Assessing Rio Grande Rift Development and Exhumation in the Southern Rocky Mountains Using Techniques in Low-temperature Thermochronometry

by

Alyssa Langford Abbey

A dissertation submitted in partial fulfillment
of the requirements for the degree of
Doctor of Philosophy
(Earth and Environmental Science)
in the University of Michigan
2018

Doctoral Committee:

Associate Professor Nathan Niemi, Chair
Associate Professor Marin Clark
Associate Professor Eric Hetland
Professor Nikolaos Katopodes
Professor Ben van der Pluijm

Figure A: *Kenosha Pass, CO. June 2014*

Alyssa Langford Abbey

alabbey@umich.edu

ORCID iD: 0000-0002-0617-4859

DEDICATION

Science, …, is made up of mistakes, but they are mistakes which it is useful to make, because they lead little by little to the truth.

---A Journey to the Center of the Earth, Jules Verne

Any planet is 'Earth' to those that live on it.

---Pebble in the Sky, Isaac Asimov

ACKNOWLEDGEMENTS

First, I'd like to acknowledge my advisor Nathan Niemi for patiently and diligently answering any and all the questions I had. His mentorship taught me to be thoughtful about designing projects and hypotheses and recognize the types of data and experiments needed to test those hypotheses. With Nathan's help and guidance I have become more confident as a scientist and my ability to articulate my research.

I would also like to thank each of my committee members for direction, inspiration, and learning opportunities.

- Marin Clark was always there with sharp and pointed questions that required me to think critically about my work.
- Ben van der Pluijm was great at encouraging me to think about various new and interesting avenues in which to apply my skills and knowledge. Plus, hosting FroST provided an amazing environment for me to learn about research applicable to myself and my peers as well as a glimpse into the inner workings of a large department at a research university.
- Eric Hetland, through short conversations and the 'Power Law Seminar', always reminded me to think about errors and uncertainties in my data.
- Nikolaos Katopodes, my cognate committee member, provided a view point that constantly reminded me that not all people, not all scientists even have the same knowledge or the same way of thinking about time and space.

My field and lab assistants were also extremely appreciated, and I would like to thank Jesse Fenno for being an amazing field assistant in my first year as a graduate student, also Forrest Gilfoy and Megan Hendrick in following years. I also very much enjoyed working with and mentoring Megan on some experimental projects. Amanda Maslyn deserves an enormous thank you for working with me on organizing lab time to avoid too many bottle neck situations and more importantly for picking many of my apatite grains as she knew that final step of mineral separation was infuriating for me.

I would also like to extend my thanks to everyone who has been a part of the SCALE lab group during my time here at the University of Michigan. Lydia Staisch, Petr Yakovlev, Sean Gallen, Scott Miller, Kate Lowe, Alex Tye, Tim Stahl, Eic Portenga, Kendra Murray, Kevin Ortiz, Kirk Townsend, Nik Midttun, Logan Knopper, and Billy Medwedeff were all extremely helpful at different times in my career at the University of Michigan.

Many other friends in the Earth department and Ultimate Frisbee community have been invaluable to me these last five years as my support crew in research, in friendship, in adventure, in commiseration, and in celebration. I value these relationships highly and would like to acknowledge these friends: Erin Lynch, Will Bender, James Jolles, Xiaofei Pu, Sarah Walker, Sam Haugland, Tristan Childress, Sam Nemkin, Clay Tabor, Ian Winkelstern, Kyle Meyer, Meeri, Tots, TZ, T-lo, Hank, Ninja, Charlotte, Ben Murphy, Joe Besser, Bailey, Talia, and Tia.

Most importantly, the support of my family has been paramount to my success. My parents shaped me into the person I am today with a love of exploration, adventure and curiosity, while my brother always strove to push my limits and drive my competitive nature. lil Sebastian has kept me on my toes with continuous and immediate transitions from loving cuddles to savage attacks, and Sheila has been with me through it all with reminders of home and my love for music. Additionally, my boyfriend Daniel has been so compassionate, reassuring, and understanding giving me complete emotional, inspirational, and loving support through my years in grad school.

Finally, I could not have accomplished any of this work without funding for various things like field work, sample analysis, and conference travel. This funding came from a National Science Foundation grant EAR-1151247 awarded to Nathan Niemi, an EarthScope AGeS research grant, a Geological Society of America research grant, and several Rackham graduate student research, travel grants, and Turner Awards from the University of Michigan awarded to myself.

Table of Contents

LIST OF FIGURES

LIST OF TABLES

ABSTRACT

I use low-temperature thermochronometry methods to assess a variety of tectonic processes including continental rifting, fault initiation and growth patterns, orogenic exhumation and reheating mechanisms. Specifically this dissertation focuses on the development of the Rio Grande rift (RGR) in New Mexico and Colorado, USA and exhumation in the southern Rocky Mountains, Colorado.

To understand rift development and distinguish between different potential rifting models in a continental rift system, we need to determine the spatial and temporal patterns of rift-related faulting and magmatism. Distinct phases of fault initiation, growth, and linkage of basin-bounding fault systems can be documented through dense vertical transect sampling and inverse thermal history modeling, which we perform in the upper Arkansas River (UAR) Basin in the northern part of the RGR (chapter 2). Fault-motion in the UAR Basin initiates on a small segment at ~25 Ma. Other segments begin to initiate and undergo fault growth via tip propagation for ~15 m.y. until ~10 Ma when the entire fault systems is integrated into a coherent 90-km-long fault system.

We apply a similar method along the entire RGR to understand fault initiation, growth, and linkage along the entire rift (chapter 3). Additionally, we evaluate spatial and temporal patterns in faulting and rift-related magmatism to obtain insight into the processes behind extension accommodation and how to differentiate between rift models.

Rift initiation begins synchronously ~25 Ma on fault segments in both the northern and southern RGR. Segment initiation, growth, and linkage continues from ~25 to ~15 Ma, at which time the entire rift system becomes linked through strike-slip faulting and magmatic accommodation in the central RGR. Trends in the locations of faulting and magmatism are spatially coincident with pre-existing weaknesses arising from previous tectonic rifting and orogenic events. Additionally, crustal and lithospheric thickness differences suggest that rift structure and geometry are at least partly controlled by both inherited structure and/or lithospheric properties. Based on these new analyses and interpretations, we do not support a northward propagation model for the development of the RGR and instead favor a synchronous model, in which a commination of an oblique strain model and a block rotation form the Rio Grande rift.

To constrain the magnitude and timing of Laramide deformation in the southern Rocky Mountains, we combine new thermochronometric, geochronologic, and clumped isotope data from the Mosquito Range, Arkansas Hills, and Arkansas River valley (Colorado, USA) (chapter 4). Analysis of these data show that during the Laramide Orogeny, ~3–5 km of differential (west side up) exhumation between the Mosquito Range–Arkansas Hills (5–7 km total exhumation from 80 and 60 Ma) and the Royal Gorge region to the east (<1–2 km exhumation since ca. 120 Ma) occurred. We also recognize an inverse trend in age-elevation relationships in our thermochronometry samples and demonstrate, through the application of clumped isotopic analysis, that this inversion likely arises from post-exhumation hydrothermal reheating driven by paleotopography and overlying late Eocene to early Miocene ignimbrite sequences.

We further use these data to propose that a paleo-surface often referred to as the Eocene erosion surface entirely formed in the Paleocene and suggest that the southern Rockies may be a useful region to study the evolution of paleo-landscapes.

CHAPTER I. INTRODUCTION

MOTIVATION AND BACKGROUND

Extensional boundaries between tectonic plates (i.e. mid-ocean ridges) make up the longest continuous plate boundary system (>80,000 km) and are associated with some of the largest mountain chains on Earth. Unfortunately, the majority of these rift systems are on the ocean floor and challenging to access (Fig. 1.1) making it difficult to study faulting and magmatism in these systems. Thus, we must turn to continental rifts, which provide information about the early stages of continental extension and tectonic plate break-up. Most rifts are unique in their combination of fault style (e.g. large interconnected systems or numerous diffuse faults), geometry, accommodation mechanisms (tectonic or magmatic) and rates of extension (e.g. Nelson et al., 1992; Muirhead et al., 2016; Molnar et al., 2017); hence, by understanding the processes that drive the different expressions of faulting and magmatism in a rift we can acquire a glimpse into the early phases of tectonic plate break-up.

Ultimately, continental rifting is caused by the interactions between mantle flow and plate movements; however, rift accommodation via tectonic (faulting and graben formation) or magmatic (dike injection and volcanism) processes. Additionally, various combinations of heat flow, lithospheric structure, far-field stresses, mantle flow and magmatism control rates of rift development (Lavecchia et al., 2017). Some rifts are wide

zones of deformation and accommodate large amounts of horizontal extension (e.g. Basin and Range or Aegean), while others are made up of narrow deep grabens (e.g. Ethiopian,

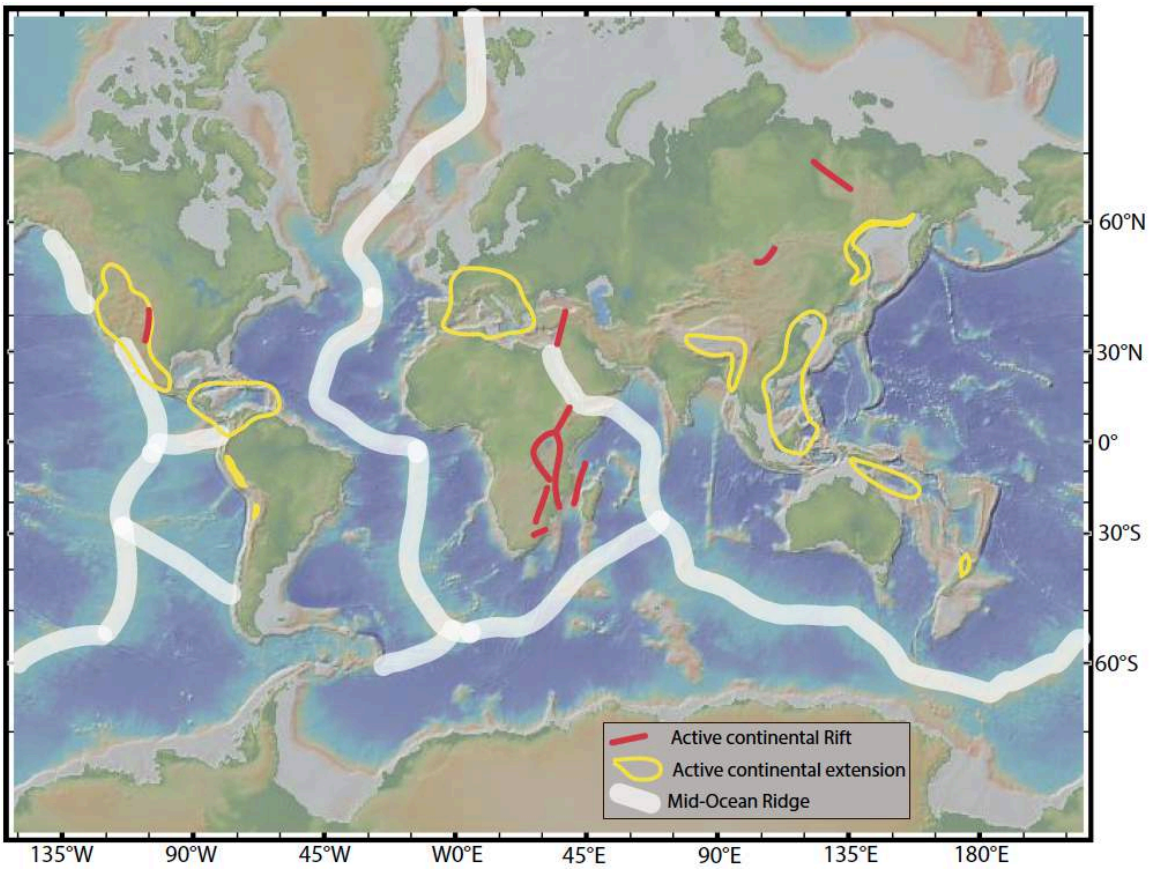

Figure 1.1: World map of mid-ocean ridges, active continental rifts and extensional regions. Note, This is schematic; see Sengor and Natal'in (2001) for comprehensive map.

Baikal, Rhine, Rio Grande rift). In addition, there are both magma rich (e.g. Red Sea, Ethiopian rift, eastern branch of the East African rift) and magma poor (e.g. Iberia-Newfoundland margin, South China Sea, western branch of the East African rift) rifts (Reston, 2005; Corti, 2012; Hart et al., 2017). Understanding the roles of different driving mechanisms in rift systems will provide insight into plate break-up, a key component to the tectonic cycle. The Rio Grande rift (RGR) in the western United States is an ideal rift system for exploring tectonic and magmatic controls in continental rifting as the rift system is currently active, easy to access, and is part of a larger extensional system across

the entirety of western North America. The entire rift is exposed on land, and there is a plethora of published data related to fault motion, basin sedimentation, volcanism, lithospheric structure, and regional strain rates that provides a thorough framework necessary for understanding the processes behind fault growth, basin linkage, and volcanism in the entire rift system (e.g. van Alstine, 1969; Tweto, 1979; Kelley and Duncan, 1986; Lindsey et al., 1986; Machette, 1988; Kelley et al., 1992; Lewis and Baldridge, 1994; Chapin and Cather, 1994; Brister and Gries, 1994; Kluth and Schaftenaar, 1994; McIntosh and Quade, 1995; Kelley and Chapin, 1995; Kelley and Chapin 1997; Machette et al., 1998; McMillan et al., 2000; Hubbard et al., 2001; House et al., 2003; Chapin et al., 2004; Peterson and Roy, 2005; Levander et al., 2011; Berglund et al., 2012; Landman and Flowers, 2013; Ricketts et al., 2016; Grauch et al., 2017; Abbey and Niemi, in review). Moreover, extension in the RGR is relatively slow, which affords the opportunity to perhaps capture discrete details about fault initiation and rates of fault growth, as well as potential relationships to compositional changes in volcanism that would otherwise be difficult to detect in more rapidly developing rift systems (e.g. Ethiopian rift, Gulf of California).

Aspects of fault initiation, segment growth, and accommodation mechanisms (i.e. tectonic or magmatic) in the RGR are not entirely clear with a debate centering around two hypotheses: (1) rifting was primarily synchronous (Landman and Flowers, 2013; Ricketts et al., 2015; Chapin and Cather, 1994) along the length of the RGR, or (2) extension began in the southern part of the rift and has propagated northward over time so that the basins in the northern RGR are the youngest in the rift system (McMillan et al., 2002; Leonard, 2002; Heller et al., 2003; Frankel and Pazzaglia, 2006; Duller et al.,

2012). To understand how extension is accommodated in the RGR, I use low-temperature thermochronometry to explore fault growth timing, along with analysis of spatial and temporal patterns of magmatism in New Mexico and Colorado. Information about relationships between faulting and magmatism, in time and space, is necessary to discriminate between different general rift models such as block rotation, oblique extension and formation of accommodation zones, fault propagation and linkage, and magma driven propagation (Fig. 3.1; Nelson et al., 1992; Brune et al., 2017; Lavecchia et al., 2017; Molnar et al., 2017). I also use low-temperature thermochronometry to assess exhumation rates and magnitudes in the southern Rocky Mountains as many researchers suggest there has been a recent rejuvenation of uplift and increase in topographic relief in the southern Rockies, which may be attributed in part to RGR activity (e.g. Leonard, 2002; McMillan et al., 2006; Karlstrom et al., 2008; Thomson et al., 2016). Furthermore, the role of structural inheritance seems to play a role in the spatial relationships between the rift basins and faulting in the southern Rockies, which we explore by assessing lithospheric properties in the region.

Physiography and Geologic Background of the Rio Grande rift and southern Rocky Mountains

The RGR is the most recent major deformation event in a protracted tectonic history across the Colorado and New Mexico region in the western United States of North America. Below is a brief geologic history of tectonic events that have occurred in the current location of the RGR and southern Rocky Mountains. Continental building and accretion of ancient terranes occurred during the middle Proterozoic (e.g. Yavapai (1.9-1.7 Ga) and Mazatzal (1.8-1.6 Ga) orogenies; Figs. 1.2 and 1.3; Robbins, 2005; Shaw and

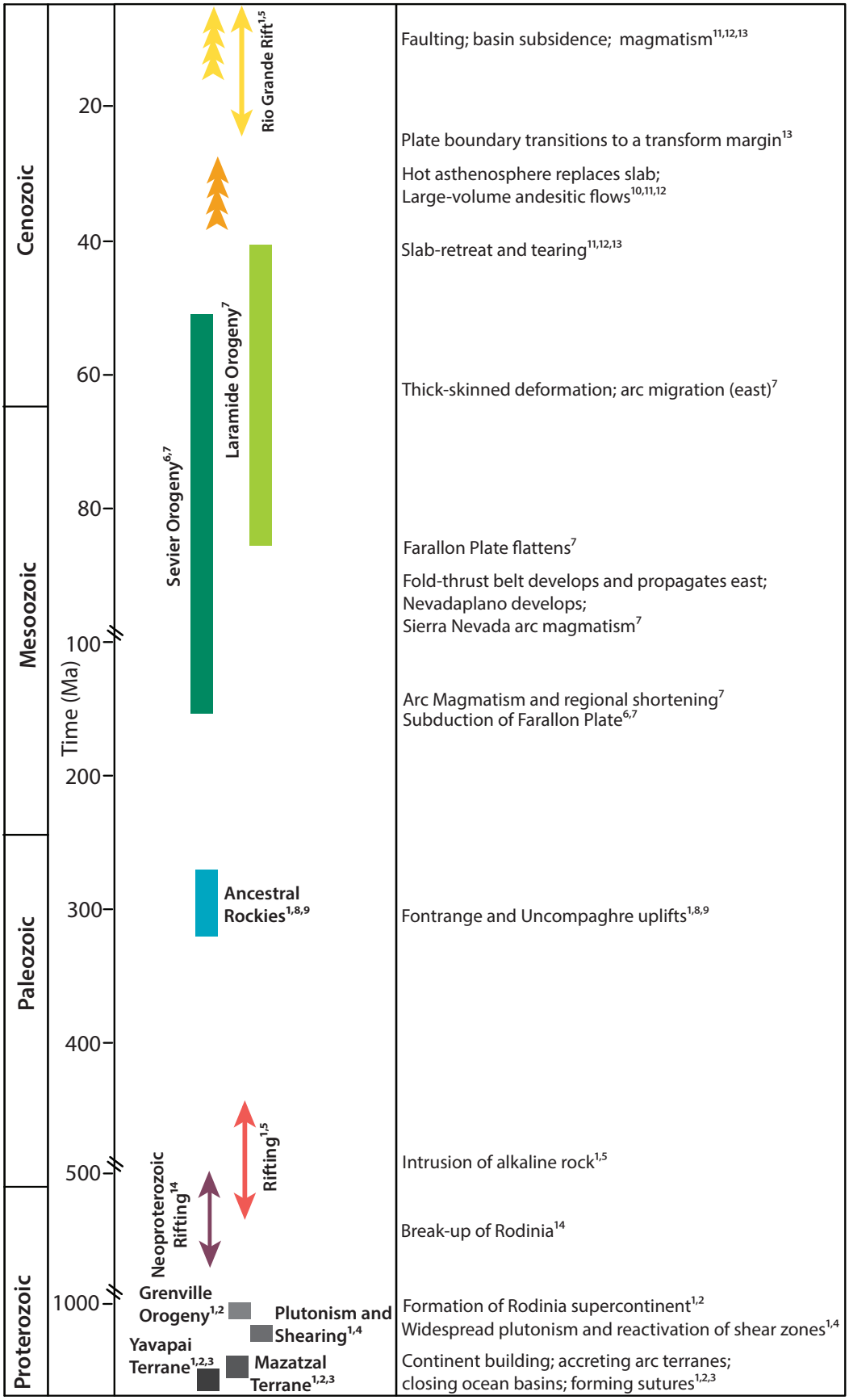
Cenozoic
Mesoozoic
Paleozoic
Proterozoic
Time (Ma)
20
40
60
80
100
200
300
400
500
1000
Rio Grande Rift[1,5]
Laramide Orogeny[7]
Sevier Orogeny[6,7]
Ancestral Rockies[1,8,9]
Rifting[1,5]
Neoproterozoic Rifting[14]
Grenville Orogeny[1,2]
Plutonism and Shearing[1,4]
Yavapai Terrane[1,2,3]
Mazatzal Terrane[1,2,3]
Faulting; basin subsidence; magmatism[11,12,13]
Plate boundary transitions to a transform margin[13]
Hot asthenosphere replaces slab;
Large-volume andesitic flows[10,11,12]
Slab-retreat and tearing[11,12,13]
Thick-skinned deformation; arc migration (east)[7]
Farallon Plate flattens[7]
Fold-thrust belt develops and propagates east;
Nevadaplano develops;
Sierra Nevada arc magmatism[7]
Arc Magmatism and regional shortening[7]
Subduction of Farallon Plate[6,7]
Fontrange and Uncompaghre uplifts[1,8,9]
Intrusion of alkaline rock[1,5]
Break-up of Rodinia[14]
Formation of Rodinia supercontinent[1,2]
Widespread plutonism and reactivation of shear zones[1,4]
Continent building; accreting arc terranes;
closing ocean basins; forming sutures[1,2,3]

Figure 1.2: Timeline of major tectonic events occurring in the western United States of North America from 2 Ga to present. Note age scale breaks. (1) Robbins, 2005; (2) Shaw and Karlstrom, 1999, (3) Chapin, 2012; (4) van Schmus et al., 1993 (5) McMillan and McLemore, 2004 (6) Dickenson, 2004; (7) DeCelles, 2004; (8) Knepper, 1974; (9) Baars and Stevenson, 1984; (10) Cosca, 2014; (11) Ricketts et al., 2015; (12) Ricketts et al., 2016 (13) Chapin et al., 2004; (14) Timmons et al., 2001.

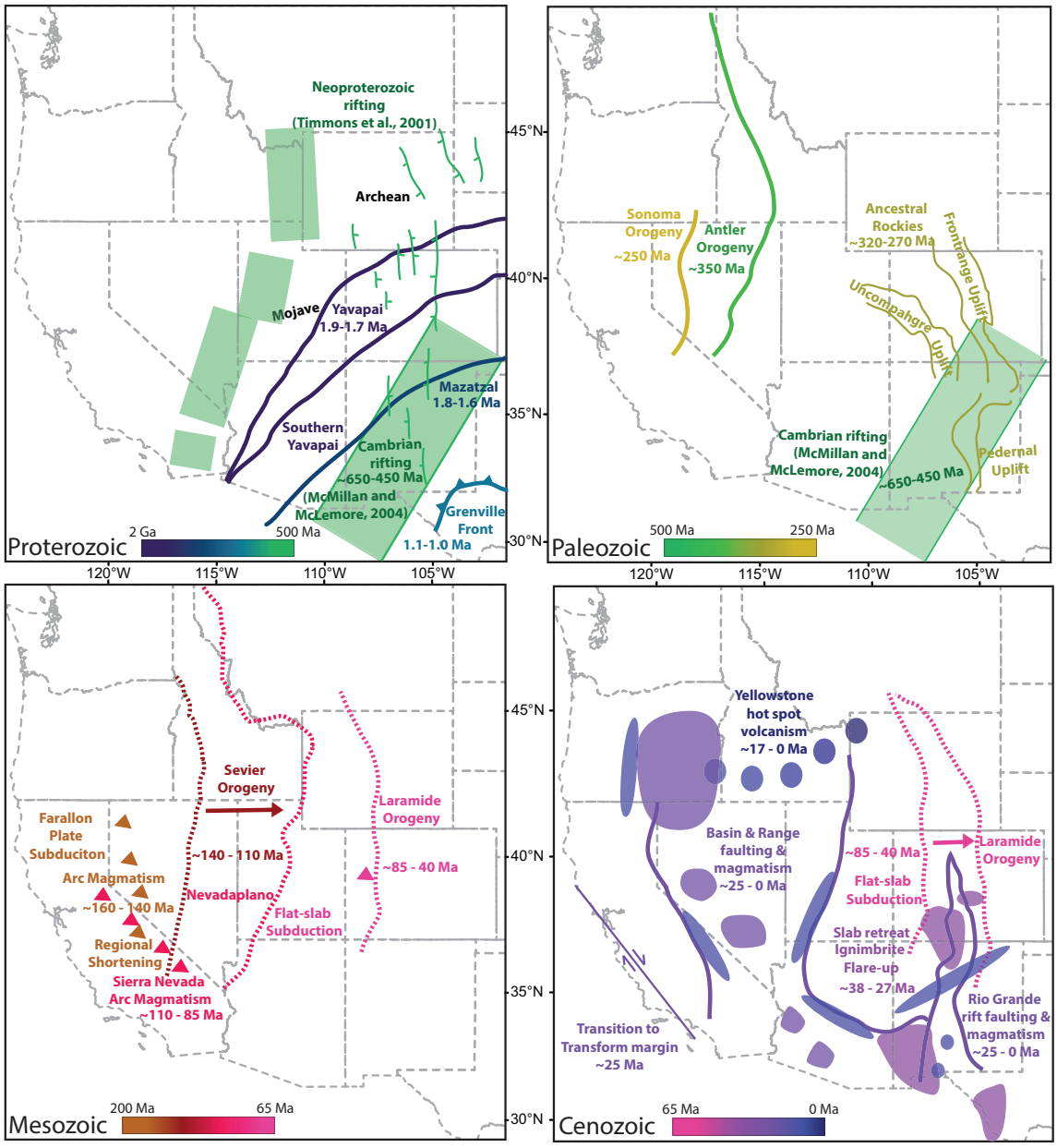

Figure 1.3: Schematic representations of main tectonic events occurring in the western United States of North America from 2 Ga to present.

Karlstrom, 1999, Chapin, 2012) followed by the formation of the supercontinent Rodinia (Grenville orogeny: ~1.1-1.0 Ga; Robbins, 2005; Shaw and Karlstrom, 1999) and subsequent break-up (~750 to 500 Ma; Figs. 1.2 and 1.3; Karlstrom et al., 1999; Timmons et al., 2001; McMillan and McLemore, 2004; Robbins, 2005). Collision and orogenesis occurred again with the formation of the Ancestral Rockies during the assemblage of the supercontinent Pangaea ~320-270 Ma (Figs. 1.2 and 1.3; Knepper, 1974; Kluth and Coney, 1981; Baars and Stevenson, 1984; Robbins, 2005). The middle Mesozoic to early Cenozoic is marked by the Sevier and Laramide orogenies, which caused deformation and construction of the Rocky Mountains (Figs. 1.2, 1.3 and 1.4; Tweto, 1975; Dickinson et al., 1988; Keller and Baldridge, 1999; Marshak et al., 2000; DeCelles, 2004, Dickenson, 2004; Robbins, 2005; Gilbert, 2012). Finally, the middle to late Cenozoic is marked by the transition to a transform plate boundary and extensional deformation driving the development of the Rio Grande rift system (Figs. 1.2, 1.3 and 1.4; Kelley and Chapin, 1995; Kelley and Chapin, 1997; Landman and Flowers, 2013; Ricketts et al., 2015; Ricketts et al., 2016).

The present-day RGR is >1000 km long from southern New Mexico to central Colorado, USA (Fig. 1.4; Kelley et al., 1992; Knepper, 1974; Limbach, 1975) and potentially exists as far north as southern Wyoming (Kellogg, 1999; Neaser et al., 2002; Leonard et al., 2002; Cosca et al., 2014). The RGR lies in the southern Rocky Mountains between the uplifted and relatively undeformed Colorado Plateau (mean elevations > 2 km) to the west and the low-relief Great Plains to the east (Fig. 1.4). The southern Rocky Mountains in Colorado embody a region of high elevation peaks and intermontane basins. The oldest rocks within the southern Rocky Mountains, Proterozoic gneisses and

granitoids, are locally disconformably overlain by sequences of lower Paleozoic sedimentary rocks, and upper Paleozoic strata (Scott et al., 1976; Green, 1992). High

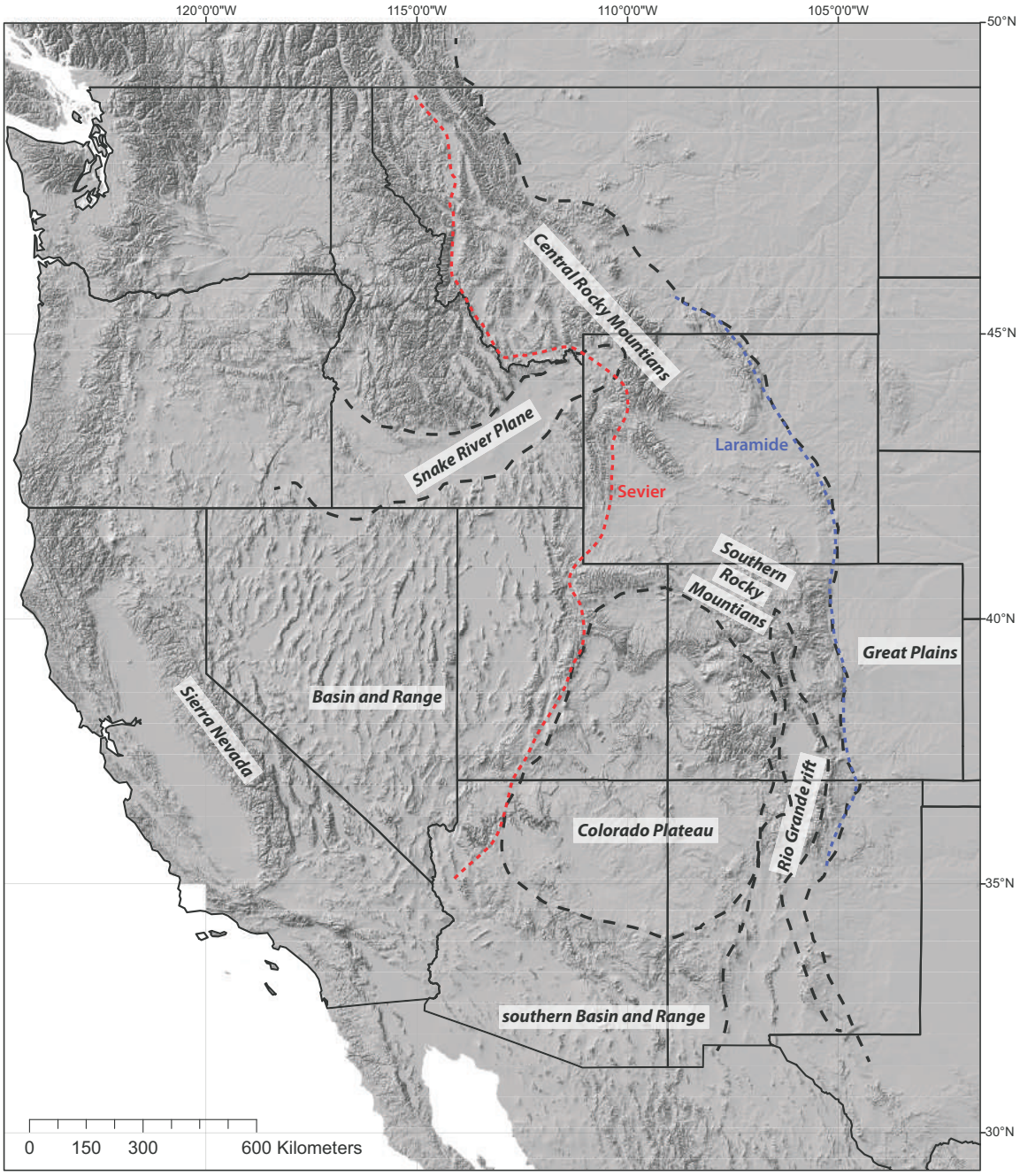

Figure 1.4: Locations of major geologic provinces in the western United States of North America (modified from Gilbert et al., 2012).

angle faults from the latest Mississippian to Permian Ancestral Rocky Mountain Orogeny cut through the basement rock (e.g. Taylor et al., 1975a; Taylor et al., 1975b; Taylor et al., 1975c; Taylor, 1975; Scott, 1975a;Green, 1992). In my primary field area within the southern Rockies, a regional low-relief erosion surface developed across the region (Epis and Chapin, 1974; Epis and Chapin 1975; McMillan et al., 2002; 2006; Gregory and Chase, 1994) after Laramide orogenic deformation and is preserved by mid-Cenozoic (~38 Ma to ~27 Ma) silicic ignimbrites (e.g. Epis and Chapin, 1974; Epis and Chapin, 1975; Epis et al., 1976; Chapin and Lowell, 1979; Shannon, 1988; Gregory and McIntosh, 1996; Wallace et al., 1997). The RGR and southern Rocky Mountain region is also impressively incised by rivers like the Arkansas River, creating >1.5 km of local relief, which provides a way to easily observe and access all the above described geologic relationships.

METHODOLOGY FOR THERMOCHRONOMETRY ANALYSES AND INVERSE THERMAL HISTORY MODELING

Sample analysis protocol and inverse thermal history modeling parameters

The low-temperature thermochronometry data in this dissertation were acquired with the following procedures: (1) sample processing, (2) analysis in the University of Michigan Thermochronology Lab and the University of Arizona Radiogenic Helium Dating Laboratory, (3) calculating corrected age and error, (4) calculating eU concentrations, and (5) selecting of interpretable data based on number of grains excluding outliers, standard error values, and the percent error for each individual sample. Inverse thermal modeling of the thermochronometric data presented here was done using two different versions of the program QTQt (version 64R5.4.6, in Chapter 4

and 5.6.2a in Chapters 2 and 3; Gallagher, 2012). Because of this version difference and the different research questions that were tested in each chapter, the model parameters varied between the different studies. These sample analysis procedures and modeling parameters, including the reasoning behind the choices we made for each project, are described below (Table 1.1).

Sample Processing

All new thermochronometric data presented in this dissertation come from rock samples processed at the University of Michigan.

1. Samples were crushed in a Jaw crusher from Sturtevant Mill Company, which breaks fist-sized samples into fragments about 1-2 cm^3.
2. The shards were run through a BICO BRAUN Direct Driven Pulverizer, which further crushed the samples into a mixture of individual mineral grains and smaller (1 mm to 1 cm) rock shards.
3. Each sample was sieved in a Rotap Sieve Shaker with sieves selected to separate the sample into size fractions of <300 μm, 300 to 500 μm and >500 μm. The 300-500 and >500 μm portions were re-run through the pulverizer and sieve if the <300 μm yield in the first round of sieving was low (determined by eye from A.L. Abbey, M. Hendrick, and A. Maslyn, who each contributed to this sample processing step).
4. The minerals with high surface area to volume ratio (e.g. clays and micas) were removed either by hand panning using Evco Geological Supply Golden Lab plastic pans, or by running them over a Holman-Wilfley Ltd water table.
5. The remaining mineral fractions were then fully dried and further refined via the

removal of magnetic minerals. This was done using a hand magnet (used primarily to remove steel fragments from the jaw crusher and pulverizer) and a Frantz magnetic separator.

6. The non-magnetic fractions recovered from the Frantz were then mechanically stirred in a separatory funnel containing the heavy liquid lithium metatungstate (LMT; 2.8 g/mL), for several hours until all minerals heavier than 2.8 g/mL had sunk through the liquid (i.e. the zircon and apatite crystals) and all minerals lighter than 2.8 g/mL had floated to the top.
7. The samples intended for zircon (U-Th)/He analysis were subjected to another round of heavy liquid mineral separation using Methyl Iodide (MI) at a density of 3.1 g/mL. This separated the denser zircons from the less dense apatite.
8. The sample fractions were cleaned with Acetone if they were run through MI and Ethanol if run through LMT prior to hand picking.
9. Many samples were run through 80 μm sieve paper in order to get rid of crystal grains that are too small to date.
10. Individual grains from each sample were picked by hand using a Leica MZ16 stereo zoom microscope. We picked individual apatite and zircon grains under the microscope using Inox stainless steel Dumont Style tweezers with high precision tips. Each grain that was picked for analysis had to meet certain criteria: (i) no inclusions (checked for under crossed-polars), (ii) larger than 80 μm in length, width and height, (iii) no obvious discoloration, and (iv) no large cracks. Studies have shown that broken grains may also be problematic in age analyses (Brown et al., 2013; Beucher et al., 2013), so we tried to avoid picking broken grains when

possible; however, in some samples this was unavoidable. Each picked grain was then photographed and measured for length and width information. The photos are saved in an archive at the University of Michigan in the Thermochronology Lab.

11. Individual grains were packed into platinum and niobium tubes (length 0.040" and diameter 0.027") for degassing.

Note that portions of rock sample from each step in the above-described processes were saved for any later re-processing that was needed and all left-over samples are stored at the University of Michigan for any further use.

Sample Analysis

Each individual grain analyzed and reported in this dissertation was de-gassed at the University of Michigan in the Thermochronology Lab on an Alphachron Helium Instrument consisting of a diode laser extraction system and quadrupole mass spectrometer. With this set-up, 23 crystals with unknown ages and two standard crystals can be degassed in a single analytical run. We use Durango apatite as a standard for the apatite (U-Th-Sm)/He dating and Fish Canyon Tuff as a standard for the zircon (U-Th)/He dating. Each apatite crystal is heated by a laser for 5 minutes at 900°C to degas helium from the crystal. Temperature is controlled by a 4-color pyrometer. After the first heating step, the apatite grain is heated a second time, following the same time and temperature schedule. The second step is used to determine whether or not helium extraction was complete during the first step, or if there are potential helium retentive inclusions within the apatite grain. Zircon crystals are heated by a a laser for 10 minutes at 1200°C three separate times, with the first two runs intended to degas the entire crystal and obtain all

the helium and the third run to detect inclusions or retentive phases. If an inclusion is detected by the presence of high levels of helium on the second (third for zircon) laser heating then the grain is not used for analysis. In addition, if the extracted helium concentration is below 0.01 ncc the grain is also not used for analysis as this value is too close to the blank values measured on the Alphachron Instrument, making it impossible to determine the precise amount of helium that was in the crystal.

To obtain information about the concentrations of U, Th, and Sm in the grains the irradiated samples were then sent to the Arizona Radiogenic Helium Dating Laboratory at the University of Arizona where they were analyzed using sector ICP-MS (Reiners and Nicolescu, 2006). Generally, the analytical methods for extracting U, Th, and Sm concentrations involves dissolving the grains in nitric acid then spiking the recovered dissolved crystal with isotopically distinctive U, Th, and Sm and then diluted (see analytical methods outlined in Reiners and Nicolescu (2006) for complete details). The diluted solutions are then measured using solution ICP-MS performed on a Thermo Finnigan Element2 in low-resolution mode. The measuring method involved EScan peak jumping with variations in parameters such as: (i) magnet mass, (ii) samples per peak, (iii) mass, averaging, search, and integration windows, and (iv) runs and passes, depending on the mineral and/or isotopes being measured (see analytical methods outlined in Reiners and Nicolescu (2006) for complete details).

Corrected age, error, and eU calculations

Observed (uncorrected) ages and errors are calculated from measured U, Th, Sm, and He quantities (number of atoms for U, Th, and Sm and ncc of He). Errors are propagated using a Monte Carlo approach where values of U, Th, Sm, and He are

iteratively drawn from normal distributions described by the reported quantity of each element and it's analytical uncertainty. For each iteration, the (U-Th-Sm)/He age is calculated using the standard age equation for helium dating, solved using a function minimization approach in Matlab. One thousand iterations of this process are undertaken, and a rough approximation of the age is made. Iterative calculations of the grain age continue in one thousand iterations increments until the subsequent addition of iterations results in the mean age of all iterations varying by less than 0.001%. When this convergence is achieved, the mean and standard deviation of ages from all iterations are taken to represent the uncorrected grain age and associated sample uncertainty. The observed (uncorrected) ages are calculated using the following equation, which is solved by searching for *t* to minimize the left-hand-side of the equation to be as close to zero as possible.

$$\left\{8\left(\frac{136.8}{137.8}\,U\left[e^{\frac{\ln(2)t}{\lambda_{238_U}}}-1\right]\right)+7\left(\frac{1}{137.8}\,U\left[e^{\frac{\ln(2)t}{\lambda_{235_U}}}-1\right]\right)+6\left(Th\left[e^{\frac{\ln(2)t}{\lambda_{232_{Th}}}}-1\right]\right)\right.$$
$$\left.+\left(\frac{1}{6.7}Sm\left[e^{\frac{\ln(2)t}{\lambda_{147_{Sm}}}}-1\right]\right)\right\}-He=0$$

To obtain 'corrected ages' we must take into account the kinetic energy that is imparted to alpha particles during decay. This is an important factor as particles can be displaced by ~20 μm within a crystal and even cause alpha particles to be ejected out of the crystal (Farley et al., 1996; Harrison and Zeitler, 2005). Therefore, we must estimate the fraction of ejected ^{4}He from the crystal and make a correction to the 'observed age' calculated from the above equation. This correction is called the F_t correction, which is an empirical expression derived by Farley et al. (1996) and primarily controlled by the

surface to volume ratio of each grain (Harrison and Zeitler, 2005). Thus, we solve for the F_t parameter and divide the calculated observed (uncorrected) ages by this parameter to obtain the corrected ages for each crystal.

Then, for each grain we compare the age to grain size and eU concentrations:

$$eU = [U] + (0.243 \times [Th]) + (0.0047 \times [Sm])$$

Data selection criteria for interpretation

The data for each sample are subjected to outlier tests to determine if there are any grains that should be excluded from mean age calculations. Samples are assessed for outliers using either the Dean and Dixon (1951) Q-test or the Boddy and Smith (2010) test for two extreme outliers. The Q-test is amenable to small data sets ($n \geq 3$), and thus useful for (U-Th-Sm)/He thermochronometry, where individual samples typically include 3–5 replicates. The drawback to this test is that it is conservative in identifying outliers, and can only be used once on each sample. Other tests are available for larger data sets ($n \geq 5$) that can identify as many as two outliers (Boddy and Smith, 2010), and we employ these tests for two extreme outliers on samples with five or more replicates. Both tests exclude samples with outliers found at the 95% confidence level comparing test results to both the Q-test table values and the two extreme outlier statistical table values to three significant figures. In Chapter 2, nine outlier grains were found out of the 163 grains that were analyzed, which is equivalent to 5.5% of the total number of analyses (Table A2). In Chapter 3, one outlier grain was found out of 20 analyzed grains, which is equivalent to 5% of the grains analyzed (Table B1). In Chapter 4, 10 outlier grains were found out of 188 analyzed grains, which is equivalent to 5.3% of the grains analyzed (Table D1). Once outliers were taken out, sample mean ages were calculated from the remaining grains.

Sample errors we then calculated by using the default standard deviation (σ) equation in Microsoft Excel:

$$\sigma_{sample} = \frac{\sqrt{abs(X - X_{mean})^2}}{n - 1}$$

This standard deviation value was then used to calculate the standard error (*SE*):

$$SE = \frac{\sigma_{sample}}{\sqrt{n}}$$

Using the standard error we calculate the percent error (*% error)*:

$$\%\ error = \left(\frac{SE}{mean\_age}\right) \times 100$$

If a sample has a percent error >15% and we do not find a useful correlation in age versus grain size or age versus eU we do not use these samples for cooling age interpretations or inverse thermal history modeling.

Inverse thermal history modeling parameters

Inverse thermal history modeling of low-temperature thermochronometric data includes three main parts: (1) the thermochronometric data, (2) any additional geologic information, and (3) system- and model-parameters. Table 1.1 describes the decisions made for each of these parts in each chapter of this dissertation.

Table 1.1: THERMAL HISTORY MODEL INPUT TABLE

Thermochronometric Data
Apatite (U-Th-Sm)/He or Zicon (U-Th)/He data: uncorrected age, error, concentrations of U, Th, Sm and He, mineral type, crystal size (length, width, height)
Apatite fission track data: all AFT data was from previously published studies, where those studies provided track count or track length data this was used, where those studies did not report the count or length data we used the resample count data function in QTQt to generate plausible track count data for the reported AFT age.
Additional Geologic Information
Most models were run without imposed constraint boxes. However, in places where there were concrete constraints on burial depths or surface exposure we did place large constrain boxes into

Table 1.1: THERMAL HISTORY MODEL INPUT TABLE

the models with information on a range of temperatures that ma have occurred over a range of times (e.g. 100 ± 50°C at 40 ± 10 Ma makes a box from 50 to 150°C and from 50 to 30 Ma; see Chapter 3 for models that include constrain boxes).
System- and Model-specific Parameters
For each model run we had QTQt resample the errors associated with each grain age.
Both apatite and zircon grains were modeled as if they were spherical crystals because the ratios between grain length, width and height did not warrant a cylindrical model which is more complex and time consuming to run.
For apatite grains the RDAAM radiation damage model from Flowers et al., 2009 was used and for zircon the ZrDAAM radiation damage model from Guenthner et al., 2013 was used.
For models run in Chapters 2 and 4 the prior temperature ranges were left at the default values set by QTQt. For Chapter 3 the priors were adjusted to have a larger range (see Chapter 3 section entitled Thermal modeling results and interpretation).
We used a 30°C/km geothermal gradient for all of our models, in Chapters 2 and 4 we made this a tight constraint allowing for variation of 1°C. In Chapter 3 we allowed the geothermal gradient to vary by 5°C so between 25°C and 35°C.
For present-day temperatures we used 7 ± 3°C (mean annual temperature for Salida, CO) in Chapters 2 and 4 and 10 ± 3°C in Chapter 3 (to account for the warmer temperatures in NM).
The present-day temperature offset was set to 6 ± 1°C/km as this is the accepted general topographic temperature effect at the surface.
The MCMC constraints we modified included the burn-in and post-burn-in values as well as the birth proposal parameters. For Chapters 2 and 4 we used 20,000 burn-in iterations, 80,000 post-burn-in iterations and a uniform birth proposal. For Chapter 3 we used 20,000 burn-in iterations, 80,000 post-burn-in iterations and a Gaussian birth proposal.

DISSERTATION OBJECTIVES AND OUTLINE

The research presented here aims to address both the debate about RGR development and explore the processes driving fault initiation, growth, and linkage with the purpose of understanding continental rifting. To resolve the debate between a synchronous versus northward propagation model for rifting, I assess spatial patterns of rift-flank fault initiation and compare them to magmatic patterns along the entire RGR. The RGR may also effect both regional and local surface deformation, and it has been suggested that thinning of the lithosphere and increased heat flow caused by rifting may drive long-wavelength doming and tilting that might be a cause for rejuvenation and

increasing topographic relief in the southern Rocky Mountains. I evaluate this hypothesis by looking into timing and rates of exhumation in the southern Rockies and do not find signal for rejuvenated exhumation, but instead unearth details about differential exhumation in the southern Rockies during the Laramide Orogeny.

Research objectives for the following chapters in this dissertation include: (1) understanding the processes involved in Rio Grande rift development through faulting and magmatism patterns, which will help resolve contention around hypotheses for Rio Grande rift growth, (2) using thermochronometry to assess fault growth and segment linkage along large normal fault systems, and (3) documenting exhumation in the southern Rocky Mountains to determine if thermochronometry can capture a recent rejuvenation phase. The majority of this work I accomplished through strategic sampling for low-temperature thermochronometry data in the form of densely spaced vertical transects and the careful application of inverse thermal history modeling to further interpret these data in order to understand the faulting and exhumation patterns in the RGR and Southern Rockies.

Chapter 2

As mentioned above, there are numerous models for how continental rifts develop. Debate surrounding the development of the Rio Grande rift (RGR) revolves around the hypotheses that rifting has either occurred synchronously or that the rift has propagated northward through time. However, with only sparse datasets from the northern part of the RGR this debate has been difficult to resolve. Therefore, before attempting to understand the processes driving evolution on the entire RGR, I initially focused on understanding the growth and development of the northern RGR. This work is

presented in Chapter 2: *Low-temperature thermochronometric constraints on fault initiation and growth in the northern Rio Grande rift, upper Arkansas River valley, Colorado*, USA, which has been accepted for publication in Geology (Abbey and Niemi, 2018). We use low-temperature thermochronometry data from the upper Arkansas River valley (UAR) and thermal history analysis, to obtain detailed information about fault exhumation timing and magnitudes to understand patterns of fault growth and basin linkage, which was not previously resolved. Our discoveries include (1) the timing of rift initiation in the northern Rio Grande rift appears to be synchronous and we infer this does not support a northward propagation model; (2) the faulting begins in small segments, which grow and link over several million years, revealing that the development of large basin-bounding faults is a slow process in the northern Rio Grande rift; and (3) the new fault geometry we propose increases the potential for higher magnitude earthquakes than was previously estimated for the region. Thus, the work presented here in Chapter 2 informs our understanding of fault growth and linkage in the upper Arkansas River basin of the northern RGR, and can be applied to understanding the growth of the entire Rio Grande rift as well as other continental rifts around the world.

Chapter 3

With the addition of new low-temperature thermochronometric data from the northern RGR we are able to further refine our understanding the development of the entire RGR by focusing on spatial and temporal patterns of faulting and magmatism, as these are the two main mechanisms for rift accommodation. These analyses are addressed in Chapter 3: *Continental rifting processes determined by faulting and magmatism in the Rio Grande rift*, which will be submitted to Tectonics as Abbey and Niemi. Using

thermochronometry data and thermal history modeling we obtain estimates for the timing of fault initiation along with magnitudes and rates of exhumation, from 14 vertical sampling transects that encompass six major normal fault systems in the RGR. We find that (1) rift initiation is tectonically controlled and that initiation is synchronous throughout the rift; (2) RGR development occurs in phases where fault segments initiate then grow and link; (3) magmatic accommodation appears to occur solely in the central RGR along the Jemez lineament; (4) lithospheric properties play a key role in the location and geometry of fault bounded basins and spatial extent of magmatism; and (5) we can differentiate between different rift models, and suggest a combination of oblique strain and block rotation play a part in RGR development. Hence the work presented in Chapter 3 informs our understanding of fault growth and linkage in the RGR, but also sheds light on the processes that control continental rifting accommodation, including pre-existing crustal weaknesses or fabrics, lithospheric properties, and mantle convection.

Chapter 4

Many have postulated that the RGR has been the cause for rejuvenation seen in the southern Rocky Mountains in the form of increased topographic relief both regionally across the Rockies and Great Plains and locally within river canyons incising these mountains (e.g. Leonard, 2002; McMillan et al., 2006; Karlstrom et al., 2008; Thomson et al., 2016). I address this idea in Chapter 4: *Early Cenozoic exhumation and paleotopography in the Arkansas River valley: southern Rocky Mountains, Colorado*, which has been published in Lithosphere (Abbey et al., 2017). We apply low-temperature apatite (U-Th-Sm)/He thermochronometry in the southern Rocky Mountains, Colorado and find that (1) significant differential exhumation between the Mosquito

Range/Arkansas Hills and the southern Front Range during the Laramide Orogeny, which potentially elucidates long-standing questions about the structural geometry and style in the region; (2) a refinement of the age and evolution of the paleotopography or "late Eocene erosion surface" in the southern Rockies; (3) the utility of densely spaced sampling and clumped isotope analysis to identify thermal resetting by ignimbrite emplacement, which adds to the growing body of literature concerned with "top-down" resetting of low-temperature thermochronometers; (4) any exhumation that has occurred after ~50 Ma, contributing to rejuvenation within the southern Rockies was most likely less than 1-2 km as it is not detected by our low-temperature thermochronometry analysis. Our work from the southern Rockies does, however, suggest that we may be able to address questions about topographic rejuvenation and record paleotopography with other methods, which are described briefly in chapter 5.

Chapter 5

Chapter 5 summarizes the findings from the previous chapters to evaluate our new understanding regarding the fault initiation and growth, as well as the processes controlling continental rift accommodation. I address the utility of low-temperature thermochronometers for documenting fault motion, exhumation and identifying basement structures. Chapter 5 concludes with ideas for continued research that will aid in our understanding of (1) the processes behind fault growth in continental rifts, (2) the control inherited structure has on deformation, (3) the progression erosion and rejuvenation documented in paleotopography, and (4) how heating or reheating may be manifested in low-temperature thermochronometers and then applied to measure the timing and duration of potential heat pulses in a system.

REFERENCES

Abbey and Niemi, 2018, Low-temperature thermochronometric constraints on fault initiation and growth in the northern Rio Grande rift, upper Arkansas River valley, Colorado, USA: Geology, doi:10.1130/G40232.1.

Abbey, A. L., Niemi, N. A., Geissman, J. W., Winkelstern, I. Z., Heizler, M., 2017, Early Cenozoic exhumation and paleotopography in the Arkansas River valley, southern Rocky Mountains, Colorado, Lithosphere, v. 10, p. 239–266, doi:10.1130/L673.1.

Baars, D. L. and Stevenson, G. M., 1984, The San Luis uplift, Colorado and New Mexico—an enigma of the ancestral Rockies: The Mountain Geologist, v. 21, p. 57-67.

Berglund, H. T., Sheehan, A. F., Murray, M. H., Roy, M., Lowry, A. R., Nerem, R. S., and Blume, F., 2012, Distributed deformation across the Rio Grande Rift, Great Plains, and Colorado Plateau, Geology, v. 40, n. 1, p. 23–26. doi: 10.1130/G32418.1.

Beucher, R., Brown, R.W., Roper, S., Stuart, F., Persano, C., 2013, Natural age dispersion arising from analysis of broken crystals. Part II: Practical application to the apatite (U-Th)/He thermochronometry: Geochimica et Cosmochimica Acta, v. 120, p. 395-416, doi:10.1016/j.gca.2013.05.042.

Brister, B. S. and Gries, R. R., 1994, Tertiary stratigraphy and tectonic development of the Alamosa basin (northern San Luis basin), Rio Grande rift, south-central Colorado, in Keller, G. R. and Cather, S. M. eds, Basins of the Rio Grande rift: Structure, stratigraphy, and tectonic setting, Geological Society of America Special Paper, v. 291, p. 39–58.

Brown, R.W., Beucher, R., Roper, S., Persano, C., Stuart, F., Fitzgerald, P., 2013, Natural age dispersion arising from analysis of broken crystals. Part I: Theoretical basis and implications for the apatite (U-Th)/He thermochronometer: Geochimica et Cosmochimica Acta, v. 122, p. 478-497, doi:10.1016/j.gca.2013.05.041.

Brune, S., Corti, G., and Ranalli, G., 2017, Controls of inherited lithospheric heterogeneity on rift linkage: Numerical and analogue models of interaction between the Kenyan and Ethiopian rifts across the turkana depression, Tectonics, v. 36, 1767-1786.

Chapin, C. E., 2012, Origin of the Colorado Mineral Belt, Geosphere, v. 8, n. 1, p. 28–43, doi: 10.1130/GES00694.1.

Chapin, D. E., and Cather, S. M., 1994, Tectonic setting of the axial Basins of northern and central Rio Grande Rift, 'in' Keller, G. R., and Cather, S. M., eds., Basins of the Rio Grande Rift: structure stratigraphy and tectonic setting: Geological Society of America Special Publication 291, p. 5-25.

Chapin, C. E., and Lowell, G. R., 1979, Primary and secondary flow structures in ash-flow tuffs of the Gribbles Run paleovalley, central Colorado: Geological Society of America Special Paper 180, p. 137–154.

Chapin, C. E., Wilks, M., and McIntosh, W. C., 2004, Space-time patterns of late Cretaceous to present magmatism in New Mexico-comparison with Andean volcanism and potential for future volcanism. In S. M. Cather, W. C. McIntosh, and S. A. Kelley, eds., Tectonics, geochronology, and volcanism in the southern Rocky Mountains and Rio Grande rift p. 13–40, Socorro, New Mexico: Bureau of Geology and Mineral Resources Bulletin 160.

Corti, G., 2012, Evolution and characteristics of continental rifting: analogue modeling-inspired view and comparison with examples from the East African Rift System, Tectonophysics, 522-523, p. 1-33.

Cosca, M. A., Thompson, R. A., Lee, J. P., Turner, K. J., Neymarl, L. A., and Premo, W. R., $^{40}Ar/^{39}Ar$ geochronology. Isotope geochemistry (Sr, Nd, Pb), and petrology of alkaline lavas near Yampa, Colorado: Migration od alkaline volcanism and evolution of the northern Rio Grande rift, Geosphere, v. 10, n. 2, p. 374-400.

DeCelles, P. G., 2004, Late Jurassic to Eocene Evolution of the Cordilleran Thrust belt and Foreland basin system, Western U.S.A.: American Journal of Science, v. 304, p. 105–168.

Dickenson W. R., Klute, M. A., Hayes, M. J., Janecke, S. U., Lundin, M. A., McKittrick, M. A., and Olivares, M. D., 1988, Paleogeographic and paleotectonic setting of Laramide sedimentary basins in the Central Rocky Mountain region: Geological Society of America Bulletin, v. 100, p. 1023-1039.

Dickenson, W. R., 2004, Evolution of the North American Cordillera: Annual Review of Earth and Planetary Sciences, v. 32, p. 13–4, doi:10.1146/annurev.earth.32.101802.120257.

Duller, R. A., Whittaker, A. C., Swinehart, J. B., Armitage, J. J., Sinclair, H. D., Bair, A., Allen, P. A., 2012; Abrupt landscape change post–6 Ma on the central Great Plains, USA. Geology, v. 40, n. 10, p. 871–874, doi: 10.1130/G32919.1.

Epis, R. C., and Chapin, C. E., 1974, Stratigraphic Nomenclature of the Thirtynine Mile Volcanic Field, Central Colorado: Geologic Survey Bulletin, p. 1–32.

Epis, R. C., and Chapin, C. E., 1975, Geomorphic and Tectonic Implications of the Post-Laramide, Late Eocene Erosion Surface in the Southern Rocky Mountains: Geological Society of America Memoir, v. 144, p. 45–74.

Epis, R. C., Scott, G. R., Taylor, R. B., and Chapin, C. E., 1976, Cenozoic Volcanic, Tectonic, and Geomorphic Features of Central Colorado: Studies in Colorado Field Geology, Professional Contributions Colorado School of Mines, p. 323–338.

Farley, K.A., Wolf, R.A., and Silver, L.T., 1996, The effects of long alpha-stopping distances on (U-Th)/He ages: Geochimica et Cosmochimica Acta, v. 60, p. 4223-4229, doi:10.1016/S0016-7037(96)00193-7.

Frankel, K. L., and Pazzaglia, F. J., 2006, Mountain fronts, base-level fall, and landscape evolution: Insights from the southern Rocky Mountains. In Special Paper 398: Tectonics, Climate, and Landscape Evolution: Geological Society of America, v. 398, p. 419–434. doi:10.1130/2006.2398(26).

Gallagher, K., 2012, Transdimensional inverse thermal history modeling for quantitative thermochronology: Journal of Geophysical Research, v. 117, B02408, doi:10.1029/2011JB008825.

Grauch, V.J.S., Bauer, P. W., Drenth, B. J., Kelson, K. I., 2017, A shifting rift—Geophysical insights into the evolution of Rio Grande rift margins and the Embudo transfer zone near Taos, New Mexico. Geosphere, v. 13, n. 3, p. 870–910, doi:10.1130/GES01425.1.

Gilbert, H., 2012, Crustal structure and signatures of recent tectonism as influenced by ancient terranes in the western United States, Geosphere, v. 8, n. 1, p. 141–157.

Green, G.N., 1992, The Digital Geologic Map of Colorado in ARC/INFO Format: U.S. Geological Survey Open-File Report 92-0507, 9 p. http://pubs.usgs.gov/of/1992/ofr-92-0507/.

Gregory, K. M., and Chase, C. G., 1994, Tectonic and climatic significance of a late Eocene low-relief, high-level geomorphic surface, Colorado: Journal of Geophysical Research, v. 99, p. 20141–20160.

Gregory, K. M., and McIntosh, W. C., 1996, Paleoclimate and paleoelevation of the Oligocene Pitch-Pinnacle flora, Sawatch Range, Colorado: Geological Society of America Bulletin, v. 108, n. 5, p. 545–561.

Harrison, T.M., Zeitler, P.K., 2005, Fundamentals of Noble Gas Thermochronometry: Reviews in Mineralogy and Geochemistry, v. 58, p. 123-149.

Hart, N. R., Stockli, D. F., Lavier, L. L., and Hayman, N. W., 2017, Thermal evolution of a hyperextended rift basin, Mauleon Basin, western Pyrenees, Tectonics, v. 36, p. 1103-1128.

Heller, P. L., Dueker, K., and McMillan, M. E., 2003, Post-Paleozoic alluvial gravel transport as evidence of continental tilting in the US Cordillera: Geological Society of America Bulletin, v. 115, n. 9, n. 1122-1132.

House, M.A., Kelley, S.A., Roy, M., 2003, Refining the footwall cooling history of a rift flank uplift, Rio Grande rift, New Mexico, Tectonics, v. 22, no. 5, 1060, doi:10.1029/2002TC001418.

Hubbard, M.S., Oviatt, C.G., Kelley, S., Perkins, M.E., Hodges, K.V., and Robbins, R., 2001, Oligocene-Miocene basin formation and modification in the northern Rio Grande rift; constraints from $^{40}Ar/^{39}Ar$, fission track, and tephrochronology: Geological Society of America Abstracts with Programs, v. 33, no. 6, p. A-257.

Karlstrom, K.E., Crow, R., Crossey, L.J., Coblentz, D., and Van Wijk, J.W., 2008, Model for tectonically driven incision of the younger than 6 Ma Grand Canyon: Geology, v. 36, p. 835–838, doi:10.1130/G25032A.1.

Karlstrom, K. E., Harlan, S., Williams, M., McClelland, J., Geissman, J. W., and Åhäll, Karl-Inge, 1999, Refining Rodinia: Geologic evidence for the Australia–Western U.S. (AUSWUS) connection for Proterozoic supercontinent reconstructions, GSA Today, v. 9, p. 1–7.

Keller, G. R., and Baldridge, W. S., 1999 The Rio Grande Rift: A Geological and Geophysical Overview: Rock Mountain Geology, v. 34, n. 1, p. 121-130.

Kelley, S. A., and Chapin, C. E., 1995, Apatite Fission-Track Thermochronology of Southern Rocky Mountain-Rio Grande Rift-Western High Plains Provinces: New Mexico Geological Society Guidebook, v. 46, p. 87–96.

Kelley, S. A., and Chapin, C. E., 1997, Cooling histories of mountain ranges in the southern Rio Grande rift based on apatite fission-track analysis—a reconnaissance survey: New Mexico Bureau of Mines Mineral Resources, v. 19, n. 1, p. 1–14.

Kelley, S. A., Duncan, I. J., 1986, Late Cretaceous to Middle Tertiary tectonic history of the northern Rio Grande rift, New Mexico: Journal of Geophysical Research, v. 91, p. 6246–6262, doi:10.1029/JB091iB06p06246.

Kelley, S. A., Chapin, C. E., and Corrigan, A. J., 1992, Late Mesozoic to Cenozoic Cooling Histories of the Flank of the Northern and Central Rio Grande Rift, Colorado and New Mexico: New Mexico Bureau of Mines Mineral Resources, v. 145, p. 1–40.

Kellogg, K.S., 1999, Neogene basins of the northern Rio Grande rift: partitioning and asymmetry inherited from Laramide and older uplifts, Tectonophysics, v. 305, p. 141-152.

Kluth, C., and Coney, P., 1981 Plate tectonics of the Ancestral Rocky Mountains: Geology, v. 9, p. 10–15.

Kluth, C.F., Schaftenaar, C.H., 1994, Depth and geometry of the northern Rio Grande Rift in the San Luis Basin, south-central Colorado, in Keller, G.R., Cather, S.M., eds., Basins of the Rio Grande Rift: Structure, stratigraphy and tectonic setting: Geological Society of America Special Paper 291, p. 27–38.

Knepper, D. H. Jr., 1974, Tectonic analysis of the Rio Grande rift zone, central Colorado, Colorado School of Mines [Ph.D. Thesis], T-1593, p. 237.

Landman, R., and Flowers, R. M., 2013, (U-Th)/He thermochronologic constraints on the evolution of the northern Rio Grande Rift, Gore Range, Colorado, and implications for rift propagation models: Geosphere, v. 9, n. 1, p. 170–187, doi:10.1130/GES00826.1.

Lavecchia, A., Thieulot, C., Beekman, F., Cloetingh, S., and Clark, S., 2017, Lithosphere erosion and continental breakup: Interaction of extension, plume upwelling and melting, Earth and Planetary Science Letters, v. 467, p. 89-98.

Leonard, E. M., 2002, Geomorphic and tectonic forcing of late Cenozoic warping of the Colorado piedmont, Geology, v. 30, n. 7, p. 595–598.

Leonard, E. M., M. S. Hubbard, S. A. Kelley, E. Evanoff, C. S. Siddoway, C. G. Oviatt, M. Heizler, and M. Timmons, 2002, High Plains to Rio Grande rift: Late Cenozoic evolution of central Colorado, in Geological Society of America Annual Meeting Field Trip Guidebook, Geological Society of America, Boulder, Colorado, 35 p.

Levander, A., Schmandt, B., Miller, M. S., Liu, K., Karlstrom, K. E., Crow, R. S., Lee, C. T. A., and Humphreys, E. D., 2011, Continuing Colorado plateau uplift by delamination style convective lithospheric downwelling, Nature, v. 472, p. 461-466.

Lewis C. J., Baldridge W. S., 1994, Crustal extension in the Rio Grande rift, New Mexico: Half-grabens, accommodation zones, and shoulder uplifts in the Ladron Peak-Sierra Lucero area, Geological Society of America, Special Paper, v. 291, p. 135-155.

Limbach, F., 1975, The geology of the Buena Vista area, Chaffee County, Colorado, Colorado School of Mines [MS thesis], 98 p.

Lindsey, D. A., Andriessen, P. A. M., and Wardlaw, B.R., 1986, Heating, cooling, and uplift during Tertiary time, northern Sangre de Cristo Range, Colorado, Geological Society of America Bulletin, v. 97, p. 1133-1143.

Machette, M. N., 1988, Quaternary movement along the La Jencia fault, central New Mexico: U.S. Geological Survey Professional Paper 1440, 82 p., 2 plates.

Machette, M. N., Personious, S. F., Kelson, K. I., Haller, K. M., Dart, R. L., 1998, Map of Quaternary faults and folds in New Mexico and adjacent areas, USGS Open-file report 98-521.

Marshak, S., Karlstrom, K., and Timmons, J.M., 2000, Inversion of Proterozoic extensional faults: an explanation of Laramide and Ancestral Rockies intracratonic deformation, United States: Geology, v. 28, p. 735-738.

McIntosh, W. C., Quade J., 1995, $^{40}Ar/^{39}Ar$ geochronology of the tephra layers in the Santa Fe Group, Española Basin, New Mexico, New Mexico Geological Society Guidebook, 46th Field Conference, p. 279-287.

McMillan, N.J., McLemore, V.T., 2004, Cambrian-Ordovician magmatism and extension in New Mexico and Colorado, New Mexico Bureau of Geology and Mineral Resources Bulletin 160, 11 p.

McMillan, M. E., Angevine, C. L., and Heller, P. L., 2002, Post-depositional tilt of the Miocene-Pliocene Ogallala Group on the western Great Plains: Evidence of late Cenozoic uplift of the Rocky Mountains: Geology, v. 30, n. 1, p. 63–66.

McMillan, M. E., Heller, P. L., and Wing, S. L., 2006, History and causes of post-Laramide relief in the Rocky Mountain orogenic plateau: Geological Society of America Bulletin, v. 118, n. 3-4, p. 393–405, doi:10.1130/B25712.1.

McMillan, N. J., Dickin, A. P., Haag, D., 2000, Evolution of magma source regions in the Rio Grande rift, southern New Mexico, GSA Bulletin, v. 112, n. 10, p. 1582–1593. doi:10.1130/0016-7606(2000)112<1582:EOMSRI>2.0.CO;2.

Molnar, N, E., Cruden, A. R., and Betts, P. G., 2017, Interactions between propagating rotational rifts and linear rheological heterogeneities: Insights from three-demensional laboratory experiments, Tectonics, v. 36, 420-443, doi:10.1002/2016TC004447.

Muirhead, J. D., Kattenhorn, S. A., Lee, H., Mana, S., Turrin, B. D., Fischer, T. P., Kianji, G., Dindi, E., and Stamps, D. S., 2016, Evolution of upper crustal faulting assisted by magmatic volatile release during early-stage continental rift development in the East African Rift, Geosphere, v. 12, n. 6, p. 1670–1700.

Naeser, C. W., Bryant, B., Kunk, M. J., Kellogg, K., Donelick, R. A., and Perry, W. J. Jr., 2002, Tertiary cooling and tectonic history of the White River uplift, Gore Range, and western Front Range, central Colorado: Evidence from fission-track and $^{39}Ar/^{40}Ar$ ages: Geological Society of America Special Papers, v. 366, p. 31–53.

Nelson, R. A., Patton, T. L., Morley, C. K., 1992, Rift-segment interaction and its relation to hydrocarbon exploration in continental rift systems, American Association of Petrolium Geologists Bulletin, v. 76, p. 1153-1160.

Peterson, C., and Roy, M., 2005, Gravity and flexure models of the San Luis, Albuquerque, and Tularosa Basins in the Rio Grande rift, New Mexico, and southern Colorado, New Mexico Geological Society, 56th Field Conference Guidebook, Geology of the Chama Basin, p. 105-114.

Reiners, P.W., and Nicolescu, S., 2006, Measurement of parent nuclides for (U-Th)/He chronometry by solution sector ICP-MS: Arizona Radiogenic Helium Dating Laboratory Report 1, http://www.geo.arizona.edu/~reiners/arhdl/Reiners_and_Nicolescu_submitted.pdf

Reston, T., 2005, Polyphase faulting during the development of the west Galicia rifted margin, Earth and Planetary Science Letters, v. 237, p. 561-576.

Ricketts, J. W., Karlstrom, K. E., Kelley, S. A., 2015 Embryonic core complexes in narrow continental rifts: The importance of low-angle normal faults in the Rio Grande rift of central New Mexico, Geosphere, v. 11, n. 2, p. 425–444 doi: 10.1130/GES01109.1.

Ricketts, J. W., Kelley, S. A., Karlstrom, K. E., Schmandt, B., Donahue, M. S., and van Wijk, J., 2016, Synchronous opening of the Rio Grande rift along its entire length at 25–10 Ma supported by apatite (U-Th)/He and fission-track thermochronology, and evaluation of possible driving mechanisms: Geological Society of America Bulletin, v. 128, n. 3-4, p. 397–424, doi:10.1130/B31223.1.

Robbins, R., 2005, Petrology, structure and exhumation of the southern Sawatch Mountains, south-central Colorado, [PhD Thesis] Kansas State University.

Scott, G. R., 1975, Cenozoic surfaces and deposits in the southern Rocky Mountains: Geological Society of America Memoirs, v. 144, p. 227-248.

Scott, G.R., Taylor, R.B., Epis, R.C., and Wobus, R.A., 1976, Geologic map of the Pueblo 1 degree x 2 degrees quadrangle, south-central Colorado, US Geological Survery, Miscellaneous Field Studies Map MF-775, 1:187,500.

Şengör, A. M. C., Natal'in, B. A., 2001, Rifts of the world, Ernst, R. E., Buchan, K. L., Eds., Mantle Plumes: Their Identification Through Time, Special Paper, Geological Society of America, Boulder, CO, v. 352, p. 389-482.

Shannon, J. R., 1988, Geology of the Mount Aetna cauldron complex, Sawatch Range, Colorado [Doctoral Thesis], Colorado School of Mines.

Shaw, C.A., and Karlstrom, K.E., 1999, The Yavapai-Mazatzal crustal boundary in the Southern Rocky Mountains: Rocky Mountain Geology, v. 34, no. 1, p. 37-52.

Taylor, R.B., Scott, G.R., and Wobus, R.A., 1975a, Reconnaissance geologic map of the Howard quadrangle, central Colorado: U.S. Geological Survey, Miscellaneous Investigations Series Map I-892, scale 1:62,500.

Taylor, R.B., Scott, G.R., Wobus, R.A., and Epis, R.C., 1975b, Reconnaissance geologic map of the Cotopaxi 15-minute quadrangle, Fremont and Custer Counties Colorado: U.S. Geological Survey, Miscellaneous Investigations Series Map I-900, scale 1:62,500.

Taylor, R.B., Scott, G.R., Wobus, R.A., and Epis, R.C., 1975c, Reconnaissance geologic map of the Royal Gorge quadrangle, Fremont and Custer Counties Colorado: U.S. Geological Survey, Miscellaneous Investigations Series Map I-869, scale 1:62,500.

Taylor, R. B., 1975, Neogene tectonism in south-central Colorado: Geological Society of America Memoirs, v. 144, p. 211-226.

Thomson, S.N., Soreghan, G.S., Reiners, P.W., Peyton, S.L., and Murray, K.E., 2016, A definitive 6 Ma start date for carving of the northeastern Colorado Plateau Canyonlands: Geological Society of America Abstracts with Programs, v. 48, no. 7, doi:10.1130/abs/2016AM-287583.

Timmons, J. M., Karlstrom, K. E., Dehler, C. M., Geissman, J. W., Heizler, M. T., 2001, Proterozoic multistage (ca. 1.1 and 0.8 Ga) extension recorded in the Grand Canyon Supergroup and establishment of northwest- and north-trending tectonic grains in the southwestern United States, GSA Bulletin, v. 113, n. 2, p. 163–181.

Tweto, O., 1975, Laramide (Late Cretaceous-Early Tertiary) orogeny in the Southern Rocky Mountains, in Curtis, B.M., ed. Cenozoic history of the Southern Rocky Mountains: Geological Society of America Memoir, v. 144, p. 1-44.

Tweto, O., 1979, The Rio Grande rift system in Colorado, in Reiker, R. E., ed., Rio Grande rift: Tectonics and magmatism: Washington D.C., American Geophysical Union, p. 33-56.

Wallace, C. A., Cappa, J. A., and Lawson, A. D., 1997, Geologic map of the Salida East quadrangle, Chaffee and Fremont Counties, Colorado: Colorado Geological Survey, Open-File Report OF-97-6, scale 1:24,000.

Van Alstine, R. E., 1969, Geology and Mineral Deposits of the Poncha Springs NE

Quadrangle, Chaffee County, Colorado, University.

Van Schmus, W.R., Bickford, M.E., Condie, K.C., 1993. Early Proterozoic crustal evolution. In: Reed, J.C., et al. (Eds.), Precambrian: Conterminous U.S. DNAG vol. C-2, Geological Society of America, Boulder, CO, p. 270–28.

CHAPTER II. LOW-TEMPERATURE THERMOCHRONOMETRIC CONSTRAINTS ON FAULT INITIATION AND GROWTH IN THE NORTHERN RIO GRANDE RIFT, UPPER ARKANSAS RIVER VALLEY, CO

ABSTRACT

Continental rifting models predict a variety of spatiotemporal patterns of rift initiation, fault development, and time scales of rift integration. The Rio Grande rift (southwestern United States) is an example of a rift for which both synchronous opening and propagation models have been proposed and, hence, offer differing predictions for the timing of rift development. Low-temperature thermochronometry data from six vertical transects in the upper Arkansas River valley reveal exhumation histories that delineate the initiation, growth, and linkage of rift-bounding faults. Extension initiates on separate fault segments between ca. 22 and 18 Ma, and spatial patterns in fault initiation and exhumation rate suggest that individual fault segments linked to form a coherent ~75-km-long fault system by ca. 13 Ma. Our results, combined with data from throughout the northern Rio Grande rift, support a model of synchronous early Miocene rift initiation, with full rift integration occurring no earlier than ca. 10 Ma. Densely spaced sampling transects and slow extension rates in the Rio Grande rift allow us to resolve differences in the timing of fault initiation and rates of exhumation that yield insight into the processes of fault growth and linkage that cannot be easily discerned in rapidly

evolving rift systems.

INTRODUCTION

The architecture of continental rifts controls hydrocarbon distribution, aquifer reserves, and, ultimately, our understanding of continental breakup; however, the processes by which rifts evolve remain highly debated (Nixon et al., 2016). End-member rift evolution models include (1) the propagation of extension and deformation at the end(s) of a rift system, or (2) synchronous onset of rifting along the entire length. Each model has been proposed for existing, well-studied rifts, such as the East African rift (Berhe, 1986; Chorowicz, 2005) and the Gulf of California rift (Umhoefer, 2011; Busby, 2013). The evolution of the Rio Grande rift (RGR, southwestern United States; Fig. 2.1A) is similarly contested despite being one of the best-exposed and accessible continental rifts. Several studies suggest rifting began in southern New Mexico between ca. 30 and 25 Ma and propagated northward to northern Colorado, and perhaps even to southern Wyoming (Leonard, 2002; Heller et al., 2003; Cosca et al., 2014). Others suggest that the onset of rifting throughout New Mexico and central Colorado was relatively synchronous, with initiation between 25 and 20 Ma, and with the most rapid rift development occurring between 20 and 10 Ma (Chapin and Cather, 1994; Landman and Flowers, 2013; Ricketts et al., 2016).

Debate surrounding the northward propagation of the RGR persists primarily because of limited constraints on the timing of rift initiation in the northern RGR (NRGR). Both poor resolution on the age of syn-rift strata, and the fairly amagmatic nature of the NRGR (e.g., Van Alstine, 1969; Cosca et al., 2014) preclude their use as proxies for the timing of rift initiation, as is done elsewhere within the rift system (e.g.,

Grauch et al., 2017). Rather, arguments for the timing of rift initiation in the NRGR have, until recently, arisen mainly from indirect proxies, such as sedimentation and regional tilting (e.g., Leonard, 2002; Heller et al., 2003). Low-temperature thermochronometry provides a method for directly measuring the onset of exhumation along major basin-bounding faults in the NRGR, clarifying the timing and spatial patterns of rift-flank fault initiation. Here we present six new low-temperature thermochronometry transects from the Sawatch Range (Fig. 2.1; Fig. A1) and estimates of fault initiation from thermal history modeling.

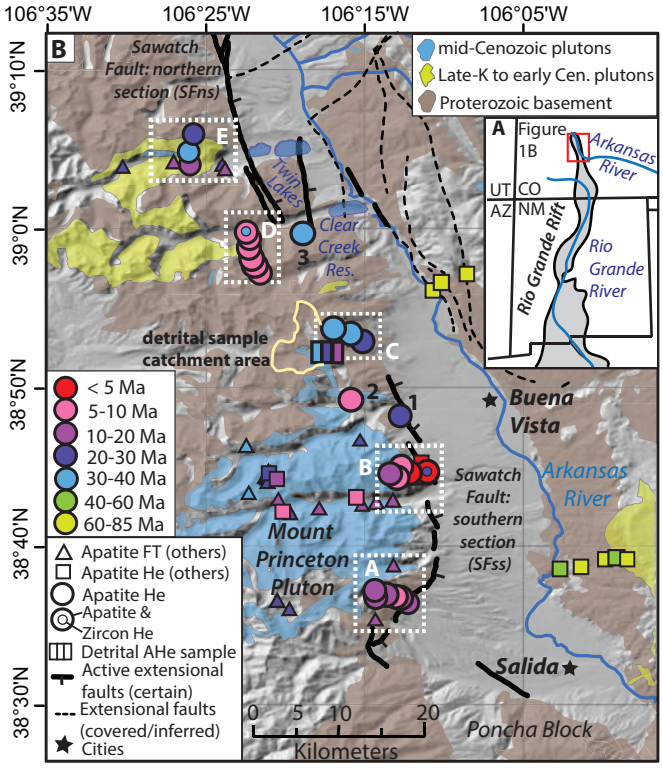

Figure 2.1. (A) Rio Grande rift extent. (B) Sample locations and simplified structure and geology in the upper Arkansas River valley. New samples: AHe – large circles, ZHe – small circles, detrital AHe – rectangle. Previously published samples: AHe – small squares (Ricketts et al., 2016; Abbey et al., 2017) and AFT – small triangles (Bryant and Naeser, 1980; Shannon, 1988; Kelley et al., 1992). Dashed boxes group samples into vertical transects (Table 2.1).

UPPER ARKANSAS RIVER VALLEY

The NRGR is comprised of three north-south–striking half grabens (from south to north: the San Luis valley, upper Arkansas River valley, and Blue River valley; Fig. A1), each bounded by high-angle normal fault systems that create >1.5 km of

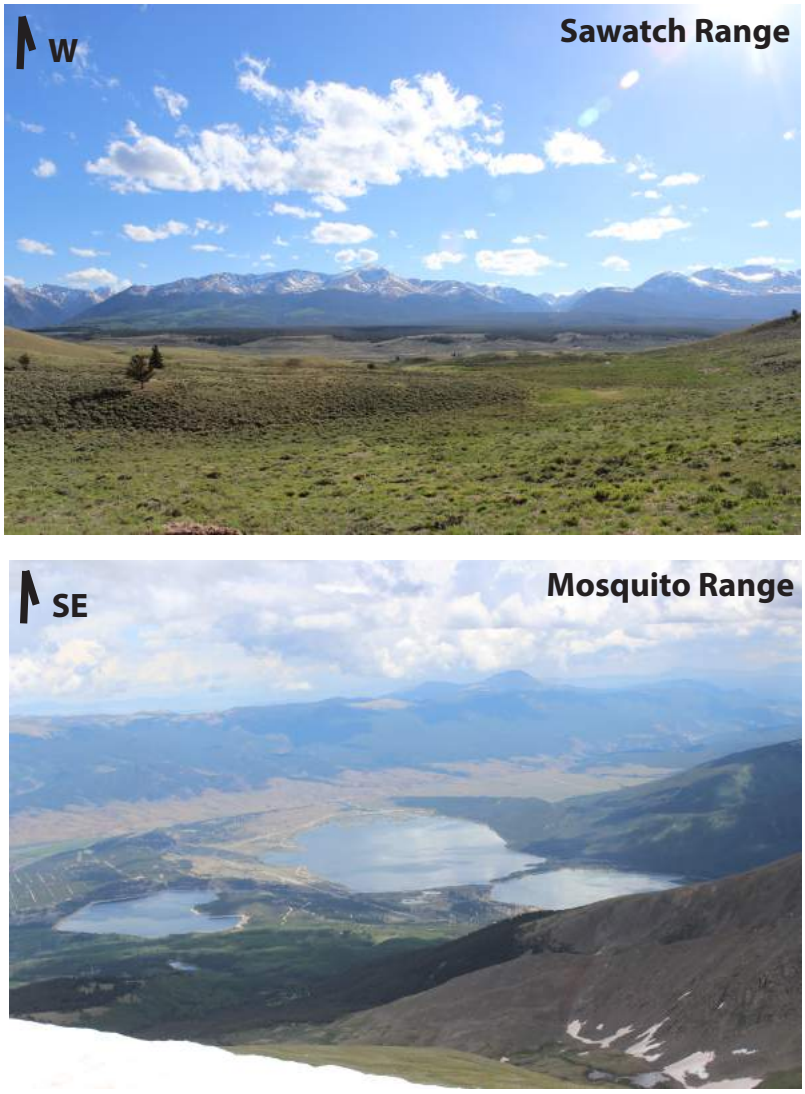

Figure 2.2: Field photos taken in the summer of 2014. Top: looking west across the upper Arkansas River valley to the Sawatch Range. Bottom: looking southwest across the Twin Lakes towards the Mosquito Range from Mount Elbert.

topographic relief (Sangre de Cristo Range, Sawatch Range, and Gore Range, respectively; Figs. 2.1 and A1). We focus here on the ~90-km-long upper Arkansas River (UAR) valley, flanked by >4200 m peaks in the Sawatch Range to the west and ~3000 m peaks in the Mosquito Range and Arkansas Hills to the east (Figs. 2.1 and 2.2). Rift-related normal faults bound the eastern margin of the Sawatch Range and are mapped as distinct fault segments ~20–30 km in length; the Sawatch fault northern section (SFns) and southern section (SFss), which have both been active in the Quaternary (Fig. 2.1; Table 2.1; U.S. Geological Survey, 2006). A continuous Quaternary fault system is not

recognized along the range front, despite the continuity of high topographic relief in the Sawatch Range. South of the UAR valley, the Poncha Block accommodation zone connects the SFss to the Sangre de Cristo fault in the San Luis valley. North of the UAR valley is a complex series of northeast-striking faults that trend toward the Blue River fault system bounding the Gore Range in the Blue River valley (Fig. A1).

TABLE 2.1. VERTICAL SAMPLING TRANSECTS

Transect	Fault Footwall	Rock Type	AHe Ages (Ma)
Mount Shavano (A)	Southern Sawatch (SFss)	1,2	9.3 - 18.7
Mount Princeton (B)	Southern Sawatch (SFss)	2	2.2 – 12.2
Mount Columbia (C)	None mapped	1	20.9 – 31.3
Mount Belford (D)	Northern Sawatch (SFns)	1	5.6 – 8.9
Mount Elbert (E)	Northern Sawatch (SFns)	1	11.5 – 32.3
Galena Mountain (F)	Northern Sawatch (SFns)	1	40.0 – 92.3

Note: Rock type: 1. Proterozoic bedrock, 2. Eocene Mt Princeton Batholith

(U-TH-SM)/HE LOW-TEMPERATURE THERMOCHRONOMETRY

Low-temperature thermochronometry can be applied to determine the timing of initiation, magnitude, and rate of exhumation along normal faults because the footwalls of these faults are progressively cooled and exposed via tectonic exhumation (e.g., Curry et al., 2016). Apatite (U-Th-Sm)/He (AHe) thermochronometry records cooling below temperatures of ~30–90 °C (Flowers et al., 2009) and zircon (U-Th)/He (ZHe) thermochronometry records cooling from ~140–220 °C (Guenthner et al., 2013). Combining helium thermochronometric methods with apatite fission-track (AFT) dating, which captures cooling between ~150 and 70 °C (Kelley et al., 1992), allows for interpretation of exhumation histories from ~7–1 km depths, depending on the geothermal gradient.

We present low-temperature thermochronometry data from six vertical transects (A to F south to north; Figs. 2.1B and A1; Table 2.1) that span ~90 km along-strike in the Sawatch Range. Our transect strategy focused on sampling in the footwall of the Sawatch fault, within a distance of 5 km from the fault surface trace, to obtain high-relief vertical transects. To address fault geometry, growth, and linkage in the NRGR, we report additional data from three single bedrock samples (not in a transect; labeled 1, 2 and 3 in Fig. 2.1B and Tables A1 and A2), and one detrital sample from the Sawatch Range (Fig. 2.1B). All samples were analyzed for AHe, and the deepest samples in two of the transects (B and D) were analyzed for ZHe (Table A1).

All AHe ages from transects A, B, and D are younger than 20 Ma (Figs. 2.1 and 2.3; Tables 2.1 and A1). ZHe data from the deepest samples in two of these transects (B and D) are 20.6 ± 0.6 Ma and 33.7 ± 1.6 Ma, respectively (Table A1). AHe ages from transect E range from 32 to 11 Ma, and from transects C and F all AHe ages are older than 20 Ma (Table 2.1). Bedrock samples 1, 2, and 3 record AHe ages of 25.0 ± 2.1 Ma, 7.7 ± 0.6 Ma, and 39.4 ± 1.4 Ma, respectively (Fig. 2.1; Table A1), and 10 AHe dates from a modern detrital sample collected near transect C has age populations of ca. 13, ca. 22, and ca. 37 Ma (Fig. 2.3; Table A2). Samples in transect F preserve Cretaceous to Eocene cooling ages that pre-date RGR initiation and are not discussed further (Fig. A1; Tables 2.1, A1 and A2).

Data from transects A, B, D, and E potentially constrain the timing of rift initiation, and rates and magnitudes of exhumation on rift-bounding faults, which we quantify with inverse thermal history models. We find AHe ages from transect C, in combination with the individual bedrock ages and the detrital AHe dates, are pertinent to

understanding fault geometry and linkage in the NRGR, and these are discussed below.

INVERSE THERMAL MODELING

To investigate exhumation histories on the Sawatch fault segments, we performed inverse thermal history modeling using the QTQt program (QTQt64R5.6.2a,

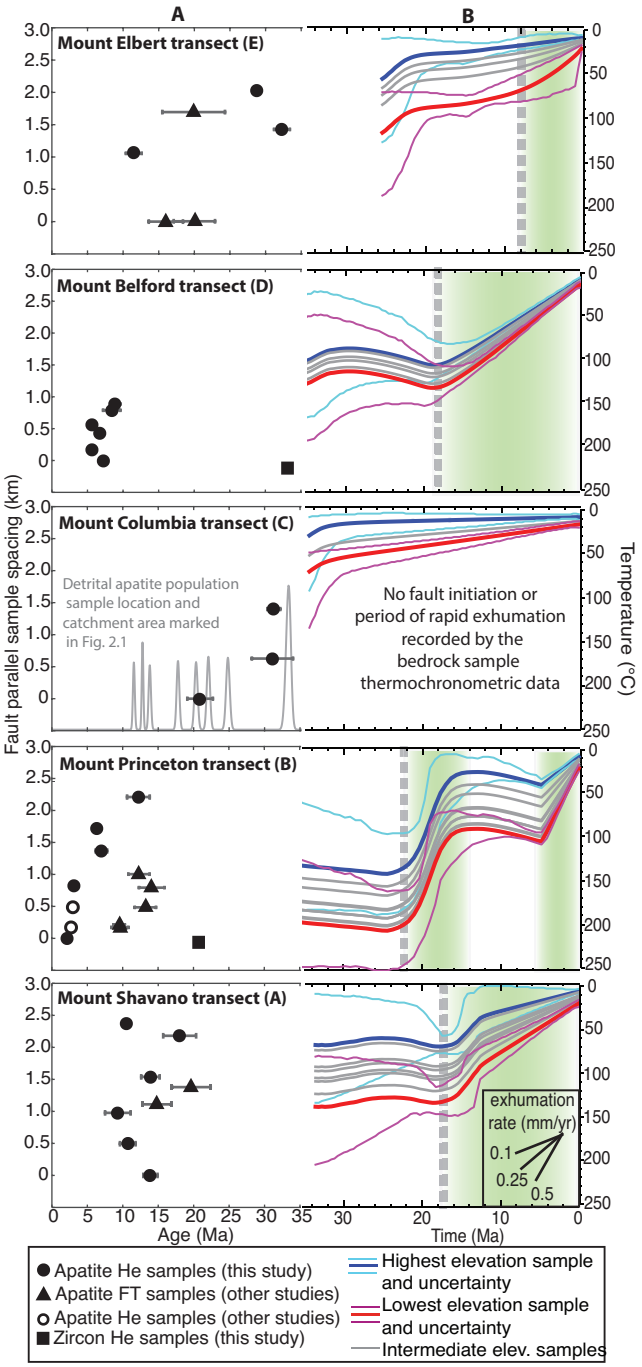

Figure 2.3. (A) Thermochronometric ages plotted as a function of fault-parallel separation after projection onto a 70°-dipping fault plane (Fig. A3). (B) Inverse thermal history models for transects A-E. Gray dashed lines indicate estimated timing of fault initiation and green shading highlights exhumation rates >0.2 mm/yr.

http://www.iearth.org.au/codes/QTQt/; Gallagher, 2012). We selected this program for its ability to simultaneously model both many samples with known vertical separation (i.e., transects) and data from multiple thermochronometers. We defined spacing between samples by projecting each sample onto its associated fault plane and determining fault-parallel separation to account for footwall tilting during exhumation (Fig. A3; e.g., Stockli et al., 2000). Published thermochronometric data were incorporated into our analysis where such data are in close proximity to our transects and consistent with our sampling strategy (Bryant and Naeser; 1980; Shannon, 1988; Kelley et al., 1992; Ricketts et al., 2016; see Appendix A). QTQt model outputs represent a suite of most-likely time-temperature paths for our vertical transects (see Appendix A).

SAWATCH FAULT INITIATON AND EVOLUTION

Thermal history modeling of our densely spaced vertical transects reveals a heterogeneous pattern of fault initiation and growth along the UAR valley. The earliest exhumation appears to initiate on the SFss at ca. 22 Ma (transect B) (thick red line in Fig. 2.3; interpretations made from the cooling path for the deepest sample). Transect A records the southward propagation of SFss, with exhumation initiating at ca. 18 Ma at this site. Faulting on the SFns initiates at ca. 18 Ma, with the earliest exhumation observed at transect D. Transect E records the northward propagation of the SFns, showing exhumation initiation at ca. 10 Ma.

Total magnitudes of exhumation mirror initiation ages, with ~5–6 km of exhumation observed at transect B, 4–5 km at transects A and D, and 2–3 km at transect E (Figs. 2.3 and 2.4). Together, these patterns of fault initiation and displacement appear to define two independent fault segments (SFss and SFns) that are growing via fault tip

propagation. Thus, possible faulting in the region between the SFss and the SFns (Fig. 2.1B) can be used to assess general fault growth and linkage models, as well as the geometry of the Sawatch fault, in particular.

Surprisingly, our sampling transect C that lies between the two active segments of the Sawatch fault system shows no evidence of post-Oligocene cooling (Fig. 2.3). We can conceive of two explanations for this observation; (1) the SFss and SFns propagated unidirectionally away from one another, implying highly asymmetric displacement gradients, and no structural linkage of the SFss and SFns; or (2) the SFss and the SFns link via a structure within the Sawatch Range, such that transect C is in the hanging wall of the Sawatch fault.

We test these alternatives by comparing ages of samples collected at the range front to ages of samples from several kilometers west of the range front at three sites between the SFss and the SFns (Fig. 2.1B). For all three sites, AHe ages at the range front are >20 Ma (from south to north: sample 1, transect C, sample 3). However, the AHe ages of paired samples west of the range front are <15 Ma (sample 2; youngest ages from the detrital sample that drains a catchment west of transect C; transect D, respectively) (Figs. 2.1, 2.3 and A4). This spatial pattern of older ages at the range front and younger ages in the range interior is consistent with the explanation that the SFss and the SFns are linked by a normal fault within the range.

We use the AHe age distribution from the detrital sample to infer the approximate onset of faulting and slip rate on this interior fault by modifying the detrital thermochronometry analysis approach of Avdeev et al. (2011) (see Appendix A). Comparing our observed distribution of detrital AHe ages to modeled age distributions

predicted from various exhumation histories and the known catchment hypsometry, we find that our observed ages are best modeled by cooling at a rate of ~0.03 mm/yr prior to ca. 14 Ma, followed by an increase in cooling rate to ~0.4 mm/yr post–14 Ma (Figs. A5 and A6). This suggests that ~5 km of exhumation has occurred on a fault segment west of the range front between the SFss and SFns since ca. 14 Ma, a magnitude consistent with that observed at adjacent transects B and D.

We propose that the SFss and SFns faults initiated as independent fault segments in the early Miocene and became linked by middle to late Miocene time. We name this integrated rift-bounding structure the Sawatch Range fault (SRF; Fig. 2.4) and infer that it extends inboard of the range front north of transect B and re-emerges at the range front north of transect D. Our data support development of the SRF by tip propagation of initially individual fault segments, followed by segment linkage and continued tip propagation (Kim and Sanderson, 2005; Curry et al., 2016). In this context, rejuvenation of exhumation near transect B at ca. 6 Ma may reflect segment linkage and adjustment of the fault displacement ratio to account for the new fault length and geometry (e.g., Kim and Sanderson, 2005; Fig. 2.4).

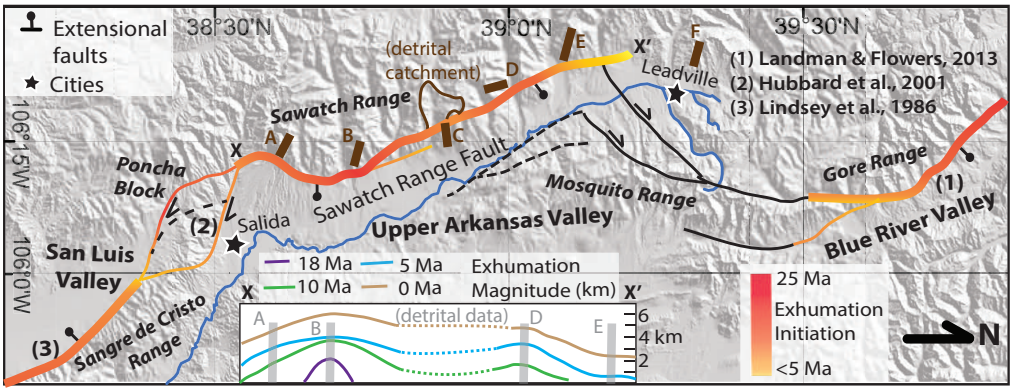

Figure 2.4. Proposed fault geometry for the UAR valley. Fault initiation indicated by fault trace color and magnitude of fault offset through time shown on inset. Thick faults are major rift-bounding normal faults, thin faults are minor structures. See text for discussion.

The inferred continuity of the SRF system has ramifications for seismic potential in the region. Empirical relationships between earthquake magnitude and rupture length would suggest earthquake magnitudes of ~M6 on the SFss or SFns, if they rupture independently (Wells and Coppersmith, 1984). A contiguous fault system with a length of 90 km, however, would be capable of an ~M7.5 earthquake. Surface displacements of 3 to 4 m per event on the SFss (McCalpin, 2016) are also consistent with earthquake magnitudes of ~M7.5 (Wells and Coppersmith, 1984), and support the inference of a contiguous fault system in the UAR graben. Occurrence of a >M7 earthquake in the UAR would have significant impacts both locally as well as on the highly populated Front Range region.

NORTHERN RIO GRANDE RIFT

Our data in the UAR valley, combined with similar data from the Gore Range and the Sangre de Cristo Range (Figs. 2.4, A1 and A3) offer an opportunity to assess whether rifting in the NRGR was synchronous or if there is evidence for northward propagation. In the Gore Range, faulting initiates at ca. 24 Ma (Landman and Flowers, 2013), while in the northern Sangre de Cristo Range, exhumation occurs at ca. 19 Ma (Lindsey et al., 1986). Together with our observation of initiation at ca. 22–18 Ma in the UAR valley, these data support contemporaneous onset of rifting throughout the NRGR, with no trend suggestive of northward propagation. These observations support rifting drivers for the RGR that predict synchronous initiation along the length of the rift such as rotation of the Colorado Plateau associated with Basin and Range extension, or mantle convection following the removal of the subducting Farallon slab (Landman and Flowers, 2013; Ricketts et al., 2016).

Although the earliest initiation of faulting on the SRF is at ca. 22 Ma, fault growth and propagation was a slow process, with some portions of the SRF not becoming active until post–10 Ma (Figs. 2.3 and 2.4), indicating that the evolution and integration of the entire SRF occurred over ~10–15 m.y. The linkage of the SRF in the middle to late Miocene appears to coincide with the development of accommodation zones connecting the three NRGR basins, including transfer faults in the Poncha Block (Fig. 2.4; Hubbard et al., 2001) and transfer faults between Leadville and the southern Gore Range (Fig. 2.4), resulting in a fully integrated NRGR between 10 and 5 Ma.

CONCLUSIONS

Low-temperature thermochronometric data from multiple transects in the UAR valley define the evolution of the 75-km-long Sawatch Range normal fault. This fault initiated at ca. 22 Ma, similar to fault initiation in other NRGR basins, and is thus indicative of a synchronous onset of rifting throughout the NRGR. In addition, dense vertical transect sampling in the UAR valley underscores the ability of low-temperature thermochronometric data to yield insight into fault growth and linkage processes in continental rifts.

ACKNOWLEDGMENTS

J. Fenno, F. Gilfoy, M. Hendrick, A. Maslyn, and W. Medwedeff provided field and analytical assistance. National Science Foundation grant EAR-1151247 (Niemi) and University of Michigan student research grants (Abbey) supported this work.

APPENDIX A: SUPPLEMENTARY DATA TABLES AND FIGURES FOR CHAPTER 2

Analytical data files and supplementary information and figures

This data repository contains two data tables, Table A1 – A2, three supplementary figures, Figs. A1 – A6, input information and data files for inverse thermal history modeling, and information pertaining to the methods and modeling used to estimate exhumation timing, rates and magnitudes from our detrital AHe sample.

Table A1: This table contains location and age data for all apatite (U-Th-Sm)/He and zircon (U-Th)/He thermochronometry results presented in this manuscript.

Table A2: This table contains analytical data for all apatite and zircon grains used for apatite (U-Th-Sm)/He and zircon (U-Th)/He thermochronometry results presented in this manuscript.

Figure A1: This figure shows the location of the northern Rio Grande rift and all published rift-related thermochronometry data.

Figure A2: This figure shows relationships between age and eU and age and grain size.

Figure A3: This figure shows a schematic representation of the sample projection correction we made for each modeled transect.

Figure A4: This figure shows the new fault geometry for the Sawatch Range fault in relation to the thermochronometric data and displays an interpretation for fault initiation and linkage between the northern rift basins.

Figure A5: This figure shows the L2-norm values used to predict the best-fit age elevation relationship for a change in exhumation rate to obtain our observed detrital AHe ages in relationship to catchment hypsometry.

Figure A6: This figure shows the cumulative density functions for our observed detrital AHe ages and the best-fit predicted ages.

TABLE A1: SAMPLE LOCATIONS AND MEAN AGES FOR APATITE (U-TH-SM)/HE AND ZIRCON (U-TH)/HE

Sample Name	Longitude	Latitude	Elevation (m)	Rock Type	Mean Age (Ma)
Mount Shavano Transect (A)					
15MTS-01	-106.1984	38.6031	3066	Granite	13.9 ± 1.0
15MTS-02	-106.2079	38.6073	3292	Gneiss	10.7 ± 1.1
15MTS-03	-106.2161	38.6119	3556	Granite	9.3 ± 1.8
15MTS-04	-106.2261	38.6139	3839	Gneiss	13.9 ± 1.3
15MTS-05	-106.2393	38.6132	4085	Gneiss	18.7 ± 1.5
15MTS-06	-106.2392	38.6189	4341	Granite	10.5 ± 0.4
Mount Princeton Transect (B)					
15MTP-01	-106.1834	38.7433	2833	Granite	2.2 ± 0.1
15MTP-01 (z)	-106.1834	38.7433	2833	Granite	20.6 ± 0.6
15MTP-02	-106.2017	38.7420	3153	Granite	3.0 ± 0.3
15MTP-03	-106.2108	38.7487	3450	Granite	7.0 ± 0.8
15MTP-04	-106.2144	38.7369	3708	Granite	6.3 ± 0.6
15MTP-05	-106.2225	38.7415	3997	Granite	12.2 ± 1.6
Individual Samples (1 and 2)					
17MCWD-01	-106.2078	38.7959	2751	Granite	25.0 ± 2.1
17MCWD-02	-106.2639	38.8123	2841	Granite	7.7 ± 0.6
Mount Columbia Transect (C) and detrital sample					
15MTC-01	-106.2419	38.8678	2966	Gneiss	--
15MTC-02	-106.2460	38.8740	3254	Gneiss	--
15MTC-03	-106.2514	38.8802	3511	Gneiss	20.9 ± 1.8
15MTC-04	-106.2637	38.8882	3784	Gneiss	31.1 ± 2.9
15MTC-05	-106.2816	38.8933	4066	Gneiss	31.3 ± 0.9
17NCWD-MR (detrital)	-106.26778	38.87101	3029	Course modern river Sand	
Mount Belford Transect (D) and individual sample (3)					
14MTB-01	-106.3751	38.9971	2957	Granite	7.3 ± 0.5
14MTB-01 (z)	-106.3751	38.9971	2957	Granite	33.7 ± 1.6
14MTB-02	-106.3719	38.9902	3230	Granite	5.7 ± 0.3
14MTB-03	-106.3731	38.9812	3460	Gneiss	6.8 ± 0.1
14MTB-04	-106.3704	38.9706	3692	Granite	5.6 ± 0.5
14MTB-04a	-106.3680	38.9657	4001	Gneiss	8.4 ± 1.2
14MTB-05	-106.3611	38.9607	4322	Gneiss	8.9 ± 0.7
17CCKR	-106.2846	39.0049	3020	Granite	39.4 ± 1.4
Mount Elbert Transect (E)					
14MTE-01	-106.4338	39.0670	2973	Granite	11.5 ± 1.1
14MTE-02	-106.4353	39.0803	3328	Granite	32.3 ± 1.1
14MTE-03	-106.4383	39.0935	3670	Gneiss	28.8 ± 0.3

Sample Name	Longitude	Latitude	Elevation (m)	Rock Type	Mean Age (Ma)
14MTE-04	-106.4330	39.0943	3879	Gneiss	--
14MTE-05	-106.4300	39.0992	4156	Granite	--
14MTE-06	-106.4454	39.1177	4409	Gneiss	--
Galena Mountain Transect (F)					
15GAM-01	-106.4300	39.3141	3902	Gneiss	83.7 ± 15.9*
15GAM-02	-106.4147	39.3122	3762	Granite	43.9 ± 0.6
15GAM-03	-106.4094	39.3099	3628	Granite	92.3 ± 20.5*
15GAM-04	-106.3973	39.3025	3382	Granite	72.9 ± 9.9
15GAM-05	-106.3866	39.2957	3219	Schist	40.0 ± 3.4

Note: Dash indicates no data obtained from sample; (z) indicates zircon helium analyses, other data from apatite helium analyses.

* Sample mean age has >15% error.

TABLE A2. INDIVIDUAL GRAIN RESULTS FOR APATITE (U-TH-SM)/HE AND ZIRCON (U-TH)/HE SAMPLES

Sample	Mass (µg)	Length (µm)	Radius (µm)	FT	U (ppm)	Th (ppm)	Sm (ppm)	He (ncc)	eU (ppm)	Raw date (Ma)	Corr. date (Ma)	Error (Ma)
Mount Shavano Transect (A)												
15MTS-01a	2.42	97.6	55.4	0.77	28.96	22.70	632.09	0.10	37.2	9.1	11.9	0.12
15MTS-01b	2.01	112.6	47.0	0.74	35.88	29.58	537.71	0.11	45.3	10.3	13.9	0.13
15MTS-01c	1.36	90.1	43.3	0.71	23.43	22.04	545.82	0.05	31.1	9.4	13.2	0.12
15MTS-01d	1.62	123.2	40.4	0.71	24.67	19.56	500.42	0.07	31.6	11.8	16.6	0.16
15MTS-02a	2.37	110.0	51.7	0.76	18.28	7.39	247.94	0.05	21.2	7.9	10.4	0.11
15MTS-02b	4.36	170.5	56.3	0.79	18.40	8.32	224.94	0.12	21.4	10.8	13.8	0.14
15MTS-02c	2.81	173.6	44.8	0.74	16.48	5.07	242.33	0.04	18.8	6.8	9.1	0.09
15MTS-02d	1.51	103.4	42.7	0.71	16.58	10.19	196.25	0.03	19.9	6.7	9.4	0.12
15MTS-03a	2.69	178.1	43.3	0.73	8.09	28.80	88.91	0.03	15.2	6.3	8.6	0.07
15MTS-03b	1.50	118.9	39.5	0.70	11.29	43.72	162.71	0.02	22.3	4.8	6.8	0.07
15MTS-03c	3.27	148.0	52.3	0.77	12.85	50.40	106.62	0.06	25.1	5.5	7.1	0.06
15MTS-03d	2.95	112.6	57.0	0.78	0.82	4.57	8.84	0.01	1.9	11.4	14.7	0.23
15MTS-04a	1.76	133.9	40.4	0.71	29.61	97.16	368.27	0.15	54.1	12.7	17.9	0.14
15MTS-04b	1.89	129.0	42.6	0.72	18.44	51.35	323.93	0.07	32.0	9.3	12.8	0.10
15MTS-04c	1.39	95.9	42.4	0.71	13.91	74.67	301.79	0.05	32.8	9.3	13.1	0.11
15MTS-04d	2.27	140.0	44.8	0.74	8.91	35.70	253.40	0.04	18.5	8.8	11.9	0.10
15MTS-05a	4.59	185.5	55.4	0.79	12.02	11.06	395.69	0.15	16.5	17.9	22.8	0.21
15MTS-05b	1.60	114.0	41.7	0.71	18.75	29.89	611.49	0.06	28.6	10.9	15.3	0.13
15MTS-05c*	2.14	112.6	48.6	0.75	5.28	9.08	306.28	0.08	8.8	39.0	52.2	0.44
15MTS-05d	2.08	116.6	47.0	0.74	13.73	19.27	521.84	0.06	20.7	11.6	15.7	0.14
15MTS-05e	2.63	162.5	44.8	0.74	29.27	40.54	583.97	0.17	41.5	13.6	18.4	0.16
15MTS-05f	3.22	155.0	50.8	0.77	10.11	16.01	460.60	0.09	16.0	16.4	21.4	0.20
15MTS-05g*	2.05	118.4	46.4	0.74	11.71	27.56	257.65	0.13	19.4	28.4	38.5	0.32
15MTS-06a	3.32	110.9	61.0	0.79	16.98	61.42	74.10	0.12	31.7	9.5	12.1	0.10

TABLE A2. INDIVIDUAL GRAIN RESULTS FOR APATITE (U-TH-SM)/HE AND ZIRCON (U-TH)/HE SAMPLES

Sample	Mass (µg)	Length (µm)	Radius (µm)	FT	U (ppm)	Th (ppm)	Sm (ppm)	He (ncc)	eU (ppm)	Raw date (Ma)	Corr. date (Ma)	Error (Ma)
15MTS-06b	2.20	115.7	48.6	0.75	32.60	31.54	33.65	0.08	40.1	7.6	10.1	0.09
15MTS-06c	1.75	125.0	41.7	0.72	27.33	130.15	132.49	0.09	58.4	7.2	10.1	0.08
15MTS-06d	3.54	179.8	49.5	0.76	20.03	57.78	55.79	0.11	33.8	7.3	9.6	0.08
15MTS-06e	3.53	197.9	47.0	0.76	21.10	75.88	86.78	0.14	39.3	8.0	10.6	0.09
Mount Princeton Transect (B) apatite grains												
15MTP-01a	1.94	147.6	40.4	0.71	24.16	100.45	204.18	0.02	48.6	1.4	2.0	0.02
15MTP-01b	1.84	91.0	50.1	0.74	11.66	32.37	57.92	0.01	19.5	1.8	2.4	0.03
15MTP-01c	1.77	80.4	52.3	0.75	21.58	59.96	97.29	0.01	36.1	1.6	2.1	0.02
15MTP-01e	1.76	139.6	39.5	0.71	24.36	110.46	231.65	0.02	51.3	1.6	2.2	0.02
15MTP-02a	2.45	162.6	43.3	0.73	17.23	36.52	88.94	0.03	26.2	3.0	4.1	0.04
15MTP-02b	3.05	149.3	50.4	0.76	22.91	37.26	78.82	0.03	32.0	2.1	2.8	0.03
15MTP-02c	1.76	129.4	41.1	0.71	30.70	44.49	58.09	0.02	41.4	2.2	3.1	0.03
15MTP-02d	3.38	182.4	47.9	0.76	12.55	29.13	75.61	0.02	19.7	2.2	2.9	0.03
15MTP-02e	2.28	115.7	49.5	0.75	15.73	39.84	64.70	0.01	25.4	1.7	2.3	0.02
15MTP-03a	1.80	137.0	40.4	0.71	8.76	31.94	158.77	0.02	17.0	4.1	5.7	0.08
15MTP-03b	1.47	91.0	44.8	0.72	14.10	18.98	56.39	0.02	18.8	6.8	9.5	0.08
15MTP-03c	2.57	133.8	48.8	0.75	12.28	16.27	51.72	0.03	16.3	6.0	8.0	0.08
15MTP-03d	2.86	115.3	55.5	0.77	4.25	5.67	23.75	0.01	5.7	5.2	6.8	0.08
15MTP-03e	2.07	164.3	39.5	0.71	9.23	33.15	146.58	0.02	17.7	3.5	4.9	0.06
15MTP-04a	1.40	84.0	45.5	0.72	4.77	19.98	47.96	0.01	9.7	4.9	6.8	0.12
15MTP-04b	2.97	158.1	48.3	0.76	16.23	46.44	118.52	0.04	27.7	4.1	5.4	0.05
15MTP-04c	2.16	109.6	49.5	0.75	2.62	15.60	38.39	0.01	6.4	4.0	5.4	0.17
15MTP-04d	2.12	130.7	44.8	0.73	9.62	29.86	90.49	0.03	17.0	5.6	7.7	0.07
15MTP-05a	1.55	104.7	42.8	0.72	39.61	57.01	96.01	0.08	53.4	7.8	10.9	0.09
15MTP-05b	1.51	115.7	40.2	0.70	44.24	72.60	147.34	0.13	61.9	11.7	16.6	0.13

TABLE A2. INDIVIDUAL GRAIN RESULTS FOR APATITE AND ZIRCON (U-TH-SM)/HE SAMPLES

Sample	Mass (µg)	Length (µm)	Radius (µm)	FT	U (ppm)	Th (ppm)	Sm (ppm)	He (ncc)	eU (ppm)	Raw date (Ma)	Corr. date (Ma)	Error (Ma)
15MTP-05c*	2.14	128.2	45.5	0.74	4.36	14.52	49.40	0.05	8.0	25.7	34.8	0.29
15MTP-05d	1.79	88.3	50.1	0.74	13.97	43.06	151.58	0.06	24.8	10.9	14.7	0.13
15MTP-05e	2.69	129.5	50.8	0.76	37.10	68.02	168.14	0.10	53.8	5.6	7.4	0.07
15MTP-05f	2.32	118.8	49.2	0.75	25.84	46.92	189.99	0.07	37.7	6.1	8.1	0.08
15MTP-05g	2.87	165.6	46.4	0.75	30.77	46.51	144.69	0.17	42.3	11.7	15.6	0.13
Mount Princeton Transect (B) zircon grains												
15MTP-01 Zra	4.19	207.2	50.1	0.77	687.95	451.09	0.00	6.01	793.5	14.9	19.4	0.19
15MTP-01 Zrb	3.09	173.6	47.0	0.75	603.83	569.44	0.00	4.43	737.1	16.0	21.3	0.20
15MTP-01 Zrc	3.03	174.9	46.4	0.75	828.82	490.77	0.00	5.52	943.7	15.9	21.2	0.20
Middle Cottonwood Creek individual samples (1 and 2)												
17MCWD-01a	6.61	167.4	70.0	0.82	11.31	0.91	406.42	0.22	13.4	22.9	27.9	0.32
17MCWD-01b	3.88	118.4	63.8	0.80	48.35	1.47	491.37	0.40	51.0	17.1	21.5	0.24
17MCWD-01c	4.55	182.4	55.7	0.79	9.00	0.84	220.65	0.13	10.2	24.9	31.7	0.35
17MCWD-01d	4.18	159.9	57.0	0.79	5.96	0.68	308.96	0.06	7.6	18.4	23.4	0.26
17MCWD-01e	5.92	167.4	66.3	0.81	8.54	0.43	233.48	0.11	9.7	16.8	20.7	0.24
17MCWD-02a	4.31	212.9	50.1	0.77	13.65	54.33	79.82	0.07	26.7	5.2	6.8	0.06
17MCWD-02b	5.74	214.7	57.6	0.80	28.95	127.48	158.19	0.22	59.5	5.3	6.7	0.05
17MCWD-02c	4.26	216.0	49.5	0.77	20.04	54.81	59.61	0.09	33.1	5.4	7.1	0.06
17MCWD-02d	2.25	108.2	50.8	0.75	34.06	122.61	129.45	0.13	63.4	7.5	9.9	0.08
17MCWD-02e	3.35	135.2	55.4	0.78	23.08	97.37	170.25	0.12	46.7	6.4	8.2	0.07
Mount Columbia Transect (C) and individual samples (detrital)												
15MTC-03a	2.90	108.2	57.6	0.78	3.66	0.49	151.73	0.02	4.5	15.0	19.3	0.22
15MTC-03b	1.71	89.2	48.8	0.74	7.37	0.53	188.94	0.03	8.4	19.3	26.2	0.33
15MTC-03c*	3.06	155.5	49.5	0.76	9.17	0.79	148.97	0.15	10.1	41.5	54.5	0.59
15MTC-03d	2.80	115.7	54.8	0.77	6.28	0.40	171.54	0.04	7.2	19.3	25.0	0.29
15MTC-03f	2.41	118.8	50.1	0.75	7.03	4.03	180.86	0.04	8.8	17.2	22.7	0.26

TABLE A2. INDIVIDUAL GRAIN RESULTS FOR APATITE AND ZIRCON (U-TH-SM)/HE SAMPLES

Sample	Mass (µg)	Length (µm)	Radius (µm)	FT	U (ppm)	Th (ppm)	Sm (ppm)	He (ncc)	eU (ppm)	Raw date (Ma)	Corr. date (Ma)	Error (Ma)
15MTC-03g	3.93	187.3	51.0	0.77	4.09	3.40	138.63	0.03	5.5	12.6	16.3	0.18
15MTC-03h	1.57	97.2	44.8	0.72	7.89	5.81	197.52	0.02	10.2	11.5	15.9	0.21
15MTC-04a	1.99	159.9	39.3	0.71	29.19	1.39	314.86	0.16	31.0	22.0	31.0	0.32
15MTC-04b	4.69	205.4	53.2	0.78	42.02	1.33	299.15	0.70	43.7	28.8	36.8	0.41
15MTC-04c	4.16	182.4	53.2	0.78	11.27	0.19	151.86	0.11	12.0	18.0	23.1	0.26
15MTC-04d	2.27	126.3	47.3	0.74	76.59	1.31	503.37	0.53	79.3	25.0	33.5	0.35
15MTC-05a	2.32	133.9	46.4	0.74	20.83	18.38	124.06	0.17	25.7	23.4	31.5	0.30
15MTC-05b	1.41	108.2	40.2	0.70	9.60	15.60	150.50	0.06	14.0	23.4	33.3	0.30
15MTC-05c	1.70	94.5	47.3	0.73	3.52	4.26	236.90	0.02	5.6	21.7	29.6	0.44
15MTC-05d	2.37	136.9	46.4	0.74	26.99	20.03	129.42	0.20	32.3	21.5	29.0	0.28
15MTC-05e	2.14	147.6	42.4	0.73	60.79	48.54	239.77	0.46	73.3	24.2	33.3	0.31
17NCWD-MRa	2.27	131.3	46.4	0.74	11.56	32.34	128.99	0.06	19.7	10.0	13.5	0.11
17NCWD-MRb	5.20	208.5	55.7	0.79	30.68	7.79	107.26	0.24	33.0	11.5	14.5	0.16
17NCWD-MRc	2.21	94.5	53.9	0.76	25.49	13.34	266.98	0.07	29.9	9.3	12.3	0.13
17NCWD-MRd	3.21	149.3	51.7	0.77	14.13	9.68	188.20	0.11	17.3	17.3	22.6	0.22
17NCWD-MRe	4.04	163.0	55.5	0.78	64.81	18.43	364.84	0.56	70.8	16.3	20.9	0.22
17NCWD-MRf	5.87	211.1	58.7	0.80	10.93	34.81	139.70	0.37	19.7	27.1	33.8	0.27
17NCWD-MRg	3.25	103.4	62.5	0.79	24.57	15.22	93.97	0.16	28.6	14.5	18.4	0.19
17NCWD-MRh	6.15	163.0	68.5	0.82	10.81	13.39	177.97	0.39	14.8	36.5	44.6	0.42
17NCWD-MRi	3.05	129.4	54.1	0.77	7.20	5.80	312.72	0.09	10.0	25.9	33.5	0.32
17NCWD-MRj	2.61	114.4	53.2	0.76	9.60	6.25	79.09	0.07	11.4	19.4	25.3	0.25
Mount Belford Transect (D) and individual sample (3) apatite grains												
14MTB-01a	2.27	140.5	44.8	0.74	22.23	11.25	215.77	0.03	25.9	4.7	6.4	0.07
14MTB-01b	2.75	135.6	50.1	0.76	55.20	19.38	324.15	0.10	61.3	5.2	6.8	0.07
14MTB-01c	4.68	174.9	57.6	0.79	26.87	11.59	174.65	0.10	30.4	5.8	7.3	0.08

TABLE A2. INDIVIDUAL GRAIN RESULTS FOR APATITE AND ZIRCON (U-TH-SM)/HE SAMPLES

Sample	Mass (µg)	Length (µm)	Radius (µm)	FT	U (ppm)	Th (ppm)	Sm (ppm)	He (ncc)	eU (ppm)	Raw date (Ma)	Corr. date (Ma)	Error (Ma)
14MTB-01d	3.76	142.7	57.2	0.79	20.22	7.28	224.91	0.07	23.0	6.7	8.5	0.09
14MTB-02a	3.14	144.9	51.9	0.77	3.85	9.26	102.16	0.01	6.5	4.0	5.2	0.07
14MTB-02d	1.73	103.9	45.5	0.73	5.36	14.19	173.57	0.01	9.5	4.9	6.7	0.11
14MTB-02e	2.44	155.0	44.2	0.74	3.87	14.96	148.00	0.01	8.1	4.5	6.1	0.08
14MTB-02f*	2.47	125.0	49.5	0.75	3.25	6.62	80.37	0.03	5.2	16.9	22.4	0.23
14MTB-02g	2.74	144.0	48.6	0.75	4.27	5.78	77.72	0.01	6.0	4.1	5.4	0.12
14MTB-02h	4.08	173.1	54.1	0.78	4.19	12.93	166.97	0.02	8.0	4.0	5.1	0.07
14MTB-03a	3.30	140.0	54.1	0.77	28.81	4.15	224.43	0.07	30.8	5.4	7.0	0.08
14MTB-03b	2.79	118.4	54.1	0.77	28.58	3.03	208.96	0.05	30.3	5.3	6.9	0.08
14MTB-03c	2.20	150.6	42.6	0.73	61.09	10.50	265.19	0.08	64.8	4.6	6.4	0.07
14MTB-03d	5.08	174.9	60.1	0.80	10.95	0.95	139.23	0.04	11.8	5.5	6.8	0.09
14MTB-04a	2.15	82.2	57.0	0.76	2.53	11.70	148.21	0.01	6.0	5.3	6.9	0.10
14MTB-04b	2.97	150.6	49.5	0.76	5.02	19.83	161.20	0.02	10.4	3.7	4.9	0.06
14MTB-04c	2.98	123.2	54.8	0.77	7.39	10.15	86.01	0.02	10.2	4.1	5.4	0.07
14MTB-04d	1.90	112.7	45.7	0.73	7.51	13.83	87.87	0.01	11.2	3.7	5.1	0.08
14MTB-04aa	1.45	102.0	42.0	0.71	45.29	24.62	258.34	0.05	52.3	5.0	7.0	0.07
14MTB-04ab	2.31	114.0	50.1	0.75	36.12	15.82	334.84	0.10	41.4	9.0	11.9	0.12
14MTB-04ac	1.66	121.5	41.2	0.71	50.25	25.24	377.58	0.06	57.9	4.8	6.7	0.06
14MTB-04ad	3.07	91.0	64.7	0.79	33.08	17.61	262.51	0.09	38.4	6.1	7.8	0.08
14MTB-05a	2.92	135.6	51.7	0.76	23.46	29.63	204.62	0.08	31.4	6.8	8.8	0.08
14MTB-05b	3.12	173.1	47.3	0.75	14.01	13.75	185.24	0.05	18.1	6.7	8.9	0.10
14MTB-05c*	1.79	126.3	42.0	0.72	7.85	11.24	205.87	0.05	11.4	21.7	30.3	0.26
14MTB-05d	3.34	146.2	53.2	0.77	4.58	4.60	97.34	0.02	6.1	8.8	11.4	0.12
14MTB-05e	1.49	87.0	46.1	0.72	4.91	7.03	116.29	0.01	7.1	5.0	6.9	0.13
14MTB-05f	1.25	95.8	40.2	0.70	13.05	20.78	140.08	0.02	18.6	5.9	8.4	0.11

TABLE A2. INDIVIDUAL GRAIN RESULTS FOR APATITE AND ZIRCON (U-TH-SM)/HE SAMPLES

Sample	Mass (µg)	Length (µm)	Radius (µm)	FT	U (ppm)	Th (ppm)	Sm (ppm)	He (ncc)	eU (ppm)	Raw date (Ma)	Corr. date (Ma)	Error (Ma)
17CCKRa	6.19	188.6	63.8	0.81	27.28	21.37	238.19	0.88	33.4	36.0	44.4	0.44
17CCKRb	3.01	121.5	55.4	0.77	18.14	7.87	277.38	0.21	21.3	28.1	36.3	0.36
17CCKRc	5.96	220.8	57.9	0.80	71.91	56.64	478.94	1.96	87.4	31.6	39.6	0.39
17CCKRd	5.83	194.8	61.0	0.80	28.00	26.29	272.94	0.76	35.4	30.9	38.5	0.37
17CCKRe	5.73	123.2	76.0	0.82	30.61	9.68	463.35	0.73	35.1	31.4	38.2	0.41
Mount Belford Transect (D) zircon grains												
14MTB-01 Zra	4.46	220.4	50.1	0.77	327.73	123.52	0.00	5.50	356.6	28.5	37.0	0.44
14MTB-01 Zrb	3.10	191.7	44.8	0.74	573.47	131.50	0.00	5.46	604.2	24.1	32.3	0.34
14MTB-01 Zrc	11.97	345.4	65.6	0.83	679.06	108.25	0.00	26.89	704.4	26.4	31.9	0.39
Mount Elbert Transect (E)												
14MTE-01a	3.70	182.9	50.1	0.77	15.20	34.15	156.52	0.11	23.9	10.7	14.0	0.12
14MTE-01b	2.80	193.0	42.4	0.73	14.12	57.82	126.94	0.06	28.2	6.5	8.9	0.07
14MTE-01c	1.42	100.3	42.0	0.71	11.62	45.13	137.16	0.03	22.8	7.6	10.7	0.11
14MTE-01d	2.08	120.1	46.4	0.74	11.61	23.66	107.72	0.04	17.7	9.2	12.4	0.12
14MTE-02a	1.90	117.5	44.8	0.73	43.79	3.12	535.41	0.24	47.0	22.6	31.0	0.32
14MTE-02b*	2.08	120.1	46.4	0.74	51.84	1.82	437.26	0.67	54.3	49.9	67.6	0.71
14MTE-02c	2.34	144.5	44.9	0.74	63.38	3.43	639.66	0.41	67.2	22.1	29.9	0.31
14MTE-02d	3.88	104.7	67.8	0.80	46.96	3.24	541.34	0.61	50.3	26.8	33.5	0.38
14MTE-02e	2.58	123.3	51.0	0.76	47.56	1.79	453.08	0.36	50.1	23.8	31.3	0.34
14MTE-02f	2.34	126.4	47.9	0.75	60.20	2.80	619.59	0.47	63.8	26.9	36.0	0.38
14MTE-05a	2.20	123.3	47.1	0.74	40.83	4.74	556.65	0.25	44.6	22.0	29.7	0.30
14MTE-05b	1.44	109.6	40.4	0.70	26.34	7.39	495.55	0.10	30.4	19.7	28.0	0.27
14MTE-05c	1.60	101.6	44.2	0.72	29.24	7.23	597.62	0.13	33.7	20.9	29.0	0.28
14MTE-05d	1.86	143.1	40.2	0.71	41.61	5.02	611.59	0.20	45.7	20.3	28.5	0.28

TABLE A2. INDIVIDUAL GRAIN RESULTS FOR APATITE AND ZIRCON (U-TH-SM)/HE SAMPLES

Sample	Mass (µg)	Length (µm)	Radius (µm)	FT	U (ppm)	Th (ppm)	Sm (ppm)	He (ncc)	eU (ppm)	Raw date (Ma)	Corr. date (Ma)	Error (Ma)
Galena Mountain Transect (F)												
15GAM-01a	5.91	163.9	66.9	0.81	2.18	10.43	313.06	0.18	6.1	49.7	61.0	0.50
15GAM-01b	2.80	109.6	56.3	0.77	1.57	3.22	71.90	0.07	2.7	88.5	114.5	1.18
15GAM-01c*	7.21	162.5	74.2	0.83	4.52	9.89	356.78	2.12	8.5	326.0	393.0	3.35
15GAM-01d	1.40	107.8	40.2	0.70	54.94	9.50	194.00	0.52	58.1	53.1	75.7	0.74
15GAM-02a*	4.98	141.8	66.1	0.81	2.82	12.09	274.86	0.31	6.9	85.5	105.7	0.83
15GAM-02b	6.32	196.7	63.2	0.81	2.22	8.09	223.19	0.12	5.2	35.0	43.2	0.62
15GAM-02c	2.50	144.5	46.4	0.74	2.07	15.07	317.06	0.06	7.1	32.5	43.6	0.37
15GAM-02d	7.63	211.6	66.9	0.82	4.24	14.14	366.71	0.28	9.3	37.0	45.1	0.36
15GAM-03a	2.74	97.2	59.2	0.78	2.58	19.52	337.16	0.25	8.7	98.6	127.0	1.14
15GAM-03b	5.48	228.4	54.6	0.79	2.33	13.35	388.83	0.30	7.3	73.9	93.8	0.72
15GAM-03c	5.50	99.0	83.1	0.83	1.79	8.97	305.90	0.13	5.3	46.4	56.1	0.50
15GAM-03d	2.07	152.0	41.1	0.72	2.98	20.50	338.10	0.15	9.4	72.0	100.2	1.37
5GAM-03e	5.82	158.1	67.6	0.82	2.48	11.67	384.30	0.19	7.0	46.0	56.5	0.45
15GAM-04a	1.23	81.3	43.3	0.71	24.81	8.47	224.33	0.23	27.8	55.5	78.5	0.75
15GAM-04b	3.90	144.4	57.9	0.79	9.60	4.68	178.54	0.20	11.5	37.8	48.0	0.59
15GAM-04c	2.53	128.1	49.5	0.75	16.52	4.49	165.16	0.21	18.3	39.1	51.9	0.55
15GAM-04d	5.50	183.8	61.0	0.80	2.10	11.21	314.76	0.28	6.2	81.9	102.0	0.81
15GAM-05a	1.76	121.5	42.4	0.72	20.67	0.89	136.38	0.11	21.5	24.1	33.5	0.35
15GAM-05b	5.16	130.8	70.0	0.81	17.36	0.27	84.96	0.35	17.8	31.6	38.8	0.45
15GAM-05c	2.19	126.3	46.4	0.74	7.26	0.35	124.32	0.06	7.9	28.3	38.2	0.41
15GAM-05d	1.47	117.1	39.5	0.70	34.33	0.83	173.70	0.22	35.3	34.7	49.5	0.51

* Failed Q-Test (Dean and Dixon, 1951) or two extreme outlier test (Boddy and Smith, 2010), not used in mean age calculation or any other data analysis or interpretations. 9 out of 163 grains were discarded.

Figure A1: Map of all published low-temperature thermochronometry around the northern Rio Grande rift including the San Luis valley, upper Arkansas River valley and Blue River valley (this study; Bryant and Naeser, 1980; Lindsey et al., 1986; Shannon 1988; Kelley et al., 1992; Robbins, 2005; Naeser et al., 2002; Klein et al., 2010; Landman and Flowers, 2013; Ricketts et al., 2016; Abbey et al., 2017). Generalized faults from Quaternary faults database (U.S Geological Survey, 2006). Inset shows general fault systems for the entire Rio Grande rift with a red box outlining the region we define as the northern Rio Grande rift.

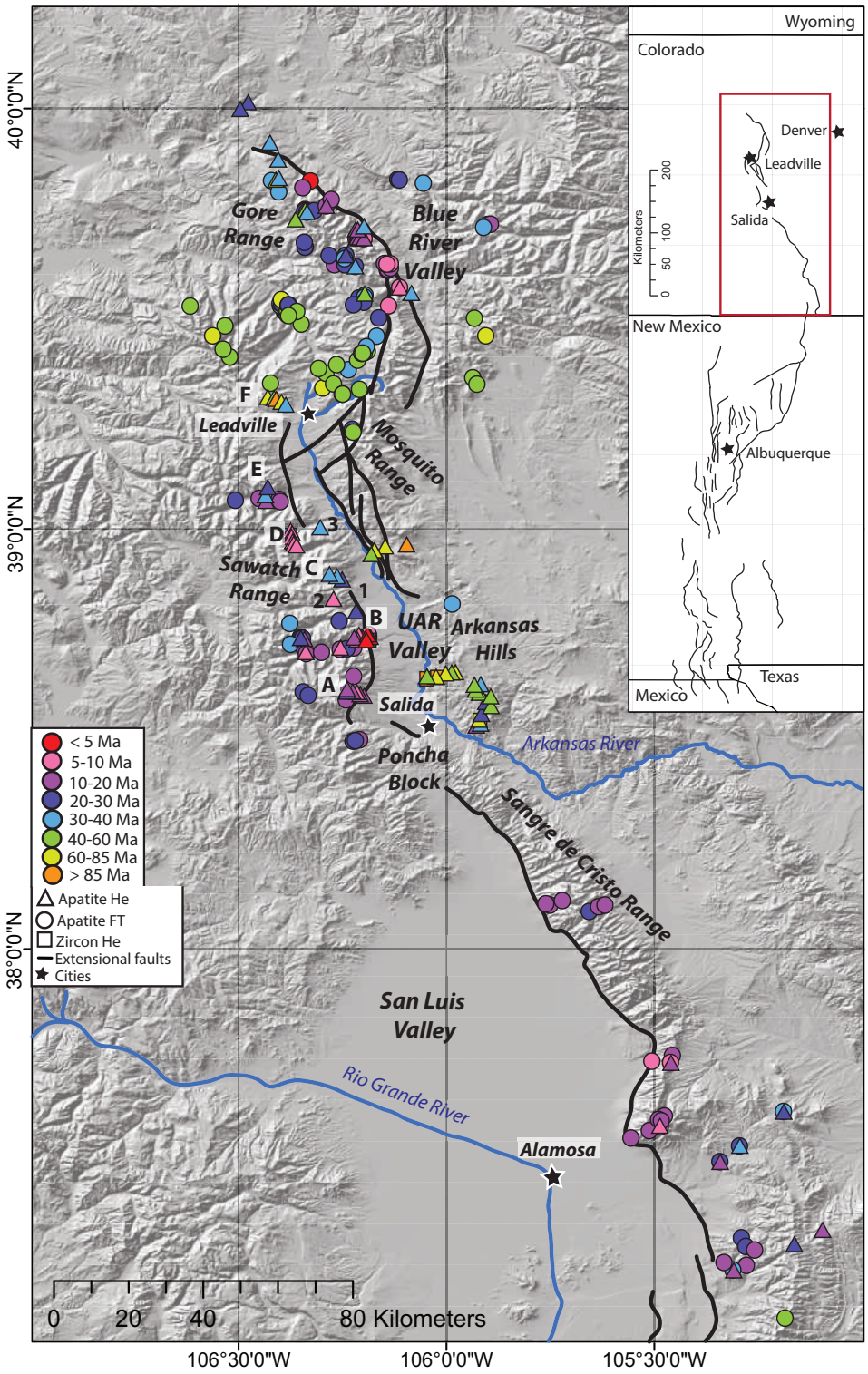

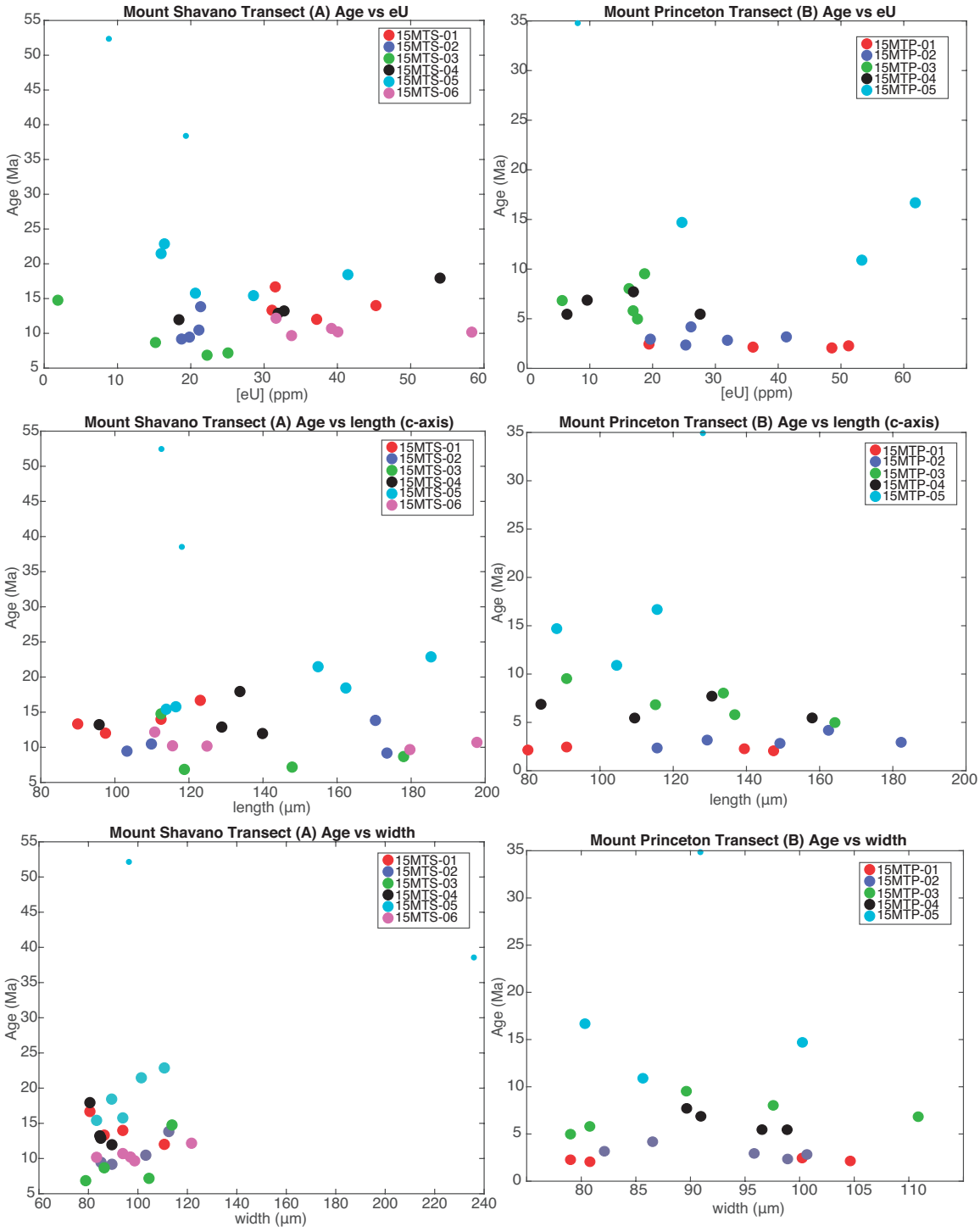

Figure A2: Scatter plots of age-eU and age-grain size relationships for new analyses presented here. Colors indicate data from one sample where each circle is data from an individual grain. The smaller circles represent the few grains that were discarded as outliers using Dean and Dixon (1951) Q-test or Boddy and Smith (2010) test for two extreme outliers. These outliers are marked in Table A2. Samples from transects A and B.

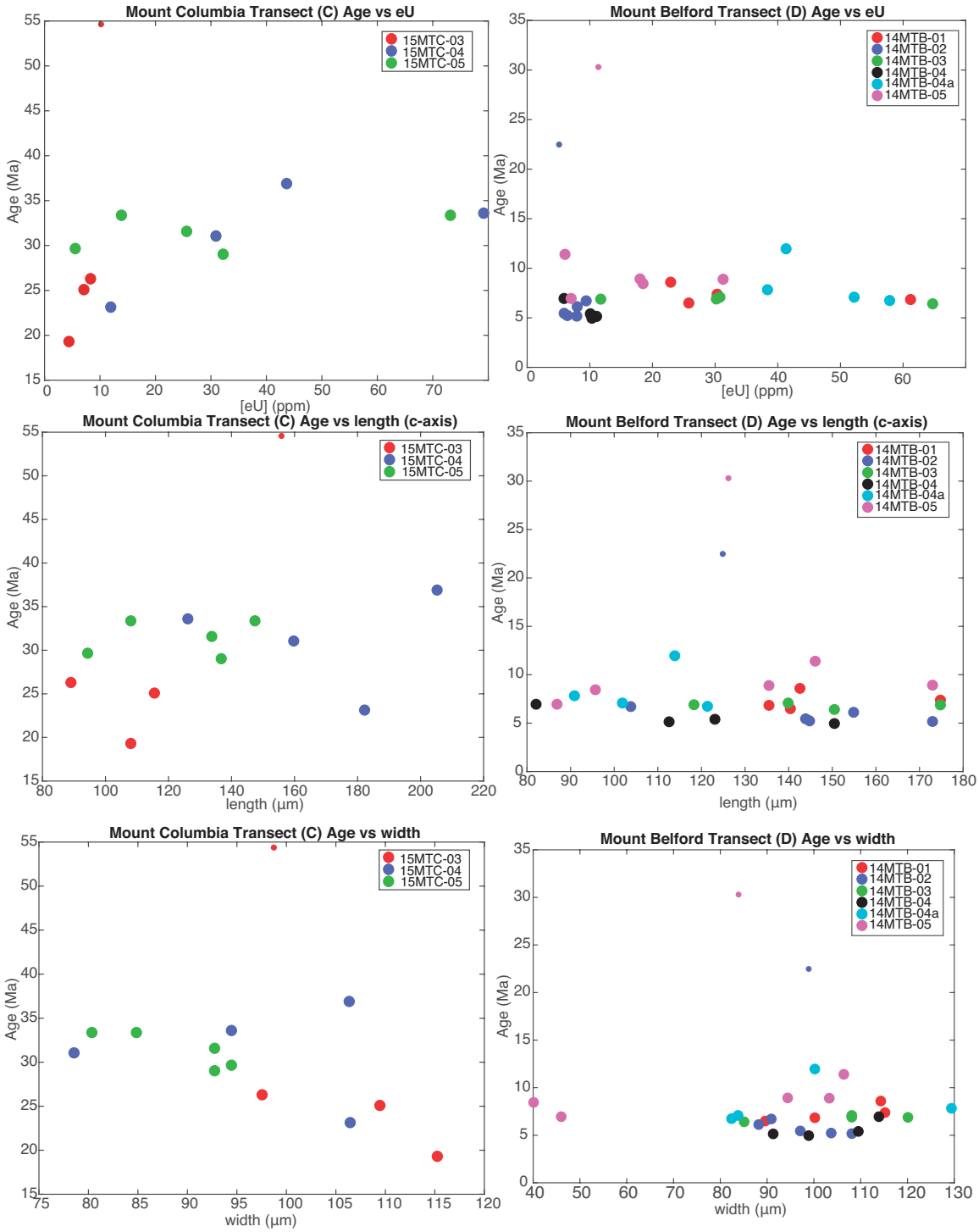

Figure A2 continued: Samples from transects C and D.

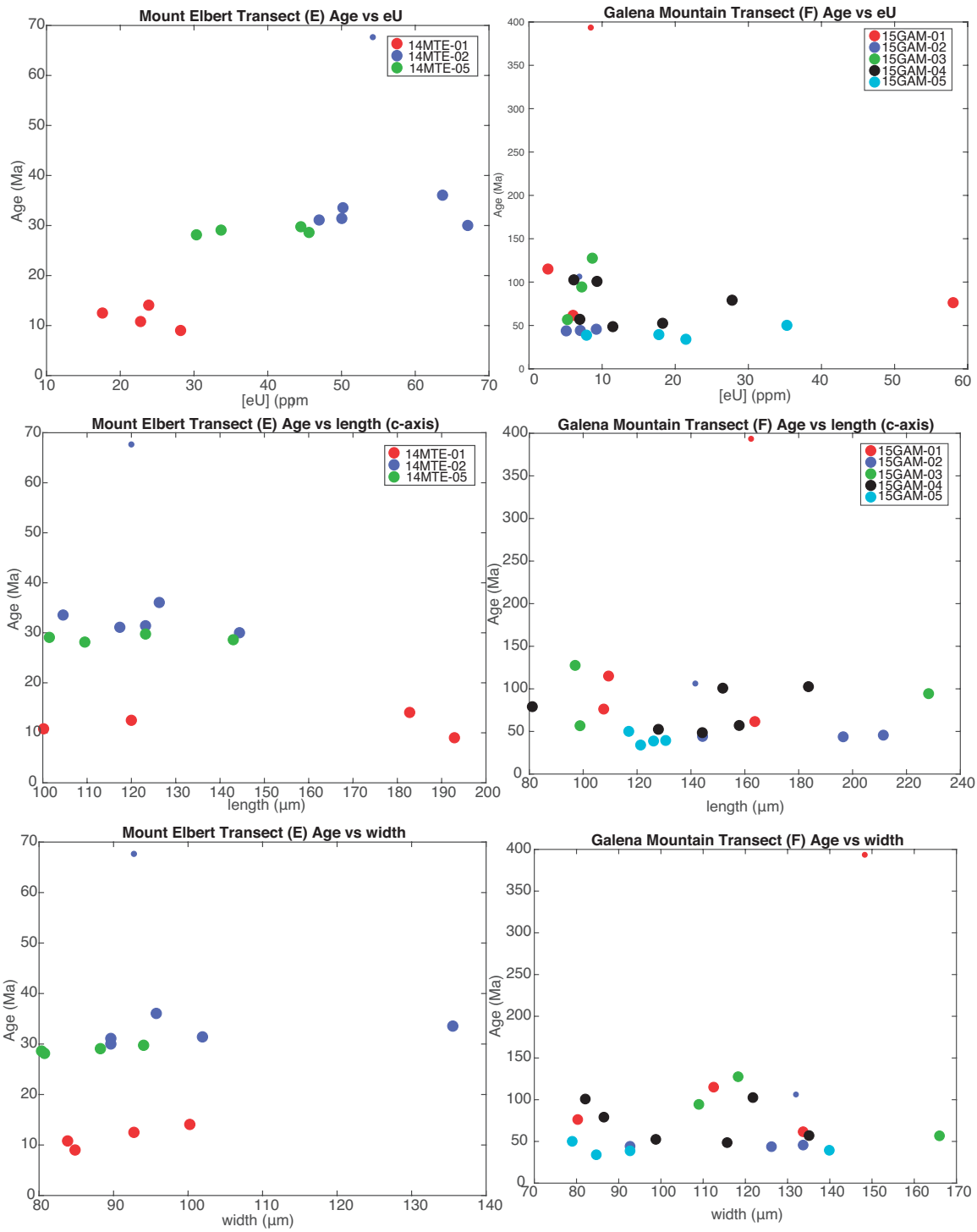

Figure A2 continued: Samples from transects E and F.

Caution must be taken when assigning elevations (extrapolated to depths) to samples that have been exhumed by normal faulting as they will likely have experienced tilting and therefore may be spatially re-oriented (Stockli et al., 2000; Stockli et al., 2003; Curry et al., 2016). Therefore, we project the location of our samples and those from other published studies proximal to our samples onto the fault plane on which they were exhumed as a reference for how samples were most-likely spatially oriented prior to exhumation and erosion.

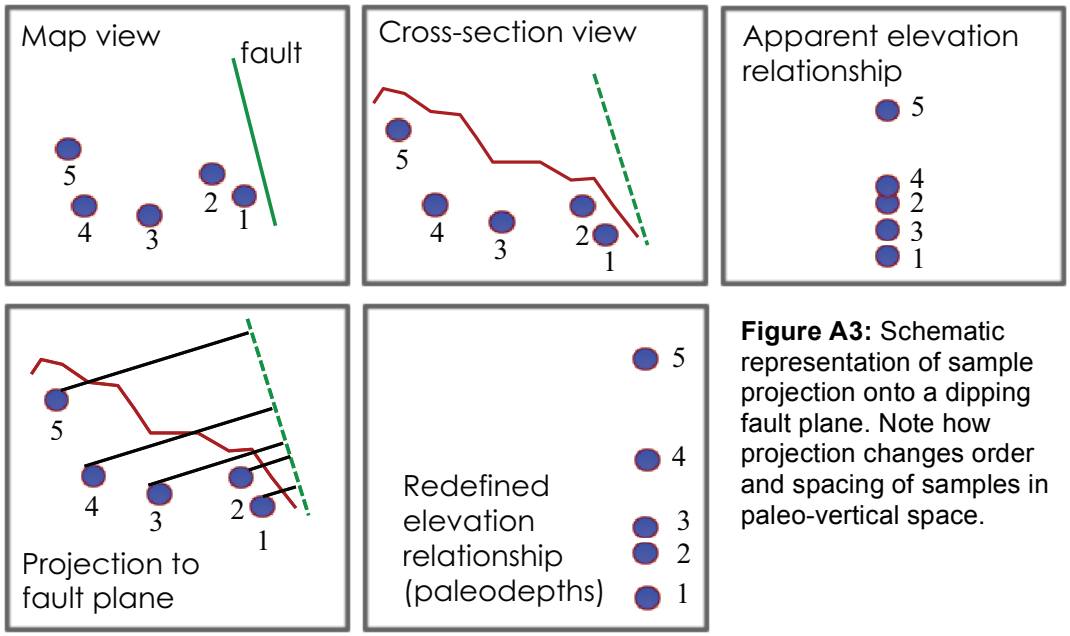

Figure A3: Schematic representation of sample projection onto a dipping fault plane. Note how projection changes order and spacing of samples in paleo-vertical space.

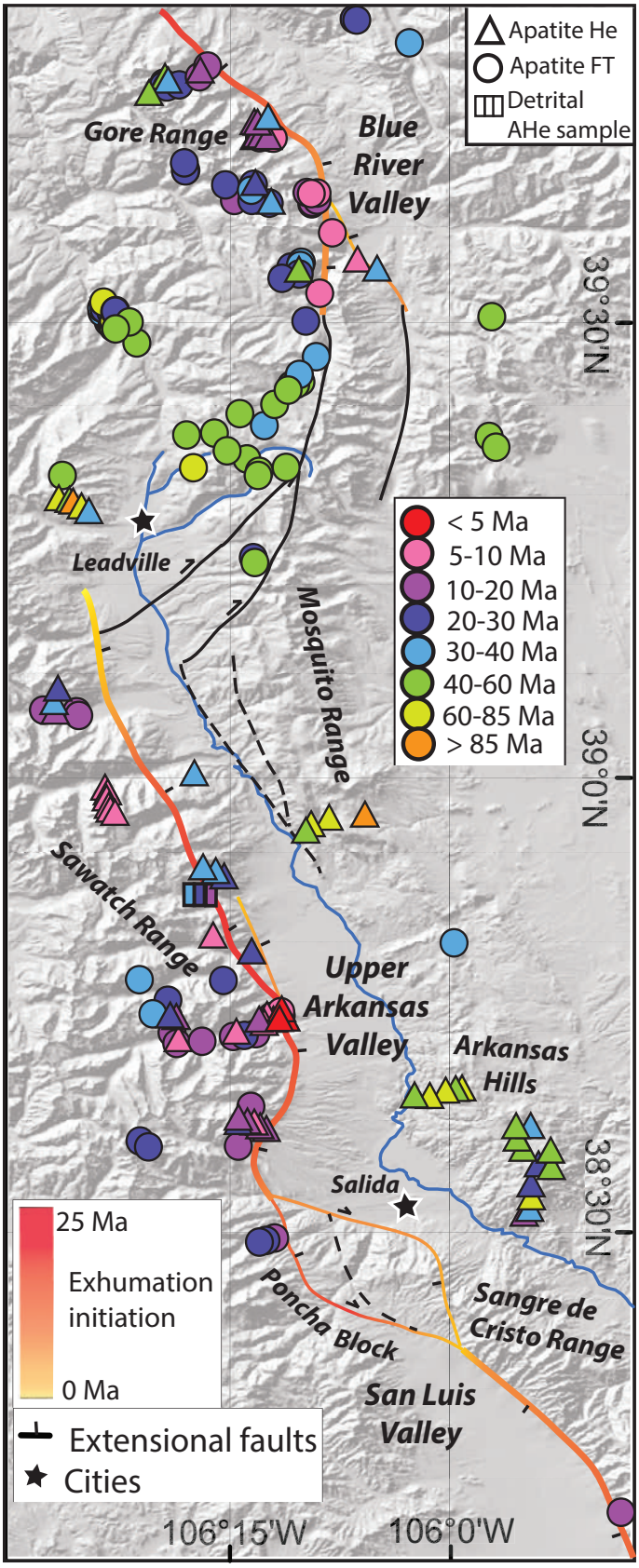

Figure A4: Map of all published low-temperature thermochronometry around the northern Rio Grande rift including the northern San Luis valley, upper Arkansas River valley, and southern Blue River valley (this study; Bryant and Naeser, 1980; Lindsey et al., 1986; Shannon 1988; Kelley et al., 1992; Robbins, 2005; Naeser et al., 2002; Klein et al., 2010; Landman and Flowers, 2013; Ricketts et al., 2016; Abbey et al., 2017). New fault geometry and exhumation story for the upper Arkansas River fault system (i.e. Sawatch Range Fault) and linkage between accommodation zones to connect with the Sangre de Cristo and Gore Range faults in the south and north respectively.

Low-temperature thermochronometry analysis

Samples were processed using standard mineral separation practices with details describing this and the analytical procedure described in Abbey et al. (2017) and Niemi and Clark (2017). Individual apatite and zircon grains were hand-selected and screened for zoning and inclusions prior to outgassing on an Alphachron Helium Instrument at the University of Michigan. Ages reported are averages based on multiple (3–7) individual replicate analyses from each sample. Average ages for apatite or zircon samples were interpreted from samples with at least three or two inclusion-free grains, respectively. All grains analyzed were >80 μm in both length and width (Table A2). Analyses of U, Th, and Sm from the apatite and zircon grains were performed at the University of Arizona following the methods outlined in Reiners and Nicolescu (2006).

Thermal History Modeling: Explanation and Constraints

The following is a detailed description of constraints and inputs for each inverse thermal history model. Imposed thermal constraints include a present-day temperature of 7 °C ± 3 °C. We chose this because the mean annual temperature (MAT) near Salida, CO is 7 °C and the ± 3 °C was chosen arbitrarily as a value that would allow for small variation in the possible present-day temperatures of the samples and still keep them near the MAT of the field area. We realize this does not encompass the full range of present-day temperatures, which our samples are exposed to (for example winter and summer temperatures vary much more than an average of ± 3 °C). However, changing the present day temperature has little to no effect on the thermal history models out-put since the temperatures never come close to temperatures in the AHe sensitivity range. We also choose 30 ± 1 °C/km for our geothermal gradient as this is a reasonable estimate for the

geothermal gradient in central Colorado near the rift (Nathenson and Guffanti, 1988). QTQt allows the user to choose whether or not the geothermal gradient can vary through time or not. We hold the geothermal gradient constant in these models to address changes in timing, magnitudes, and rates of exhumation on fault segments. Exploring a range of geothermal gradients between 20 and 40°C/km does not change the general form of each thermal history model. The primary difference in thermal history models with different geothermal gradients is the inferred depth from which the rocks are exhuming. Thus, we choose to tightly constrain the geothermal gradient because we are evaluating relative differences in timing and rates of exhumation and we find that a 30°C/km geothermal gradient is reasonable for such a comparison.

Each model we run with 20,000 burn-in iterations and 80,000 post-burn-in iterations, with no other added constraints.

Below we include all of the data files used in each of the thermal history models for all of our transects in the UAR.

Mount Shavano Transect (A) inverse thermal history modeling included samples: 15MTS-01, 15MTS-02, 15MTS-03, 15MTS-04, 15MTS-05,15MTS-06 (this study), 84-300_Tag, 84-280_Tnfg (Shannon, 1988)

```
15MTS-01
0.0 0.0 0.0
0 0 0 0.000000 0.000000 0.000000
105
0 2.000000 0.000000
1 16.300000
-1
0
1
0.000000 0
0.000000 0
0.000000 0
4
2
0.0700 24.670019.5600 500.4200 11.8000 -0.1600 123.2000 80.8000 80.8000
A 19.27 6.071400e-05 122300 2 2 0
0.1100 35.8800 29.5800 537.7100 10.3000 -0.1300 112.6000 94.1000 94.1000
A 19.33 6.071400e-05 122300 2 2 0
0.0500 23.4300 22.0400 545.8200 9.4000 -0.1200 90.1000 86.6000 86.6000
A 19.32 6.071400e-05 122300 2 2 0
0.1000 28.9600 22.7000 632.0900 9.1000 -0.1200 97.6000 110.9000 110.9000
A 19.25 6.071400e-05 122300 2 2 0
```

```
15MTS-02
0.000000 0.000000 495.000000
0 0 0 0.000000 0.000000 0.000000
105
0 2.000000 0.000000
1 16.300000
-1
0
1
0.000000 0
0.000000 0
0.000000 0
4
2
0.1200 18.4000 8.3200 224.9400 10.8000 -0.1400 170.5000 112.7000 112.7000
A 19.13 6.071400e-05 122300 2 2 0
0.0500 18.2800 7.3900 247.9400 7.9000 -0.1100 110.0000 103.4000 103.4000
A 19.09 6.071400e-05 122300 2 2 0
0.0300 16.5800 10.1900 196.2500 6.7000 -0.1200 103.4000 85.3000 85.3000
A 19.23 6.071400e-05 122300 2 2 0
0.0400 16.4800 5.0700 242.3300 6.8000 -0.0900 173.6000 89.7000 89.7000
A 19.01 6.071400e-05 122300 2 2 0
```

```
15MTS-03
0.000000 0.000000 977.000000
0 0 0 0.000000 0.000000 0.000000
105
0 2.000000 0.000000
1 16.300000
-1
0
1
0.000000 0
0.000000 0
0.000000 0
4
2
0.0100 0.8200 4.5700 8.8400 11.4000 -0.2300 112.6000 114.0000 114.0000
A 20.74 6.071400e-05 122300 2 2 0
0.0300 8.0900 28.8000 88.9100 6.3000 -0.0700 178.1000 86.6000 86.6000
A 20.36 6.071400e-05 122300 2 2 0
0.0600 12.8500 50.4000 106.6200 5.5000 -0.0600 148.0000 104.7000 104.7000
A 20.46 6.071400e-05 122300 2 2 0
0.0200 11.2900 43.7200 162.7100 4.8000 -0.0700 118.9000 79.1000 79.1000
A 20.41 6.071400e-05 122300 2 2 0
```

```
15MTS-04
0.000000 0.000000 1539.000000
0 0 0 0.000000 0.000000 0.000000
105
0 2.000000 0.000000
1 16.300000
-1
0
1
0.000000 0
0.000000 0
0.000000 0
4
2
0.1500 29.6100 97.1600 368.2700 12.7000 -0.1400 133.9000 80.8000 80.8000
A 20.28 6.071400e-05 122300 2 2 0
0.0500 13.9100 74.6700 301.7900 9.3000 -0.1100 95.9000 84.8000 84.8000
A 20.66 6.071400e-05 122300 2 2 0
0.0700 18.4400 51.3500 323.9300 9.3000 -0.1000 129.0000 85.2000 85.2000
A 20.11 6.071400e-05 122300 2 2 0
0.0400 8.9100 35.7000 253.4000 8.8000 -0.1000 140.0000 89.7000 89.7000
A 20.36 6.071400e-05 122300 2 2 0
```

```
15MTS-05
0.000000 0.000000 2181.000000
0 0 0 0.000000 0.000000 0.000000
105
0 2.000000 0.000000
1 16.300000
-1
0
1
0.000000 0
0.000000 0
0.000000 0
5
2
0.1500 12.0200 11.0600 395.6900 17.9000 -0.2100 185.5000 110.9000 110.900
A 19.23 6.071400e-05 122300 2 2 0
0.0900 10.1100 16.0100 460.6000 16.4000 -0.2000 155.0000 101.6000 101.600
A 19.47 6.071400e-05 122300 2 2 0
0.1700 29.2700 40.5400 583.9700 13.6000 -0.1600 162.5000 89.6000 89.6000
A 19.57 6.071400e-05 122300 2 2 0
0.0600 13.7300 19.2700 521.8400 11.6000 -0.1400 116.6000 94.1000 94.1000
A 19.44 6.071400e-05 122300 2 2 0
0.0600 18.7500 29.8900 611.4900 10.9000 -0.1300 114.0000 83.5000 83.5000
A 19.57 6.071400e-05 122300 2 2 0
```

```
15MTS-06
0.000000 0.000000 2378.000000
0 0 0 0.000000 0.000000 0.000000
105
0 2.000000 0.000000
1 16.300000
-1
0
1
0.000000 0
0.000000 0
0.000000 0
5
2
0.1200 16.9800 61.4200 74.1000 9.5000 -0.1000 110.9000 121.9000 121.9000
A 20.41 6.071400e-05 122300 2 2 0
0.1400 21.1000 75.8800 86.7800 8.0000 -0.0900 197.9000 94.1000 94.1000
A 20.41 6.071400e-05 122300 2 2 0
0.0800 32.6000 31.5400 33.6500 7.6000 -0.0900 115.7000 97.2000 97.2000
A 19.52 6.071400e-05 122300 2 2 0
0.0900 27.3300 130.1500 132.4900 7.2000 -0.0800 125.0000 83.5000 83.5000
A 20.64 6.071400e-05 122300 2 2 0
0.1100 20.0300 57.7800 55.7900 7.3000 -0.0800 179.8000 98.9000 98.9000
A 20.24 6.071400e-05 122300 2 2 0
```

```
Tag
0 0 1110
0 0 200 340 122020 58.723
105
3 0.040 0.000
1 16.3
0
0
1
14.67 2.00
0.00 0
0.000 0
6 10.169
7 6.021
3 10.106
4 4.363
5.5 9.81
6 10.468
4 7.86
5.5 10.373
5.5 9.103
7.5 9.926
6 7.148
6 6.18
3 4.159
6.5 6.973
6.5 5.616
3.5 8.241
5 7.356
6 7.456
4 8.958
4.5 8.988
5 5.55
6.5 12.331
4 7.096
6 8.045
3.5 5.038
6 6.927...
...
5 9.929
8.5 7.664
4.5 7.84
5 7.771
5 6.281
3 6.253
4.5 6.167
7.5 6.973
5.5 8.262
8 7.714
4.5 11.397
6.5 4.897
7 6.732
4 7.161
5 7.693
3 4.628
3.5 9.277
5.5 6.283
4.5 12.51
7 8.665
5 7.682
4.5 7.5
4.5 7.61
4.5 6.314
6 8.884
4.5 7.226
4 5.432
5.5 11.846
4.5 7.303
6.5 6.874
5.5 9.69
4.5 7.127
5 8.975
5 7.434
5.5 7.908
7.5 5.799
3.5 11.478 ...
...
3.5 12.936
6.5 4.691
5 6.977
4 8.397
6.5 8.25
5.5 10.336
6.5 9.325
4.5 7.396
6.5 6.693
6.5 7.683
6 9.139
5 6.599
6.5 11.698
9.5 6.357
4.5 8.623
1.5 7.199
7 7.537
8 9.111
5.5 4.259
4.5 4.147
5 7.743
4.5 7.7
8.5 8.855
5 8.649
3 4.226
8.5 7.619
5.5 9.121
8 8.311
5.5 8.642
4.5 10.435
4.5 12.781
3.5 8.602
3 9.337
5 7.819
7 10.012
5 8.178
5 6.649
```

```
Tnfg
0 0 1379
0 0 200 340 125742 56.573
105
3 0.040 0.000
1 16.3
0
0
1
19.80 2.74
0.00 0
0.000 0
3 8.497
9 10.422
3 4.705
5 6.862
8 10.39
5 6.45
7 6.34
7 10.94
8 6.556
7 10.563
7 4.373
5 5.696
6 4.116
6 4.173
6 4.348
6 2.693
5 5.352
11 9.29
6 12.407
9 7.022
4 4.996
8 7.801
5 5.164
9 8.16
6 1.816
5 10.479 ...
...
7 5.711
5 10.737
4 3.028
8 6.878
7 6.768
5 12.731
5 4.619
9 5.359
6 5.063
6 6.574
8 6.606
11 5.211
4 4.368
7 9.073
7 8.118
3 4.57
5 6.085
9 8.701
2 7.179
10 10.603
9 11.524
3 5.725
7 5.802
7 12.566
4 4.964
3 4.38
9 4.902
8 11.345
5 4.621
6 8.654
7 9.766
7 7.234
2 5.762
8 4.779
12 5.732
11 7.018
9 7.534 ...
...
9 10.371
5 4.408
3 7.765
10 10.499
8 5.303
4 3.957
5 5.634
5 4.057
2 6.59
8 6.45
9 10.729
4 10.021
4 4.579
3 5.862
6 5.707
7 7.502
8 6.051
12 7.602
13 6.366
6 8.938
7 8.137
7 11.035
7 9.639
4 4.16
4 7.136
6 5.914
5 2.26
6 6.963
3 5.266
7 8.216
9 9.623
6 7.979
8 5.491
6 8.008
6 6.245
5 5.643
4 3.563
```

Mount Princeton Transect (B) inverse thermal history modeling: 15MTP-01, 15MTP-02, 15MTP-03, 15MTP-04, 15MTP-05 (this study), 84MP02, 84MP04 (Kelley et al., 1992), 84MP03, 84MP05 (Kelley et al., 1992; Ricketts et al., 2016)

```
15MTP-01
0 0 0
0 0 0 0 0 0
105
0 2 0
1 16.3
0
0
1
0.00 0
0.00 0
0.000 0
7
7
0.01 11.66 32.37 57.92 1.79 -0.03 91.004 100.28 100.28
A 20.19 6.0714e-05 122300 2 2 0
0.02 24.36 110.46 231.65 1.57 -0.02 139.572 79.06 79.06
A 20.57 6.0714e-05 122300 2 2 0
0.01 21.58 59.96 97.29 1.56 -0.02 80.430 104.69 104.69
A 20.2 6.0714e-05 122300 2 2 0
0.02 24.16 100.45 204.18 1.43 -0.02 147.555 80.84 80.84
A 20.51 6.0714e-05 122300 2 2 0
6.01 687.95 451.09 0.0 14.9 -0.19 207.2 100.2 100.2
Z 16.19 19.3188 165000 3 2 0
4.43 603.83 569.44 0.0 16.0 -0.2 173.6 94 94
Z 16.19 19.3188 165000 3 2 0
5.52 828.82 490.77 0.0 15.9 -0.2 174.9 92.8 92.8
Z 16.19 19.3188 165000 3 2 0
```

```
15MTP-02
0.000000 0.000000 836.000000
0 0 0 0.000000 0.000000 0.000000
105
0 2.000000 0.000000
1 16.300000
-1
0
1
0.000000 0
0.000000 0
0.000000 0
5
2
0.0300 17.2300 36.5200 88.9400 3.0200 -0.0400 162.5690 86.5800 86.5800
A 19.98 6.071400e-05 122300 2 2 0
0.0200 30.7000 44.4900 58.0900 2.2300 -0.0300 129.4130 82.1640 82.1640
A 19.75 6.071400e-05 122300 2 2 0
0.0200 12.5500 29.1300 75.6100 2.1900 -0.0300 182.4200 95.8820 95.8820
A 20.04 6.071400e-05 122300 2 2 0
0.0300 22.9100 37.2600 78.8200 2.1200 -0.0300 149.2950 100.7130 100.7130
A 19.81 6.071400e-05 122300 2 2 0
0.0100 15.7300 39.8400 64.7000 1.7300 -0.0200 115.7290 98.9460 98.9460
A 20.13 6.071400e-05 122300 2 2 0
```

```
15MTP-03
0.000000 0.000000 1367.000000
0 0 0 0.000000 0.000000 0.000000
105
0 2.000000 0.000000
1 16.300000
-1
0
1
0.000000 0
0.000000 0
0.000000 0
5
2
0.0200 14.1000 18.9800 56.3900 6.8200 -0.0800 91.0040 89.6720 89.6720
A 19.68 6.071400e-05 122300 2 2 0
0.0300 12.2800 16.2700 51.7200 6.0100 -0.0800 133.8420 97.6280 97.6280
A 19.67 6.071400e-05 122300 2 2 0
0.0100 4.2500 5.6700 23.7500 5.2300 -0.0800 115.2790 110.9060 110.9060
A 19.66 6.071400e-05 122300 2 2 0
0.0200 8.7600 31.9400 158.7700 4.0900 -0.0800 136.9570 80.8280 80.8280
A 20.34 6.071400e-05 122300 2 2 0
0.0200 9.2300 33.1500 146.5800 3.5100 -0.0600 164.3160 79.0610 79.0610
A 20.34 6.071400e-05 122300 2 2 0
```

```
15MTP-04
0.000000 0.000000 1724.000000
0 0 0 0.000000 0.000000 0.000000
105
0 2.000000 0.000000
1 16.300000
-1
0
1
0.000000 0
0.000000 0
0.000000 0
4
2
0.0300 9.6200 29.8600 90.4900 5.6000 -0.0700 130.7000 89.7000 89.7000
A 20.25 6.071400e-05 122300 2 2 0
0.0100 4.7700 19.9800 47.9600 4.9000 -0.1200 84.0000 91.0000 91.0000
A 20.50 6.071400e-05 122300 2 2 0
0.0400 16.2300 46.4400 118.5200 4.1000 -0.0500 158.1000 96.6000 96.6000
A 20.20 6.071400e-05 122300 2 2 0
0.0100 2.6200 15.6000 38.3900 4.0000 -0.1700 109.6000 98.9000 98.9000
A 20.78 6.071400e-05 122300 2 2 0
```

```
15MTP-05
0.000000 0.000000 2210.000000
0 0 0 0.000000 0.000000 0.000000
105
0 2.000000 0.000000
1 16.300000
-1
0
1
0.000000 0
0.000000 0
0.000000 0
7
2
0.1300 44.2400 72.6000 147.3400 11.7200 -0.1300 115.7350 80.3860 80.3860
A 20.30 6.071400e-05 122300 2 2 0
0.1727 30.7700 46.5100 144.6900 11.7000 -0.1300 165.6000 92.8000 92.8000
A 19.81 6.071400e-05 122300 2 2 0
0.0600 13.9700 43.0600 151.5800 10.9000 -0.1300 88.3000 100.3000 100.3000
A 19.75 6.071400e-05 122300 2 2 0
0.0800 39.6100 57.0100 96.0100 7.7700 -0.0900 104.6790 85.6910 85.6910
A 20.24 6.071400e-05 122300 2 2 0
0.0653 25.8400 46.9200 189.9900 6.1000 -0.0800 118.8000 98.4000 98.4000
A 19.74 6.071400e-05 122300 2 2 0
0.1003 37.1000 68.0200 168.1400 5.6000 -0.0700 129.5000 101.6000 101.6000
A 19.85 6.071400e-05 122300 2 2 0
```

```
84MP02
0 0 793
0 0 20 351 627378 108.096
105
3 0.040 0.000
1 16.3
0
0
1
13.73 1.78
0.00 0
0.000 0
6.5 58.965
6 59.111
10 67.356
7 69.527
8.5 59.559
9.5 51.675
9.5 56.302
6 54.059
9 81.872
7 56.107
3 55.157
6 68.291
2.5 36.581 ...
...
8.5 57.233
5.5 53.717
5.5 53.462
7.5 46.163
8.5 68.277
11.5 58.72
10 69.365
```

```
84MP03
0 0 485
0 0 20 351 634294 142.921
105
3 0.040 0.000
1 16.3
-1
0
1
13.08 1.51
0.00 0
0.000 0
8.5 67.402
12.5 94.514
6.5 77.823
9 82.805
10 77.655
5.5 46.512
12 73.742
4.5 43.875
6.5 75.786
8.5 73.259
6.5 88.641
11.5 95.293
7 75.551
7.5 51.757 ...
...
8.5 83.029
6.5 55.381
10 72.295
9 83.31
15.5 90.107
12 100.762
5
2
0.6150 20.6500 97.3100 28.2100 2.6000 -0.2600 217.5000 116.2000 116.2000
A 20.65 6.071400e-05 122300 2 2 0
0.2870 10.7100 42.4600 13.1200 2.5500 -0.2500 177.6000 118.2000 118.2000
A 20.51 6.071400e-05 122300 2 2 0
0.1420 6.5000 24.3600 11.1300 2.1400 -0.2500 209.5000 85.7000 85.7000
A 20.46 6.071400e-05 122300 2 2 0
0.2580 11.0000 51.5400 27.1000 2.0400 -0.2200 206.4000 91.8000 91.8000
A 20.64 6.071400e-05 122300 2 2 0
0.2870 14.9800 70.4600 14.7300 1.6700 -0.2200 147.1000 82.8000 82.8000
A 20.65 6.071400e-05 122300 2 2 0
```

```
84MP04                                  ...
0 0 210                                 26.5 251.625
0 0 20 351 644892 233.388               14.5 147.467
105                                     15 253.761
3 0.040 0.000                           23.5 237.875
1 16.3                                  23.5 263.543
0                                       21 187.098
0                                       17 217.011
1                                       10.5 178.078
9.45 0.80
0.00 0
0.000 0
18 192.826
26.5 279.94
19 207.312
25.5 291.168
13 186.186
22 275.954
20 303.168
12 136.965
17 221.401
14 207.229
13.5 210.217
17.5 172.676 ...
```

```
84MP05                                  ...
0 0 172                                 7.5 82.892
0 0 20 351 649367 109.781               10.5 108.92
105                                     12 119.394
3 0.040 0.000                           11.5 137.316
1 16.3                                  5 67.738
-1                                      9.5 104.638
0                                       6 113.48
1                                       5.5 101.429
9.54 1.20                               4
0.00 0                                  2
0.000 0                                 0.2200 13.5100 29.0100 12.2100 -1.9900 -0.4000 152.4000 73.3000 73.3000
10.5 121.586                            A 20.02 6.071400e-05 122300 2 2 0
7 67.688                                0.1150 5.8000 22.0400 15.8900 -1.9100 -0.2100 185.2000 88.9000 88.9000
6 82.69                                 A 20.46 6.071400e-05 122300 2 2 0
5 81.575                                0.1880 12.1600 28.3900 10.1600 -1.8400 -0.2500 140.5000 84.6000 84.6000
9 78.423                                A 20.09 6.071400e-05 122300 2 2 0
9 100.77                                0.1400 14.5800 20.6100 6.7600 -1.3300 -0.2700 152.7000 71.6000 71.6000
8 104.209                               A 19.74 6.071400e-05 122300 2 2 0
11 90.585
5 75.013
9.5 110.611
4 62.989
7.5 86.053...
```

Mount Columbia Transect (C) inverse thermal history modeling: 15MTC-03, 15MTC-04, 15MTC-05, (this study)

```
15MTC-03
0.000000 0.000000 0.000000
0 0 0 0.000000 0.000000 0.000000
105
0 2.000000 0.000000
1 16.300000
-1
0
1
0.000000 0
0.000000 0
0.000000 0
7
2
0.0300 7.3700 0.5300 188.9400 19.3000 -0.3300 89.2000 97.6000 97.6000
A 18.83 6.071400e-05 122300 2 2 0
0.0400 6.2800 0.4000 171.5400 19.3000 -0.2900 115.7000 109.5000 109.5000
A 18.73 6.071400e-05 122300 2 2 0
0.0400 7.0300 4.0300 180.8600 17.2000 -0.2600 118.8000 100.2000 100.2000
A 18.71 6.071400e-05 122300 2 2 0
0.0200 3.6600 0.4900 151.7300 15.0000 -0.2200 108.2000 115.3000 115.3000
A 19.09 6.071400e-05 122300 2 2 0
0.0300 4.0900 3.4000 138.6300 12.6000 -0.1800 187.3000 102.0000 102.0000
A 18.64 6.071400e-05 122300 2 2 0
0.0200 7.8900 5.8100 197.5200 11.5000 -0.2100 97.2000 89.6000 89.6000
A 19.17 6.071400e-05 122300 2 2 0
```

```
15MTC-04
0.000000 0.000000 627.000000
0 0 0 0.000000 0.000000 0.000000
105
0 2.000000 0.000000
1 16.300000
-1
0
1
0.000000 0
0.000000 0
0.000000 0
4
2
0.7000 42.0200 1.3300 299.1500 28.8000 -0.4100 205.4000 106.4000 106.4000
A 19.19 6.071400e-05 122300 2 2 0
0.5300 76.5900 1.3100 503.3700 25.0000 -0.3500 126.3000 94.5000 94.5000
A 18.88 6.071400e-05 122300 2 2 0
0.1600 29.1900 1.3900 314.8600 22.0000 -0.3200 159.9000 78.6000 78.6000
A 18.87 6.071400e-05 122300 2 2 0
0.1100 11.2700 0.1900 151.8600 18.0000 -0.2600 182.4000 106.5000 106.5000
A 18.86 6.071400e-05 122300 2 2 0
```

```
15MTC-05
0.000000 0.000000 1400.000000
0 0 0 0.000000 0.000000 0.000000
105
0 2.000000 0.000000
1 16.300000
-1
0
1
0.000000 0
0.000000 0
0.000000 0
5
2
0.0600 9.6000 15.6000 150.5000 23.4000 -0.3000 108.2000 80.4000 80.4000
A 18.81 6.071400e-05 122300 2 2 0
0.4600 60.7900 48.5400 239.7700 24.2000 -0.3100 147.6000 84.9000 84.9000
A 19.71 6.071400e-05 122300 2 2 0
0.1700 20.8300 18.3800 124.0600 23.4000 -0.3000 133.9000 92.8000 92.8000
A 19.41 6.071400e-05 122300 2 2 0
0.0200 3.5200 4.2600 236.9000 21.7000 -0.4400 94.5000 94.5000 94.5000
A 19.44 6.071400e-05 122300 2 2 0
0.2000 26.9900 20.0300 129.4200 21.5000 -0.2800 136.9000 92.8000 92.8000
A 19.12 6.071400e-05 122300 2 2 0
```

Mount Belford Transect (D) inverse thermal history modeling included samples: 14MTB-01, 14MTB-02, 14MTB-03, 14MTB-04, 14MTB-04a, 14MTB-05 (this study)

```
14MTB-01
0.000000 0.000000 0.000000
0 0 0 0.000000 0.000000 0.000000
105
0 2.000000 0.000000
1 16.300000
0
0
1
0.000000 0
0.000000 0
0.000000 0
7
7
0.0700 20.2200 7.2800 224.9100 6.7000 -0.0900 142.7000 114.4000 114.4000
A 19.08 6.071400e-05 122300 2 2 0
0.1000 26.8700 11.5900 174.6500 5.8000 -0.0800 174.9000 115.3000 115.3000
A 19.17 6.071400e-05 122300 2 2 0
0.1000 55.2000 19.3800 324.1500 5.2000 -0.0700 135.6000 100.3000 100.3000
A 19.12 6.071400e-05 122300 2 2 0
0.0300 22.2300 11.2500 215.7700 4.7000 -0.0700 140.5000 89.7000 89.7000
A 19.19 6.071400e-05 122300 2 2 0
5.4957 327.73 123.5200 0.00 28.5000 -0.4400 220.4000 100.2000 100.2000
Z 15.87 4.6e-05 169000 0 2 0
5.4607 573.47 131.500 0.00 24.1000 -0.3400 191.7000 89.6000 89.6000
Z 15.65 4.6e-05 169000 0 2 0
26.8858 679.06 108.2500 0.00 26.4000 -0.3900 345.400 131.2000 131.2000
Z 15.75 4.6e-05 169000 0 2 0
```

```
14MTB-02
0.000000 0.000000 165.000000
0 0 0 0.000000 0.000000 0.000000
105
0 2.000000 0.000000
1 16.300000
-1
0
1
0.000000 0
0.000000 0
0.000000 0
6
2
0.0100 5.3600 14.1900 173.5700 4.9000 -0.1100 103.9000 91.0000 91.0000
A 19.81 6.071400e-05 122300 2 2 0
0.0100 3.8700 14.9600 148.0000 4.5000 -0.0800 155.0000 88.3000 88.3000
A 19.97 6.071400e-05 122300 2 2 0
0.0100 4.2700 5.7800 77.7200 4.1000 -0.1200 144.0000 97.2000 97.2000
A 20.27 6.071400e-05 122300 2 2 0
0.0100 3.8500 9.2600 102.1600 4.0000 -0.0700 144.9000 103.8000 103.8000
A 19.57 6.071400e-05 122300 2 2 0
0.0200 4.1900 12.9300 166.9700 4.0000 -0.0700 173.1000 108.2000 108.2000
A 19.93 6.071400e-05 122300 2 2 0
```

```
14MTB-03
0.000000 0.000000 422.000000
0 0 0 0.000000 0.000000 0.000000
105
0 2.000000 0.000000
1 16.300000
-1
0
1
0.000000 0
0.000000 0
0.000000 0
4
2
0.0700 28.8100 4.1500 224.4300 5.4000 -0.0800 140.0000 108.2000 108.2000
A 20.06 6.071400e-05 122300 2 2 0
0.0500 28.5800 3.0300 208.9600 5.3000 -0.0800 118.4000 108.2000 108.2000
A 18.96 6.071400e-05 122300 2 2 0
0.0400 10.9500 0.9500 139.2300 5.5000 -0.0900 174.9000 120.2000 120.2000
A 18.94 6.071400e-05 122300 2 2 0
0.0800 61.0900 10.5000 265.1900 4.6000 -0.0700 150.6000 85.2000 85.2000
A 18.87 6.071400e-05 122300 2 2 0
```

```
14MTB-04
0.000000 0.000000 565.000000
0 0 0 0.000000 0.000000 0.000000
105
0 2.000000 0.000000
1 16.300000
-1
0
1
0.000000 0
0.000000 0
0.000000 0
4
2
0.0100 2.5300 11.7000 148.2100 5.3000 -0.1000 82.2000 114.0000 114.0000
A 19.01 6.071400e-05 122300 2 2 0
0.0200 7.3900 10.1500 86.0100 4.1000 -0.0700 123.2000 109.6000 109.6000
A 20.33 6.071400e-05 122300 2 2 0
0.0100 7.5100 13.8300 87.8700 3.7000 -0.0800 112.7000 91.4000 91.4000
A 19.63 6.071400e-05 122300 2 2 0
0.0200 5.0200 19.8300 161.2000 3.7000 -0.0600 150.6000 99.0000 99.0000
A 19.83 6.071400e-05 122300 2 2 0
```

```
14MTB-04a
0.000000 0.000000 789.000000
0 0 0 0.000000 0.000000 0.000000
105
0 2.000000 0.000000
1 16.300000
-1
0
1
0.000000 0
0.000000 0
0.000000 0
4
2
0.1000 36.1200 15.8200 334.8400 9.0000 -0.1200 114.0000 100.3000 100.3000
A 20.33 6.071400e-05 122300 2 2 0
0.0900 33.0800 17.6100 262.5100 6.1000 -0.0800 91.0000 129.5000 129.5000
A 19.15 6.071400e-05 122300 2 2 0
0.0500 45.2900 24.6200 258.3400 5.0000 -0.0700 102.0000 83.9000 83.9000
A 19.22 6.071400e-05 122300 2 2 0
0.0600 50.2500 25.2400 377.5800 4.8000 -0.0600 121.5000 82.5000 82.5000
A 19.25 6.071400e-05 122300 2 2 0
```

```
14MTB-05
0.000000 0.000000 887.000000
0 0 0 0.000000 0.000000 0.000000
105
0 2.000000 0.000000
1 16.300000
-1
0
1
0.000000 0
0.000000 0
0.000000 0
6
2
0.0200 4.5800 4.6000 97.3400 8.8000 -0.1200 146.2000 106.5000 106.5000
A 19.20 6.071400e-05 122300 2 2 0
0.0500 14.0100 13.7500 185.2400 6.7000 -0.1000 173.1000 94.5000 94.5000
A 19.55 6.071400e-05 122300 2 2 0
0.0800 23.4600 29.6300 204.6200 6.8000 -0.0800 135.6000 103.4000 103.4000
A 19.38 6.071400e-05 122300 2 2 0
0.0200 13.0500 20.7800 140.0800 5.9000 -0.1100 95.800000 40.2000 40.2000
A 19.43 6.071400e-05 122300 2 2 0
0.0100 4.9100 7.0300 116.2900 5.0000 -0.1300 87.0000 46.1000 46.1000
A 19.61 6.071400e-05 122300 2 2 0
```

Mount Elbert Transect (E) inverse thermal history modeling included samples: 14MTE-01, 14MTE-02, 14MTE-05 (this study), 73N7, 73N9, TL-F-6-16 (Bryant and Naeser, 1980)

```
14MTE-01
0.000000 0.000000 1057.000000
0 0 0 0.000000 0.000000 0.000000
105
0 2.000000 0.000000
1 16.300000
-1
0
1
0.000000 0
0.000000 0
0.000000 0
4
2
0.1100 15.2000 34.1500 156.5200 10.7000 -0.1200 182.9000 100.3000 100.300
A 19.99 6.071400e-05 122300 2 2 0
0.0400 11.6100 23.6600 107.7200 9.2000 -0.1200 120.1000 92.8000 92.8000
A 19.92 6.071400e-05 122300 2 2 0
0.0300 11.6200 45.1300 137.1600 7.6000 -0.1100 100.3000 83.9000 83.9000
A 20.43 6.071400e-05 122300 2 2 0
0.0600 14.1200 57.8200 126.9400 6.5000 -0.0700 193.0000 84.9000 84.9000
A 20.49 6.071400e-05 122300 2 2 0
```

```
14MTE-02
0.000000 0.000000 1427.000000
0 0 0 0.000000 0.000000 0.000000
105
0 2.000000 0.000000
1 16.300000
-1
0
1
0.000000 0
0.000000 0
0.000000 0
6
2
0.4700 60.2000 2.8000 619.5900 26.9000 -0.3800 126.4000 95.8000 95.8000
A 18.87 6.071400e-05 122300 2 2 0
0.6100 46.9600 3.2400 541.3400 26.8000 -0.3800 104.7000 135.6000 135.6000
A 18.86 6.071400e-05 122300 2 2 0
0.3600 47.5600 1.7900 453.0800 23.8000 -0.3400 123.3000 102.0000 102.0000
A 18.87 6.071400e-05 122300 2 2 0
0.2400 43.7900 3.1200 535.4100 22.6000 -0.3200 117.5000 89.7000 89.7000
A 18.86 6.071400e-05 122300 2 2 0
0.4100 63.3800 3.4300 639.6600 22.1000 -0.3100 144.5000 89.7000 89.7000
A 18.86 6.071400e-05 122300 2 2 0
```

```
14MTE-05
0.000000 0.000000 2036.000000
0 0 0 0.000000 0.000000 0.000000
105
0 2.000000 0.000000
1 16.300000
-1
0
1
0.000000 0
0.000000 0
0.000000 0
4
2
0.2500 40.8300 4.7400 556.6500 22.0000 -0.3000 123.3000 94.1000 94.1000
A 18.87 6.071400e-05 122300 2 2 0
0.1300 29.2400 7.2300 597.6200 20.9000 -0.2800 101.6000 88.3000 88.3000
A 18.88 6.071400e-05 122300 2 2 0
0.2000 41.6100 5.0200 611.5900 20.3000 -0.2800 143.1000 80.4000 80.4000
A 18.91 6.071400e-05 122300 2 2 0
0.1000 26.3400 7.3900 495.5500 19.7000 -0.2700 109.6000 80.8000 80.8000
A 18.88 6.071400e-05 122300 2 2 0
```

```
73N7                    ...             ...
0 0 1695                3.5 8.801       2.5 10.977
0 0 50 340 303102 2506.96 3 9.211       2.5 6.306
105                     2 5.878         3 10.395
3 0.040 0.000           3.5 9.264       4.5 8.065
1 16.3                  2.5 11.072      6.5 9.198
0                       3 6.334         2.5 8.475
0                       4 10.457        6 7.118
1                       3 5.817         2 6.351
19.05 1.79              3.5 11.053      3.5 7.776
0.00 0                  4 8.378         2.5 5.558
0.000 0                 6 8.499         4.5 4.247
2 9.508                 2.5 7.897       4.5 9.86
4 9.755                 5.5 8.816       5.5 10.497
5 10.345                3.5 9.485
2 6.255                 3 10.531
2 6.981                 3 10.342
3 13.579                3 9.739
2.5 7.468               2 7.575
4 5.328                 4 12.821
2.5 9.559               2.5 5.794
1.5 8.511               3.5 11.55
2.5 10.137              3 9.655
1.5 8.891               2 8.884
3.5 12.336 ...          2 10.169 ...
```

```
73N9                    ...             ...
0 0 0                   9 35.977        4 12.986
0 0 50 340 299395 52.053 6 35.791       5 13.08
105                     8 13.972        10 32.499
3 0.040 0.000           7 11.949        10 18.254
1 16.3                  8 20.664        6 25.051
0                       7 28.827
0                       2 18.16
1                       6 12.364
15.90 2.41              5 15.783
0.00 0                  5 11.925
0.000 0                 5 19.21
5 38.379                6 29.77
7 23.347                6 25.862
5 16.698                8 30.804
7 29.537                5 11.548
6 23.349                11 33.615
10 33.645               2 16.269
7 14.087                13 26.232
10 31.844               15 15.979
2 16.638                3 16.047
9 27.591                10 33.302
5 22.743                12 29.614
8 20.119                6 18.633
4 13.506                5 13.126
13 31.262               7 10.453
4 14.607                5 24.777
6 20.594                11 30.569
9 30.326 ...            5 17.636 ...
```

```
TL-F-6-16               ...             ...
0 0 5                   6 15.723        9.5 11.564
0 0 50 340 204566 57.057 12.5 14.89     8 15.587
105                     5 7.98          9 19.391
3 0.040 0.000           7 14.385        11.5 15.057
1 16.3                  7 16.429        14 16.946
0                       6 14.317        5.5 12.377
0                       4 10.602        6.5 14.774
1                       5 9.045         6.5 13.193
19.91 2.94              10.5 11.848     7.5 12.05
0.00 0                  7.5 9.381       11.5 14.21
0.000 0                 4 10.938        6 10.411
6 10.945                4 10.336        6 7.603
6 13.38                 7.5 10.77       7 15.239
10.5 18.146             7 11.405        6 11.264
8.5 12.172              6 10.407        6.5 12.561
3 10.339                7.5 11.614
8 13.46                 11 15.252
9 12.877                4.5 11.778
4.5 10.103              5.5 11.591
8 15.724                6 16.75
9.5 15.389              9 10.729
4.5 12.152              11 13.163
6.5 11.54 ...           8.5 12.216 ...
```

Modeling exhumation rate changes using detrital AHe populations and catchment hypsometry

To obtain cooling ages from west of the Sawatch Range front, we collected bedrock samples both at the range front and several km west of the range front. However, collecting bedrock near transect C was logistically difficult because of restricted access and difficult terrain, so we collected a detrital sample from a stream draining the catchment west of transect C. The ages from grains in that detrital sample ranged from 12 Ma to 45 Ma (Table A2) indicating that the region west of the range front experienced cooling at least into the middle to late Miocene.

To assess the most-likely exhumation history that could produce our observed distribution of detrital AHe ages, we used a modified version of the method proposed by Avdeev et al. (2011) to predict expected AHe ages based on an assumed age-elevation relationship and the observed catchment hypsometry. We tested hypothetical age-elevation relationships that were constrained by the youngest observed detrital age (assumed to be at the lowest elevation in the catchment) and the oldest observed detrital age (assumed to be at the highest elevation in the catchment). Using a simple grid search, we modeled two-piece age elevation relationships by defining a "break-in-slope" in the age-elevation relationship at all combinations of ages and elevations between the lowest and highest ages and elevations. For each step in the search, we calculated the expected distribution of detrital AHe ages for the given age-elevation relationship (assuming uniform sampling across the catchment) and compared the CDF of this expected distribution to the CDF of the observed distribution of detrital ages that we analyzed. The L2-norm was determined for each pair of CDFs and we determined that the best-fit age-

elevation relationship to our data required a change in exhumation rate at ~13.6 Ma (with this age being presently located at an elevation of ~3365 m; Figs. A5 and A6) This relationship requires an average exhumation rate of ~0.03 mm/yr from ~45 Ma to ~14 Ma followed by an increase in exhumation rate to ~0.4 mm/yr post-14 Ma. At a constant rate of 0.4 mm/yr from ~14 Ma, the magnitude of exhumation would amount to ~5 km.

This timing for a change in exhumation rate is a rough estimation as we are limited by the number of analyses in our detrital sample. The timing for onset of increased rates of exhumation coincides well with a model for fault growth via tip propagation. In addition, the estimated rates and magnitudes of predicted exhumation from this model compare well with the rates and magnitudes of exhumation we interpret from the SFss and SFns, which are much better constrained with bedrock vertical transects (A, B, C, D and E; Kim and Sanderson, 2005; Curry et al., 2016).

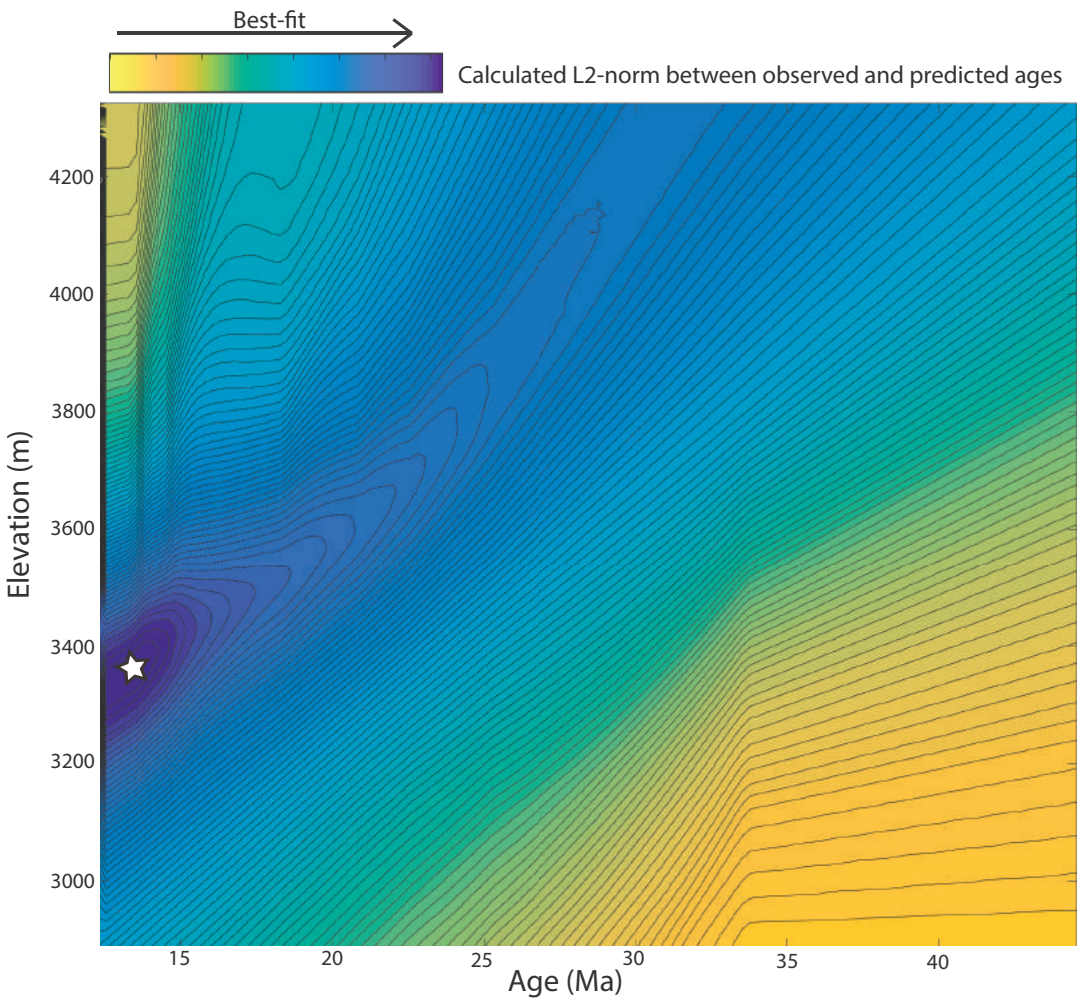

Figure A5: Filled contour plot of L2-norm comparison for predicted populations from all tested age-elevation points (representing a change in exhumation rate) compared to our observed detrital AHe ages. The best-fit age and elevation combination that matches the catchment hypsometry is marked by a white star indicating that the most-likely exhumation history to produce the ages observed in the catchment is one with a change in exhumation rate occurring ~14 Ma when the rate of exhumation goes from and average of ~0.03 mm/yr prior to ~14 Ma to an average of ~0.4 mm/yr post-14 Ma.

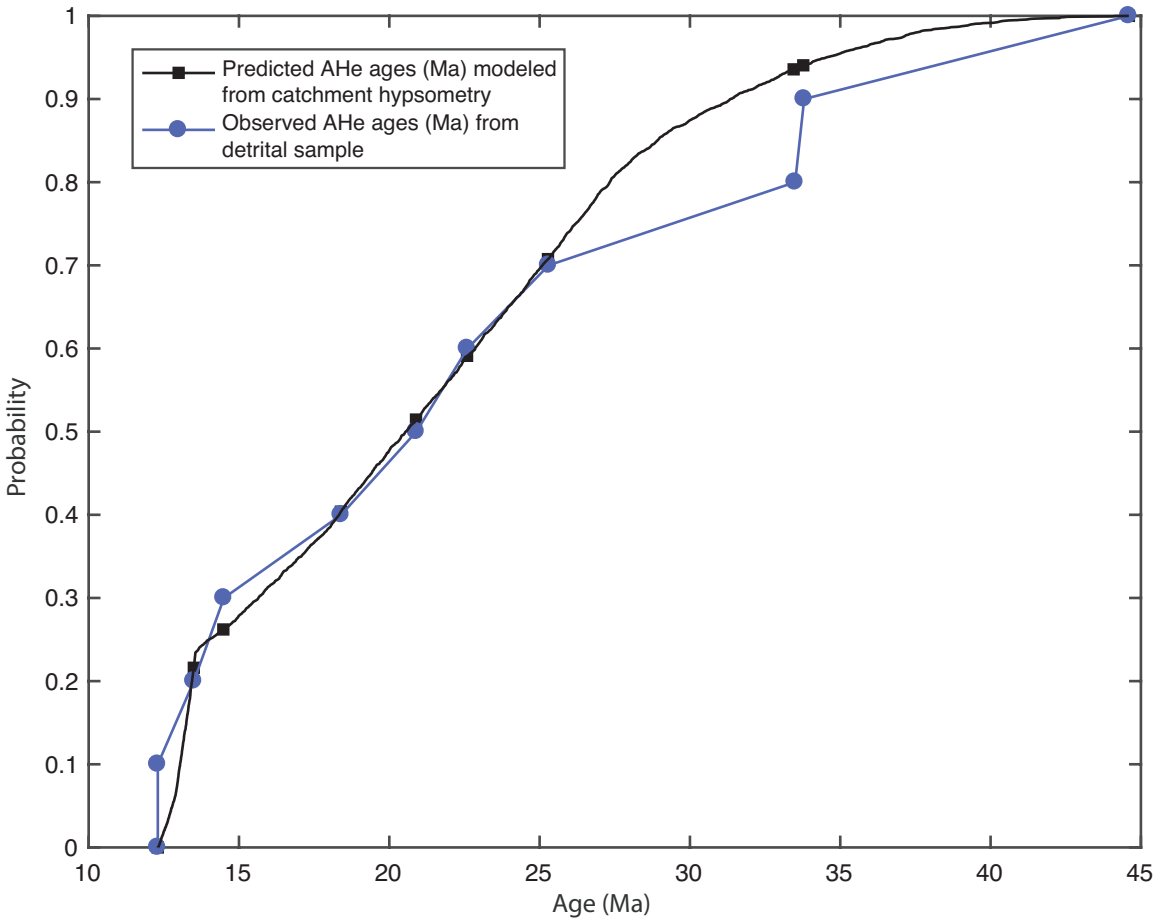

Figure A6: Cumulative density plot (CDF) for our observed detrital AHe ages (blue circles) and CDF for the best-fit predicted ages (calculated from L2-norm; Fig. A5) that incorporate the catchment hypsometry where the detrital sample was collected.

REFERENCES

Abbey, A.L., Niemi, N.A., Geissman, J.W., Winkelstern, I.Z., and Heizler, M., 2017, Early Cenozoic exhumation and paleotopography in the Arkansas River valley, southern Rocky Mountains, Colorado: Lithosphere, v. 10, p. 239–266, doi:10.1130/L673.1.

Avdeev, B., Niemi, N.A., and Clark, M.K., 2011, Doing more with less: Bayesian estimation of erosion models with detrital thermochronometric data: Earth and Planetary Science Letters, v. 305, p. 385–395, doi:10.1016/j.epsl.2011.03.020.

Berhe, S.M., 1986, Geologic and geochronologic constraints on the evolution of the Red Sea-Gulf of Aden and Afar depression: Journal of African Earth Sciences, v. 5, p. 101–117, doi:10.1016/0899-5362(86)90001-1.

Bryant, B., and Naeser, C.W., 1980, The significance of fission-track ages of apatite in relation to the tectonic history of the Front and Sawatch Ranges, Colorado: Geological Society of America Bulletin, v. 91, p. 156–164, doi:10.1130/0016-7606(1980)91<156:TSOFAO>2.0.CO;2.

Busby, C.J., 2013, Birth of a plate boundary ca. 12 Ma in the ancestral Cascades arc, Walker Lane belt of California and Nevada: Geosphere, v. 9, p. 1147–1160, doi:10.1130/GES00928.1.

Chapin, C.E., and Cather, S.M., 1994, Tectonic setting of the axial basins of the northern and central Rio Grande rift, in Keller, G.R., and Cather, S.M., eds., Basins of the Rio Grande Rift: Structure, Stratigraphy, and Tectonic Setting: Geological Society of America Special Papers, v. 291, p. 5–26, doi:10.1130/SPE291-p5.

Chorowicz, J., 2005, The East African Rift system: Journal of African Earth Sciences, v. 43, p. 379–410, doi:10.1016/j.jafrearsci.2005.07.019.

Cosca, M.A., Thompson, R.A., Lee, J.P., Turner, K.J., Neymark, L.A., and Premo, W.R., 2014, $^{40}Ar/^{39}Ar$ geochronology, isotope geochemistry (Sr, Nd, Pb), and petrology of alkaline lavas near Yampa, Colorado: Migration od alkaline volcanism and evolution of the northern Rio Grande rift: Geosphere, v. 10, p. 374–400, doi:10.1130/GES00921.1.

Curry, M.A., Barnes, J.B., and Colgan, J.P., 2016, Testing fault growth models with low-temperature thermochronology in the northwest Basin and Range, USA: Tectonics, v. 35, p. 2467–2492, doi:10.1002/2016TC004211.

Flowers, R.M., Ketcham, R.A., Shuster, D.L., and Farley, K.A., 2009, Apatite (U-Th)/He thermochronometry using a radiation damage accumulation and annealing model:

Geochimica et Cosmochimica Acta, v. 73, p. 2347–2365, doi:10.1016/j.gca.2009.01.015.

Gallagher, K., 2012, Transdimensional inverse thermal history modeling for quantitative thermochronology: Journal of Geophysical Research, v. 117, B02408, doi:10.1029/2011JB008825.

Grauch, V.J.S., Bauer, P.W., Drenth, B.J., and Kelson, K.I., 2017, A shifting rift—Geophysical insights into the evolution of Rio Grande rift margins and the Embudo transfer zone near Taos, New Mexico: Geosphere, v. 13, p. 870–910, doi:10.1130/GES01425.1.

Guenthner, W.R., Reiners, P.W., Ketcham, R.A., Nasdala, L., and Giester, G., 2013, Helium diffusion in natural zircon: Radiation damage, anisotropy and the interpretation of zircon (U-Th)/He thermochronology: American Journal of Science, v. 313, p. 145–198, doi:10.2475/03.2013.01.

Heller, P.L., Dueker, K., and McMillan, M.E., 2003, Post-Paleozoic alluvial gravel transport as evidence of continental tilting in the US Cordillera: Geological Society of America Bulletin, v. 115, p. 1122–1132, doi:10.1130/B25219.1.

Hubbard, M.S., Oviatt, C.G., Kelley, S., Perkins, M.E., Hodges, K.V., and Robbins, R., 2001, Oligocene-Miocene basin formation and modification in the northern Rio Grande rift; constraints from 40Ar/39Ar, fission track, and tephrochronology: Geological Society of America Abstracts with Programs, v. 33, no. 6, p. A-257.

Kelley, S.A., Chapin, C.E., and Corrigan, A.J., 1992, Late Mesozoic to Cenozoic Cooling Histories of the Flank of the Northern and Central Rio Grande Rift, Colorado and New Mexico: Socorro, New Mexico, New Mexico Bureau of Mines Mineral Resources, Bulletin 145, p. 1–40.

Kim, Y.S., and Sanderson, D.J., 2005, The relationship between displacement and length of faults: A review: Earth-Science Reviews, v. 68, p. 317–334, doi:10.1016/j.earscirev.2004.06.003.

Landman, R., and Flowers, R.M., 2013, (U-Th)/He thermochronologic constraints on the evolution of the northern Rio Grande Rift, Gore Range, Colorado, and implications for rift propagation models: Geosphere, v. 9, p. 170–187, doi:10.1130/GES00826.1.

Leonard, E.M., 2002, Geomorphic and tectonic forcing of late Cenozoic warping of the Colorado piedmont: Geology, v. 30, p. 595–598, doi:10.1130/0091-7613(2002)030<0595:GATFOL>2.0.CO;2.

Lindsey, D.A., Andriessen, P.A.M., and Wardlaw, B.R., 1986, Heating, cooling, and uplift during Tertiary time, northern Sangre de Cristo Range, Colorado: Geological Society of America Bulletin, v. 97, p. 1133–1143, doi:10.1130/0016-7606(1986)97<1133:HCAUDT>2.0.CO;2.

Nixon, C.W., et al., 2016, Rapid spatiotemporal variations in rift structure during development of the Corinth Rift, Central Greece: Tectonics, v. 35, p. 1225– 1248, doi:10.1002/2015TC004026.

Ricketts, J.W., Kelley, S.A., Karlstrom, K.E., Schmandt, B., Donahue, M.S., and van Wijk, J., 2016, Synchronous opening of the Rio Grande rift along its entire length at 25–10 Ma supported by apatite (U-Th)/He and fission-track thermochronology, and evaluation of possible driving mechanisms: Geological Society of America Bulletin, v. 128, p. 397–424, doi:10.1130/B31223.1.

Shannon, J.R., 1988, Geology of the Mount Aetna cauldron complex, Sawatch Range, Colorado [Ph.D. thesis]: Golden, Colorado, Colorado School of Mines, 434 p.
Stockli, D.F., Farley, K.A., and Dumitru, T.A., 2000, Calibration of the apatite (U-Th)/He thermochronometer on an exhumed fault block, White Mountains, California: Geology, v. 28, p. 983–986, doi:10.1130/0091-7613(2000)28<983:COTAHT>2.0.CO;2.

Umhoefer, P.J., 2011, Why did the Southern Gulf of California rupture so rapidly?—Oblique divergence across hot, weak lithosphere along a tectonically active margin: GSA Today, v. 21, p. 4–10, doi:10.1130/G133A.1.

U.S. Geological Survey, 2006, Quaternary fault and fold database for the United States: http://earthquake.usgs.gov/hazards/qfaults/ (accessed February 2018).

Van Alstine, R.E., 1969, Geology and Mineral Deposits of the Poncha Springs NE Quadrangle, Chaffee County: Colorado: U.S. Geological Survey Professional Paper 626, 52 p.

Wells, D. L., Coppersmith, K. J., 1994, New empirical relationships among magnitude, rupture length, rupture width, rupture area, and surface displacement: Bulletin of the Seismological Society of America, v. 84, n. 4, p.

CHAPTER III: CONTINENTAL RIFTING PROCESSES DETERMINED BY FAULTING AND MAGMATISM IN THE RIO GRANDE RIFT, USA

ABSTRACT

Analysis of low-temperature thermochronometric data in the Rio Grande rift (RGR) in New Mexico and Colorado, USA provides the means to assess the timing of fault initiation, as well as patterns in growth and linkage of rift faults. Evaluating spatiotemporal patterns in faulting and rift-related magmatism reveals insights into processes behind extension accommodation and helps to distinguish between possible rift models. We separate the RGR into three sections (north, central, and south) based on physiographic differences in faulting and volcanism and combine new apatite (U-Th-Sm)/He (AHe) and zircon (U-Th)/He (ZHe) thermochronometric data with previously published AHe and apatite fission track (AFT) data to compile 14 vertical transects, spanning more than >800 km along the RGR axis. Rift initiation is contemporaneous at ca. 25 Ma on fault segments in both the northern and southern RGR. Fault initiation continues with segment growth and linkage from ca. 25 to ca. 15 Ma. At ca. 15 Ma the entire rift system becomes linked through strike-slip faulting and magmatic accommodation in the central RGR. The faulting accommodation occurs along a north to south strike while the magmatic accommodation occurs along the Jemez lineament trending northeast to southwest. These strike trends of the faulting and magmatism are

spatially coincident with pre-existing weaknesses from previous tectonic rifting and orogenic events. In contrast, the physiographic differences between the three sections of the rift appear to be related to crustal and lithospheric characteristics, namely lithospheric thickness. This suggests that rift structure and geometry are at least partly controlled by both inherited structure and/or lithospheric properties. These new analyses and interpretations provide a framework for assessing rifting models, and we suggest that a possible RGR model involves initiation of fault accommodated extension by oblique strain followed by block rotation, where extension in the RGR is accommodated by faulting (southern and northern RGR) and magmatism (central RGR).

INTRODUCTION

Continental rifting may eventually lead to tectonic plate break-up, an essential part of the tectonic cycle, and yet, the processes behind rift initiation, geometry or style of faulting, location of extension, and accommodation mechanisms remain unclear (Nelson et al., 1992; Molnar et al., 2017). Ultimately, continental rifting is caused by the interactions between mantle flow and plate movements; accordingly, rifting accommodation, rates of development, and the manner of fault growth are controlled by various combinations of heat flow, lithospheric structure, far-field stresses, mantle flow and magmatism (Lavecchia et al., 2017). The different expressions of rifting (wide, narrow, magma dominated, faulting in the form of large basin-bounding faults, or numerous intra-basin faults, en echelon geometries; e.g. Ebinger 1984; Ebinger 1989; Nelson et al., 1992; Molnar et al., 2017; Brune et al., 2017) are seen in numerous locations around the Earth, emphasizing the roles various processes like faulting and magmatism can have on the geometry and extension accommodation of a rift system

(Fig. 3.1). For example, some rifts are wide zones of deformation and accommodate large amounts of horizontal extension (e.g. Basin and Range or Aegean) while others are comprised of narrow deep grabens (e.g. Ethiopian, Baikal, Rhine), differences that may be controlled by lithospheric strength or rates of extension (Buck, 1991; Brun, 1999; Corti, 2012). Additionally, many rift systems are associated with voluminous magmatism (e.g. Red Sea, Ethiopian rift, eastern branch of the East African rift), while others are magma poor (e.g. Iberia-Newfoundland margin, South China Sea, western branch of the East African rift; Reston, 2005; Corti, 2012; Hart et al., 2017). Furthermore, rifts may development through multiple phases of extension or through continuous deformation during a single extension phase (e.g. fault block rotation and locking, or ductile to brittle; Færseth, 1996; Morley et al., 2004; Reston, 2005; Lavier and Manatschal, 2006; Corti, 2009; Beltrando et al., 2015; Claringbould et al., 2017). Therefore, acquiring detailed information about faulting and magmatism processes and their controls on fault growth, basin linkage, and rift geometry will provide the opportunity to understand the processes that drive rift initiation and accommodation in continental rifts.

One region where rift initiation and fault growth (e.g. tip propagation, segment linkage or constant length with increasing vertical displacement; Kim and Sanderson, 2005) can be well documented is the Rio Grande rift (RGR) in the western United States. The entire rift system is exposed on land and there is a plethora of published data related to fault motion, basin sedimentation, volcanism, lithospheric structure and regional strain rates that provides a thorough framework necessary for understanding the relationships between faulting, magmatism and lithospheric structure in a rift system (Table 3.1). Moreover, extension in the RGR is relatively slow (Woodward, 1977; Savage et al.,

1980; Golombek et al., 1983; Shirvell et al., 2009; Kreemer et al., 2010; Muirhead et al., 2016; Nixon et al., 2016), which affords the opportunity to perhaps capture discrete details about fault growth and rift basin linkage that might otherwise be difficult to detect in more rapidly developing systems (e.g. Ethiopian rift, Gulf of California).

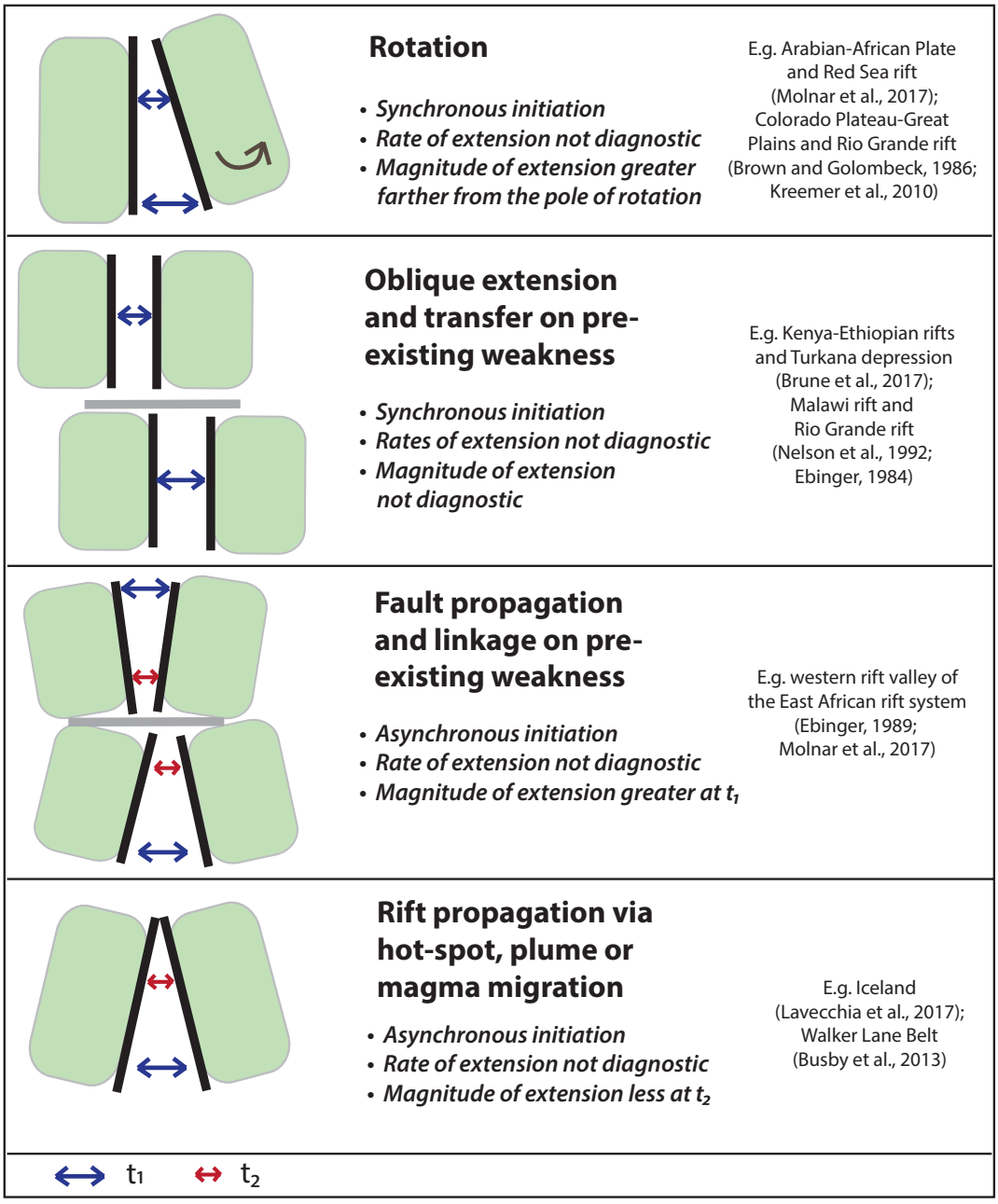

Figure 3.1: Generalized models of different forcings that may cause continental rifting. Each model has diagnostic characteristics in the timing of initiation, rate of extension and magnitude of extension, which can be used to differentiate between possible rift models.

Aspects related to the timing of RGR development are highly disputed, with debate centering around two main hypotheses: (1) rifting was primarily synchronous along the length of the RGR (Landman and Flowers, 2013; Ricketts et al., 2015; Chapin and Cather, 1994), or (2) extension began in the southern part of the rift and has propagated northward over time so that the basins in the northern RGR are the youngest in the rift system (McMillan et al., 2002; Leonard, 2002; Heller et al., 2003; Frankel and Pazzaglia, 2006; Duller et al., 2012). Processes that could support a synchronous model would include either a rotation model or and oblique extension model, whereas a propagation model would gain support from fault initiation moving in a specific direction either by connecting pre-existing weak zones or from migration of magma (Fig 3.1; Ebinger 1984; Brown and Golombeck, 1986; Ebinger, 1989; Nelson et al., 1992; Kreemer et al., 2010; Busby et al., 2013; Molnar et al., 2017; Lavecchia et al., 2017; Brune et al., 2017). To distinguish between these different processes we must understand the spatial and temporal relationships between faulting and magmatism and determine how those relationships are controlled by things like mantle plumes, lithospheric properties, or inherited crustal weaknesses.

Within the RGR, inter-basin syn-rift sedimentation signatures, and thermochronometry data from along the rift flanks, have been invoked to support the model of synchronous rift initiation (Ricketts et al., 2015; Chapin and Cather, 1994; Landman and Flowers 2013). Conversely, far field tilting of Miocene sediments, increased sedimentation in the Great Plains, and the existence of rift-related magmatism

in northern Colorado have been invoked as evidence for a northward propagation model (McMillan et al., 2002; Leonard 2002; Heller et al., 2003; Duller et al., 2012; Kellogg, 1999; Neaser et al., 2002; Leonard et al., 2002; Cosca et al., 2014). Syn-rift strata, in individual basins of the RGR, often have poor age resolution (van Alstine et al., 1960; van Alstine, 1969) and, rift related magmatism is sparse in many RGR basins (McMillan et al., 2000; Cosca et al., 2014). Regional tilting or far-removed erosion and sedimentation are indirect proxies for rift activity, and thus, the above mentioned proxies do not provide thorough details along the entire length of the rift and cannot be used reliably for distinguishing between rift models.

To resolve the timing, magnitudes, and rates of exhumation on rift faults in the RGR, we must maintain a consistent approach for quantifying fault initiation and growth, as much of the debate surrounding RGR development models comes from drawing inferences from several different data types recording different aspects of rifting (described above). Low-temperature thermochronometry is one such approach that provides a method for directly measuring the onset of exhumation of major basin-bounding faults along the entire RGR. Here we synthesize all of the low-temperature thermochronometry data available along the RGR to clarify spatial patterns of rift-flank fault initiation, growth, and linkage. We add new thermochronometry samples to complement existing data and perform inverse thermal history modeling to obtain information about timing, magnitudes, and rates of exhumation along the rift faults, which we use to infer the processes of fault growth and basin linkage. Understanding the fault growth processes is helpful for assessing possible controls on rift geometry and accommodation through time, such as lithospheric properties, inherited crustal structure,

TABLE 3.1. SUMMARY OF INFORMATION FROM EACH RIO GRANDE RIFT BASIN

Faulting	Sedimentation	Magmatism	Low-temperature Thermochronometry	Rifting Interpretations
Southern Rio Grande rift				
Palomas Basin				
Cabaillo Fault (W)[3]	From the Black Range primarily[1]	Mogollon-Datil volcanic field (VF) (late Eocene to early Miocene)	Black Range, west side: AFT 20-40 Ma[1]; ZFT ~68 Ma[1]; AHe 45-52 Ma[2] Cabaillo Mountains, east side: AFT 5-18 Ma[1]	Rift related exhumation primarily occurred on the east side of the basin and AFT suggest the PAZ was 3-3.5 km deep in the late Eocene.[1]
Jornada Basin				
Jornada Draw Fault (E)[3]	Primarily from the San Andreas Mountains[1]	Jornada del Muerto VF (Quaternary) Potrillo VF (south of distinct basin area) (Quaternary)	Sparse data in the central and southern part of the basin and Las Uvas Mountains: 6-18 Ma[1]	Rapid erosion and fault block tilting occurred in the middle Miocene.[1]
Tularosa Basin				
San Andreas Fault (60?E)[1,3] Alamogordo Fault (W)[3]	2-3 km thick[30]	Carrizozo VF (Quaternary)	San Andreas Mountains: ZFT 49 Ma[1]; AFT 8-22 Ma[1]; AHe 9-16 Ma[2] Organ Mountains: AFT 10-29 Ma[1]; AHe 10-16 Ma[2] Sacramento Mountains: AFT 40-67 Ma[1] Sierra Blanca intrusion: AFT 23-33 Ma; AHe 15-23 Ma[2]	Onset of rifting indicated by the younger AFT in Sierra Blanca and suggest rapid denudation rates of 200-400m/my.[1] Combined the AFT and AHe data imply rapid cooling and rift extension occurred between 25 and 10 Ma.[2]
Southern Albuquerque Basin				
La Jencia Fault (80-85°E)[3,4] Ladron Fault (E)[5] Jeter fault (15-30°E)[5] Coyote Springs Fault (E)[3] Santa Fe Fault (E)[3]	Basin fill is mostly middle Miocene age and includes the Popotosa fm. and Santa Fe fm. (interbedded with 14.5 Ma volcanic	Socorro Magma Body (subsurface)[5,40,41]	Magdalena Mountains: AFT 46-4 Ma[6] Lemitar Mountians: AFT 13-6 Ma[6] Sierra Ladrones: AFT 32-9 Ma[6]; AHe ~9-12 Ma[5] Joyita Hills: AFT 8-26 Ma[6]; AHe ~18 Ma[2]	Two phases of exhumation (1) late Laramide, (2) post-18 Ma.[7] Two phases of rift exhumation (1) late Oligocene to early Miocene, (2) middle Miocene to Present.[8] Continuous exhumation 25-2 Ma with high rates 20-10 Ma and slower rates 10-5 Ma.[5]

TABLE 3.1. SUMMARY OF INFORMATION FROM EACH RIO GRANDE RIFT BASIN

Faulting	Sedimentation	Magmatism	Low-temperature Thermochronometry	Rifting Interpretations
Socorro Canyon (E)[3] Loma Pelada Fault (E)[3] West Joyita Fault (W)[3] Los Piños fault (W)[3,6] Manzano Fault (W)[3,6]	rocks[32]). Rift fill thicknesses are ~8 km[8,31]		Los Piños Mountains: AFT 37-65 Ma[6] Manzano Mountains: AFT 20-47 Ma[6]; AHe 25-41 Ma[2]	
Central Rio Grande rift				
Northern Albuquerque Basin				
Knife Edge Fault (W)[3,5,7,9] San Francisco Fault (NW)[3,7,9] La Bajada Fault (W)[3,7,9] Sand Hill Fault zone (E)[3]	Santa Fe fm. at the base of the Sandias (interbedded with 16.1 Ma basalt flows) is ~4200m thick[9,33,34]	Lucero VF, Albuquerque-Cat Hills VF, San Felipe VF, Cienega VF (late-Miocene to Quaternary)	Sandia Mountains: AFT 15-30 Ma[7] 16-22 Ma[9]; AHe 12-18 Ma[9] Ortiz Mountains: AFT 25-32 Ma[9]; AHe 17-18 Ma[9]	Rapid cooling in two phases (1) 22-17 Ma (2) 14-13 Ma.[9] 3.1 km of material was exhumed and 2.4 km of rock uplift has occurred in the Sandia Mountains since the middle Miocene.[9]
Española Basin				
Pajarito Fault (E)[3,10] Embudo Fault (left lateral)[3,10] Picuris-Pecos Fault (W)[3,10] Tijeras Fault (left lateral)[3,9,10] Nambe Fault (W)[3]	Santa Fe fm. is 3km thick on the west side of the basin[33] and 2 km thick on the east side[10]	Mount Taylor VF, Jemez VF, Taos Plateau VF, Ocate VF (late-Miocene to Quaternary)	Santa Fe Mountains: AFT 55-75 Ma[7]; AHe 44-115 Ma[2] Nacimiento Mountains: AFT (south) 46-33 Ma[6]; AFT (north) 81-46 Ma[6]	Cooling in the Santa Fe Mountains occurred during the Laramide Orogeny.[11]
Northern Rio Grande Rift				
San Luis Basin				
Sangre de Cristo Fault (60-70°W)[3,6,7,10,12,13]	Santa Fe fm. was deposited from 26-2 Ma[35,36] Sedimentation peaks in middle to late Miocene[15,18,19,36] Thicknesses range	Taos Plateau VF (late-Miocene to Quaternary), San Juan VF (late-Eocene to early Miocene)	Sangre de Cristo Mountains: AFT (south) 18-34 Ma[7]; AHe (central) 9-33 Ma[2]; AFT (north) 15-23 Ma[12,13]; AHe (north) ~11 Ma[2]	Multi-phase cooling in the southern Sangre de Cristo Mountains: (1) Laramide driven cooling and exhumation from the late Cretaceous to early cenozoic[6,11] (2) rift initiated cooling from the Oligocene to Miocene[6,11,12,13,14] (3) continued rifting from late Miocene to present.[11,12,13,15.16,17,18,19] In the central Sangre de Cristo Mountains rapid cooling occurs from 28-0 Ma[2]

TABLE 3.1. SUMMARY OF INFORMATION FROM EACH RIO GRANDE RIFT BASIN

Faulting	Sedimentation	Magmatism	Low-temperature Thermochronometry	Rifting Interpretations
	from 3 km over the Alamosa horst in the center of the basin[35,37] and up to 9 km closer to the basins edges[12,15,35,37]			In the northern Sangre de Cristo Mountains some interpretations suggest a late Laramide cooling pulse followed by a rifting pulse from the late Oligocene to early Miocene[11], while others suggest rifting in this part of the basin was not fully established until the Miocene.[13,14]
Upper Arkansas River Basin				
Sawatch Range Fault (70°E)[20,27]	Dry Union fm. late Miocene in age[38] is 900-1800m thick[18,26,39,38]	San Juan VF, 39 Mile VF (late-Eocene to early Miocene)	Sawatch Range: AFT 9-37 Ma[6,21,22,23]; AHe 2-33 Ma[2,20] Arkansas Hills: AHe 54-65 Ma[24] Mosquito Range (south): AHe 59-260 Ma[24]	Interpretations include fault initiation ~28-29 Ma[15,21], continuous rapid cooling from 28 to 5 Ma[2]; as well as pulsed exhumation (1) 22-16 Ma and (2) 8-0 Ma[20,25,26]
Blue River Basin				
Blue River Fault (50-75°E)[27,28]	Valley deposition began ~27 Ma and continued until at least the early Miocene[29]	North Park VF (late-Eocene to early Miocene), Flat Top VF (Miocene), Yampa VF (late-Miocene)	Williams Fork Mountains: AFT 21-37 Ma[29] Gore Range: AFT (east) 5-20 Ma[29]; AHe (east) 5-20 Ma[28]; AFT (west) 17-37 Ma[29]; AHe (west) 27-51 Ma[28]	Fault initiation in the Oligocene with major cooling and unroofing until at least 7 Ma with 2.3 km of displacement on the Blue River Fault and 3-5.4 km of exhumation.[28]

(1) Kelley and Chapin 1997; (2) Ricketts et al., 2016; (3) Machette et al., 1998; (4) Machette, 1988; (5) Ricketts et al, 2015; (6) Kelley et al., 1992; (7) Kelley and Duncan, 1986; (8) Lewis and Baldridge, 1994; (9) House et al., 2003; (10) Grauch et al., 2017; (11) Kelley, 1990; (12) Lindsey et al., 1983; (13) Lindsey et al., 1986; (14) Kelley and Chapin, 1995; (15) Tweto, 1979; (16) Chapin and Seager, 1975 (17) Morgan et al., 1986 (18) Taylor, 1975 (19) Epis et al., 1976; (20) Abbey and Niemi, in review; (21) Shannon, 1988; (22) Bryant and Naeser, 1980; (23) Cunningham, 1977; (24) Abbey et al., 2017; (25) Hubbard et al., 2001; (26) Knepper, 1974; (27) Morgan, 2017 (28) Landman and Flowers, 2013; (29) Naeser et al., 2002; (30) Peterson and Roy, 2005; (31) Lozinsky, 1988 (32) McIntosh and Quade, 1995; (33) Chapin and Cather, 1994; (34) May and Russell, 1994; (35) Brister and Gries, 1994; (36) Smith, 2004; (37) Kluth and Schaftenaar, 1994; (38) van Alstine, 1969; (39) Scott, 1975; (40) Sanford et al., 1977; (41) Balch et al., 1997.

or mantle convection. To further differentiate between possible rift models (Fig. 3.1), we evaluate spatial, temporal, and compositional patterns in magmatism along the RGR. By exploring the details of faulting and magmatism in the RGR, we are not only able to resolve the debate between a synchronous versus northward propagation model for rifting, but we are also able to gain knowledge about the manner and timing of fault growth and basin linkage as well as controls on rift geometry and accommodation mechanisms, which can be applied to other continental rift systems where there is perhaps less available data or limited access.

PHYSIOGRAPHY OF THE RIO GRANDE RIFT

The Rio Grande rift (RGR) is >1000 km long spanning from southern New Mexico to central Colorado, USA (Fig. 3.2; Kelley et al., 1992; Knepper, 1974; Limbach, 1975) and possibly as far north as southern Wyoming (Kellogg, 1999; Neaser et al., 2002; Leonard et al., 2002; Cosca et al., 2014). The RGR penetrates the significantly deformed southern Rocky Mountains, between the uplifted and relatively undeformed Colorado Plateau (mean elevations > 2 km) to the west and the low-relief Great Plains to the east (Fig. 3.2). The majority of the basins formed from rift extension are asymmetric half grabens (Kellogg, 1999) with significant exhumation occurring along north-south striking basin-bounding normal fault systems connected by various accommodation zones (Fig. 3.2; Lewis and Baldridge, 1994; Kellogg, 1999; Neaser et al., 2002; Ricketts et al., 2016). On closer inspection the physiography of the RGR changes along trend, displaying distinct differences in extension magnitudes, magmatism signature and faulting style.

We separate the RGR into three regions (north, central and south) based on the above physiographic differences. The southern RGR in southern and central New Mexico includes the Palomas, Jornada, Tularosa and southern Albuquerque Basins (Figs. 3.2, 3.3 and 3.4). The southern RGR has the most horizontal extension (Chapin and Cather, 1994), minimal rift-related volcanism, and accommodates extension across several large normal fault bounded basins at the same latitude (Figs. 3.2, and 3.4). The central RGR

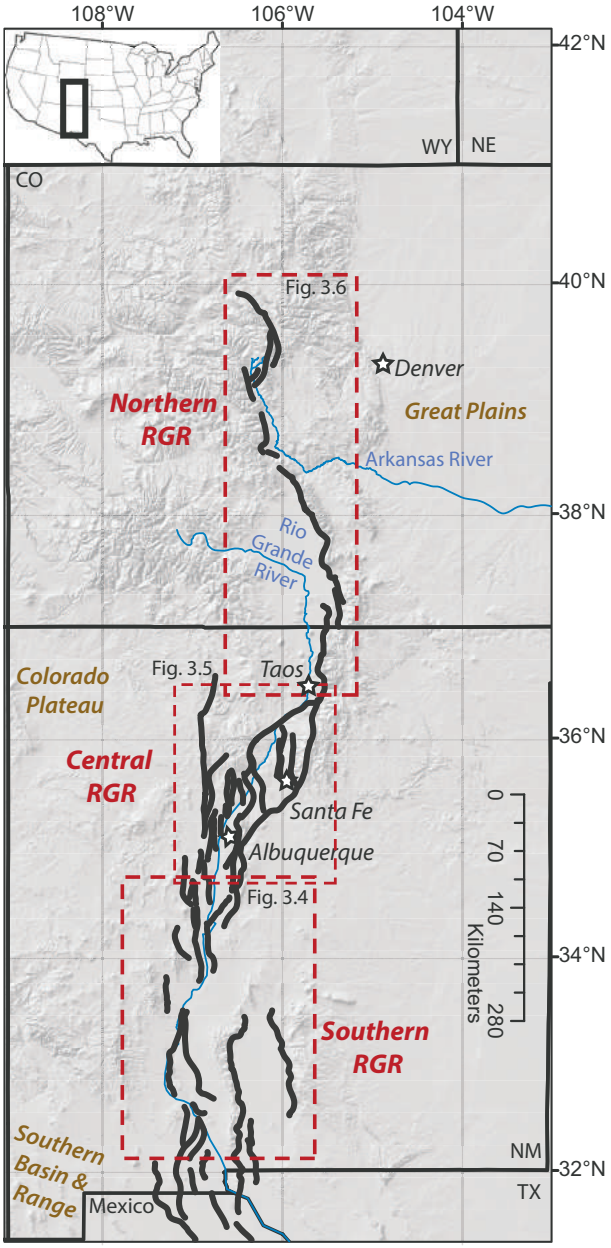

Figure 3.2: Location of the Rio Grande rift (RGR) in New Mexico and Colorado, sandwiched between the Colorado Plateau and Great Plains. Dashed red outlines mark the regions defined as the northern, central and southern RGR.

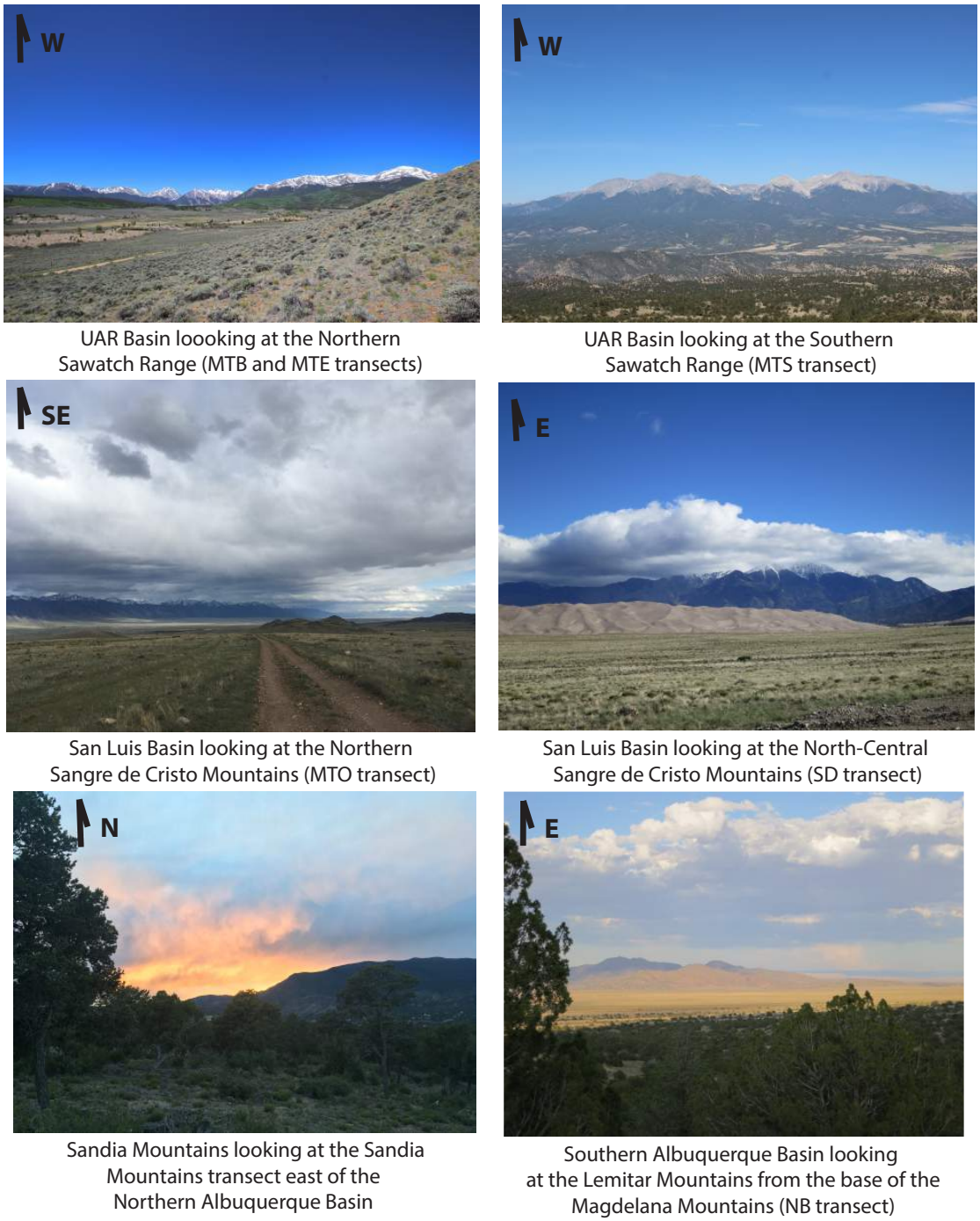

Figure 3.3: Field photos from the Rio Grande rift. Top row: the Sawatch Range and Mosquito Range from the upper Arkansas River Basin (top row), the Sangre de Cristo Range from the San Luis Basin (middle row), the Sandia Mountains flanking the northern Albuquerque Basin (bottom left), and the Lemitar Mountains from the Magdalena Mountains on the southwest side of the southern Albuquerque Basin.

includes the northern Albuquerque basin and the Española basin (Figs. 3.2, 3.3 and 3.5).

The central RGR basins are characterized by left-lateral strike-slip faults oriented northeast to southwest, numerous intra-basin normal faults with minimal vertical offset, large-volume magmatism, and less extension than the southern RGR (Chapin and Cather, 1994). The northern RGR is defined as the rift basins in northern New Mexico and Colorado including the San Luis, upper Arkansas River, and Blue River Basins (Figs. 3.2, 3.3 and 3.6). The northern RGR accommodates the least amount of extension (Chapin and Cather, 1994), is essentially amagmatic, and has one narrow basin bounded by a single large normal fault system at any given latitude (Figs. 3.2 and 3.6).

APPROACH TO RESOLVING SPATIAL AND TEMPORAL PATTERS OF FAULTING AND MAGMATISM IN THE RIO GRANDE RIFT

We use low-temperature thermochronometry, throughout the RGR to constrain timing, rates and magnitudes of faulting. Low-temperature thermochronometers are powerful tools for understanding the near-surface thermal histories of the crust. Apatite (U-Th-Sm)/He (AHe) records cooling between ~30 and 90 °C depending on radiation damage (Farley, 2002; Shuster et al., 2006; Flowers et al., 2009), apatite fission track (AFT) thermochronometry records sample ages associated with cooling between ~70 and 150 °C (Kelley and Chapin, 1995; Ehlers, 2005), and zircon (U-Th)/He (ZHe) records temperatures from ~130 to ~230 °C (Reiners et al., 2002; Reiners, 2005; Guenthner et al., 2013). Together, this suite of thermochronometers allows us to resolve rock thermal histories for the upper ~7 km of the Earth's crust, depending on the local geothermal gradient. Using these methods we can directly track fault movement as thermochronometers can directly record exhumation from footwalls of normal faults.

Here we primarily compile published low-temperature thermochronometry data, and complement these data with new analyses that expand the temperature ranges of the existing data. We analyzed 4-5 grains per AHe sample and three grains per ZHe sample. Outliers in each of the samples were identified using Dean and Dixon's q-test (Dean and Dixon, 1951) and grains were excluded if they were considered outliers with 95% confidence (Table B1). Sample age results are highly reproducible with percent errors of <8% after removal of outliers (Table 3.3).

We also assemble published data on volcanic ages and compositions to investigate spatiotemporal patterns of rift-related volcanism to use as an indication for rift timing and as a possible mode of extensional strain accommodation. In the following sections we describe the results from our new data as well as the spatial and temporal patterns in existing low-temperature thermochronometry and volcanism data.

Summary of Thermochronometry, Magmatism and Extension in the RGR basins

Low-temperature thermochronometry and magmatism analyses are ubiquitous throughout the area surrounding the RGR (Table 3.1). Useful proxies and data published from the RGR basins are briefly summarized in Table 3.1; however, because the aim of this work is to document fault growth and linkage through timing and magnitudes of exhumation and assess rift accommodation via faulting or magmatism, we focus on those datasets below.

Southern Rio Grande rift

The southern RGR is the widest extensional region in the rift with 50% extension accommodated by several grabens at a specific latitude (i.e. the Palomas, Jornada, and Tularosa basins; Chapin and Cather, 1994; Fig. 3.4). The faults bounding these basins are

north-south striking high angle (>60° dips) normal faults. Volcanism within the southern RGR is sparse with a few Quaternary basalt flows (the Jornada del Muerto, Carrizozo, and Potrillo volcanic fields; Fig. 3.7). To the west of the three southern-most basins are the mid-Cenozoic Mogollon-Datil ignimbrites, which are often attributed to slab retreat and slowing plate convergence rates at the end of the Laramide Orogeny rather than related to RGR extension (Fig. 3.7; McMillan et al., 2000; Chapin et al., 2004).

Palomas Basin

The Palomas basin is ~20 km wide and ~80 km long, flanked by the Caballo Mountains on the east side and the Black Range on the west side (Fig. 3.4). The west dipping Caballo fault system uplifts the Caballo Mountains and otherwise little deformation is documented in the Palomas Basin (Fig. 3.4).

Published low-temperature thermochronometry data from the basin-bounding ranges include minimal AFT and AHe that show early Cenozoic cooling ages to the west in the Black Range and middle to late Miocene cooling in the Caballo Mountains to the east (Table 3.1; Fig. 3.4; Kelley and Chapin, 1997; Ricketts et al., 2016).

There is no rift-related volcanism in the Palomas Basin; however, the Black Range is capped by the Mogollon-Datil intermediate to felsic ignimbrites and southwest of the basin are a few minor Quaternary basalt flows (McMillan et al., 2000; NM Bureau of Geology and Mineral Resources, 2003).

Jornada Basin

The Jornada Basin, lies to the east of the Palomas Basin, and is ~40 km wide and ~150 km long. Active faulting in the Jornada Basin is along the Jornada Draw fault, a normal fault that cuts from northwest to southeast across the center of the basin (Fig. 3.4;

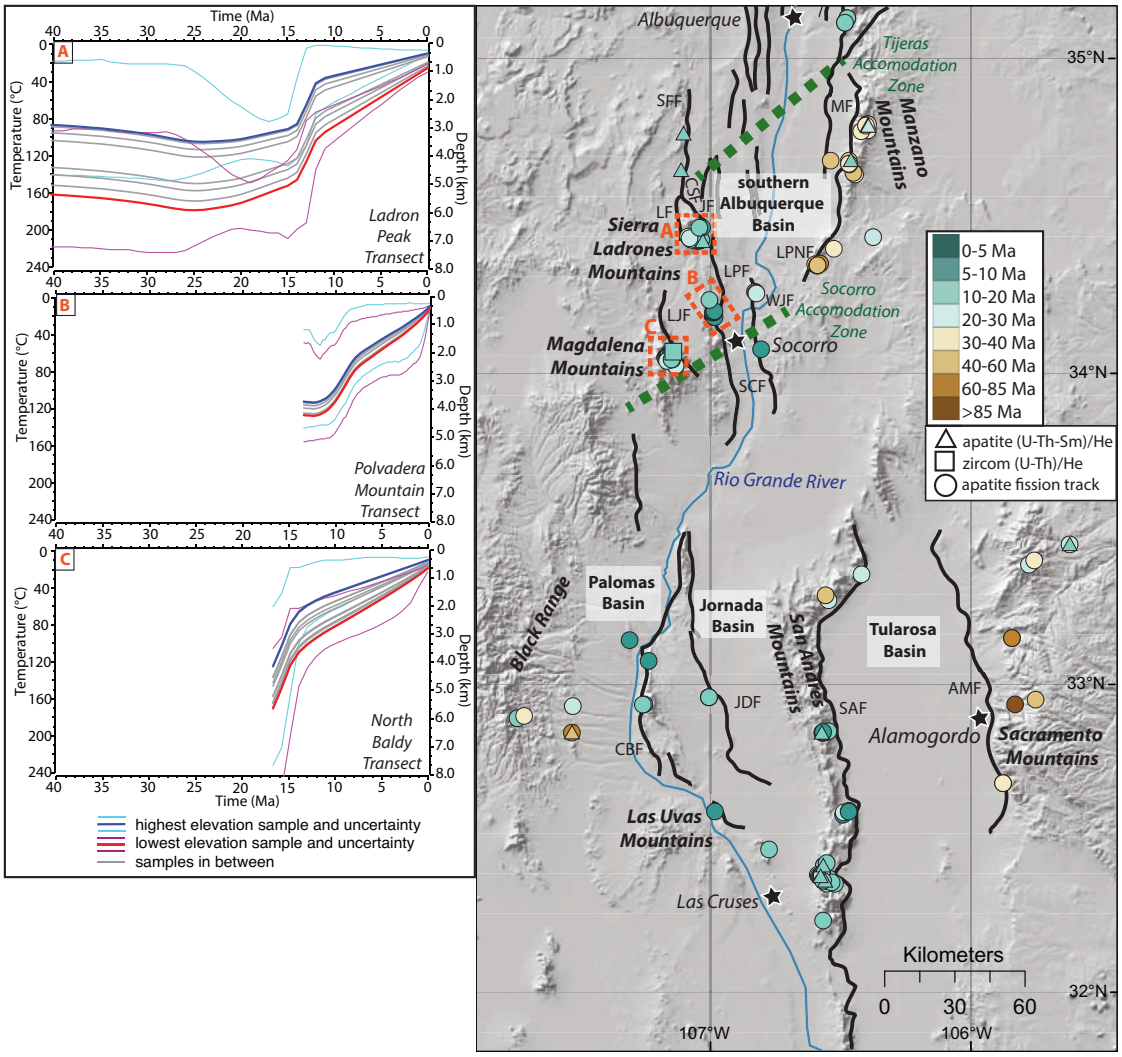

Figure 3.4: Southern Rio Grande rift (RGR). Low-temperature thermochronometry (published and this study) colored by cooling age. Inverse thermal history modeling was performed for three vertical transects from the southern Albuquerque basin, where samples were determined suitable for inverse thermal modeling as described in the text (dashed orange boxes and letters: (A) Ladron Peak transect; (B) Polvadera Mountain transect; (C) North Baldy transect). Accommodation zones indicated by dashed green line and major faults named with the following abbreviations: LJF-La Jencia fault; LPF-Loma Pelada fault; CBF-Cabaillo fault; SAF-San Andreas Fault; AMF-Alamagodo fault,;SCF-Socorro Canyon fault; WJF-West Joyita fault; MF-Manzano fault; Loma Paleda fault, LF-Ladron fault; JF-Jeter fault; CSF-Coyote Springs fault; SFF-Santa Fe Fault; LPNF-Los Pinos fault.

Machette et al., 1998; US Geological Survey, 2006; NM Bureau of Geology and Mineral Mesources, 2003).

The minimal thermochronometric data here is from Las Uvas Mountains on the southwest side of the basin, and records Miocene cooling (Table 3.1; Fig. 3.4).

The Jornada del Muerto volcanic field in the northern part of the basin and the Potrillo volcanic field south of the Jornada Basin on the New Mexico-Mexico border were formed from Quaternary basaltic eruptions (Fig; 3.7; NM Bureau of Geology and Mineral Resources, 2003).

Tularosa Basin

The Tularosa Basin is the easternmost of the southern RGR extensional basins and is ~50 km wide and ~140 km long (Fig. 3.4). The western side of the basin is bounded by the east-dipping San Andreas normal fault at the base of the San Andreas and Organ Mountains, and the eastern side is bounded by the west dipping Alamagordo fault at the base of the Sacramento Mountains (Fig. 3.4; Machette et al., 1998; US Geological Survey, 2006; NM Bureau of Geology and Mineral Resources, 2003).

Of the three southern RGR basins the Tularosa Basin has the most AFT and AHe data. These data record middle to late Cenozoic cooling in the San Andreas and Organ Mountains, and no cooling in the Sacramento Mountains since the early Cenozoic with the exception of middle Miocene cooling ages found in the Sierra Blanca intrusion in the northern part of the Sacramento Mountains (Table 3.1; Fig. 3.4; Kelley and Chapin, 1997; Ricketts et al., 2016).

The only rift related volcanism in the Tularosa basin is in the Quaternary basalts of the Carrizozo volcanic field in the northern part of the basin (Fig. 3.7; NM Bureau of Geology and Mineral Resources, 2003).

Southern Albuquerque Basin

The northernmost basin in the southern RGR is the southern Albuquerque basin, which we define as the area from south of Socorro, NM to Albuquerque, NM (Figs. 3.2 and 3.4). It is the widest of any of the individual rift basins spanning ~80 km from east to west and has undergone ~28% extension (Chapin and Cather, 1994). This basin contains numerous faults along many small mountain ranges including from west to east the high angle (>80°) east-dipping La Jencia Fault at the base of the Magdalena Mountains, the east-dipping high-angle Ladron Fault and west-dipping low-angle Jeter fault that bracket the Sierra Ladrones Mountains, the high-angle east-dipping Socorro Canyon normal fault system at the base of the Lemitar Mountains, and the west-dipping Los Piños and Manzano normal faults at the base of the Los Piños Mountains and Manzano Mountains (Figs. 3 and 4; Table 1; Machette, 1988; Ricketts et al., 2015).

Low-temperature thermochronometry data from these mountains show the western side of the basin is dominated by Oligocene to Miocene cooling ages in the Magdalena, Lemitar and Sierra Ladrones Mountains as opposed to the eastern side where Paleocene to Oligocene ages are preserved in the Los Piños and Manzano Mountains (Table 3.1; Fig. 3.4; Kelley et al., 1992; Ricketts et al., 2015; Ricketts et al., 2016). At the base of the Magdalena Mountains we collected a sample for ZHe analysis and obtained a cooling age of 14.4 ± 0.6 Ma (Tables 3.2 and 3.3; Fig 3.4).

Although there are minor low-volume extrusive deposits in the southern Albuquerque Basin, there is no significant quantity of rift-related volcanism. However, the Socorro magma body sits ~19 km below the surface of the southern Albuquerque Basin under an area of ~3400 km^2 (Sanford et al., 1977; Balch et al., 1997).

Central Rio Grande rift

The central RGR includes the northern Albuquerque Basin and the Española basin. The faulting in the central RGR is quite different from the southern RGR fault pattern. There are two northeast-southwest striking left-lateral strike-slip faults; the Embudo fault and the Tijeras fault (Fig. 3.5). In addition, both basins are full of diffuse intra-basin north-south striking normal faults (~10-20 km long), which accommodate minimal vertical offset (Figs. 3.2 and 3.5; Grauch et al., 2017). Volcanism in the central RGR is voluminous and dominated by basalt flows mainly <10 Ma, along the Jemez Lineament (Fig. 3.7; e.g. Chapin et al., 2004; Grauch et al., 2017).

Northern Albuquerque Basin

We separate the northern Albuquerque basin from the southern Albuquerque basin because the transition from a rift system of large basin-bounding normal faulting and little to no magmatism to one dominated by strike-slip faulting, minor intra-basin faulting and voluminous volcanism occurs in the middle of the Albuquerque Basin. This continuation of the Tijeras left lateral strike-slip fault that separates the Manzano Mountains in the southern Albuquerque basin and the Sandia Mountains on the east side of the northern Albuquerque basin, or an oblique anticlinal accommodation zone in the basin (Fig. 3.5; Grauch and Connell 2013; Ricketts et al., 2015). The Sandia Mountains on the east side of the northern Albuquerque basin are uplifted by the high-angle Knife Edge normal fault (Figs. 3.3 and 3.5), and the central and west side of the northern Albuquerque Basin is dominated by near-vertical-dipping normal faults that accommodate minimal vertical offset (Machette et al., 1998). Horizontal extension in the northern Albuquerque Basin is 17% (Chapin and Cather, 1994).

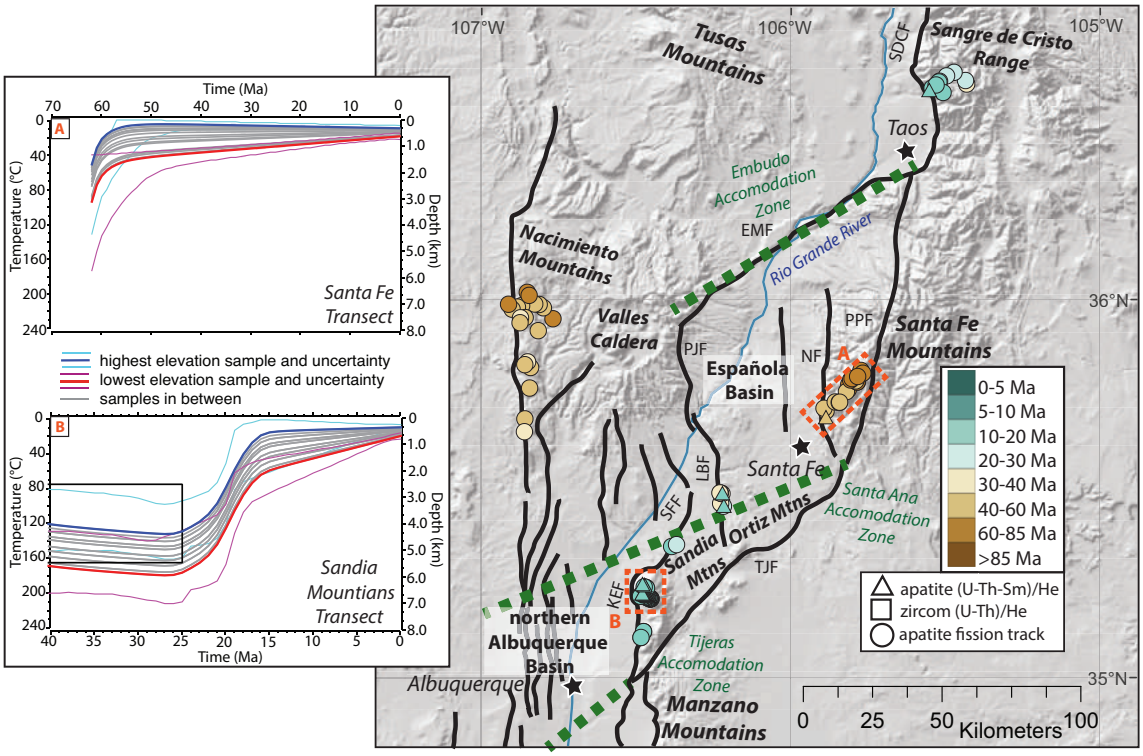

Figure 3.5: Central Rio Grande rift (RGR). Low-temperature thermochronometry (published and this study) colored by cooling age. Inverse thermal history modeling was performed for two vertical transects from the Española basin, where samples were determined suitable for inverse thermal modeling as described in the text (dashed orange boxes and letters: (A) Santa Fe transect; (B) Sandia Mountains transect). Accommodation zones indicated by dashed green line and major faults named with the following abbreviations: PJF-Pajarito fault; SDCF-Sangre de Cristo fault; PPF-Picuris-Pecos fault; LBF-La Bajada fault; SFF-San Francisco fault; KEF-Knife edge fault; TJF-Tijeras fault; NF-Nambe fault.

Low-temperature thermochronometry data from the Sandia and Ortiz Mountains reveal Miocene cooling on the east side of the northern Albuquerque Basin interpreted as extension and vertical displacement along the Knife-edge and La Bajada faults (Table 3.1; Fig. 3.5; Kelley and Duncan, 1986; House et al., 2003).

Rift related volcanism is in the form of Quaternary basalts flows, which increase in surface area to the north in the basin (Fig. 3.7; NM Bureau of Geology and Mineral Resources, 2003).

Española:

The Española Basin lies northeast of the northern Albuquerque basin (Figs. 3.2 and 3.5; Machette et al., 1998, Grouch et al., 2017). The north side of the basin is defined by a northeast-southwest striking left-lateral strike-slip fault (the Embudo fault), which has been dominated by left-lateral slip since ~12-11 Ma (Kelson et al., 2004; Grauch et al., 2017), although, it may have had an earlier phase of normal motion (Brown and Golombek, 1986). The Santa Fe Mountains are on the east side of the basin, cut by the north-south striking Picuris-Pecos fault (Fig. 3.5). The southern part of the basin is defined by the northeast-southwest striking left-lateral strike-slip Tijeras fault, and the west side is marked by the active east dipping Nacimiento fault that bounds the west side of the Nacimiento Mountains (Fig. 3.5). There are no extension estimates published for the Española Basin.

Low-temperature thermochronometry in the Santa Fe Mountains and Nacimiento Mountains record cooling ages from the late Cretaceous to the Eocene (Table 3.1; Fig.

TABLE 3.2: SAMPLE LOCATIONS AND MEAN AGES FOR APATITE (U-TH-SM)/HE AND ZIRCON (U-TH)/HE

Sample Name	Longitude	Latitude	Elevation (m)	Mineral	Mean Age (Ma)
17NSdC	-105.7667	38.1008	2675	Apatite	7.4 ± 0.5
17SD	-105.5066	37.7334	2559	Zircon	19.4 ± 0.4
17WEEL	-105.5586	36.5407	2332	Apatite	11.2 ± 2.4
17SFe	-105.8480	35.6881	2286	Apatite	58.7 ± 3.6
17NB	-107.1419	34.0764	2048	Zircon	14.4 ± 0.6

3.5; Kelley and Duncan, 1986; Kelley 1992; Ricketts et al 2016). We collected a sample at the base of the Santa Fe Mountains for AHe analysis, which yielded a cooling age of 58.7 ± 3.6 Ma (Tables 3.2 and 3.3; Fig. 3.5).

The Española Basin has the largest volcanic deposits within the RGR. Volcanism occurs not only in the basin but also along a northeast-southwest trend from Arizona to Kansas (Fig. 3.5). Magmatism began along this trend in the Española Basin in the middle Miocene and deposits range in composition from felsic to mafic (Fig. 3.7; Chapin et al., 2004; Grauch et al., 2017).

Northern Rio Grande rift

The northern RGR is relatively narrow in comparison to basins of the southern and central RGR and each basin of the three extensional grabens (from south to north: San Luis, upper Arkansas River and Blue River) is bounded by a single dominant normal fault. The three basins range from 60 km to 200 km in length, with high angle (>60°) north south striking normal faults producing high-relief mountains along the basin flanks (Figs. 3.2 and 3.6). Rift-related volcanism in these northern basins is essentially non-existent, although the mid-Cenozoic San Juan and Thirty-nine Mile volcanic fields, on the west and east margins of the rift respectively, are expansive and have the same source mechanisms as those invoked for the Mogollon-Datil volcanic field in southern New Mexico (Chapin et al., 2004). Some researchers have proposed the northern extent of the RGR reaches into northern Colorado, and possibly as far north as Wyoming, based on extensional features similar in age to rifting (Tweto, 1979) as well as a few sparse volcanic deposits with rift related chemical signatures and ages (Fig. 3.7; Leat et al., 1989; Leat et al.1990; Cosca et al., 2014). However, no clearly defined range-bounding normal faults are targets for low-temperature thermochronometry at northern latitudes.

San Luis basin:

The San Luis Basin is the longest of the RGR basins, >200 km long and ~75 km wide at the widest part (Tweto, 1979). The high angle (60°-70°) west dipping Sangre de Cristo normal fault bounds the east side of the basin exhuming the Sangre de Cristo Mountain range (Figs. 3.3 and 3.6). The west side of the basin has no active faulting, however the Tusas Mountains and San Juan Mountains tower over the valley at elevations >600-1200m above the basin floor. Extension across the San Luis Basin is 8-12% (Kluth and Schaftenaar, 1994; Chapin and Cather, 1994) and the basin has little internal deformation (Kluth and Schaftenaar, 1994) although there is a central horst (Alamosa Horst) in the middle of the basin that causes the deepest parts of the basin to be on the edges (Brister and Gries, 1994; Kluth and Schaftenaar, 1994).

In the Sangre de Cristo Mountains, AFT and AHe thermochronometry record Oligocene to Miocene cooling (Fig. 3.6; Lindsey et al., 1983; Lindsey et al., 1986; Kelley and Duncan, 1986; Ricketts et al., 2016). The low-temperature thermochronometry show Oligocene to Miocene cooling ages at the base of the Sangre de Cristo Mountains on both the west and east side (Lindsey et al., 1983; Kelley and Chapin, 1995; Ricketts et al., 2016) suggesting the possibility of active normal faults on both sides of the range during that time (Lindsey et al., 1983). In the San Luis Basin, we collected an AHe sample from the base of the northern Sangre de Cristo Mountains, which has a cooling age of 7.4 ± 0.5 Ma (Tables 3.2 and 3.3; Fig. 3.6). We also sampled at the base of the central Sangre de Cristo Mountains for ZHe analysis obtaining a cooling age of 19.4 ± 0.4 Ma (Tables 3.2 and 3.3; Fig. 3.6). A sample collected for AHe analysis was added to the base of the southern Sangre de Cristo Mountains near Taos, NM, and yielded a cooling age of 8.8 ± 0.5 Ma (Tables 3.2 and 3.3; Fig. 3.6).

TABLE 3.3: IDENTIFIED VERTICAL TRANSECTS

Sample Name	Source	Analysis Method	Mean Age ± Error	Latitude	Longitude	Original Elevation (m)	Fault Parallel Distance (m)
Keller Mountain Transect; Blue River fault (75°E) Blue River valley, northern RGR							
GRWL1	1	AHe	18.5 ± 0.6	39.6917	-106.2181	3911	1234
GRWL2	1	AHe	18.8 ± 1.2	39.6953	-106.2150	3755	1013
GRWL3	1	AHe	16.9 ± 0.7	39.6942	-106.2114	3603	787
GRWL8	1	AHe	11.6 ± 1.0	39.6917	-106.2019	3230	217
GR-WL-1	2	AFT	15.9 ± 2.2	39.6917	-106.2181	3911	1234
GR-WL-2	2	AFT	13.5 ± 2.2	39.6953	-106.2150	3755	1013
GR-WL-3	2	AFT	16.8 ± 3.4	39.6942	-106.2114	3603	787
GR-WL-4	2	AFT	11.9 ± 1.5	39.6936	-106.2075	3433	536
GR-WL-8	2	AFT	11.7 ± 2.0	39.6917	-106.2019	3230	217
GR-WL-9	2	AFT	9.2 ± 1.8	39.6908	-106.1978	3100	0
Buffalo Mountain Transect; Blue River fault (75°E); Blue River valley, northern RGR							
GR-WL-5	2	AFT	8.8 ± 2.6	39.6314	-106.1344	3066	0
GR-WL-7	2	AFT	6.7 ± 1.5	39.6303	-106.1431	3152	275
GR-WL-6	2	AFT	10.9 ± 2.4	39.6319	-106.1492	3364	615
GR-WL-12	2	AFT	11.0 ± 2.8	39.6214	-106.1350	3621	552
GR-WL-11	2	AFT	19.2 ± 6.7	39.6181	-106.1419	3871	949
GR-WL-10	2	AFT	19.4 ± 5.1	39.6161	-106.1425	3889	979
Mount Elbert Transect; Sawatch Range fault (70°E); upper Arkansas River valley, northern RGR							
14MTE-01	3	AHe	11.5 ± 1.1	39.0670	-106.4338	2973	1057
14MTE-02	3	AHe	32.2 ± 1.1	39.0803	-106.4353	3328	1427
14MTE-05	3	AHe	28.8 ± 0.3	39.0992	-106.4454	4156	2036
73N7	4	AFT	19.9 ± 4.4	39.0731	-106.4508	3121	1695
73N9	4	AFT	16.0 ± 2.4	39.0706	-106.4031	2819	0
TL-F-6-16	4	AFT	20.0 ± 2.9	39.0656	-106.3997	2926	5

TABLE 3.3: IDENTIFIED VERTICAL TRANSECTS

Sample Name	Source	Analysis Method	Mean Age ± Error	Latitude	Longitude	Original Elevation (m)	Fault Parallel Distance (m)
Mount Belford Transect; Sawatch Range fault (70°E); upper Arkansas River valley, northern RGR							
14MTB-01	3	AHe	7.2 ± 0.5	38.9971	-106.3751	2957	0
14MTB-01	3	ZHe	33.7 ± 1.6	38.9971	-106.3751	2957	0
14MTB-02	3	AHe	5.7 ± 0.3	38.9902	-106.3719	3230	165
14MTB-03	3	AHe	6.8 ± 0.1	38.9812	-106.3731	3460	422
14MTB-04	3	AHe	5.6 ± 0.5	38.9706	-106.3704	3692	565
14MTB-04a	3	AHe	8.4 ± 1.2	38.9657	-106.3680	4001	789
14MTB-05	3	AHe	8.9 ± 0.7	38.9607	-106.3611	4322	887
Mount Princeton Transect; Sawatch Range fault (70°E); upper Arkansas River valley, northern RGR							
15MTP-01	3	AHe	2.2 ± 0.1	38.7433	-106.1834	2833	0
15MTP-01	3	ZHe	20.6 ± 0.6	38.7433	-106.1834	2833	0
15MTP-02	3	AHe	3.0 ± 0.3	38.7420	-106.2017	3153	836
15MTP-03	3	AHe	7.0 ± 0.8	38.7487	-106.2108	3450	1367
15MTP-04	3	AHe	6.3 ± 0.6	38.7369	-106.2144	3708	1724
15MTP-05	3	AHe	12.2 ± 1.6	38.7415	-106.2225	3997	2210
84MP02	5	AFT	14.1 ± 1.8	38.7420	-106.2007	3133	793
84MP03	5	AFT	13.2 ± 1.5	38.7422	-106.1928	3055	485
84MP03	6	AHe	3.1 ± 0.3	38.7422	-106.1928	3055	485
84MP04	5	AFT	9.5 ± 0.8	38.7428	-106.1865	2963	210
84MP05	5	AFT	9.6 ± 1.2	38.7485	-106.1873	2899	172
84MP05	6	AHe	2.7 ± 0.5	38.7485	-106.1873	2800	172
Mount Shavano Transect; Sawatch Range fault (70°E); upper Arkansas River valley, northern RGR							
15MTS-01	3	AHe	13.9 ± 1.0	38.6031	-106.1984	3066	0
15MTS-02	3	AHe	10.7 ± 1.1	38.6073	-106.2079	3292	495
15MTS-03	3	AHe	9.3 ± 1.8	38.6119	-106.2161	3556	977
15MTS-04	3	AHe	13.9 ± 1.3	38.6139	-106.2261	3839	1539
15MTS-05	3	AHe	18.7 ± 1.5	38.6132	-106.2393	4085	2181
15MTS-06	3	AHe	10.5 ± 0.4	38.6189	-106.2392	4341	2378
84-300_Tag	7	AFT	14.8 ± 2.0	38.6493	-106.2231	3487	1110
84-280_Tnfg	7	AFT	19.7 ± 2.7	38.5929	-106.2416	3158	1379
Mount Owen Transect; northern Sangre de Cristo fault (60°W); San Luis valley, northern RGR							
G	8	AFT	17.3 ± 5.0	38.1053	-105.7508	2770	776

TABLE 3.3: IDENTIFIED VERTICAL TRANSECTS

Sample Name	Source	Analysis Method	Mean Age ± Error	Latitude	Longitude	Original Elevation (m)	Fault Parallel Distance (m)
H	8	AFT	20.0 ± 4.6	38.1081	-105.7608	2710	287
17SdC	this study	AHe	7.4 ± 0.5	38.1008	-105.7667	2675	0
Sand Dunes Transect; northern Sangre de Cristo fault (60°W); San Luis valley, northern RGR							
88SG01	5	AFT	12.8 ± 2.3	37.7470	-105.4567	3299	2784
88SG03	5	AFT	10.4 ± 1.3	37.7307	-105.4612	2927	2320
88SG03	6	AHe	11.5 ± 2.2	37.7307	-105.4612	2927	2320
88SG05	5	AFT	5.6 ± 1.4	37.7333	-105.5060	2536	0
17SD	this study	ZHe	19.4 ± 0.4	37.7334	-105.5066	2559	65
Wheeler Peak Transect; southern Sangre de Cristo fault (70°W); San Luis valley, northern RGR							
81WP7	9	AFT	18.5 ± 3.4	36.5433	-105.5558	2335	89
NM/H-1	9	AFT	17.6 ± 3.6	36.5533	-105.5287	2414	997
80L-6a	9	AFT	11.5 ± 2.2	36.5632	-105.5277	2457	1070
81WP6	9	AFT	21.3 ± 3.6	36.5658	-105.5250	2470	1164
81WP5	9	AFT	21.8 ± 3.6	36.5830	-105.4972	2683	2219
81WP4	9	AFT	22.9 ± 3.6	36.5950	-105.4667	2805	3269
17WEEL	this study	AHe	8.8 ± 0.5	36.5407	-105.5586	2332	0
Santa Fe Transect; Nambe fault (near vertical dip W); Española basin, central RGR							
81SF1	9	AFT	55.1 ± 12.2	35.6983	-105.8988	2256	N/A
81SF2	9	AFT	57.4± 10.6	35.7075	-105.9067	2296	N/A
81SF3	9	AFT	55.6 ± 11.4	35.7282	-105.8612	2421	N/A
81SF4	9	AFT	59.0 ± 9.2	35.7267	-105.8452	2488	N/A
81SF5	9	AFT	61.6 ± 13.4	35.7688	-105.8085	2985	N/A
81SF6	9	AFT	61.0 ± 8.6	35.7858	-105.8065	3128	N/A
81SF7	3	AFT	59.4 ± 10.2	35.7620	-105.8162	2924	N/A
81SF8	9	AFT	68.2 ± 14.2	35.7945	-105.7715	3732	N/A
81SF9	9	AFT	74.0 ± 12.2	35.7937	-105.7728	3744	N/A
81SF10	9	AFT	57.6 ± 10.6	35.7973	-105.7973	3634	N/A
81SF11	9	AFT	62.0 ± 10.6	35.8005	-105.7997	3610	N/A
81SF12	9	AFT	64.6 ± 10.6	35.8048	-105.7937	3415	N/A
81SF13	9	AFT	62.9 ± 15.0	35.8320	-105.7580	3848	N/A
81SF14	3	AFT	69.3 ± 20.0	35.8230	-105.7505	3543	N/A
81SF15	9	AFT	63.7 ± 16.6	35.8122	-105.7712	3238	N/A

TABLE 3.3: IDENTIFIED VERTICAL TRANSECTS

Sample Name	Source	Analysis Method	Mean Age ± Error	Latitude	Longitude	Original Elevation (m)	Fault Parallel Distance (m)
81SF16	9	AFT	43.8 ± 10.4	35.7272	-105.8440	2524	N/A
17SFe	this study	AHe	58.7 ± 3.6	35.6881	-105.8480	2286	N/A
Sandia Mountains Transect; Knife Edge fault (70°W); northern Albuquerque basin, central RGR							
81SAN1	9&10	AFT	19.1 ± 2.0	35.2045	-106.4470	3095	1639
81SAN1	10	AHe	17.3± 1.3	35.2045	-106.4470	3095	1639
81SAN2	9&10	AFT	21.7 ± 2.3	35.2045	-106.4492	3006	1489
81SAN3	9&10	AFT	19.3 ± 1.9	35.2045	-106.4515	2933	1347
81SAN3	10	AHe	17.1 ± 1.2	35.2045	-106.4515	2933	1347
81SAN4	9&10	AFT	21.5 ± 1.8	35.2062	-106.4540	2805	1150
81SAN4	10	AHe	17.1 ± 0.8	35.2062	-106.4540	2805	1150
81SAN5	9&10	AFT	18.5 ± 1.8	35.2078	-106.4557	2726	1025
81SAN5	10	AHe	15.9 ± 0.5	35.2078	-106.4557	2726	1025
81SAN6	9&10	AFT	19.2 ± 1.8	35.2093	-106.4607	2616	766
81SAN6	10	AHe	18.5 ± 1.3	35.2093	-106.4607	2616	766
81SAN7	9&10	AFT	18.9 ± 2.0	35.2108	-106.4643	2549	590
81SAN7	10	AHe	12.9 ± 0.9	35.2108	-106.4643	2549	590
81SAN8	9&10	AFT	16.9 ± 1.8	35.2113	-106.4678	2439	378
81SAN8	10	AHe	13.9 ± 0.5	35.2113	-106.4678	2439	378
81SAN9	9&10	AFT	16.3 ± 1.8	35.2138	-106.4733	2354	128
81SAN9	10	AHe	12.9 ± 1.3	35.2138	-106.4733	2354	128
81SAN10	9&10	AFT	17.4 ± 1.8	35.2132	-106.4747	2262	0
81SAN10	10	AHe	14.5 ± 1.5	35.2132	-106.4747	2262	0
Ladron Peak Transect; Loma Pelada fault (70°E); southern Albuquerque basin, southern RGR							
88LAD01	5	AFT	12.0 ± 1.2	34.4238	-107.0390	1866	357
88LAD02	5	AFT	10.6 ± 1.5	34.4242	-107.0500	1927	760
88LAD03	5	AFT	10.0 ± 1.1	34.4258	-107.0563	2012	1038
88LAD04	5	AFT	11.2 ± 1.5	34.4313	-107.0807	2574	2364
88LAD05	5	AFT	13.4 ± 1.8	34.4282	-107.0765	2439	2071
88LAD06	5	AFT	14.1 ± 2.0	34.4275	-107.0288	1829	0
88LAD08	5	AFT	32.2 ± 11.9	34.4403	-107.0925	2476	2599
88LAD11	5	AFT	29.1 ± 10.1	34.4338	-107.0850	2796	2669
TM(88LAD06)	11	AHe	12.4 ± 0.3	34.4275	-107.0288	1829	0

TABLE 3.3: IDENTIFIED VERTICAL TRANSECTS

Sample Name	Source	Analysis Method	Mean Age ± Error	Latitude	Longitude	Original Elevation (m)	Fault Parallel Distance (m)
Polvadera Mountain Transect; Socorro Canyon fault (60°E); southern Albuquerque basin, southern RGR							
90LEM01	5	AFT	12.5 ± 2.0	34.1802	-106.9895	1957	493
90LEM02	5	AFT	8.0 ± 1.8	34.1823	-106.9865	1982	374
90LEM03	5	AFT	6.7 ± 1.7	34.1808	-106.9855	1902	260
90LEM04	5	AFT	8.6 ± 1.8	34.1795	-106.9815	1823	9
90LEM05	5	AFT	6.1 ± 1.7	34.1978	-106.9898	1921	458
90LEM06	5	AFT	6.4 ± 1.7	34.1990	-106.9830	1847	78
90LEM07	5	AFT	6.5 ± 1.7	34.2029	-106.9830	1762	0
North Baldy Transect; La Jencia fault (80°E); southern Albuquerque basin, southern RGR							
88MAG05	5	AFT	26.7 ± 6.2	34.0732	-107.1613	2195	424
88MAG06	5	AFT	16.1 ± 4.4	34.0773	-107.1513	2109	211
88MAG07	5	AFT	16.9 ± 7.8	34.0767	-107.1422	2055	11
88MAG09	5	AFT	31.3 ± 11.0	34.0577	-107.1785	2988	1520
88MAG10	5	AFT	46.5 ± 8.4	34.0578	-107.1778	2963	1485
88MAG11	5	AFT	9.6 ± 1.6	34.0613	-107.1722	2695	1118
88MAG12	5	AFT	13.4 ± 3.5	34.0623	-107.1715	2695	1129
88MAG13	5	AFT	19.1 ± 4.6	34.0643	-107.1663	2591	934
88MAG14	5	AFT	18.7 ± 4.7	34.0663	-107.1622	2530	804
88MAG15	5	AFT	15.6 ± 2.9	34.0717	-107.1487	2366	458
88MAG16	5	AFT	11.7 ± 3.3	34.0755	-107.1452	2226	228
88MAG17	5	AFT	5.3 ± 2.4	34.0757	-107.1493	2104	175
88MAG18	5	AFT	4.6 ± 2.3	34.0808	-107.1437	2061	40
17NB	this study	ZHe	14.4 ± 0.6	34.0764	-107.1419	2048	0

(1) Landman and Flowers 2013; (2) Naeser et al., 2002; (3) Abbey and Niemi, 2018; (4) Bryant and Naeser, 1980; (5) Kelley et al., 1992; (6) Ricketts et al., 2016 (7) Shannon, 1988; (8) Lindsey at el., 1986; (9) Kelley and Duncan, 1986; (10) House et al., 2003; (11) Ricketts et al., 2015; (12) Kelley and Chapin, 1997.

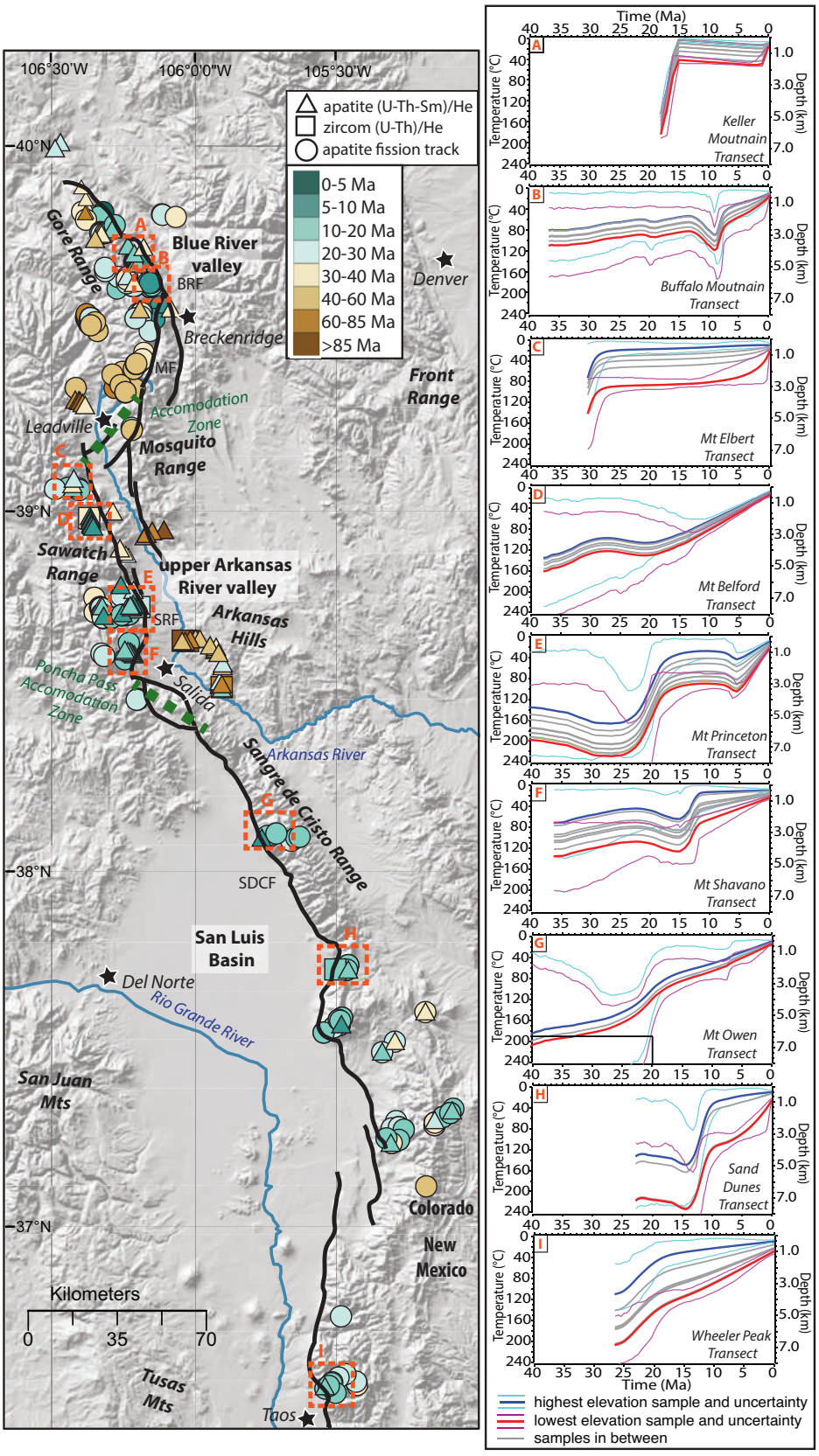
106°30'W
106°0'0"W
105°30'W
40°N
39°N
38°N
37°N
apatite (U-Th-Sm)/He
zircom (U-Th)/He
apatite fission track
0-5 Ma
5-10 Ma
10-20 Ma
20-30 Ma
30-40 Ma
40-60 Ma
60-85 Ma
>85 Ma
Gore Range
Blue River valley
BRF
Breckenridge
Denver
Front Range
MF
Accomodation Zone
Leadville
Mosquito Range
Sawatch Range
upper Arkansas River valley
SRF
Arkansas Hills
Poncha Pass Accomodation Zone
Salida
Arkansas River
Sangre de Cristo Range
SDCF
San Luis Basin
Del Norte
Rio Grande River
San Juan Mts
Colorado
New Mexico
Kilometers
0
35
70
Tusas Mts
Taos
Time (Ma)
Temperature (°C)
Depth (km)
Keller Moutnain Transect
Buffalo Moutnain Transect
Mt Elbert Transect
Mt Belford Transect
Mt Princeton Transect
Mt Shavano Transect
Mt Owen Transect
Sand Dunes Transect
Wheeler Peak Transect
highest elevation sample and uncertainty
lowest elevation sample and uncertainty
samples in between

Figure 3.6: Northern Rio Grande rift (RGR). Low-temperature thermochronometry (published and this study) colored by cooling age. Inverse thermal history modeling was performed for two vertical transects from the Española basin, where samples were determined suitable for inverse thermal modeling as described in the text (dashed orange boxes and letters: (A) Keller Mountain transect; (B) Buffalo Mountain transect; (C) Mount Elbert transect; (D) Mount Belford transect; (E) Mount Princeton transect; (F) Mount Shavano transect; (G) Mount Owen transect; (H) Sand Dunes transect; (I) Wheeler Peak transect). Accommodation zones indicated by dashed green line and major faults named with the following abbreviations: SDCF-Sangre de Cristo fault; SRF-Sawatch Range fault; MF-Mosquito fault; BRF-Blue River fault.

Volcanic deposits within the basin are in the southern-most part where the Miocene-aged Taos Plateau volcanic field blankets the basin fill, and to the west of the basin are the large volume ignimbrites of the Oligocene aged San Juan volcanic field (Table 3.1; Figs. 3.7).

Upper Arkansas River Basin

The upper Arkansas River (UAR) Basin is ~90 km long, stretching from Salida to Leadville, Colorado and is 5-10 km wide (Fig. 3.6). The graben is bounded on the west side at the base of the Sawatch Range, by the east dipping high angle (~70°E) Sawatch Range Fault (Fig. 3.3; Miller, 1999; U.S. Geological Survey, 2006; Abbey and Niemi, 2018). The northeast side of the graben has minor faults in the Mosquito Range (Fig. 3.6) that are thought to be re-activated Laramide structures (Tweto, 1979).

Low-temperature thermochronometry cooling ages in the UAR Basin are Cretaceous to Eocene in the Mosquito Range and Arkansas Hills on the east side (Table 3.1; Fig. 3.6; Abbey et al., 2017), and Oligocene to Quaternary in the Sawatch Range (Table 3.1; Fig. 3.6; Cunningham, 1977; Bryant and Naeser, 1980; Shannon, 1988; Kelley et al., 1992; Ricketts et al., 2016; Abbey and Niemi, 2018).

There is no rift-related volcanism around the UAR valley; however, the Oligocene ignimbrites in the San Jan and Thirty-nine Mile volcanic fields are well preserved on both the east and west sides of the UAR basin (Fig. 3.7).

Blue River Basin

The Blue River Basin is the farthest north expression of a basin forming fault system of the RGR. It is ~60 km long and 5-9 km wide. The Blue River fault, on the west side of the Blue River Basin at the base of the Gore Range, dips ~50-75° to the east (Fig. 3.6; Landman and Flowers, 2013; Morgan, 2017) and is interpreted to have had many phases of activity including throughout the late-Cretaceous and entire Cenozoic (Tweto, 1979), with possibly >1.4 km of vertical displacement along the southern Blue River fault occurring in the Pliocene (Kellogg et al., 2011).

Low-temperature thermochronometry in the Gore Range show that fault exhumation initiated in the Oligocene, continued to at least the late Miocene and was concentrated at the range front near the Blue River Fault trace (Table 3.1; Fig. 3.6; Naeser et al., 2002; Landman and Flowers, 2013).

There is no rift-related volcanism in the Blue River Basin; however, there are small-volume volcanic deposits at the same latitude about 50 km to the west of the Blue River Basin that are Miocene or younger in age and which have similar chemical signatures to other rift-related volcanics (Fig. 3.7; Leat et al., 1989; Leat et al.1990; Cosca et a., 2014).

INVERSE THERMAL HISTORY MODELING OF LOW-TEMPERATURE THERMOCHRONOMETRY DATA TO OBTAIN FAULT INITIATION TIMING AND ESTIMATES FOR EXHUMATION MAGNITUDES

To obtain the most information on fault initiation and magnitudes and rates of exhumation from the thermochronometric data, we focus on published data that can be assembled into coherent vertical transects (Ehlers, 2005). The more space covered along

the exhumed fault block the more information can be gleaned about the timing of the onset of fault motion as well as the minimum temperatures to which the rock were exposed at depth. Traditionally, age-elevation relationships of vertical transects have been used to estimate initiation timing and rates of exhumation (Fitzgerald and Gleadow, 1990). Advances in the field, however, have progressed to include inverse thermal history modeling (Ketcham, 2005; Gallagher, 2012) and a better understanding of diffusion kinetics in both apatite and zircon, provides a way to explore many possible cooling histories for a given sample or group of samples.

In this study, we define a vertical transect as including at least three thermochronometric samples that are within 5 km of the fault trace at the surface. We targeted places where >500 m was traversed in vertical space across <5 km of horizontal space to ensure a high relief relationship between the samples. We identified one to four groups of samples that fit our criteria for a vertical transect in each RGR basin (Table 3.3) except for the three southern-most basins (Palomas, Jonada and Tularosa basins) where there were no such spatial relationships in the published samples from those basins.

Inverse Thermal History Modeling

We use the program QTQt (QTQt64R5.6.2a; Gallagher, 2012) for inverse thermal history modeling of our selected vertical transects. QTQt was preferred for this study because it has the ability to incorporate several samples with a known spatial relationship (i.e. vertical transects) and can integrate different thermochronometers simultaneously within the same model. In addition, newer versions (post-QTQt64R5.5) of the program are helpful for including early AFT data published in the region, because these early

publications often omitted the detailed track count and track length needed for inverse modeling to obtain thermal histories. QTQt can perform a resampling of published track count data for AFT samples to generate synthetic spontaneous and induced track length data with statistics that match the reported data, and thus provides a way to use early AFT data in new thermal history models. Outputs from these inverse thermal history models are most-likely time-temperature paths that a sample or group of samples may have undergone, which help to resolve questions related to timing, magnitudes, and rates of exhumation.

To obtain estimates for timing and magnitudes of fault motion, via inverse thermal history modeling, we must have a thorough understanding of the spatial relationships between samples in each vertical transect. We assume sample location relationships have not changed as the rocks are exhumed to the surface and that each sample in the entire transect has undergone the same exhumation history. However, exhumation along a normal fault implies the footwall samples have experienced some amount of tilting that is related to the dip of the fault (Stockli et al., 2000; Shirvell et al., 2009), which means the paleo-vertical distance between the samples is different from the present vertical distance. To account for this difference in paleo versus modern vertical distance we project the samples from a single transect onto the fault plane on which they were exhumed (Abbey and Niemi, 2018). This projection allows us to determine the fault parallel distance (i.e. the paleo-vertical distance between the samples) at the time the samples were undergoing exhumation. These new sample distance relationships are what we use in our inverse thermal history model runs (Table 3.3).

Thermal modeling results and interpretations

Inverse thermal model inputs include raw age information, grain size, and concentrations of He, U, Th and Sm. In all model runs we implemented the Flowers et al. (2009) model for radiation damage in apatite and the Guenthner et al. (2013) damage model for zircon. Our defined model parameters include the present-day surface temperatures between 7°C and 13°C (temperatures that encompass the mean annual temperatures in the rift basins in Colorado and New Mexico), and a geothermal gradient between 25°C and 35°C/km (30°C/km is a reasonable estimate for the RGR based on modern regional heat flow as well as elevated heat flow estimates for the region during the Oligocene; House et al., 2003). Additionally, the prior temperature range for each model (i.e. the temperature space in which a single model run can start) was dependent on the types of data included in the runs (with only AHe data temperature prior was set to between 0°C and 100°C, if a run included AFT data temperature priors were between 0°C and 150°C and if ZHe was included the temperature prior was 0°C and 250°C). In select cases where there is other useful information related to past temperatures or depths that can be incorporated into the models as a constraint, the individual data for each constraint is discussed below (Figs. 3.5 and 3.6). Models were run with a burn-in of 20,000 iterations then sampled over 100,000 iterations and the birth proposal parameters were picked using a Gaussian distribution.

Southern Rio Grande rift

The three southern most RGR basins (Palomas, Jornada, and Tularosa) do not have thermochronometry samples that fit our criteria for a vertical transect, so we did not perform any inverse thermal history modeling on thermochronometry data from those basins, but we note that the cooling ages from the thermochronometric data on the active

basin-bounding faults are generally between ~20 Ma and 5 Ma (Fig. 3.4; Kelley and Chapin, 1997; Ricketts et al., 2016).

Southern Albuquerque Basin

Three vertical transects were identified and used for inverse thermal history modeling in the southern Albuquerque Basin (Table 3.3). The North Baldy transect from the Magdalena Mountains was exhumed on the La Jencia fault with the earliest onset of faulting ca. 25 Ma (Fig. 3.4). Exhumation proceeded from ~25-19 Ma at a rate of ~0.3 mm/yr, bringing up rocks from ~7 km depth, then from ~19-16 Ma the exhumation rate increased to ~0.5 mm/yr. From 16 Ma to present we cannot resolve a specific pulse of cooling; however, fault exhumation continued, bringing rocks from ~3.5 km depth up to the surface at an average rate of 0.2 mm/yr (Fig 3.4).

The Polvadera Mountain transect, from the Lemitar Mountains eastward, closer to the center of the basin, records exhumation on the Socorro Canyon fault. Fault initiation appears to occur at ~12 Ma, bringing up rocks from >4 km depth at an exhumation rate of ~0.4 mm/yr until ~8 Ma at which point the exhumation rate decreased to an average of 0.3 mm/yr from 8-0 Ma (Fig. 3.4).

To the north, along the Loma Pelada fault, the Ladron Peak transect shows fault initiation at ~14 Ma, exhuming the footwall from ~5 km depth at a rate of ~0.7 mm/yr from 14 to 11 Ma followed by slower exhumation at an average rate of 0.2-0.3 mm/yr from 11 Ma to present (Fig. 3.4).

Central Rio Grande rift

Northern Albuquerque Basin

We performed inverse thermal history modeling on one group of samples in the Sandia Mountains (Table 3.3; Fig. 3.5). This model incorporates a constraint box to account for burial estimates made by House et al. (2003), who suggest that ~2.4 km of section was overlying the Sandia Mountains at the end of the Cretaceous and that another 1-2.5 km was added to that cover during the end of the Laramide Orogeny and Oligocene volcanism. Motion along the Knife Edge fault appears to initiate at ~24 Ma, with exhumation proceeding until ~16 Ma at a rate of ~0.4 mm/yr, bringing rock from ~5 km depth to within <1 km of the surface. From ~16 Ma to present there was <1 km of exhumation recorded in the Sandia Mountains (Fig. 3.5).

Española Basin

Based on the new AHe ages obtained from the base of the Santa Fe transect and published AFT ages in the Santa Fe Mountains (Kelley and Duncan, 1986), cooling around the Española Basin seems to be entirely associated with the Laramide Orogeny. Thermal history modeling confirms this and shows that all of the samples were at near surface temperatures by 50 Ma (Table 3.3; Fig. 3.5), which suggests that the Nambe Fault at the range front of the Santa Fe Mountains does not accommodate a large enough amount of rift-related vertical displacement, associated with rifting, to detect with low-temperature thermochronometry. This places a limit on rift related exhumation of <~1.5 km in the western Santa Fe Mountains.

Northern Rio Grande rift

San Luis Basin

In the San Luis Basin, we identified three areas where data could be considered part of a vertical transect and used for inverse thermal history modeling (Table 3.3). In

the southern San Luis Basin, the Wheeler Peak transect shows exhumation of rock from >6 km depth at a rate of ~0.4 mm/yr from 25 to 20 Ma. Post-20 Ma the thermal modeling does not recover any discrete pulses of cooling, with exhumation from ~4 km depth occurring at an average rate of 0.2 mm/yr (Fig. 3.6).

In the north-central part of the San Luis Basin, the Sand Dunes transect reveals fault initiation occurred at ~14 Ma and rocks were exhumed from >7 km depth at a rate of ~1.0 mm/yr from 14 to 11 Ma. From 8 Ma to present another exhumation pulse exhumes footwall rocks from ~4 km depth at a rate of 0.5 mm/yr (Fig. 3.6).

The Mount Owens transect, farther north, includes a constraint to represent conodont analyses from Lindsey et al. (1986) that indicates burial to temperatures of 200-300°C. Thermal history modeling shows that from ~25-20 Ma exhumation brought rocks from ~5.5 km depth at a rate of 0.4 mm/yr. After 20 Ma the thermal history path is less detailed, similar to the Wheeler Peak transect thermal history, and the footwall continued to exhume at average rates of ~0.15-0.2 mm/yr to present-day (Fig. 3.6).

Upper Arkansas River Basin

The UAR Basin has the highest density of low-temperature thermochronometry data and we identified four transects useful for assessing rift-related exhumation (Table 3.3). In the south, the Mount Shavano transect reveals fault initiation at ~16 Ma, exhuming the footwall from ~4 km depth at a rate of ~0.5 mm/yr until ~12 Ma. After ~12 Ma, exhumation slows and definitive cooling pulses are not captured in the thermal model, which shows an average exhumation rate of <0.2 mm/yr (Fig. 3.6).

In the south-central part of the Sawatch Range fault system, the Mount Princeton transect records fault initiation at ~24 Ma. Rapid exhumation occured from >7 km depth

at a rate of ~0.6 mm/yr until ~19 Ma. A second pulse of exhumation began at ~5 Ma, exhuming rock from 3.5 km depth to the surface at a rate ~0.7 mm/yr (Fig. 3.6).

In the northern part of the Sawatch Range, the Mount Belford transect records onset of cooling at ~20 Ma, and although no distinct cooling pulses are discernable in the thermal history post-20-Ma, samples were exhumed from ~4 km depth to the surface at an average rate of 0.2 mm/yr from 20-0 Ma.

The farthest north expression of exhumation recorded by low-temperature thermochronometry in the UAR Basin is seen at the Mount Elbert transect, where exhumation is observed from ~3 km depth at a rate of ~0.4 mm/yr from 7 Ma to present (Fig. 3.6).

Blue River Basin

In the Blue River Basin, which is the farthest north asymmetric rift-basin, we identified two vertical transects in the southern part of the Gore Range (Table 3.3). The Buffalo Mountain transect reveals heating possibly by burial at ~14 Ma followed by rapid exhumation from ~4 km depth at a rate of ~0.5 mm/yr beginning ~10 Ma and slowing to a rate of ~0.3-0.4 mm/yr from 7 Ma to present (Fig. 3.6).

The Keller Mountain transect chronicles exhumation from at least 6 km depth from 18 to 15 Ma at a rate of ~1.3 mm/yr. The thermal history model also uncovers a pulse of exhumation from 2-0 Ma at a rate of ~1.0 mm/yr (Fig. 3.6).

Summary of low-temperature thermochronometry data and inverse modeling

The standardization we have applied to interpreting the plethora of low-temperature thermochronometry data in the RGR (i.e. vertical transects in close proximity to the active rift fault), provides a way to pinpoint onset of faulting and

estimate magnitudes and rates of fault motion in each separate rift basin. We find that fault initiation occurs in the northern and southern RGR at ca. 25 Ma, although only portions of what are now linked and through-going faults were active at that early stage (Figs. 3.4, 3.5 and 3.6). For many of these faults that were active in the early stages of rifting, this pulse of exhumation lasted for ~5-10 m.y. with rapid cooling recorded until the middle Miocene. Other parts of the individual rift basins did not become active until the middle Miocene with exhumation initiating between ca. 18 and 10 Ma. In such cases, the cooling pulse was often at a higher rate compared to the early pulse (Figs. 3.4 and 3.6). Finally, in several basins, especially the northern rift basins, there is a noticeable cooling pulse occurring at <7 Ma (Fig. 3.6).

In summary, we find that faulting initiates fairly contemporaneously along the rift and that exhumation rates increase as new segments initiate and link together. This helps to differentiate between rift models and reveals that a northward propagation model is not supported where faulting accommodates extension. To further discriminate between rift models we must understand rift accommodation via magmatism and then compare the spatial and temporal relationships between the rift related faulting and volcanism.

RIO GRANDE RIFT MAGMATISM

Continental rifting is often accompanied by magmatic activity, which is thought to play a role in extension accommodation in rift systems (e.g. Buck, 2004; Reyners et al., 2007; Ebinger et al., 2013; Muirhead et al., 2016). Volcanic activity within rifts is commonly localized along major boundary faults, transfer zones and limited portions of rift shoulders (off-axis volcanism)(Corti, 2012). In addition, magmatism in continental rift zones, grabens, and other manifestations of extensional tectonism is generally

dominated by mafic alkaline compositions (indicating an asthenospheric source) or bi-modal where low silica basalts and high silica rhyolites are erupted in the same location (e.g. Bailey, 1974; Tweto, 1979; Johnson and Thompson, 1991; Kellogg, 1999; Cosca et al., 2014).

Previous studies suggest that rift-related magmatism begins between 29 and 26 Ma when the style and chemical signature of the magmatic events changed from intermediate andesitic ignimbrites to alkaline basalt and bi-modal eruptions and lava flows in CO and NM (Epis and Chapin 1974; Lipman and Mehnert, 1975; Tweto, 1979; Lindsey et al., 1983; Miggins et al., 2002; Chapin et al., 2004). This transition is proposed to be associated with slab-rollback, retreat or detachment and development of the RGR (Cosca et al., 2014; Ricketts et al., 2015). However, because most of the magmatic activity seen in CO and NM during the Cenozoic seems to exist outside the boundaries of the rift flanks we look into the patterns in volcanic ages and chemical compositions to determine the role magmatism has played or possibly will play in accommodating extension in the RGR.

Published data on the Cenozoic volcanic rocks in the southwestern US is ubiquitous and has been compiled into large databases that facilitate data sharing and in our case provide a means for assessing general spatial and temporal patterns of mafic and bi-modal volcanism in a large-scale system. Using EarthChem (http://www.earthchem.org/portal; accessed February, 2018) we searched for chemical and age data related to all volcanic rocks in NM and CO with ages from 0 to 70 Ma (Table 3.4). The generated data table from EarthChem Portal included rock age, major oxide percentages, isotopic and rare earth element concentrations; however, all data types

were not available for every sample in the table, and we were mainly interested in the ages and major oxide compositions. We note that although every reported sample had an age associated with it, not every reported study performed independent age dating so many of the reported ages were assigned through regional correlations with previously dated rocks related to a specific event or stratigraphic relationship. We accept this method for assigning ages and use these data in our assessment of spatial and temporal patterns of magmatism.

Table 3.4. EarthChem Portal Search Query

Location (box defined by coordinates)	42°N; 30°N; 109°W; 103°W
Age (Ma)	0 to 70
Rock type	All categories within the EarthChem categories of Igneous > volcanic
Results (source and number of reported samples)	NAVDAT: 3984 GEOROC: 1741 USGS: 1685 Total: 7410

To evaluate the conclusions drawn from previous studies, that rift related volcanism begins with a bi-modal alkaline signal ~29-26 Ma we filtered the data from EarthChem to assess only samples with major oxide composition data. This is a useful filter because it allows us to focus on the SiO_2 content of the rocks, which is one simple way to look for a mafic and/or bi-modal signals. Major oxides are reported in weight percent (wt%) so summing concentrations should produce a total of 100%. Therefore, we performed another filter and retained samples with total major oxide concentrations between 98% and 102%. The remaining samples (5064 data points in total) were used in our assessment of patterns in age and SiO_2 content (Figs. 3.7 and 3.8). We did not filter for reported for a single flow event we did not exclude those. Chapin et al. (2004)

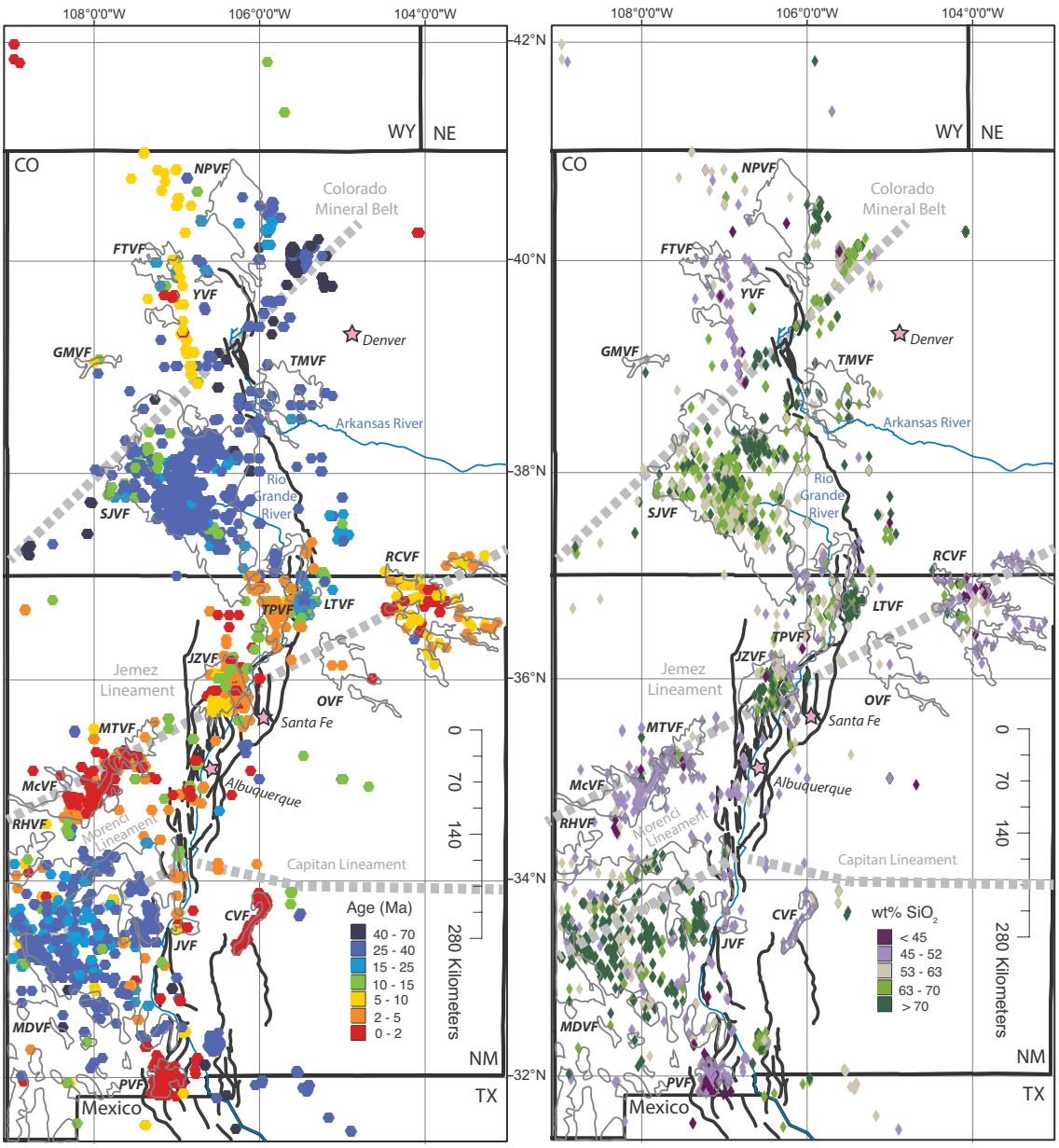

Figure 3.7: Age and SiO_2 content for Cenozoic volcanic deposits in Colorado and New Mexico from EarthChem database (see text and table 3.4 for information on search query). Major lineaments indicated by dashed grey lines and large-scale volcanic fields named with the following abbreviations: PVF-Potrillo volcanic field; MDVF-Mogollon-Datil volcanic field; JVF-Jornada volcanic field; CVF-Carrizozo volcanic field; RHVF-Red Hills volcanic field; McVF-McCarty's volcanic field; MTVF-Mount Taylor volcanic field; JZVF-Jemez volcanic field; TPVF-Taos Plateau volcanic field; OVF-Ocate volcanic field; LTVF-Latir volcanic field; RCVF-Raton-Clayton volcanic field; SJVF-San Juan volcanic field; TMVF-Thirty-nine Mile volcanic field; GMVF-Grande Mesa volcanic field; YVF-Yarmony volcanic field; FTVF-Flat Tops volcanic field; NPVF-North Park volcanic field.

perform a similar compilation for Cenozoic magmatic rocks in New Mexico and they do filter the data so that they only have one point to represent an event or specific stratigraphic unit and the trends in their compilation for NM data are similar to ours from both NM and CO, thus we do not suggest there is a large bias by not further filtering the results from our EarthChem query (Table 3.4).

Interestingly, we see that the spatial pattern of dominantly intermediate to felsic compositions coincides with the spatial pattern for volcanic rocks with ages greater than ~15 Ma and the pattern of low silica compositions aligns well with the pattern for volcanic rocks younger than ~15 Ma (Fig. 3.7). The oldest volcanics (70-40 Ma) have a small spatial extent, are intermediate to felsic in composition, and are found almost exclusively along the Colorado Mineral Belt lineament, with minor deposits in southern NM and along the TX and Mexico boarder (Fig. 3.7). Ignimbrites form large volcanic fields (Thirty-nine Mile, San Juan and Mogollon-Datil) after ~40 Ma (e.g. Chapin et al., 2004), which are mainly active between ~38 and 27 Ma and are composed almost entirely of intermediate and felsic compositions (Figs. 3.7 and 3.8). From ~27 to ~21 Ma volcanism is seen almost exclusively in the Mogollon-Datil volcanic field in the form of rhyolite eruptions (Fig. 3.7; Chapin et al., 2004). From ~21 to ~15 Ma there is a lull in volcanism with only a few small felsic- intermediate eruptions scattered around the Mogollon-Datil, San Juan, and Latir volcanic fields. At ca.15 Ma magmatic activity returns and mafic compositions become more prevalent (the mafic, intermediate and felsic categories are equally represented; Fig. 3.8; Chapin et al., 2004). Magmatism at this time is focused in the central RGR with minor eruptions in the Jemez, Taos, and Latir

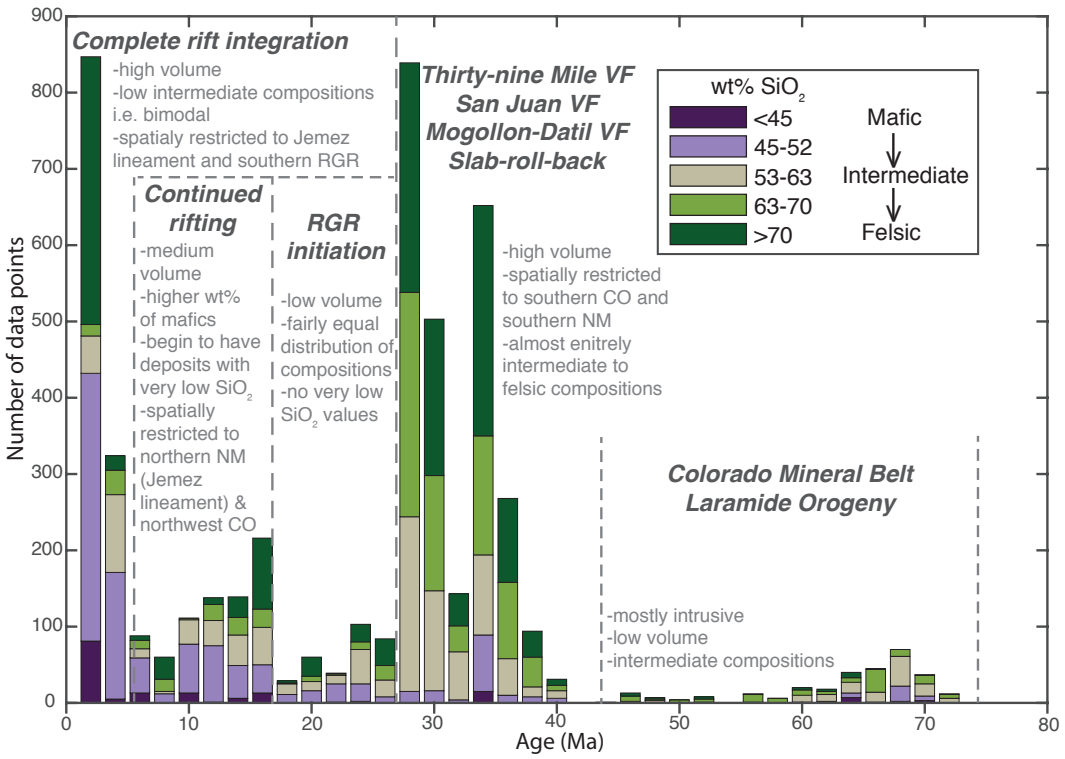

Figure 3.8: Stacked histogram with age and SiO_2 data for volcanic points gathered from EarthChem database (see text and Table 3.4 for information on search query). Note: this is all data published in EarthChem with no filter to single out each specific flow event and the number of points for each age bin is not directly related to volume of magmatism.

volcanic fields and areas of the southern Albuquerque Basin (Fig. 3.7 and 3.8). At ca. 10 Ma mafic volcanism begins to dominate while the volume of intermediate and felsic eruptions greatly decreases (Fig. 3.7 and 3.8). The location of volcanic sources shifts around 10 Ma, with major eruptions along the Jemez lineament in the Raton, Taos and Jemez volcanic fields as well as in minor eruptions in northwest CO along the same strike as the RGR but >50 km west of the Blue River Basin (Fig. 3.7). Magmatic activity continues unabated and by ~5 Ma basalts are erupted all along the northeast southwest striking Jemez Lineament, (Figs. 3.7 and 3.8). From 2 Ma to present the activity in the Jemez Lineament volcanic fields remain active as primarily mafic eruptions with the exception of rhyolite eruptions in the Jemez volcanic field (i.e. Bandelier tuff; Chapin et

al., 2004). Post-2 Ma volcanic activity begins in the southern RGR as well, with eruption of the low silica volcanic rock in the Jornada, Carrizozo, and Potrillo volcanic fields (Fig. 3.7).

INITIATION, GROWTH AND LINKAGE OF RIO GRANDE RIFT NORMAL FAULTS

RGR development begins ca. 25 Ma with motion on fault segments in the northern and southern parts of the RGR. It appears that faulting occurs at higher rates in the northern RGR at ~0.4 to 0.6 mm/yr, compared to the southern RGR at ~0.3 mm/yr (Figs. 3.4, 3.6 and 3.9) and there no evidence for faulting in the central RGR at 25 Ma (Fig. 3.9). Faulting continues in the north and south with initiation on more segments by ~18 to 14 Ma and many segments record faster exhumation rates at ~0.5 mm/yr to ~1.3 mm/yr (Figs. 3.4, 3.5, 3.6 and 3.9). This pattern mimics the detailed fault growth pattern seen in the upper Arkansas River (UAR) Basin where there are a high density of thermochronometric samples and thermal history models (Abbey and Niemi, 2018).

In the UAR phases of segment initiation occur at ~25 Ma, and ~18 Ma, and fault exhumation acceleration is inferred to be related to fault growth via tip propagation and segment linkage (Abbey and Niemi, 2018). This process of segment initiation, growth, and linkage appears to occur over several million years (Abbey and Niemi, 2018). We hypothesize that many of the basin bounding faults in the entire RGR may have the same growth patterns, which can be observed in other RGR basins where we have multiple vertical transects (e.g. San Luis Basin, Blue River Basin and southern Albuquerque Basin; Figs. 3.4 and 3.6). This rift-wide observation of late Oligocene to early Miocene fault initiation does not support the northward propagation hypothesis.

Our method of identifying rift initiation and quantifying fault growth patterns in the RGR is more accurate when using a multiple-transect approach. Initiation ages from a single transect may be misleading, as they will only reflect growth on that specific fault segment. Thus a multi-transect approach is preferable for understanding fault initiation and propagation patterns in rift systems.

DEVELOPMENT OF A FULLY-LINKED RIFT SYSTEM

Linkage of fault segments followed by the linking of separate rift basins via accommodation zones is seen in many continental rifts (e.g. Nelson et al., 1992; Ebinger 1989; Chapin and Cather, 1994; Lewis and Baldridge; 1994), as well as detailed in the northern RGR (Abbey and Niemi, 2018). In the northern RGR, through-going fault systems develop over million of years; however, by the middle to late Miocene these systems appear to be fully interconnected (Abbey and Niemi, 2018). This fault growth and linkage and pattern is mirrored in the apparent linkage of the northern and southern parts of the RGR around 15 Ma. This linkage occurs in the region we define as the central RGR and appears to be accommodated by magmatism. The major faulting in the central RGR is in the form of left-lateral strike slip faults and large-scale eruptive volcanism begins in this region at ca. 15 Ma (Figs. 3.5 and 3.9). In fact, some researchers suggest the entire region between the Embudo fault in the northern Española Basin and the Tijeras fault that cuts through the Albuquerque Basin is one large accommodation zone within in the rift (Figs. 3.5 and 3.9; Kelson et al., 2004; Grauch et al., 2017).

By the middle to late Miocene the RGR was fully linked, and the southern, central and northern parts of the rift have been actively accommodating extension as one

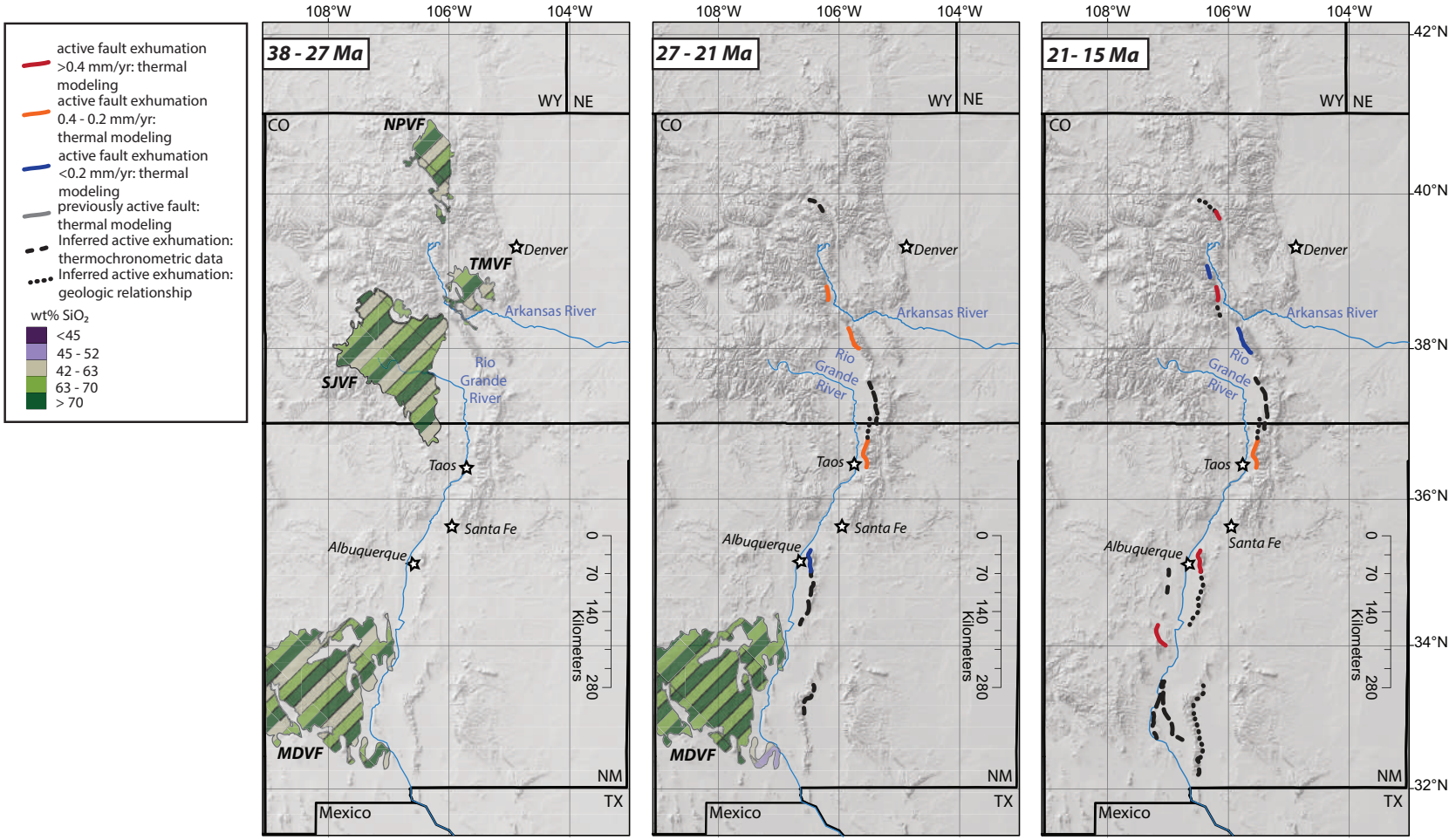

Figure 3.9: Evolution of faulting and magmatism along the Rio Grande rift (RGR) presented in time-steps. Faults patterned based on data source and colored by rate of exhumation where information from thermal modeling was available. Schematic versions of the active volcanic fields in each time step are colored to represent general eruption compositions and named with the following abbreviations: MDVF-Mogollon-Datil volcanic field; SJVF-San Juan volcanic field; TMVF-Thirty-nine Mile volcanic field; NPVF-North Park volcanic field.

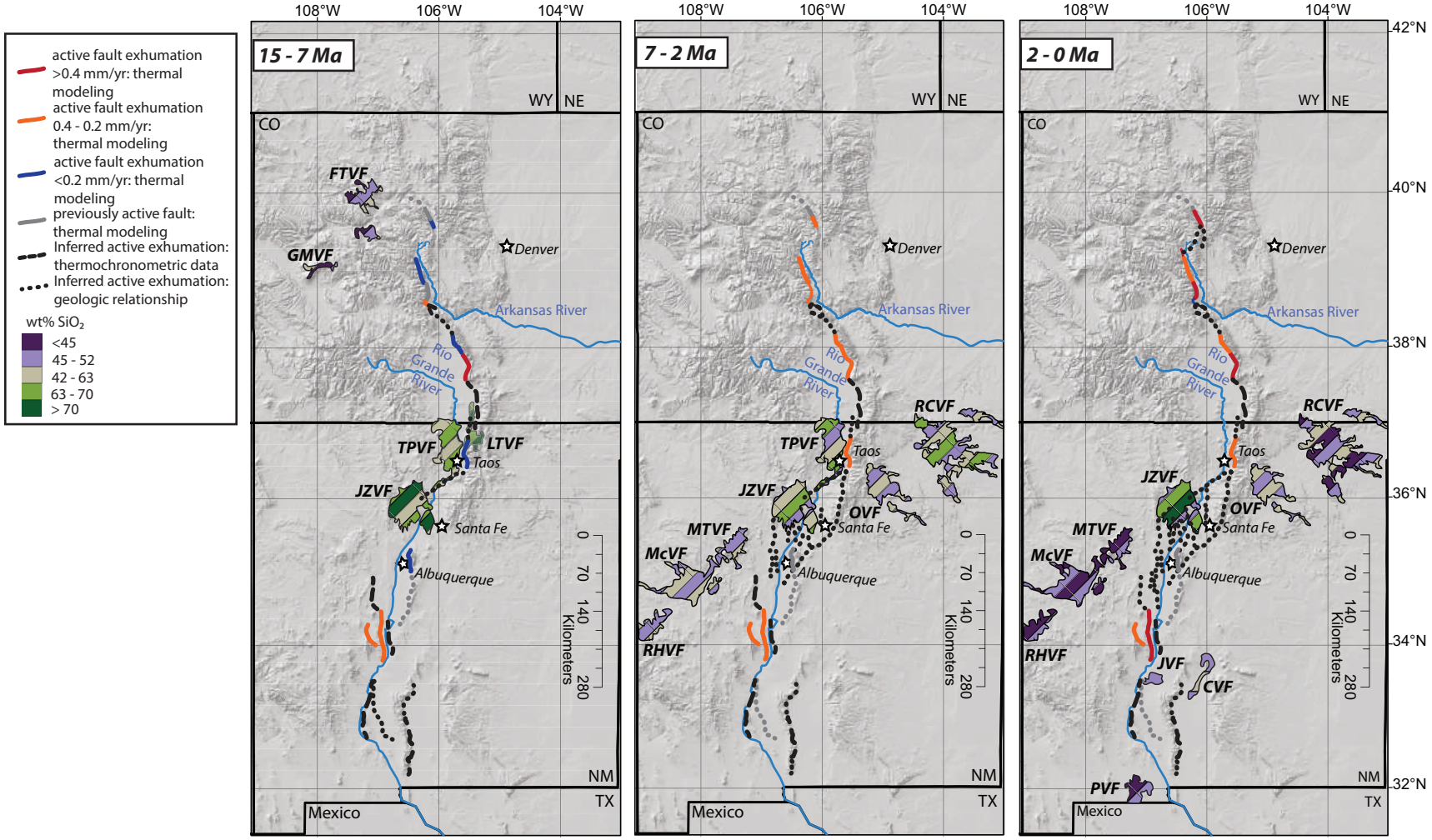

Figure 3.9 continued: Schematic versions of the active volcanic fields are named with the following abbreviations: JZVF-Jemez volcanic field; TPVF-Taos Plateau volcanic field; LTVF-Latir volcanic field; GMVF-Grande Mesa volcanic field; FTVF-Flat Tops volcanic field; RHVF-Red Hills volcanic field; McVF-McCartys volcanic field; MTVF-Mount Taylor volcanic field; OVF-Ocate volcanic field; RCVF-Raton-Clayton volcanic field; JVF-Jornada volcanic field; CVF-Carrizozo volcanic field; PVF-Potrillo volcanic field.

integrated system since then. The central part of the rift remains the only part where magmatism accommodates rifting, as there is no obvious volcanic accommodation in the early phases of rifting and from the mid-Miocene to present the majority of volcanism has been along the Jemez lineament, and not within any part of the RGR beside the central part (Figs. 3.7 and 3.9). Hence, magmatism does not seem to be a compelling proxy for the onset for rifting in the RGR system.

RIFT PHYSIOGRAPHY AND CRUSTAL INHERITANCE

Despite the above evidence that rifting initiated contemporaneously along numerous fault segments, there remain distinct physiographic differences between the southern, central, and northern parts of the RGR. We propose that these physiographic differences may be controlled partly by inherited crustal structures and partly by lithospheric properties.

We find that the RGR faults and general basin geometries are spatially coincident with mapped Ancestral Rockies uplifts and basins (Kottlowski, 1968; Knepper, 1974; Kluth and Coney, 1981; Baars and Stevenson, 1984; Shaw and Karlstrom, 1999; Dickerson, 2003; Huffman, 2003; Robbins, 2005; Kluth and DuChene, 2009). In New Mexico, the southern RGR basins and uplifted footwall margins are well aligned with Neoproterozoic rift features (Karlstrom et al., 1999; Timmons et al., 2001), a possible Cambrian rift system (McMillan and McLemore, 2004), and features from the Ancestral Rocky Mountain Orogen (the Orogrande and Estancia Basins and Pedernal uplift; Kottlowski, 1968; Dickerson, 2003; Fig. 1.3). The northern RGR basins and rift flanks appear in similar locations to the Ancestral Rockies Frontrange, Apishipa and Sierra Grande uplifts and Central Colorado Trough while the northeastern edge of the Colorado

Plateau and the middle to late Cenozoic rift related volcanism in northwestern Colorado align well with the Neoproterozoic rift features (Timmons et al., 2001) and Uncompahgre uplift (Kottlowski, 1968; Knepper, 1974; Kluth and Coney, 1981; Baars and Stevenson, 1984; Dickerson, 2003; Huffman, 2003; Robbins, 2005; Kluth and DuChene, 2009; Fig. 1.3).

In contrast, the magmatism in the central RGR and along the northeast-southwest trend of the Jemez lineament is spatially coincident with Proterozoic terrane boundaries (e.g. the suture between the Yavapai and Mazatzal terranes; Tweto and Sims, 1963; Warner, 1978; Karlstrom and Bowring, 1988; Karlstrom and Humphreys, 1998; Chapin et al., 2004; Magnani et al., 2004; Robbins, 2005; Chapin, 2012; Fig. 1.3). Therefore, it appears that the geometry and location of faulting and magmatism in the RGR may be partly controlled by pre-existing structure.

In addition, the crust and lithosphere are of markedly different character along the length of the RGR. The Jemez lineament separates thick lithosphere under the northern RGR, similar to that found beneath the Colorado Plateau, and thinner lithosphere beneath the southern RGR, more geophysically similar to that under the Basin and Range (Ander, 1980; Levander et al., 2011). Consequently, the northern RGR faults are rupturing a region where crustal thicknesses are ~50 km (Sheehan et al., 1995) and lithospheric thicknesses are >100 km (Levander et al., 2011), and the southern RGR faults are breaking ~40 km thick crust (Tousson and Sanford, 1976 and Sanford et al., 1977) and 70 km thick lithosphere (Fig. 3.10; Levander et al., 2011). These differences in thickness may account for the differences in the styles of faulting seen in the northern and southern RGR, because wider more diffuse rift zones are often associated with thinner warmer

underlying lithosphere as opposed to narrow deep grabens that are found in areas with a cold thick lithosphere beneath (Ebinger, 1991).

Such a difference in lithospheric properties can be a mechanism for driving magmatism as well, for example, through edge-driven convection as seen all along the sides of the Colorado Plateau (van Wijk et al., 2010; Rudzitis et al., 2016), where there is also an abrupt step in lithospheric thickness (Levander et al., 2011).

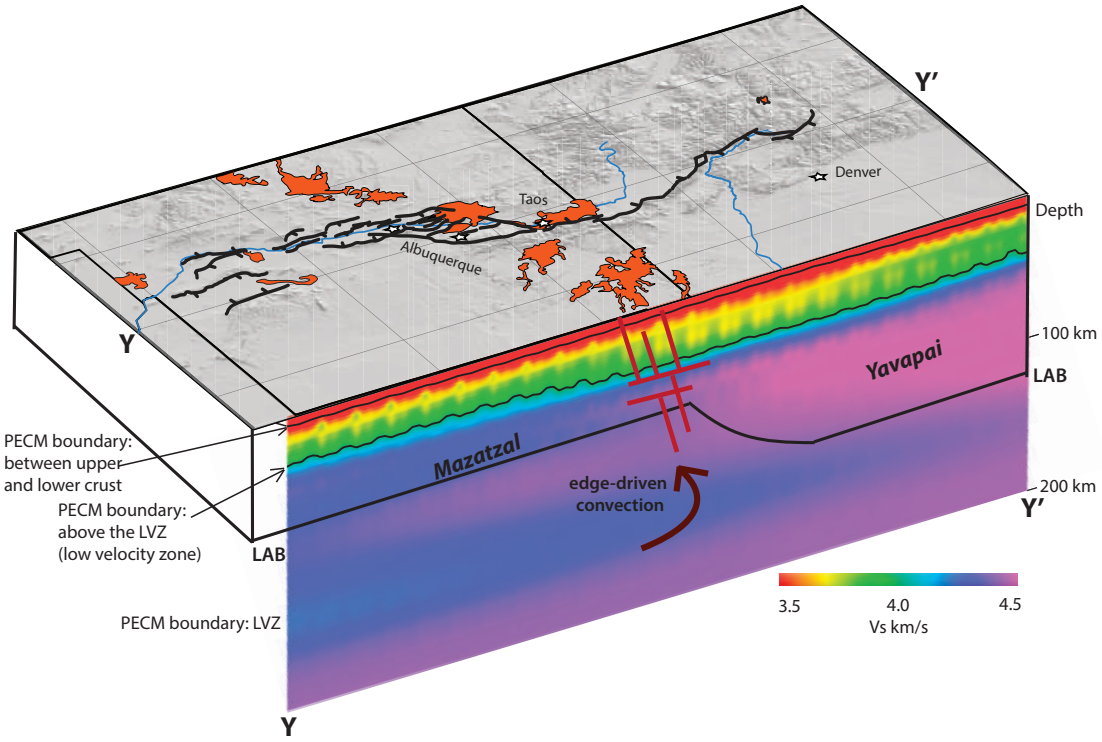

Figure 3.10: Block diagram showing simplified Quaternary faulting and volcanism at the surface and a depth profile from the cross-section between 42°N and 32°N at 106°W. The depth profile colors are Vs speeds in km/s from the WUS-CAMHI-2015 model obtained through IRIS (http://ds.iris.edu/dms/products/emc/gcross-section.html)(Chai et al., 2015) with different properties of continental upper mantle marked by the PECM boundaries: PECM—Continental Parametric Earth Model. Note the lithospheric thickness difference beneath the northern and southern parts of the RGR drawn at depths taken from the lithosphere-asthenosphere boundary estimates (Levander et al., 2011): LAB—Lithosphere-Asthenosphere boundary. The majority of the volcanism occurs along a lineament above the step in lithospheric thickness (Levander et al., 2011), which may be aided by edge-driven convection: arrow and red lines (Van Wijk et al., 2010; Rudzitis et al., 2016). This change in lithospheric thickness occurs at the Yavapai Mazatzal terrane boundary.

In summary, we propose that lithospheric properties control rift style and accommodation (Fig. 3.10) with crustal faults initiating along pre-existing weaknesses created by previous deformation events including Neoproterozoic and Cambrian rifting and the Ancestral Rocky Mountain Orogenic uplifts in Colorado and New Mexico. Faulting in the northern RGR is characterized by long narrow deep grabens indicating a strong and cold lithosphere (e.g. Ebinger, 1991), while in the south many large faults at the same latitude form to accommodate more extension in the southern RGR (Fig. 3.10). Strike-slip faulting and basin linkage across the Jemez Lineament occurs similarly where the transition in lithospheric properties is abrupt, and magmatism takes advantage of this character difference to accommodate rifting via dike injection, magma ejection and diffuse intra-basin faulting (Fig. 3.9 and 3.10; Corti, 2009; Murihead et al., 2016). Therefore, rift accommodation mechanisms and styles of deformation seem to be highly spatially controlled by pre-existing weaknesses and lithospheric structure.

RIO GRANDE RIFT MODEL

Our analysis of thermochronometry and magmatism patterns helps to identify and refine general continental rifting models (Fig. 3.1). Our thermal history modeling reveals fault initiation on segments throughout the rift, which do not support propagation models for the RGR. General synchronous rifting models suggest rifting may be driven by rotation of a block (e.g. Molnar et al., 2017) or oblique strain (e.g. Brune et al., 2017) causing rift segments to initiate simultaneously and link across accommodation zones. Several researchers support a block rotation model for the RGR, in which the Colorado Plateau acts as the rotating block with respect to the Great Plains (Hamilton, 1981; Cordell, 1982; Lewis and Baldridge, 1994; Chapin and Cather, 1994; Kreemer et al.,

2010). This interpretation involves a phase of clockwise rotation of the Colorado Plateau in the middle to late Miocene, which was accommodated along the Jemez lineament and which added to the development of the central RGR accommodation zone (Hamilton, 1981; Cordell, 1982; Lewis and Baldridge, 1994; Chapin and Cather, 1994; Kreemer et al., 2010). Another event of clockwise rotation of the Colorado plateau and counter clockwise rotation of the central RGR appears to have occurred between 7 and 4 Ma (Zoback and Thompson, 1978; Brown and Golombek 1986; Chapin et al., 2004). Therefore, rotation of the Colorado Plateau, and the fact that there is greater extension in the southern RGR (Chapin and Cather, 1994) seems to support a model for synchronous rifting via block rotation. However, RGR faulting initiated ~25 Ma (Fig. 3.9), ca. 10 m.y. before the proposed initial rotation of the Colorado Plateau. Therefore, we suggest a model in which there is a combination of oblique strain initiating the rifting and linkage of the rift segments that was later followed by the rotation of the Colorado Plateau, accounting for the increased extension in the south and enhanced magmatism occurring along the Jemez lineament (Fig. 3.1).

This detailed analysis of low-temperature thermochronometry data along rift flank faults affords the opportunity to understand fault initiation, growth, and linkage throughout the RGR, in both time and space. Moreover, because the RGR is a fairly slowly evolving system we are able to capture distinct phases of rift development, which may be difficult to discern in other rapidly evolving continental rift systems. We find that understanding rift accommodation via spatiotemporal patterns in faulting and magmatism is necessary to distinguish between different rift initiation and growth models and may be

useful for discriminating between models for continental rifts that have less available data or are difficult to access.

CONCLUSIONS

Inverse thermal history modeling from new and existing low-temperature thermochronometry data along the length of the entire Rio Grande rift provide detailed information on the initiation, growth, and linkage of basin-bounding fault systems. In addition, the analysis of spatiotemporal relationships between faulting and rift-related magmatism provide the opportunity to understand the processes behind extension accommodation. These analyses suggest that rift initiation occurred synchronously ca. 25 Ma on several small fault segments within each basin. Fault segment initiation, growth and linkage continued through the middle to late Miocene at which point the rift became fully integrated into one system with the linkage across the central RGR via magmatic accommodation. Tectonic accommodation in the northern and southern parts of the RGR and magmatic accommodation in the central RGR has continued from ca. 10 Ma to present.

The RGR also has different physiographic characteristics between the northern, central and southern parts, and these differences are not dictated by the timing of rift development but rather by inherited crustal structure and lithospheric properties. For example, there may be possible reactivation of previous weaknesses from ancient rifting and orogenesis events and/or differences in the thickness of crust and lithosphere between the northern and southern RGR could be an explanation for the physiographic variation along the rift. We suggest a rifting model beginning with contemporaneous extension accommodated on numerous fault segments in the both the northern and southern RGR

driven by oblique strain. Then in the middle to late Miocene the system transitions to more of a block rotation model with clockwise rotation of the Colorado Plateau causing increased extension accommodated by faulting in the northern and southern RGR and magmatism in the central RGR.

ACKNOWLEDGEMENTS

Thank you to K. E. Murray for assistance with sample collection and for insightful conversations about western U.S. geology. Thanks to Amanda Maslyn (University of Michigan) and Victor Valencia (ZirChron LLC) for assistance with sample processing and analysis. This work was partially supported by NSF grant EAR- 1151247 (NAN), as well as a Rackham graduate student research grant and a Turner Award from the Department of Earth and Environmental Sciences at the University of Michigan (ALA).

APPENDIX B: SUPPLEMENTARY DATA TABLES AND FIGURES FOR CHAPTER 3

This appendix contains one data table, Table B1, and two supplementary figures, Figs. B1 – B2. Appendix A shows examples of data files for inverse thermal history modeling, those files can be generated in the program QTQt with the information from Table B1 and data from the previously published data incorporated into each model run (Table 3.3). Alternatively, A.L. Abbey is willing to share the input text files used for these model runs and may be contacted at alabbey@umich.edu.

Table B1: This table contains analytical data for all apatite and zircon grains used for apatite (U-Th-Sm)/He and zircon (U-Th)/He thermochronometry results presented in this manuscript.

Figure B1: This figure shows relationships between age and eU and age and grain size.

Figure B2: This figure shows relationships between the observed age the predicted age from the maximum likelihood model output from QTQt.

TABLE B1: INDIVIDUAL GRAIN RESULTS FOR APATITE AND ZIRCON HE SAMPLES

Sample Name & Mineral (A or Z)	Mass (µg)	Length (µm)	Radius (µm)	FT	U (ppm)	Th (ppm)	Sm (ppm)	He (ncc)	eU (ppm)	Raw date (Ma)	Corr. date (Ma)	Error (Ma)
17NSdCb (A)	4.04	156.8	56.5	0.79	28.05	35,57	419.19	0.11	37.9	6.1	7.76	0.07
17NSdCd (A)	6.54	173.1	68.5	0.82	1.71	5.28	32.73	0.02	3.1	5.4	6.63	0.08
17NSdCg (A)	1.99	146.2	41.1	0.72	19.92	36.03	501.63	0.05	30.7	6.3	8.75	0.07
17NSdCh (A)	2.32	121.9	48.6	0.75	15.55	30.24	292.77	0.03	24.0	4.9	6.49	0.06
17SDa (Z)	2.25	114.4	49.5	0.75	3897.93	55.37	--	16.00	3910.9	15.0	20.03	0.23
17SDb (Z)	4.83	174.9	58.5	0.79	196.76	108.21	--	1.94	222.1	14.9	18.80	0.20
17SDc (Z)	2.34	144.4	44.8	0.74	411.42	255.22	--	1.89	471.1	14.2	19.22	0.19
17WEELa (A)	2.39	114.0	51.0	0.76	14.98	6.33	50.23	0.03	16.7	6.1	8.00	0.09
17WEELb (A)*	3.68	129.4	59.4	0.79	19.48	3.58	40.21	0.15	20.5	16.4	20.83	0.23
17WEELc (A)	2.76	155.0	47.0	0.75	20.25	4.75	39.82	0.05	21.5	6.5	8.71	0.09
17WEELd (A)	4.81	121.9	70.0	0.81	16.67	3.17	30.56	0.07	17.6	6.6	8.16	0.09
17WEELe (A)	2.15	151.9	42.0	0.72	53.11	6.59	61.56	0.11	54.9	7.5	10.30	0.10
17SFea (A)	1.55	109.5	42.0	0.71	11.93	6.60	122.85	0.08	14.1	32.3	45.30	0.44
17SFeb (A)	1.02	249.6	71.3	0.83	40.01	1.66	269.97	2.78	41.7	55.0	66.01	0.78
17SFec (A)	2.81	137.4	50.4	0.76	17.87	3.92	148.89	0.29	19.5	44.6	58.65	0.66
17SFed (A)	5.00	181.1	58.5	0.80	20.01	2.27	220.27	0.60	21.8	47.3	59.41	0.67
17SFee (A)	6.17	222.2	58.7	0.80	13.78	1.98	119.62	0.55	14.8	51.2	63.92	0.79
17NBa (Z)	3.44	219.2	44.2	0.74	722.54	506.39	--	4.09	841.0	11.7	15.66	0.16
17NBb (Z)	3.01	162.5	47.9	0.75	874.10	430.11	--	3.66	974.7	10.3	13.68	0.14
17NBc (Z)	4.06	198.8	50.4	0.77	596.02	384.66	--	3.63	686.0	10.8	13.98	0.14

* Failed Q-Test for outliers, not used in mean age calculation or any other data analysis or interpretations.

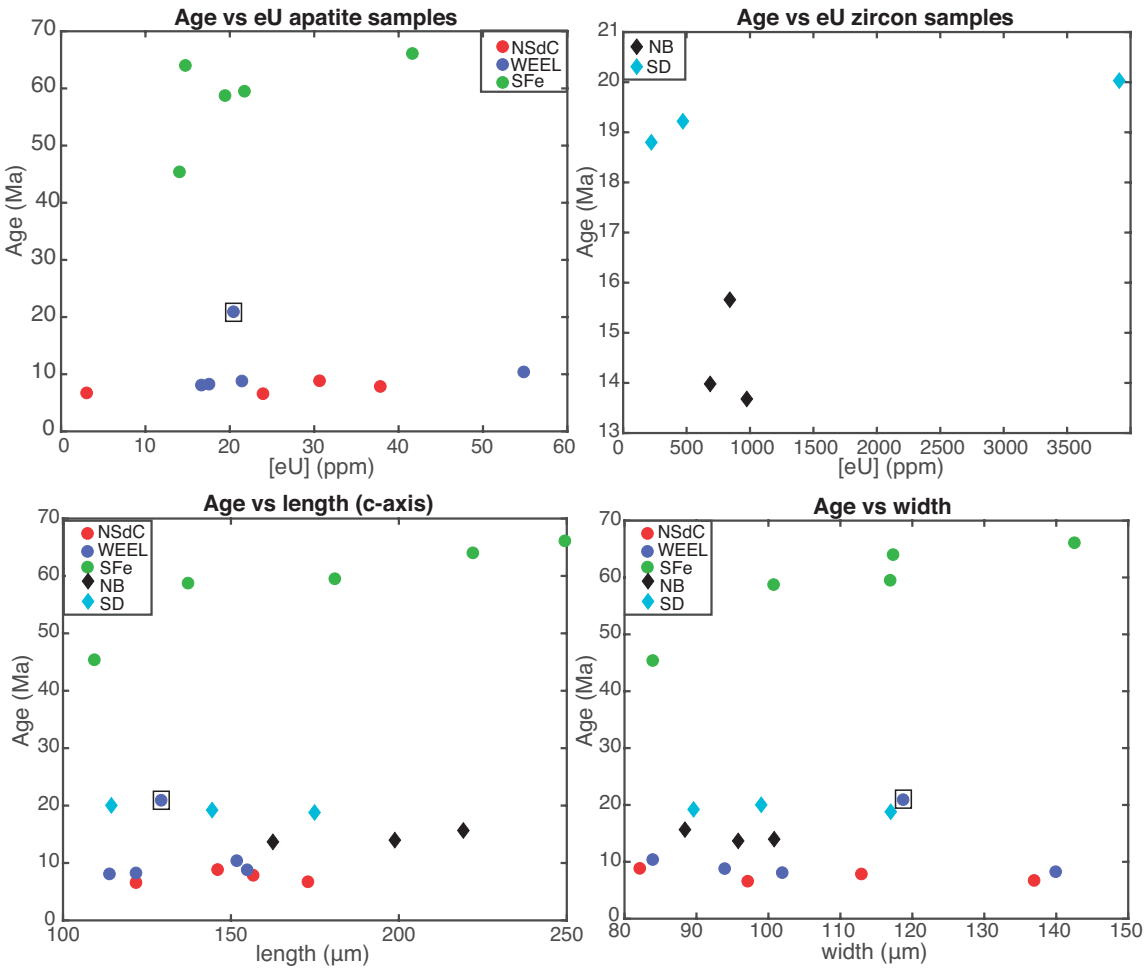

Figure B1: Plots of age-eU relationships for new thermochronometry data. Top panel: apatite grains—filled circles (left), zircon grains—filled diamonds (right). Bottom panel: age and grain size relationships (length and width, left and right respectively) for both apatite and zircon crystals (circles and diamonds respectively). Note one of the WEEL samples failed the q-test for outliers (blue circle with black box).

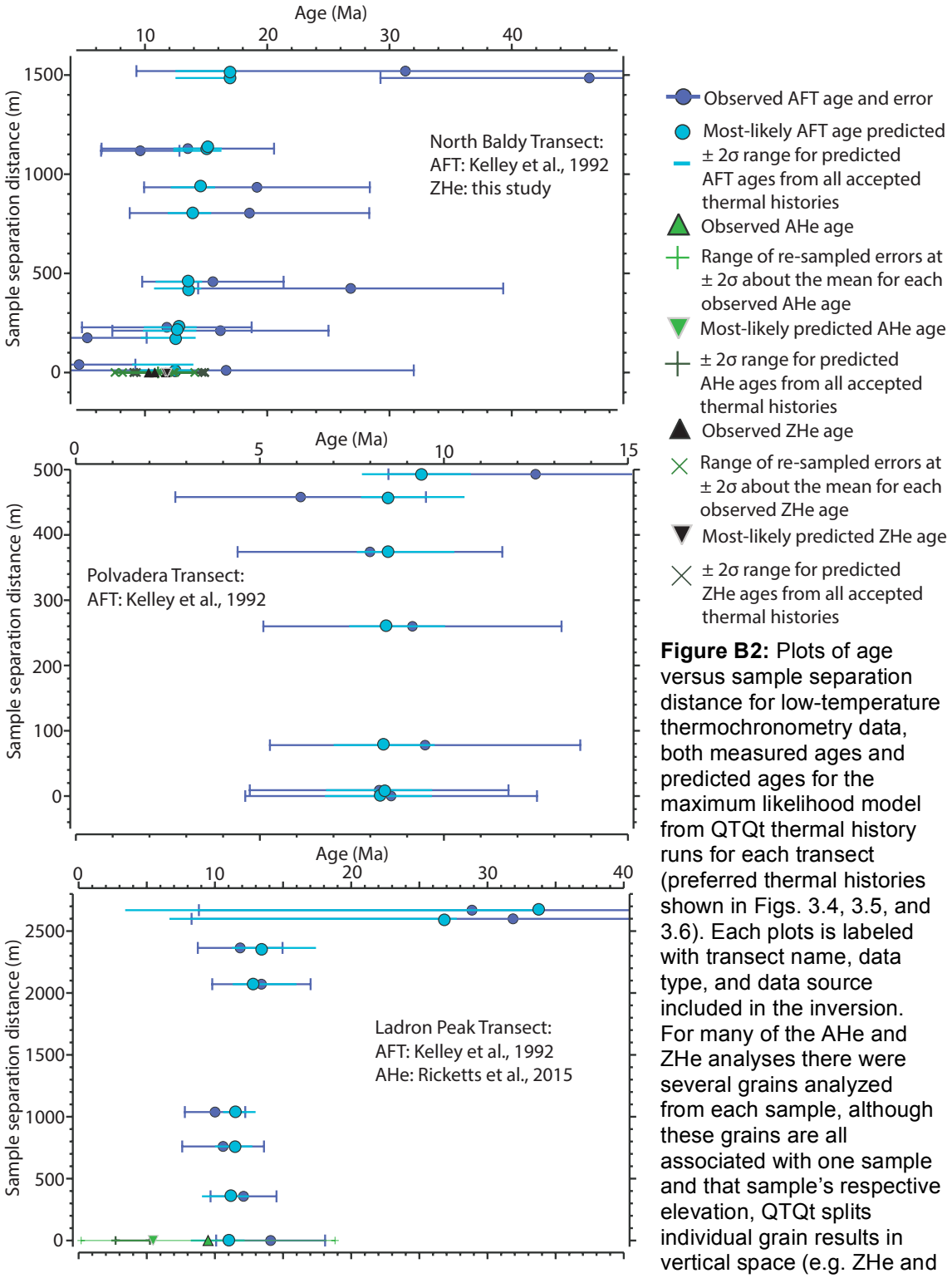

Figure B2 continued: AFT—apatite fission track; AHe—apatite (U-Th-Sm)/He; ZHe—zircon (U-Th)/He. This figure presents results from transects going south to north in the RGR. The above plots are all from the southern Albuquerque basin.

Figure B2: Plots of age versus sample separation distance for low-temperature thermochronometry data, both measured ages and predicted ages for the maximum likelihood model from QTQt thermal history runs for each transect (preferred thermal histories shown in Figs. 3.4, 3.5, and 3.6). Each plots is labeled with transect name, data type, and data source included in the inversion. For many of the AHe and ZHe analyses there were several grains analyzed from each sample, although these grains are all associated with one sample and that sample's respective elevation, QTQt splits individual grain results in vertical space (e.g. ZHe and AHe data in Sand Dunes transect). This does not mean the grains are representing different sample separation distance. Note, axes values are not the same for each plot.

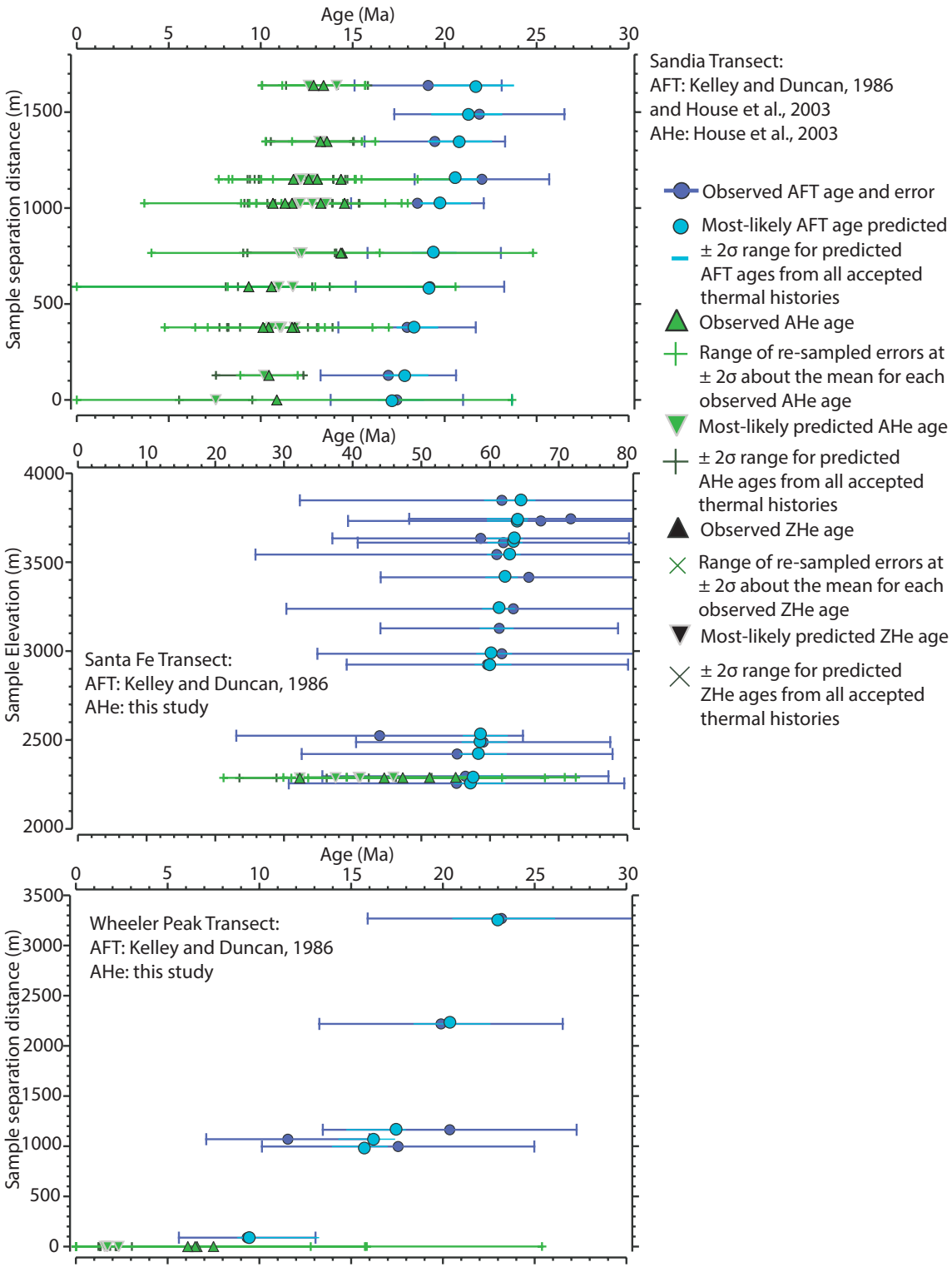

Figure B2 continued: The above plots are from the northern Albuquerque basin (Sandia Transect), Española basin (Santa Fe Transect), and San Luis basin (Wheeler Peak Transect).

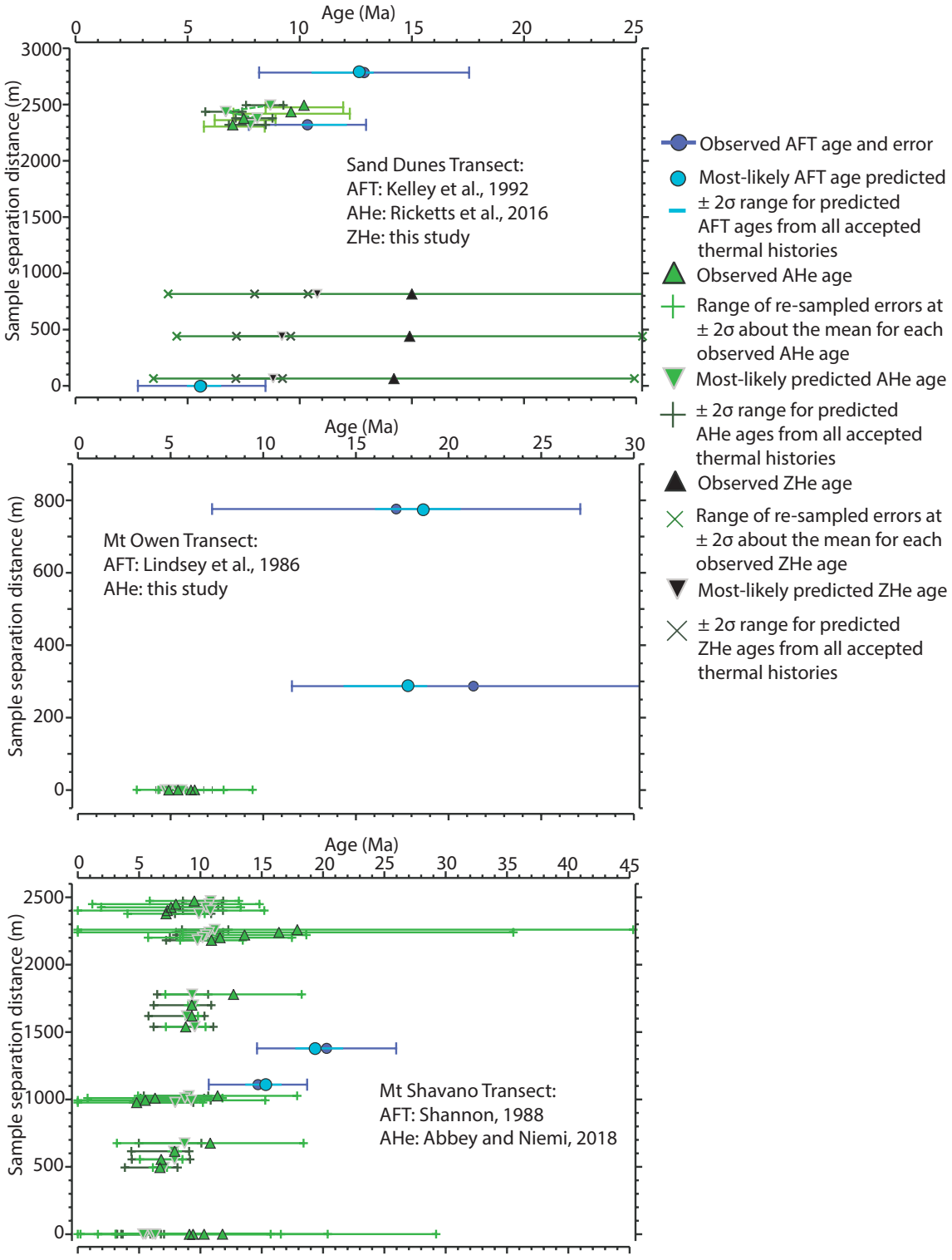

Figure B2 continued: The above plots are from the San Luis basin (Sand Dunes and Mount Owens Transects), and the upper Arkansas River basin (Mount Shavano Transect).

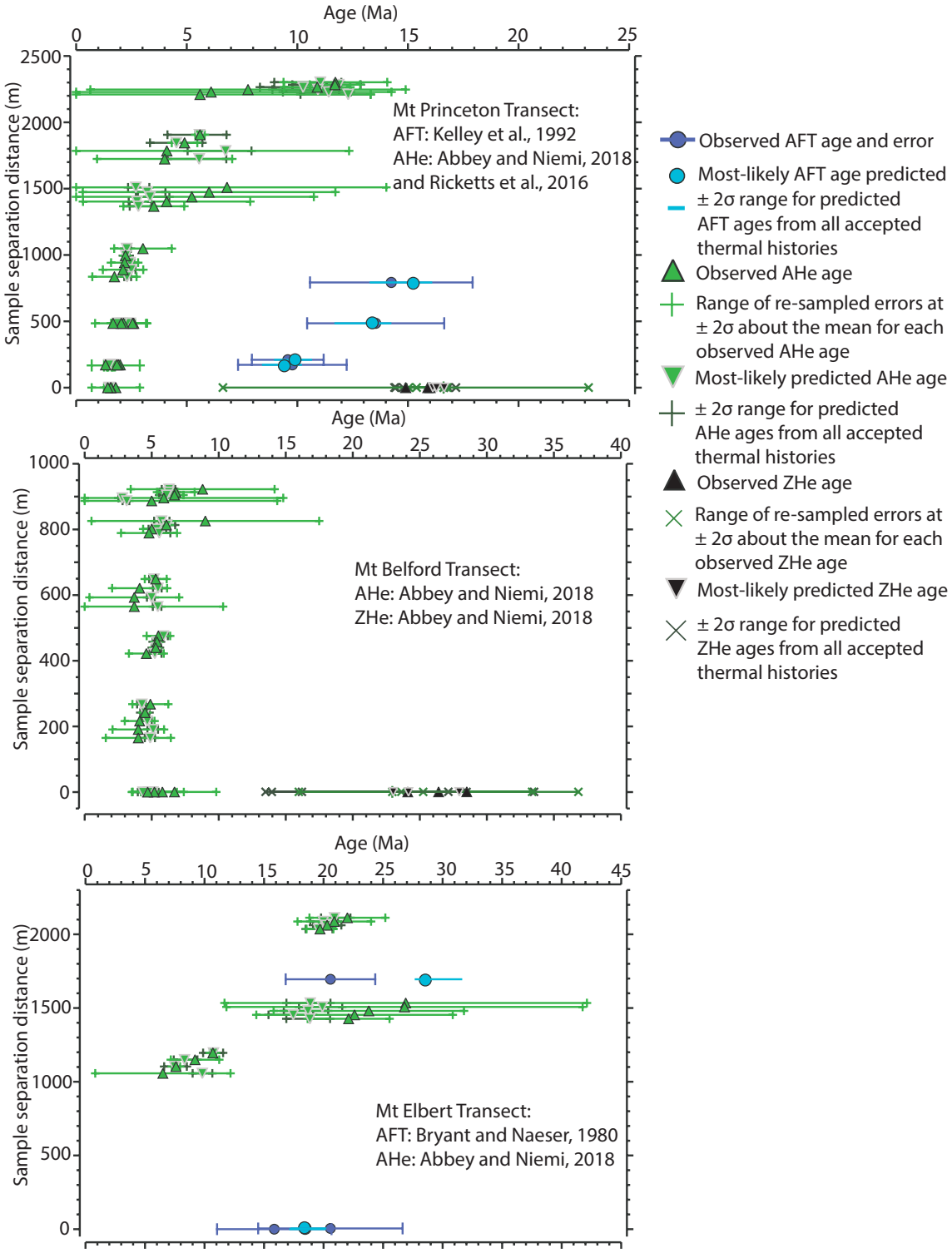

Figure B2 continued: The above plots are all from the upper Arkansas River basin.

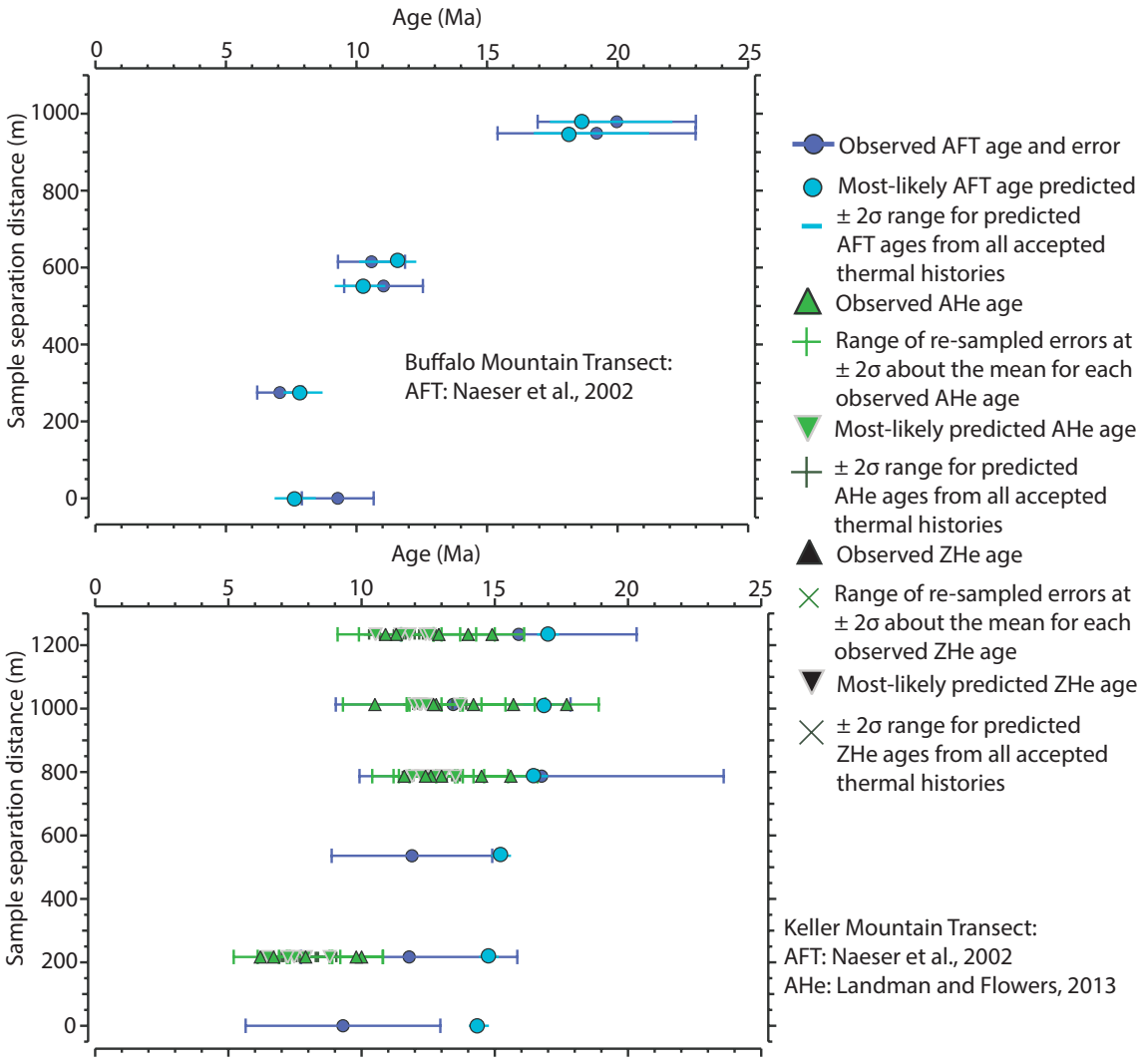

Figure B2 continued: The above plots are both from the Blue River basin.

REFERENCES

Abbey, A.L., Niemi, N.A., Geissman, J.W., Winkelstern, I.Z., Heizler, M., 2017, Early Cenozoic exhumation and paleotopography in the Arkansas River valley, southern Rocky Mountains, Colorado: Lithosphere, v. 10, n. 2, p. 239-266, doi:10.1130/L673.1.

Abbey, A.L., and Niemi, N.A. 2018, Low-temperature thermochronometric constraints on fault initiation and growth in the northern Rio Grande rift, upper Arkansas River valley, Colorado, USA: Geology, doi:10.1130/G40232.1.

Ander, M.E., 1980, Geophysical study of the crust and upper mantle beneath the central Rio Grande rift and adjacent Great Plains and Colorado Plateau: [Doctoral Thesis] University of New Mexico, Albuquerque.

Baars, D.L., and Stevenson, G.M., 1984, The San Luis Uplift, Colorado and New Mexico—an enigma of the Ancestral Rockies: Geology, v. 21, p. 57-67.

Bailey, D.K., 1974, Continental rifting and alkaline magmatism, in Sorensen, H., ed., The alkaline rocks: New York, Wiley, p. 148–159.

Balch, R.S., Hartse, H.E., Sanford, A.R., and Lin, K., 1997, A new map of the geographical extent of the Socorro mid-crustal magma body: Bulletin of Seismological Society of America, v. 87, p. 174-182.

Beltrando, M., Stockli, D.F., Decarlis, A. and Manatschal, G., 2015, A crustal-scale view at rift localization along the fossil Adriatic margin of the Alpine Tethys preserved in NW Italy: Tectonics, v. 34, p. 1927-1951.

Block, L., and Royden, L.H., 1990, Core complex geometries and regional scale flow in the lower crust: Tectonics, v. 9, p. 557-567.

Brister, B.S. and Gries, R.R., 1994, Tertiary stratigraphy and tectonic development of the Alamosa basin (northern San Luis basin), Rio Grande rift, south-central Colorado, in Keller, G. R. and Cather, S. M. eds, Basins of the Rio Grande rift: Structure, stratigraphy, and tectonic setting: Geological Society of America Special Paper, v. 291, p. 39–58.

Brown, L.L., Golombek, M.P., 1986, Block rotations in the Rio Grande rift, New Mexico: Tectonics, v. 5, p. 423-438.

Brun, J.P., 1999, Narrow rifts versus wide rifts: inferences for the mechanics of rifting from laboratory experiments, Philosophical Transactions of the Royale Society

London Series A-Mathematical, Physical and Engineering Sciences, v. 357, p. 695-710.

Brune, S., Corti, G., and Ranalli, G., 2017, Controls of inherited lithospheric heterogeneity on rift linkage: Numerical and analogue models of interaction between the Kenyan and Ethiopian rifts across the turkana depression: Tectonics, v. 36, p. 1767-1786.

Bryant, B., and Naeser, C.W., 1980, The significance of fission-track ages of apatite in relation to the tectonic history of the Front and Sawatch Ranges, Colorado: Geological Society of America Bulletin, v. 91, p. 156–164.

Buck, W.R., 1991, Modes of continental lithospheric extension, Journal of Geophysical Research: Solid Earth, v. 96, n. B12, p. 20161–20178.

Buck, W.R., 2004, Consequences of asthenospheric variability on continental rifting, G.D. Karner, B. Taylor, N.W. Droscoll, D.L. Kohlstedt, eds., Rheology and Deformation of the Lithosphere at Continental Margins: Columbia University Press, New York, p. 1-30.

Busby, C.J., 2013 Birth of a plate boundary at ca. 12 Ma in the Ancestral Cascades arc, Walker Lane belt of California and Nevada: Geosphere, v. 9, n. 5, p. 1147–1160.

Chai, C., Ammon, C.J., Maceira, M., Herrmann, R.B., 2015, Inverting interpolated receiver functions with surface wave dispersion and gravity: application to the western US and adjacent Canada and Mexico: Geophysical Research Letters, v. 42, n. 11, p. 4359- 4366.

Chapin, D.E., and Cather, S.M., 1994, Tectonic setting of the axial Basins of northern and central Rio Grande Rift, 'in' Keller, G. R., and Cather, S. M., eds., Basins of the Rio Grande Rift: structure stratigraphy and tectonic setting: Geological Society of America Special Publication 291, p. 5-25.

Chapin, C.E., and Seager, W.R, 1975, Evolution of the Rio Grande rift in the Socorro and Las Cruces areas, 26th Field Conference, New Mexico Geological Society, p. 297-321.

Chapin, C.E., Wilks, M., and McIntosh, W.C., 2004, Space-time patterns of late Cretaceous to present magmatism in New Mexico-comparison with Andean volcanism and potential for future volcanism. In S. M. Cather, W. C. McIntosh, and S. A. Kelley, eds., Tectonics, geochronology, and volcanism in the southern Rocky Mountains and Rio Grande rift p. 13–40, Socorro, New Mexico: Bureau of Geology and Mineral Resources Bulletin 160.

Claringbould, J.S., Bell, R.E., Jackson, C.A.L., Gawthorpe, R.L., and Odinsen, T., 2017, Pre-existing normal faults have limited control on the rift geometry of the northern North Sea: Earth and Planetary Science Letters, v. 475, p. 190-206.

Cordell, L., 1982, Extension in the Rio Grande rift: Journal of Geophysical Research, v. 87, p. 8561–8569.

Corti, G., 2009, Continental rift evolution: from rift initiation to incipient break-up in the Main Ethiopian Rift, East Africa: Earth Science Reviews, v. 96, p. 1-53.

Corti, G., 2012, Evolution and characteristics of continental rifting: analogue modeling-inspired view and comparison with examples from the East African Rift System: Tectonophysics, v. 522-523, p. 1-33.

Cosca, M.A., Thompson, R.A., Lee, J.P., Turner, K.J., Neymarl, L.A., and Premo, W.R., $^{40}Ar/^{39}Ar$ geochronology. Isotope geochemistry (Sr, Nd, Pb), and petrology of alkaline lavas near Yampa, Colorado: Migration of alkaline volcanism and evolution of the northern Rio Grande rift: Geosphere, v. 10, n. 2, p. 374-400.

Cunningham, C.G., Naeser, C.W., and Marvin, R.F., 1977, New ages for intrusive rocks in the Colorado mineral belt: U.S. Geological Survey Open-File Report 77-573, 7p.

Dean, R.B., and Dixon, W.J., 1951, Simplified Statistics for Small Numbers of Observations: Analytical Chemistry, v. 23 n. 4, p. 636–638.

Dickerson, W., 2003, Intraplate mountain building in response to continent–continent collision — the Ancestral Rocky Mountains (North America) and inferences drawn from the Tien Shan (Central Asia): Tectonophysics, v. 365, p. 129-142.

Duller, R.A., Whittaker, A.C., Swinehart, J.B., Armitage, J.J., Sinclair, H.D., Bair, A., Allen, P.A., 2012, Abrupt landscape change post–6 Ma on the central Great Plains, USA: Geology, v. 40, n. 10, p. 871–874.

Ebinger, C., Crow, M., Rosendahl, B., Livingstone, D., Le Fournier, J., 1984, Structural evolution of Lake Malawi: Nature, v. 308, p. 627-629.

Ebinger, C.J., Karner, G.D., and Weissel, G.D., 1991, Mechanical strength of extended continental lithosphere: constraints from the western rift system, Africa: Tectonics, v. 10, p. 1239-1256.

Ebinger, C.J., 1989, Tectonic development of the western branch of the East African rift system: GSA Bulletin, v. 101, n. 7, p. 885–903.

Ebinger, C.J., van Wijk, J., and Keir, D., 2013, The time scales of continental rifting: Implications for global processes, in Bickford, M.E., ed., The Web of Geological Sciences: Advances, Impacts, and Interactions: Geological Society of America Special Paper 500, p. 371–396.

Ehlers, T.A., 2005, Crustal Thermal Processes and the Interpretation of Thermochronometer Data: Reviews in Mineralogy and Geochemistry, v. 58 n. 1, 315–350.

Epis, R.C., and Chapin, C.E., 1974, Stratigraphic Nomenclature of the Thirtynine Mile Volcanic Field, Central Colorado: Geologic Survey Bulletin, p. 1–32.

Epis, R.C., Scott, G.R., Taylor, R.B., and Chapin, C.E., 1976, Cenozoic Volcanic, Tectonic, and Geomorphic Features of Central Colorado: Studies in Colorado Field Geology, Professional Contributions Colorado School of Mines, p. 323–338.

Færseth, R.B., 1996, Interaction of Permo–Triassic and Jurassic extensional fault-blocks during development of the North Sea: Journal of the Geological Society, v. 153, p. 931–944.

Farley, K.A., 2002, (U-Th)/He Dating: Techniques, Calibrations, and Applications: Reviews in Mineralogy and Geochemistry, v. 47, n. 1, p. 819–844.

Fitzgerald, P.G., and Gleadow, A.J.W., 1990, New approaches in fission-track geochronology as a tectonic tool: examples from the transantarctic mountains: International Journal of Radiation Applications and Instrumentation, Part D. Nuclear Tracks Radiation Measurements, v. 17, n. 3, p. 351–357.

Flowers, R.M., Ketcham, R.A., Shuster, D.L., and Farley, K.A., 2009, Apatite (U–Th)/He thermochronometry using a radiation damage accumulation and annealing model: Geochimica et Cosmochimica Acta, v. 73, n. 8, p. 2347–2365.

Frankel, K.L., and Pazzaglia, F.J., 2006, Mountain fronts, base-level fall, and landscape evolution: Insights from the southern Rocky Mountains. In Special Paper 398: Tectonics, Climate, and Landscape Evolution: Geological Society of America, v. 398, p. 419–434.

Gallagher, K., 2012, Transdimensional inverse thermal history modeling for quantitative thermochronology: Journal of Geophysical Research, v. 117, n. B2.

Golombek M.D., McGill G.E., and Brown L., 1983, Tectonic and geologic evolution of the Espanola Basin, Rio Grande Rift: structure, rate of extension and relation to the state of stress in the Western United States: Tectonophysics, v. 94, p. 483-507.

Gómez-Vasconcelos, M.G., Villamor, P., Cronin, S., Procter, J., Palmer, A., Townsend, D., and Leonard, G., 2017, Crustal extension in the Tongariro graben, New Zealand: Insights into volcano-tectonic interactions and active deformation in a young continental rift: GSA Bulletin, v. 129, n. 9-10, p. 1085–1099.

Grauch, V.J.S., Connell, S.D., 2013, New perspectives on the geometry of the Albuquerque Basin, Rio Grande rift, New Mexico: Insights from geophysical models of rift-fill thickness, in Hudson, M.R., Grauch, V.J.S, eds., New Perspectives on Rio Grande Rift Basins: From Tectonics to Groundwater: Geological Society of America Special Paper 494, p. 427-462.

Grauch, V.J.S., Bauer, P.W., Drenth, B.J., Kelson, K.I., 2017, A shifting rift—Geophysical insights into the evolution of Rio Grande rift margins and the Embudo transfer zone near Taos, New Mexico: Geosphere, v. 13, n. 3, p. 870–910.

Guenthner, W.R., Reiners, P.W., Ketcham, R.A., Nasdala, L., and Giester, G., 2013, Helium diffusion in natural zircon: Radiation damage, anisotropy, and the interpretation of zircon (U-Th)/He thermochronology: American Journal of Science, v. 313, n. 3, p. 145-198.

Hamilton, W., 1981, Plate-tectonic mechanism of Laramide deformation: Contributions in Geology, v. 19, p. 87-92.

Hart, N.R., Stockli, D.F., Lavier, L.L., and Hayman, N.W., 2017, Thermal evolution of a hyperextended rift basin, Mauleon Basin, western Pyrenees: Tectonics, v. 36, p. 1103-1128.

Heller, P. L., Dueker, K., and McMillan, M.E., 2003, Post-Paleozoic alluvial gravel transport as evidence of continental tilting in the US Cordillera: Geological Society of America Bulletin, v. 115, n. 9, n. 1122-1132.

Hodgson, I., Illsley-Kemp, F., Keir, D., Ebinger, C.J., and Mtelela, K., 2017, Crustal structure at a young continental rift: A receiver function study from the Tanganyika Rift: Tectonics, v. 36, p. 2806-2822.

House, M.A., Kelley, S.A., Roy, M., 2003, Refining the footwall cooling history of a rift flank uplift, Rio Grande rift, New Mexico: Tectonics, v. 22, n. 5, p. 1060.

Hubbard, M.S., Oviatt, C.G., Kelley, S., Perkins, M.E., Hodges, K.V., and Robbins, R., 2001, Oligocene-Miocene basin formation and modification in the northern Rio Grande rift; constraints from $^{40}Ar/^{39}Ar$, fission track, and tephrochronology: Geological Society of America Abstracts with Programs, v. 33, no. 6, p. A-257.

Huffman, A.C., 2003, Middle Pennsylvanian tectonics of the conterminous United States, in C. B., Cecil and N. T., Edgar, eds., Advances in carbonate sequence stratigraphy, application to reservoirs, outcrops and models: Society for Sedimentary Geology (SEPM), v. 77, p. 73–94.

Hyndman, R.D., 2017, Lower-crustal flow and detachment in the North American Cordillera: a consequence of Cordillera-wide high temperatures: Geophysical Journal International, v. 209, n. 3, 1, p. 1779–1799.

Johnson, C.M., and Thompson, R.A., 1991, Isotopic composition of Oligocene mafic volcanic rocks in the northern Rio Grande rift: Evidence of contributions of ancient intraplate and subduction magmatism to evolution of the lithosphere: Journal of Geophysical Research, v. 96, p. 13,593-13,608.

Karlstrom, K.E., Harlan, S., Williams, M., McClelland, J., Geissman, J.W., and Åhäll, Karl-Inge, 1999, Refining Rodinia: Geologic evidence for the Australia–Western U.S. (AUSWUS) connection for Proterozoic supercontinent reconstructions: GSA Today, v. 9, p. 1–7.

Karlstrom, K.E., and Bowring, S.A., 1988, Early Proterozoic Assembly of Tectonostratigraphic Terranes in Southwestern North America: The Journal of Geology, v. 96, n. 5, p. 561-576.

Karlstrom, K.E., and Humphreys, E.D., 1998, Persistent influence of Proterozoic accretionary boundaries in the tectonic evolution of southwestern North America, Interaction of cratonic grain and mantle modification events: Rocky Mountain Geology, v. 33, n. 2, p. 161–179.

Kelley, S., 1990, Late Mesozoic to Cenozoic cooling histories of the Sangre de Cristo Mountains, Colorado and New Mexico, in Bauer, P. W., Lucas, S. G., Mawer, C. K., McIntosh, W. C., eds Tectonic Development of the Southern Sangre de Cristo Mountains, New Mexico: New Mexico Geological Society 41st Annual Fall Fields Conference Guidebook, p. 123-132.

Kelley, S.A., Chapin, C.E., and Corrigan, A.J., 1992, Late Mesozoic to Cenozoic Cooling Histories of the Flank of the Northern and Central Rio Grande Rift,

Colorado and New Mexico: New Mexico Bureau of Mines Mineral Resources, v. 145, p. 1–40.

Kelley, S.A., and Chapin, C.E., 1995, Apatite Fission-Track Thermochronology of Southern Rocky Mountain-Rio Grande Rift-Western High Plains Provinces: New Mexico Geological Society Guidebook, v. 46, p. 87–96.

Kelley, S.A., and Chapin, C.E., 1997, Cooling histories of mountain ranges in the southern Rio Grande rift based on apatite fission-track analysis—a reconnaissance survey: New Mexico Bureau of Mines Mineral Resources, v. 19, n. 1, p. 1–14.

Kelley, S.A., Duncan, I.J., 1986, Late Cretaceous to Middle Tertiary tectonic history of the northern Rio Grande rift, New Mexico: Journal of Geophysical Research, v. 91, p. 6246-6262.

Kellogg, K.S., 1999, Neogene basins of the northern Rio Grande rift: partitioning and asymmetry inherited from Laramide and older uplifts: Tectonophysics, v. 305, p. 141-152.

Kellogg, K.S., Shroba, R.R., Premo, W.R. Bryant B., 2011, Geologic map of the eastern half of the Vail 30′ × 60′ quadrangle, Eagle, Summit, and Grand Counties, Colorado: U.S. Geological Survey Scientific Investigations Map SIM-3170, 1 sheet, scale 1:100 000, 49 p.

Kelson, K.I., Bauer, P.W., Unruh, J.R., and Bott, D.J., 2004, Late Quaternary characteristics of the northern Embudo fault, Taos County, New Mexico, in Brister, B.S., Bauer, P.W., Read, A.S., and Lueth, V.W., eds., New Mexico Geological Society Guidebook: 55th Field Conference, Geology of the Taos Region, p. 147–157.

Ketcham, R., 2005, Forward and inverse modeling of low temperature thermochronometry data, in Reiners, P.W., Ehlers, T.A., eds., Low-temperature thermochronology: Techniques, interpretations, and applications: Reviews in Mineralogy and Geochemistry, v. 58, p. 275-314.

Kim, Y.S., Sanderson, D.J., 2005, The relationship between displacement and length of faults: a review: Earth-Science Reviews, v. 68, n. 3–4, p. 317-334.

Kluth, C.F., and Coney, P.J., 1981, Plate tectonics of the Ancestral Rocky Mountains: Geology, v. 9, n. 1, p. 10–15.

Kluth, C.F., and DuChene, H.R., 2009, late Pennsylvanian and early Permian structural geology and tectonic history of the Paradox Basin and Uncompahgre uplift, Colorado and Utah, in: The Paradox Basin Revisited: New Developments in Petroleum Systems and Basin Analysis, eds. W. S., Houston, L. L., Wray and P. G., Moreland: Rocky Mountain Association of Geology, Special Publications, p. 178-197.

Kluth, C.F., Schaftenaar, C.H., 1994, Depth and geometry of the northern Rio Grande Rift in the San Luis Basin, south-central Colorado, in Keller, G.R., Cather, S.M., eds., Basins of the Rio Grande Rift: Structure, stratigraphy and tectonic setting: Geological Society of America Special Paper 291, p. 27–38.

Knepper, D.H. Jr., 1974, Tectonic analysis of the Rio Grande rift zone, central Colorado: [Doctoral Thesis] Colorado School of Mines.

Kottlowski, E., 1968, Influence of the Pedernal Uplift on sedimentation, in Basins of the Southwest, 1: West Texas Geological Society, p. 21-40.

Kreemer, C., Blewitt, G., and Bennett, R.A., 2010, Present-day motion and deformation of the Colorado Plateau: Geophysical Research Letters, v. 37, n. 10, p. 1-5.

Landman, R., and Flowers, R.M., 2013, (U-Th)/He thermochronologic constraints on the evolution of the northern Rio Grande Rift, Gore Range, Colorado, and implications for rift propagation models: Geosphere, v. 9, n. 1, p. 170–187.

Lavecchia, A., Thieulot, C., Beekman, F., Cloetingh, S., and Clark, S., 2017, Lithosphere erosion and continental breakup: Interaction of extension, plume upwelling and melting: Earth and Planetary Science Letters, v. 467, p. 89-98.

Lavier, L.L., and Manatschal, G., 2006, A mechanism to thin the continental lithosphere at magma-poor margins: Nature, v. 440, n. 7082, p. 324-328.

Leat P.T., Thompson, R.N., Dickin, A.P., Morrison, M.A., and Hendry, G.L., 1989, Quaternary volcanism in northwestern Colorado: Implications for the roles of asthenosphere and lithosphere in the genesis of continental basalts: Journal of Volcanism Geothermal Research, v. 37, p. 291-310.

Leat P.T., Thompson, R.N., Morrison, M.A., Hendry, G.L., and Dickin A.P., 1990, Geochemistry of mafic lavas in the early Rio Grande rift, Yarmony Mountain, Colorado, U.S.A.: Chemical Geology, v. 81, p. 23-43.

Leonard, E.M., 2002, Geomorphic and tectonic forcing of late Cenozoic warping of the Colorado piedmont: Geology, v. 30, n. 7, p. 595–598.

Leonard, E.,M., Hubbard, M.S., Kelley, S.A., Evanoff, E., Siddoway, C.S., Oviatt, C.G., Heizler, M., and Timmons, M., 2002, High Plains to Rio Grande rift: Late Cenozoic evolution of central Colorado, in Geological Society of America Meeting Field Trip Guidebook: Geological Society of America, Boulder, Colorado, 35 p.

Levander, A., Schmandt, B., Miller, M.S., Liu, K., Karlstrom, K.E., Crow, R.S., Lee, C.T.A., and Humphreys, E.D., 2011, Continuing Colorado plateau uplift by delamination style convective lithospheric down-welling: Nature, v. 472, p. 461-466.

Lewis C.J., Baldridge W.S., 1994, Crustal extension in the Rio Grande rift, New Mexico: Half-grabens, accommodation zones, and shoulder uplifts in the Ladron Peak-Sierra Lucero area: Geological Society of America, Special Paper, v. 291, p. 135-155.

Limbach, F.W., 1975, The geology of the Buena Vista area, Chaffee county, Colorado: [Doctoral Thesis] T-1692, Colorado School of Mines, Golden, Colorado.

Lipman, P.W., Mehnert, H.H., 1975, Late Cenozoic basaltic volcanism and development of the Rio Grande depression in the Southern Rocky Mountains, in Curtis, B.F.,

ed., Cenozoic history of the southern Rocky Mountains: Geological Society of America Memoir, 144, p. 119–154.

Lindsey, D.A., Lohnson, B.R., and Andriessen, P.A.M., 1983, Laramide and Neogene structure of the northern Sangre de Cristo Range, south-central Colorado. In: Lowell, J.D. (Ed.), Rocky Mountain Foreland Basins and Uplifts: Rocky Mountain Association of Geology, Denver, CO, p. 219–228.

Lindsey, D.A., Andriessen, P.A.M., and Wardlaw, B.R., 1986, Heating, cooling, and uplift during Tertiary time, northern Sangre de Cristo Range, Colorado: Geological Society of America Bulletin, v. 97, p. 1133-1143.

Lozinsky, R.P., 1988, Stratigraphy, sedimentology, and sand petrology of the Santa Fe Group and pre-Santa Fe Tertiary deposits in the Albuquerque basin, central New Mexico [Doctoral Thesis], New Mexico Institute of Mining and Technology, Socorro, New Mexico.

Machette, M.N., 1988, Quaternary movement along the La Jencia fault, central New Mexico: U.S. Geological Survey Professional Paper 1440, 82 p., 2 plates.

Machette, M.N., Personious, S.F., Kelson, K.I., Haller, K.M., Dart, R.L., 1998, Map of Quaternary faults and folds in New Mexico and adjacent areas: USGS Open-file report 98-521.

Magnani, M.B., Miller, K.C., Levander, A., and Karlstrom, K., 2004, The Yavapai-Mazatzal boundary: A long-lived tectonic element in the lithosphere of southwestern North America: GSA Bulletin, v. 116, n. 9-10, p. 1137–1142.

May, S.J., and Russell, L.R., 1994, Thickness of the syn-rift Santa Fe Group in the Albuquerque Basin and its relation to structural style, in Keller, G. R., Cather, S. M., eds. Basins of the Rio Grande rift: Structure, stratigraphy, and tectonic setting: Geological Society of America Special Paper 291, p. 113-124.

McIntosh, W.C., Quade J., 1995, $^{40}Ar/^{39}Ar$ geochronology of the tephra layers in the Santa Fe Group, Española Basin, New Mexico: New Mexico Geological Society Guidebook, 46th Field Conference, p. 279-287.

McMillan, N.J., and McLemore, V.T., 2004, Cambrian-Ordovician magmatism and extension in New Mexico and Colorado: New Mexico Bureau of Geology and Mineral Resources Bulletin 160, 11 p.

McMillan, N.J., Dickin, A.P., Haag, D., 2000, Evolution of magma source regions in the Rio Grande rift, southern New Mexico: GSA Bulletin, v. 112, n. 10, p. 1582-1593.

McMillan, M.E., Angevine, C.L., and Heller, P.L., 2002, Post depositional tilt of the Miocene-Pliocene Ogallala Group on the western Great Plains: Evidence of late Cenozoic uplift of the Rocky Mountains: Geology, v. 30, n. 1, p. 63–66.

Miggins, D.P., Thompson, R.A., Pillmore, C.L., Snee, L.W., Stern, C.R., 2002, Extension and uplift of the northern Rio Grande rift: Evidence from $^{40}Ar/^{39}Ar$ geochronology from the Sangre de Cristo Mountains, south-central Colorado and northern New Mexico, in Menzies, M.A., Klemperer, S.L., Ebinger, C.J., Baker,

J., eds., Volcanic Rifted Margins: Geological Society of America Special Paper 362, p. 47–64.

Miller, M.G., 1999, Active breaching of a geometric segment boundary in the Sawatch Range normal fault, Colorado, USA: Journal of Structural Geology, v. 21, p. 769–776.

Molnar, N,E., Cruden, A.R., and Betts, P.G., 2017, Interactions between propagating rotational rifts and linear rheological heterogeneities: Insights from three-dimensional laboratory experiments: Tectonics, v. 36, p. 420-443.

Morgan, M.L., 2017, Colorado Earthquake Map Server: http://dnrwebmapgdev.state.co.us/CGSOnline/

Morgan, P.W., Seager, R., and Golombek, M.P., 1986, Cenozoic thermal, mechanical and tectonic evolution of the Rio Grande rift: Journal of Geophysical Research, v. 91, p. 6263–6276.

Morley, C.K., Haranya, C., Phoosongsee, W., Pongwapee, S., Kornsawan, A., and Wonganan, N., 2004, Activation of rift oblique and rift parallel pre-existing fabrics during extension and their effect on deformation style: examples from the rifts of Thailand: Journal of Structural Geology, v. 26, n. 10, p. 1803-1829.

Mortimer, E., Kirstein, L.A., Stuart, F.M., and Strecker, M.R., 2016, Spatio-temporal trends in normal-fault segmentation recorded by low-temperature thermochronology: Livingstone fault scarp, Malawi Rift, East African Rift System: Earth and Planetary Science Letters, v. 455, p. 62-72.

Muirhead, J.D., Kattenhorn, S.A., Lee, H., Mana, S., Turrin, B.D., Fischer, T.P., Kianji, G., Dindi, E., and Stamps, D.S., 2016, Evolution of upper crustal faulting assisted by magmatic volatile release during early-stage continental rift development in the East African Rift: Geosphere, v. 12, n. 6, p. 1670-1700.

Naeser, C.W., Bryant, B., Kunk, M.J., Kellogg, K., Donelick, R.A., and Perry, W.J. Jr., 2002, Tertiary cooling and tectonic history of the White River uplift, Gore Range, and western Front Range, central Colorado: Evidence from fission-track and $^{39}Ar/^{40}Ar$ ages: Geological Society of America Special Papers, v. 366, p. 31-53.

Nelson, R.A., Patton, T.L., Morley, C.K., 1992, Rift-segment interaction and its relation to hydrocarbon exploration in continental rift systems: American Association of Petrolium Geologists Bulletin, v. 76, p. 1153-1160.

New Mexico Bureau of Geology and Mineral Resources, 2003, Geologic Map of New Mexico, Scale 1:500,000.

Nixon, C.W., et al., 2016, Rapid spatiotemporal variations in rift structure during development of the Corinth Rift, Central Greece: Tectonics, v. 35, n. 5, p. 1225-1248.

Peterson, C., and Roy, M., 2005, Gravity and flexure models of the San Luis, Albuquerque, and Tularosa Basins in the Rio Grande rift, New Mexico, and

southern Colorado: New Mexico Geological Society, 56th Field Conference Guidebook, Geology of the Chama Basin, p. 105-114.

Reiners, P.W., Farley, K.A., and Hickes, H.J., 2002, He diffusion and (U–Th)/He thermochronometry of zircon: initial results from Fish Canyon Tuff and Gold Butte: Tectonophysics, v. 349, n. 1, p. 297-308.

Reiners, P.W., 2005, Zircon (U-Th)/He thermochronometry: Reviews in Mineralogy and Geochemistry, v. 58, n. 1, p. 151-179.

Reston, T., 2005, Polyphase faulting during the development of the west Galicia rifted margin: Earth Planetary Science Letters, v. 237, p. 561-576.

Reyners, M., Eberhart-Phillips, D., and Stuart, G., 2007, The role of fluids in lower-crustal earthquakes near continental rifts: Nature, v. 446, p. 1075-1078.

Ricketts, J.W., Karlstrom, K.E., Kelley, S.A., 2015, Embryonic core complexes in narrow continental rifts: The importance of low-angle normal faults in the Rio Grande rift of central New Mexico: Geosphere, v. 11, n. 2, p. 425-444.

Ricketts, J.W., Kelley, S.A., Karlstrom, K.E., Schmandt, B., Donahue, M.S., and van Wijk, J., 2016, Synchronous opening of the Rio Grande rift along its entire length at 25–10 Ma supported by apatite (U-Th)/He and fission-track thermochronology, and evaluation of possible driving mechanisms: Geological Society of America Bulletin, v. 128, n. 3-4, p. 397–424.

Robbins, R., 2005, Petrology, structure and exhumation of the southern Sawatch mountains, south-central Colorado: [Masters Thesis], Kansas State University.

Rudzitis, S., Reid, M.R., and Blichert-Toft, J., 2016, On edge melting under the Colorado Plateau margin: Geochemistry, Geophysics, Geosystems, v. 17, p. 2835-2854.

Sanford, A.R., Mott, R.P., Shuleski, P.J., Rinehart, E.J., Caravella, F.J., Ward, R.M. and Wallace, T.C., 1977, Geophysical Evidence for a Magma Body in the Crust In the Vicinity of Socorro, New Mexico, in The Earth's Crust eds. J.G. Heacock, G.V. Keller, J.E. Oliver and G. Simmons: American Geophysical Union, Washington, D.C.

Savage. M.K., Silver, P.G., and Meyer, R.P., 1990, Observations of teleseismic shear-wave splitting in the Basin and Range from portable and permanent stations: Geophysical Research Letters, v. 17, p. 21-24.

Scott, G.R., 1975, Reconnaissance geologic map of the Buena Vista quadrangle, Chaffee and Park Counties, Colorado: U.S. Geological Survey, Miscellaneous Field Studies Map MF-657, scale 1:62,500.

Shannon, J.R., 1988, Geology of the Mount Aetna cauldron complex, Sawatch Range, Colorado: [Doctoral Thesis], Colorado School of Mines.

Shaw, C.A., and Karlstrom, K.E., 1999, The Yavapai-Mazatzal crustal boundary in the Southern Rocky Mountains: Rocky Mountain Geology, v. 34, no. 1, p. 37-52.

Sheehan, A.F., Abers, G.A., Jones, C.H., and Lerner-Lam, A.L., 1995, Crustal thickness variations across the Colorado Rocky Mountains from teleseismic receiver functions: Journal of Geophysical Research, v. 100, p. 20,391-20,404.

Shirvell, C., Stockli, D.F., Axen, G.J., and Grove, M., 2009, Miocene–Pliocene exhumation along the West Salton Detachment Fault (WSDF), Southern California, from (U–Th)/He thermochronometry of Apatite and Zircon: Tectonics, v. 28.

Shuster, D.L., Flowers, R.M., and Farley, K.A., 2006, The influence of natural radiation damage on helium diffusion kinetics in apatite: Earth and Planetary Science Letters, v. 249, n. 3-4, p. 148-161.

Smith, G.A., 2004, Middle to late Cenozoic development of the Rio Grande rift and adjacent regions in northern New Mexico: in Mack, G.H., and Giles, K.A., eds., The geology of New Mexico: A geologic history: New Mexico Geological Society, Special Publication 11, p. 331-358.

Stamps, D.S., Iaffaldano, G., and Calais, E., 2015, Role of mantle flow in Nubia-Somalia plate divergence: Geophysical Research Letters, v. 42, p. 290-296.

Stockli, D.F., Farley, K.A., and Dumitru, T.A., 2000, Calibration of the apatite (U-Th)/He thermochronometer on an exhumed fault block, White Mountains, California: Geology, v. 28, n. 11, p. 983-986.

Szymanski, E., Stockli, D.F., Johnson, P.R., and Hager, C., 2016, Thermochronometric evidence for diffuse extension and two-phase rifting within the Central Arabian Margin of the Red Sea Rift: Tectonics, v. 35, p. 2863-2895.

Taylor, R.B., 1975, Neogene tectonism in south-central Colorado: Geological Society of America Memoirs, v. 144, p. 211-226.

Timmons, J.M., Karlstrom, K.E., Dehler, C.M., Geissman, J.W., Heizler, M.T., 2001, Proterozoic multistage (ca. 1.1 and 0.8 Ga) extension recorded in the Grand Canyon Supergroup and establishment of northwest- and north-trending tectonic grains in the southwestern United States: GSA Bulletin, v. 113, n. 2, p. 163-181.

Tousson R.T., A.R. Sanford; Crustal structure in central New Mexico interpreted from the gas buggy explosion: Bulletin of the Seismological Society of America, v. 66, n. 3, p. 877-886.

Tweto, O., 1979, The Rio Grande rift system in Colorado, in Reiker, R. E., ed., Rio Grande rift: Tectonics and magmatism: Washington D.C.: American Geophysical Union, p. 33-56.

Tweto, O., Sims, P.K, 1963, Precambrian Ancestry of the Colorado Mineral Belt: GSA Bulletin, v. 74, n. 8, p. 991–1014.

U.S. Geological Survey, 2006, Quaternary fault and fold database for the United States, accessed February 2018 from USGS web site: http//earthquake.usgs.gov/hazards/qfaults/.

van Alstine, R.E., 1969, Geology and Mineral Deposits of the Poncha Springs NE Quadrangle, Chaffee County, Colorado: U. S. Geological Survey Special Paper 626, p. 1-52.

van Alstine, R.E., and Lewis, G.E., 1960, Pliocene sediments near Salida, Chaffee County, Colorado: U.S. Geological Survey Professional Paper 400-B, p. B245.

van Wijk, J.W., Baldridge, W.S., van Hunen, J., Goes, S., Aster, R., Coblentz, D.D., Grand, S.P., and Ni, J., 2010, Small-scale convection at the edge of the Colorado Plateau: Implications for topography, magmatism, and evolution of Proterozoic lithosphere: Geology, v. 38, n. 7, p. 611–614.

Warner, L.A., 1978, The Colorado Lineament: A middle Precambrian wrench fault system: Geological Society of America Bulletin, v. 89, p. 161-171.

Woodward, L.A., 1977, Rate of crustal extension across the Rio Grande rift near Albuquerque, New Mexico: Geology, v. 5, p. 269-272.

Zoback, M.L., and Thompson, G.A., 1978, Basin and Range rifting in northern Nevada: Clues from a mid-Miocene rift and its subsequent offsets: Geology, v. 6, n. 2, p. 111-116.

CHAPTER IV. EARLY CENOZOIC EXHUMATION AND PALEOTOPOGRAPHY IN THE ARKANSAS RIVER VALLEY, SOUTHERN ROCKY MOUNTAINS, COLORADO

ABSTRACT

New thermochronometric, geochronologic, and clumped isotope data from the Mosquito Range, Arkansas Hills, and Arkansas River valley (Colorado, USA) constrain the magnitude and timing of Laramide deformation in this region, as well as the development of a low-relief Eocene erosion surface found throughout the southern Rocky Mountains. Apatite (U-Th-Sm)/He thermochronometry from seven vertical transects near the lower Arkansas River valley were collected to assess exhumation histories. New paleomagnetic data from the latest Cretaceous Whitehorn Granodiorite is presented to assess the effect of possible upper crustal tilting on these transects. These data, in combination with new zircon (U-Th)/He thermochronometry and $^{40}Ar/^{39}Ar$ and zircon U-Th-Pb geochronology from the Whitehorn Granodiorite support inverse thermal history models that imply ~3–5 km of differential (west side up) exhumation between the Mosquito Range–Arkansas Hills (5–7 km total exhumation from 80 and 60 Ma) and the Royal Gorge region to the east (<1–2 km exhumation since ca. 120 Ma). Challenges in extracting reliable thermal histories from this data set include samples with significant grain-to-grain age variability, and the observation of upward younging

age-elevation relationships in parts of several vertical transects. The former problem is common in Proterozoic crystalline rocks with protracted cooling histories, deriving from complications including helium implantation and radiation damage. We demonstrate, through the application of clumped isotopic data on co-located carbonate samples, that the latter complication likely arises from post-exhumation hydrothermal reheating driven by paleotopography and overlying late Eocene to early Miocene ignimbrite sequences. By comparing multiple closely spaced vertical transects in Proterozoic rocks including a transect collected in Cretaceous plutonic rocks and transects overlain by mid-Cenozoic ignimbrites with those that are not, we demonstrate that reliable thermal histories can be obtained from complex thermochronometric data sets through careful data evaluation and inter-transect thermal history comparisons.

Interpreting the thermochronometric data in the context of the spatial distribution of mid-Cenozoic ignimbrites in this region also provides new insights into the development of the low-relief Eocene erosion surface in the Rocky Mountains. We observe rapid and extensive Laramide exhumation while ignimbrite deposition is confined to narrow paleovalleys within a paleosurface of moderate relief in the Arkansas Hills and Mosquito Range. Where Laramide exhumation is minimal, the ignimbrites blanket a low-relief paleoerosion surface. The former paleolandscape was entirely formed in the Paleocene, based on our low-temperature thermochronometric data, while the latter paleosurface may well record a much longer evolutionary history, possibly partially inheriting an older paleolandscape. The compound nature of the Eocene erosion surface in this region may provide insight into the development of such surfaces throughout the Rocky Mountains.

INTRODUCTION

Significant debate surrounds the timing and cause of present-day elevation and relief generation in the southern Rocky Mountains (Colorado, USA). The physiography of much of the region appears to be young, with assumed recent high-relief generation, high elevations, and local evidence of young cooling and fast exhumation rates (Karlstrom et al., 2012; Landman and Flowers, 2013; Ricketts et al., 2016). However, Late Cretaceous to early Cenozoic low-temperature thermochronologic ages (Kelley and Chapin, 2004; Landman and Flowers, 2013), the demonstration of a well-defined Eocene erosion surface (Epis and Chapin, 1974, 1975), and the preservation of widespread, relatively undeformed mid-Cenozoic volcanic rocks all imply that the exhumation and relief development may have been generated much earlier. These features suggest that the topography of the Rocky Mountains is long lived and possibly inherited from previous orogenic deformation (i.e., the latest Cretaceous to early Cenozoic Laramide orogeny) and that any exhumation or topographic change after the Eocene has been relatively minor.

Distinguishing between ancient and youthful relief is of key importance in our understanding of the topographic evolution of large mountain belts (Pazzaglia and Brandon, 1996). Long-term decay (10^8 yr.) in the topography of orogens is governed by crustal thickness and buoyancy (Fischer, 2002; Blackburn et al., 2012). On shorter time scales (10^6–10^7 yr.), however, the destruction, preservation, or development of local relief can vary depending on the type of erosional processes that dominate across the landscape (e.g., planation, river incision, glaciation, and mass wasting; Whipple et al., 1999; Baldwin et al., 2003; Babault et al., 2007; Egholm et al., 2009, 2013), making it

difficult to ascertain the timing of relief development. Although such challenges are not unique to the southern Rocky Mountains, this region is a prime example of the range of processes and time scales that conceivably could be proposed for uplift and relief generation.

Crustal shortening associated with latest Cretaceous to early Cenozoic Laramide orogenesis is one of the most frequently cited causes for the development of high elevations and relief in the southern Rocky Mountains (e.g., Bird, 1984). Thickening of the lithosphere resulting from crustal shortening (e.g., Brewer et al., 1982; Hamilton, 1988), and buoyancy changes arising from mantle and crustal processes (e.g., Liu et al., 2010; Jones et al., 2015) contributed to regional elevation gain during the Laramide orogeny. Development of a high-elevation mountain range during this time is supported by isotopic and paleobotanical studies of paleoelevation change (e.g., Gregory and Chase, 1992; Sjostrom et al., 2006; Fan et al., 2014) and the generation of topographic relief is indirectly supported by increased exhumation rates observed through the application of low-temperature thermochronometry, specifically apatite fission track (AFT) studies in the Front Range and Sangre de Cristo Mountains (Kelley and Chapin, 1995; 2004).

Crustal shortening within most of the Laramide orogenic belt ceased by the mid-Eocene (e.g., Tweto, 1975). However, an increase in erosion rates across the southern Rocky Mountains and Colorado Plateau in the late Miocene (Murray et al., 2016) and arguments that at least some of the relief in major fluvial drainages traversing this region developed over the same time interval (e.g., Karlstrom et al., 2008; Thomson et al., 2016) have been used as evidence of post–late Miocene regional uplift and post-orogenic

relief development in the central and southern Rocky Mountains (Rockies). One line of argument arises from eastward tilting of the Miocene Ogallala Formation along the eastern range front of the Rockies (McMillan et al., 2002). This tilting has been attributed to regional doming, associated with Rio Grande rift propagation and possibly augmented by surface erosion and isostatic response (McMillan et al., 2006). The magnitude of differential uplift associated with this regional tilting is ~700 m down to the east determined by a 250 km transect in southern Wyoming from Cheyenne to the western Great Plains in Nebraska (McMillan et al., 2002). Mantle-driven dynamic uplift has also been invoked as a mechanism for generating 500–1000 m of surface uplift across the Rocky Mountains and Colorado Plateau since the late Miocene (Karlstrom et al., 2012; Heller and Liu, 2016), although controversy remains over the magnitude of surface topography that can be generated by dynamic forces (Molnar et al., 2015).

Processes that may continue to drive relief development in the southern Rocky Mountains include ongoing erosional and isostatic response to Rio Grande rift propagation (Leonard, 2002), distal base-level fall (Frankel and Pazzaglia, 2006), and climate change that modulates glacial-interglacial cycles (Small and Anderson, 1998).

Here we focus on the tectonic development of the southern Rocky Mountains in the vicinity of the Arkansas River (Fig. 4.1). This region exhibits >1 km of local relief, produced by river incision, exposing profiles of many key geologic relationships such as high-angle faults, extensional grabens, and erosional contacts. Such a setting provides an ideal location to address the time scales and potential driving processes of topographic evolution and relief generation.

Physiography and Geology of the Lower Arkansas River Valley

The southern Rocky Mountains in Colorado represent a region of high elevation peaks and intermontane basins, with an abrupt transition into the lower elevation Great Plains expanse to the east, and the relatively undeformed Colorado Plateau to the west (Fig. 4.1). Within the southern Rocky Mountains, the Arkansas River divides the Mosquito Range from the Sawatch Range, with headwaters near Leadville, Colorado. It flows south until reaching Salida, Colorado, where the river makes an abrupt directional change and flows east (Figs. 4.2 and 4.3). The river has two clear physiographic segments. We define the upper Arkansas River (UAR) valley as the southward-flowing

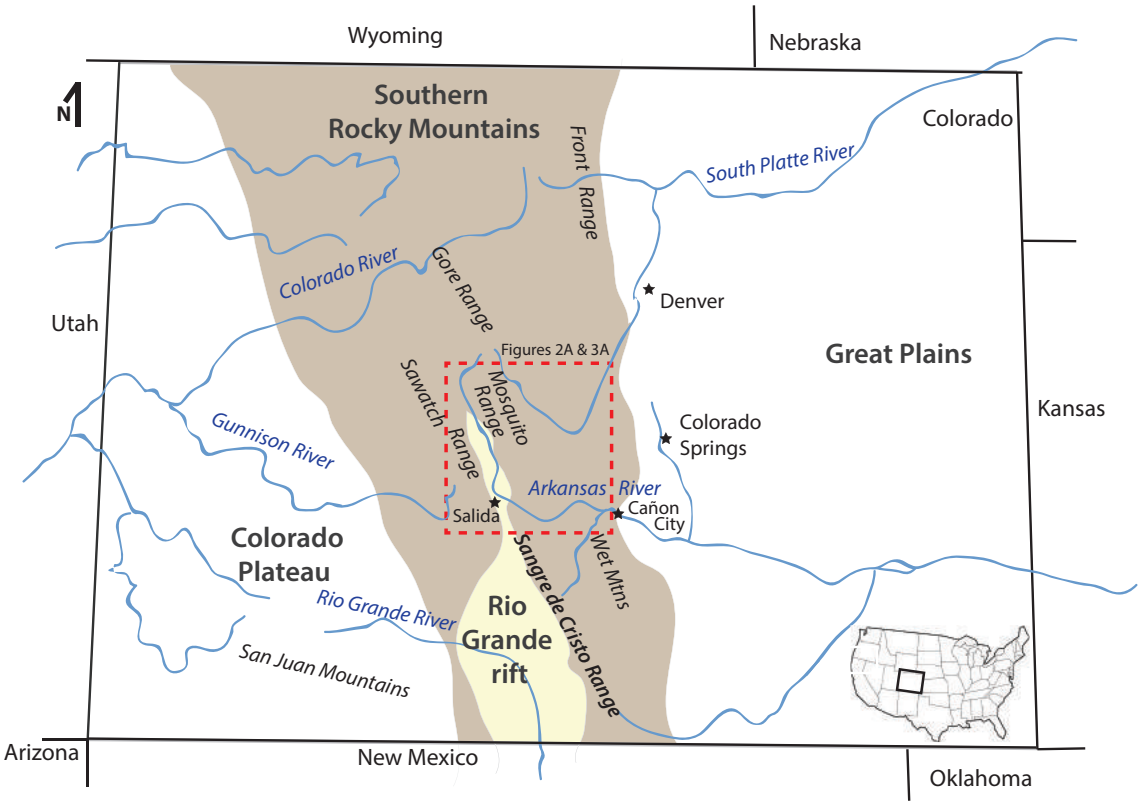

Figure 4.1: Location map showing the state of Colorado, US with major rivers in blue. General geologic provinces include the Great Plains, the southern Rocky Mountains (light brown shading), the Colorado Plateau and the northern extent of the Rio Grande rift (light yellow shading within the southern Rocky Mountain province). Dashed red box marks area of study (Figs. 4.2A and 4.3A).

section of the river, which flows through a broad normal-fault-bounded valley defined by high-elevation peaks associated with extensional features in the northern Rio Grande rift. The lower Arkansas River (LAR) valley is the eastward flowing section of the river from Salida to Cañon City, Colorado (Fig. 4.3). The LAR valley, in contrast to the UAR, is defined by a narrow, steep, fluvially incised gorge that exposes rocks spanning ~1.7 b.y. of geologic time.

The oldest rocks within the LAR valley are Proterozoic gneisses and granitoids (Scott, 1975b; Taylor et al., 1975a, 1975b, 1975c; Bryant and Naeser, 1980; Wallace et al., 1997). These Proterozoic crystalline rocks are locally disconformably overlain by relatively thin sequences of lower Paleozoic sedimentary rocks, as well as thicker sequences of upper Paleozoic strata. High-angle, basement-cutting faults record the latest Mississippian to Permian Ancestral Rocky Mountain orogeny (Baars and Stevenson, 1984; Kluth and Coney, 1981; Fig. 4.2). Paleozoic sections are sparsely preserved, but remnants of Ordovician to Permian carbonate and detrital sedimentary rocks are exposed in and along the LAR canyon (Taylor et al., 1975a, 1975b, 1975c; Wallace et al., 1997; Fig. 4.2). Middle to upper Mesozoic sediments associated with the Cretaceous Interior Seaway (ca. 72 Ma; Blakey et al., 1988; Dickinson et al., 1988; Blakey, 1996, 2008; DeCelles, 2004) are preserved in the eastern part of the LAR valley (Fig. 4.2).

Deformation in the form of crustal shortening, high-angle thrust faulting, and local folding of the crystalline basement, all related to the Laramide orogeny, took place during the latest Cretaceous to middle Eocene time (ca. 85–40 Ma; Tweto, 1975; Dickinson et al., 1988; Keller and Baldridge, 1999; Marshak et al., 2000; DeCelles,

2004), eroding and dissecting Paleozoic and Mesozoic strata. Laramide deformation in southern Colorado was also associated with small volume plutonism, including the emplacement of the latest Cretaceous Whitehorn Granodiorite in the Arkansas Hills and

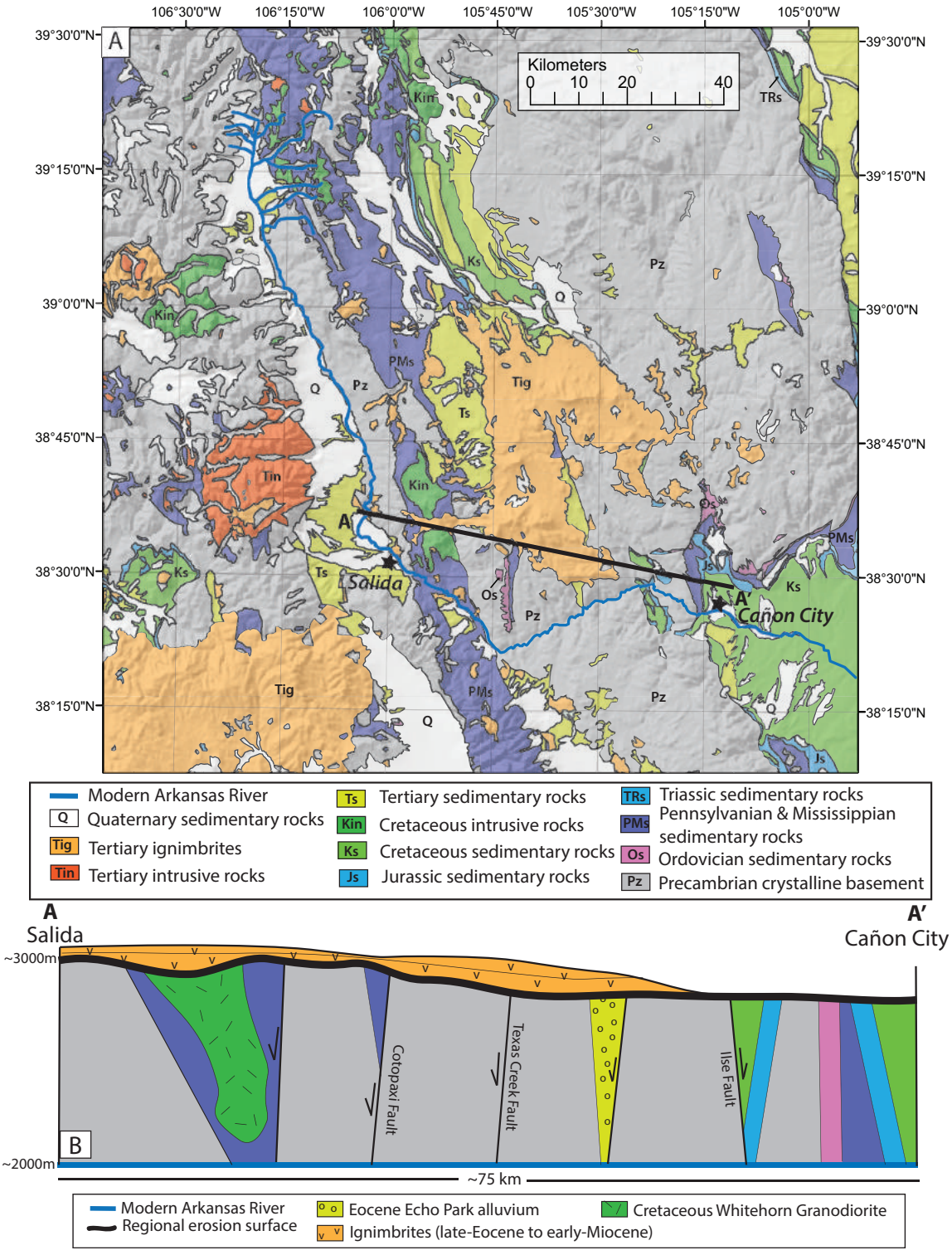

Figure 4.2: (A) Simplified Geologic map of the upper and lower Arkansas River valleys. (B) Schematic representation of geologic relationships in the lower Arkansas River valley is shown in cross-section. Note vertical exaggeration with actual distances on figure (structure orientations are not exaggerated). Large faults and fault systems represented by black lines with displacement shown by black arrows (Taylor et al., 1975b and 1975c) dissect the Proterozoic, Paleozoic and Mesozoic rock. Early Cenozoic deformation includes graben formation (i.e. Echo Park Canyon). The regional Eocene erosion surface is indicated with a thick black line overlain by relatively undeformed late-Eocene to early-Miocene ignimbrite deposits. Blue line at the base of the cross-section represents the modern lower Arkansas River.

Mosquito Range (Wallace et al., 1997; Fridrich et al., 1998; Fig. 4.3).

Laramide orogenic deformation was followed by the development of a regional low-relief erosion surface across the southern Rocky Mountains (Epis and Chapin, 1974, 1975; McMillan et al., 2002, 2006; Gregory and Chase, 1994). This erosion surface was blanketed in the mid-Cenozoic (ca. 36 to ca. 20 Ma) by volcanic deposits, primarily silicic ignimbrites and andesitic porphyritic flows and lahars, originating from calderas located in the present-day Sawatch Range (Epis and Chapin, 1974, 1975; Taylor et al., 1975a, 1975b, 1975c; Taylor, 1975; Scott, 1975a; Epis et al., 1976; Chapin and Lowell, 1979; Shannon, 1988; Gregory and McIntosh, 1996; Wallace et al., 1997; McIntosh and Chapin, 2004; Fig. 4.2). Following this phase of volcanic activity, extension associated with the Rio Grande rift initiated in southern Colorado during the early Miocene (Kelley and Chapin, 1995, 1997; Landman and Flowers, 2013; Ricketts et al., 2016).
These geologic relationships are exposed in the >1 km of local relief along the LAR valley and provide relative timing constraints on the regional geologic evolution. However, in order to better resolve the processes that have led to local and broad-scale relief in the southern Rockies, quantitative information on the time scales and magnitude of relief generation are needed. Our study is focused on the application of low-

temperature thermochronometry in this region to evaluate the timing and amount of near-surface exhumation in a region where such data sets are limited.

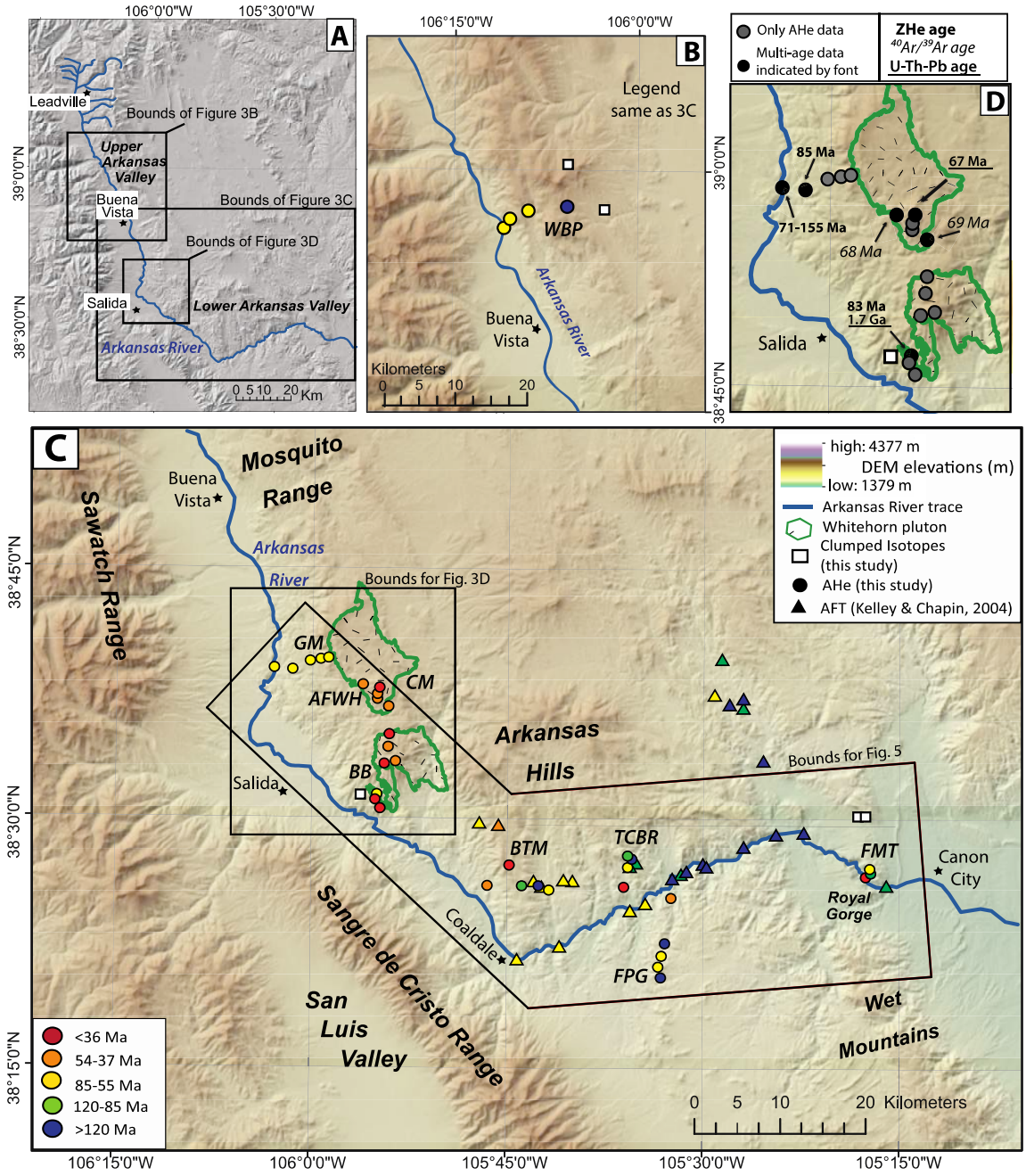

Figure 4.3: 90 m digital elevation model (DEM) showing study region and sample localities. (A) Location of the upper and lower Arkansas River (UAR and LAR respectively) near its headwaters in Colorado. (B) UAR Valley marked by black box outline in 3A, showing apatite helium (AHe) data (colored circles) and clumped isotope sample locations (white squares) for the West Buffalo Peak (WBP) transect. (C) LAR Valley marked by rectangle in 3A, showing sample locations of clumped isotopes (white squares) and AHe data (colored circles) collected in vertical transects. GM—Green Mountain, CM—Cameron Mountain, BB—Big Baldy, BTM—Burned Timber Mountain, TCBR—Texas Creek-Bull Ridge, FPG—Five Point Gulch, FMT—Fremont Peak. Some apatite fission track (AFT) data for this region have been published (triangles; Kelley and Chapin, 2004). Colors signify sample mean ages. Two additional AHe samples were collected from quarries in the Whitehorn Granodiorite (AFWH). Other analyses (ZHe, U-Th-Pb of zircon and $^{40}Ar/^{39}Ar$ of biotite, hornblende and K-feldspar) were performed on many samples in both the GM and WH (Whitehorn) transects shown in D. (D). Gray circles indicate samples with only AHe data while black circles indicate samples analyzed with multiple techniques: ZHe ages (bold font; Table D1), $^{40}Ar/^{39}Ar$ (italicized; Table D3) and U-Th-Pb (semi bold and underlined; Tables D5 and D6).

Thermochronometric Approach to Assess Topographic Evolution in the Southern Rocky Mountains

In this paper, new apatite (U-Th-Sm)/He (AHe) and zircon (U-Th)/He (ZHe) data provide a unique low-temperature thermochronometric record from this region of the southern Rockies. In an attempt to develop a detailed data set bearing on the geologic evolution of this region, we sampled multiple closely spaced vertical transects throughout the LAR valley. The complexity of this region has been well documented; for example, Precambrian rocks are known to be problematic for low-temperature thermochronometry studies because there may be problems with helium retention in old grains and recorded temperatures can be related to late-stage resetting (Peyton et al., 2012). Furthermore, vertical spatial relationships may not be maintained through time (Fitzgerald et al., 2006; Stanley et al., 2013). With the assumption that we may have similar problems with samples from Proterozoic rocks in our study region, we use a number of other approaches ($^{40}Ar/^{39}Ar$, U-Th-Pb, paleomagnetism, clumped isotopes) to help assess any complex behavior displayed by the low-temperature thermochronometry data. We also present

new zircon U-Th-Pb and $^{40}Ar/^{39}Ar$ analyses from biotite hornblende and K-feldspar in the Whitehorn Granodiorite to address timing of emplacement and early cooling history of the intrusion. Paleomagnetic data from the Whitehorn Granodiorite are used to evaluate the magnitude of post-Cretaceous tilting in the region. Clumped and oxygen isotope analyses of carbonate rocks, in conjunction with forward thermal models of thermochronometry data, are useful for assessing potentially reset AHe ages, and reveal a cooling signature unrelated to exhumation.

LOW-TEMPERATURE THERMOCHRONOMETRIC DATA FROM THE VICINITY OF THE LOWER ARKANSAS RIVER

Low-temperature thermochronometers are powerful tools for understanding the near-surface thermal histories of the crust. AHe records cooling between ~30 and 90 °C depending on radiation damage (Farley, 2002; Shuster et al., 2006; Flowers et al., 2009), while AFT thermochronometry records sample ages associated with cooling between ~70 and 150 °C (Kelley and Chapin, 1995; Ehlers, 2005), and ZHe records temperatures from ~130 to ~230 °C (Reiners et al., 2002; Reiners, 2005). $^{40}Ar/^{39}Ar$ thermochronometry records thermal histories between 200 °C and ~500 °C, depending on the mineral phase analyzed (McDougall and Harrison, 1988), providing constraints on the higher temperature thermal history of a given sample. Together, this suite of thermochronometers affords the ability to resolve thermal histories for the upper 15–20 km of the Earth's crust, depending on the local geothermal gradient.

Thermochronometric data from the southern Rockies are abundant, but available data are predominantly K-Ar and $^{40}Ar/^{39}Ar$ age determinations that record higher temperature information (Klein et al., 2010). Extant low-temperature thermochronometric

data from the southern Rockies come mostly from AFT analyses (see Klein et al., 2010; much of the data from rocks in the Arkansas River region are from Kelley and Chapin, 2004, 1995), which record pre-Cenozoic cooling ages. Only a few studies incorporating AHe ages have been published for the southern Rocky Mountains (Landman and Flowers, 2013; Ricketts et al., 2016), thus, our suite of AHe and ZHe data from the LAR region provides a more complete picture of the near-surface thermal histories of the rocks in the locality of the LAR valley.

Analytical Methods for Helium and Argon Thermochronometry

Apatite (U-Th-Sm)/He and Zircon (U-Th)/He Procedures

Samples were processed using standard mineral separation practices. Individual apatite and zircon grains were hand-selected and screened for zoning and inclusions prior to outgassing on an Alphachron Helium Instrument at the University of Michigan. Ages reported are averages based on multiple (3–9) individual replicate analyses from each sample. We only interpret apatite or zircon ages from samples with at least three or two inclusion-free grains, respectively. All grains analyzed were >80 μm in both length and width (Table 4.1; Table D11). Additional details of the analytical procedure are described in Appendix 1 and Niemi and Clark (2017). Analyses of U, Th, and Sm from the apatite and zircon grains were performed at the University of Arizona following the methods outlined in Reiners and Nicolescu (2006).

$^{40}Ar/^{39}Ar$ Procedures

Mineral separates were obtained using standard mineral separation practices followed by step-heating using a Mo double vacuum resistance furnace at the New Mexico Bureau of Geology and Mineral Resources. Biotite and hornblende crystals were

heated in 11 and 10 min increments, respectively, whereas K-feldspar analyses involved a detailed 42-step heating schedule to retrieve data necessary for multiple diffusion domain (MDD) modeling. The $^{40}Ar/^{39}Ar$ analytical method follows that of McIntosh and Cather (1994) and Sanders et al. (2006; see Appendix 1 for details). Argon closure in K-feldspar is treated following the MDD method developed by Lovera et al. (1989).

Thermochronometric Data Quality Assessment and Interpretation

Interpretation of low-temperature thermochronometric data is complicated in data sets with protracted or non-monotonic thermal histories (Fitzgerald et al., 2006; Peyton et al., 2012; Stanley et al., 2013). Proterozoic rocks especially may be subject to an array of processes that give rise to scatter in single-grain apatite dates from a given sample. Such processes include radiation damage (Flowers et al., 2009; Shuster et al., 2006), He implantation (Reiners et al., 2008; Spiegel et al., 2009; Kohn et al., 2009), zonation (Hourigan et al., 2005), or U-rich inclusions (House et al., 1997). In some cases, relationships between grain size and date (e.g., Reiners and Farley, 2001) or radiation damage (eU) and date (e.g., Flowers et al., 2009; Gautheron et al., 2009) can effectively explain the observed variation in single-grain apatite dates from the same bulk sample. When this is the case, each grain records a specific part of the thermal evolution of the sample, and these variations can be exploited to derive the thermal history of the sample (Flowers et al., 2007). In other cases, the cause of scatter in measured dates cannot be ascribed to any of the processes described here (e.g., Peyton et al., 2012), and limited thermochronometric information may be gleaned from such analyses.

In interpreting thermochronometric data, determining how much weight to place on samples with significant scatter has historically been a subjective decision (Galbraith

TABLE 4.1. APATITE AND ZIRCON RESULTS

Sample name	Longitude	Latitude	Elevation (m)	Rock type	Grains analyzed per sample	Mean age (Ma)
West Buffalo Peak (WBP) Transect						
15WBP-02*	-106.09601	38.96303	3453	Alkali Feldspar Granite	4	260 ± 41
15WBP-04*	-106.14741	38.95847	3132	Granite	5†	60 ± 2
15WBP-05*	-106.17333	38.94917	2856	Granite	4	72 ± 10
15WBP-06*	-106.18095	38.94075	2565	Granite	3	60 ± 4
Green Mountain (GM) Transect						
14GM-01*	-105.9790	38.6592	3081	Granite	5	60 ± 5
14GM-02*	-105.9878	38.6586	2784	Granite	4	57 ± 1
14GM-03*	-106.0026	38.6564	2646	Granite	4	62 ± 3
14GM-04*	-106.0249	38.6485	2440	Granite	6†	65 ± 3
14GM-04 (z)*	-106.0249	38.6485	2440	Granite	3§	85 ± 1
14GM-05*	-106.0474	38.6499	2251	Granite	9	55 ± 6
14GM-05 (z)	-106.0474	38.6499	2251	Granite	3	115 ± 24#
Whitehorn (WH) Transects and individual samples						
14BB-01	-105.8933	38.5574	3215	Granodiorite	0	--
14BB-02	-105.9079	38.5544	2932	Granite / Granodiorite	4	28 ± 3
14BB-03*	-105.9163	38.5253	2586	Tonalite	4	63 ± 3
14BB-03 (z)*	-105.9163	38.5253	2586	Tonalite	3§	83 ± 1
14BB-04	-105.9178	38.5198	2462	Intermediate Granite	7	34 ± 8#
15BB-04a	-105.9135	38.5100	2338	Quartz Diorite	4	19 ± 4#
15AFWH2	-105.9426	38.6353	2940	Granite/Granodiorite	4	42 ± 3
15AFWH26	-105.9057	38.6087	2892	Granite / Granodiorite	4	48 ± 4
15CM-01	-105.9043	38.5729	3134	Quartz Monzonite	7	51 ± 3
15CM-02	-105.9027	38.5824	3081	Quartz Diorite / Granodiorite	7†	27 ± 2
15CM-03	-105.9187	38.6198	3029	Granite	5	46 ± 1

TABLE 4.1. APATITE AND ZIRCON RESULTS

Sample name	Longitude	Latitude	Elevation (m)	Rock type	Grains analyzed per sample	Mean age (Ma)
15CM-04	-105.9163	38.6236	3151	Granite	7	40 ± 4
15CM-05	-105.9156	38.6298	3338	Granite	7	35 ± 6[#]
Burned Timber Mountain Transect						
14BTM-01*	-105.6954	38.4291	2318	Phyllite / Granite	7†	62 ± 3
14BTM-02	-105.7089	38.4329	2446	Quartzite	2	327 ± 41
14BTM-03*	-105.7292	38.4330	2597	Granite	5†	110 ± 14
14BTM-04	-105.7468	38.4539	2844	Diorite	5	28 ± 3
14BTM-05	-105.7557	38.4596	3032	Granite	0	--
14BTM-06	-105.7742	38.4323	2201	Granite	4	41 ± 3
Texas Creek / Bull Ridge Transect						
14TCBR-01*	-105.5977	38.4634	2607	Granite	4	101 ± 9
14TCBR-02*	-105.5952	38.4621	2494	Granite	4	135 ± 11
14TCBR-03*	-105.5919	38.4529	2238	Granodiorite	4	67 ± 0.3
14TCBR-04	-105.6001	38.4362	2083	Alkali Feldspar Granite	6	23 ± 6[#]
14TCBR-05	-105.5875	38.4156	1927	Alkali Feldspar Granite	**	--
Five Point Gulch Transect						
14FPG-01	-105.5356	38.4394	1884	Quartzite	1	48 ± 1
14FPG-03	-105.5406	38.4201	2039	Phyllite / Schist	**	--
14FPG-04	-105.5382	38.4086	2105	Mafic Intrusive	0	--
14FPG-05	-105.5405	38.3905	2187	Intermediate Igneous	4	320 ± 106[#]
14FPG-06*	-105.5467	38.3749	2227	Intermediate Igneous	4	63 ± 5
14FPG-08*	-105.5518	38.3631	2320	Granite	4	61 ± 5
14FPG-09	-105.5552	38.3507	2529	Granite	4	126 ± 4[#]
14LOM-01	-105.5551	38.3469	2457	Intermediate Metamorphic	**	--
14LOM-02	-105.5518	38.3433	2383	Intermediate Metamorphic	**	--

TABLE 4.1. APATITE AND ZIRCON RESULTS

Sample name	Longitude	Latitude	Elevation (m)	Rock type	Grains analyzed per sample	Mean age (Ma)
Echo Canyon Samples						
14EC-03a	-105.5527	38.4637	2005	Siltstone	4	--
14EC-04	-105.5477	38.4795	2160	Very coarse sandstone	1	33 ± 0.3
14EC-05	-105.5487	38.4939	2401	Sublitharenite Volcanic	**	--
Fremont Peak Transect						
14FMT-01	-105.2915	38.4419	1703	Quartz Monzonite	5§	27 ± 2
14FMT-02	?	?		Granodiorite	3	110 ± 29#
14FMT-03	-105.2887	38.4432	1806	Diorite	4	70 ± 27#
14FMT-04	-105.2861	38.4457	1992	Quartz Monzonite	**	--
14FMT-05	-105.2875	38.4515	1982	Quartz Monzonite	**	--

* Used in thermal models (reasoning described in text).

† 4 or more grains were included in mean age calculation, but some grains were excluded due to outlier rejection (Table D1).

§ Fewer than 4 grains were included in mean age calculation, due to outlier rejection for apatite samples and due to number of grains analyzed for zircon samples (Table D1).

Sample mean age has a percent error > 15%.

(z) Indicates zircon helium analyses, all the rest of the data is from apatite helium analyses.

-- No data obtained from sample.

** No apatite in sample.

Note: Sample EC-03a produced four datable grains, however, they are detrital and cannot be averaged together as a mean age; individual grain dates reported in Table D1.

and Laslett, 1993; Gallagher, 1995). We describe our statistical approach to assess scatter in our data set. As a general rule, we place limited confidence in the geologic relevance of thermochronometric ages derived from samples with mean age standard errors that exceed 15%, and we exclude these samples from thermal modeling (Flowers et al., 2015).

Data quality of individual samples is assessed through a multistep procedure to remove outliers and test for typical causes of data scatter. Samples are assessed for outliers using either the Dean and Dixon (1951) Q-test or the Boddy and Smith (2010) test for two extreme outliers. The Q-test is amenable to small data sets ($n \geq 3$), and thus useful for (U-Th-Sm)/He thermochronometry, where individual samples typically include 3–5 replicates. The drawback to this test is that it is conservative in identifying outliers, and can only be used once on each sample. Other tests are available for larger data sets ($n \geq 5$) that can identify as many as two outliers (Boddy and Smith, 2010), and we employ these tests for two extreme outliers on samples with five or more replicates. Both tests exclude samples with outliers found at the 95% confidence level.

Once individual grain outliers are identified, date-eU and date–grain size correlation plots are generated, with outliers flagged (Fig. D1). These plots are visually inspected for trends in grain date versus eU and grain date versus size. If correlations between these parameters are observed, previously identified outliers may be retained in the data set. If no trends are observed, the outliers are excluded from further analysis, and the sample age and standard error are recalculated from the retained grain dates.

Samples are also inspected for indications of He implantation. Implantation from surrounding U-rich phases can bias date determinations, particularly on apatite grains with low eU (<5 ppm; Table D1; Spiegel et al., 2009). We observe low-eU grains

primarily in samples from the Whitehorn transect (discussed in the following), although these samples did not display high degrees of age scatter (Table 4.1; Table D1; Fig. 4.4). To address concerns of potential He implantation in the low-eU grains from the Whitehorn transect, we acquired whole-rock trace element analyses for three samples that exhibited low eU (14BB-03, 15CM-05, and 15AFWH2; Table D1). Trace element analyses by inductively coupled plasma–mass spectrometry (ICPMS) indicate that U concentrations in the whole rocks are no greater than the concentrations observed in individual apatite grains (<5 ppm; Table D2). Given the low concentration of U in the whole rock, He implantation is unlikely to have an effect on the dates of the apatite grains that we analyzed.

Following the data quality procedure outlined here, we define four different stages through which our sample ages are filtered prior to use in interpretations and thermal modeling.

1. Samples with no outliers and exhibiting little scatter (<15% standard errors) are accepted at face value, with high confidence in the mean age calculated from the individual grain dates.
2. Samples for which scatter can be reduced to less than 15% by outlier removal are subject to age recalculation, with high confidence in the mean age calculated from the retained individual grain dates.
3. Samples with high scatter (>15% standard error) after outlier tests, but that exhibit a correlation between data and eU or date and grain size, are retained for thermal modeling, but mean ages for these samples are treated cautiously with respect to geologic interpretations.

4. Samples with high scatter, to which no clear cause can be ascribed, are given little confidence in the mean age calculated and are not used in any thermal modeling.

Low-Temperature Thermochronometric Results

New AHe low-temperature thermochronometric data are presented for 39 samples from the LAR valley, in addition to ZHe data for 3 of those samples. These samples were collected from seven vertical transects along the LAR from Salida to Cañon City, as well as along two additional vertical transects located on the eastern side of the UAR valley near Salida and Buena Vista, respectively (Fig. 4.3; Table 4.1; Table D1). Furthermore, AHe data and $^{40}Ar/^{39}Ar$ analyses on hornblende, biotite, and K-feldspar are reported for samples from two quarries located in high-elevation exposures of the Whitehorn Granodiorite, northeast of Salida (Fig. 3; Table 4.2; Tables D3 and D4).

All samples were collected from rocks in the hanging wall of the northern Rio Grande rift extensional system (southwest Front Range, Arkansas Hills, and Mosquito Range; Fig. 4.3), with most transects gathered in Proterozoic granitoids and gneissic basement rocks (Scott, 1975b; Taylor et al., 1975a, 1975b, 1975c; Wallace et al., 1997). Exceptions include two transects that were collected within the Cretaceous Whitehorn Granodiorite (Taylor et al., 1975b), and another in Eocene sedimentary rocks in Echo Canyon (Fig. 4.2; Wallace et al., 1997). All transects in the LAR valley were collected below the Eocene erosion surface and overlying volcanic rock sequences. The two sample transects in the UAR valley are not covered by these volcanic flow deposits.

AHe and ZHe results from each transect and $^{40}Ar/^{39}Ar$ data from the Whitehorn Granodiorite are described in the following (Fig. 4.3); in some cases, geographically proximal transects are described and discussed jointly. Results are presented in

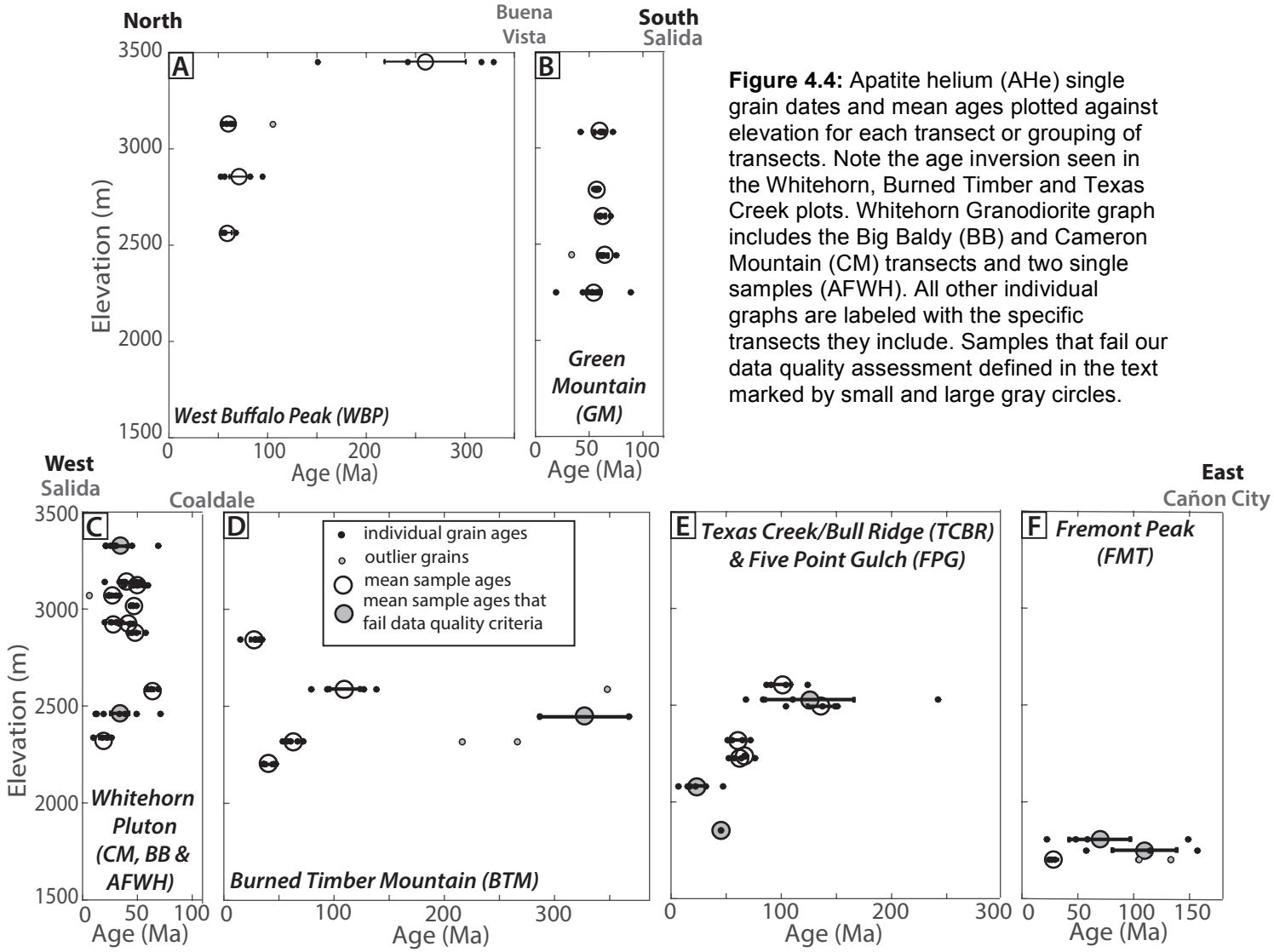

Figure 4.4: Apatite helium (AHe) single grain dates and mean ages plotted against elevation for each transect or grouping of transects. Note the age inversion seen in the Whitehorn, Burned Timber and Texas Creek plots. Whitehorn Granodiorite graph includes the Big Baldy (BB) and Cameron Mountain (CM) transects and two single samples (AFWH). All other individual graphs are labeled with the specific transects they include. Samples that fail our data quality assessment defined in the text marked by small and large gray circles.

downstream order along the Arkansas River (i.e., transects farthest from Cañon City are described first).

West Buffalo Peak Transect

The West Buffalo Peak (WBP) transect is the northernmost transect (Fig. 4.3B) spanning ~900 m of elevation. AHe analyses were performed on apatite extracted from Precambrian basement located disconformably below Carboniferous strata (Tweto, 1974; Scott, 1975b) and the data record apparent ages of 60 ± 4 Ma, 72 ± 10 Ma, and 60 ± 2 Ma for the three samples collected at the lowest elevations. The highest elevation sample, however, yields a much older age, 260 ± 41 Ma (Table 4.1; Table D1; Figs. 4.3B and 4.4A).

Green Mountain Transect

The Green Mountain (GM) transect is located just north of Salida (Fig. 4.3C). The vertical transect includes 5 samples that span >830 m of elevation. The transect extends eastward from the river (Fig. 4.3C) and all collected samples are in Paleoproterozoic granodiorite (Wallace and Lawson, 2008). The AHe ages for all GM samples investigated are Paleocene (oldest: 65 ± 3 Ma, youngest: 55 ± 6 Ma) with no obvious elevation trend (Table 4.1; Table D1; Figs. 4.3C, 4.3D, 4.4B, and 4.5). ZHe analyses were performed on the lowest two samples in the transect (GM-04 and GM-05) with three grains analyzed per sample. Dates range from 84 to 144 Ma in GM-04 and from 71 to 155 Ma in GM-05 (Table 4.1; Table D1).

Whitehorn Granodiorite Transects

We sampled two vertical transects in the Whitehorn Granodiorite (WH). The Big Baldy (BB samples) transect encompasses the south flank of Big Baldy Mountain from

2073 m (river level) to 2932 m (Table 4.1; Table D1) and includes samples within the Cretaceous granodiorite as well as adjacent samples in the surrounding Paleoproterozoic basement rock (14BB-03, also analyzed for ZHe). The Cameron Mountain (CM samples) transect extends the elevation range of samples collected in the Whitehorn Granodiorite

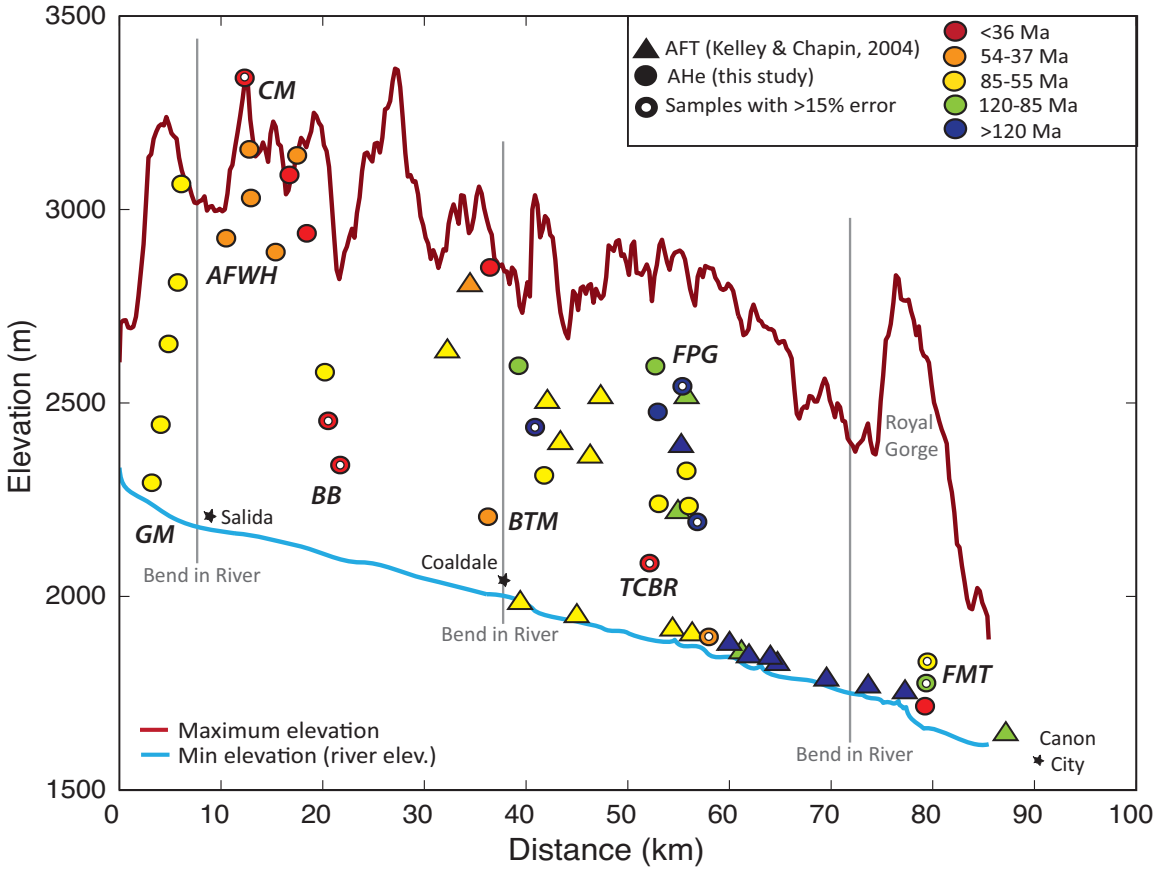

Figure 4.5: Cross-section of lower Arkansas River (LAR) Valley (outlined by black polygon from Fig. 4.3C). Symbol colors and shapes are the same as in Fig. 4.3 showing apatite helium (AHe) ages for analyzed samples in the LAR and published apatite fission track (AFT) data (Kelley and Chapin, 2004). Thin gray lines mark bends in the river (see Fig. 4.3).

to 3338 m along the southern ridge of Cameron Mountain (Table 4.1). Combined, these transects span ~1.3 km of elevation. Two additional samples (AFWH; Table 4.1; Table D1) were taken from rock quarries between these two transects, at the localities of previously collected samples for $^{40}Ar/^{39}Ar$ geochronology and paleomagnetic data (WH; Table 4.2; Table D3). AHe data were obtained from BB, CM, and AFWH quarry samples (Table 4.1; Table D1), while $^{40}Ar/^{39}Ar$ data is presented for the WH quarry samples (Table 4.2).

AHe thermochronometry data show that the lower 3 BB samples progressively decrease in age with decreasing elevation, from 63 ± 3 Ma at 2586 m to 19 ± 4 Ma at 2338 m (Table 4.1; Figs. 4.4 and 4.5). In contrast, all 8 samples at higher elevations yield a range of ages from 27 ± 2 Ma to 51 ± 3 Ma and do not show a correlation with elevation (these samples include sample 14BB-02 and all CM and AFWH samples) (Table 4.1; Figs. 4.3C, 4.4C, and 4.5). The ZHe data from sample 14BB-03 record an age of 83 ± 1 Ma (Fig. 4.3D; Table 4.1; Table D1).

The $^{40}Ar/^{39}Ar$ incremental heating data reveal relatively flat spectra for biotite and hornblende from both samples (Fig. 4.6). Biotite from WH-2 and WH-26 yield plateau spectra for >90% of the ^{39}Ar released and give apparent ages of 69.3 ± 0.2 Ma and 69.8 ± 0.2 Ma, respectively (Figs. 4.3D and 4.6; Table 4.2; Table D3). The hornblende spectra are somewhat more complex than the biotite spectra and are slightly saddle shaped (Fig. 4.6). The intermediate steps of WH-26 hornblende yield a plateau age of 70.0 ± 0.4 Ma, while the preferred age of the hornblende from sample WH-2 is 69.1 ± 0.6 Ma, determined from the isochron analysis (Fig. 4.6; Table 4.2; Fig. D3).

K-feldspar age spectra reveal variable age gradients for the two samples (Fig.

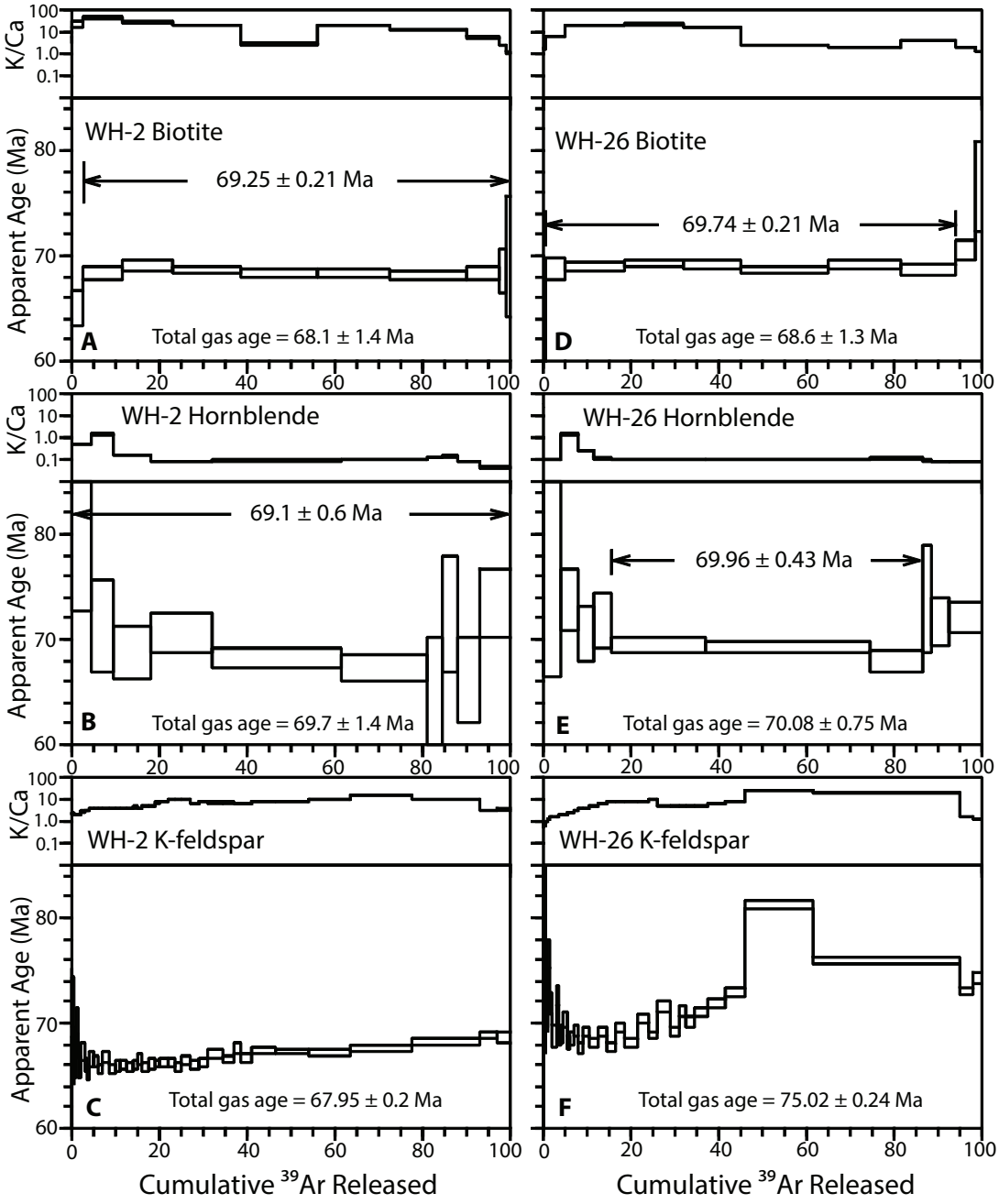

Figure 4.6: (A-F) $^{40}Ar/^{39}Ar$ age spectra and K/Ca diagrams for hornblende, biotite and K-feldspar in two single samples (WH-2 and WH-26) collected in the Whitehorn Granodiorite. All ages are weighted mean ages from the steps indicated by arrows except WH-2 hornblende, which is an isochron age (Fig. D2).

4.6). K-feldspar from sample WH-2 shows a gradual increase from ca. 66.3 to ca. 70 Ma over the entire spectrum (Fig. 4.7; Table 4.2; Table D4). In contrast, WH-26 yields initial minimum ages of ca. 69.4 Ma over the first 20% of the spectrum, followed by a sharp increase to ca. 82 Ma before falling to ca. 76 Ma during the final 50% of the spectrum (Fig. 4.7). The shape of the release spectrum for sample WH-26 has been observed in other K-feldspars and is interpreted to be caused by excess argon trapped within large diffusion domains (Foster et al., 1990). Thus, we do not further consider the K-feldspar age data from sample WH-26.

Burned Timber Mountain Transect

North of Coaldale, the Burned Timber Mountain (BTM) transect was collected over 600 vertical meters along a traverse that is parallel to the Arkansas River (Fig. 4.3C). The lowest elevation sample (BTM-06, 2201 m) records a mean age of 41 ± 3 Ma, while two samples at higher elevations (BTM-01, 2318 m and BTM-03, 2597 m) have mean ages of 62 ± 3 Ma and 110 ± 14 Ma, respectively. The highest elevation sample in the transect (BTM-04, 2844 m) yields a younger age of 28 ± 3 Ma (Table 4.1; Table D1; Figs. 4.4D and 4.5).

Texas Creek–Bull Ridge and Five Point Gulch Transects

The Texas Creek–Bull Ridge (TCBR) and Five Point Gulch (FPG) traverses are considered together here, as they are at similar downstream distances along the river (Fig. 4.3C and 4.5) and span the same elevation range. The FPG traverse is located south of the Arkansas River and the TCBR traverse is on the north side (Fig. 4.3C). Many of the samples collected in these two transects are at similar elevations (Table 4.1; Figs. 4.4E and 4.5), and the data from them indicate a consistent cooling history both north and

TABLE 4.2. ARGON DATA RESULTS

Analysis Identifiers			Preferred Age						Integrated Age		
Sample	Lab#	Irrad	Analysis	n	$\%^{39}Ar$	MSWD	Age (Ma)	± 1σ	n	Age (Ma)	± 1σ
WH-2 Biotite	53009-01	NM-149	Plateau	10	97.3	1.58	69.25	0.21	11	69.00	1.40
WH-26 Biotite	53012-01	NM-149	Plateau	10	91.9	1.99	69.74	0.21	11	69.50	1.30
WH-2 Hornblende	53010-01	NM-149	Plateau	10	100.0	2.8	69.10	0.60	10	70.60	1.40
WH-26 Hornblende	53013-01	NM-149	Plateau	3	71.1	3.36	70.99	0.43	10	69.96	0.75
WH-2 K-feldspar	53008-01	NM-149	Total gas age	42	100.0	N/A	67.95	0.20	42	67.95	0.20
WH-26 K-feldspar	53011-01	NM-149	Total gas age	42	100.0	N/A	75.12	0.24	42	75.12	0.24

Lab# - lab identifier

Irrad - irradiation package identifier

n - number of steps used to calculate preferred age

$\%^{39}Ar$ - % of ^{39}Ar comprising the preferred age

MSWD - Mean Square Weighted Deviation

± 1σ - 1 sigma errors calculated for the age

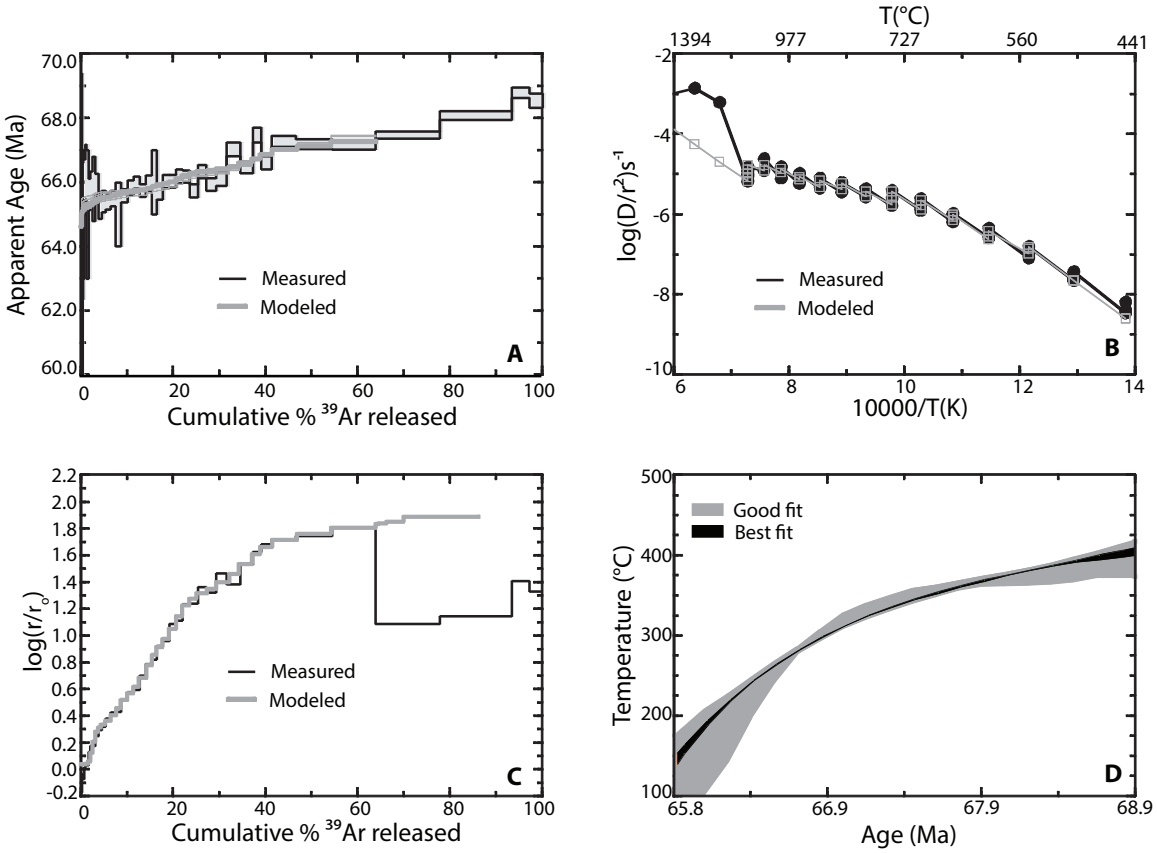

Figure 4.7: Detailed analysis of K-feldspar in WH-2 sample from the Whitehorn Granodiorite. (A) Age spectrum, (B) Arrhenius plot (*T* is temperature), (C) $\log(r/r_o)$ plot, and (D) thermal history from multiple diffusion domain MDD modeling.

south of the LAR valley. The three lowest elevation samples from both transects combined did not yield reproducible data (Table 4.1), with low apatite yield (only one grain; 48 ± 1 Ma, FPG-01; Table 4.1; Table D1) and high percent error (23 ± 6 Ma, TCBR-04 and 320 ± 106, FPG-05; Table 4.1; Table D1). The mid-elevation samples within these two transects record late Cretaceous and early Cenozoic ages (FPG-06, 63 ± 5 Ma; TCBR-03, 67 ± 0.3 Ma; FPG-08, 61 ± 5 Ma; Table 4.1; Fig. 4.4). The TCBR transect continues to higher elevations than the FPG transect, yielding older AHe dates in the two samples at these higher elevations (135 ± 11 Ma and 101 ± 9 Ma; Table 4.1; Figs. 4.4 and 4.5). In summary, for all samples from these two transects that fit our data quality

criteria, the AHe dates are latest Cretaceous to Paleocene in age (Table 4.1; Table D1; Figs. 4.3C, 4.4E, and 4.5).

Echo Canyon

Five samples were collected in Echo Canyon (EC) from the coarse, unconsolidated sandstone mapped as the Eocene Echo Park Alluvium (Taylor et al., 1975b). Apatite yields from these samples were poor, and thus dates were only obtained from two samples. Of these two, only one sample (EC-03a) yielded multiple grains acceptable for analysis. The four dates obtained from sample EC-03a range from 406 ± 4 Ma to 3486 ± 26 Ma (Table 4.1; Table D1), while the one AHe date obtained from EC-04 yielded a date of 33 ± 0.3 Ma (Table 4.1; Table D1). The Paleozoic and older dates of the individual apatite grains, combined with the geologic age constraints on the unit from which these samples were collected, indicate that these dates reflect the thermal evolution of the source terrain from which they were derived (and not the thermal history of the Echo Park Alluvium). Because we lack any geologic context for this source terrain, and because the detrital nature of these grains prevents us from treating them statistically as an integrated sample, we exclude these dates from further analyses.

Fremont Transect

The Fremont transect (FMT) samples were collected in a vertical transect on Fremont Peak near Royal Gorge, Colorado (Fig. 4.3C). Only three of the five samples collected yielded apatite (Table 4.1; Table D1). The AHe dates for the three samples range from Early Cretaceous to late Paleogene (27 ± 2 Ma, FMT-01; 110 ± 29 Ma, FMT-02; ± 27 Ma, FMT-03; Table 4.1; Figs. 4.4F and 4.5) and show no correlation between age and elevation. All three samples, however, have poor reproducibility (Table 4.1;

Table D1) and were not incorporated into thermal models or subject to further interpretation.

ASSESSMENT OF REGIONAL DIFFERENCES ON THE INTERPRETATION OF THERMOCHRONOMETRIC DATA

Interpretations of low-temperature thermochronometric data from Proterozoic rocks that most likely have complex or protracted thermal histories can be complicated. Often dates from a single sample will have low reproducibility (Fitzgerald et al., 2006; Peyton et al., 2012; Flowers et al., 2009; Shuster et al., 2006; Reiners et al., 2008; Spiegel et al., 2009; Kohn et al., 2009; Hourigan et al., 2005; House et al., 1997), and although samples may be collected along vertical transects, it is not always clear that their present spatial relationships are representative of those at the time of cooling and exhumation (e.g., Reiners and Farley, 2001; Niemi et al., 2013).

Interpretations of paleo-isotherm geometries from low-temperature thermochronometric data can also be affected by long-wavelength regional tilting (e.g., House et al., 2001; Roy et al., 2004). Because much of the southern Rocky Mountain region is composed of Paleoproterozoic and Mesoproterozoic crystalline rocks that have undergone significant metamorphic and deformation events, and because these rocks are not typically overlain by sedimentary strata that provide constraints on the orientation of paleo-horizontal, accurate information on regional tilting is critical to the valid interpretation of the spatial relationships among our low-temperature thermochronometric samples. Regional deformation and tilting could compromise assumed age-elevation relationships in our sampling transects, and regional-scale down-to-the west tilting has been proposed to have affected much of the Front Range of Colorado (Naeser et al.,

2002). To assess the degree of tilting that may have been imposed on our sampling transects, we employ a joint geochronologic and paleomagnetic study of the Cretaceous Whitehorn Granodiorite. New U-Th-Pb geochronologic analyses from zircon collected from the Whitehorn Granodiorite define the emplacement age of this pluton. These geochronologic analyses, together with paleomagnetic data, can be used to assess the magnitude of post-emplacement tilting of the granodiorite by comparison with expected paleomagnetic directions for the study area based on North American paleomagnetic poles of comparable age. This exercise has potential implications for the effects of post–latest Cretaceous deformation on our low-temperature thermochronometric sampling.

Emplacement and Tilting of the Cretaceous Whitehorn Granodiorite

The Whitehorn Granodiorite intruded into the Arkansas Hills (Fig. 4.3C; Wallace and Lawson, 2008; Wallace et al., 1997) and is ~8 km (east-west) by 25 km (north-south) in surface exposure. The stock is granodioritic in composition (Wrucke, 1974), and was emplaced in the Late Cretaceous (ca. 70 Ma), as initially inferred by K-Ar dates on biotite (cf. Chualaowanich, 1997, for a summary of new and recalculated K-Ar age determinations on the Whitehorn stock).

Zircon U-Th-Pb data from the Whitehorn Granodiorite

We analyzed two samples for zircon U-Th-Pb data, one from the Whitehorn Granodiorite pluton (15CM-05) and one from Proterozoic gneiss in the wall rock adjacent to the pluton (14BB-03; Table 4.1; Fig. 4.3D).

Igneous Zircon U-Th-Pb Analytical Methods

Analyses were performed using laser ablation–ICP-MS on both the Nu Plasma multi-collector ICP-MS (14BB-03) and the Thermo Element 2 single-collector ICP-MS

(15CM-05) at the University of Arizona's LaserChron Center following the procedures outlined in their procedures manuals (Gehrels and Pecha, 2014; Ibanez-Mejia et al., 2015).

Zircon U-Th-Pb Results

The sample from the Whitehorn Granodiorite (15CM-05) yields an age of 67.31 + 0.57/–0.78 Ma (2σ; Table D5; Fig. 4.8), confirming the previously inferred Late Cretaceous age for the intrusion of the pluton. The wall-rock sample (14BB-03) yields zircon U-Th-Pb ages of ca. 1.7 Ga (Table D6), which is consistent with U-Th-Pb ages

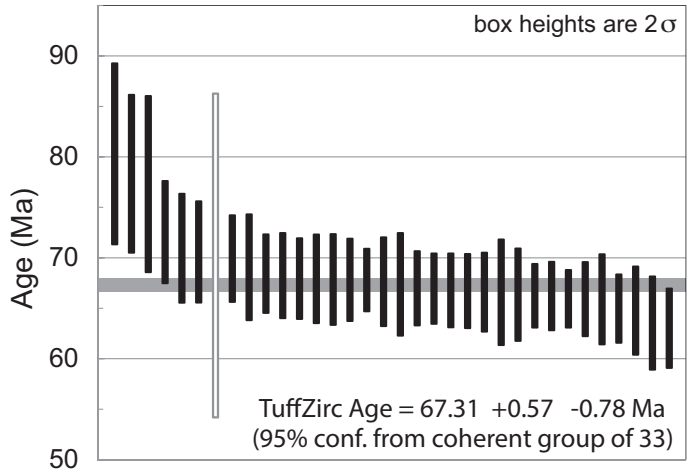

Figure 4.8: Mean age determined by U-Th-Pb analyses of 34 individual zircon grains from 15CM-05 taken from the Whitehorn Granodiorite. TuffZirc Age is calculated in Isoplot 3.6 (Ludwig, 2008) from 33 of these grains (black bars) with one grain rejected from age calculation due to high error (white bar); conf.—confidence.

from basement rocks in the surrounding area (Klein et al., 2010). The zircon U-Th-Pb ages and the biotite and hornblende $^{40}Ar/^{39}Ar$ ages are analytically indistinguishable and suggest that the Whitehorn Granodiorite was emplaced at, and cooled to, ambient temperatures below ~300 °C by ca. 67 Ma.

Paleomagnetism of the Whitehorn Granodiorite

Paleomagnetic Analytical Methods

We collected independently oriented samples from more than 50 sites in the Whitehorn Granodiorite and related thin intermediate composition dikes, as well as

intrusion host rocks, including Proterozoic metaigneous rocks and hornfels developed in Pennsylvanian strata in contact with the pluton. At all sites, sampling involved the use of a portable field drill with a nonmagnetic diamond drill bit that was water-cooled. At most sites, azimuthal orientation of independent cores (samples) was obtained by both magnetic and solar compasses. Core specimens were prepared in the laboratory into 2.5-cm-diameter, 2.25-cm-high right cylinders for anisotropy of magnetic susceptibility (AMS) and all remanence measurements. AMS measurements were made on an AGICO KLY-4A automated susceptibility unit. All remanence measurements were made on a 2G Enterprises Model 760R superconducting rock magnetometer equipped with an online 2G Enterprises alternating field (AF) demagnetization system and automated specimen handler. Thermal demagnetization employed on a Shaw MMTD instrument or an ASC TD48 instrument. Measurements of bulk susceptibility, as a continuous function of heating and cooling, were conducted on an AGICO MFK1-A susceptibility unit equipped with a CS4 furnace attachment. All heating and cooling experiments were conducted in an inert (argon) atmosphere.

Paleomagnetic Results

For samples of the Whitehorn Granodiorite that contain a single component of magnetization, as revealed in progressive demagnetization, the intensity of the natural remanent magnetization (NRM) is typically between 0.5 and 5 A/m. Several sites established in the pluton yield NRM intensities that are considerably higher (>10 A/m) and demagnetization results yield highly scattered directions of remanence. We interpret this behavior to be the effect of one or more lightning strikes, resulting in a lightning-induced RM, and the results from these sites are deemed uninterpretable (the results from

these sites are omitted from Table D7). For those sites not affected by lightning, alternating field (AF) demagnetization typically isolates a remanence of north-northwest to northwest declination and moderate to slightly steep positive inclination over a range of peak (AF) fields up to at least 80 mT, if not higher (Fig. 4.9). A similar magnetization is isolated in thermal demagnetization over a range of laboratory unblocking temperatures between ~450 °C and 580 °C (Fig. 4.9). Most sites in the Whitehorn Granodiorite that were not affected by lightning yield well-grouped magnetizations at the site level, with a 95% confidence in values of ~7° or less and k values >75 for typical sample populations between 7 and 10 independent samples (Fig. 4.10; Table D7). Sites in adjacent Paleozoic sedimentary rocks or Precambrian crystalline rocks that we interpret to have been remagnetized during pluton emplacement typically yield the most dispersed population of directions. On the basis of demagnetization behavior and monitoring bulk susceptibility continuously in heating and cooling (Fig. D3), we infer that the remanence characteristic of the pluton is carried by low-Ti magnetite. Reflected light microscopy and scanning electron microscopy both show that magnetite is typically unoxidized and exhibits textures that are consistent with a primary magmatic origin (Fig. D4). AMS data from the pluton exhibit a range of fabric orientations and fabric types, as well as a variable dispersion of principal susceptibility axes (Fig. D5). Consequently, it is difficult to interpret these data in the context of a model of homogeneous magma emplacement; further sampling, at very high spatial resolution, if possible, may result in a refinement of the data set to more fully assess the emplacement mechanism for the pluton. Notably, the degree of anisotropy and magnitude of fabric parameters (e.g., L and F) are acceptably

low and do not warrant concern about a strong magnetic fabric influencing the direction of a thermoremanent magnetization blocked in the granodiorite.

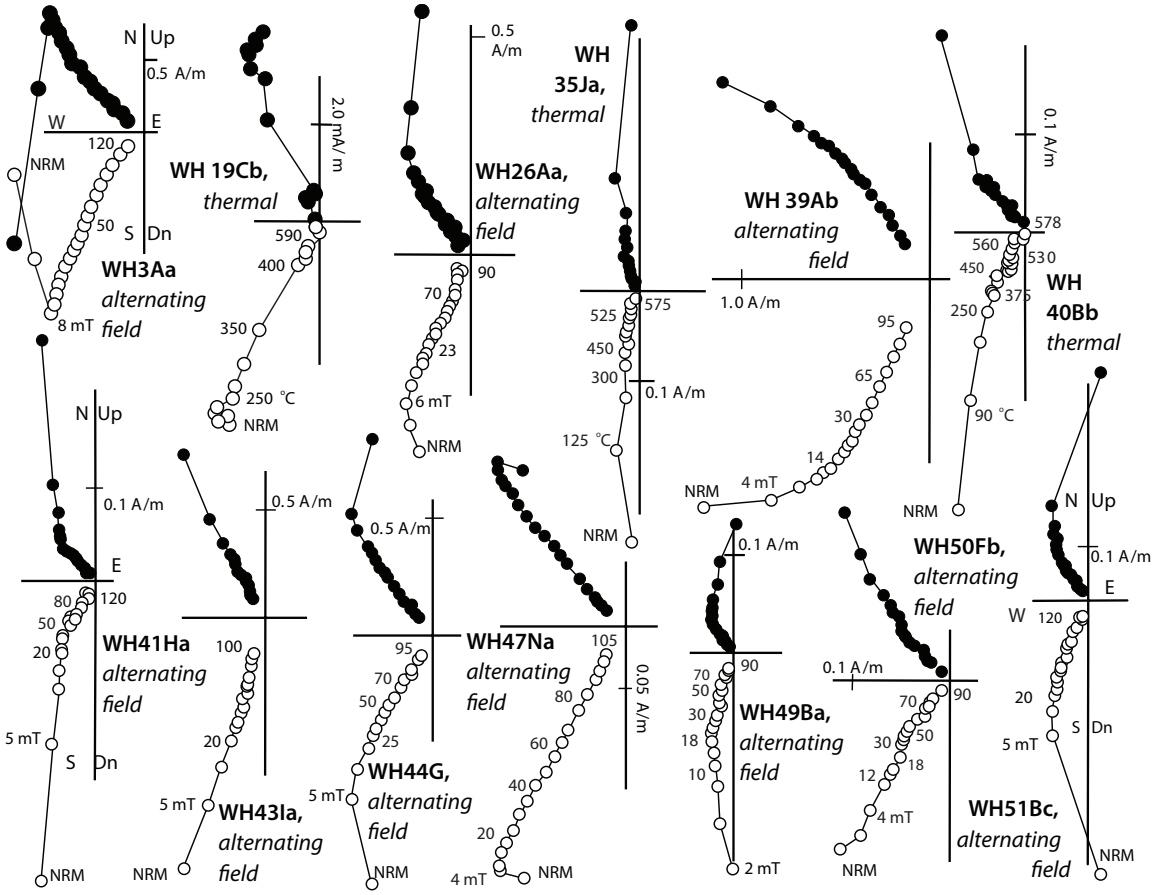

Figure 4.9: Representative examples of response to progressive alternating field (AF) and thermal demagnetization of specimens from samples from the Whitehorn Granodiorite from selected sampling sites. NRM—natural remanent magnetization. Each orthogonal demagnetization diagram plots the endpoint of the magnetization vector measured after successive demagnetization steps onto the horizontal (filled symbols) and vertical (open symbols) planes. Selected demagnetization steps are indicated along vertical projections. All projections are in geographic coordinates and all projections have the same coordinate scheme.

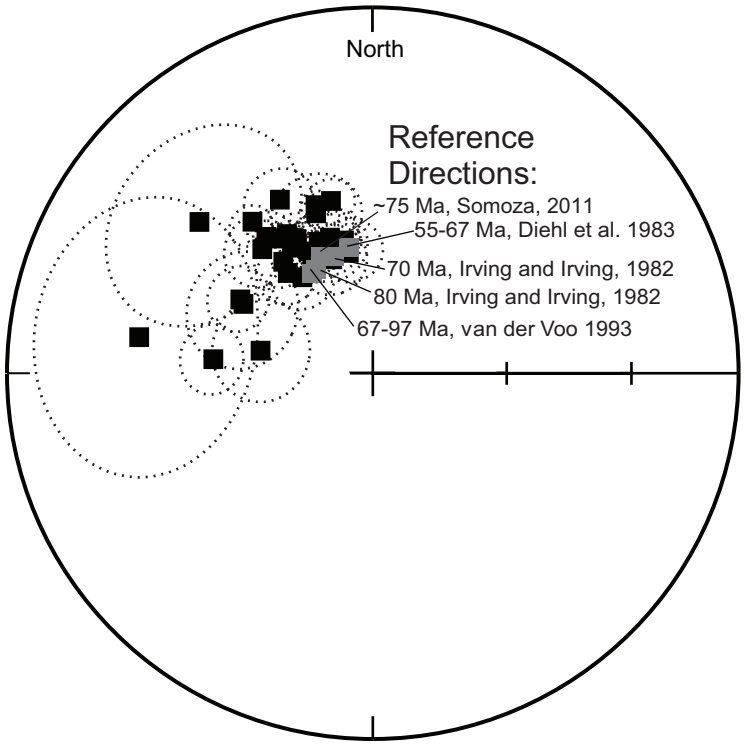

Figure 4.10: Equal area projection of estimated site mean directions and associated projected cones at 95% confidence of paleomagnetic data from sites in the Whitehorn Granodiorite and adjacent host rocks. Black squares show sample projections onto the lower hemisphere. Paleomagnetic data from the Whitehorn Granodiorite are compared with examples of expected directions (gray squares) of the locality for latest Cretaceous time. All paleomagnetic data from the Whitehorn Granodiorite are of north to north-northwest declination and moderate positive inclination (normal polarity).

Paleomagnetic Interpretations

The in situ magnetization characteristic of the Whitehorn Granodiorite, as defined by results from 32 sites in granodiorite and contact host rocks, is of north-northwest declination and moderate positive inclination (Dec. = 324.2°, Inc. = +56.5°, α95 = 4.1°, k = 38.6). All magnetizations resolved from the pluton are exclusively of normal polarity, consistent with the interpreted age of emplacement of the pluton as ca. 67 Ma, with magnetization acquisition during magnetic polarity Chron 31/30 time interval, which is dominated by normal polarity (Gradstein et al., 2012). The direction of the in situ magnetization differs slightly from expected latest Cretaceous (ca. 70–66 Ma) directions (~340/62–347/61) derived from paleomagnetic poles for North America for this time period (Fig. 4.10). The discordance is tentatively interpreted as indicating a slight (<10°) down to the east tilting of the Whitehorn Granodiorite and host rocks since emplacement.

Whitehorn Granodiorite Emplacement and Tilting Summary

Based on the paleomagnetic data presented here, which show that analyses from the Whitehorn Granodiorite are not statistically distinguishable from expected directions for the latest Cretaceous time, it is unlikely that tilting occurred southwest of the Front Range in the LAR valley. Given the location of the Whitehorn Granodiorite and immediately surrounding Proterozoic rocks, gentle tilting to the east may be related to the development of the broad Sawatch anticline that developed during Laramide deformation or regional flexure associated with the Rio Grande rift. The sense of tilting is opposite that previously proposed for the Front Range (Naeser et al., 2002) and of magnitude small enough that it should not affect the interpretation of thermochronometric data collected along vertical transects.

GENERAL SPATIAL PATTERNS OF THERMOCHRONOMETRIC AGES

The paleomagnetic results here show that little tilting has affected the rocks in the LAR valley. In addition, the base of the Wall Mountain Tuff, which is preserved across the LAR region and as much as 130 km east at Castle Rock (just south of Denver), has a regional tilt of <1°. Therefore, we conclude that our sampling transects, with a possible exception for transects west of the Mosquito Range ridgeline (discussed in detail in the following), approximate true vertical profiles and that their respective vertical spatial relationships reflect paleodepth relationships.

Spatial Patterns of Low-Temperature Thermochronometric Data Along the Arkansas River

In general, the AHe data reveal older ages at the east end of the LAR valley (ca. 135 Ma to ca. 60 Ma) and younger ages to the west (ca. 65 to ca. 40 Ma; Table 4.1; Figs. 4.3C and 4.5). The boundary between the older and younger age domains is

approximately located west of Texas Creek (transects TCBR and FPG) and east of Burned Timber Mountain (BTM transect), in the vicinity of Coaldale (Fig. 4.3C). This spatial pattern of AHe ages is also notable in the vertical relationships of these transects. We discuss these vertical relationships and the hypothesis that there was differential exhumation in the LAR valley during Laramide tectonism, with greater exhumation taking place toward the western end of the LAR valley.

Vertical Patterns in Low-Temperature Thermochronometric Transects

In contrast to a fairly clear-cut overall spatial pattern in the AHe ages, vertical age patterns in the individual transects suggest a more complex and nuanced thermal history. Vertical transects are often interpreted to reflect the cooling history of rocks, with the slope of sample data in age elevation space being proportional to the exhumation rate (Fitzgerald and Gleadow, 1990). Sample suites with steep or elevation-invariant ages are interpreted as the rapid exhumation of samples that cooled quickly through the partial retention zone (PRZ; Fitzgerald and Gleadow, 1990). Sample suites with steep age-elevation gradients at lower elevations and shallow age-elevation gradients at higher elevations are inferred to record lesser amounts of total exhumation, for a given thermochronometer, with partial preservation of the PRZ. In such cases, the onset of exhumation is marked by the time of change in slope from a shallow to steep elevation gradient (Fitzgerald and Gleadow, 1990). In all cases of simple cooling histories driven by tectonic or erosional exhumation, thermochronometric ages in vertical transects are predicted to increase monotonically with higher elevation (Fitzgerald and Gleadow, 1990).

We observe aspects of all of these expected behaviors in the vertical transects

from the Arkansas River valley; however, there are also some notable deviations from these expectations. In the UAR valley, the WBP transect records elevation invariant ages below ~3200 m (Fig. 4.4A), indicating rapid cooling ca. 70–60 Ma. The uppermost sample in this transect yields a cooling age that is significantly older than the rest of the transect samples (ca. 260 Ma), implying that the change from Paleozoic ages to Cretaceous– Paleocene ages records the location of the base of the PRZ and places a limit on the amount of exhumation in this region to ~3 km in the Cenozoic.

The GM, WH, and BTM transects also exhibit rapid exhumation ca. 60 Ma. None of these transects preserve older ages at higher elevations (Figs. 4.4 and 4.5), suggesting that these transects may have undergone greater total exhumation than the WBP transect, which is farther to the north. Samples at higher elevations in the WH and BTM transects display anomalous behavior, which we discuss in the following.

In the Texas Creek transects (TCBR and FPG), samples collected below ~2600 m display cooling from ca. 135 Ma to ca. 60 Ma at a rate slower than that observed in transects to the west (Fig. 4.4E). These transects do not display a change in exhumation rate as a function of time or depth, suggesting that they may reflect a fossil PRZ. In addition, the fact that the Echo Canyon (EC) gravel samples show varying ages from the Proterozoic and Paleozoic as well as the mid-Cenozoic (Table D1) indicates that the samples in the east were never buried deeply enough, after the Cretaceous, to reset the AHe ages. Thus, the eastern part of the LAR valley appears to have undergone less exhumation in comparison to the rocks included in the transects from the western end of the LAR valley.

Younging of Apatite Helium Ages Below and Adjacent to Ignimbrites

At elevations above ~2600 m in multiple transects (WH, BTM, TCBR) we observe that thermochronometric ages no longer monotonically increase, but are instead younger than the samples below them (Table 4.1; Figs. 4.4 and 4.5), and in some cases (e.g., BTM) are younger than all other samples in the vertical transect. These highest elevation ages range from ca. 50 to 28 Ma in the WH and BTM samples, while the highest elevation sample in the TCBR transect is ca. 100 Ma (35 m.y. younger than a sample <120 m below it). This inflection in the age-elevation relationship is inconsistent with simple tectonic or erosional exhumation, and requires further exploration.

EVALUATION AND INTERPRETATION OF LOW-TEMPERATURE THERMOCHRONOMETRIC DATA

To further refine the thermal histories recorded by our low-temperature thermochronometry data, we wish to understand the age inversion seen in many of our vertical transects and to decide how samples or transects displaying this behavior should be interpreted. Notably, transects that display this age inversion were collected beneath or adjacent to thick exposures of mid-Cenozoic ignimbrites (Fig. 4.11).

Circulation of hydrothermal fluids has been proposed to partially reset low-temperature thermochronometers to depths of at least several hundred meters (Arne et al., 1990; Foster et al., 1994; Gallagher, 1998; Whipp and Ehlers, 2007; Hickey et al., 2014; Ault et al., 2016), and large-volume ignimbrites are observed to generate short-lived (tens to thousands of years), high-temperature (200–500 °C) hydrothermal systems (Gazis et al., 1996; Holt and Taylor, 1998; Keating, 2005). To assess whether hydrothermal circulation may have been a factor in partially resetting AHe samples collected directly below or adjacent to the nonconformity and overlying ignimbrites, we combine clumped

isotope analyses of Paleozoic carbonate rocks (both adjacent to and distal from the ignimbrites) with thermal modeling to evaluate if the temperatures and isotopic signatures they record can be linked to hydrothermal fluid circulation.

Application of Clumped Isotope Thermometry to Assess Paleohydrothermal Fluid Circulation

Clumped isotope analysis is a tool that can be used to determine the temperature of formation waters, diagenetic temperatures, metamorphic cooling temperatures, and recrystallization conditions for carbonate rocks (e.g., Passey and Henkes, 2012; Winkelstern and Lohmann, 2016). If the age inversion in the AHe ages can be attributed to circulating high-temperature fluids, the hydrothermal fluid signature should be manifested as diagenetic alteration of carbonate rocks from the LAR valley. Thus, sampling and analysis of carbonate rocks proximal to our AHe sampling transects can potentially quantify the thermal and diagenetic conditions undergone by these rocks.

Carbonate clumped isotope analysis uses the tendency of heavier oxygen and carbon isotopes (^{18}O and ^{13}C) to clump together within the same carbonate molecule at lower temperatures (Schauble et al., 2006). This method offers a way of measuring carbonate formation temperature without additional assumptions, thereby making possible calculation of the isotopic composition of precipitating waters. Geologically ancient fine-grained carbonates are unlikely to preserve clumped isotope temperatures indicative of original Earth surface conditions (Winkelstern and Lohmann, 2016). Instead, such samples may preserve clumped isotope conditions that range from some combination of original near-surface conditions and temperatures at depth (arising from shallow diagenesis), to extensive resetting by solid-state reordering at temperatures above

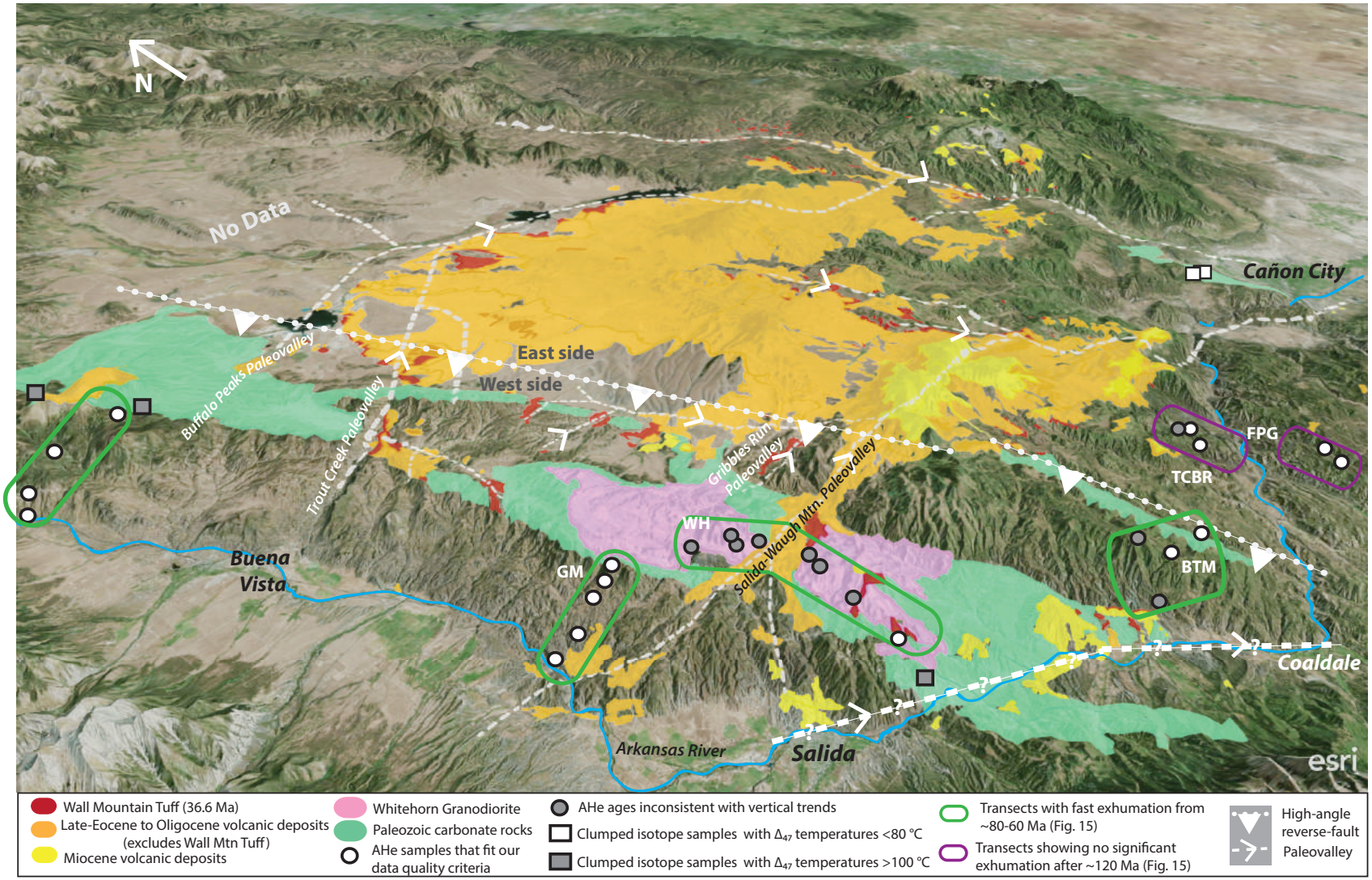
N
No Data
Cañon City
East side
West side
Buffalo Peaks Paleovalley
Trout Creek Paleovalley
Gribbles Run Paleovalley
Salida-Waugh Mtn. Paleovalley
FPG
TCBR
WH
GM
BTM
Buena Vista
Coaldale
Salida
Arkansas River
esri
Wall Mountain Tuff (36.6 Ma)
Late-Eocene to Oligocene volcanic deposits (excludes Wall Mtn Tuff)
Miocene volcanic deposits
Whitehorn Granodiorite
Paleozoic carbonate rocks
AHe samples that fit our data quality criteria
AHe ages inconsistent with vertical trends
Clumped isotope samples with Δ_{47} temperatures <80 °C
Clumped isotope samples with Δ_{47} temperatures >100 °C
Transects with fast exhumation from ~80-60 Ma (Fig. 15)
Transects showing no significant exhumation after ~120 Ma (Fig. 15)
High-angle reverse-fault
Paleovalley

Figure 4.11: Prospective ArcEarth view with 3× exaggerated topography. Late-Eocene to early-Miocene ignimbrites are draped over topography (red—Wall Mountain Tuff, orange—Oligocene, yellow—Miocene). Dashed white lines indicate paleovalleys proposed to have existed prior to ignimbrite deposition (Chapin and Lowell, 1979). On the basis of differential exhumation recorded by the low-temperature thermochronometry and the clumped isotope signatures we propose and east-west boundary in the LAR valley, marked by dotted white line with high-angle reverse fault symbols, we propose that the Salida–Waugh Mountain paleovalleys do not extend as far west as previously mapped and that another paleovalley from Salida to Coaldale may have existed (marked by the white dashed line with question marks) where ignimbrite deposits are still preserved at modern river level. AHe—apatite helium; WH—Whitehorn; TCBR—Texas Creek–Bull Ridge; FPG—Five Point Gulch; BTM—Burned Timber Mountain; GM—Green Mountain.

~150 °C, to complete recrystallization at a range of burial depths (Passey and Henkes, 2012; Winkelstern and Lohmann, 2016). Experimental data show that solid-state reordering of carbonate bonds only occurs at temperatures >~150 °C and that the clumped isotope composition preserved in a given sample is a function of both temperature and time (Passey and Henkes, 2012; Stolper and Eiler, 2015). Essentially, the carbonate Δ_{47} value of a given rock will equilibrate with ambient conditions more quickly if temperatures are higher. Thus a carbonate rock, if slowly cooled over millions of years, will continually re-equilibrate to a final temperature near the ~150 °C blocking threshold, below which the bonds can no longer reorder. Alternatively, the rock can be rapidly cooled to a temperature below 150 °C, in which case the clumped isotope temperature recorded will be hot (at or near the peak burial or heating temperature of the sample; Passey and Henkes, 2012; Henkes et al., 2014; Lloyd et al., 2017). Fundamentally, as soon as solid-state reordering has resulted in a carbonate clumped isotope temperature in excess of the ~150 °C blocking temperature, solid-state reordering during cooling cannot yield a clumped isotope temperature lower than ~150 °C without subsequent recrystallization or diagenetic alteration (cf. Lloyd et al., 2017). We present clumped isotope data from carbonate rocks in the LAR region, including from the contact metamorphic aureole of the Cretaceous Whitehorn Granodiorite. We demonstrate that the

clumped isotope Δ_{47} temperatures preserved in the contact aureole are cooler than independently determined peak metamorphic temperatures, requiring a post-metamorphic diagenetic alteration of the carbonate samples in post-Cretaceous time.

Stable Isotope Methods and Analysis

We analyzed bulk micritic limestone samples from Mississippian carbonates in the LAR region. These samples were taken from localities near several of our vertical transects (Fig. 4.3). Two samples were collected from the Mississippian Williams Canyon Limestone near the easternmost extent of the Arkansas River gorge and Cañon City (MOX-02 and MOX-03 near the FMT AHe transect; Fig. 4.3C; Table 4.3; Table D7). An additional sample was collected in the Mississippian Leadville Limestone at the base of the Whitehorn Granodiorite east of Salida (14BB-04; Fig. 4.3; Table 4.3; Table D7). Two samples were collected from the Leadville Limestone on West Buffalo Peak (overlying the WBP transect; Fig. 4.3B; Table 4.3; Table D7).

Our analytical methods follow those described in Defliese et al. (2015). Three ~5 mg subsamples of each carbonate sample were measured for their conventional and clumped stable isotopic composition. Following reaction with 75 °C phosphoric acid, evolved CO_2 was cryogenically purified and passed through Porapak resin held at −10 °C (instead of the colder temperature used by Defliese et al. 2015; see Petersen et al., 2016). The clumped isotope acid fractionation factor and ≥75 °C acid temperature calibration of Defliese et al. (2015) were applied to all data. Final clumped isotope measurements are reported as Δ_{47} values (Table 4.3) in the absolute reference frame of Dennis et al. (2011). Carbonate $\delta^{18}O$ and $\delta^{13}C$ values are measured concurrently with clumped isotope analyses. These data are reported relative to the Vienna Pee Dee belemnite (VPDB)

standard and are interpreted using the calcite acid fractionation factor of Kim and O'Neil (1997). Calculated $\delta^{18}O$ water values employ the revised calcite water fractionation factor of Friedman and O'Neil (1977) and are reported relative to Vienna standard mean ocean water (VSMOW).

Clumped Isotope Δ_{47} Temperatures and $\delta^{18}O$ Water Values

All samples record clumped isotope temperatures in excess of 65 °C (Table 4.3) and therefore no longer record surface conditions and have been diagenetically altered. The three western samples (BB-04, WBP-03, and WBP-02; Fig. 4.3) record temperatures in excess of 100 °C (Table 4.3), significantly warmer than the ~70 °C temperatures recorded by the samples from the east end of the valley (MOX-02 and MOX-03; Fig. 4.3; Table 4.3). Calculated water $\delta^{18}O$ values for the fluids from which these carbonates formed also differ substantially. Western samples precipitated from ~3‰ more positive waters than those in the east.

Constraints on Late-Stage Hydrothermal Circulation from Clumped Isotope Temperatures and $\delta^{18}O$ Values

The clumped isotope temperatures from our samples are all below the ~150 °C blocking threshold, indicating that the samples have either (1) never equilibrated to temperatures in excess of 150 °C, or (2) equilibrated in the past to temperatures above 150 °C but were subsequently altered via dissolution and re-precipitation, thereby erasing previous diagenetic or metamorphic temperatures. However, the differences in both clumped isotope Δ_{47} temperatures and calculated water $\delta^{18}O$ values (Table 4.3; Fig. 4.12) between the eastern and western samples implies possible different thermal histories, particularly because the sample suite is collected from carbonate rocks of roughly the

same age, with presumably similar initial Δ_{47} values. We interpret the clumped isotope temperatures in light of our thermochronometric data and other independent geologic evidence to resolve the genesis of the observed clumped isotope variability.

Eastern carbonate samples

The elevated temperatures recorded by samples collected near Cañon City (~70 °C) are consistent with alteration under shallow burial conditions and are consistent with observations from other fine-grained carbonate rocks (e.g., Quade et al., 2013; Winkelstern and Lohmann, 2016). Calculated water δ18O values of ~+7‰ (relative to VSMOW) are also consistent with waters that have partially equilibrated with surrounding rock (e.g., Clayton et al., 1966; Sousa et al., 2016), likely indicating that some recrystallization of these samples has occurred. Together these results are broadly what one would expect for clumped isotope alteration of geologically ancient rocks that have never undergone deep burial or complete solid-state reordering. Their current Δ_{47} and water $\delta^{18}O$ values likely reflect diagenetic background conditions, i.e., the result of partial recrystallization at a range of depths, potentially along with minor solid-state alteration (without reaching equilibrium).

Western carbonate samples

The temperatures recorded by all three of the western samples are significantly warmer than the eastern samples, although all are still distinctly lower than the blocking temperature (~150 °C) for calcite (Table 4.3). We can further divide discussion of the western samples into northern and southern samples. The southern samples, typified by sample BB-04, we collected in close proximity (tens of meters) to the intrusive contact of the Whitehorn Granodiorite. Sedimentary rocks in the contact metamorphic aureole of the

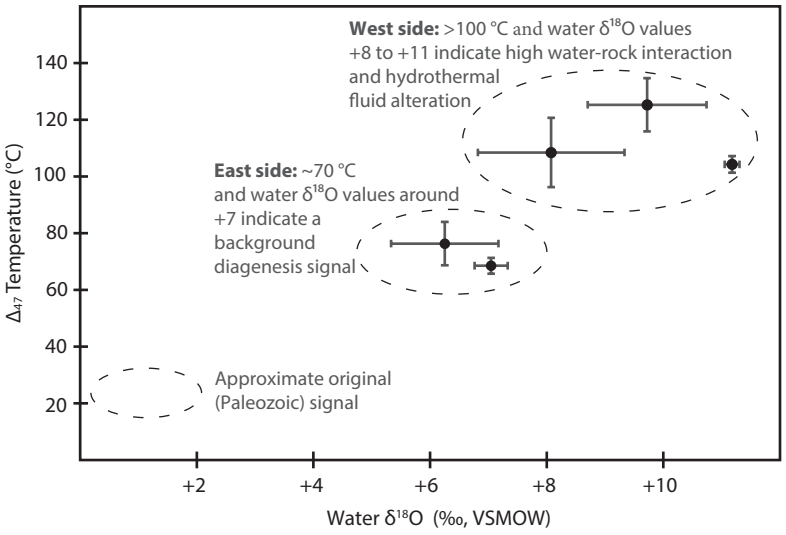

Figure 4.12: Clumped isotope temperatures plotted with calculated $\delta^{18}O$ of formation waters. Samples collected near Cañon City (MOX-02 and MOX-03) reflect typical diagenetic conditions of shallow burial we refer to as background diagenesis. The other three samples (BB-04, WBP-03, and WBP-01) have been further altered by high-temperature fluids. VSMOW—Vienna standard mean ocean water.

Whitehorn Granodiorite are inferred to have undergone peak metamorphic temperatures of ~600 °C (Wofford, 1986). This observation, combined with our $^{40}Ar/^{39}Ar$ biotite, hornblende, and K-feldspar data, as well as our ZHe data, imply that the Whitehorn Granodiorite and its associated metamorphic aureole cooled rapidly (from ~600 °C to ambient temperatures of <200 °C in ~2 m.y.). Such a cooling history should preserve clumped isotope Δ_{47} temperatures at or near peak metamorphic conditions (Passey and Henkes 2012; Lloyd et al., 2017). Therefore, the relatively cold temperatures from BB-04 (~50 °C below the blocking temperature for solid-state reordering of clumped isotope bonds) necessitate post-metamorphic alteration or recrystallization to overprint the metamorphic clumped isotope temperature. The more positive water $\delta^{18}O$ values involved in precipitating this carbonate, relative to the eastern samples, are also consistent with more extensive recrystallization via waters equilibrated with (isotopically heavy) rock $\delta^{18}O$.

The carbonate samples collected farther north from West Buffalo Peak also exhibit Δ_{47} temperatures of ~100 °C and heavy water $\delta^{18}O$ values, but were collected

TABLE 4.3. CARBONATE CLUMPED ISOTOPE AND STABLE ISOTOPE RESULTS

Sample ID	Longitude	Latitude	Elevation (m)	$\delta^{13}C$ (‰, VPDB)	Rock $\delta^{18}O$ (‰, VPDB)	Δ_{47} (‰, ARF)	Δ_{47} Temperature (° C)	Water $\delta^{18}O$ (‰, VSMOW)
MOX-02	-105.2916	38.4946	1899	-1.3 ± 0.1	-2.5 ± 0.1	0.597 ± 0.005	68 ± 3	7.0 ± 0.3
MOX-03	-105.2893	38.4949	1899	+0.3 ± 0.1	-4.2 ± 0.1	0.584 ± 0.013	76 ± 8	6.2 ± 0.9
BB-04b	-105.9146	38.5082	2314	+2.4 ± 0.1	-2.7 ± 0.3	0.539 ± 0.004	104 ± 3	11.2 ± 0.1
WBP-03	-106.1150	38.9997	3574	+1.7 ± 0.1	-6.0 ± 0.1	0.536 ± 0.017	108 ± 12	8.1 ± 1.3
WBP-01	-106.0808	38.9596	3258	-0.6 ± 0.1	-6.0 ± 0.2	0.514 ± 0.011	125 ± 9	9.7 ± 1.0

Clumped isotope temperatures are calculated using the > 75 °C acid calibration of Defliese et al. (2015).

Δ_{47} values are reported in the absolute reference frame (ARF) of Dennis et al. (2011).

Conventional stable isotope values are reported relative to the Vienna Pee Dee Belemnite (VPDB) and Vienna Standard Mean Ocean Water (VSMOW) standards.

from an area devoid of post-Mississippian intrusions. There is also no evidence that these samples were ever deeply buried, as AHe sample WBP-02 (collected from Proterozoic basement rock that underlies the carbonate samples) has individual grain ages as old as Late Mississippian (Table D1), suggesting that regional burial has not attained temperatures hot enough to reset AHe ages (~60 °C) since the late Paleozoic. We would therefore expect the northern carbonate samples to reflect roughly the same background diagenetic temperatures as the eastern samples. However, the elevated Δ_{47} temperatures and heavier oxygen isotope values of precipitating waters indicate alteration under conditions similar to those of sample BB-04 (Fig. 4.12). From these observations, we infer that carbonate samples in the western LAR region record a late-stage (post Cretaceous Whitehorn Granodiorite emplacement) clumped isotope signal that overprints earlier values. From the similarity of clumped isotope temperatures recorded by all the western samples, we infer that the present-day signal was post-Cretaceous (younger than the peak metamorphic temperature that should have been recorded in sample BB 04) and was imparted at shallow depths by recrystallization. This inference is supported because the recorded temperature is less than the 150 °C blocking temperature for solid-state reordering, and because carbonate samples near West Buffalo Peak record clumped isotope temperatures hotter than would be required to reset structurally deeper, but not reset, AHe thermochronometric data. The most likely cause for this alteration is heating during mid-Cenozoic magmatism and ignimbrite emplacement arising from hydrothermal fluid circulation driven in the near surface sedimentary strata by the combination of the overlying volcanic rocks and local paleorelief (Sousa et al., 2016). Circulation of hydrothermal fluids, as implied by the clumped isotope results, could also potentially

affect AHe results from samples collected near the overlying ignimbrites. Such a process could potentially explain the observed inversion in age-elevation data in several vertical transects, as described here, and is explored quantitatively in the following.

Effects of Short-Lived, Top-Down Heating and Hydrothermal Circulation

The effect of advective heat transport by topography-driven fluid flow has been found to modify the crustal thermal field (Whipp and Ehlers, 2007). In such scenarios, ages from low-temperature thermochronometers could be biased toward younger cooling ages by being reset or partially reset by the influx of heat from circulating fluids rather than by conductive cooling arising from exhumation. In the models of Whipp and Ehlers (2007), fluid circulation was driven by significant topographic relief, and transported heat that was advected toward the surface by rapid exhumation in an active orogenic belt. Near-surface hydrothermal circulation, however, can also be established by other processes. Volcanic eruptive centers and large-volume ignimbrites can both generate short-lived (10 yr. to 10 k.y.) hydrothermal systems, with temperatures from 70 to 150 °C, depending on local meteoric water temperatures (Keith, 1991; Keith et al., 1992; Gazis et al., 1996; Holt and Taylor, 1998; Keating, 2005). Even short-lived modest temperature perturbations can alter low-temperature thermochronometers and partially, or completely, reset AHe ages (Hickey at al., 2014; Ault et al., 2016).

Late Eocene to early Miocene volcanism and ignimbrite emplacement are prevalent, and voluminous, throughout the Mosquito Range and the LAR (Epis and Chapin, 1975; Gregory and McIntosh, 1996), and these eruptive products are deposited on highly dissected and fractured Proterozoic basement rocks, which may form copious pathways for fluid penetration and circulation. Such hydrothermal systems have

previously been invoked to explain regional mineralization and, to a lesser extent, local remagnetization (e.g., DeVoto, 1990; Geissman and Harlan, 2002). We explore the impact of potential hydrothermal fluid circulation on AHe ages arising from the emplacement of hot ignimbrites (~750 °C) on cold (~7 °C; modern mean annual surface temperature at Salida) basement rock. We employ a forward thermal model, implemented in QTQt (version 64R5.4.6; Gallagher, 2012), to explore the effects of short-lived thermal pulses on AHe ages. The thermal models initiate with instantaneous cooling from temperatures >200 °C to 0 °C at 100 Ma, which establishes a baseline thermochronometric age of 100 Ma. This cooling is followed by thermal perturbations beginning at 36.6 Ma of varying duration (103–107 yr.) and magnitude (40 to 200 °C), after which the AHe age is recalculated. The results of these experiments (Fig. 4.13) show that short-lived (<105 yr.) thermal pulses >100 °C could measurably reset the AHe ages recorded in a given sample. Thus, taking these data into account we infer that hydrothermal systems in the upper hundreds of meters of Proterozoic basement were driven during emplacement and cooling of the ignimbrite sheets (Fig. 4.13), partially resetting the AHe ages in samples adjacent to the ignimbrite base (Figs. 4.11 and 4.14). Therefore, the data from these samples cannot be used for interpretations related to cooling from exhumation.

Selection of Low-Temperature Thermochronometric Data for Thermal Modeling

To extract thermal histories related to the tectonic evolution in our study area, it is critical to identify samples from our data set that have thermochronometric ages that may reflect heating associated with the hydrothermal processes described here. The clumped carbonate thermometry data (Table 4.3; Fig. 4.12), age inversions observed in our vertical

transects (Figs. 4.4 and 4.5; Table 4.1), and numerical modeling of pulse heating events (Fig. 4.13) raise concerns that samples collected in proximity to the regionally extensive ignimbrite deposits (Chapin et al., 2004; McIntosh and Chapin, 2004) may have been subject to resetting by hydrothermal fluid circulation, as proposed here.

We first note that there are two AHe transects where we observe no evidence of anomalous behavior or potential resetting. Samples from the Green Mountain (GM) and West Buffalo Peak (WBP) transects (Figs. 4.4 and 4.5) both display typical age-elevation relationships, and are spatially removed from the confined paleovalleys that appear to have captured much of the deposition of ignimbrites in the western part of our study area (although the view in Fig. 4.11 seems to display a close proximity between the base of the GM transect and the ignimbrite deposits in the UAR valley north of Salida, they are in fact separated by nearly 2 km; Epis et al., 1976; Chapin and Lowell, 1979). In the case of the WBP transect, hydrothermal fluid circulation appears to have altered clumped isotope temperatures in late Paleozoic carbonate rocks overlying this transect. However, given the late Paleozoic AHe age for the highest elevation sample in the WBP transect (older than 260 Ma; Table 4.1; Fig. 4.4), either such fluids did not penetrate into the Proterozoic igneous rock in this region, or they had minimal effect on the thermochronometric ages (Fig. 4.14). In either case, the potential effects on the highest elevation sample in this transect, if any, will not alter the thermal modeling of the Late Cretaceous to recent thermal history.

Each of the other transects, however, show an indication of hydrothermal resetting, as evidenced by an age inversion pattern, with relatively younger ages observed in the highest elevation samples (WH, BTM, TCBR; Figs. 4.4 and 4.5). In several cases,

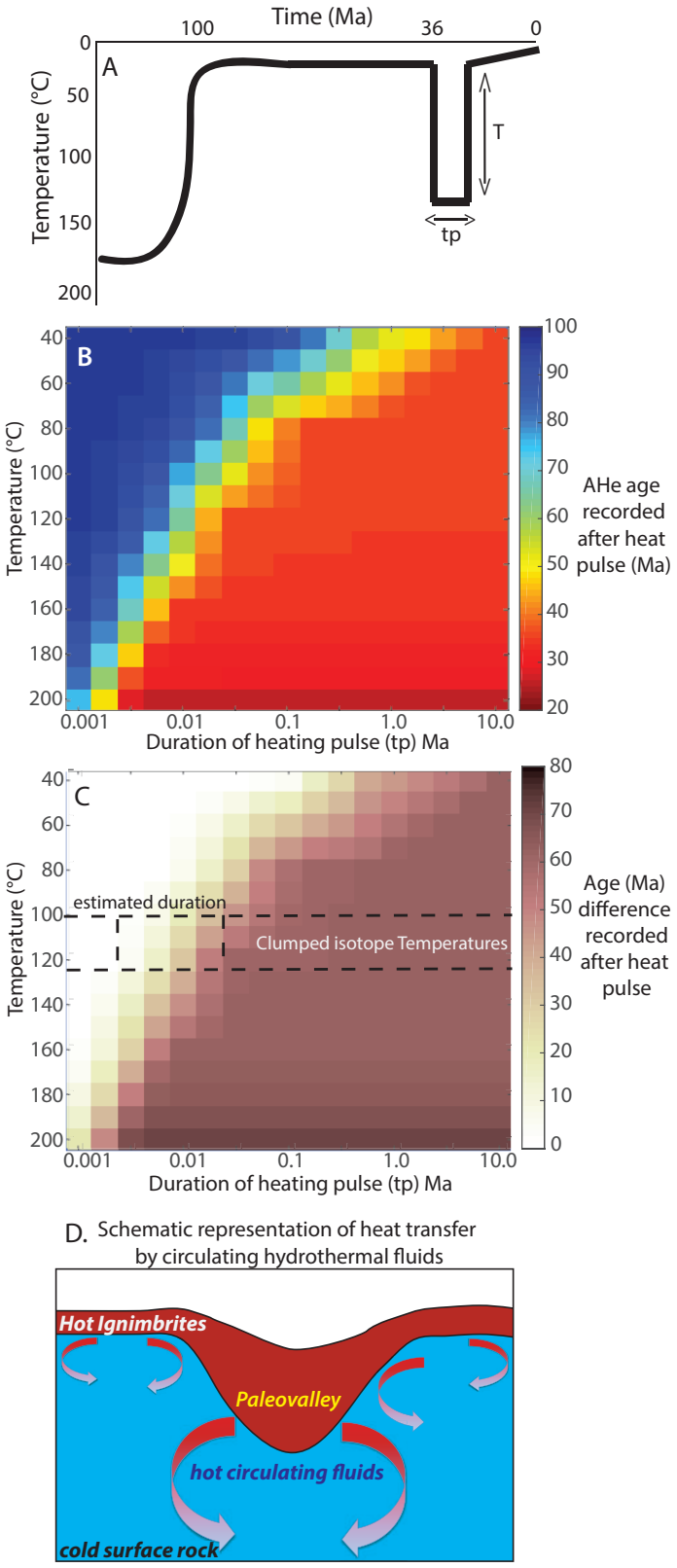

Figure 4.13: Numerical experiment demonstrating the effect of short-lived heat pulses on apatite helium (AHe) ages using forward thermal modeling in QTQt version 64R5.4.6 (Gallagher, 2012) . (A) Example time-temperature path for experiment. Sample is rapidly cooled at 100 Ma, then reheated for varying times (*t*p) and magnitudes (temperature). (B) Variations in AHe ages are determined for a variety of *t*p and temperature values, and compared to the AHe ages predicted with no reheating pulse. (C) Deviation of AHe age in B from predicted age without a heating pulse. Dashed lines mark the approximate duration needed to reproduce the deviation in AHe ages we observe in the vicinity of ignimbrite deposits in the lower Arkansas River, if exposed to hydrothermal fluid circulation temperatures similar to those recorded by carbonate clumped isotope temperatures in the region (~100-125 °C; Fig. 12). (D) Schematic diagram of hydrothermal fluid circulation in the vicinity of ignimbrite deposits, driven by the paleorelief from pre-existing paleovalleys and thickness of the ignimbrite deposit. Arrows represent the proportional relationship between heat penetration, topography and thickness of the heat source.

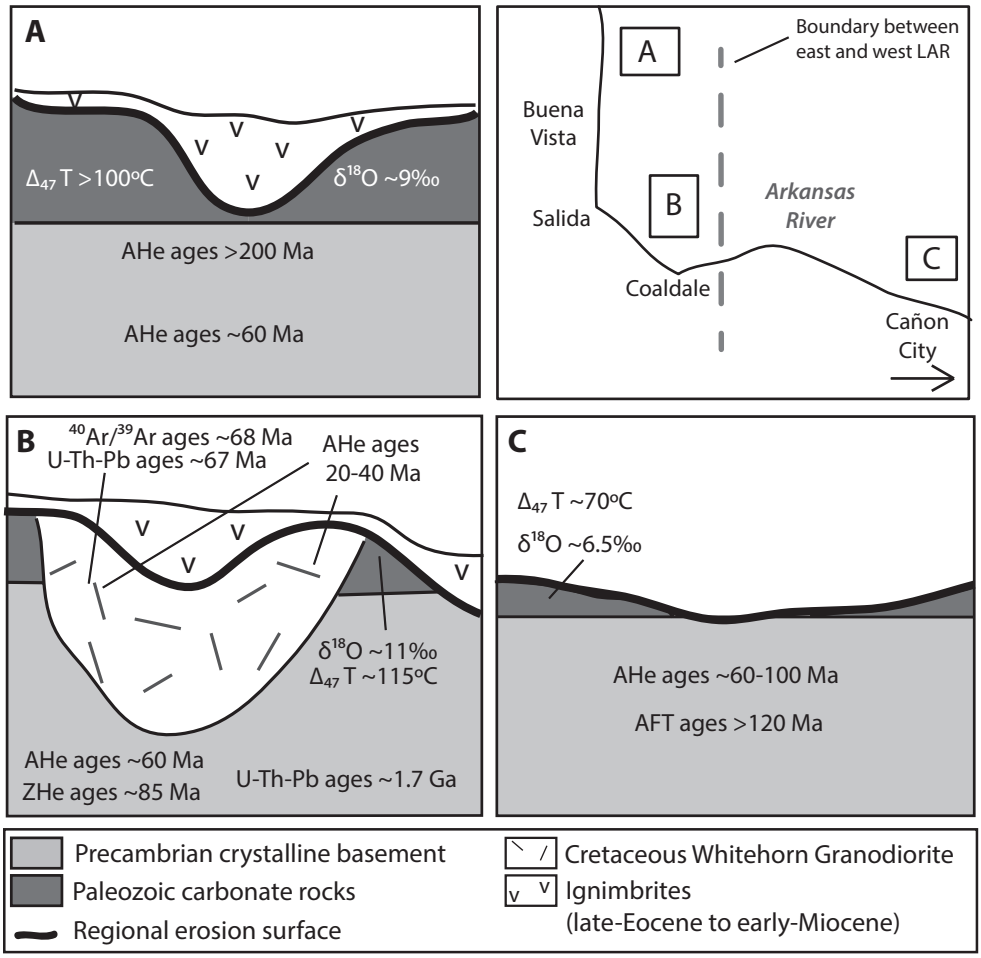

Figure 4.14: Summary of clumped isotope results, thermochronometry data (*T* is temperature), and geologic relationships seen in three regions from the study area. East-west boundary shown in upper right box separates regions in the east (C) recording pre-Laramide apatite helium (AHe) and apatite fission track (AFT) ages as well as a background diagenesis signal in the clumped isotopes from western regions (in A and B), which record thermochronometry ages related to the Laramide Orogeny and clumped isotope temperatures and $\delta^{18}O$ signatures indicative of hydrothermal fluid alteration. (A) The region near West Buffalo Peak (WBP) in the upper Arkansas River valley (UAR). (B) The Whitehorn Granodiorite transect in the western lower Arkansas River valley (LAR). (C) The eastern LAR, west of Cañon City.

these highest elevation samples are in close proximity to the regional Eocene erosion surface, blanketed by late Eocene to early Miocene ignimbrites (Fig. 4.11). To exclude the potential biasing of our thermal models by hydrothermally mediated reheating, we exclude the results from the highest elevation samples of these transects.

In addition to concerns about samples in close proximity to the erosion surface

and ignimbrite base, we are also wary of samples collected along the walls of regional paleovalleys (Fig. 4.11; Chapin and Lowell, 1979), which are currently filled by hundreds of meters of ignimbrite deposits. Samples collected along the flanks of these paleovalleys, particularly the samples to the north and south of the preserved ignimbrite valley fill in the Salida–Waugh Mountain paleovalley (Fig. 4.11; McIntosh and Chapin, 2004), also appear to have been subjected to hydrothermal resetting, based on their position relative to ignimbrite deposition and the inverse age-elevation relationship that they preserve. Thus, samples collected along paleovalley walls should also be excluded from thermal modeling. These criteria potentially exclude a number of samples collected along the north side of the Arkansas River between Salida and Coaldale, where remnants of ignimbrite deposits mantle the canyon wall from summit to river level (Fig. 4.11). An implication of this observation is that at least part of the modern Arkansas River canyon may be a re-incised Eocene paleovalley, an interpretation that we discuss in greater detail in the following.

Given these criteria, we identify samples that may have been affected by hydrothermal circulation. Then, with our data quality criteria established previously, we combine acceptable samples from our vertical transects of AHe and ZHe data and K-feldspar $^{40}Ar/^{39}Ar$ data with relevant published AFT data (Kelley and Chapin, 2004) to extract Cretaceous to present thermal histories. We describe the results in the following, with a focus first on the two transects that display no data quality issues or hydrothermal resetting signatures (WBP and GM), and compare these models to those derived from the complex thermochronometric data sets that characterize the remaining transects.

QTQt Thermal Modeling

Thermal modeling was undertaken in QTQt Macintosh version 64R5.4.6 (Gallagher, 2012). One advantage of this software is the ability to simultaneously solve for the thermal histories of multiple samples collected along a vertical transect. Model inputs include raw age information, grain size, and concentrations of He, U, Th, and Sm. In all model runs we implemented the Flowers et al. (2009) model for radiation damage in apatite and no radiation damage model for zircon. Model parameters that we define include the present-day surface temperature of 7 °C ± 3 °C (mean annual surface temperature at Salida), and a 30 °C/km geothermal gradient (a reasonable estimate for continental regions that are tectonically active but not undergoing igneous activity or extension; Bryant and Naeser, 1980; and similar to the present-day mean geothermal gradient for the southern Rockies; Nathenson and Guffanti, 1988). Models were run with a burn-in of 20,000 iterations then sampled over 80,000 iterations with a thinning of 1.

Thermal Modeling Results and Summary

Two transects from the westernmost part of our study area (WBP and GM) do not show evidence of the hydrothermal resetting signature in samples from other transects (Figs. 4.3 and 4.5; Table 4.1), and are spatially removed from the emplacement of ignimbrites. Ages along these two transects display expected age-elevation relationships, and we assume that the thermal histories derived from these samples will be the most representative of the tectonic exhumation of the region. Inverse thermal modeling of data from these two transects reveals rapid cooling from ca. 80 to 60 Ma (Fig. 4.15). After this rapid exhumation event both regions remained at near-surface temperatures from the Paleocene to the present (Fig. 4.15), recording no younger thermal perturbations.

The preservation of Paleozoic ages at the highest elevations in transect WBP and

the existence of partially reset ZHe ages at the base of transect GM reflect differential exhumation from north to south along the western flank of the Mosquito Range. Transect WBP records cooling since ca. 80 Ma from temperatures as high as ~100 °C, while transect GM records cooling from temperatures in excess of 160 °C over the same time period. For a 30 °C/km geothermal gradient, this implies a southward increase in the depth of exhumation from ~3 km at WBP to ~5 km at GM.

The above interpretation assumes that the present-day vertical relationships in the GM transect reflect paleo-depth relationships. Previously we discussed evidence that supports this assumption; however, others have proposed that the southern Mosquito Range–Arkansas Hills may have undergone tilting or step faulting related to Rio Grande rift extension (Chapin and Lowell, 1979; Keller and Baldridge, 1999; McIntosh and Chapin, 2004; Kelley, 2012). Such deformation could decrease the paleo-depth range sampled along the GM transect. However, basement contacts are not mapped as offset by faults (Van Alstine and Cox, 1969; Wallace et al., 1997; Wallace and Lawson, 2008), and although we cannot definitively rule out regional folding and/or tilting, both AHe and ZHe data from the second-lowest elevation sample on the GM transect (GM-04) indicate the need for exhumation from depths >4 km from ca. 80–60 Ma, regardless of the spatial relationship to other samples within the transect (Fig. D6). Thus, both the interpretation of differential exhumation between the eastern and western LAR valley and the timing of that exhumation are not dependent on the assumption of a vertical sample transect. If paleo-depth relationships along the transect are not preserved, then our preferred interpretation overestimates the magnitude of differential exhumation by ~1 km (Fig. 4.15; Fig. D6).

The other western LAR transects (WH and BTM) are below or in close proximity to the thickest volcanic deposits and deepest paleovalleys. As a result, many of the samples in these two transects have been omitted from inverse thermal modeling based on the likelihood that they were affected by hydrothermal fluid circulation. Thermal modeling for these two transects, therefore, only includes unaffected samples. The Whitehorn model contains AHe and ZHe from 14BB-03, and the BTM model incorporates our AHe data as well as AFT data from six nearby samples reported by Kelley and Chapin (2004; Figs. 4.3 and 4.5). To include the AFT data in the thermal models generated by QTQt, we performed a resampling of the published track count data to generate synthetic spontaneous and induced track length data with statistics that match the reported data. The WH and BTM transects reveal thermal histories similar to those observed at WBP and GM, with rapid cooling from ca. 80 to 60 Ma (Fig. 4.15). Both the WH and BTM transects were exhumed from temperatures of at least ~120–150 °C, implying between 4 and 5 km of Laramide-age exhumation.

Modeling the easternmost transects (TCBR and FPG) together, we observe that all of the samples in these vertical transects were near the surface (above the PRZ) from at least ca. 120 Ma to the present (Fig. 4.15). Because these samples all resided below the closure temperature of the AHe system (~70 °C) we have limited resolution on the thermal histories of these samples. However, it appears that these samples have undergone <2 km of exhumation (and perhaps <1 km in some cases) since the Late Cretaceous.

All thermal models, except for those from the easternmost transects, show that the most likely thermal history for these transects involves rapid exhumation between ca. 80

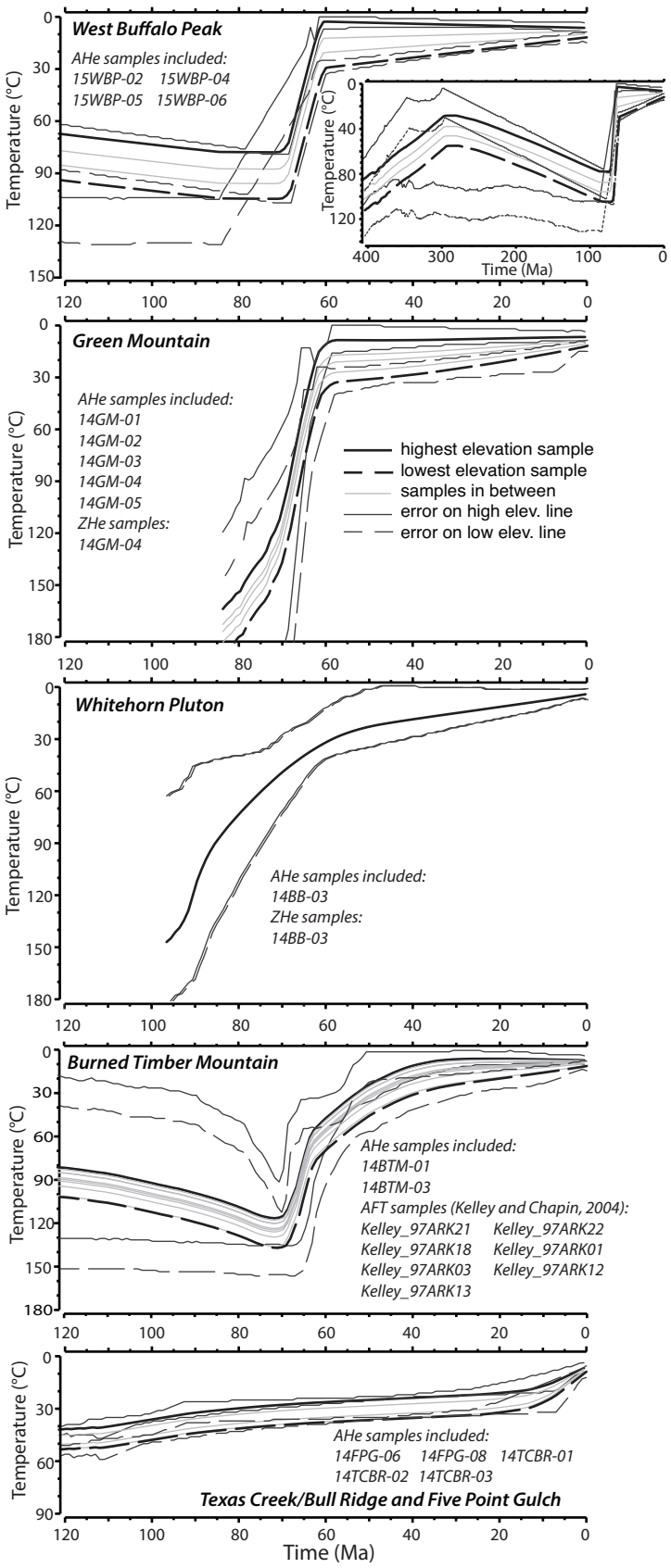

Figure 4.15: Inverse thermal models run in QTQt version 64R5.4.6 (Gallagher, 2012). Pathways indicate the best-fit thermal history for each transect or set of transects as a whole (only modeled samples fitting data quality criteria and unmodified by hydrothermal fluids). All the thermal histories except for the Texas Creek group show rapid exhumation from temperatures >80 °C occurring between ca. 80 and 60 Ma. The West Buffalo Peak (WBP) model has data adding information to the thermal histories (older AHe samples) so the model can make predictions farther back in time (inset at top). AHe—apatite helium; ZHe—zircon helium; AFT—apatite fission track; elev.—elevation.

and 60 Ma. Along the western reach of the LAR, three transects record 4–6 km of exhumation over this time interval. The magnitude of exhumation appears to diminish northward toward West Buffalo Peak, where Laramide-age exhumation is limited to no more than ~3 km. In contrast, the eastern samples show <2 km of exhumation. Together the thermal models imply ~2–5 km of differential exhumation from ca. 80 to 60 Ma between the western and eastern parts of the LAR region.

TECTONIC AND TOPOGRAPHIC EVOLUTION OF THE LOWERARKANSAS RIVER VALLEY

We discuss the implications that our new low-temperature thermochronometry data set has for improving our quantitative understanding of the timing and magnitude of exhumation related to Laramide tectonism beginning in the latest Cretaceous. We are also able to examine the formation of the Eocene erosion surface and the general paleotopography of the southern Rocky Mountains prior to mid-Cenozoic ignimbrite deposition and their relation to Laramide tectonism.

Laramide Tectonism in the Lower Arkansas River Valley

Low-temperature thermochronometers provide a way to assess exhumation magnitudes and rates through the upper crust and also have the ability to quantify differential exhumation, which may reflect structural offsets that are not recorded by obvious structural or stratigraphic piercing points. Such differential exhumation is observed along the LAR where the magnitude and rate of crustal cooling differ significantly between the eastern and western parts of the valley (Figs. 4.3, 4.4, 4.11, and 4.15). Three transects in the southern part of the western LAR (GM, WH, and BTM) show rapid cooling from 80 to 60 Ma from peak temperatures of ~130 to ~180 °C to

temperatures <~60 °C (Fig. 4.15). For an assumed geothermal gradient of ~30 °C/km, this equates to exhumation from depths of 4–6 km. The northernmost transect in the western LAR (WBP) shows similar timing and rates of exhumation, but from a lower initial temperature (~100 °C), reflecting a smaller total magnitude of exhumation (~3 km).

In contrast, the eastern LAR valley transects (TCBR, FPG) show no rapid cooling during the latest Cretaceous to early Cenozoic (Fig. 4.15). AFT ages from this region are principally older than Early Cretaceous (Figs. 4.3 and 4.4), indicating that the samples were cooled below the AFT closure temperature before Laramide deformation. Thermal modeling of the AHe ages from the eastern part of the valley defines a cooling history from <60 °C ca. 120 Ma to present-day surface temperatures, which is equivalent to <1 to no more than 2 km of exhumation throughout the Cenozoic (Fig. 4.15). The magnitude of exhumation inferred from the AHe thermal models is consistent with the lack of burial indicated by carbonate clumped isotope temperatures measured in this region. Thus, the magnitude of differential exhumation between the eastern and western parts of the LAR valley is at least 2 to possibly 5 km.

We can further constrain the magnitude of differential exhumation between the eastern and western transects by using our geochronologic and thermochronologic data to refine estimates of the emplacement depth of the Whitehorn Granodiorite. Thermal models for the WH transect permit cooling from peak temperatures >150 °C. Such temperatures are potentially compatible with a range of proposed geobarometry estimates for the Cretaceous Whitehorn Granodiorite, which vary from ~3.7 kbar (indicating >10 km of overlying rock; Workman, 1997) to ~1.4 kbar (indicating ~4 km of overlying rock;

Wofford, 1986). The closure temperature of existing K-Ar ages on the Whitehorn Granodiorite does not constrain the emplacement depth (or temperature) of the pluton, because these results could be interpreted as either emplacement or cooling ages. Our zircon U-Th-Pb dates from the Whitehorn Granodiorite record a mean age of ca. 67 Ma (Table D5; Fig. 4.8), which is unambiguously interpreted as the timing of emplacement. In combination with our new $^{40}Ar/^{39}Ar$ ages from the Whitehorn Granodiorite, which are indistinguishable from the zircon U-Th-Pb ages, we can infer that the $^{40}Ar/^{39}Ar$ ages also represent the timing of emplacement, and imply that this emplacement occurred at ambient temperatures below the closure temperature of K-feldspar (~190–350 °C; Table 4.2; Figs. 4.6 and 4.7). This inference is supported by our ZHe ages from Proterozoic basement samples collected adjacent to the pluton that record a cooling age of ca. 83 Ma, older than the emplacement age of the Whitehorn Granodiorite (Table 4.1; Table D1; Fig. 4.14). This suggests that prior to pluton emplacement, the Proterozoic host rock was cooler than the ZHe closure temperature (150–180 °C) or at ~5–6 km depth. Thus, our thermochronometric data are consistent with geobarometric pressures closer to the lower end of previously proposed values (e.g., Wofford, 1986).

These data also appear to define an upper limit to the peak exhumation temperatures of the WH transects to not be significantly greater than 180 °C, and imply that maximum depths of exhumation are likely in the 5–6 km range. Therefore, our preferred estimate of the magnitude of differential exhumation between the eastern and western transects is between ~3 and 5 km. Such a magnitude of differential exhumation over a relatively short lateral distance is indicative of structural displacement between the western and eastern regions, and should be accommodated by reverse faulting.

Identifying a discrete structure on which this deformation was accommodated is hampered by the lack of preserved exposures of overlying Phanerozoic strata in the LAR valley and the difficulty of tracing structures through crystalline basement rock (Brady et al., 2000), but we hypothesize that the structure is somewhere east of transect BTM (Fig. 4.11).

The timing of exhumation in the western region indicates that this differential exhumation was accommodated by displacement along reverse faults active during Laramide shortening (Fig. 4.16). Data from the AHe transects and the spatial distribution of ignimbrite filled paleovalleys (Fig. 4.11) imply that the structures responsible for this differential exhumation are located near the longitude of Coaldale (Fig. 4.11). West of Coaldale, rapid Cretaceous exhumation is observed in all thermochronometry transects, and mid-Cenozoic ignimbrites are primarily confined to narrow paleovalleys. East of Coaldale, AHe data show minimal Cretaceous exhumation and mid-Cenozoic ignimbrites are distributed broadly across the presumed Eocene erosion surface.

In combination, these data suggest differential uplift of the western LAR region relative to the east, with the magnitude of this differential uplift dissipating northward (Figs. 4.14 and 4.15). Such a pattern of deformation is consistent with the south to north transfer of strain between known Laramide structural systems. South of the LAR, east-directed, Laramide-aged high-angle reverse faults bound both the Wet Mountains and northern Sangre de Cristo Range (Lindsey et al., 1984; Jacob and Albertus, 1985; Bedford, 1994; Lindsey, 2010; Rasmussen, 2016). Conversely, to the north of the LAR valley, Laramide-aged deformation is accommodated on the west-directed Elkhorn and Elk-Sawatch thrust systems (Bryant, 1966; Bryant and Naeser, 1980; Bedford, 1994).

The structural link between these two systems has long been a topic of debate (e.g., Bedford, 1994) and the transfer or linking is suggested to be in the vicinity of the LAR (Bedford, 1994). We propose that the west-side-up differential exhumation observed in the LAR (Fig. 4.11) is a continuation of the well-defined east-directed thrust systems to the south in the Sangre de Cristo Mountains, and that this deformation dies out to the north of West Buffalo Peak as strain is transferred to the west-directed Elkhorn and Elk-Sawatch thrust systems. Our interpretation is consistent with the observed structural style in the region arising from Laramide tectonism and provides a new solution to the question of fault linkage between Laramide structures in the Sangre de Cristo Mountains and the Front Range.

Formation of Late Eocene Erosion Surface

There are many low-relief surfaces documented throughout the southern Rocky Mountains that have been assigned an Eocene age (Epis and Chapin, 1974; Epis and Chapin, 1975; Gregory and Chase, 1994; Chapin and Kelley, 1997; Leonard, 2002; McMillan et al., 2002, 2006; Landman and Flowers, 2013). These surfaces often are lumped together as one large surface throughout the entire southern Rockies, i.e., the late Eocene erosion surface (Epis and Chapin, 1974, 1975). However, debate is ongoing regarding the synchroneity and mechanistic similarity in the development of these surfaces (Gregory and Chase, 1994; Leonard, 2002; McMillan et al., 2002, 2006). In the LAR region, mid-Cenozoic ignimbrites blanket and preserve an erosion surface of low to moderate relief (e.g., Epis and Chapin, 1974). The combination of this ignimbrite cover and our new low-temperature thermochronometry data afford an opportunity to estimate the timing and duration of this paleosurface formation.

Development of the distinctive paleotopography preserved in and near the LAR valley appears to have a nonsynchronous evolution. Our low-temperature thermochronometry data imply rapid erosion from ca. 80 to 60 Ma (Fig. 4.15) in the western LAR valley and little contemporaneous erosion in the eastern part. The distribution and geometry of the western LAR volcanic deposits define a surface of moderate local relief (hundreds of meters) established by the incision of numerous paleovalleys (Chapin and Lowell, 1979). Modeling of our thermochronometry data requires the removal of several kilometers of rock in the western LAR since the time of emplacement of the Whitehorn Granodiorite (ca. 67 Ma). However, these models also place many of the higher elevation samples from the western LAR below the AHe closure temperature (60 °C or even cooler; ~30 °C or less) by ca. 60 Ma (Fig. 4.15), thus minimizing additional exhumation after that time. These constraints, combined with the modest paleorelief preserved in the paleovalleys, suggest that the simplest explanation for the timing of formation of the preserved paleolandscape is coeval with cessation of rapid exhumation. Because there is minimal exhumation after ca. 60 Ma, we infer that landscape evolution slowed following Laramide deformation and the western surface largely stabilized for ~20 m.y., until the inception of ignimbrite deposition and surface preservation ca. 37 Ma. Thus, the western paleosurface is a preserved remnant of the late Eocene, post-Laramide landscape.

The erosion surface across the eastern LAR, however, does not have a thermochronometric record of significant exhumation in the past 120 m.y., and may in fact record the evolution of a much older, more slowly evolving surface that is also preserved by mid-Cenozoic ignimbrite deposition. The evolution of this surface is less well determined with the available thermochronometric data, due to the minimal

exhumation in Cretaceous and Cenozoic time. Mesozoic strata are deposited on

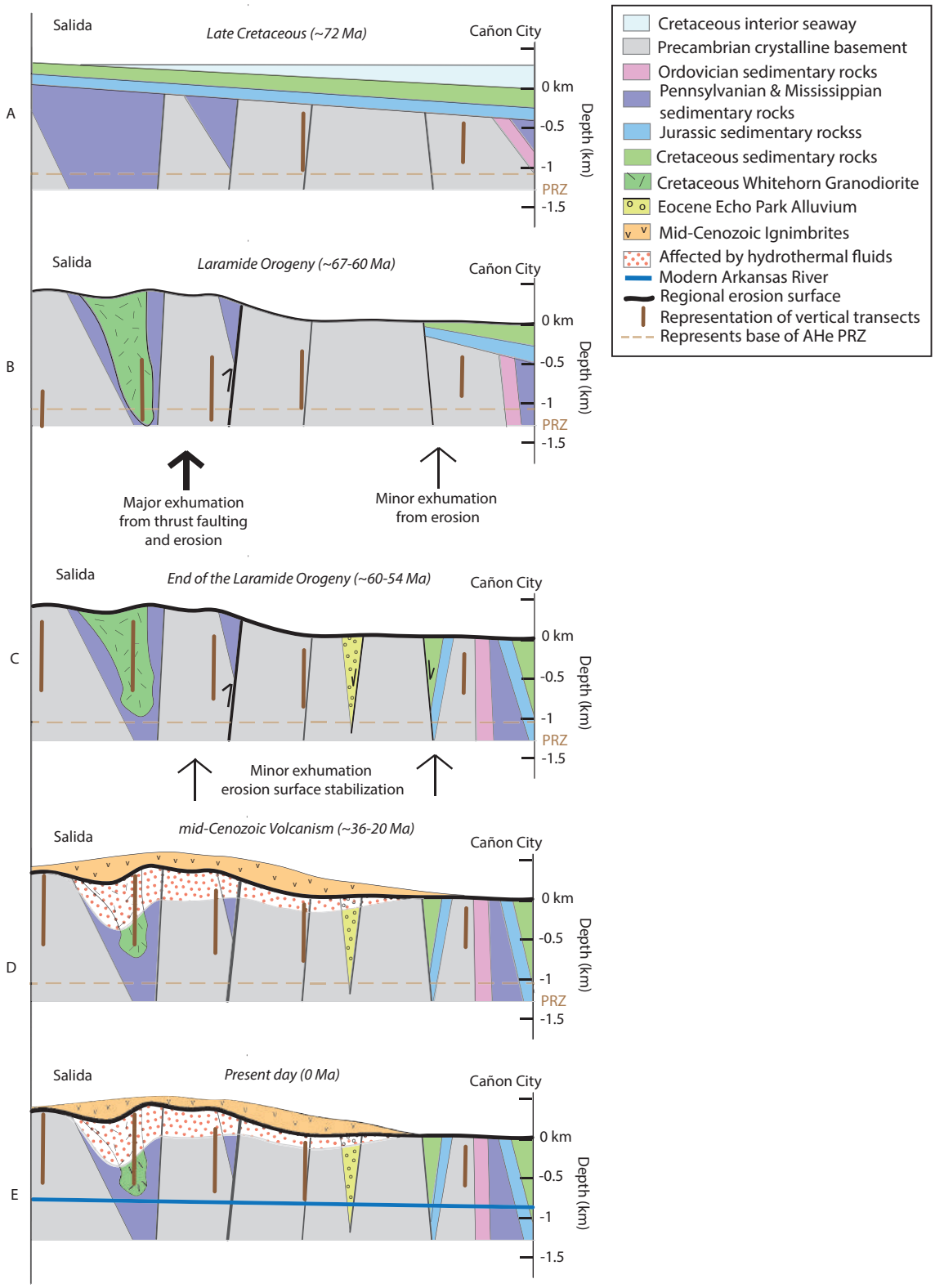

Figure 4.16: Schematic representation of lower Arkansas River (LAR) valley evolution from the Late Cretaceous to present. Time moves forward from top to bottom. AHe—apatite helium. (A) The region is covered by the interior seaway (light blue) until ca. 72 Ma and has already undergone Ancestral Rockies deformation seen in the Paleozoic deposits while the Mesozoic sediments are still flat lying. PRZ—partial retention zone. (B) Middle of the Laramide Orogeny: the Cretaceous Whitehorn Granodiorite has been emplaced and major erosion begins to strip off the overlying sediments with large amounts of exhumation occurring in the western half of the LAR valley while only minimal amounts are recorded in the east. (C) By the end of Laramide deformation significant erosion has taken place, forming most of the Eocene erosion surface and incising many paleovalleys in the western LAR. (D) Ignimbrites blanket the surface in large eruptive events from ca. 36 to 29 Ma (Thirty-nine Mile volcanic field) and continue with smaller events until ca. 20 Ma. Although not extremely thick (a few hundred meters at most), high temperatures from these deposits and the existing topography drive hydrothermal fluid circulation causing re-setting and alteration of the samples nearby (red dots). (E) General present day setting showing a small amount of regional erosion occurs post mid-Cenozoic volcanism while the major erosion is taken up by the Arkansas River, which cuts >1 km down into the basement rock.

Proterozoic basement throughout much of the eastern LAR, and the magnitude of exhumation implied by our thermochronometric data is consistent with the removal of these strata (Taylor, 1975). Thus, one plausible interpretation of the eastern LAR erosion surface is that it reoccupies the pre-Mesozoic depositional surface, a paleolandscape presumably the age of the Ancestral Rockies. Stripping of this Mesozoic cover during the Laramide orogeny would be consistent with stratigraphic records of Late Cretaceous to Paleocene erosion recorded both north and south of the LAR (Johnson, 1959; Cole et al., 2010). Although localized post-Laramide deformation can be seen in the form of extensional graben formation (i.e., Echo Park Canyon; Fig. 4.2), the thermochronometric data from the eastern LAR valley suggest these phases of deformation had minimal extent and did not amount to major landscape evolution during the Eocene. The differences in the rates of formation and erosional magnitudes represented by the western and eastern LAR erosion surfaces suggest that they may in fact be two separate surfaces, characterized by different timing and rates of formation, as well as possible different

formation mechanisms.

The question arises as to how this composite paleosurface was preserved between the cessation of Laramide tectonism and the inception of late Eocene to Oligocene ignimbrite eruptions. Debate about the formation of planation surfaces, whether such low-relief surfaces can be long lived and how they might remain low relief over long time periods, is not new or unique to the Rockies (Jolivet et al., 2007; Landis et al., 2008). A recent hypothesis for the long-term stabilization of a paleosurface in an active mountain rage has been proposed for the southern Sierra Nevada, USA, where a low-relief surface is argued to have been maintained for more than 20 m.y. (Sousa et al., 2016). This preservation is attributed to a perpetual, but thin, layer of sediment being continually deposited on and stripped off the erosion surface, armoring it and preventing erosion of the underlying paleosurface topography (Sousa et al., 2016). A similar mechanism may have played a role in stabilizing the Laramide topography of the LAR region, as supported by exposures of thin Eocene to Oligocene fluvial deposits found in the South Park basin just north of the Arkansas Hills (Ruleman and Bohannon, 2008; Kirkham et al., 2006), and even preserved between ignimbrites as fluvial conglomerates in the LAR region (Hon, 1984).

The excellent preservation of the regional paleosurface beneath the mid-Cenozoic ignimbrites, as well as the present-day distribution of these ignimbrites, suggests minimal landscape evolution since Oligocene time (Fig. 4.11). The two major topographic features that appear to disrupt the erosion surface and overlying volcanic rocks are the Rio Grande rift valley north of Salida and the >1 km incision of the modern LAR canyon between Salida and Cañon City. Remarkably, deposits and eruptive products related to the mid-

Cenozoic volcanic rocks that overlie the Eocene erosion surface are also exposed as remnants on the walls of the Arkansas River canyon down to present-day river level between Salida and Coaldale (Fig. 4.11). The east-west orientation of this segment of the Arkansas River, along with the presence of ignimbrite valley fill, are characteristics that it shares in common with many previously identified paleovalleys in this region (Chapin and Lowell, 1979). Thus, we tentatively suggest that a part of the modern Arkansas River valley from Salida to Coaldale may have been an early Cenozoic paleovalley (Fig. 4.11). As with the other paleovalleys, the Salida-Coaldale paleovalley was likely filled at one time with late Eocene to early Miocene ignimbrites, but these have been excavated by canyon re-incision. In such a scenario, the modern-day Arkansas River canyon may have resulted from the headward migration of the LAR (Cañon City to Coaldale) and subsequent stream capture of the UAR (Sak et al., 2005; Kelley, 2012; Fig. 4.11) in the late Cenozoic, possibly associated with Rio Grande rifting.

In summary, the late Eocene topography in the eastern LAR valley, as preserved by the mid-Cenozoic volcanism, shows the signature of a low to moderate-relief erosion surface, similar to those documented in other parts of the southern Rockies. The western Eocene surface is characterized by numerous paleovalleys of not insignificant relief and most likely developed rapidly near the end of the Laramide orogeny, ca. 60 Ma in this area, and was preserved by ignimbrite deposition beginning ca. 37 Ma. The eastern low-relief surface may have developed over a much longer period of time, or may even have been inherited from an earlier history of landscape development. The late Eocene erosion surface of the LAR valley thus appears to be two possibly distinct paleosurfaces that formed at different times and rates, and suggests that the many late Eocene erosion

surfaces found within the Rocky Mountains could have dissimilar evolutionary histories in terms of both formation mechanisms and timing. The only major landscape development that has occurred from the middle-Cenozoic to present in the LAR valley region is the >1 km of modern river incision, which may have been accelerated by a combination of re-incising a paleovalley through headward erosion from east to west and stream capture aided by Rio Grande rifting to the west.

CONCLUSIONS

New geochronologic, thermochronometric, and stable isotope data from the Mosquito Range, Arkansas Hills, and lower Arkansas River valley in the southern Colorado Rocky Mountains provide further clarification on timing of exhumation and paleotopography development in a complex region of the Rocky Mountains. The thermochronometric data we present here suggest that Laramide orogenic deformation was the main driver of rapid exhumation in the LAR valley by the early Cenozoic (ca. 60 Ma). Throughout the rest of the Cenozoic, the LAR valley underwent only small perturbations of burial and re-exhumation that are not recorded in our low-temperature thermochronometric data. There is a significant difference between the exhumation histories of the west part of the LAR compared to the east part. Based on our AHe data and the AFT data of Kelley and Chapin (2004), we estimate that the amount of exhumation could not have been more than ~1–2 km in the eastern segment of the LAR (east of Coaldale). Considering the AHe, ZHe, and $^{40}Ar/^{39}Ar$ presented here, along with geobarometry estimates from the Whitehorn Granodiorite (Wofford, 1986), we estimate that ~5–6 km of exhumation occurred in the western segment. Thus, we estimate that ~3–5 km of differential exhumation between the east and west of the LAR valley occurred

during the Laramide orogeny.

This east-west differentiation is also seen in the paleotopographic surface preserved beneath mid-Cenozoic ignimbrite deposits. Moderate relief, in the form of east-flowing paleovalleys, characterizes the western part of the LAR, while the eastern part displays much lower relief paleotopography. We infer that rapid topographic evolution of the western paleosurface took place near the end of the Laramide, driven by rapid uplift and exhumation, and formation of the eastern paleosurface may have been an older, more slowly and more completely evolving topographic surface.

The conclusions here are drawn from complex low-temperature thermochronometric data sets. However, by comparing samples and transects that have not undergone complex thermal perturbations, and by comparing transects in both older (Proterozoic) and younger (Cretaceous) rocks, we can disentangle the series of events and complex heating histories that may have affected our samples, and develop an approach to extract meaningful thermal histories. The LAR valley reveals this kind of complex system. Mid-Cenozoic ignimbrites perfectly preserve paleotopography, yet they also caused significant thermal modification of near-surface rocks, and Proterozoic basement rocks yield poorly reproducible samples that likely reflect radiation damage and protracted cooling histories. Our findings that ignimbrites acted as a heat source for fluids circulating in the near-surface crust (particularly below the erosion surface and adjacent to the paleovalleys), resulting in resetting of AHe ages, builds on several studies concerned with the potential impact of top-down heating on recorded thermochronometric ages. The incorporation of clumped isotope analyses in our study reveals its potential as a tool to test for such an effect, and to then identify and omit from

further analysis data from possibly altered samples.

High-density vertical sampling for thermochronometric data was critical for unraveling the tectonic history of the LAR, and such an approach may be necessary in other regions of complex thermal histories. From 7 different transects in the LAR valley, spanning ~80 km distance, we identify multiple thermal histories, which record information on rapid exhumation, differential exhumation over relatively small spatial scales, and local near-surface thermal perturbations. These diverse thermal signatures would most likely not have been revealed with a sparse sampling strategy.

ACKNOWLEDGMENTS

Jesse Fenno and Forrest Gilfoy assisted in sample collection. Megan Hendrick and Amanda Maslyn assisted with sample processing and analysis. S. Nehring, S. Muggleton, and C. Porreca assisted with sampling of the Whitehorn Granodiorite for paleomagnetic study, and Nehring and Muggleton assisted with laboratory measurements. This work was partially supported by National Science Foundation grant EAR-1151247 (Niemi), as well as a GSA Student Research Award, a Rackham graduate student research grant, and a Turner Award from the Department of Earth and Environmental Sciences at the University of Michigan (Abbey).

APPENDIX C. SAMPLE PREPARATION AND ANALYSIS

Apatite (U-Th-Sm)/He and Zircon (U-Th)/He

Samples were crushed and sieved to small (<300 μm) size fractions, followed by water density separation (panning by hand) to remove clays and lighter materials. Magnetic grains were removed with the use of a Frantz magnetic separator and apatite was separated using the high-density liquid lithium metatungstate (LMT) (2.8 g/mL). Using a Leica MZ16 stereo zoom microscope, at least 3 inclusion free apatite grains, >80 μm (width and length along c-axis), with little to no discoloring were picked for each sample (note that unbroken grains were difficult to find, so many grains of apatite had 1 or 2 terminations). Individual grains were packaged into Pt tubes for He extraction, which was conducted at the University of Michigan's thermochronometry lab using an Alphachron Helium Instrument. Each grain underwent extraction through heating to 900 °C for 5 min using a diode laser with temperatures monitored via a 4-color optical pyrometer. A second heating step under the same conditions was conducted to make sure all the 4He was released from the grain. In this process we spike the Alphachron with an internal 3He standard for measuring $^{4}He/^{3}He$ ratios on a Pfeiffer quadropole mass spectrometer. Durango apatite age standards were run with each batch of unknown grains to ensure age measurement accuracy.

$^{40}Ar/^{39}Ar$

Minerals were separated by standard heavy liquid, magnetic and hand-picking techniques. Separates were loaded into a machined Al disc and irradiated for 6 h in L-67 position at the Ford Reactor, University of Michigan. Fish Canyon Tuff sanidine (FC-1) with an assigned age of 28.201 Ma (Kuiper et al., 2008), relative to Mmhb-1 with an age of 520.4 Ma (Samson and Alexander, 1987), was used as a neutron flux monitor. Samples were step heated in a Mo resistance furnace with heating times of 10 min for biotite and hornblende analyses and 5-235 min for K-feldspars. Electron multiplier sensitivity averaged 1.9 x 10-16 mol/pA and J-factors were determined to a precision of ± 0.1% by CO_2 laser-fusion of 4 single crystals from each of 4 radial positions around the irradiation tray. Correction factors for interfering nuclear reactions were determined using K-glass and CaF_2 and are as follows: 0.0247 ± 0.0002 for $(^{40}Ar/^{39}Ar)_K$, 0.00027 ± 0.00001 for $(^{36}Ar/^{37}Ar)_{Ca}$ and 0.00070 ± 0.00005 for $(^{39}Ar/^{37}Ar)Ca$. Weighted mean age was calculated by weighting each age analysis by the inverse of the variance while the weighted mean error was calculated using the method of Taylor (1982). Mean squares of weighted deviates evaluated for n-1 degrees of freedom for single crystal data and n-2 for isochron data. Isochron analyses follow those of York (1968). The ^{40}K total decay constant is 5.463e-10 yr^{-1} (Min et al., 2001) and isotopic abundances follow Steiger and Jäger (1977). All final plateau and isochron errors reported at ± 2σ, unless otherwise noted.

APPENDIX D: SUPPLEMENTARY DATA TABLES AND FIGURES FOR CHAPTER 4

This appendix contains eight data tables, Table D1 – D8 and six supplementary figures, Figs D1 – D6.

Table D1: This table contains analytical data for all apatite and zircon grains used for apatite (U-Th-Sm)/He and zircon (U-Th)/He thermochronometry results presented in this manuscript.

Table D2: This table contains analytical data for bulk rock analyses performed by Activation Laboratories.

Table D3: This table contains analytical data for $^{40}Ar/^{39}Ar$ analyses of hornblende and biotite thermochronometry results presented in this manuscript.

Table D4: This table contains analytical data for $^{40}Ar/^{39}Ar$ analyses of K-feldspar thermochronometry results presented in this manuscript.

Table D5: This table contains analytical data for U-Th-Pb analyses of zircon geochronology from sample 15CM-05 results presented in this manuscript.

Table D6: This table contains analytical data for U-Th-Pb analyses of zircon geochronology from sample 14BB-03 results presented in this manuscript.

Table D7: This table contains analytical data for paleomagnetic results presented in this manuscript.

Table D8: This table contains analytical data for clumped isotope results presented in this manuscript.

Figure D1: This figure shows apatite helium dates for each grain compared to eU and grain size.

Figure D2: This figure shows argon ratios from the hornblende analyses of WH-2 to calculate the isochron age for this sample.

Figure D3: This figure shows the magnetic susceptibility for each paleomagnetic sample analyzed.

Figure D4: This figure shows reflected light photomicrographs representative of the assemblages in the Whitehorn Granodiorite.

Figure D5: This figure shows AMS data for paleomagnetic samples in the Whitehorn Granodiorite.

Figure D6: This figure shows the thermal model for the apatite and zircon He data from sample GM-04.

TABLE D1: INDIVIDUAL GRAIN RESULTS FOR APATITE AND ZIRCON HE SAMPLES

Sample Name	Mass (µg)	Length (µm)	Radius (µm)	FT	U (ppm)	Th (ppm)	Sm (ppm)	He (ncc)	eU (ppm)	Raw Date (Ma)	Corr. Date (Ma)	Error (Ma)
West Buffalo Peak transect samples												
15WBP-02a	2.0048	115.7	46.4	0.74	3.21	8.76	315.09	0.33	6.7	233.8	317.1	3.56
15WBP-02b	1.8460	117.5	44.2	0.73	5.76	12.15	376.00	0.50	10.4	239.3	329.1	2.61
15WBP-02c	2.9764	171.8	46.4	0.75	3.03	9.54	531.84	0.39	7.8	181.4	242.1	1.82
15WBP-02d	4.3243	201.0	51.7	0.78	6.72	7.97	428.42	0.56	10.6	116.8	150.6	1.34
15WBP-04a	2.5509	143.1	47.0	0.75	11.16	24.32	132.13	0.23	17.5	43.5	58.2	0.48
15WBP-04b	2.3293	139.6	45.5	0.74	16.22	28.62	160.78	0.31	23.7	46.3	62.6	0.52
15WBP-04c	6.0117	237.2	56.1	0.79	20.38	39.93	319.38	0.96	31.2	43.6	54.9	0.46
15WBP-04d	4.6455	173.6	57.6	0.79	9.78	12.86	130.60	0.38	13.4	51.5	65.0	0.58
15WBP-04e*	3.1308	150.6	50.8	0.76	28.28	57.23	236.86	1.29	42.8	80.7	105.6	0.86
15WBP-05a	2.6990	114.4	54.1	0.77	1.58	7.24	276.60	0.09	4.6	72.7	94.7	0.80
15WBP-05b	2.0663	127.7	44.8	0.73	1.99	4.57	374.58	0.06	4.8	60.4	82.4	0.82
15WBP-05c	2.8327	138.7	50.4	0.76	10.88	18.36	489.18	0.22	17.5	39.8	52.4	0.44
15WBP-05d	1.7916	127.7	41.7	0.72	30.89	40.43	441.78	0.36	42.4	40.5	56.4	0.48
15WBP-06a	3.4451	164.3	51.0	0.77	12.16	29.64	167.41	0.35	19.9	43.4	56.5	0.45
15WBP-06c	1.2867	87.9	42.6	0.71	23.50	58.39	283.30	0.28	38.5	47.9	67.7	0.50
15WBP-06d	1.4813	87.9	45.7	0.72	12.14	30.17	178.67	0.14	20.0	39.1	54.1	0.43
Green Mountain transect apatite samples												
14GM-01b	5.7	199.2	59.4	0.80	11.4	14.0	190.9	0.50	15.6	48.6	60.7	0.6
14GM-01c	2.1	102.9	50.2	0.75	8.6	12.4	97.9	0.14	12.0	47.0	62.8	0.5
14GM-01d	2.1	98.9	51.0	0.75	2.5	3.1	54.1	0.04	3.5	45.5	60.6	0.6
14GM-01e	2.6	137.0	48.6	0.75	10.4	17.1	153.3	0.25	15.1	54.3	72.2	0.6
14GM-01f	1.1	82.6	40.4	0.69	1.7	8.8	57.1	0.02	4.0	29.3	42.4	0.5
14GM-02a	3.8	110.0	65.4	0.80	18.5	18.5	261.2	0.50	24.0	46.4	58.1	0.5

Sample Name	Mass (µg)	Length (µm)	Radius (µm)	FT	U (ppm)	Th (ppm)	Sm (ppm)	He (ncc)	eU (ppm)	Raw Date (Ma)	Corr. Date (Ma)	Error (Ma)
14GM-02b	2.5	136.9	47.9	0.75	72.2	60.4	417.2	1.18	88.3	44.1	58.8	0.5
14GM-02c	4.7	140.0	64.7	0.81	28.6	25.0	312.7	0.91	35.9	45.5	56.5	0.5
14GM-02d	2.4	120.6	49.5	0.75	45.3	44.6	343.5	0.66	57.4	40.8	54.2	0.5
14GM-03a	2.3	151.5	43.3	0.73	15.7	8.2	144.6	0.22	18.3	44.2	60.5	0.6
14GM-03b	7.6	178.0	72.9	0.83	40.3	20.3	398.5	2.05	46.9	48.6	58.6	0.6
14GM-03c	1.5	88.3	46.4	0.73	28.6	13.8	254.3	0.27	33.1	44.0	60.7	0.6
14GM-03d	2.6	132.5	49.5	0.76	29.1	16.4	201.6	0.56	33.9	52.7	69.8	0.7
14GM-04a	8.5	205.4	71.6	0.83	12.6	2.7	176.8	0.73	14.1	52.3	62.9	0.7
14GM-04b	7.2	185.9	69.1	0.82	11.5	4.3	178.4	0.56	13.3	50.9	61.9	0.7
14GM-04c*	2.4	104.7	53.9	0.76	15.6	8.9	260.3	0.14	18.9	25.5	33.4	0.3
14GM-04d	2.9	140.0	51.0	0.76	35.5	12.8	248.0	0.67	39.6	48.8	63.9	0.6
14GM-04e	2.7	97.2	59.2	0.78	20.2	6.7	174.4	0.34	22.5	46.6	59.9	0.6
14GM-04f	2.6	132.1	49.5	0.76	106.0	31.2	475.8	2.04	115.5	56.4	74.7	0.8
14GM-05a	2.5	144.4	46.6	0.75	24.3	1.4	58.9	0.11	24.9	14.6	19.6	0.3
14GM-05b	3.1	89.7	65.4	0.79	5.7	1.2	36.3	0.08	6.2	35.1	44.5	0.5
14GM-05c	2.0	126.3	44.8	0.73	11.7	2.6	51.7	0.20	12.6	65.1	88.8	0.9
14GM-05d	7.9	170.5	76.0	0.83	5.5	1.4	34.7	0.28	6.0	49.4	59.3	0.7
14GM-05e	4.3	182.5	54.1	0.78	7.7	4.1	36.5	0.21	8.9	46.1	58.9	0.6
14GM-05f	2.5	155.5	44.8	0.74	9.5	3.2	55.4	0.12	10.5	39.1	52.9	0.6
14GM-05g	3.7	155.0	54.1	0.78	11.5	3.9	53.8	0.23	12.7	41.2	53.0	0.6
14GM-05h	2.7	149.3	47.3	0.75	13.3	5.7	85.5	0.21	15.0	44.0	58.7	0.6
14GM-05i	6.9	232.3	60.7	0.81	14.1	3.8	76.3	0.58	15.3	45.9	56.8	0.6
Green Mountain transect zircon samples												
14GM-04 Zra*	5.1	216.4	54.1	0.79	654.3	191.8	0.0	49.29	699.2	113.2	144.0	1.5
14GM-04 Zrb	2.8	186.8	42.8	0.73	572.3	221.1	0.0	13.15	624.1	62.8	85.6	0.8

Sample Name	Mass (µg)	Length (µm)	Radius (µm)	FT	U (ppm)	Th (ppm)	Sm (ppm)	He (ncc)	eU (ppm)	Raw Date (Ma)	Corr. Date (Ma)	Error (Ma)
14GM-04 Zrc	5.4	225.3	54.8	0.79	462.3	177.1	0.0	22.09	503.8	66.3	84.1	0.9
14GM-05 Zra	3.1	167.4	47.9	0.76	363.0	75.8	0.0	7.69	380.7	53.7	71.1	0.7
14GM-05 Zrb	6.4	226.1	59.4	0.80	354.2	97.2	0.0	28.28	377.0	95.8	119.3	1.3
14GM-05 Zrc	3.4	192.1	47.0	0.76	411.0	97.0	0.0	21.21	433.7	117.1	155.0	1.6
Whitehorn transects apatite samples												
14BB-02a	2.5	120.1	51.0	0.76	2.6	9.4	96.0	0.03	5.3	20.2	26.6	0.3
14BB-02b	1.8	109.1	44.8	0.73	3.2	10.0	132.8	0.03	6.1	25.9	35.7	0.4
14BB-02c	2.3	118.8	48.8	0.75	0.9	5.4	49.2	0.02	2.4	22.7	30.3	0.4
14BB-02d	3.2	109.5	60.1	0.78	3.8	8.8	123.7	0.04	6.4	16.1	20.6	0.2
14BB-03a	1.5	110.9	40.4	0.70	15.2	37.3	613.8	0.19	26.8	43.8	62.2	0.5
14BB-03b	2.2	100.3	51.7	0.75	4.6	16.0	52.8	0.10	8.6	44.2	58.7	0.5
14BB-03c	4.1	140.0	60.1	0.79	4.5	22.9	135.1	0.27	10.5	54.5	68.7	0.6
14BB-03d	3.1	146.2	51.7	0.77	9.0	26.5	113.5	0.27	15.8	45.9	59.8	0.5
14BB-04a	3.0	124.6	54.8	0.77	1.8	2.9	12.1	0.04	2.5	38.4	49.7	0.6
14BB-04b	1.3	92.8	42.0	0.71	2.0	5.2	10.7	0.02	3.3	27.8	39.4	0.6
14BB-04c	3.4	127.6	57.6	0.78	2.0	3.7	13.5	0.07	2.9	55.3	70.7	0.7
14BB-04d	1.7	105.1	44.2	0.72	2.8	7.4	17.7	0.02	4.6	24.6	34.0	0.3
14BB-04e	3.5	134.3	56.8	0.78	3.4	9.9	129.8	0.03	6.3	9.8	12.5	0.1
14BB-04f	2.6	130.7	49.2	0.75	5.1	11.7	107.9	0.02	8.4	8.9	11.8	0.2
14BB-04g	2.2	136.9	44.9	0.74	6.7	12.7	120.0	0.04	10.2	13.9	18.9	0.2
15BB-04aa	2.5	153.7	44.8	0.74	0.9	3.2	55.9	0.01	1.9	19.8	26.7	0.5
15BB-04ab	3.5	144.9	54.8	0.78	2.4	5.1	63.6	0.02	3.9	14.1	18.1	0.2
15BB-04ac	3.4	150.6	53.2	0.77	1.0	3.7	54.0	0.02	2.2	17.5	22.6	0.3
15BB-04ad	1.9	115.7	45.7	0.73	0.9	4.3	48.7	0.01	2.2	7.3	10.0	0.2
15AF-WH2a	2.1	142.7	42.6	0.73	6.1	35.9	181.2	0.12	15.3	32.2	44.3	0.3

Sample Name	Mass (µg)	Length (µm)	Radius (µm)	FT	U (ppm)	Th (ppm)	Sm (ppm)	He (ncc)	eU (ppm)	Raw Date (Ma)	Corr. Date (Ma)	Error (Ma)
15AF-WH2b	3.0	168.7	47.3	0.75	5.0	24.4	121.0	0.14	11.3	35.1	46.6	0.4
15AF-WH2c	3.1	146.2	51.0	0.76	4.5	23.4	148.8	0.10	10.7	25.5	33.3	0.3
15AF-WH2d	2.4	150.6	44.2	0.74	2.9	19.3	262.5	0.07	8.7	31.9	43.4	0.4
15AF-WH26a	2.8	132.5	51.0	0.76	4.9	14.5	276.2	0.10	9.6	34.1	44.8	0.5
15AF-WH26b	2.4	153.7	44.2	0.74	5.0	15.9	220.4	0.10	9.8	36.1	49.1	0.4
15AF-WH26c	3.2	158.2	50.1	0.76	8.4	13.8	331.4	0.21	13.2	44.0	57.7	0.5
15AF-WH26d	3.5	170.5	50.1	0.77	8.7	15.6	222.9	0.17	13.4	31.9	41.6	0.4
15CM-01a	1.6	123.2	40.4	0.71	25.0	30.0	122.9	0.27	32.6	42.2	59.6	0.5
15CM-01b	1.1	83.5	40.2	0.69	6.4	10.9	122.6	0.04	9.5	31.5	45.7	0.5
15CM-01c	1.5	105.1	41.5	0.71	3.1	11.2	98.8	0.03	6.2	26.6	37.5	0.4
15CM-01d	2.2	147.5	42.6	0.73	15.7	25.5	94.4	0.20	22.1	35.5	48.9	0.4
15CM-01e	1.5	110.9	41.1	0.71	7.9	21.9	242.3	0.09	14.1	35.2	49.8	0.4
15CM-01f	2.4	155.0	44.2	0.74	30.7	38.1	157.8	0.49	40.3	41.6	56.5	0.5
15CM-01g	2.0	155.0	40.4	0.72	32.0	23.2	176.2	0.38	38.2	40.9	57.2	0.5
15CM-02a	2.3	124.6	47.9	0.75	8.1	9.1	264.4	0.08	11.4	25.3	33.9	0.3
15CM-02b	2.1	91.4	53.2	0.75	5.7	12.4	287.8	0.04	9.9	18.1	24.0	0.4
15CM-02c	1.4	94.1	43.3	0.71	10.7	21.2	136.2	0.05	16.3	18.6	26.1	0.2
15CM-02d	2.1	125.0	45.5	0.74	5.1	10.2	156.7	0.04	8.3	17.9	24.3	0.2
15CM-02e	1.9	143.1	41.1	0.72	6.1	15.8	118.1	0.04	10.4	16.4	22.8	0.2
15CM-02f	2.4	109.5	51.7	0.76	11.5	19.8	66.5	0.11	16.4	23.3	30.8	0.3
15CM-02g*	1.8	136.9	40.0	0.71	10.9	20.8	127.7	0.02	16.4	3.9	5.5	0.1
15CM-03a	1.3	94.5	41.1	0.70	10.1	30.0	219.6	0.09	18.2	30.9	44.1	0.3
15CM-03b	1.5	116.6	40.2	0.70	7.0	19.9	178.9	0.07	12.5	31.3	44.5	0.4
15CM-03c	1.9	147.6	40.2	0.71	5.0	19.3	183.0	0.08	10.4	32.6	45.8	0.4
15CM-03d	2.1	132.1	44.2	0.73	10.0	30.9	253.2	0.16	18.4	36.2	49.5	0.4

Sample Name	Mass (µg)	Length (µm)	Radius (µm)	FT	U (ppm)	Th (ppm)	Sm (ppm)	He (ncc)	eU (ppm)	Raw Date (Ma)	Corr. Date (Ma)	Error (Ma)
15CM-03e	2.1	125.9	45.7	0.74	7.3	21.9	176.9	0.11	13.3	33.9	46.0	0.4
15CM-04a	1.3	102.0	40.0	0.70	29.6	52.0	167.0	0.18	42.6	26.0	37.2	0.3
15CM-04b	1.6	114.4	41.3	0.71	10.3	30.1	264.0	0.12	18.6	35.0	49.2	0.4
15CM-04c	1.6	98.9	44.2	0.72	7.7	24.3	222.2	0.10	14.4	38.2	53.0	0.4
15CM-04d	2.8	132.5	51.0	0.76	8.2	23.9	219.3	0.12	14.8	25.8	33.9	0.4
15CM-04e	2.5	191.8	40.2	0.72	15.6	34.8	266.1	0.26	25.0	35.0	48.7	0.4
15CM-04f	2.8	173.7	44.8	0.74	15.2	35.9	203.4	0.24	24.5	29.1	39.2	0.3
15CM-04g	2.7	141.7	48.8	0.75	16.3	35.4	175.4	0.12	25.4	15.0	19.9	0.2
15CM-05a	2.4	126.3	48.6	0.75	5.6	26.7	176.1	0.07	12.6	19.4	25.8	0.2
15CM-05b	2.2	158.2	41.7	0.72	2.4	12.8	34.1	0.02	5.6	15.0	20.8	0.2
15CM-05c	2.2	141.4	44.0	0.73	4.6	19.9	53.3	0.06	9.6	22.4	30.6	0.2
15CM-05d	1.6	134.3	38.6	0.70	8.1	27.2	91.2	0.09	14.9	31.2	44.6	0.3
15CM-05e	1.6	126.3	39.6	0.70	3.4	19.4	68.4	0.03	8.3	15.3	21.7	0.2
15CM-05f	2.5	100.3	55.4	0.77	3.4	19.6	38.0	0.06	8.2	22.2	29.0	0.3
15CM-05g	2.7	135.6	49.5	0.76	5.0	24.2	56.8	0.18	10.9	51.9	68.6	0.6
Whitehorn transects zircon samples												
14BB-03 Zra*	4.7	114.0	71.6	0.81	1.8	5.9	0.0	7.21	3.2	3015.2	3708.5	29.1
14BB-03 Zrb	1.8	114.4	44.2	0.73	307.4	216.6	0.0	4.68	358.1	59.8	82.4	0.7
14BB-03 Zrc	4.0	208.0	48.8	0.76	134.0	47.2	0.0	4.52	145.0	64.1	83.9	0.9
Burned Timber Mountain transect samples												
14BTM-01a*	1.7	129.5	40.4	0.71	13.2	5.2	69.5	0.46	14.8	152.5	214.9	2.1
14BTM-01b	2.1	131.2	44.2	0.73	5.5	3.8	50.6	0.07	6.6	41.7	57.1	0.6
14BTM-01c	2.0	120.1	45.8	0.74	8.7	3.7	47.8	0.09	9.8	39.3	53.4	0.6
14BTM-01d	2.2	140.0	44.6	0.74	5.2	4.6	37.0	0.08	6.4	44.5	60.5	0.6
14BTM-01e*	1.5	120.2	39.8	0.70	7.0	2.7	63.3	0.27	7.9	186.3	264.9	3.8

Sample Name	Mass (µg)	Length (µm)	Radius (µm)	FT	U (ppm)	Th (ppm)	Sm (ppm)	He (ncc)	eU (ppm)	Raw Date (Ma)	Corr. Date (Ma)	Error (Ma)
14BTM-01f	2.3	135.6	45.7	0.74	6.2	2.2	70.5	0.10	7.1	49.5	67.0	0.7
14BTM-01h	1.8	121.5	43.3	0.72	31.0	12.9	129.7	0.40	34.6	52.3	72.2	0.7
14BTM-02a	2.2	117.0	48.8	0.75	0.9	3.2	176.2	0.11	2.4	214.2	286.2	3.7
14BTM-02b	3.2	179.3	46.7	0.75	2.3	2.1	121.6	0.32	3.3	276.2	367.2	3.4
14BTM-03a	6.7	133.8	79.1	0.83	1.8	4.7	85.2	0.16	3.3	65.7	78.9	0.7
14BTM-03b	3.6	138.7	57.0	0.78	2.6	8.7	84.0	0.16	5.0	73.8	94.2	0.8
14BTM-03c	3.1	118.4	57.2	0.78	4.6	13.2	128.1	0.30	8.3	99.2	127.3	1.1
14BTM-03d	1.6	80.4	49.5	0.73	28.6	63.1	262.6	0.86	44.6	101.4	138.1	1.0
14BTM-03e*	1.8	100.3	47.3	0.74	6.2	22.4	110.1	0.66	11.9	256.1	348.2	2.7
14BTM-04a	1.4	89.7	44.0	0.71	4.3	9.6	17.7	0.03	6.7	23.1	32.4	0.3
14BTM-04b	1.4	109.6	40.5	0.70	1.9	3.5	16.1	0.01	2.8	10.4	14.8	0.3
14BTM-04c	2.1	103.8	50.1	0.75	5.2	8.5	21.7	0.04	7.3	21.6	28.8	0.3
14BTM-04d	2.0	111.3	47.3	0.74	3.8	5.8	16.1	0.03	5.2	20.9	28.3	0.3
14BTM-04e	1.9	98.5	48.6	0.74	5.1	7.0	22.4	0.04	6.9	25.4	34.3	0.4
14BTM-06a	2.0	133.8	42.6	0.72	17.9	17.7	244.2	0.18	23.2	34.3	47.5	0.4
14BTM-06b	4.1	185.5	52.3	0.78	26.3	38.0	273.0	0.49	36.5	27.4	35.4	0.3
14BTM-06c	4.1	166.1	55.7	0.78	24.8	48.9	342.2	0.53	37.8	28.6	36.4	0.3
14BTM-06d	2.1	158.1	41.1	0.72	38.8	56.5	385.6	0.44	53.9	32.1	44.6	0.4
Texas Creek / Bull Ridge transect samples												
14TCBR-01a	1.3	87.1	42.7	0.71	1.2	4.1	19.1	0.03	2.2	87.6	124.0	1.8
14TCBR-01b	2.0	98.9	49.5	0.74	19.3	8.4	102.5	0.33	21.7	64.5	86.7	0.8
14TCBR-01c	1.6	82.2	49.5	0.74	10.7	4.5	78.0	0.16	12.1	66.5	90.4	0.9
14TCBR-01d	5.5	121.5	74.6	0.82	17.2	4.4	103.2	1.04	18.7	85.7	104.3	1.1
14TCBR-02a	1.8	121.9	42.4	0.72	20.1	16.0	208.1	0.51	24.8	98.8	137.4	1.2
14TCBR-02b	1.8	102.0	46.4	0.73	29.4	16.0	374.9	0.55	34.9	76.3	104.2	1.0

Sample Name	Mass (µg)	Length (µm)	Radius (µm)	FT	U (ppm)	Th (ppm)	Sm (ppm)	He (ncc)	eU (ppm)	Raw Date (Ma)	Corr. Date (Ma)	Error (Ma)
14TCBR-02c	2.3	111.3	50.2	0.75	16.8	8.9	340.4	0.60	20.5	113.2	150.5	1.5
14TCBR-02d	1.4	100.7	41.7	0.71	1.1	4.4	67.5	0.04	2.4	105.6	149.2	2.1
14TCBR-03a	2.1	112.6	47.9	0.74	18.7	4.1	78.2	0.25	20.1	49.5	66.6	0.7
14TCBR-03b	2.4	140.0	46.4	0.74	139.5	5.9	147.4	2.10	141.5	50.6	68.0	0.7
14TCBR-03c	3.2	107.8	61.0	0.79	13.6	2.2	29.6	0.30	14.3	53.2	67.7	0.7
14TCBR-03d	1.1	83.5	41.1	0.70	88.7	12.4	102.9	0.59	92.1	46.5	66.9	0.6
14TCBR-04a	1.4	105.2	40.9	0.70	7.8	16.3	81.2	0.02	12.0	10.4	14.7	0.2
14TCBR-04b	2.0	135.6	43.3	0.73	3.5	12.6	113.8	0.01	7.0	4.9	6.8	0.1
14TCBR-04c	2.0	130.7	43.3	0.73	5.5	12.5	97.0	0.03	8.9	12.1	16.6	0.2
14TCBR-04d	1.7	92.8	47.7	0.73	12.7	10.2	196.9	0.05	16.0	16.4	22.3	0.2
14TCBR-04e	1.6	82.2	49.3	0.73	1.9	5.8	13.9	0.02	3.3	23.6	32.1	0.5
14TCBR-04f	1.8	123.2	42.6	0.72	3.4	8.0	17.4	0.04	5.4	33.7	46.8	0.5
Five Point Gulch transect samples												
14FPG-01a	3.5	129.0	57.9	0.78	0.6	1.3	6.7	0.02	0.9	37.2	47.5	0.6
14FPG-05a	2.0	115.7	46.4	0.74	2.8	1.8	6.5	0.08	3.3	99.2	134.6	1.4
14FPG-05b	1.7	100.7	45.7	0.73	3.4	5.0	29.0	0.11	4.7	116.3	159.6	1.7
14FPG-05c	2.3	97.2	54.2	0.76	4.4	1.2	48.4	0.60	4.9	444.0	583.2	6.1
14FPG-05d	1.9	114.4	45.7	0.73	3.3	1.4	16.1	0.26	3.7	294.1	400.8	4.5
14FPG-06a	3.3	135.2	55.4	0.78	6.8	3.9	30.4	0.16	7.9	49.2	63.3	0.7
14FPG-06b	3.1	118.4	57.0	0.78	8.4	5.6	38.7	0.22	9.9	59.5	76.4	0.8
14FPG-06c	2.9	135.2	51.7	0.76	11.8	5.7	37.9	0.21	13.3	44.1	57.7	0.6
14FPG-06d	2.1	110.9	47.9	0.74	3.2	3.4	19.7	0.04	4.1	39.2	52.8	0.6
14FPG-08a	2.4	115.7	50.8	0.76	2.1	7.4	22.8	0.05	4.0	42.2	55.8	0.6
14FPG-08b	1.7	100.8	45.7	0.73	1.5	7.3	28.6	0.03	3.3	37.1	50.9	0.6
14FPG-08c	3.6	117.5	61.6	0.79	1.6	5.4	17.3	0.07	2.9	57.0	72.0	0.7

Sample Name	Mass (µg)	Length (µm)	Radius (µm)	FT	U (ppm)	Th (ppm)	Sm (ppm)	He (ncc)	eU (ppm)	Raw Date (Ma)	Corr. Date (Ma)	Error (Ma)
14FPG-08d	3.6	118.8	61.6	0.79	2.4	8.9	26.8	0.11	4.7	51.1	64.6	0.6
14FPG-09a	2.4	171.8	41.3	0.72	50.1	51.5	252.7	1.43	63.4	79.6	110.1	0.9
14FPG-09b	2.9	141.4	50.1	0.76	9.5	11.4	110.7	0.80	12.7	184.2	242.3	2.1
14FPG-09c	2.2	143.1	43.3	0.73	15.2	22.0	236.2	0.27	21.4	49.8	68.4	0.6
14FPG-09d	1.3	94.1	41.1	0.70	22.7	29.4	275.6	0.28	30.9	58.9	83.9	1.0
Echo Canyon samples												
14EC-03aa	2.2	138.7	44.0	0.73	5.7	3.8	39.7	5.75	6.7	2550.2	3486.1	26.1
14EC-03ab	2.0	94.5	51.0	0.75	5.6	2.1	46.7	1.32	6.3	829.1	1107.9	10.3
14EC-03ac	1.3	82.2	45.1	0.72	25.4	7.9	115.1	1.33	27.7	290.7	406.1	3.8
14EC-03ad	1.7	95.8	47.0	0.73	20.7	4.2	98.2	1.64	22.1	353.7	482.9	4.9
14EC-04a	2.3	177.6	40.2	0.72	9.8	30.9	36.3	0.12	17.2	24.0	33.4	0.3
Fremont Peak transect samples												
14FMT-01a	2.5	102.0	55.4	0.77	13.8	1.6	179.5	0.09	15.0	20.2	26.3	0.3
14FMT-01b	1.5	103.4	42.6	0.71	11.7	1.6	181.5	0.04	12.9	17.1	23.9	0.3
14FMT-01c	4.7	204.1	53.2	0.78	8.2	2.4	144.8	0.12	9.5	23.2	29.7	0.3
14FMT-01d*	2.9	171.8	45.5	0.75	15.8	1.6	180.8	0.57	17.0	98.9	132.7	1.4
14FMT-01e*	2.0	106.5	47.9	0.74	13.0	1.4	174.4	0.25	14.1	77.1	104.1	1.1
14FMT-02a	2.2	103.4	51.8	0.76	19.1	1.1	118.4	0.23	19.9	43.5	57.6	0.6
14FMT-02b	3.3	188.6	46.4	0.75	18.4	1.6	94.5	0.89	19.2	117.9	156.8	1.6
14FMT-02c	1.5	126.3	38.9	0.70	30.0	2.0	123.8	0.46	31.0	80.3	114.8	1.2
14FMT-03a	4.6	138.2	63.9	0.80	5.4	2.7	170.6	0.06	6.9	18.1	22.6	0.3
14FMT-03b	4.0	147.6	57.9	0.79	5.2	1.8	131.6	0.11	6.2	38.2	48.5	0.5
14FMT-03c	4.3	159.9	57.6	0.79	4.5	1.2	90.0	0.12	5.2	46.4	58.8	0.6
14FMT-03d	2.6	126.3	50.8	0.76	2.8	1.2	157.4	0.12	3.9	112.7	148.5	1.7

Note: eU = [U] + 0.234[Th] + 0.0047[Sm]; * Grains that failed the outlier tests

TABLE D2: BULK ROCK ANALYSES

Analyte Symbol	SiO2	Al2O3	Fe2O3(T)	MnO	MgO	CaO	Na2O	K2O	TiO2	P2O5	LOI	Total
Unit Symbol	%	%	%	%	%	%	%	%	%	%	%	%
Detection Limit	0.01	0.01	0.01	0.001	0.01	0.01	0.01	0.01	0.001	0.01		0.01
14BB-03	64.42	16.67	6.51	0.065	1.86	0.3	1.19	3.88	0.998	0.12	2.79	98.81
15CM-05	55.89	17.95	8.09	0.148	3.11	7.65	3.59	1.73	1.071	0.37	0.76	100.4
15AF-WH2	60.06	16.83	7.55	0.114	2.79	6.34	3.03	2.31	0.878	0.4	0.64	100.9

Analyte Symbol	Sc	Be	V	Cr	Co	Ni	Cu	Zn	Ga	Ge	As	Rb
Unit Symbol	ppm	ppm	ppm	ppm	ppm	ppm	ppm	ppm	ppm	ppm	ppm	ppm
Detection Limit	1	1	5	20	1	20	10	30	1	0.5	5	1
14BB-03	14	3	123	100	15	30	< 10	40	22	1.6	< 5	101
15CM-05	22	1	208	50	16	< 20	10	50	22	1.7	< 5	33
15AF-WH2	18	2	128	30	14	< 20	< 10	80	21	1.7	< 5	53

Analyte Symbol	Sr	Y	Zr	Nb	Mo	Ag	In	Sn	Sb	Cs	Ba	La
Unit Symbol	ppm	ppm	ppm	ppm	ppm	ppm	ppm	ppm	ppm	ppm	ppm	ppm
Detection Limit	2	0.5	1	0.2	2	0.5	0.1	1	0.2	0.1	2	0.05
14BB-03	60	46.7	402	20.7	< 2	1.1	< 0.1	3	0.8	2.1	890	38.7
15CM-05	753	27.2	164	10.9	< 2	< 0.5	< 0.1	1	1.1	0.5	611	28.8
15AF-WH2	690	37.6	210	11.2	< 2	< 0.5	< 0.1	2	0.7	0.4	766	53.2

Analyte Symbol	Ce	Pr	Nd	Sm	Eu	Gd	Tb	Dy	Ho	Er	Tm	Yb
Unit Symbol	ppm	ppm	ppm	ppm	ppm	ppm	ppm	ppm	ppm	ppm	ppm	ppm
Detection Limit	0.05	0.01	0.05	0.01	0.005	0.01	0.01	0.01	0.01	0.01	0.005	0.01
14BB-03	82.8	9	36.1	7.42	1.38	7.08	1.16	7.46	1.58	4.78	0.738	4.91
15CM-05	61.2	7.62	30.8	6.52	2.15	5.84	0.83	4.92	0.93	2.71	0.379	2.5
15AF-WH2	90	10.2	39.8	8.18	1.89	7.08	1.07	6.2	1.27	3.66	0.527	3.25

TABLE D2: BULK ROCK ANALYSES

Analyte Symbol	Lu	Hf	Ta	W	Tl	Pb	Bi	Th	U
Unit Symbol	ppm	ppm	ppm	ppm	ppm	ppm	ppm	ppm	ppm
Detection Limit	0.002	0.1	0.01	0.5	0.05	5	0.1	0.05	0.01
14BB-03	0.77	10.1	1.76	2.7	0.36	7	0.1	18.8	4.66
15CM-05	0.382	4	0.77	0.8	0.09	10	< 0.1	3.52	0.89
15AF-WH2	0.52	5.2	0.8	0.8	0.17	6	< 0.1	7.61	0.64

Analysis Method: FUS-MS

TABLE D3: HORNBLENDE AND BIOTITE ARGON DATA

ID	Temp (°C)	$^{40}Ar/^{39}Ar$	$^{37}Ar/^{39}Ar$	$^{36}Ar/^{39}Ar$ (x 10^{-3})	$^{39}Ar_K$ (x 10^{-15}mol)	K/Ca	$^{40}Ar^*$ (%)	^{39}Ar (%)	Age (Ma)	±1σ (Ma)
WH-2 biotite, wt. = 1.47 mg, J=0.0009758, NM-149, Lab#=53009-01										
A	650	208.1	0.1356	648.8	0.136	3.8	7.9	0.5	26.2	6.9
B	750	41.01	0.0246	11.36	0.635	20.8	91.8	2.7	64.82	0.83
C	850	39.6	0.0128	0.4344	2.52	39.9	99.7	11.7	68.33	0.31
D	920	39.71	0.0189	-0.5662	3.23	27	100.4	23.2	68.98	0.23
E	1000	39.86	0.028	0.6727	4.37	18.2	99.5	38.7	68.57	0.19
F	1075	39.83	0.2027	1.323	4.94	2.5	99.1	56.2	68.21	0.2
G	1110	39.83	0.0283	1.178	4.62	18	99.1	72.7	68.26	0.19
H	1180	39.81	0.0467	1.535	4.88	10.9	98.9	90	68.05	0.19
I	1210	39.67	0.1007	1.071	2.19	5.1	99.2	97.8	68.18	0.3
J	1250	39.46	0.2255	1.644	0.462	2.3	98.8	99.4	68.4	1
K	1300	39.94	0.4891	4.864	0.159	1	96.5	100	69.7	2.9
Total gas age			n=11		28.1	15.7			68.1	1.4
Plateau		MSWD= 1.58	n=9	steps C-K	27.4	15.7		97.3	**68.36**	**0.21**
WH-26 biotite, wt. = 1.77 mg, J=0.0009760, NM-149, Lab#=53012-01										
A	650	457	0.3329	1461	0.18	1.5	5.5	0.6	40.9	7.6
B	750	51.8	0.0939	39.79	1.37	5.4	77.3	5.2	68.67	0.54
C	850	41.78	0.0283	6.555	3.88	18	95.4	18.2	68.79	0.22
D	920	41.01	0.0251	3.17	3.98	20.3	97.7	31.5	69.19	0.2
E	1000	40.84	0.0342	2.706	3.83	14.9	98	44.4	69.13	0.22
F	1075	40.6	0.2365	3.139	5.77	2.2	97.8	63.7	68.54	0.16
G	1110	40.74	0.309	2.55	4.79	1.7	98.2	79.8	69.07	0.2
H	1180	40.45	0.1354	3.563	3.79	3.8	97.4	92.5	68.49	0.25
I	*1210*	*40.78*	*0.2719*	*2.607*	*1.6*	*1.9*	*98.2*	*97.9*	*70.36*	*0.47*
J	*1250*	*43.62*	*0.315*	*9.583*	*0.503*	*1.6*	*93.6*	*99.6*	*76.5*	*2.1*
K	*1300*	*51.35*	*0.5695*	*30.21*	*0.134*	*0.9*	*82.7*	*100*	*8*	*15*
Total gas age			n=11		29.8	8.5			68.6	1.3
Plateau		MSWD= 1.99	n=7	steps B-H	27.4	9.1		91.9	**68.85**	**0.21**
WH-2 hornblende, wt. = 3.94 mg, J=0.0009785, NM-149, Lab#=53010-01										
A	800	619.4	1.08	1916.2	0.235	0.47	8.6	4.8	87.8	7.6
B	900	63.6	0.3875	68.73	0.232	1.3	68.1	9.5	71.2	2.2
C	1000	56.92	3.382	56.91	0.428	0.15	70.9	18.3	68.7	1.3
D	1030	54.65	7.222	47.6	0.671	0.071	75.3	32	70.48	0.92
E	1060	43.39	6.436	14.69	1.45	0.079	91.2	61.8	68.16	0.45
F	1090	42.93	5.62	14.54	0.93	0.091	91	80.8	67.15	0.62
G	1120	53.06	4.265	48.49	0.181	0.12	73.6	84.5	64.9	2.6

ID	Temp (°C)	$^{40}Ar/^{39}Ar$	$^{37}Ar/^{39}Ar$	$^{36}Ar/^{39}Ar$ (x 10^{-3})	$^{39}Ar_K$ (x 10^{-15}mol)	K/Ca	$^{40}Ar^*$ (%)	^{39}Ar (%)	Age (Ma)	±1σ (Ma)
H	1170	51.64	4.231	23.09	0.174	0.12	87.4	88.1	72.2	2.8
I	1200	51.5	6.954	39.09	0.254	0.073	78.6	93.2	66.1	2
J	1250	52.36	12.65	31.08	0.33	0.04	84.4	100	73.4	1.6
Total gas age			n=10		4.89	0.16			69.7	1.4
Isochron		MSWD= 2.8	n=10	steps A-J	4.89	0.16		100	**68.2**	**0.6**
WH-26 hornblende, wt. = 4.07 mg, J=0.0009741, NM-149, Lab#=53013-01										
A	800	296.5	5.316	854.9	0.346	0.096	14.9	4.1	76.4	5
B	900	44.96	0.4136	7.696	0.337	1.2	95	8.2	73.7	1.4
C	1000	44.03	2.115	8.327	0.306	0.24	94.8	11.8	70.5	1.3
D	1030	40.48	5.074	-5.1894	0.318	0.1	104.8	15.6	71.7	1.3
E	1060	41.47	5.994	5.118	1.82	0.085	97.5	37.4	69.45	0.36
F	1090	40.65	5.879	3.083	3.1	0.087	98.9	74.6	69.17	0.27
G	1120	40.2	5.132	3.423	1.02	0.099	98.5	86.7	67.86	0.52
H	*1170*	*40.32*	*6.4*	*-1.6397*	*0.145*	*0.08*	*102.5*	*88.5*	*73.8*	*2.5*
I	*1200*	*41.18*	*6.688*	*2.668*	*0.367*	*0.076*	*99.4*	*92.9*	*71.5*	*1.1*
J	*1250*	*41.05*	*6.569*	*0.5949*	*0.595*	*0.078*	*100.8*	*100*	*71.94*	*0.74*
Total gas age			n=10		8.35	0.14			70.08	0.75
Plateau		MSWD= 3.36	n=3	steps E-G	5.94	0.09		71.1	**69.06**	**0.43**

Isotopic ratios corrected for blank, radioactive decay and mass discrimination.

Isotopic ratios not corrected for interfering reactions.

Plateau, total gas and isochron age errors include error in J and irradiation parameters.

Plateau and isochron errors are 2σ.

Analyses in italics are excluded from mean age calculations.

TABLE D4: K-FELDSPAR ARGON DATA

ID	Temp (°C)	$^{40}Ar/^{39}Ar$	$^{40}Ar/^{39}Ar$	$^{37}Ar/^{39}Ar$ (x 10-3)	$^{39}Ar_K$ (x 10-15mol)	K/Ca	$^{40}Ar^*$ (%)	^{39}Ar (%)	Age (Ma)	±1σ (Ma)	Time (min)
WH-2 K-feldspar, wt. = 11.79 mg, J=0.0009739, NM-149, Lab#=53008-01											
A	450	508.5	0.2611	1596	0.539	2	7.3	0.2	63.7	5.6	10.2
B	450	89.93	0.2523	194.5	0.266	2	36.1	0.3	56.1	2.1	20.3
C	450	71.58	0.2297	115.8	0.239	2.2	52.2	0.4	64.5	2.1	28.6
D	500	69.52	0.2289	94.02	0.612	2.2	60	0.7	71.9	1.1	10.1
E	500	47.7	0.2633	32.23	0.566	1.9	80.1	0.9	65.86	0.86	20.1
F	500	45.44	0.2901	23.67	0.552	1.8	84.7	1.2	66.32	0.86	28.5
G	550	54.47	0.2672	46.73	1.04	1.9	74.7	1.6	70.07	0.62	9.8
H	550	42.28	0.282	14.37	1.02	1.8	90	2	65.62	0.48	20
I	550	41.5	0.2452	11.29	0.959	2.1	92	2.4	65.84	0.5	28.3
J	600	45.32	0.2082	21.32	1.47	2.5	86.1	3.1	67.29	0.42	9.8
K	600	39.95	0.1883	5.799	1.71	2.7	95.7	3.8	65.94	0.33	19.9
L	600	39.67	0.1686	6.295	1.62	3	95.3	4.4	65.21	0.34	28.1
M	650	41.14	0.1502	8.694	2.05	3.4	93.8	5.3	66.51	0.34	10.3
N	650	39.36	0.1458	3.118	2.55	3.5	97.7	6.4	66.28	0.24	20.3
O	650	38.83	0.1351	2.867	2.51	3.8	97.8	7.4	65.51	0.24	28.6
P	700	40.4	0.1387	5.846	2.87	3.7	95.7	8.6	66.67	0.24	10.1
Q	700	38.77	0.1419	2.525	3.37	3.6	98.1	10.1	65.58	0.2	20.2
R	700	38.81	0.1383	2.153	3.06	3.7	98.4	11.4	65.83	0.23	28.5
S	750	39.19	0.1405	3.122	3.16	3.6	97.7	12.7	65.99	0.19	10.3
T	750	38.57	0.1369	1.508	3.45	3.7	98.9	14.1	65.74	0.19	20.4
U	750	38.71	0.1296	1.533	2.95	3.9	98.9	15.4	65.98	0.23	28.8
V	800	39.39	0.1331	2.866	2.6	3.8	97.9	16.5	66.46	0.27	10.3
W	800	38.71	0.118	2.136	2.96	4.3	98.4	17.7	65.68	0.22	20.3

TABLE D4: K-FELDSPAR ARGON DATA

ID	Temp (°C)	$^{40}Ar/^{39}Ar$	$^{40}Ar/^{39}Ar$	$^{37}Ar/^{39}Ar$ (x 10-3)	$^{39}Ar_K$ (x 10-15mol)	K/Ca	$^{40}Ar^*$ (%)	^{39}Ar (%)	Age (Ma)	±1σ (Ma)	Time (min)
X	850	39.54	0.1126	4.202	3.27	4.5	96.9	19.1	66.03	0.21	10.5
Y	850	39.17	0.083	2.974	3.4	6.2	97.8	20.5	66.03	0.19	20.6
Z	900	39.89	0.0707	5.102	3.62	7.2	96.2	22	66.19	0.21	10.5
ZA	900	39.5	0.0593	3.767	3.7	8.6	97.2	23.6	66.19	0.2	20.5
ZB	950	40.48	0.0574	7.953	4.2	8.9	94.2	25.3	65.74	0.21	10.7
ZC	950	40.48	0.0615	6.801	4.28	8.3	95	27.1	66.33	0.2	20.7
ZD	1000	41.8	0.0842	12.05	5.31	6.1	91.5	29.4	65.93	0.19	10.6
ZE	1000	41.76	0.0718	11.57	5.03	7.1	91.8	31.5	66.1	0.22	20.6
ZF	1050	43.38	0.0795	15.22	7.29	6.4	89.6	34.6	67.03	0.22	10.7
ZG	1050	42.42	0.0813	13.09	6.51	6.3	90.9	37.3	66.46	0.17	20.7
ZH	1100	42.27	0.0859	10.56	3.97	5.9	92.6	39	67.47	0.23	10.7
ZI	1100	41.39	0.0909	9.314	5.7	5.6	93.4	41.4	66.61	0.21	20.6
ZJ	1100	41.35	0.0759	7.826	12.5	6.7	94.4	46.6	67.28	0.18	59.6
ZK	1100	41.06	0.0657	7.018	18.5	7.8	95	54.4	67.19	0.15	115.2
ZL	1100	41.09	0.0628	7.195	22.7	8.1	94.8	63.9	67.16	0.14	235.1
ZM	1200	40.55	0.0399	4.742	33	12.8	96.6	77.8	67.48	0.12	5.2
ZN	1300	41.07	0.0605	5.314	37.2	8.4	96.2	93.4	68.07	0.14	5.9
ZO	1400	42.47	0.1816	8.653	9.19	2.8	94	97.3	68.79	0.16	5.7
ZP	1685	45.95	0.1658	18.54	6.48	3.1	88.1	100	68.54	0.22	5.4
Total gas age			n=42		238	7.2			**67.08**	**0.2**	
WH-26 K-feldspar, wt. = 10.01 mg, J=0.0009786, NM-149, Lab#=53011-01											
A	450	1122.1	0.7461	3234.3	0.197	0.68	14.8	0.1	272.2	12.6	10.1
B	450	191.8	0.9082	474.2	0.073	0.56	27	0.1	89.1	6.7	20.1

TABLE D4: K-FELDSPAR ARGON DATA

ID	Temp (°C)	$^{40}Ar/^{39}Ar$	$^{40}Ar/^{39}Ar$	$^{37}Ar/^{39}Ar$ (x 10-3)	$^{39}Ar_K$ (x 10-15mol)	K/Ca	$^{40}Ar^*$ (%)	^{39}Ar (%)	Age (Ma)	±1σ (Ma)	Time (min)
C	450	155.2	0.9058	346.1	0.053	0.56	34.2	0.2	91.3	8.8	28.3
D	500	133	0.9202	234.4	0.101	0.55	48	0.2	109.3	4.6	9.9
E	500	74.46	0.8855	122.2	0.124	0.58	51.6	0.3	66.5	3.8	20
F	500	73.02	0.9164	99.16	0.122	0.56	60	0.3	75.7	3.7	28.3
G	550	90.77	1.006	132.6	0.208	0.51	56.9	0.4	88.9	2.5	9.7
H	550	55.49	0.9462	45.23	0.242	0.54	76	0.6	73	1.9	19.7
I	550	55.06	0.9129	48.88	0.259	0.56	73.9	0.7	70.4	1.7	28.1
J	600	73.31	0.7363	80.62	0.443	0.69	67.6	0.9	85.4	1.2	9.5
K	600	50.39	0.6047	30.77	0.5	0.84	82	1.2	71.51	0.99	19.7
L	600	47.51	0.4839	22.25	0.566	1.1	86.2	1.4	70.88	0.87	28
M	650	56.06	0.4356	40.09	0.885	1.2	78.9	1.9	76.43	0.67	10.1
N	650	45.95	0.3802	15.16	1.07	1.3	90.3	2.4	71.77	0.52	20.1
O	650	43.73	0.3468	13.86	1.22	1.5	90.7	3	68.65	0.48	28.4
P	700	45.17	0.3312	11.02	1.08	1.5	92.8	3.6	72.52	0.5	9.9
Q	700	41.66	0.3139	6.85	1.3	1.6	95.2	4.2	68.65	0.45	20
R	700	41.39	0.3069	5.599	1.14	1.7	96.1	4.8	68.82	0.44	28.2
S	750	42.93	0.2713	7.869	1.64	1.9	94.6	5.6	70.29	0.36	10.2
T	750	39.68	0.2432	1.418	1.67	2.1	99	6.5	68.01	0.3	20.3
U	750	40.05	0.2121	1.71	1.68	2.4	98.8	7.3	68.49	0.33	28.6
V	800	40.46	0.1869	1.832	1.83	2.7	98.7	8.2	69.12	0.28	10.1
W	800	39.57	0.1552	2.049	2.33	3.3	98.5	9.4	67.48	0.26	20.2
X	850	41.23	0.1519	4.438	3.12	3.4	96.8	10.9	69.11	0.23	10.4
Y	850	40.11	0.1104	2.815	3.59	4.6	97.9	12.7	68.01	0.2	20.4
Z	900	41.26	0.0949	4.402	3.67	5.4	96.9	14.6	69.16	0.21	10.3

TABLE D4: K-FELDSPAR ARGON DATA

ID	Temp (°C)	$^{40}Ar/^{39}Ar$	$^{40}Ar/^{39}Ar$	$^{37}Ar/^{39}Ar$ (x 10-3)	$^{39}Ar_K$ (x 10-15mol)	K/Ca	$^{40}Ar^*$ (%)	^{39}Ar (%)	Age (Ma)	±1σ (Ma)	Time (min)
ZA	900	39.95	0.0711	3.129	4.59	7.2	97.7	16.9	67.58	0.19	20.4
ZB	950	41.55	0.0712	4.915	3.72	7.2	96.5	18.7	69.41	0.21	10.5
ZC	950	40.64	0.0686	4.677	6.18	7.4	96.6	21.8	67.97	0.2	20.6
ZD	1000	43.04	0.0755	8.298	4.84	6.8	94.3	24.2	70.24	0.2	10.4
ZE	1000	40.88	0.0562	3.963	4.4	9.1	97.1	26.4	68.75	0.18	20.4
ZF	1050	45.78	0.1116	15.07	5.26	4.6	90.3	29.1	71.49	0.24	10.6
ZG	1050	43.54	0.1254	12.39	4.8	4.1	91.6	31.5	69.03	0.23	20.6
ZH	1100	43.92	0.114	9.859	2.67	4.5	93.4	32.8	70.96	0.26	10.5
ZI	1100	43.64	0.1176	10.69	3.44	4.3	92.8	34.5	70.07	0.24	20.6
ZJ	1100	44.01	0.1044	10.28	6.42	4.9	93.1	37.7	70.9	0.19	55.1
ZK	1100	44.91	0.0826	11.59	8.38	6.2	92.4	41.9	71.76	0.19	115.1
ZL	1100	46.86	0.0739	16.05	8.83	6.9	89.9	46.3	72.84	0.19	235.1
ZM	1200	50.03	0.0229	10.19	31.2	22.3	94	61.9	81.12	0.18	6.6
ZN	1300	45.96	0.0263	6.907	66.4	19.4	95.6	95.1	75.88	0.17	5.7
ZO	1400	45.07	0.3889	9.929	6.2	1.3	93.6	98.2	72.91	0.2	5.7
ZP	1685	46.98	0.4151	13.83	3.52	1.2	91.4	100	74.19	0.26	5.4
Total gas age			n=42		200	12.4			**74.16**	**0.24**	

Isotopic ratios corrected for blank, radioactive decay and mass discrimination.

Isotopic ratios not corrected for interfering reactions.

Total gas age errors include error in J and irradiation parameters.

TABLE D5: U-TH-PB GEOCHRONOLOGIC ANALYSES SAMPLE 15CM-05

Analysis	U (ppm)	^{206}Pb ^{204}Pb	U/Th	$^{206}Pb^*$ $^{207}Pb^*$	± (%)	Isotope Ratios $^{207}Pb^*$ $^{235}U^*$	± (%)	$^{206}Pb^*$ ^{238}U	± (%)	Error Corr.	Apparent Ages (Ma) $^{206}Pb^*$ $^{238}U^*$	± (Ma)	$^{207}Pb^*$ ^{235}U	± (Ma)	$^{206}Pb^*$ $^{207}Pb^*$	± (Ma)	Best Age (Ma)	± (Ma)
15CM-05-SAMPLE 1 Spot 28	29	279	1.4	219.78	370.2	0.01	370.2	0.01	3.1	0.01	63.0	2.0	6.2	23.0	NA	NA	63.0	2.0
15CM-05-SAMPLE 1 Spot 16	49	478	1.2	33.66	13.0	0.04	13.5	0.01	3.6	0.27	63.5	2.3	40.3	5.3	NA	NA	63.5	2.3
15CM-05-SAMPLE 1 Spot 13	88	2379	0.9	24.25	3.4	0.06	4.8	0.01	3.4	0.71	64.7	2.2	56.6	2.6	NA	NA	64.7	2.2
15CM-05-SAMPLE 1 Spot 29	69	747	0.8	33.37	7.6	0.04	8.0	0.01	2.6	0.33	64.9	1.7	41.6	3.3	NA	NA	64.9	1.7
15CM-05-SAMPLE 1 Spot 9	116	465	0.7	73.58	6.2	0.02	7.0	0.01	3.4	0.48	65.8	2.2	19.3	1.3	NA	NA	65.8	2.2
15CM-05-SAMPLE 1 Spot 7	70	555	0.8	41.49	17.8	0.03	18.1	0.01	2.8	0.15	65.9	1.8	34.1	6.0	NA	NA	65.9	1.8
15CM-05-SAMPLE 1 Spot 21	167	2353	0.6	23.71	3.1	0.06	3.8	0.01	2.2	0.57	65.9	1.4	58.9	2.2	NA	NA	65.9	1.4
15CM-05-SAMPLE 1 Spot 25	87	741	0.7	34.47	35.0	0.04	35.1	0.01	2.6	0.07	66.2	1.7	41.0	14.1	NA	NA	66.2	1.7
15CM-05-SAMPLE 1 Spot 26	144	4935	0.7	22.88	2.8	0.06	3.7	0.01	2.4	0.65	66.2	1.6	61.2	2.2	NA	NA	66.2	1.6

TABLE D5: U-TH-PB GEOCHRONOLOGIC ANALYSES SAMPLE 15CM-05

Analysis	U (ppm)	$^{206}Pb/^{204}Pb$	U/Th	$^{206}Pb^*/^{207}Pb^*$	± (%)	Isotope Ratios $^{207}Pb^*/^{235}U^*$	± (%)	$^{206}Pb^*/^{238}U$	± (%)	Error Corr.	Apparent Ages (Ma) $^{206}Pb^*/^{238}U^*$	± (Ma)	$^{207}Pb^*/^{235}U$	± (Ma)	$^{206}Pb^*/^{207}Pb^*$	± (Ma)	Best Age (Ma)	± (Ma)
15CM-05-SAMPLE 1 Spot 2	53	1371	0.9	29.65	3.9	0.05	5.2	0.01	3.5	0.66	66.3	2.3	47.7	2.4	NA	NA	66.3	2.3
15CM-05-SAMPLE 1 Spot 15	39	1134	1.1	22.61	5.3	0.06	6.6	0.01	3.9	0.59	66.5	2.6	62.3	4.0	NA	NA	66.5	2.6
15CM-05-SAMPLE 1 Spot 3	40	792	1.1	36.35	7.9	0.04	8.5	0.01	2.9	0.35	66.5	1.9	39.2	3.3	NA	NA	66.5	1.9
15CM-05-SAMPLE 1 Spot 22	175	853	0.6	34.48	5.2	0.04	5.9	0.01	2.8	0.47	66.7	1.8	41.3	2.4	NA	NA	66.7	1.8
15CM-05-SAMPLE 1 Spot 10	116	2949	0.9	23.18	2.7	0.06	3.8	0.01	2.7	0.72	66.7	1.8	60.9	2.3	NA	NA	66.7	1.8
15CM-05-SAMPLE 1 Spot 1	113	1210	0.6	27.05	11.6	0.05	11.9	0.01	2.6	0.22	66.9	1.7	52.6	6.1	NA	NA	66.9	1.7
15CM-05-SAMPLE 1 Spot 4	165	1515	0.6	25.47	3.1	0.06	4.2	0.01	2.8	0.66	66.9	1.8	55.8	2.3	NA	NA	66.9	1.8
15CM-05-SAMPLE 1 Spot 35	50	451	0.9	83.21	54.4	0.02	54.6	0.01	3.8	0.07	67.3	2.5	17.5	9.5	NA	NA	67.3	2.5
15CM-05-SAMPLE 1 Spot 12	194	3337	0.7	22.24	2.6	0.07	4.2	0.01	3.3	0.78	67.6	2.2	64.2	2.6	NA	NA	67.6	2.2

TABLE D5: U-TH-PB GEOCHRONOLOGIC ANALYSES SAMPLE 15CM-05

Analysis	U (ppm)	$^{206}Pb/^{204}Pb$	U/Th	$^{206}Pb^*/^{207}Pb^*$	± (%)	Isotope Ratios $^{207}Pb^*/^{235}U^*$	± (%)	$^{206}Pb^*/^{238}U$	± (%)	Error Corr.	Apparent Ages (Ma) $^{206}Pb^*/^{238}U^*$	± (Ma)	$^{207}Pb^*/^{235}U$	± (Ma)	$^{206}Pb^*/^{207}Pb^*$	± (Ma)	Best Age (Ma)	± (Ma)
15CM-05-SAMPLE 1 Spot 23	103	6629	0.7	21.61	2.6	0.07	3.4	0.01	2.3	0.67	67.7	1.5	66.2	2.2	11.9	61.7	67.7	1.5
15CM-05-SAMPLE 1 Spot 8	89	1588	0.8	25.76	5.2	0.06	6.1	0.01	3.0	0.50	67.8	2.0	55.8	3.3	NA	NA	67.8	2.0
15CM-05-SAMPLE 1 Spot 32	32	819	1.4	34.67	9.7	0.04	10.2	0.01	3.3	0.32	67.8	2.2	41.8	4.2	NA	NA	67.8	2.2
15CM-05-SAMPLE 1 Spot 31	69	1124	0.8	29.36	3.9	0.05	5.1	0.01	3.2	0.64	67.9	2.2	49.2	2.4	NA	NA	67.9	2.2
15CM-05-SAMPLE 1 Spot 24	132	728	0.6	38.66	37.1	0.04	37.2	0.01	2.9	0.08	67.9	2.0	37.6	13.7	NA	NA	67.9	2.0
15CM-05-SAMPLE 1 Spot 17	75	1815	0.8	25.01	4.0	0.06	5.1	0.01	3.1	0.61	68.2	2.1	57.8	2.9	NA	NA	68.2	2.1
15CM-05-SAMPLE 1 Spot 14	63	809	0.8	31.50	25.2	0.05	25.4	0.01	2.9	0.11	68.4	1.9	46.3	11.5	NA	NA	68.4	1.9
15CM-05-SAMPLE 1 Spot 27	68	3733	0.8	13.42	4.2	0.11	5.6	0.01	3.8	0.67	69.0	2.6	106.4	5.7	1054.9	83.9	69.0	2.6
15CM-05-SAMPLE 1 Spot 6	43	1058	1.0	27.76	4.5	0.05	5.5	0.01	3.1	0.56	69.9	2.1	53.5	2.9	NA	NA	69.9	2.1

TABLE D5: U-TH-PB GEOCHRONOLOGIC ANALYSES SAMPLE 15CM-05

Analysis	U (ppm)	^{206}Pb ^{204}Pb	U/Th	$^{206}Pb^*$ $^{207}Pb^*$	± (%)	Isotope Ratios $^{207}Pb^*$ $^{235}U^*$	± (%)	$^{206}Pb^*$ ^{238}U	± (%)	Error Corr.	Apparent Ages (Ma) $^{206}Pb^*$ $^{238}U^*$	± (Ma)	$^{207}Pb^*$ ^{235}U	± (Ma)	$^{206}Pb^*$ $^{207}Pb^*$	± (Ma)	**Best Age** (Ma)	± (Ma)
15CM-05-SAMPLE 1 Spot 19	65	493	0.9	46.78	14.2	0.03	18.3	0.01	11.5	0.63	70.2	8.0	32.2	5.8	NA	NA	70.2	8.0
15CM-05-SAMPLE 1 Spot 33	108	4884	1.3	12.72	6.2	0.12	7.1	0.01	3.6	0.50	70.5	2.5	114.3	7.7	1162.1	122.8	70.5	2.5
15CM-05-SAMPLE 1 Spot 5	57	5696	0.9	20.75	4.6	0.07	6.0	0.01	3.8	0.64	70.9	2.7	72.0	4.2	108.2	108.6	70.9	2.7
15CM-05-SAMPLE 1 Spot 18	46	2969	0.9	21.22	4.5	0.07	5.7	0.01	3.5	0.61	72.5	2.5	72.0	4.0	55.1	107.2	72.5	2.5
15CM-05-SAMPLE 1 Spot 34	57	265	1.0	2.15	30.0	0.77	30.6	0.01	5.7	0.19	77.3	4.4	582.4	136.3	NA	NA	77.3	4.4
15CM-05-SAMPLE 1 Spot 30	77	372	0.9	9.45	12.5	0.18	13.5	0.01	5.0	0.37	78.3	3.9	166.4	20.7	1727.7	230.5	78.3	3.9
15CM-05-SAMPLE 1 Spot 20	88	685	0.7	7.98	9.7	0.22	11.2	0.01	5.6	0.50	80.3	4.5	198.9	20.2	2033.5	171.4	80.3	4.5
15CM-05-SAMPLE 1 Spot 11	86	116	0.9	2.34	21.4	1.45	33.3	0.02	25.5	0.77	156.9	39.5	909.6	202.5	NA	NA	156.9	39.5

TABLE D6: U-TH-PB GEOCHRONOLOGIC ANALYSES SAMPLE 14BB-03

Analysis	U (ppm)	^{206}Pb ^{204}Pb	U/Th	$^{206}Pb^*$ $^{207}Pb^*$	± (%)	Isotope Ratios $^{207}Pb^*$ $^{235}U^*$	± (%)	$^{206}Pb^*$ ^{238}U	± (%)	Error Corr.	Apparent Ages (Ma) $^{206}Pb^*$ $^{238}U^*$	± (Ma)	$^{207}Pb^*$ ^{235}U	± (Ma)	$^{206}Pb^*$ $^{207}Pb^*$	± (Ma)	Best Age (Ma)	± (Ma)
14BB03-12	73	34482	1.0	11.15	1.3	3.13	1.6	0.25	0.9	0.55	1456.5	11.4	1441.2	12.3	1418.7	25.5	1418.7	25.5
14BB03-07	112	56465	1.2	11.03	2.0	3.12	3.6	0.25	3.0	0.84	1435.7	39.2	1437.3	28.0	1439.7	38.1	1439.7	38.1
14BB03-15	93	36110	3.3	9.92	1.5	3.97	1.8	0.29	1.0	0.53	1620.6	13.7	1628.5	14.7	1638.8	28.7	1638.8	28.7
14BB03-11	317	111523	14.7	9.89	0.6	4.08	1.2	0.29	1.1	0.89	1655.0	16.1	1650.3	10.1	1644.4	10.3	1644.4	10.3
14BB03-08	76	38315	1.6	9.80	2.3	4.11	3.7	0.29	2.8	0.77	1650.6	41.0	1655.4	29.9	1661.5	43.5	1661.5	43.5
14BB03-09	64	35923	1.5	9.73	2.5	3.66	8.8	0.26	8.5	0.96	1481.1	112.2	1562.9	70.7	1675.1	46.7	1675.1	46.7
14BB03-03	154	103265	3.8	9.71	0.5	4.24	1.6	0.30	1.5	0.95	1683.7	22.2	1681.7	13.0	1679.2	9.3	1679.2	9.3
14BB03-10	224	50638	3.1	9.69	0.5	4.22	1.6	0.30	1.5	0.95	1675.8	21.7	1678.6	12.8	1682.0	9.1	1682.0	9.1
14BB03-21	38	10332	2.6	9.65	3.2	4.24	3.3	0.30	0.7	0.23	1677.4	11.1	1682.6	27.2	1689.2	59.6	1689.2	59.6
14BB03-16	105	33164	1.5	9.65	0.8	4.29	1.5	0.30	1.2	0.82	1693.1	17.8	1691.7	12.0	1689.8	15.2	1689.8	15.2
14BB03-02	94	35556	1.4	9.64	0.5	4.37	0.9	0.31	0.7	0.79	1719.3	10.6	1706.7	7.3	1691.3	9.9	1691.3	9.9
14BB03-06	137	81867	3.0	9.63	0.8	4.30	1.7	0.30	1.4	0.87	1692.5	21.6	1692.7	13.6	1693.0	14.8	1693.0	14.8
14BB03-20	194	55036	4.1	9.63	0.5	4.32	1.1	0.30	1.0	0.91	1701.3	15.1	1697.8	9.1	1693.5	8.3	1693.5	8.3
14BB03-19	122	40914	4.6	9.63	0.7	4.27	1.3	0.30	1.0	0.81	1682.8	15.3	1687.7	10.4	1693.7	13.6	1693.7	13.6
14BB03-13	22	6898	1.7	9.61	3.5	4.48	3.8	0.31	1.5	0.40	1752.0	22.9	1727.5	31.3	1697.9	63.7	1697.9	63.7
14BB03-17	210	104079	3.0	9.59	0.3	4.39	1.3	0.31	1.2	0.97	1717.8	18.7	1710.4	10.6	1701.3	6.0	1701.3	6.0
14BB03-14	126	57052	1.3	9.57	0.6	4.44	1.3	0.31	1.1	0.90	1731.6	17.3	1720.2	10.5	1706.3	10.2	1706.3	10.2
14BB03-18	227	96108	3.8	9.56	0.4	4.29	0.9	0.30	0.8	0.90	1679.7	12.5	1691.9	7.8	1707.0	7.7	1707.0	7.7
14BB03-05	65	55480	1.6	9.52	1.2	4.48	1.7	0.31	1.2	0.73	1738.2	18.9	1728.0	14.2	1715.6	21.5	1715.6	21.5
14BB03-04	359	217034	2.7	9.46	0.7	4.32	1.2	0.30	1.0	0.82	1671.4	15.0	1696.3	10.2	1727.3	12.9	1727.3	12.9
14BB03-01	153	78001	3.2	9.35	0.5	4.63	1.1	0.31	1.0	0.89	1760.2	15.4	1754.8	9.3	1748.4	9.1	1748.4	9.1

Table D7. SUMMARY OF PALEOMAGNETIC DATA FROM SITES IN THE WHITEHORN GRANODIORITE AND HOST METASEDIMENTARY ROCKS

Site	Rock Type	N/No	Decl.	Incl.	a_{95}	*k*	a_{951-3}, a_{951-2}
WH1	metaign5/8	279.1	+35.3	28.0	8.4	17.7,	22.5
WH2	gd	7/7	331.2	+58.8	3.3	331.4	2.3, 3.4
WH3	gd	9/9	320.7	+57.5	5.9	75.9	1.7/8.6
WH4	gd	10/11	349.3	+62.0	7.2	46.2	5.5, 10.0
WH5	gd	7/8	346.1	+49.9	5.2	134.8	2.4, 5.5
WH6	gd	7/7	323.6	+63.5	7.0	75.5	4.6, 6.6
WH8	gd	8/10	281.4	+64.4	11.1	25.8	3.9, 12.5
WH10	gd	8/8	343.1	+58.0	5.9	90.6	2.9, 6.3
WH12	gd	9/9	274.9	+53.5	7.4	49.7	4.1, 7.9
WH13	hornfls	6/8	311.2	+37.4	21.9	10.3	9.2, 22.4
WH15	gd	6/7	339.6	+62.9	7.9	73.6	5.0, 8.5
WH18	gd	9/9	340.5	+52.0	9.6	29.6	6.3, 9.8
WH19	gd	6/7	341.3	+49.9	3.4	382.3	1.3, 3.6
WH20	gd	12/12	347.8	+59.4	3.6	142.5	2.7, 3.7
WH25	gd	7/7	330.7	+56.0	4.5	183.8	2.2, 4.6
WH26	gd	10/10	328.8	+53.3	2.9	272.8	1.9, 3.0
WH27	gd	10/11	337.9	+57.7	2.8	303.2	1.3, 3.1
WH29	gd	9/9	326.4	+56.3	5.0	107.5	2.8, 5.3
WH30	gd	4/6	331.4	+54.2	4.8	366.7	1.8, 4.1
WH31	gd	8/9	295.8	+57.3	12.7	20.0	5.3, 14.0
WH32	gd	8/8	341.0	+59.5	7.0	63.5	5.4, 9.8
WH39	gd	8/8	321.3	+49.8	3.1	276.4	1.3, 3.3
WH40	gd	8/8	331.4	+45.1	7.3	50.4	5.6, 9.7
WH41	gd	8/8	318.2	+52.5	8.4	38.4	4.7, 9.2
WH43	gd	8/9	328.3	+62.6	3.0	286.4	1.2, 3.3
WH44	gd	8/8	331.4	+55.9	3.8	180.4	1.5, 3.7
WH46	gd	8/8	299.0	+55.4	7.1	53.4	5.5, 9.7
WH47	gd	8/8	319.3	+60.6	6.8	31.3	5.3, 9.6
WG48	gd	8/8	341.0	+59.5	8.4	30.3	4.5, 9.5
WH49	gd	8/8	330.5	+61.7	4.4	99.1	1.8, 4.4
WH50	gd	8/9	320.3	+46.5	4.6	112.4	1.8, 4.7
WH51	gd	8/8	322.8	+50.9	3.3	195.4	1.4, 3.5

Site, number of the specific sampling site, typically spread over 5-10 square meters, where some 7-10 independently oriented samples, usually as standard paleomagnetic cores, were obtained; Rock type, metaign, Proterozoic meta-igneous host rock, gd, Whitehorn Granodiorite, hornfls, Paleozoic contact sedimentary rock; N/No, ratio of the number of samples accepted to provide an estimated site mean direction and associated statistics to the total number of independent samples measured (with typically one specimen per sample utilized); Decl., declination of the estimated site mean direction, measured east from geographic north (0^{o}); Incl., inclination of the estimated site mean direction, measured positive downwards from the horizontal; a95, semi-angle, in degrees of the estimated circle of 95 percent confidence about the estimated site mean direction, assuming a circular distribution of independent directions about the true mean direction (from Fisher, 1953); k, the best estimate of Fisher's (1953) confidence parameter, assuming a circular distribution of independent directions about the true mean direction; a_{951-3}, $a_{951-2,}$, the angle, in degrees, of the semi-minor and semi-major angles of 95 percent confidence about the estimated site mean direction, following a non-circular, Bingham distribution (Onstott, 1980).

TABLE D8: RAW CLUMPED ISOTOPE DATA

FEB. 2016 RUN

Date	Sample Name	δ13C (PDB)	δ18O (raw)	δ18O PDB	δ45	δ46	δ47	δ48	δ49	Δ47	Δ48	Δ49	Window
2/26	MOX-02-1	-1.505	37.483	-2.17	2.132	2.421	4.207	4.739	7.234	-0.377	-0.107	0.186	1
2/26	WBP-01-1	-0.478	33.944	-5.58	2.982	-0.993	1.563	3.672	8.969	-0.531	5.668	7.743	1
2/28	WBP-01-2 *	-0.908	32.984	-6.50	2.548	-1.921	0.389	-4.71	-0.129	-0.343	-0.875	0.944	1
2/28	MOX-03-1	0.057	35.153	-4.42	3.523	0.174	3.365	-0.324	8.493	-0.439	-0.672	4.379	1
2/29	MOX-02-2	-1.09	36.957	-2.68	2.505	1.913	4.07	3.625	7.238	-0.399	-0.204	0.79	1
2/29	BB-O4-2	2.19	37.497	-2.16	5.601	2.442	7.819	56.536	2.676	-0.371	51.395	-8.039	1
2/29	WBP-03-3	1.573	33.705	-5.81	4.9	-1.219	3.4	-0.118	6.1	-0.446	2.325	3.283	1
2/29	WBP-01-3	-0.751	33.177	-6.32	2.701	-1.734	0.569	-4.178	5.933	-0.505	-0.716	6.477	1
3/1	BB-04-3	2.49	37.199	-2.45	5.874	2.155	7.82	316.764	-21.501	-0.368	311.107	-31.691	1
3/1	MOX-03-2	0.372	35.535	-4.05	3.831	0.544	4.114	11.108	-2.612	-0.373	10.009	-7.726	1
3/1	MOX-03-3	0.553	35.398	-4.18	3.997	0.412	4.129	-0.036	9.487	-0.398	-0.859	4.394	1
3/1	MOX-02-3	-1.186	37.129	-2.52	2.42	2.08	4.162	4.013	6.581	-0.383	-0.15	-0.1	1
3/6	WBP-01-4	-0.654	33.257	-6.24	2.795	-1.657	0.72	-3.128	6.58	-0.527	0.183	6.872	1

Transfer Functions:

Window	Start Date	End Date	SlopeEGL	SlopeETF	IntETF
1	2/24/16	03/04/16	0.017922	1.079029	1.027081

Equilibrated and Heated Gasses:

Date	Name	δ13C	δ18O	δ45	δ46	δ47	δ48	δ49	Δ47	Δ48	Δ49
2/22	Evap HG (leaky)	-41.105	39.391	-34.985	4.18	-33.598	7.883	12.412	-1.529	-0.49	43.005
2/22	Carrara HG	1.88	34.962	5.228	-0.006	4.519	-1.604	7.286	-0.862	-1.592	1.721
2/22	Ooids HG	4.325	26.173	7.241	-8.484	-1.872	-20.389	8.129	-0.928	-3.554	17.322
2/23	2xEV HG	-41.113	50.749	-34.628	15.142	-22.602	34.089	6.075	-1.27	3.47	14.2
2/24	Evap HG	-41.061	37.454	-35.006	2.31	-35.411	3.742	13.986	-1.552	-0.88	48.484
2/26	MATH HG	-3.756	30.698	-0.2	-4.134	-5.273	-10.835	9.714	-1.005	-2.606	18.189
2/27	Ooids HG	4.7	36.167	7.915	1.163	8.549	0.986	8.425	-0.76	-1.339	-2.286

2/28	2x EV HG	-40.643	62.144	-33.822	26.141	-11.247	60.416	8.875	-1.175	7.075	-5.171
2/29	MATH HG	-3.959	30.073	-0.411	-4.736	-6.108	-11.757	8.733	-1.031	-2.329	18.64
3/5	Evap HG	-40.842	31.877	-34.98	-3.073	-40.624	-8.779	14.391	-1.704	-2.659	60.03
3/6	MDIW HG	-40.76	26.64	-35.073	-8.127	-45.631	-20.715	14.095	-1.841	-4.602	70.467
2/22	2xEV 25C	-41.082	70.604	-33.967	34.306	-2.656	79.343	2.481	-0.159	8.931	-26.591
2/23	MDIW 25C	-41.218	29.913	-35.397	-4.969	-41.99	-12.704	16.856	-0.813	-2.82	67.079
2/23	Evap 25C	-41.342	46.124	-34.991	10.678	-26.479	23.864	8.748	-0.525	2.344	26.15
2/23	MDIW 25C	-41.084	30.505	-35.251	-4.397	-41.286	-11.259	16.578	-0.798	-2.507	65.413
2/25	2x EV 25C	-40.5	71.364	-33.405	35.04	-1.336	81.49	3.755	-0.134	9.504	-27.317
2/26	Evap 25C	-40.702	46.987	-34.363	11.512	-25.041	25.73	9.713	-0.531	2.516	24.755
2/28	MDIW 25C	-40.789	30.417	-34.978	-4.482	-41.106	-11.644	16.389	-0.82	-2.725	65.07
2/29	2xEV 25C	-40.671	71.169	-33.563	34.851	-1.731	84.043	-0.094	-0.181	12.256	-30.53
3/1	Evap 25C	-40.976	46.198	-34.645	10.749	-26.07	24.31	9.023	-0.545	2.639	25.894
3/2	MDIW 25C	-40.934	30.283	-35.118	-4.612	-41.413	-11.897	13.825	-0.861	-2.72	62.822
3/4	2xEV 25C	-40.572	71.099	-33.472	34.784	-1.665	82.303	2.754	-0.149	10.762	-27.742
3/6	Evap 25C	-40.924	46.194	-34.596	10.746	-26.068	24.492	10.685	-0.591	2.822	27.534

SEPT. 2015 RUN

Date	Sample Name	δ13C (PDB)	δ18O (raw)	δ18O PDB	δ45	δ46	δ47	δ48	δ49	Δ47	Δ48	Δ49	Window
09/16/15	BB-04-1	2.451	36.17	-3.44	5.804	1.161	6.709	265.885	-11.184	-0.422	262.95	-19.497	2
09/16/15	WBP-03-1	1.858	33.662	-5.85	5.167	-1.26	3.569	55.086	7.228	-0.51	57.75	4.205	2
09/19/15	WBP-03-2	1.757	33.164	-6.33	5.056	-1.741	2.984	18.938	8.795	-0.505	22.495	6.839	2

Transfer Functions:

Window	Start Date	End Date	SlopeEGL	SlopeETF	IntETF
2	9/16/15	09/20/15	0.019941	1.013510	1.063380

Equilibrated and Heated Gasses:

Date	Name	δ13C	δ18O	δ45	δ46	δ47	δ48	δ49	Δ47	Δ48	Δ49
09/09/15	Carrara HG	1.93	33.565	5.23	-1.354	3.107	-4.842	10.752	-0.944	-2.142	7.836
09/09/15	Evap HG	-41.025	43.044	-34.792	7.705	-30.055	15.227	15.939	-1.52	-0.239	39.234

09/10/15	2xEV HG	-41.124	62.552	-34.262	26.534	-11.392	58.422	12.434	-1.227	4.412	-1.927
09/11/15	Ooids HG	4.211	37.333	7.494	2.287	9.176	6.244	9.312	-0.811	1.657	-3.165
09/13/15	Evap HG	-40.955	37.782	-34.896	2.626	-35.1	3.582	18.645	-1.657	-1.669	52.52
09/14/15	Carrara HG	2.047	30.272	5.235	-4.532	-0.057	-12.239	12.214	-0.97	-3.225	15.637
09/16/15	MDIW HG	-40.948	28.142	-35.201	-6.678	-44.467	-18.209	25.052	-1.92	-4.965	79.085
09/18/15	Evap HG	-40.836	35.306	-34.864	0.237	-37.435	-1.935	17.964	-1.768	-2.408	56.723
09/20/15	2xEV HG	-40.944	54.811	-34.34	19.063	-18.703	42.465	12.091	-1.387	3.827	12.242
09/21/15	Carrara HG	1.664	35.612	5.047	0.622	4.957	-0.077	6.751	-0.857	-1.319	0.147
09/22/15	MDIW HG	-41.182	28.147	-35.42	-6.674	-44.746	-17.228	15.402	-1.981	-3.978	69.178
09/24/15	Evap HG	-40.961	43.721	-34.711	8.359	-29.439	17.528	15.117	-1.611	0.728	36.978
09/26/15	Carrara HG	2.253	32.121	5.487	-2.747	1.994	-9.737	16.017	-0.943	-4.275	15.595
09/28/15	Carrara HG	2.304	34.739	5.619	-0.22	4.655	-3.147	12.808	-0.917	-2.708	7.221
09/29/15	MDIW HG	-41.205	23.629	-35.588	-11.035	-49.186	-28.892	18.958	-2.133	-7.101	82.441
09/30/15	2xEV HG	-41.185	60.442	-34.386	24.497	-13.539	55.367	18.968	-1.316	5.501	8.581
10/01/15	Evap HG	-41.227	41.378	-35.036	6.097	-31.974	12.756	9.568	-1.67	0.517	36.242
10/03/15	Carrara HG	2.011	32.542	5.274	-2.342	2.238	-8.564	11.148	-0.881	-3.904	10.149
10/04/15	Ooids HG	4.482	35.953	7.704	0.956	8.141	36.894	8.666	-0.744	34.914	-1.419
09/10/15	Evap 25C #1	-41.578	46.483	-35.202	11.023	-26.436	22.836	19.741	-0.59	0.653	36.878
09/10/15	MDIW 25C	-41.514	30.727	-35.649	-4.184	-41.598	-11.696	25.912	-0.909	-3.374	75.216
09/10/15	2xEV 25C #1	-41.651	70.564	-34.501	34.266	-3.265	76.926	5.528	-0.16	6.749	-22.98
09/10/15	Evap 25C #2	-41.393	46.823	-35.017	11.352	-25.943	23.926	18.537	-0.602	1.068	34.78
09/11/15	2xEV 25C #2	-41.46	71.026	-34.308	34.712	-2.678	77.957	9.134	-0.201	6.845	-20.516
09/13/15	2xEV 25C	-41.414	71.086	-34.262	34.77	-2.579	78.415	10.866	-0.206	7.16	-18.992
09/14/15	Evap 25C	-41.12	47.187	-34.749	11.704	-25.372	25.145	13.03	-0.645	1.563	28.178
09/15/15	MDIW 25C	-41.497	30.287	-35.646	-4.608	-42.056	-12.979	21.576	-0.97	-3.819	71.565
09/17/15	Evap 25C	-41.779	46.155	-35.4	10.706	-27.026	23.638	13.777	-0.676	2.066	31.675
09/18/15	2xEV 25C	-41.396	71.57	-34.231	35.237	-2.112	81.743	7.417	-0.216	9.356	-23.24
09/19/15	MDIW 25C	-41.481	30.102	-35.638	-4.788	-42.282	-13.146	17.729	-1.038	-3.628	67.898
09/20/15	Evap 25C	-41.688	46.366	-35.309	10.911	-26.753	23.461	15.683	-0.692	1.487	33.1
09/21/15	MDIW 25C	-41.514	30.119	-35.667	-4.771	-42.278	-12.578	16.575	-1.019	-3.089	66.687

09/23/15	Evap 25C	-41.353	46.822	-34.979	11.351	-25.988	24.656	15.46	-0.687	1.784	31.614
09/24/15	2xEV 25C	-41.087	70.614	-33.97	34.315	-2.683	80.946	5.866	-0.191	10.41	-23.318
09/26/15	MDIW 25C	-41.211	30.517	-35.371	-4.386	-41.71	-11.501	13.129	-1.123	-2.772	61.917
09/27/15	Evap 25C	-41.134	46.685	-34.778	11.219	-25.946	25.769	9.714	-0.732	3.134	25.809
09/28/15	2xEV 25C	-41.052	71.223	-33.919	34.903	-2.118	82.517	10.932	-0.239	10.73	-19.55
09/29/15	MDIW 25C	-41.303	30.925	-35.444	-3.992	-41.382	-11.693	18.797	-1.091	-3.754	67.114
10/01/15	Evap25C	-41.313	46.206	-34.961	10.757	-26.542	23.783	11.944	-0.698	2.108	29.209
10/02/15	2xEV 25C	-41.274	70.704	-34.143	34.402	-2.796	81.087	7.958	-0.201	10.373	-21.26
10/06/15	Evap 25C	-41.267	46.489	-34.909	11.03	-26.282	23.757	14.901	-0.752	1.541	31.609

* Not used: bad data.

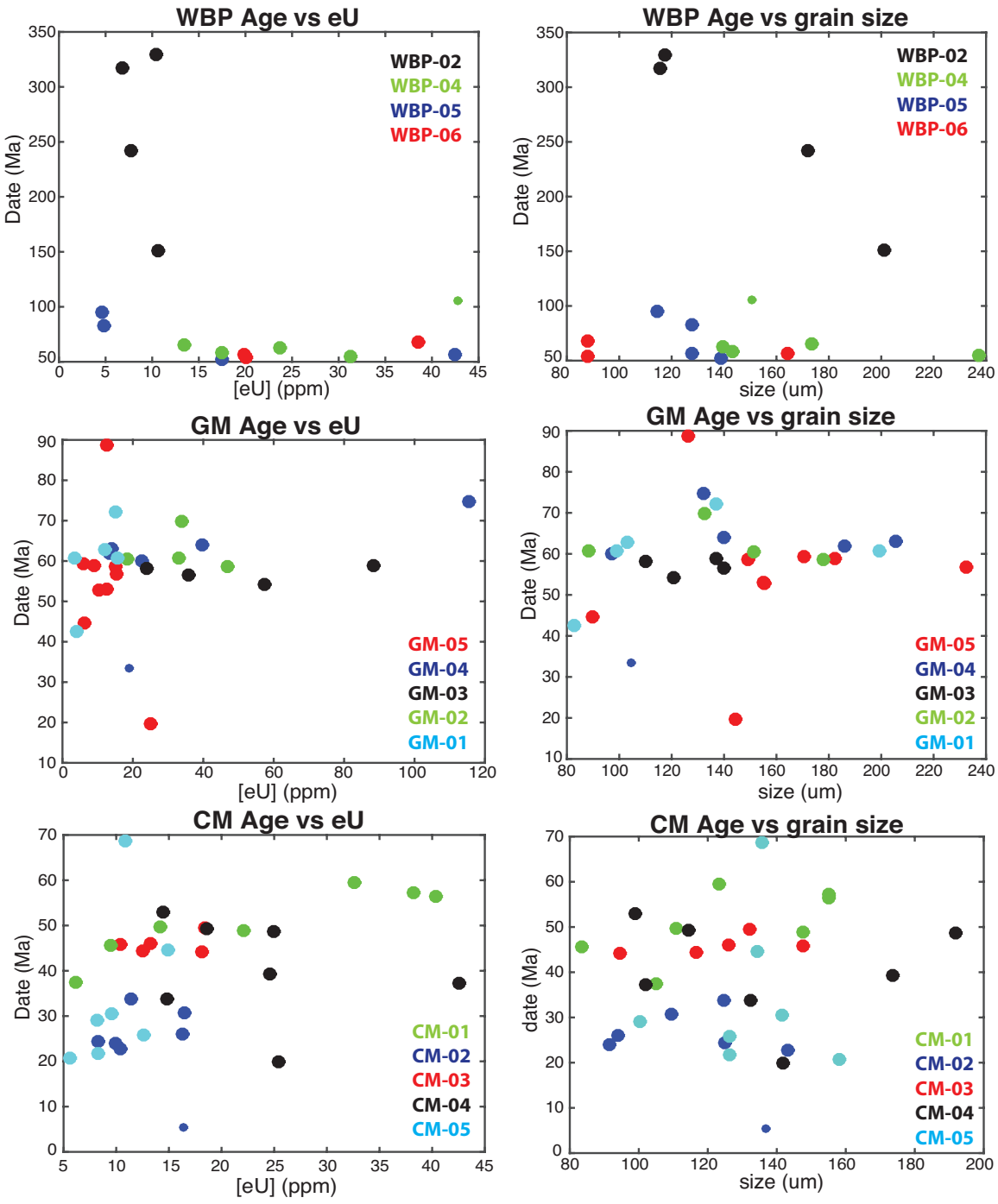

Figure D1: Plots show eU (left column) and grain size (right column) plotted against the reported AHe date for each grain analyzed in each transect. Color corresponds to separate grains from the same sample. Large circles represent grains used in the mean age calculation and small circles are outliers at 95% confidence. Data for samples WBP, GM, and CM (see table D1)

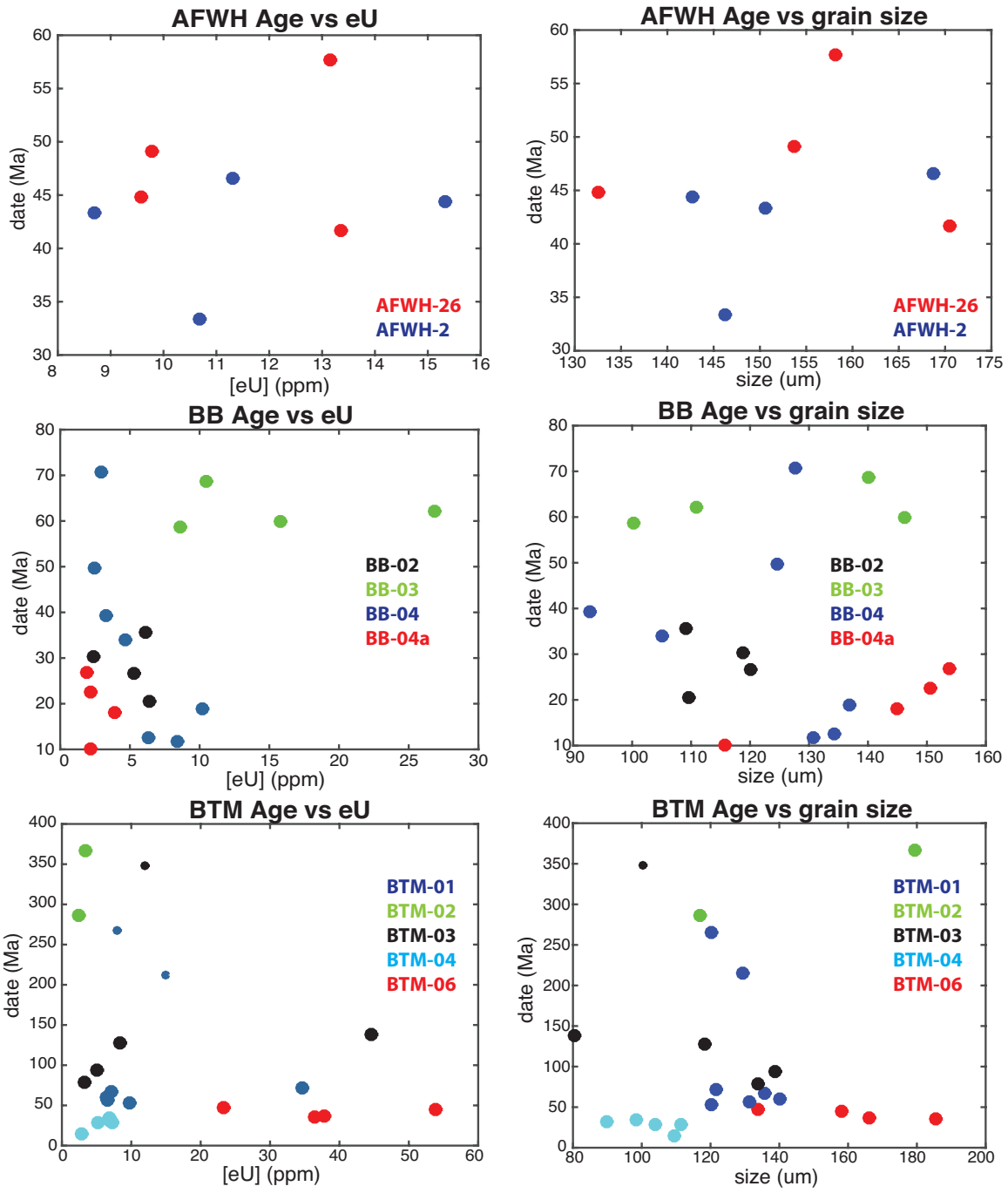

Figure D1 continued: Data for samples AFWH, BB, and BTM (see table D1)

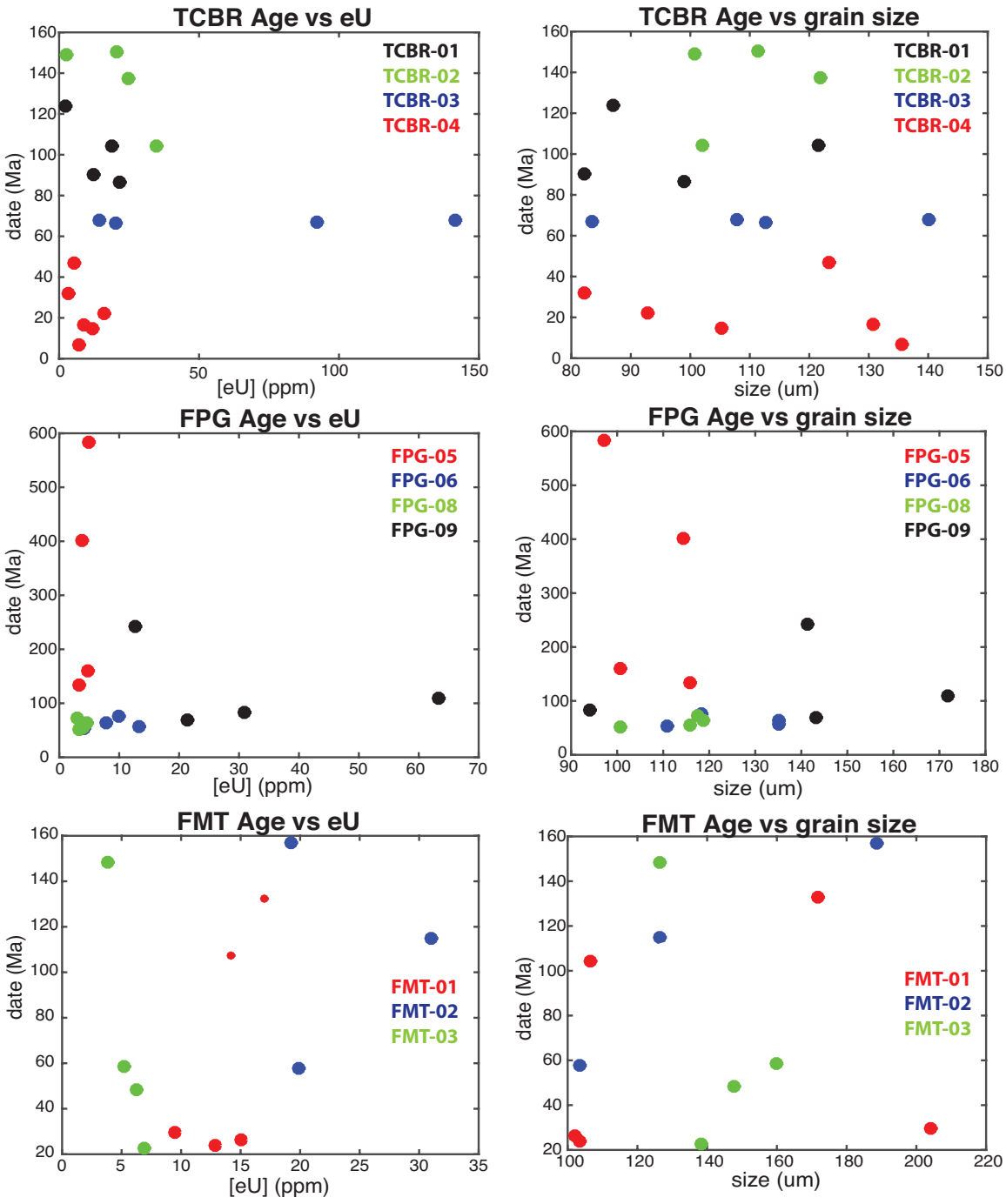

Figure D1 continued: Data for samples TCBR, FPG, and FMT (see table D1)

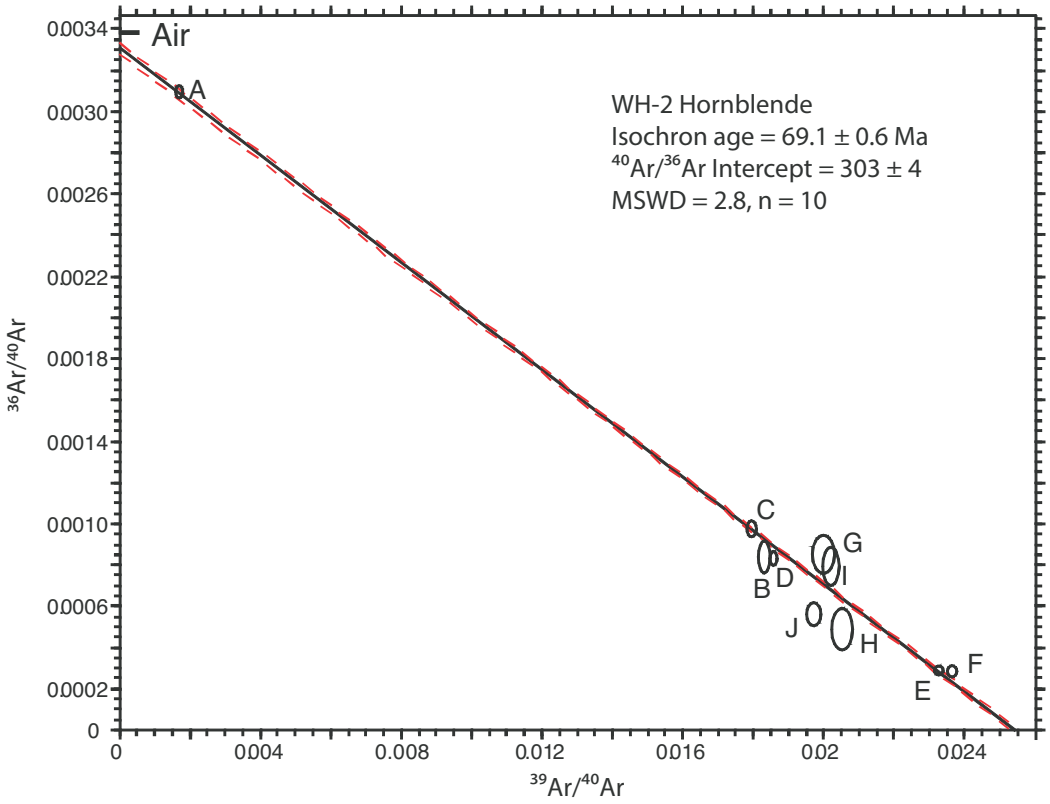

Figure D2: WH-2 hornblende isotope correlation diagram. Age spectrum discordance may be from minor excess argon contamination, as suggested by the data array.

Figure D3: Plots showing the variation of bulk susceptibility as a function of increasing (heating, indicated by red data points and line) and decreasing (cooling, indicated by blue data points and line) temperature for powders (about 0.75 gm each) prepared from fragments of core samples from selected sites collected from the Whitehorn Granodiorite. All runs are conducted in an inert (argon) atmosphere. “mg” denotes a magnetic separate, in which case about 0.1 to 0.2 gms of powder was used.

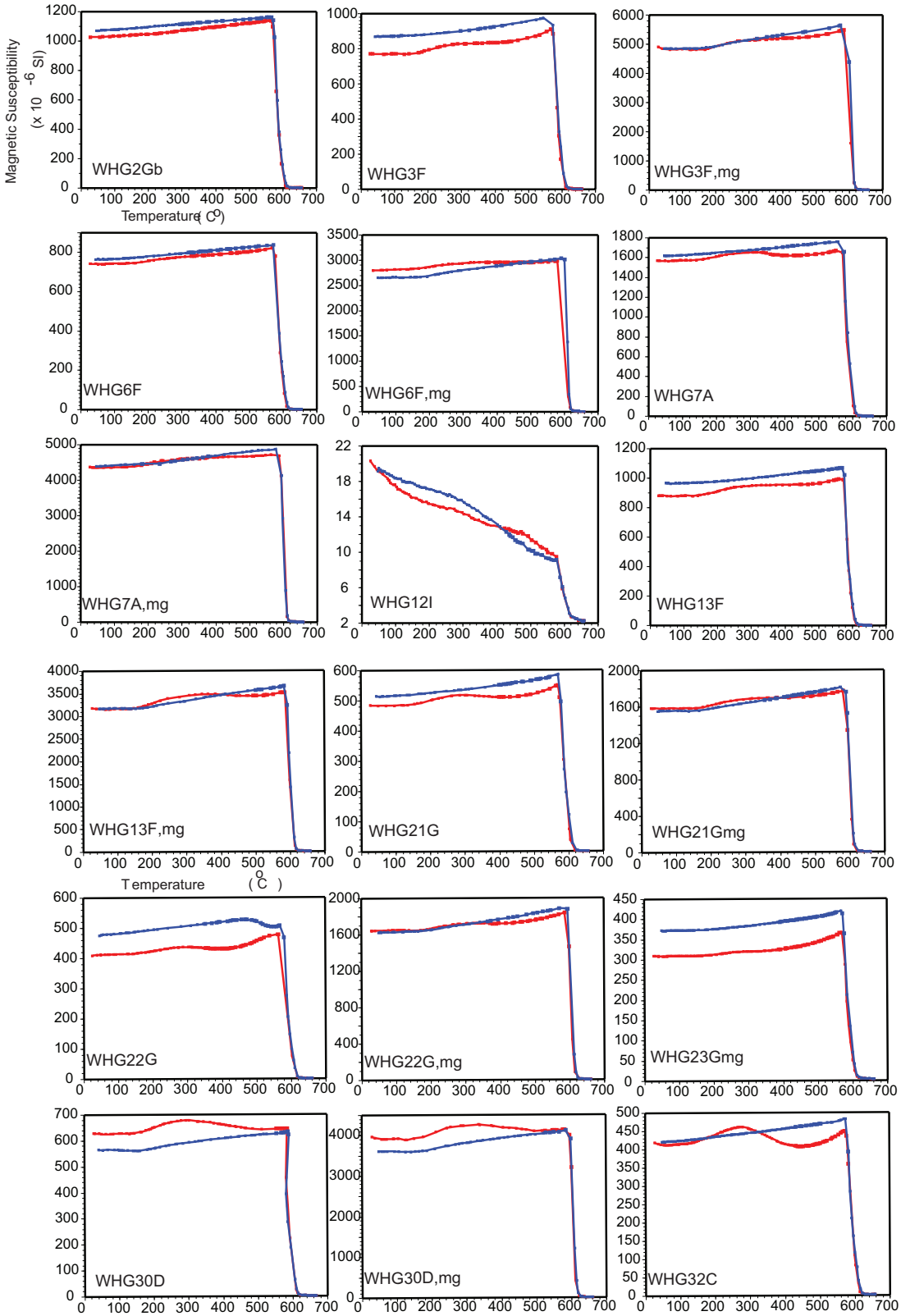
Magnetic Susceptibility (x 10 -6 SI)
Temperature (C°)
WHG2Gb
WHG3F
WHG3F,mg
WHG6F
WHG6F,mg
WHG7A
WHG7A,mg
WHG12I
WHG13F
WHG13F,mg
WHG21G
WHG21Gmg
Temperature (°C)
WHG22G
WHG22G,mg
WHG23Gmg
WHG30D
WHG30D,mg
WHG32C

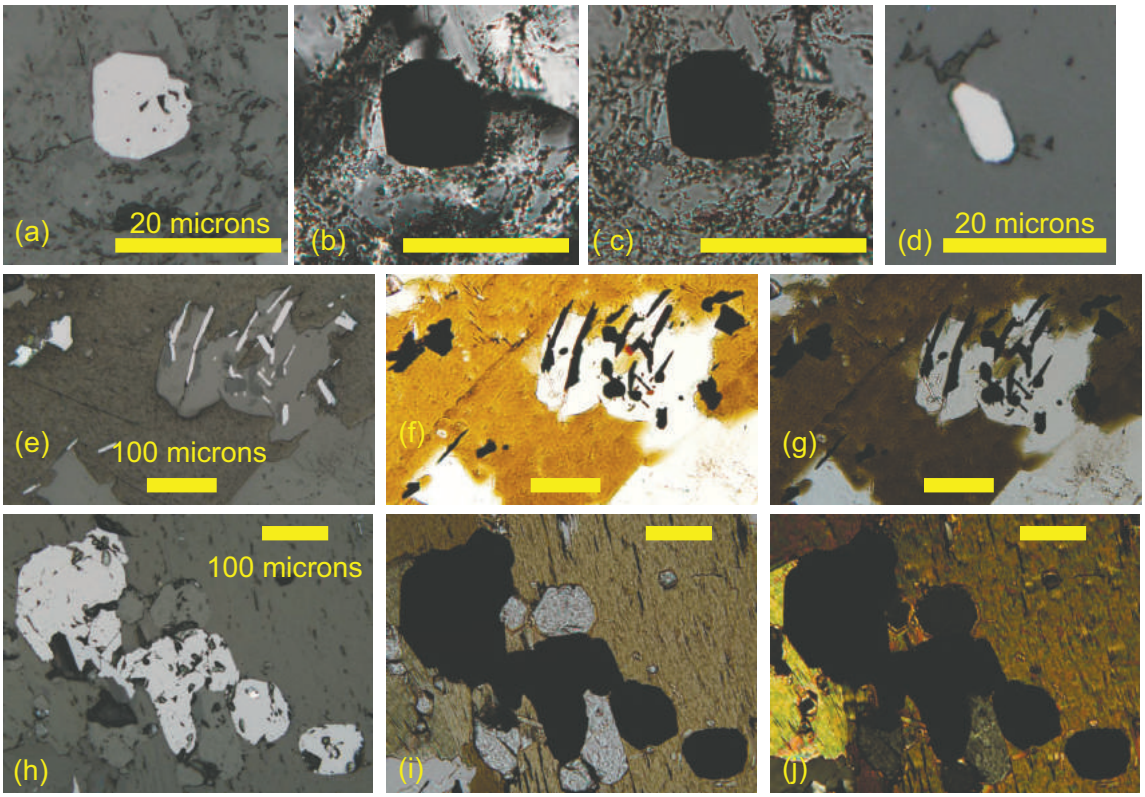

Figure D4: Transmitted and reflected light photomicrographs showing typical, representative paragenesis of iron titanium oxide assemblages in the Whitehorn Granodiorite. In most examples, a transmitted light (uncrossed polars), transmitted light (crossed polars), and reflected light image of the identical area are shown.

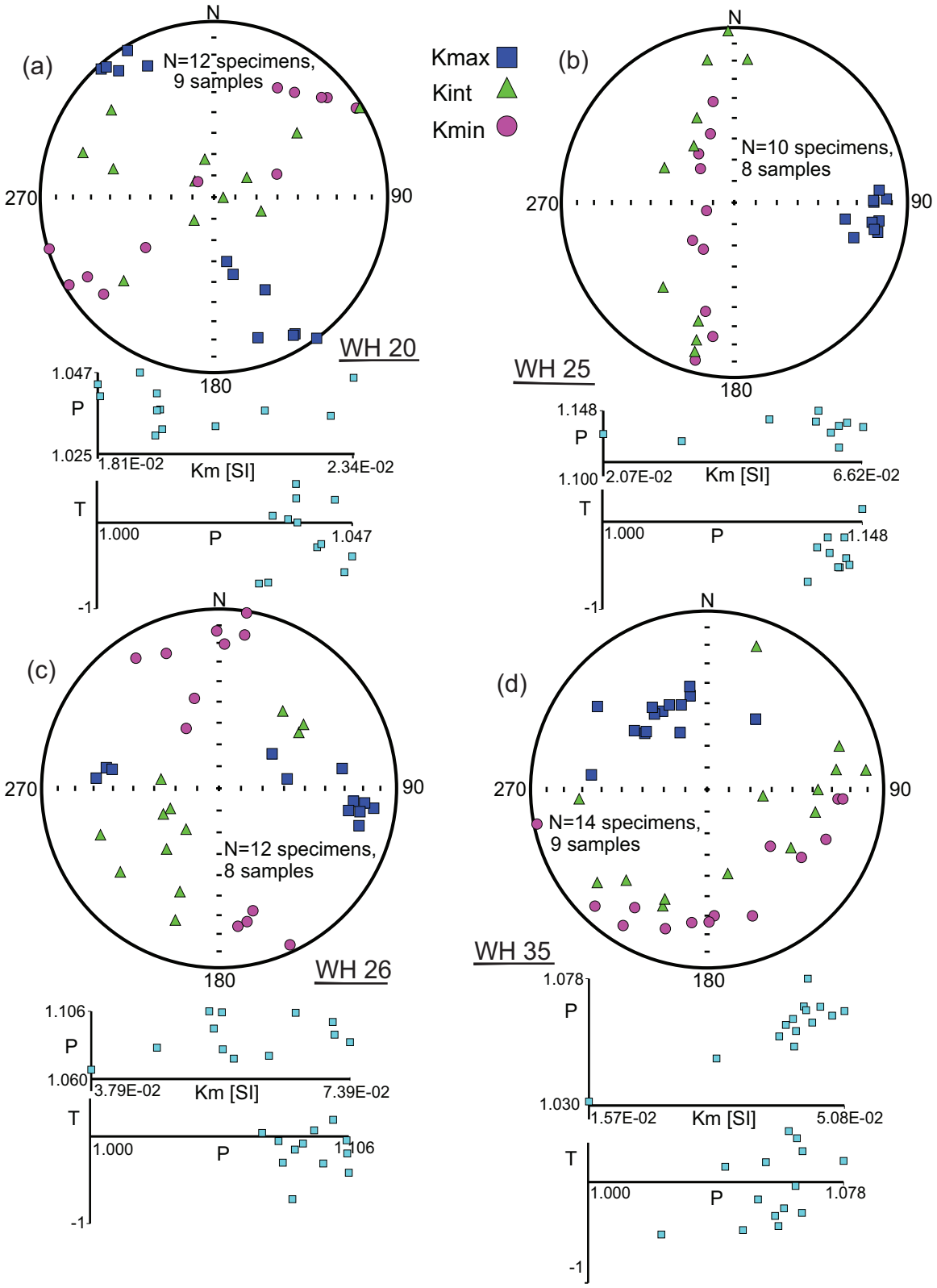
(a)
N=12 specimens,
9 samples
N
270
90
180
Kmax
Kint
Kmin
WH 20
1.047
P
1.025
1.81E-02
Km [SI]
2.34E-02
T
1.000
P
1.047
-1
(b)
N=10 specimens,
8 samples
N
270
90
180
WH 25
1.148
P
1.100
2.07E-02
Km [SI]
6.62E-02
T
1.000
P
1.148
-1
(c)
N=12 specimens,
8 samples
N
270
90
180
WH 26
1.106
P
1.060
3.79E-02
Km [SI]
7.39E-02
T
1.000
P
1.106
-1
(d)
N=14 specimens,
9 samples
N
270
90
180
WH 35
1.078
P
1.030
1.57E-02
Km [SI]
5.08E-02
T
1.000
P
1.078
-1

Figure D5: Anisotropy of magnetic susceptibility (AMS) data from representative sites in the Whitehorn Granodiorite (a, b, c, d). Examples of data from individual sites in the granodiorite, with equal area projection of directions of maximum, intermediate, and minimum principal susceptibility axes for each specimen (all on lower hemisphere). Also shown are plots of the anisotropy parameter P (anisotropy degree, Kmax/Kmin) vs. bulk susceptibility (Km) and the T parameter (shape parameter,T = (ln L – ln F) / (lnL + ln F), where L Kmax/Kint and F is Kint/Kmin) is plotted against P.

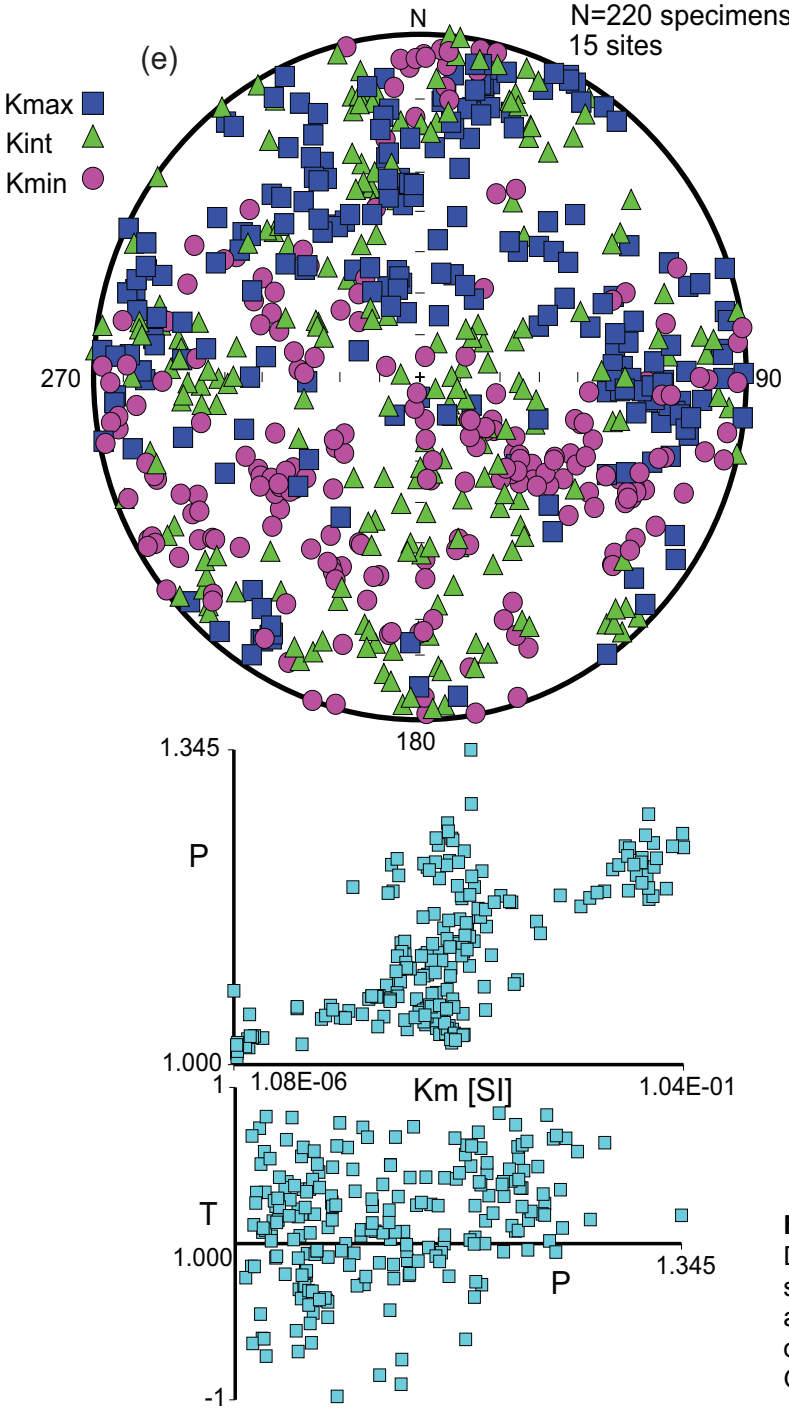

Figure D5 continued: (e) Data from a collection of sites (N = 15) distributed across the exposed area of the Whitehorn Granodiorite.

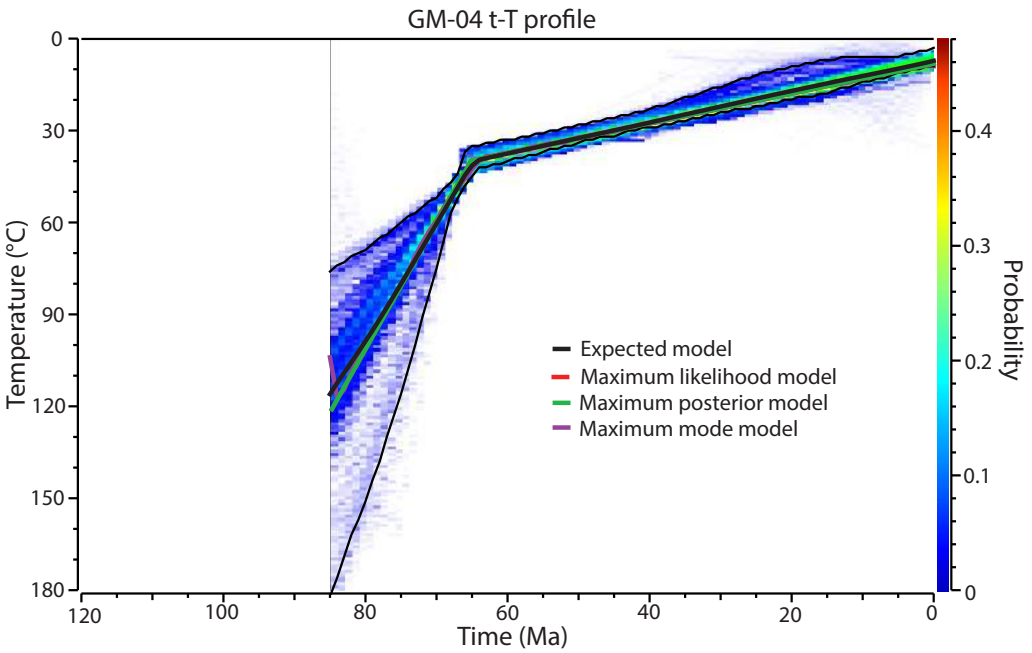

Figure D6: QTQt time-Temperature model for sample GM-04 with both apatite and zircon He data.

REFERENCES

Arne, D.C., Green, P.F., and Duddy, I.R., 1990, Thermochronologic constraints on the timing of Mississippi Valley–type ore formation from apatite fission track analysis: International Journal of Radiation Applications and Instrumentation, Part D: Nuclear Tracks and Radiation Measurements, v. 17, p. 319–323, doi:10.1016/1359-0189 (90)90053-Z.

Ault, A.K., Frenzel, M., Reiners, P.W., Woodcock, N.H., and Thomson, S.N., 2016, Record of paleo-fluid circulation in faults revealed by hematite (U-Th)/He and apatite fission-track dating: An example from Gower Peninsula fault fissures, Wales: Lithosphere, v. 8, p. 379– 385, doi:10.1130/L522.1.

Baars, D.L., and Stevenson, G.M., 1984, The San Luis uplift, Colorado and New Mexico—An enigma of the ancestral Rockies: The Mountain Geologist, v. 21, p. 57–67.

Babault, J., Bonnet, S., Driessche, J.V.D., and Crave, A., 2007, High elevation of low-relief surfaces in mountain belts: Does it equate to post-orogenic surface uplift?: Terra Nova, v. 19, p. 272–277, doi:10.1111/j.1365-3121.2007.00746.x.

Baldwin, J.A., Whipple, K.X., and Tucker, G.E., 2003, Implications of the shear stress river incision model for the timescale of post-orogenic decay of topography: Journal of Geophysical Research, v. 108, p. 2158, doi:10.1029/2001JB000550.

Bedford, L.M., 1994, Linkages of Laramide thrusts, Northern Sangre de Cristo Range, Colorado [M.S. thesis]: Tucson, University of Arizona, 39 p.

Bird, P., 1984, Laramide crustal thickening event in the Rocky Mountain foreland and Great Plains: Tectonics, v. 3, p. 741–758, doi:10.1029/TC003i007p00741.

Blackburn, T.J., Bowring, S.A., Perron, J.T., Mahan, K.H., Dudas, F.O., and Barnhart, K.R., 2012, An exhumation history of continents over billion-year time scales: Science, v. 335, no. 6064, p. 73–76, doi:10.1126/science.1213496.

Blakey, R.C., 1996, Permian eolian deposits, sequences, and sequence boundaries, Colorado Plateau, in Sonnenfeld, M.D., and Longman, M.W., eds., Paleozoic systems of the Rocky Mountain region: Rocky Mountain Section, Society for Sedimentary Geology, p. 405–426.

Blakey, R.C., 2008, Pennsylvanian-Jurassic sedimentary basins of the Colorado Plateau and southern Rocky Mountains, in Miall, A.D., ed., Sedimentary basins of United States and Canada: Amsterdam, Elsevier, p. 245–296, doi:10.1016/S1874-

5997(08)00007-5.

Blakey, R.C., Peterson, F., and Kocurek, G., 1988, Late Paleozoic and Mesozoic eolian deposits of the Western Interior of the United States: Sedimentary Geology, v. 56, p. 3–125, doi:10.1016/0037-0738(88)90050-4.

Boddy, R., and Smith, G., 2010, Effective experimentation: For scientists and technologists: Chichester, West Sussex, U.K., John Wiley, 257 p., doi:10.1002/9780470666654.

Brady, R., Wernicke, B.P., and Fryxell, J., 2000, Kinematic evolution of a large-offset continental normal fault system, South Virgin Mountains, Nevada: Geological Society of America Bulletin, v. 112, p. 1375–1397, doi:10.1130/0016-7606(2000)112<1375:KEOALO>2.0.CO;2.

Brewer, J.A., Allmendinger, R.W., Brown, L.D., Oliver, J.E., and Kaufman, S., 1982, COCORP profiling across the Rocky Mountain Front in southern Wyoming, Part 1: Laramide structure: Geological Society of America Bulletin, v. 93, p. 1242–1252, doi:10.1130/0016-7606(1982)93<1242:CPATRM>2.0.CO;2.

Bryant, B., 1966, Possible window in the Elk Range thrust sheet near Aspen, Colorado: U.S. Geological Survey Professional Paper 550-D, p. D1–D7.

Bryant, B., and Naeser, C.W., 1980, The significance of fission track ages of apatite in relation to the tectonic history of the Front Range and the Sawatch Range, Colorado: Geologic Society of America Bulletin, v. 91, p. 156–164, doi:10.1130/0016-7606(1980)91<156:TSOFAO>2.0.CO;2.

Chapin, C.E., and Kelley, S. A., 1997, The Rocky Mountain erosion surface in the Front Range of Colorado, in Colorado Front Range guidebook: Denver, Colorado, Rocky Mountain Association of Geologists, p. 101–114.

Chapin, C.E., and Lowell, G.R., 1979, Primary and secondary flow structures in ash-flow tuffs of the Gribbles Run paleovalley, central Colorado, in Chapin, C.E., and Elston, W.E., eds., Ash-flow tuffs: Geological Society of America Special Paper 180, p. 137–154, doi:10.1130/SPE180-p137.

Chapin, C.E., Wilks, M., and McIntosh, W.C., 2004, Space-time patterns of Late Cretaceous to present magmatism in New Mexico—Comparison with Andean volcanism and potential for future volcanism, in Cather, S.M., et al., eds., Tectonics, geochronology, and volcanism in the southern Rocky Mountains and Rio Grande Rift: New Mexico Bureau of Geology and Mineral Resources Bulletin, v. 160, p. 13–40.

Chualaowanich, T., 1997, Geochemical characteristics and magma evolution of the Whitehorn Stock, Chaffee, Fremont, and Park Counties, Colorado [M.S. thesis]: Golden, Colorado School of Mines, 312 p.

Clayton, R.N., Friedman, I., Graf, D.L., Mayeda, T.K., Meents, W.F., and Shimp, N.F., 1966, The origin of saline formation waters: 1. Isotopic composition: Journal of Geophysical Research, v. 71, p. 3869–3882, doi:10.1029/JZ071i016p03869.

Cole, J.C., Trexler, J.H., Cashman, P.H., Miller, I.M., Shroba, R.R., Cosca, M.A., and

Workman, J.B., 2010, Beyond Colorado's Front Range—A new look at Laramide basin subsidence, sedimentation, and deformation in north-central Colorado, in Morgan, L.A., and Quane, S.L., eds., Through the generations: Geologic and anthropogenic field excursions in the Rocky Mountains from modern to ancient: Geological Society of America Field Guide 18, p. 55–76, doi:10.1130/2010.0018(03).

Dean, R.B., and Dixon, W.J., 1951, Simplified statistics for small numbers of observations: Analytical Chemistry, v. 23, p. 636–638, doi:10.1021/ac60052a025.

DeCelles, P.G., 2004, Late Jurassic to Eocene evolution of the Cordilleran thrust belt and foreland basin system, western U.S.A.: American Journal of Science, v. 304, p. 105–168, doi:10.2475/ajs.304.2.105.

Defliese, W.F., Hren, M.T., and Lohmann, K.C., 2015, Compositional and temperature effects of phosphoric acid fractionation on Δ47 analysis and implications for discrepant calibrations: Chemical Geology, v. 396, p. 51–60, doi:10.1016/j.chemgeo.2014.12.018.

Dennis, K.J., Affek, H., Passey, B.H., Schrag, D.P., and Eiler, J.M., 2011, Defining an absolute reference frame for 'clumped' isotope studies of CO2: Geochimica et Cosmochimica Acta, v. 75, p. 7117–7131, doi:10.1016/j.gca.2011.09.025.

DeVoto, R.H., 1990, Paleozoic stratigraphy, tectonism, thermal history, and basin evolution of central Colorado, in Beaty, D.W., et al., eds., Carbonate-hosted sulfide deposits of the central Colorado Mineral Belt: Economic Geology Monograph, v. 7, p. 29–44, doi:10.5382/Mono.07.03.

Dickinson, W.R., Klute, M.A., Hayes, M.J., Janecke, S.U., Lundin, M.A., McKittrick, M.A., and Olivares, M.D., 1988, Paleogeographic and paleotectonic setting of Laramide sedimentary basins in the central Rocky Mountain region: Geological Society of America Bulletin, v. 100, p. 1023–1039, doi:10.1130/0016-7606(1988)100<1023:PAPSOL>2.3.CO;2.

Diehl, J.F., Beck, M.E., Beske-Diehl, S., Jacobson, D., and Hearn, B.C., 1983, Paleomagnetism of the Late Cretaceous–early Tertiary north-central Montana alkalic province: Journal of Geophysical Research, v. 88, p. 10593–10609, doi:10.1029/JB088iB12p10593.

Egholm, D.L., Nielsen, S.B., Pedersen, V.K., and Lesemann, J.E., 2009, Glacial effects limiting mountain height: Nature, v. 460, no. 7257, p. 884–887, https:// doi .org /10 .1038 /nature08263. Egholm, D.L., Knudsen, M.F., and Sandiford, M., 2013, Lifespan of mountain ranges scaled by feedbacks between land sliding and erosion by rivers: Nature, v. 498, no. 7455, p. 475–478, doi:10.1038/nature12218.

Ehlers, T.A., 2005, Crustal thermal processes and the interpretation of thermochronometer data: Reviews in Mineralogy and Geochemistry, v. 58, p. 315–350, doi:10.2138/rmg.2005.58.12.

Epis, R.C., and Chapin, C.E., 1974, Stratigraphic nomenclature of the Thirty-nine Mile Volcanic Field, central Colorado: U.S. Geological Survey Bulletin 1395C, 32 p.

Epis, R.C., and Chapin, C.E., 1975, Geomorphic and tectonic implications of the post-Laramide, late Eocene erosion surface in the southern Rocky Mountains, in Curtis, B.F., ed., Cenozoic history of the southern Rocky Mountains: Geological Society of America Memoir 144, p. 45–74, doi:10.1130/MEM144-p45.

Epis, R.C., Scott, G.R., Taylor, R.B., and Chapin, C.E., 1976, Cenozoic volcanic, tectonic, and geomorphic features of central Colorado, in Epis, R.C., and Weimer, R. J., eds., Studies in Colorado field geology: Colorado School of Mines Professional Contribution no. 8, p. 323–338.

Fan, M., Hough, B.G., and Passey, B.H., 2014, Middle to late Cenozoic cooling and high topography in the central Rocky Mountains: Constraints from clumped isotope geochemistry: Earth and Planetary Science Letters, v. 408, p. 35–47, doi:10.1016/j.epsl.2014.09.050.

Farley, K.A., 2002, (U-Th)/He dating: Techniques, calibrations, and applications: Reviews in Mineralogy and Geochemistry, v. 47, p. 819–844, doi:10.2138/rmg.2002.47.18.

Fischer, K.M., 2002, Waning buoyancy in the crustal roots of old mountains: Nature, v. 417, no. 6892, p. 933–936, https://doi.org/10.1038/nature00855.

Fisher, R., 1953, Dispersion on a sphere: In Proceedings of the Royal Society of London A: Mathematical, Physical and Engineering Sciences, The Royal Society, v. 217, n. 1130, p. 295-305, doi:10.1098/rspa.1953.0064.

Fitzgerald, P.G., and Gleadow, A.J.W., 1990, New approaches in fission-track geochronology as a tectonic tool: Examples from the transantarctic mountains: International Journal of Radiation Applications and Instrumentation, Part D: Nuclear Tracks and Radiation Measurements, v. 17, p. 351–357, doi:10.1016/1359-0189(90)90057-5.

Fitzgerald, P.G., Baldwin, S.L., Webb, L.E., and O'Sullivan, P.B., 2006, Interpretation of (U–Th)/He single grain ages from slowly cooled crustal terranes: A case study from the Transantarctic Mountains of southern Victoria Land: Chemical Geology, v. 225, p. 91–120, doi:10.1016/j.chemgeo.2005.09.001.

Flowers, R.M., Shuster, D.L., Wernicke, B.P., and Farley, K.A., 2007, Radiation damage control on apatite (U-Th)/He dates from the Grand Canyon region, Colorado Plateau: Geology, v. 35, p. 447–450, doi:10.1130/G23471A.1.

Flowers, R.M., Ketcham, R.A., Shuster, D.L., and Farley, K.A., 2009, Apatite (U-Th)/He thermochronometry using a radiation damage accumulation and annealing model: Geochimica et Cosmochimica Acta, v. 73, p. 2347–2365, doi:10.1016/j.gca.2009.01.015.

Flowers, R.M., Farley, K.A., and Ketcham, R.A., 2015, A reporting protocol for thermochronologic modeling illustrated with data from the Grand Canyon: Earth and Planetary Science Letters, v. 432, p. 425–435, doi:10.1016/j.epsl.2015.09.053.

Foster, D.A., Harrison, T.M., Miller, C.F., and Howard, K.A., 1990, The $^{40}Ar/^{39}Ar$ thermochronology of the eastern Mojave Desert, California, and adjacent western

Arizona with implications for the evolution of metamorphic core complexes: Journal of Geophysical Research, v. 95, p. 20,005–20,024, doi:10.1029/JB095iB12p20005.

Foster, D.A., Murphy, J.M., and Gleadow, A.J.W., 1994, Middle Tertiary hydrothermal activity and uplift of the northern flinders ranges, South Australia: Insights from apatite fission track thermochronology: Australian Journal of Earth Sciences, v. 41, p. 11–17, doi:10.1080/08120099408728108.

Frankel, K.L., and Pazzaglia, F.J., 2006, Mountain fronts, base-level fall, and landscape evolution: Insights from the southern Rocky Mountains, in Willett, S.D., et al., eds., Tectonics, climate, and landscape evolution: Geological Society of America Special Paper 398, p. 419–434, doi:10.1130/2006.2398(26).

Fridrich, C.J., DeWitt, E., Bryant, B., Richard, S., and Smith, R.P., 1998, Geologic map of the Collegiate Peaks Wilderness Area and the Grizzly Peak Caldera, Sawatch Range, central Colorado: U.S. Geological Survey Miscellaneous Investigations Map MI I-2565, scale 1:50,000. Friedman, I., and O'Neil, J.R., 1977, Compilation of stable isotope fractionation factors of geochemical interest: U.S. Geological Survey Professional Paper 440-KK, 11 p.

Galbraith, R.F., and Laslett, G.M., 1993, Statistical models for mixed fission track ages: Nuclear Tracks and Radiation Measurements, v. 21, p. 459–470, doi:10.1016/1359-0189(93)90185-C.

Gallagher, K., 1995, Evolving temperature histories from apatite fission-track data: Earth and Planetary Science Letters, v. 136, p. 421–435, doi:10.1016/0012-821X(95)00197-K.

Gallagher, K.L., 1998, The subsidence history and thermal state of the Eromanga and Cooper Basins [Ph.D. thesis]: Canberra, Australian National University, 82 p.

Gallagher, K., 2012, Trans dimensional inverse thermal history modeling for quantitative thermochronology: Journal of Geophysical Research, v. 117, B02408, doi:10.1029/2011JB008825.

Gautheron, C., Tassan-Got, L., Barbarand, J., and Pagel, M., 2009, Effect of alpha-damage annealing on apatite (U-Th)/He thermochronology: Chemical Geology, v. 266, p. 157–170, doi:10.1016/j.chemgeo.2009.06.001.

Gazis, C., Taylor, H.P., Hon, K., and Tsvetkov, A., 1996, Oxygen isotopic and geochemical evidence for a short-lived, high-temperature hydrothermal event in the Chegem caldera, Caucasus Mountains, Russia: Journal of Volcanology and Geothermal Research, v. 73, p. 213–244, doi:10.1016/0377-0273(96)00023-6.

Gehrels, G., and Pecha, M., 2014, Detrital zircon U-Pb geochronology and Hf isotope geochemistry of Paleozoic and Triassic passive margin strata of western North America: Geosphere, v. 10, n. 1, p. 49–65, doi:10.1130/GES00889.1.

Geissman, J.W., and Harlan, S.S., 2002, Late Paleozoic remagnetization of Precambrian crystalline rocks along the Precambrian/Carboniferous nonconformity, Rocky Mountains: A relationship among deformation, remagnetization, and fluid migration: Earth and Planetary Science Letters, v. 203, p. 905–924,

doi:10.1016/S0012-821X(02)00932-9.

Gradstein, F.M., Ogg, J.G., Schmitz, M., and Ogg, G., eds., 2012, The geologic time scale 2012: Boston, Elsevier, 1176 p.

Gregory, K.M., and Chase, C.G., 1992, Tectonic significance of paleobotanically estimated climate and altitude of the late Eocene erosion surface, Colorado: Geology, v. 20, p. 581–585, doi:10.1130/0091-7613(1992)020 <0581: TSOPEC>2.3.CO;2.

Gregory, K.M., and Chase, C.G., 1994, Tectonic and climatic significance of a late Eocene low-relief, high-level geomorphic surface, Colorado: Journal of Geophysical Research, v. 99, p. 20,141–20,160, doi:10.1029/94JB00132.

Gregory, K.M., and McIntosh, W.C., 1996, Paleoclimate and paleoelevation of the Oligocene Pitch-Pinnacle flora, Sawatch Range, Colorado: Geological Society of America Bulletin, v. 108, p. 545–561, doi:10.1130/0016-7606(1996)108<0545:PAPOTO>2.3.CO;2.

Hamilton, W.B., 1988, Laramide crustal shortening, in Schmidt, C.J., and Perry, W.J., Jr., eds., Interaction of the Rocky Mountain foreland and the Cordilleran thrust belt: Geological Society of America Memoir 171, p. 27–40, doi:10.1130/MEM171-p27.

Heller, P.L., and Liu, L., 2016, Dynamic topography and vertical motion of the US Rocky Mountain region prior to and during the Laramide orogeny: Geological Society of America Bulletin, v. 128, p. 973–988, doi:10.1130/B31431.1.

Henkes, G.A., Passey, B.H., Grossman, E.L., Shenton, B.J., Pérez-Huerta, A., and Yancey, T.E., 2014, Temperature limits for preservation of primary calcite clumped isotope paleotemperatures: Geochimica et Cosmochimica Acta, v. 139, p. 362–382, doi:10.1016/j.gca.2014.04.040.

Hickey, K.A., Barker, S.L., Dipple, G.M., Arehart, G.B., and Donelick, R.A., 2014, The brevity of hydrothermal fluid flow revealed by thermal halos around giant gold deposits: Implications for Carlin-type gold systems: Economic Geology and the Bulletin of the Society of Economic Geologists, v. 109, p. 1461–1487, doi:10.2113/econgeo.109.5.1461.

Holt, E.W., and Taylor, H.P., 1998, 18O/16O mapping and hydrogeology of a short-lived (≈10 years) fumarolic (>500Åã C) meteoric-hydrothermal event in the upper part of the 0.76 Ma Bishop Tuff outflow sheet, California: Journal of Volcanology and Geothermal Research, v. 83, p. 115–139, doi:10.1016/S0377-0273(98)00014-6.

Hon, K., 1984, Geology of volcanogenic uranium deposits within the Tallahassee Creek Conglomerate, Tallahassee Creek uranium district, Colorado: U.S. Geological Survey Open- File Report 84-219, 58 p.

Hourigan, J.K., Reiners, P.W., and Brandon, M.T., 2005, U-Th zonation-dependent alpha-ejection in (U-Th)/He chronometry: Geochimica et Cosmochimica Acta, v. 69, p. 3349–3365, doi:10.1016/j.gca.2005.01.024.

House, M.A., Wernicke, B.P., Farley, K.A., and Dumitru, T.A., 1997, Cenozoic thermal

evolution of the central Sierra Nevada, California, from (U-Th)/He thermochronometry: Earth and Planetary Science Letters, v. 151, p. 167–179, doi:10.1016/S0012-821X(97)81846-8.

House, M.A., Wernicke, B.P., and Farley, K.A., 2001, Paleo-geomorphology of the Sierra Nevada, California, from (U-Th)/He ages in apatite: American Journal of Science, v. 301, p. 77–102, doi:10.2475/ajs.301.2.77.

Ibanez-Mejia, M., Pullen, A., Arenstein, J., Gehrels, G.E., Valley, J., Ducea, M.N., Mora, A.R., Pecha, M., and Ruiz, J., 2015, Unraveling crustal growth and reworking processes in complex zircons from orogenic lower-crust: The Proterozoic Putumayo orogen of Amazonia: Precambrian Research, v. 267, p. 285–310, doi:10.1016/j.precamres.2015.06.014.

Irving, E., and Irving, G.A., 1982, Apparent polar wander paths from Carboniferous through Cenozoic and the assembly of Gondwana: Geophysical Surveys, v. 5, p. 141–188, doi:10.1007/BF01453983.

Jacob, A.F., and Albertus, R.G., 1985, Thrusting, petroleum seeps, and seismic exploration: Front Range south of Denver, Colorado, in Macke, D.L., and Maughan, E.K., eds., Rocky Mountain Section field trip guide 1985: Rocky Mountain Section, Society of Economic Paleontologists and Mineralogists, p. 77–96.

Johnson, R.B., 1959, Geology of the Huerfano Park area, Huerfano and Custer Counties, Colorado: U.S. Geological Survey Bulletin 1071-D, 118 p.

Jolivet, M., et al., 2007, Mongolian summits: An uplifted, flat, old but still preserved erosion surface: Geology, v. 35, p. 871–874, doi:10.1130/G23758A.1.

Jones, C.H., Mahan, K.H., Butcher, L.A., Levandowski, W.B., and Farmer, G.L., 2015, Continental uplift through crustal hydration: Geology, v. 43, p. 355–358, doi:10.1130/G36509.1.

Karlstrom, K.E., Crow, R., Crossey, L.J., Coblentz, D., and Van Wijk, J.W., 2008, Model for tectonically driven incision of the younger than 6 Ma Grand Canyon: Geology, v. 36, p. 835–838, doi:10.1130/G25032A.1.

Karlstrom, K.E., et al., 2012, Mantle-driven dynamic uplift of the Rocky Mountains and Colorado Plateau and its surface response: Toward a unified hypothesis: Lithosphere, v. 4, p. 3–22, doi:10.1130/L150.1.

Keating, G.N., 2005, The role of water in cooling ignimbrites: Journal of Volcanology and Geothermal Research, v. 142, p. 145–171, doi:10.1016/j.jvolgeores.2004.10.019.

Keith, T.E., 1991, Fossil and active fumaroles in the 1912 eruptive deposits, Valley of Ten Thousand Smokes, Alaska: Journal of Volcanology and Geothermal Research, v. 45, p. 227–254, doi:10.1016/0377-0273(91)90061-4.

Keith, T.E.C., Thompson, J.M., Hutchinson, R.A., and White, L.D., 1992, Geochemistry of waters in the Valley of Ten Thousand Smokes region, Alaska: Journal of Volcanology and Geothermal Research, v. 49, p. 209–231, doi:10.1016/0377-

0273(92)90015-6.

Keller, G.R., and Baldridge, W.S., 1999, The Rio Grande Rift: A geological and geophysical overview: Rocky Mountain Geology, v. 34, p. 121–130, doi:10.2113/34.1.121.

Kelley, S.A., and Chapin, C.E., 1995, Apatite fission-track thermochronology of southern Rocky Mountain–Rio Grande Rift–Western High Plains Provinces, in Bauer, P.W., et al., eds., Geology of the Santa Fe region: New Mexico Geological Society 46th Annual Fall Field Conference Guidebook, p. 87–96.

Kelley, S.A., and Chapin, C.E., 1997, Cooling histories of mountain ranges in the southern Rio Grande rift based on apatite fission-track analysis—A reconnaissance survey: New Mexico Geology, v. 19, p. 1–14.

Kelley, S.A., and Chapin, C.E., 2004, Denudation history and internal structure of the Front Range and Wet Mountains, Colorado, based on apatite-fission-track thermochronology, in Cather, S.M., et al., eds., Tectonics, geochronology, and volcanism in the southern Rocky Mountains and Rio Grande Rift: New Mexico Bureau of Geology and Mineral Resources Bulletin, v. 160, p. 41–68.

Kelley, S.A., 2012, Conceptual models of the Rio Grande Rift: New Mexico Bureau of Geology and Mineral Resources Lite Geology, n. 31, p. 2–5.

Kim, S.T., and O'Neil, J.R., 1997, Equilibrium and nonequilibrium oxygen isotope effects in synthetic carbonates: Geochimica et Cosmochimica Acta, v. 61, p. 3461–3475, doi:10.1016/S0016-7037(97)00169-5.

Kirkham, R.M., Keller, J.W., Houck, K.J., and Lindsay, N.R., 2006, Geologic map of the Fairplay East quadrangle, Park County, Colorado: Colorado Geological Survey Open-File Report OF-06–09, scale 1:24,000.

Klein, T.L., Evans, K.V., and DeWitt, E.H., 2010, Geochronology database for central Colorado: U.S. Geological Survey Data Series 489, 17 p.

Kluth, C., and Coney, P., 1981, Plate tectonics of the Ancestral Rocky Mountains: Geology, v. 9, p. 10–15, doi:10.1130/0091-7613(1981)9<10:PTOTAR>2.0.CO;2.

Kohn, B.P., Lorencak, M., Gleadow, A.J., Kohlmann, F., Raza, A., Osadetz, K.G., and Sorjonen- Ward, P., 2009, A reappraisal of low-temperature thermochronology of the eastern Fennoscandia Shield and radiation-enhanced apatite fission-track annealing, in Lisker, F., et al., eds., Thermochronological methods: From palaeotemperature constraints to landscape evolution models: Geological Society of London Special Publication 324, p. 193–216, doi:10.1144/SP324.15.

Kuiper, K.F., Deino, A., Hilgen, F.J., Krijgsman, W., Renne, P.R., and Wijbrans, J.R., 2008, Synchronizing rock clocks of Earth history: Science, v. 320, no. 5875, p. 500–504, doi:10.1126/science.1154339.

Landis, C.A., Campbell, H.J., Begg, J.G., Mildenhall, D.C., Paterson, A.M., and Trewick, S.A., 2008, The Waipounamu erosion surface: Questioning the antiquity of the New Zealand land surface and terrestrial fauna and flora: Geological Magazine, v. 145, p. 173–197, doi:10.1017/S0016756807004268.

Landman, R., and Flowers, R.M., 2013, (U-Th)/He thermochronologic constraints on the evolution of the northern Rio Grande Rift, Gore Range, Colorado, and implications for rift propagation models: Geosphere, v. 9, p. 170–187, doi:10.1130/GES00826.1.

Leonard, E.M., 2002, Geomorphic and tectonic forcing of late Cenozoic warping of the Colorado piedmont: Geology, v. 30, p. 595–598, doi:10.1130/0091-7613(2002)030<0595:GATFOL>2.0.CO;2.

Lindsey, D.A., 2010, The geologic story of Colorado's Sangre de Cristo Range: U.S. Geological Survey Circular 1349, 14 p.

Lindsey, D.A., Johnson, B.R., and Andriessen, P.A.M., 1984, Laramide and Neogene structure of northern Sangre de Cristo Range, south-central Colorado: American Association of Petroleum Geologists Bulletin, v. 68, p. 941.

Liu, L., Gurnis, M., Seton, M., Saleeby, J., Müller, R.D., and Jackson, J.M., 2010, The role of oceanic plateau subduction in the Laramide orogeny: Nature Geoscience, v. 3, p. 353–357, doi:10.1038/ngeo829.

Lloyd, M.K., Eiler, J.M., and Nabelek, P.I., 2017, Clumped isotope thermometry of calcite and dolomite in a contact metamorphic environment: Geochimica et Cosmochimica Acta, v. 197, p. 323–344, doi:10.1016/j.gca.2016.10.037.

Lovera, O.M., Richter, F.M., and Harrison, T.M., 1989, The 40Ar/39Ar thermochronometry for slowly cooled samples having a distribution of diffusion domain sizes: Journal of Geophysical Research, v. 94, p. 17,917–17,935, doi:10.1029/JB094iB12p17917.

Ludwig, K.R., 2008, User's Manual for Isoplot 3.6: A geochronological toolkit for Microsoft Excel: Berkeley Geochronology Center Special Publication 4.

Marshak, S., Karlstrom, K., and Timmons, J.M., 2000, Inversion of Proterozoic extensional faults: An explanation of Laramide and Ancestral Rockies intracratonic deformation, United States: Geology, v. 28, p. 735–738, doi:10.1130/0091-7613(2000)28<735:IOPEFA>2.0.CO;2.

McDougall, I., and Harrison, T.M., 1988, Geochronology and thermochronology by the $^{40}Ar/^{39}Ar$ method: New York, Oxford University Press, 269 p.

McIntosh, W.C., and Cather, S.M., 1994, $^{40}Ar/^{39}Ar$ geochronology of basaltic rocks and constraints on late Cenozoic stratigraphy and landscape development in the Red Hill–Quemado area, New Mexico, in Chamberlin, R.M., et al., eds., Mogollon slope, west-central New Mexico: New Mexico Geological Society Fall Field Conference Guidebook 45, p. 1–18.

McIntosh, W.C., and Chapin, C.E., 2004, Geochronology of the central Colorado volcanic field, in Cather, S.M., et al., eds., Tectonics, geochronology, and volcanism in the southern Rocky Mountains and Rio Grande Rift: New Mexico Bureau of Geology and Mineral Resources Bulletin, v. 160, p. 205–238.

McMillan, M.E., Angevine, C.L., and Heller, P.L., 2002, Post-depositional tilt of the Miocene–Pliocene Ogallala Group on the western Great Plains: Evidence of late

Cenozoic uplift of the Rocky Mountains: Geology, v. 30, p. 63–66, doi:10.1130/0091-7613(2002)030<0063:PTOTMP>2.0.CO;2.

McMillan, M.E., Heller, P.L., and Wing, S.L., 2006, History and causes of post-Laramide relief in the Rocky Mountain orogenic plateau: Geological Society of America Bulletin, v. 118, p. 393–405, doi:10.1130/B25712.1.

Min, K., Renne, P.R., and Huff, W.D., 2001, $^{40}Ar/^{39}Ar$ dating of Ordovician K-bentonites in Laurentia and Baltoscandia: Earth and Planetary Science Letters, v. 185, p. 121–134, doi:10.1016/S0012-821X(00)00365-4.

Molnar, P., England, P.C., and Jones, C.H., 2015, Mantle dynamics, isostasy, and the support of high terrain: Journal of Geophysical Research, v. 120, p. 1932–1957, doi:10.1002/2014JB011724.

Murray, K.E., Reiners, P.W., and Thomson, S.N., 2016, Rapid Pliocene–Pleistocene erosion of the central Colorado Plateau documented by apatite thermochronology from the Henry Mountains: Geology, v. 44, p. 483–486, doi:10.1130/G37733.1.

Naeser, C.W., Bryant, B., Kunk, M.J., Kellogg, K., Donelick, R.A., and Perry, W.J., Jr., 2002, Tertiary cooling and tectonic history of the White River uplift, Gore Range, and western Front Range, central Colorado: Evidence from fission-track and $^{39}Ar/^{40}Ar$ ages, in Kirkham, R.M., et al., eds., Late Cenozoic evaporite tectonism and volcanism in west-central Colorado: Geological Society of America Special Paper 366, p. 31–53, doi:10.1130/0-8137-2366-3.31.

Nathenson, M., and Guffanti, M., 1988, Geothermal gradients in the conterminous United States: Journal of Geophysical Research, v. 93, p. 6437–6450, doi:10.1029/JB093iB06p06437.

Niemi, N.A., and Clark, M.K., 2017, Long-term exhumation rates exceed paleoseismic slip rates in the central Santa Monica Mountains, Los Angeles County, California: Geology, v. 46, n. 1, p. 63-66, doi:10.1130/G39388.1.

Niemi, N.A., Buscher, J.T., Spotila, J.A., House, M.A., and Kelley, S.A., 2013, Insights from low-temperature thermochronometry into transpressional deformation and crustal exhumation along the San Andreas fault in the western Transverse Ranges, California: Tectonics, v. 32, p. 1602–1622, doi:10.1002/2013TC003377.

Onstott, T. C., 1980, Application of the Bingham distribution function in paleomagnetic studies: Journal of Geophysical Research: Solid Earth, v. 85, n. B3, p. 1500-1510, doi:10.1029/JB085iB03p01500.

Passey, B.H., and Henkes, G.A., 2012, Carbonate clumped isotope bond reordering and geospeedometry: Earth and Planetary Science Letters, v. 351–352, p. 223–236, doi:10.1016/j.epsl.2012.07.021.

Pazzaglia, F.J., and Brandon, M.T., 1996, Macrogeomorphic evolution of the post-Triassic Appalachian Mountains determined by deconvolution of the offshore basin sedimentary record: Basin Research, v. 8, p. 255–278, doi:10.1046/j.1365-2117.1996.00274.x.

Petersen, S.V., Winkelstern, I.Z., Lohmann, K.C., and Meyer, K.W., 2016, The effects of

Porapak™ trap temperature on δ18O, δ13C, and Δ47 values in preparing samples for clumped isotope analysis: Rapid Communications in Mass Spectrometry, v. 30, p. 199–208, doi:10.1002/rcm.7438.

Peyton, S.L., Reiners, P.W., Carrapa, B., and DeCelles, P.G., 2012, Low-temperature thermochronology of the northern Rocky Mountains, western U.S.A.: American Journal of Science, v. 312, p. 145–212, doi:10.2475/02.2012.04.

Quade, J., Eiler, J., Daeron, M., and Achyuthan, H., 2013,The clumped isotope geothermometer in soil and paleosol carbonate: Geochimica et Cosmochimica Acta, v. 105, p. 92–107, doi:10.1016/j.gca.2012.11.031.

Rasmussen, D.A., 2016, Depositional environments and provenance of early Paleogene strata in the Huerfano Basin: Implications for uplift of the Wet Mountains, Colorado, USA [M.S. thesis]: Bellingham, Western Washington University, 72 p.

Reiners, P.W., 2005, Zircon (U-Th)/He thermochronometry: Reviews in Mineralogy and Geochemistry, v. 58, p. 151–179, https://doi.org/10.2138/rmg.2005.58.6.

Reiners, P.W., and Farley, K.A., 2001, Influence of crystal size on apatite (U-Th)/He thermochronology: An example from the Bighorn Mountains, Wyoming: Earth and Planetary Science Letters, v. 188, p. 413–420, doi:10.1016/S0012-821X(01) 00341-7.

Reiners, P.W., and Nicolescu, S., 2006, Measurement of parent nuclides for (U-Th)/He chronometry by solution sector ICP-MS: Arizona Radiogenic Helium Dating Laboratory Report 1, http://www.geo.arizona.edu/~reiners/arhdl/Reiners_and_Nicolescu_submitted.pdf

Reiners, P.W., Farley, K.A., and Hickes, H.J., 2002, He diffusion and (U-Th)/He thermochronometry of zircon: Initial results from Fish Canyon Tuff and Gold Butte: Tectonophysics, v. 349, p. 297–308, doi:10.1016 /S0040-1951(02)00058-6.

Reiners, P.W., Thompson, S.N., Tipple, B.J., Peyton, S.L., Rahl, J.M., and Mulch, A., 2008, Secondary weathering phases and apatite (U-Th)/He ages: Geochimica et Cosmochimica Acta, v. 72, no. 12, Supplement, p. A784.

Ricketts, J.W., Kelley, S.A., Karlstrom, K.E., Schmandt, B., Donahue, M.S., and van Wijk, J., 2016, Synchronous opening of the Rio Grande rift along its entire length at 25–10 Ma supported by apatite (U-Th)/He and fission-track thermochronology, and evaluation of possible driving mechanisms: Geological Society of America Bulletin, v. 128, p. 397–424, doi:10.1130/B31223.1.

Roy, M., Kelley, S., Pazzaglia, F., Cather, S., and House, M., 2004, Middle Tertiary buoyancy modification and its relationship to rock exhumation, cooling, and subsequent extension at the eastern margin of the Colorado Plateau: Geology, v. 32, p. 925–928, doi:10.1130/G20561.1.

Ruleman, C.A., and Bohannon, R.G., 2008, Geologic map of the Elkhorn quadrangle, Park County, Colorado: U.S. Geological Survey Scientific Investigations Map SIM-3043, scale 1:24,000.

Sak, P.B., Leonard, E.M., Miller, S.R., Biscontini, A.J., and Jemison, E., 2005, Late

Cenozoic drainage reorganization of the Arkansas River, central Colorado, and history of the Royal Gorge: Geological Society of America Abstracts with Programs, v. 37, no. 7, p. 295. Samson, S.D., and Alexander, E.C., 1987, Calibration of the inter-laboratory $^{40}Ar/^{39}Ar$ dating standard, MMhb-1: Chemical Geology. Isotope Geoscience Section, v. 66, p. 27–34, doi:10.1016/0168-9622 (87)90025-X.

Sanders, R.E., Heizler, M.T., and Goodwin, L.B., 2006, $^{40}Ar/^{39}Ar$ thermochronology constraints on the timing of Proterozoic basement exhumation and fault ancestry, southern Sangre de Cristo Range, New Mexico: Geological Society of America Bulletin, v. 118, p. 1489–1506, doi:10.1130/B25857.1.

Schauble, E.A., Ghosh, P., and Eiler, J.M., 2006, Preferential formation of ^{13}C-^{18}O bonds in carbonate minerals, estimated using first-principals lattice dynamics: Geochimica et Cosmochimica Acta, v. 70, p. 2510–2529, doi:10.1016/j.gca.2006.02.011.

Scott, G.R., 1975a, Cenozoic surfaces and deposits in the southern Rocky Mountains, in Curtis, B.F., ed., Cenozoic history of the southern Rocky Mountains: Geological Society of America Memoir 144, p. 227–248, doi:10.1130/MEM144-p227.

Scott, G.R., 1975b, Reconnaissance geologic map of the Buena Vista quadrangle, Chaffee and Park Counties, Colorado: U.S. Geological Survey Miscellaneous Field Studies Map MF-657, scale 1:62,500.

Shannon, J.R., 1988, Geology of the Mount Aetna cauldron complex, Sawatch Range, Colorado [Ph.D. thesis]: Golden, Colorado School of Mines, 434 p.

Shuster, D.L., Flowers, R.M., and Farley, K.A., 2006, The influence of natural radiation damage on helium diffusion kinetics in apatite: Earth and Planetary Science Letters, v. 249, p. 148–161, doi:10.1016/j.epsl.2006.07.028.

Sjostrom, D.J., Hren, M.T., Horton, T.W., Waldbauer, J.R., and Chamberlain, C.P., 2006, Stable isotopic evidence for a pre–late Miocene elevation gradient in the Great Plains–Rocky Mountain region, USA, in Willett, S.D., et al., eds., Tectonics, climate, and landscape evolution: Geological Society of America Special Paper 398, p. 309–319, doi:10.1130/2006.2398(19).

Small, E.E., and Anderson, R.S., 1998, Pleistocene relief production in Laramide mountain ranges, western United States: Geology, v. 26, p. 123–126, doi:10.1130/009-7613(1998)026<0123:PRPILM>2.3.CO;2.

Somoza, R., 2011, The Late Cretaceous paleomagnetic field in North America: A South American perspective: Canadian Journal of Earth Sciences, v. 48, p. 1483–1488, doi:10.1139/e11-051.

Sousa, F.J., Saleeby, J., Farley, K.A., Unruh, J.R., and Lloyd, M.K., 2016, The southern Sierra Nevada pediment, central California: Geosphere, v. 13, p. 1–20, doi:10.1130/GES01369.1.

Spiegel, C., Kohn, B., Belton, D., Berner, Z., and Gleadow, A., 2009, Apatite (U-Th-Sm)/He thermochronology of rapidly cooled samples: The effect of He implantation: Earth and Planetary Science Letters, v. 285, p. 105–114,

doi:10.1016/j.epsl.2009.05.045.

Stanley, J.R., Flowers, R.M., and Bell, D.R., 2013, Kimberlite (U-Th)/He dating links surface erosion with lithospheric heating, thinning, and metasomatism in the southern African Plateau: Geology, v. 41, p. 1243–1246, doi:10.1130/G34797.1.

Steiger, R.H., and Jäger, E., 1977, Subcommission on geochronology: Convention on the use of decay constants in geo- and cosmochronology: Earth and Planetary Science Letters, v. 36, p. 359–362, doi:10.1016/0012-821X(77)90060-7.

Stolper, D.A., and Eiler, J.M., 2015, The kinetics of solid-state isotope-exchange reactions for clumped isotopes: A study of inorganic calcites and apatites from natural and experimental samples: American Journal of Science, v. 315, p. 363–411, doi:10.2475/05.2015.01.

Taylor, J.R., 1982, An introduction to error analysis: Mill Valley, California, University Science Books, 270 p.

Taylor, R.B., 1975, Neogene tectonism in south-central Colorado, in Curtis, B.F., ed., Cenozoic history of the southern Rocky Mountains: Geological Society of America Memoir 144, p. 211–226, doi:10.1130/MEM144-p211.

Taylor, R.B., Scott, G.R., and Wobus, R.A., 1975a, Reconnaissance geologic map of the Howard quadrangle, central Colorado: U.S. Geological Survey Miscellaneous Investigations Series Map I-892, scale 1:62,500.

Taylor, R.B., Scott, G.R., Wobus, R.A., and Epis, R.C., 1975b, Reconnaissance geologic map of the Cotopaxi 15-minute quadrangle, Fremont and Custer Counties, Colorado: U.S. Geological Survey Miscellaneous Investigations Series Map I-900, scale 1:62,500.

Taylor, R.B., Scott, G.R., Wobus, R.A., and Epis, R.C., 1975c, Reconnaissance geologic map of the Royal Gorge quadrangle, Fremont and Custer Counties, Colorado: U.S. Geological Survey Miscellaneous Investigations Series Map I-869, scale 1:62,500.

Thomson, S.N., Soreghan, G.S., Reiners, P.W., Peyton, S.L., and Murray, K.E., 2016, A definitive 6 Ma start date for carving of the northeastern Colorado Plateau Canyonlands: Geological Society of America Abstracts with Programs, v. 48, n. 7, doi:10.1130/abs/2016AM-287583.

Tweto, O., 1974, Reconnaissance geologic map of Fairplay West, Mount Sherman, South Peak, and Jones Hill 7–1/2 minute quadrangles, Park, Lake, and Chaffee Counties, Colorado: U.S. Geological Survey Miscellaneous Field Studies Map MF-555, scale 1:62,500.

Tweto, O., 1975, Laramide (Late Cretaceous–early Tertiary) orogeny in the Southern Rocky Mountains, in Curtis, B.M., ed. Cenozoic history of the southern Rocky Mountains: Geological Society of America Memoir 144, p. 1–44, doi:10.1130/MEM144-p1.

Van Alstine, R.E., and Cox, D.C., 1969, Geology and mineral deposits of the Poncha Springs Quadrangle, Chaffee County, Colorado, with a section on fluorspar mines

and prospects: U.S. Geological Survey Professional Paper PP-626, scale 1:24,000.

van der Voo, R., 1993, Paleomagnetism of the Atlantic, Tethys, and Iapetus Oceans: Cambridge, Cambridge University Press, 411 p., doi:10.1017/CBO9780511524936.

Wallace, C.A., and Lawson, A.D., 2008, Geologic map of the Cameron Mountain quadrangle, Chaffee, Fremont and Park Counties, Colorado: Colorado Geological Survey Open-File Report OF-08-12, scale 1:24,000.

Wallace, C.A., Cappa, J.A., and Lawson, A.D., 1997, Geologic map of the Salida East quadrangle, Chaffee and Fremont Counties, Colorado: Colorado Geological Survey Open-File Report OF-97-6, scale 1:24,000.

Whipp, D.M., and Ehlers, T.A., 2007, Influence of groundwater flow on thermochronometer-derived exhumation rates in the central Nepalese Himalaya: Geology, v. 35, p. 851–854, doi:10.1130/G23788A.1.

Whipple, K.X., Kirby, E., and Brocklehurst, S.H., 1999, Geomorphic limits to climate-induced increases in topographic relief: Nature, v. 401, n. 6748, p. 39–43, doi:10.1038/43375.

Winkelstern, I.Z., and Lohmann, K.C., 2016, Shallow burial alteration of dolomite and limestone clumped isotope geochemistry: Geology, v. 44, p. 467–470, doi:10.1130/G37809.1.

Wofford, M.K.Y., 1986, Skarn formation adjacent to the Whitehorn Stock, Chaffee County, Colorado [Ph.D. thesis]: Lubbock, Texas Tech University, 80 p.

Workman, J.B., 1997, Contact metamorphism and conditions of emplacement for the Whitehorn Granodiorite, and tectonic implications for Colorado in the Laramide [M.S. thesis]: Golden, Colorado School of Mines, 134 p.

Wrucke, C.T., 1974, The Whitehorn granodiorite of the Arkansas Valley in central Colorado: U.S. Geological Survey Bulletin 1394-H, 16 p.

York, D., 1968, Least squares fitting of a straight line with correlated errors: Earth and Planetary Science Letters, v. 5, p. 320–324, doi:10.1016/S0012-821X(68)80059-7.

CHAPTER V: SYNTHESIS, CONCLUSIONS AND OUTSTANDING IDEAS

PRINCIPAL FINDINGS

Using low-temperature thermochronometry data, along with information on the age and composition of magmatism, I have explored the processes behind fault initiation, growth, and linkage, as well as rifting accommodation mechanisms (chapters 2 and 3). Low-temperature thermochronometry is also shown to be a powerful tool for determining rates and magnitudes of exhumation, along with identifying basement structures and possible post-exhumation reheating stories (chapter 4). Through the analyses and interpretations made in the previous chapters, I have been able to (1) define a detailed history for fault growth and linkage in the northern Rio Grande rift (RGR), (2) resolve debate about rift development by synchronous extension initiation versus northward propagation, (3) differentiate between continental rifting models, (4) assess the effect of rifting on proposed rejuvenation in the southern Rocky Mountains, (5) determine the timing and magnitudes for exhumation in the southern Rocky Mountains, and (6) describe the recent post-orogenic paleotopography in the southern Rockies.

DEVELOPMENT OF THE RIO GRANDE RIFT

In this dissertation I address questions about rift development to understand the processes behind rift accommodation through extensional faulting or magmatism. Low-temperature thermochronometry is one method that can directly measure fault motion and

inverse thermal history modeling of these data provides information on the timing of fault initiation, as well as the rates and magnitudes of exhumation. In addition, this method can be easily applied throughout the RGR where the rift flanks are dominantly exposed Proterozoic basement granitoids and gneisses. In fact, in the past few decades this method has been applied throughout many of the RGR basins (Cunningham et al., 1977; Bryant and Naeser, 1980; Kelley and Duncan, 1986; Kelley et al., 1992; Kelley and Chapin, 1997; House et al., 2003; Naeser et al., 2002; Landman and Flowers, 2013; Ricketts et al., 2016). However, prior to the work presented here, the upper Arkansas River (UAR) Basin in the northern RGR was not well-studied with low-temperature thermochronometry data, with most of the previous data solely from the Mount Princeton batholith in the southern UAR basin (Kelley et al., 1992; Ricketts et al., 2016). Hence, to better understand faulting in the northern RGR, we developed a sampling strategy to not only populate the UAR basin with more thermochronometry data, but also to obtain a thorough understanding of fault initiation and growth within the basin, as presented in chapter 2.

Chapter 2

In the UAR basin, we collected samples along five densely spaced vertical transects, both perpendicular and parallel to the mapped fault structures at the base of the Sawatch Range (Fig. 2.1). Inverse thermal modeling of these data revealed that fault initiation began the southern Sawatch fault segment at ~24 Ma (Fig. 2.3). That segment continued to grow via tip propagation both to the north and to the south, while the northern Sawatch fault segment initiated at ~18 Ma (Fig. 2.3). In addition, a few single AHe samples (i.e. not in vertical transects) revealed that the central part of the UAR basin

appears to have recent exhumation relative to at the range front (Fig. 2.1). Moreover, the lack of younger ages or exhumation recorded in samples at the range front in the central part of the basin (Samples 1, 3 and the MTC transect; Fig. 2.3) suggests that the northern and southern Sawatch faults shift westward into the range along this section of the basin. We inferred that the two faults are now linked and that the UAR basin is bounded by one contiguous fault system that developed through the initiation of faulting on small separate segments, which then grew and became linked by ~10 Ma (Fig. 2.4). We further apply this segment growth and linkage model to the accommodation zones connecting the UAR basin and the Blue River and San Luis Basins in the northern RGR. Thus through this work we suggest that the northern RGR shows synchronous initiation on fault segments in the early Miocene, and that fault growth and linkage occurred in each of the basins from that time through the middle the late Miocene when the basins themselves began to link via the accommodation zone north of Leadville, CO and the Poncha Block accommodation zone (Fig. 2.4). We use this same approach to understanding fault growth and linkage in each of the RGR basins in Chapter 3 in order to resolve the debate about rift development and address questions about rift accommodation and geometry.

Chapter 3

Unfortunately, performing a high density sampling campaign throughout all the RGR basins, like we did in the UAR Basin presented in Chapter 2, was not feasible. However, we were able to compile 14 vertical transects useful for inverse thermal history modeling, from the plethora of published low-temperature thermochronometric data. With the addition of age and composition data from magmatism studies compiled in the EarthChem database, we assessed faulting and magmatic patterns both spatially and

temporally. We found that faulting began in both the northern and southern parts of the Rio Grande rift ~27 Ma (Figs. 3.4, 3.5, 3.6, 3.9). The initiation occurred on many small fault segments flanking the rift basins. From ~27 Ma to ~15 Ma rifting was entirely accommodated by faulting, as more segments began to initiate and link with an increase in the rates of exhumation on many of the rift flank faults (Fig. 3.9). At ~15 Ma it appears that the northern and southern parts of the RGR link through the formation of a large accommodation zone in the central RGR and that this extension and linkage is almost entirely accommodated by magmatism as expressed in the formation of the Jemez volcanic field (Fig. 3.9). Magmatism occurs along a northeast-southwest trend, the Jemez lineament, and the thermal history modeling shows that the rift faults continue to grow, with several segments showing slip-rate increases leading us to suggest that by ~10 to 5 Ma the RGR was fully integrated as one rift system.

We conclude that the synchronous initiation of faulting and patterns of volcanism in space and time does not support a northward propagation model and that most of the rift accommodation is tectonically controlled, especially in the early phases of rifting. In fact, in the central RGR, where accommodation is mainly controlled by magmatism, we observe that these volcanic eruptions are localized on a trend spatially coincident with mapped Proterozoic terrane boundaries (Fig. 1.3). Additionally, RGR faulting appears to be dictated by inherited structure and pre-existing crustal weaknesses as the geometry coincides well with mapped structures from previous tectonic events including the Laramide Orogeny, Ancestral Rockies uplifts, and Cambrian and Neoproterozoic rifting. Such coincidences do not necessarily explain the characteristic differences in faulting, rift geometry and magmatism in the southern, central and northern RGR. We postulate that

these characteristics are mainly controlled by lithospheric properties. The narrow and deep grabens and amagmatic nature of the northern RGR results from extension of a cold, thick lithosphere. In contrast, the southern RGR is underlain by much warmer and thinner lithosphere, allowing for the formation of many fault-bounded basins at a given latitude. The transition between a cold and thick to warm and thin lithosphere occurs abruptly along the trend of the Jemez lineament, which we speculate induces edge driven convection and magmatic eruptions all along that trend, allowing for magma accommodated rifting in the central RGR (Fig. 3.10).

Combining our integration of large datasets and our interpretations for rift development, we are able to differentiate between general rifting models and propose that an acceptable rifting model for the RGR would be a combination of oblique extension and block rotation (Fig. 3.1). Thus rifting began synchronously from oblique strain and produced the faulting in the northern and southern RGR. Rotation of the Colorado Plateau in the middle to late Miocene was accommodated on the Jemez lineament, encouraging the magmatic flare up, increasing extension in the south, and aiding in the linkage of the northern and southern RGR.

EXHUMATION IN THE SOUTHERN ROCKY MOUNTAINS

Chapter 4

The Rio Grande rift has often been called on as a mechanism to drive Miocene rejuvenation of uplift and increases in topographic relief in the surrounding southern Rocky Mountains region. We hoped to capture such a signal in the southern Rockies, by sampling for low-temperature thermochronometry analyses in the deeply incised lower Arkansas River canyon (chapter 4). These data, however, did not reveal exhumation

occurring post-Eocene, which may mean that little to no Miocene exhumation rejuvenation occurred, or it may simply mean that the rocks recording the exhumation are not exposed for sampling. Our thermochronometry data instead revealed a story of differential exhumation during the Laramide Orogeny.

Through the use of densely spaced vertical transects collected along the canyon walls, we were able to identify a possible reverse fault, which has not previously been well mapped, in the basement of the southern Front Range (Figs. 4.11 and 4.16). This structure appears to accommodate differential exhumation from the east, where less than 1-2 km of exhumation has occurred since >100 Ma, and the west, where 4-6 km of exhumation occurred from ~80 to 60 Ma (Fig. 4.15). Furthermore, our vertical transects revealed an unexpected relationship between age and elevation (Figs. 4.4 and 4.5), which we determined was due to reheating via hydrothermal circulation beneath thick Oligocene ignimbrite flows (Fig. 4.13). These volcanic flows also preserve the paleotopography prior to the Oligocene, often referred to as the Eocene erosion surface; however, we propose that this paleosurface can be described in greater detail thanks to the preservation by the volcanic flows. We suggest that the paleotopography that developed after the Laramide Orogeny and before the Oligocene ignimbrites were erupted was planar in the eastern part of the Front Range. However, to the west there was much more topographic variation with many high relief paleovalleys, including a paleovalley between Salida and Coaldale where the current Arkansas River flows (Fig. 4.11).

SIGNIFICANT CONTRIBUTIONS

Sampling strategies for low-temperature thermochronometry

The work presented in this dissertation relied heavily on a strategy of collecting sampling in densely spaced vertical transects. This is not often a strategy used for low-temperature thermochronometry methods, especially in the regions where I worked. However, I found that it was a completely necessary approach to understand the nuances within this region, where the geologic history has been dictated by fairly near-surface changes, known because of the uniformly old (~1.4 Ga) ages in the higher temperature thermochronometers across the region (Klein et al., 2010). This work shows that low-temperature thermochronometers are useful tools for understanding phases of fault initiation, growth, and linkage, as we showed by the analysis of the faulting in the RGR in Chapters 2 and 3. This method may also provide a way to recognize structures in basement rock, which are difficult to find by surface mapping (e.g. Brady et al., 2000). Additionally, the ability for thermochronometers to give information about exhumation timing, rates, and magnitudes may also help to identify the relationships between basement structures and how stress may be transferred spatially and temporally.

Implications for Understanding Continental Rifts

The analytical results and interpretations presented in this dissertation provide a comprehensive history for the Rio Grande rift. Previous work in the RGR focused on various aspects and expressions of rifting including: faulting, magmatism, sedimentation responses, far-field tilting, crustal and lithospheric properties, and local and regional strain (Table 3.1). It follows that although the other above mentioned proxies may be useful for understanding particular phases of or responses to rifting, I suggest that focusing on understanding fault growth and magmatism in a rift will provide more useful

information for determining possible rift models, as well as resolve debate about the timing and processes behind rift development.

Several generalized rifting models have been proposed for rift systems around the world (Fig. 3.1). We were able to distinguish between these rift models by determining information about fault initiation, magmatism and relationships between faults and lithospheric structure and pre-existing weaknesses, as we did in the RGR (Chapter 3). These relationships can be compared to and applied in other continental rift systems that are difficult to access, have little data or various types of data that may be of use in discriminating between possible rift models.

FUTURE DIRECTIONS

Fault growth

My work in Chapter 2, along the Sawatch Range, showed that normal fault systems can have complex and long development histories, which can be detected with low-temperature thermochronometers. High density vertical transect sampling for low-temperature thermochronometry data will be useful to apply to other fault systems in the RGR to see if there are patterns in the locations of segment initiation (i.e. center or edges of the now fully established system), or if rates of growth in each of the basins are similar to the Sawatch Range Fault system in the UAR Basin. This would help to better understand more precisely how and when the rift basins linked. It is important to note that the RGR fault systems are slow developing, which may be a reason we are able to detect such a long and detailed history about the fault growth patterns. I would be interested to see if such details can also be obtained from rapidly evolving normal fault systems,

establishing whether or not low-temperature thermochronometers can be as equally informative in rapidly evolving fault systems as they are in slower growing fault systems.

Paleotopography

Understanding paleotopography has been a topic of great interest for researchers studying tectonics, geomorphology and paleoclimate. In the southern Rocky Mountains we can get a glimpse at some of the paleotopography that existed in the region during the late Eocene to early Oligocene. In Chapter 4, I describe this preserved paleotopography through the use of previously mapped and newly proposed paleovalleys. However, this work only covers a snapshot of one area that has a well preserved paleosurface. We may be able to use river systems and the gravel deposits they leave behind to further describe the paleotopography at different times, thereby developing a more comprehensive understanding of how the topography evolved from its paleo-expression to that seen today. I have done some work on this front in trying understand the evolution of the Arkansas River by tracing sources and flow patterns in the gravels through the use of U-Th-Pb detrital zircon dating. Preliminary results suggest we may be able to reconstruct parts of paleo-surfaces and that changes in the paleotopography may be related to drainage capture and changes in flow direction which could have been aided by RGR faulting and basin linkage (Appendix 5).

Inherited structure

The coincidence of rift fault structures and magmatic eruptions with many pre-existing structures has led many to postulate that they are rejuvenated structures on pre-existing weaknesses or fabrics that have been inherited in the basement in the region of Colorado and New Mexico (e.g. Leonard, 2002; McMillan et al., 2006; Karlstrom et al.,

2008; Thomson et al., 2016). However, many of the proposed pre-existing older structures or weaknesses are difficult to locate in old basement rock (Brady et al., 2000). In Chapter 4 we found that low-temperature thermochronometry was useful for identifying basement structures and in one location we were able to estimate the magnitude of exhumation on the structure. This idea could be useful for trying to find and map pre-existing weaknesses from ancient structures that may have been involved in deformation during any of the major tectonic events like the Laramide orogeny, Ancestral Rockies uplifts, or Neoproterozoic rifting from the break-up of Rodinia (Fig. 1.3).

Reheating of thermochronometers

An intriguing line of research for the use of low-temperature thermochronometers is measuring heating and reheating events. This method can be used for more than documenting burial and exhumation, as we discussed in Chapter 4 with reheating via hydrothermal circulation. However, the community does not have a full understanding of how this record of reheating may be expressed in specific thermochronometers, or how different heating mechanisms may or may not cause reheating and age resetting within thermochronometers. In Chapter 4 we were able to explore this by combining thermochronometry and clumped and stable isotope analysis to help constrain the amount of heat needed and the length of time a sample would need to be exposed to those temperatures to record resetting or partial resetting (Figs. 4.12 and 4.13). A rift system provides an ideal setting for these types experiments as there is elevated heat flow and the formation of many hydrothermal systems. Thus one interesting route to go in the future would be to combine low-temperature thermochronometry analyses with other hydrothermal alteration indicators in order to assess how strong or pervasive of a

reheating signal can come from, for example, locations around hot-springs. Establishing an understanding of how reheating can affect the age signatures obtained from low-temperature thermochronometers will be invaluable information useful for assessing the use of thermochronometers in different tectonic scenarios.

CONCLUSION

The plethora of geologic mapping and data available in both the Rio Grande rift and Southern Rocky Mountains was paramount to the interpretations and conclusions drawn in this dissertation. We were able to address specific questions about faulting and rift development, but we also found surprises in the data and geologic relationships in a region where much of the geology is said to be 'figured out'. Instead the development of new techniques and methods like low-temperature thermochronometry has led to exciting discoveries in both newly explored and well-studied areas.

APPENDIX E: SUPPLEMENTARY DATA TABLES AND FIGURES FOR CHAPTER 5

This appendix contains three supplementary figures, Figs E1 – E3 and two data tables, Table E1 and E2. These figures and tables are preliminary results from a study of paleo-topography and river evolution of the Arkansas River.

Figure E1: This figure shows sample locations of detrital and igneous samples for zircon U-Th-Pb dating.

Figure E2: This figure shows field photos of each of the gravel (detrital) samples collected.

Figure E3: This figure shows PDFs of the zircon U-Th-Pb analyses.

Table E1: This table contains location data for each of the collected samples.

Table E2: This table contains analytical data for the samples analyzed for zircon U-Th-Pb dates.

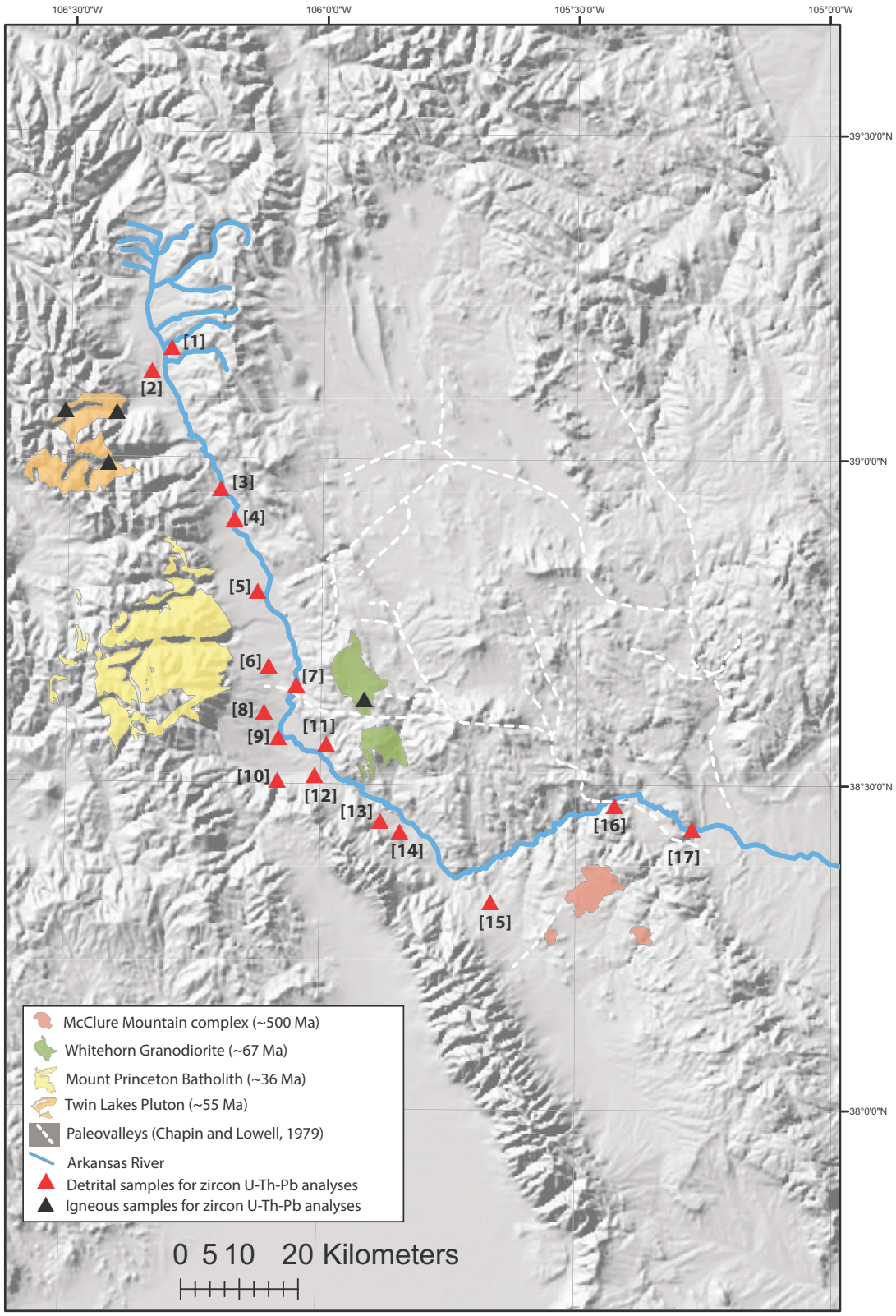

Figure E1: Sample locations for zircon U-Th-Pb analyses along the Arkansas River. Source plutons for specific ages are marked by colored polygons.

Figure E2: Field photos of gravel samples collected form the Tertiary Dry Union formation.

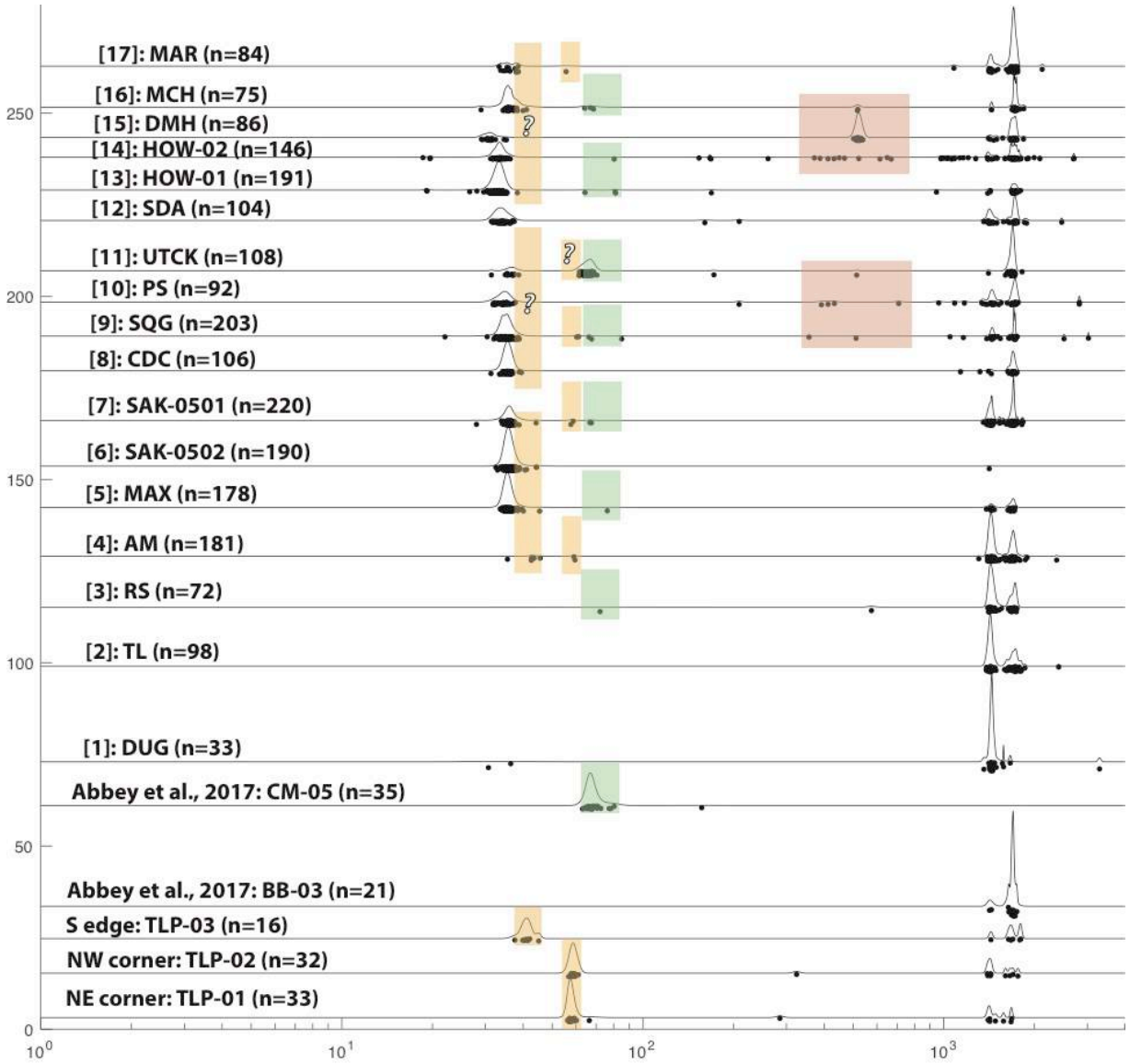

Figure E3: PDFs of detrital and igneous U-Th-Pb analyses. Sample numbers correspond to those in figure E1 Colored squares indicate correlations in age with the plutons on Fig E1.

TABLE E1: BEDROCK AND DETRITAL SAMPLES ANALYZED FOR ZIRCON U-TH-Pb

Sample Name	Longitude	Latitude	Elevation (m)	Rock unit and description
Bedrock Samples				
16TLP-01	-106.4086	39.0677	2889	Ttl: Twin Lakes Pluton, granodiorite
16TLP-02	-106.5107	39.0691	3106	Ttl: Twin Lakes Pluton, granodiorite
16TLP-03	-106.4241	38.9896	3083	Ttl: Twin Lakes Pluton, granodiorite
Detrital Samples				
16DUG	-106.3018	39.1682	2945	Tdu: calcite cemented gravel
16TL	-106.3405	39.1319	2872	Tdu: silty gravel
16RS	-106.2021	38.9509	2564	Tdu: calcite semi-cemented gravel
16AM	-106.1743	38.9055	2504	Tdu: unconsolidated gravel
16MAX	-106.1274	38.7946	2427	Tdu: sandy gravel
16SAK-0502	-106.1039	38.6802	2494	Tdu: calcite semi-cemented gravel
16SAK-0501	-106.0648	38.6533	2345	Tdu: unconsolidated gravel
16CDC	-106.1184	38.6090	2379	Tdu: coarse gravel
16SQG	-106.0833	38.5706	2240	Tdu: sandy gravel
16PS	-106.0849	38.5047	2339	Tdu: sandy gravel
16SDA	-106.0115	38.5124	2275	Tdu: coarse gravel
16UTCK	-105.9899	38.5608	2265	Tdu: coarse gravel
16HOW-01	-105.8821	38.4424	2328	Tdu or Qs?: calcite cemented gravel
16HOW-02	-105.8444	38.4269	2134	Tdu: calcite cemented gravel
16DMH	-105.6658	38.3198	2245	Tdu: calcite cemented gravel
16MCH	-105.4233	38.4678	2109	Tdu(mapped): unconsolidated gravel
16MAR	-105.2724	38.4318	1651	Modern river sand and gravel

TABLE E2: U-TH-PB GEOCHRONOLOGIC ANALYSES

Analysis	U (ppm)	$^{206}Pb/^{204}Pb$	U/Th	$^{206}Pb^*/^{207}Pb^*$	± (%)	Isotope Ratios $^{207}Pb^*/^{235}U^*$	± (%)	$^{206}Pb^*/^{238}U$	± (%)	Error Corr.	Apparent Ages (Ma) $^{206}Pb^*/^{238}U^*$	± (Ma)	$^{207}Pb^*/^{235}U$	± (Ma)	$^{206}Pb^*/^{207}Pb^*$	± (Ma)	Best Age (Ma)	± (Ma)
TLP-01																		
Spot 70	1590	8896	7.8	21.2380	1.3	0.0569	3.0	0.0088	2.6	0.89	56.3	1.5	56.2	1.6	53.6	31.9	56.3	1.5
Spot 64	1006	19305	10.0	20.5045	1.0	0.0592	2.1	0.0088	1.9	0.88	56.5	1.1	58.4	1.2	136.8	23.8	56.5	1.1
Spot 37	1060	3122	5.4	22.4431	3.6	0.0544	4.0	0.0089	1.9	0.46	56.9	1.0	53.8	2.1	NA	NA	56.9	1.0
Spot 62	947	5497	8.7	21.2373	2.3	0.0576	2.9	0.0089	1.7	0.58	56.9	0.9	56.8	1.6	53.7	55.5	56.9	0.9
Spot 67	1085	4527	9.2	21.6465	3.1	0.0565	3.8	0.0089	2.2	0.59	56.9	1.3	55.8	2.1	7.9	73.5	56.9	1.3
Spot 39	1209	4524	7.9	21.9372	1.4	0.0558	2.4	0.0089	2.0	0.83	57.0	1.2	55.1	1.3	NA	NA	57.0	1.2
Spot 47	1384	12699	7.5	20.7966	1.5	0.0589	3.0	0.0089	2.5	0.86	57.0	1.4	58.1	1.7	103.5	35.8	57.0	1.4
Spot 44	787	8402	14.5	20.8375	1.5	0.0588	3.1	0.0089	2.7	0.87	57.1	1.5	58.0	1.8	98.8	35.8	57.1	1.5
Spot 55	1694	14589	7.7	21.0193	1.2	0.0584	2.4	0.0089	2.0	0.87	57.1	1.2	57.6	1.3	78.2	27.7	57.1	1.2
Spot 38	850	42292	15.7	20.6821	1.5	0.0596	2.3	0.0089	1.7	0.74	57.4	1.0	58.8	1.3	116.5	35.7	57.4	1.0
Spot 66	1335	56023	11.5	20.8517	1.2	0.0592	2.4	0.0090	2.0	0.85	57.5	1.2	58.4	1.3	97.2	29.4	57.5	1.2
Spot 58	1891	29437	6.7	20.7104	1.0	0.0596	2.4	0.0090	2.2	0.91	57.5	1.3	58.8	1.4	113.3	24.2	57.5	1.3
Spot 63	1496	110192	10.7	20.7345	0.9	0.0597	2.6	0.0090	2.4	0.93	57.6	1.4	58.9	1.5	110.5	22.2	57.6	1.4
Spot 59	1803	26294	6.6	21.0954	1.3	0.0587	2.3	0.0090	1.9	0.84	57.6	1.1	57.9	1.3	69.6	30.1	57.6	1.1
Spot 48	834	2111	10.4	23.5251	1.7	0.0526	2.9	0.0090	2.4	0.82	57.6	1.4	52.1	1.5	NA	NA	57.6	1.4
Spot 49	1555	19651	6.8	20.7072	1.1	0.0599	2.9	0.0090	2.7	0.92	57.7	1.6	59.0	1.7	113.6	26.9	57.7	1.6
Spot 54	1564	5196	8.6	21.9655	3.4	0.0565	4.2	0.0090	2.5	0.59	57.8	1.4	55.8	2.3	NA	NA	57.8	1.4
Spot 46	1253	11079	9.2	21.1330	1.5	0.0589	2.3	0.0090	1.7	0.74	58.0	1.0	58.1	1.3	65.4	36.3	58.0	1.0
Spot 61	1127	3602	13.5	22.3311	1.2	0.0562	2.3	0.0091	2.0	0.86	58.5	1.2	55.6	1.3	NA	NA	58.5	1.2

TABLE E2: U-TH-PB GEOCHRONOLOGIC ANALYSES

Analysis	U (ppm)	^{206}Pb ^{204}Pb	U/Th	$^{206}Pb^*$ $^{207}Pb^*$	± (%)	Isotope Ratios $^{207}Pb^*$ $^{235}U^*$	± (%)	$^{206}Pb^*$ ^{238}U	± (%)	Error Corr.	Apparent Ages (Ma) $^{206}Pb^*$ $^{238}U^*$	± (Ma)	$^{207}Pb^*$ ^{235}U	± (Ma)	$^{206}Pb^*$ $^{207}Pb^*$	± (Ma)	Best Age (Ma)	± (Ma)
Spot 50	945	54761	13.9	20.1098	1.0	0.0628	2.5	0.0092	2.3	0.91	58.8	1.3	61.8	1.5	182.2	23.8	58.8	1.3
Spot 36	511	3178	5.4	21.5924	4.0	0.0589	4.6	0.0092	2.4	0.52	59.2	1.4	58.1	2.6	13.9	95.3	59.2	1.4
Spot 65	364	4230	4.2	21.3427	4.1	0.0599	5.0	0.0093	2.9	0.58	59.5	1.7	59.1	2.9	41.8	97.7	59.5	1.7
Spot 40	114	3381	1.8	21.8133	2.7	0.0593	3.8	0.0094	2.7	0.70	60.2	1.6	58.5	2.2	NA	NA	60.2	1.6
Spot 41	224	311	2.1	6.0397	8.7	0.2364	10.8	0.0104	6.4	0.59	66.4	4.2	215.4	20.9	2513.3	146.5	66.4	4.2
Spot 60	1205	15453187	6.4	11.0638	1.3	0.5640	3.1	0.0453	2.8	0.90	285.5	7.7	454.1	11.2	1433.7	25.4	285.5	7.7
Spot 43	110	49826	1.2	11.2348	0.9	3.0128	3.0	0.2456	2.9	0.96	1415.7	36.6	1410.9	23.0	1404.3	17.0	1404.3	17.0
Spot 52	90	8709	0.8	11.2074	1.2	2.8298	2.4	0.2301	2.1	0.86	1335.1	24.8	1363.5	18.0	1409.0	23.4	1409.0	23.4
Spot 57	149	37466	1.6	11.1350	1.0	2.5574	2.9	0.2066	2.7	0.93	1210.8	29.6	1288.6	21.0	1421.4	20.0	1421.4	20.0
TLP-02																		
Spot 13	1088	13688	9.6	20.4413	1.6	0.0596	3.2	0.0088	2.8	0.87	56.7	1.6	58.8	1.8	144.0	37.0	56.7	1.6
Spot 23	871	10574	8.7	20.5946	1.4	0.0601	3.1	0.0090	2.8	0.90	57.6	1.6	59.3	1.8	126.5	32.2	57.6	1.6
Spot 25	977	10109	11.9	20.7405	1.5	0.0598	3.3	0.0090	2.9	0.89	57.8	1.7	59.0	1.9	109.8	36.0	57.8	1.7
Spot 32	1016	4769	5.9	21.6676	1.6	0.0573	3.2	0.0090	2.7	0.85	57.8	1.6	56.6	1.7	5.6	39.7	57.8	1.6
Spot 22	712	4592	9.5	21.5248	2.1	0.0578	3.5	0.0090	2.8	0.81	58.0	1.6	57.1	1.9	21.4	49.8	58.0	1.6
Spot 9	1005	278804	7.4	20.0720	1.6	0.0620	3.3	0.0090	2.9	0.87	58.0	1.7	61.1	2.0	186.6	37.9	58.0	1.7
Spot 19	964	8052	8.9	21.4161	1.6	0.0584	3.4	0.0091	3.0	0.88	58.2	1.7	57.6	1.9	33.6	38.3	58.2	1.7
Spot 15	1581	9712	5.2	21.0548	1.1	0.0594	2.6	0.0091	2.3	0.90	58.3	1.3	58.6	1.5	74.2	26.9	58.3	1.3
Spot 3	919	25485	7.5	20.6462	1.7	0.0608	3.1	0.0091	2.6	0.84	58.4	1.5	59.9	1.8	120.6	39.3	58.4	1.5
Spot 29	778	38263	9.1	20.9600	1.5	0.0601	2.7	0.0091	2.2	0.84	58.6	1.3	59.2	1.5	84.9	34.8	58.6	1.3

TABLE E2: U-TH-PB GEOCHRONOLOGIC ANALYSES

Analysis	U (ppm)	^{206}Pb ^{204}Pb	U/Th	$^{206}Pb^*$ $^{207}Pb^*$	± (%)	Isotope Ratios $^{207}Pb^*$ $^{235}U^*$	± (%)	$^{206}Pb^*$ ^{238}U	± (%)	Error Corr.	Apparent Ages (Ma) $^{206}Pb^*$ $^{238}U^*$	± (Ma)	$^{207}Pb^*$ ^{235}U	± (Ma)	$^{206}Pb^*$ $^{207}Pb^*$	± (Ma)	Best Age (Ma)	± (Ma)
Spot 14	938	6558	12.4	21.3161	1.9	0.0592	3.1	0.0092	2.5	0.81	58.8	1.5	58.4	1.8	44.8	44.3	58.8	1.5
Spot 31	969	11824	12.0	21.1098	1.5	0.0598	3.0	0.0092	2.7	0.87	58.8	1.6	59.0	1.7	68.0	35.1	58.8	1.6
Spot 20	1233	15735	10.8	20.9412	1.3	0.0603	3.1	0.0092	2.8	0.91	58.8	1.6	59.5	1.8	87.1	29.8	58.8	1.6
Spot 17	1101	10737	4.4	20.5051	1.2	0.0617	3.1	0.0092	2.9	0.92	58.9	1.7	60.8	1.8	136.7	27.8	58.9	1.7
Spot 18	902	7181	13.9	21.3326	2.0	0.0594	3.2	0.0092	2.5	0.79	59.0	1.5	58.6	1.8	42.9	46.9	59.0	1.5
Spot 35	912	61492	8.5	20.4408	1.7	0.0623	3.3	0.0092	2.9	0.86	59.3	1.7	61.4	2.0	144.1	39.8	59.3	1.7
Spot 34	1029	30266	7.2	21.1023	1.3	0.0605	2.9	0.0093	2.6	0.89	59.4	1.5	59.6	1.7	68.8	30.9	59.4	1.5
Spot 4	1260	11007	10.7	20.8488	1.3	0.0612	3.7	0.0093	3.4	0.94	59.4	2.0	60.3	2.2	97.5	30.1	59.4	2.0
Spot 21	832	37274	7.9	20.0901	1.7	0.0636	3.8	0.0093	3.4	0.90	59.5	2.0	62.6	2.3	184.5	39.0	59.5	2.0
Spot 10	924	11400	8.6	19.4764	1.8	0.0667	3.3	0.0094	2.8	0.85	60.5	1.7	65.6	2.1	256.3	40.5	60.5	1.7
Spot 5	1193	11563	6.8	20.8351	1.5	0.0630	2.5	0.0095	2.0	0.80	61.1	1.2	62.0	1.5	99.1	35.5	61.1	1.2
Spot 16	1014	39873	11.1	11.4526	1.1	0.6206	3.1	0.0516	2.9	0.93	324.2	9.0	490.2	11.9	1367.5	21.9	324.2	9.0
Spot 11	424	70343	54.7	11.2930	0.9	2.7147	3.4	0.2224	3.2	0.96	1294.7	37.8	1332.5	24.9	1394.4	17.8	1394.4	17.8
Spot 24	274	81742	6.7	11.2537	0.8	2.9470	2.4	0.2406	2.2	0.94	1390.0	28.1	1394.1	18.2	1401.1	15.9	1401.1	15.9
Spot 26	199	1453035	1.9	11.1267	1.2	3.0378	3.4	0.2453	3.2	0.94	1413.9	40.4	1417.2	26.0	1422.8	23.0	1422.8	23.0
Spot 12	1340	289807	3.0	11.0947	0.9	2.8909	2.7	0.2327	2.6	0.95	1348.8	31.4	1379.5	20.6	1428.3	16.9	1428.3	16.9
Spot 12	1340	289807	3.0	11.0947	0.9	2.8909	2.7	0.2327	2.6	0.95	1348.8	31.4	1379.5	20.6	1428.3	16.9	1428.3	16.9
Spot 6	232	58116	2.9	11.0677	1.3	2.7581	2.9	0.2215	2.6	0.89	1289.7	29.9	1344.3	21.3	1433.0	24.6	1433.0	24.6
Spot 8	195	29011	1.7	11.0648	0.8	2.9777	2.7	0.2391	2.5	0.95	1381.8	31.5	1401.9	20.3	1433.5	16.2	1433.5	16.2

TABLE E2: U-TH-PB GEOCHRONOLOGIC ANALYSES

Analysis	U (ppm)	^{206}Pb / ^{204}Pb	U/Th	$^{206}Pb^*$ / $^{207}Pb^*$	± (%)	Isotope Ratios: $^{207}Pb^*$ / $^{235}U^*$	± (%)	$^{206}Pb^*$ / ^{238}U	± (%)	Error Corr.	Apparent Ages (Ma): $^{206}Pb^*$ / $^{238}U^*$	± (Ma)	$^{207}Pb^*$ / ^{235}U	± (Ma)	$^{206}Pb^*$ / $^{207}Pb^*$	± (Ma)	Best Age (Ma)	± (Ma)
Spot 27	221	113568	2.0	10.1143	0.8	3.6839	2.5	0.2704	2.4	0.95	1542.6	32.3	1567.9	19.8	1602.9	14.5	1602.9	14.5
Spot 33	543	221935	63.8	9.8147	0.9	3.5628	2.1	0.2537	2.0	0.91	1457.6	25.6	1541.3	17.0	1658.8	16.2	1658.8	16.2
Spot 7	692	649999	107.5	9.6101	0.8	3.4401	3.2	0.2399	3.1	0.96	1386.0	38.1	1513.6	24.9	1697.7	15.4	1697.7	15.4
Spot 28	633	56280	5.5	9.2730	0.9	4.1539	3.1	0.2795	2.9	0.96	1588.8	41.4	1665.0	25.2	1763.2	16.6	1763.2	16.6
TLP-03																		
Spot 33	100	361	1.6	90.0941	19.3	0.0090	19.5	0.0059	3.3	0.17	37.6	1.3	9.1	1.8	NA	NA	37.6	1.3
Spot 32	371	4549	1.2	21.5469	2.8	0.0397	3.8	0.0062	2.6	0.68	39.9	1.0	39.5	1.5	19.0	68.0	39.9	1.0
Spot 10	2259	39777	6.3	20.3902	1.1	0.0425	2.8	0.0063	2.6	0.92	40.4	1.0	42.3	1.2	149.9	25.0	40.4	1.0
Spot 26	592	9521	2.7	20.4728	2.4	0.0427	4.2	0.0063	3.5	0.83	40.7	1.4	42.4	1.8	140.4	55.7	40.7	1.4
Spot 9	1166	83171	4.5	20.4016	1.7	0.0431	4.4	0.0064	4.1	0.93	41.0	1.7	42.8	1.9	148.6	38.9	41.0	1.7
Spot 16	641	26359	2.2	20.3703	2.4	0.0435	4.0	0.0064	3.2	0.80	41.4	1.3	43.3	1.7	152.2	56.2	41.4	1.3
Spot 1	445	26628	3.4	21.1824	2.3	0.0420	3.4	0.0065	2.5	0.74	41.5	1.0	41.8	1.4	59.8	54.9	41.5	1.0
Spot 15	773	2836	2.4	21.1273	1.9	0.0422	4.1	0.0065	3.6	0.89	41.5	1.5	41.9	1.7	66.0	44.6	41.5	1.5
Spot 14	1134	24977	3.9	20.6671	1.7	0.0437	3.0	0.0066	2.5	0.82	42.1	1.0	43.4	1.3	118.2	40.7	42.1	1.0
Spot 21	1232	31325	3.8	20.7178	1.5	0.0467	2.3	0.0070	1.7	0.75	45.1	0.8	46.4	1.0	112.4	36.0	45.1	0.8
Spot 6	765	139647	14.6	11.0600	1.0	2.9154	3.1	0.2340	3.0	0.95	1355.2	36.4	1385.9	23.8	1434.3	19.2	1434.3	19.2
Spot 30	420	209588	3.0	9.9115	1.2	3.6543	3.7	0.2628	3.5	0.95	1504.2	47.4	1561.4	29.7	1640.6	22.1	1640.6	22.1
Spot 31	606	537665	13.9	9.7462	1.1	3.5721	3.6	0.2526	3.4	0.95	1451.9	43.9	1543.4	28.2	1671.7	20.8	1671.7	20.8
Spot 27	518	34899	7.6	9.6183	1.4	3.4262	3.5	0.2391	3.3	0.92	1382.1	40.5	1510.4	27.8	1696.1	25.2	1696.1	25.2
Spot 3	604	48858	4.8	9.1415	1.3	4.2085	3.9	0.2791	3.7	0.95	1587.1	51.5	1675.7	31.8	1789.3	22.9	1789.3	22.9

TABLE E2: U-TH-PB GEOCHRONOLOGIC ANALYSES

Analysis	U (ppm)	$^{206}Pb/^{204}Pb$	U/Th	$^{206}Pb^*/^{207}Pb^*$	± (%)	Isotope Ratios: $^{207}Pb^*/^{235}U^*$	± (%)	$^{206}Pb^*/^{238}U$	± (%)	Error Corr.	Apparent Ages (Ma): $^{206}Pb^*/^{238}U^*$	± (Ma)	$^{207}Pb^*/^{235}U$	± (Ma)	$^{206}Pb^*/^{207}Pb^*$	± (Ma)	Best Age (Ma)	± (Ma)
Spot 22	473	122743	4.6	9.0791	1.0	4.1858	3.4	0.2757	3.3	0.95	1569.9	45.5	1671.2	28.1	1801.8	19.0	1801.8	19.0
DUG																		
16DUG-20	220	5672	0.7	18.1283	24.7	0.0363	27.6	0.0048	12.3	0.44	30.7	3.8	36.2	9.8	418.8	559.3	30.7	3.8
16DUG-27	116	2005	0.7	30.5864	89.9	0.0255	92.9	0.0057	23.2	0.25	36.4	8.4	25.6	23.5	-902.2	1797.3	36.4	8.4
16DUG-39	59	39279	2.7	11.5020	0.8	2.9284	1.2	0.2443	0.9	0.72	1409.0	11.0	1389.3	9.1	1359.2	16.1	1359.2	16.1
16DUG-21	68	54285	0.7	11.1935	1.3	3.0866	1.6	0.2506	0.8	0.53	1441.5	10.8	1429.4	12.1	1411.4	25.5	1411.4	25.5
16DUG-25	455	549589	4.1	11.1546	0.4	3.0447	7.2	0.2463	7.2	1.00	1419.4	91.3	1418.9	54.9	1418.0	7.8	1418.0	7.8
16DUG-19	115	66894	1.8	11.1158	0.7	3.1369	1.2	0.2529	1.0	0.82	1453.4	13.1	1441.8	9.5	1424.7	13.5	1424.7	13.5
16DUG-03	147	101233	1.5	11.0964	0.7	2.8111	1.8	0.2262	1.7	0.92	1314.7	20.2	1358.5	13.8	1428.0	13.5	1428.0	13.5
16DUG-16	54	115005	0.6	11.0756	2.5	3.1149	2.6	0.2502	0.8	0.31	1439.6	10.5	1436.4	20.3	1431.6	48.0	1431.6	48.0
16DUG-05	214	132371	0.9	11.0711	0.5	3.1134	1.1	0.2500	0.9	0.86	1438.4	11.7	1436.0	8.1	1432.4	10.1	1432.4	10.1
16DUG-04	86	54938	1.2	11.0709	1.2	3.1191	1.3	0.2504	0.4	0.28	1440.8	4.6	1437.4	9.9	1432.4	23.6	1432.4	23.6
16DUG-23	57	70723	0.8	11.0632	1.4	3.1125	1.8	0.2497	1.2	0.66	1437.1	15.7	1435.8	14.2	1433.8	26.4	1433.8	26.4
16DUG-26	212	372417	2.2	11.0445	0.4	3.1517	0.5	0.2525	0.3	0.57	1451.1	4.1	1445.4	4.2	1437.0	8.6	1437.0	8.6
16DUG-17	152	172172	1.1	11.0411	0.7	3.0543	1.9	0.2446	1.7	0.93	1410.5	22.0	1421.3	14.4	1437.6	13.5	1437.6	13.5
16DUG-30	376	501394	2.2	11.0373	0.6	3.1285	6.2	0.2504	6.2	1.00	1440.7	79.7	1439.7	47.7	1438.2	10.6	1438.2	10.6
16DUG-06	198	263693	0.7	11.0362	0.8	3.2246	1.3	0.2581	1.1	0.81	1480.1	14.3	1463.1	10.4	1438.4	15.1	1438.4	15.1
16DUG-18	177	156499	0.4	11.0247	0.8	3.1971	1.2	0.2556	0.9	0.73	1467.5	11.7	1456.5	9.4	1440.4	15.9	1440.4	15.9
16DUG-28	193	101467	0.4	11.0104	0.3	3.1137	0.7	0.2486	0.6	0.88	1431.5	8.3	1436.1	5.6	1442.9	6.6	1442.9	6.6
16DUG-	168	14284	2.8	11.003	0.6	3.1544	0.8	0.2517	0.5	0.61	1447.5	6.0	1446.1	5.9	1444.0	11.5	1444.0	11.5

TABLE E2: U-TH-PB GEOCHRONOLOGIC ANALYSES

Analysis	U (ppm)	$^{206}Pb/^{204}Pb$	U/Th	$^{206}Pb^*/^{207}Pb^*$	± (%)	Isotope Ratios $^{207}Pb^*/^{235}U^*$	± (%)	$^{206}Pb^*/^{238}U$	± (%)	Error Corr.	Apparent Ages (Ma) $^{206}Pb^*/^{238}U^*$	± (Ma)	$^{207}Pb^*/^{235}U$	± (Ma)	$^{206}Pb^*/^{207}Pb^*$	± (Ma)	Best Age (Ma)	± (Ma)
33		3		8														
16DUG-36	119	88675	0.8	10.9976	0.7	3.2958	1.0	0.2629	0.7	0.71	1504.6	9.7	1480.1	7.9	1445.1	13.5	1445.1	13.5
16DUG-31	291	385134	0.4	10.9962	0.4	3.1638	1.0	0.2523	0.9	0.91	1450.4	11.3	1448.4	7.4	1445.3	7.3	1445.3	7.3
16DUG-38	115	207538	1.4	10.9880	1.1	3.2100	1.3	0.2558	0.6	0.45	1468.4	7.7	1459.6	10.0	1446.8	21.9	1446.8	21.9
16DUG-34	76	53228	0.9	10.9820	0.9	3.2280	1.2	0.2571	0.8	0.70	1475.0	11.1	1463.9	9.4	1447.8	16.5	1447.8	16.5
16DUG-13	133	125606	0.4	10.9768	0.9	3.1180	1.2	0.2482	0.7	0.58	1429.3	8.6	1437.1	8.9	1448.7	18.0	1448.7	18.0
16DUG-08	180	175171	1.8	10.9546	0.7	3.1535	1.4	0.2505	1.2	0.87	1441.3	16.1	1445.9	11.1	1452.6	13.6	1452.6	13.6
16DUG-22	340	269789	1.0	10.9479	0.4	3.2565	4.0	0.2586	4.0	0.99	1482.5	53.0	1470.7	31.2	1453.7	7.8	1453.7	7.8
16DUG-40	93	190899	1.2	10.9241	0.5	3.2241	0.9	0.2554	0.7	0.85	1466.5	9.6	1463.0	6.7	1457.9	8.8	1457.9	8.8
16DUG-32	126	137528	1.3	10.9041	1.2	3.2341	1.5	0.2558	0.8	0.55	1468.1	10.7	1465.4	11.5	1461.3	23.5	1461.3	23.5
16DUG-24	416	704815	2.3	10.8249	0.4	3.3570	1.2	0.2636	1.1	0.93	1508.0	15.0	1494.4	9.3	1475.2	8.1	1475.2	8.1
16DUG-10	346	502205	1.0	10.7220	1.7	3.1695	2.6	0.2465	2.1	0.78	1420.2	26.2	1449.8	20.4	1493.3	31.5	1493.3	31.5
16DUG-29	351	214671	7.6	10.3138	3.9	3.4664	5.3	0.2593	3.6	0.68	1486.2	48.1	1519.6	42.0	1566.4	73.2	1566.4	73.2
16DUG-37	282	333649	5.9	10.2426	0.2	3.7189	2.5	0.2763	2.5	1.00	1572.5	35.2	1575.4	20.3	1579.4	4.4	1579.4	4.4
16DUG-01	115	143314	0.5	9.7969	0.7	4.1112	0.8	0.2921	0.5	0.63	1652.1	7.8	1656.5	6.9	1662.1	12.1	1662.1	12.1
16DUG-11	223	449115	1.5	3.7350	2.3	20.2274	2.4	0.5479	0.8	0.32	2816.6	17.4	3102.3	23.4	3292.8	36.1	3292.8	36.1
TL																		
Spot 21	944	356136	2.7	11.3597	0.8	3.0051	2.5	0.2477	2.3	0.94	1426.5	29.8	1408.9	18.8	1383.1	15.8	1383.1	15.8
Spot 82	296	65855	5.1	11.3501	1.0	2.9940	2.3	0.2466	2.1	0.90	1420.8	26.3	1406.1	17.4	1384.8	18.9	1384.8	18.9
Spot 42	1116	679098	0.7	11.3406	1.0	3.0033	2.9	0.2471	2.7	0.94	1423.6	34.3	1408.5	21.9	1386.4	19.5	1386.4	19.5

TABLE E2: U-TH-PB GEOCHRONOLOGIC ANALYSES

						Isotope Ratios					Apparent Ages (Ma)						Best Age	
Analysis	U (ppm)	^{206}Pb / ^{204}Pb	U/Th	$^{206}Pb^*$ / $^{207}Pb^*$	± (%)	$^{207}Pb^*$ / $^{235}U^*$	± (%)	$^{206}Pb^*$ / ^{238}U	± (%)	Error Corr.	$^{206}Pb^*$ / $^{238}U^*$	± (Ma)	$^{207}Pb^*$ / ^{235}U	± (Ma)	$^{206}Pb^*$ / $^{207}Pb^*$	± (Ma)	(Ma)	± (Ma)
Spot 56	73	52122	0.5	11.3390	1.0	2.9725	2.4	0.2446	2.1	0.90	1410.3	27.1	1400.6	18.0	1386.6	19.3	1386.6	19.3
Spot 57	116	33874	1.5	11.3257	1.0	3.0733	3.0	0.2526	2.9	0.95	1451.7	37.2	1426.1	23.2	1388.9	18.9	1388.9	18.9
Spot 100	100	391202	0.5	11.2898	0.8	3.0993	2.2	0.2539	2.0	0.92	1458.5	26.1	1432.5	16.6	1395.0	15.9	1395.0	15.9
Spot 47	76	65123	1.0	11.2860	0.8	3.0729	2.1	0.2516	1.9	0.93	1446.9	25.0	1426.0	15.9	1395.6	14.4	1395.6	14.4
Spot 50	120	60967	0.5	11.2701	1.1	3.0040	3.1	0.2456	2.9	0.93	1416.0	36.7	1408.6	23.6	1398.3	21.9	1398.3	21.9
Spot 60	124	173419	0.9	11.2146	0.8	3.0281	2.4	0.2464	2.3	0.94	1419.9	29.1	1414.7	18.5	1407.8	15.3	1407.8	15.3
Spot 76	184	80472	1.6	11.1999	0.8	3.1596	2.4	0.2568	2.2	0.94	1473.3	29.4	1447.4	18.4	1410.3	16.0	1410.3	16.0
Spot 85	128	108091	1.1	11.1989	0.9	2.9972	2.2	0.2435	2.0	0.90	1405.1	24.8	1406.9	16.6	1410.5	18.2	1410.5	18.2
Spot 33	212	68672	2.6	11.1948	0.8	3.0946	2.4	0.2514	2.3	0.94	1445.5	29.3	1431.4	18.5	1411.2	16.0	1411.2	16.0
Spot 15	262	266123	0.6	11.1939	0.9	3.1512	2.7	0.2559	2.6	0.95	1469.1	33.5	1445.3	20.8	1411.3	16.6	1411.3	16.6
Spot 35	63	21182	1.1	11.1847	1.1	2.9992	2.2	0.2434	1.9	0.87	1404.3	24.4	1407.4	16.9	1412.9	20.8	1412.9	20.8
Spot 11	186	60700	0.4	11.1775	0.7	3.0024	2.8	0.2435	2.7	0.97	1404.9	33.9	1408.2	21.1	1414.1	13.3	1414.1	13.3
Spot 12	96	78338	1.2	11.1752	0.7	3.0281	2.3	0.2455	2.2	0.95	1415.4	28.4	1414.7	17.9	1414.5	13.9	1414.5	13.9
Spot 65	304	530219	1.5	11.1590	0.9	3.0996	2.4	0.2510	2.2	0.92	1443.5	28.1	1432.6	18.0	1417.3	17.1	1417.3	17.1
Spot 103	99	77073	1.4	11.1577	0.8	3.0028	2.3	0.2431	2.1	0.94	1402.8	26.6	1408.3	17.2	1417.5	15.0	1417.5	15.0
Spot 32	89	70767	0.5	11.1557	1.0	3.0798	2.3	0.2493	2.0	0.91	1434.8	26.2	1427.7	17.3	1417.9	18.2	1417.9	18.2
Spot 105	105	38196	0.7	11.1551	1.0	2.9878	2.9	0.2418	2.7	0.94	1396.2	34.2	1404.5	22.1	1418.0	18.7	1418.0	18.7
Spot 87	140	202653	0.5	11.1470	1.0	3.0308	3.4	0.2451	3.2	0.95	1413.3	40.7	1415.4	25.7	1419.4	19.2	1419.4	19.2
Spot 1	141	24076	0.5	11.1392	0.9	3.1326	2.6	0.2532	2.5	0.94	1454.9	32.4	1440.7	20.3	1420.7	16.6	1420.7	16.6

TABLE E2: U-TH-PB GEOCHRONOLOGIC ANALYSES

Analysis	U (ppm)	$^{206}Pb/^{204}Pb$	U/Th	$^{206}Pb^*/^{207}Pb^*$	± (%)	Isotope Ratios $^{207}Pb^*/^{235}U^*$	± (%)	$^{206}Pb^*/^{238}U$	± (%)	Error Corr.	Apparent Ages (Ma) $^{206}Pb^*/^{238}U^*$	± (Ma)	$^{207}Pb^*/^{235}U$	± (Ma)	$^{206}Pb^*/^{207}Pb^*$	± (Ma)	Best Age (Ma)	± (Ma)
Spot 84	142	83688	1.4	11.1289	0.7	2.9684	2.1	0.2397	2.0	0.94	1385.1	24.6	1399.6	15.9	1422.5	13.4	1422.5	13.4
Spot 69	341	154916	4.6	11.1274	0.9	3.0295	2.4	0.2446	2.2	0.93	1410.6	28.2	1415.1	18.3	1422.7	17.3	1422.7	17.3
Spot 67	239	338506	0.8	11.1259	0.8	3.0928	2.5	0.2497	2.4	0.94	1436.8	30.4	1430.9	19.2	1423.0	15.7	1423.0	15.7
Spot 49	358	183757	1.0	11.1256	0.9	3.0586	2.3	0.2469	2.1	0.92	1422.5	26.5	1422.4	17.2	1423.0	16.7	1423.0	16.7
Spot 40	64	64936	0.9	11.1198	1.2	2.9585	2.6	0.2387	2.3	0.89	1379.9	28.9	1397.0	19.8	1424.0	22.6	1424.0	22.6
Spot 4	75	36738	0.5	11.1182	0.9	2.9824	2.5	0.2406	2.3	0.93	1389.8	28.9	1403.1	19.0	1424.3	17.9	1424.3	17.9
Spot 104	138	2428654	1.0	11.1166	0.9	3.0543	2.8	0.2464	2.6	0.94	1419.7	33.0	1421.3	21.1	1424.6	18.1	1424.6	18.1
Spot 20	141	1092473	5.7	11.0975	1.0	3.0973	2.4	0.2494	2.2	0.92	1435.4	28.5	1432.0	18.5	1427.9	18.2	1427.9	18.2
Spot 48	194	250533	1.6	11.0971	0.9	3.1041	2.3	0.2499	2.2	0.92	1438.2	27.7	1433.7	17.9	1427.9	17.2	1427.9	17.2
Spot 13	392	1049944	2.4	11.0915	0.9	3.0608	2.6	0.2463	2.4	0.94	1419.5	31.0	1422.9	19.8	1428.9	17.0	1428.9	17.0
Spot 30	272	424343	1.3	11.0898	1.0	3.0915	2.6	0.2488	2.4	0.92	1432.1	30.4	1430.6	19.6	1429.2	18.6	1429.2	18.6
Spot 89	143	490658	1.2	11.0870	0.9	3.0911	2.2	0.2487	2.0	0.91	1431.6	25.8	1430.5	16.9	1429.7	17.2	1429.7	17.2
Spot 14	274	337529	0.8	11.0807	1.0	3.1015	2.8	0.2494	2.6	0.94	1435.2	33.7	1433.1	21.5	1430.7	18.4	1430.7	18.4
Spot 78	273	740511	2.5	11.0799	1.0	3.0000	2.2	0.2412	2.0	0.90	1392.9	25.1	1407.6	17.0	1430.9	18.4	1430.9	18.4
Spot 108	66	16101	1.4	11.0798	0.9	3.0416	2.9	0.2445	2.8	0.95	1410.2	35.3	1418.1	22.3	1430.9	16.5	1430.9	16.5
Spot 2	113	359251	0.9	11.0786	0.9	3.0633	2.7	0.2462	2.5	0.94	1419.0	32.2	1423.6	20.5	1431.1	16.9	1431.1	16.9
Spot 27	191	433263	1.7	11.0712	0.8	3.1747	3.1	0.2550	3.0	0.96	1464.4	38.7	1451.0	23.7	1432.4	15.5	1432.4	15.5
Spot 73	608	290582	7.7	11.0674	0.7	3.0632	2.3	0.2460	2.2	0.95	1417.7	27.5	1423.5	17.5	1433.0	14.0	1433.0	14.0
Spot 86	390	103583	2.9	11.0639	1.0	3.0538	2.7	0.2452	2.5	0.93	1413.4	32.2	1421.2	20.9	1433.6	19.2	1433.6	19.2

TABLE E2: U-TH-PB GEOCHRONOLOGIC ANALYSES

Analysis	U (ppm)	^{206}Pb / ^{204}Pb	U/Th	$^{206}Pb^*$ / $^{207}Pb^*$	± (%)	Isotope Ratios: $^{207}Pb^*$ / $^{235}U^*$	± (%)	$^{206}Pb^*$ / ^{238}U	± (%)	Error Corr.	Apparent Ages (Ma): $^{206}Pb^*$ / $^{238}U^*$	± (Ma)	$^{207}Pb^*$ / ^{235}U	± (Ma)	$^{206}Pb^*$ / $^{207}Pb^*$	± (Ma)	Best Age (Ma)	± (Ma)
Spot 38	127	1205000	1.3	11.0563	1.0	3.1133	1.8	0.2498	1.5	0.84	1437.2	19.4	1436.0	13.7	1435.0	18.2	1435.0	18.2
Spot 95	98	60393	1.1	11.0548	0.7	3.0138	2.5	0.2417	2.4	0.96	1395.8	30.5	1411.1	19.3	1435.2	13.6	1435.2	13.6
Spot 91	189	78826	0.7	11.0522	1.0	3.0701	2.8	0.2462	2.6	0.93	1418.8	32.8	1425.2	21.1	1435.7	18.7	1435.7	18.7
Spot 109	236	119257	1.5	11.0518	0.8	3.1167	1.9	0.2499	1.7	0.90	1438.1	22.2	1436.8	14.7	1435.7	15.8	1435.7	15.8
Spot 77	257	117253	2.2	11.0508	0.8	3.1525	2.3	0.2528	2.2	0.94	1452.8	28.7	1445.6	18.0	1435.9	14.9	1435.9	14.9
Spot 22	344	129685	0.7	11.0491	0.9	3.0672	2.6	0.2459	2.4	0.93	1417.3	30.9	1424.5	19.9	1436.2	17.7	1436.2	17.7
Spot 10	221	225226	0.4	11.0334	0.9	3.1729	2.6	0.2540	2.5	0.94	1459.1	32.0	1450.6	20.1	1438.9	16.9	1438.9	16.9
Spot 45	56	58152	0.6	11.0318	0.9	2.9957	2.7	0.2398	2.6	0.94	1385.6	31.8	1406.5	20.6	1439.2	17.3	1439.2	17.3
Spot 55	310	445694	0.9	11.0316	0.7	3.0804	2.1	0.2466	2.0	0.94	1420.7	25.1	1427.8	16.0	1439.2	13.7	1439.2	13.7
Spot 80	83	100719	0.6	11.0257	0.9	3.0531	2.4	0.2443	2.2	0.93	1408.8	28.3	1421.0	18.3	1440.2	16.5	1440.2	16.5
Spot 51	174	95146	0.5	11.0208	0.9	3.0597	2.5	0.2447	2.3	0.92	1410.9	28.8	1422.7	18.8	1441.1	18.0	1441.1	18.0
Spot 110	165	262466	0.9	11.0059	0.9	3.0829	2.7	0.2462	2.6	0.94	1418.8	32.8	1428.4	20.9	1443.7	17.5	1443.7	17.5
Spot 75	274	5366812	1.2	10.9824	1.1	3.1200	3.0	0.2486	2.8	0.93	1431.4	36.1	1437.6	23.2	1447.7	20.4	1447.7	20.4
Spot 106	74	32212	0.4	10.9782	1.0	3.1342	2.4	0.2497	2.2	0.91	1436.7	28.7	1441.1	18.8	1448.5	19.1	1448.5	19.1
Spot 96	206	628361	2.0	10.9768	1.1	3.1567	3.7	0.2514	3.5	0.96	1445.8	45.7	1446.6	28.4	1448.7	20.3	1448.7	20.3
Spot 59	324	98061	3.4	10.9630	0.9	3.0895	2.7	0.2458	2.5	0.94	1416.6	31.9	1430.1	20.5	1451.1	17.9	1451.1	17.9
Spot 93	604	275208	8.8	10.8716	0.8	3.1127	2.2	0.2455	2.0	0.92	1415.4	25.2	1435.8	16.5	1467.0	15.8	1467.0	15.8
Spot 81	396	238727	3.7	10.8124	1.0	3.0576	2.5	0.2399	2.3	0.92	1386.1	29.1	1422.1	19.5	1477.4	19.1	1477.4	19.1
Spot 58	184	577365	1.4	10.8067	1.6	3.0932	2.6	0.2425	2.1	0.80	1399.9	26.6	1431.0	20.3	1478.4	30.0	1478.4	30.0

TABLE E2: U-TH-PB GEOCHRONOLOGIC ANALYSES

						Isotope Ratios					Apparent Ages (Ma)						Best Age	
Analysis	U (ppm)	^{206}Pb ^{204}Pb	U/Th	$^{206}Pb^*$ $^{207}Pb^*$	± (%)	$^{207}Pb^*$ $^{235}U^*$	± (%)	$^{206}Pb^*$ ^{238}U	± (%)	Error Corr.	$^{206}Pb^*$ $^{238}U^*$	± (Ma)	$^{207}Pb^*$ ^{235}U	± (Ma)	$^{206}Pb^*$ $^{207}Pb^*$	± (Ma)	(Ma)	± (Ma)
Spot 3	306	92658	2.1	10.8005	1.0	3.1710	2.5	0.2485	2.2	0.91	1430.7	28.8	1450.1	19.1	1479.5	19.8	1479.5	19.8
Spot 61	456	29040	1.9	10.7344	0.9	2.9989	2.4	0.2336	2.3	0.93	1353.2	27.5	1407.3	18.5	1491.1	16.9	1491.1	16.9
Spot 44	492	748151	74.2	10.1776	0.8	3.8270	2.3	0.2826	2.2	0.93	1604.5	30.7	1598.4	18.7	1591.2	15.9	1591.2	15.9
Spot 26	390	110516	6.3	10.0522	0.7	3.6828	2.4	0.2686	2.3	0.95	1533.8	31.1	1567.7	19.1	1614.4	13.4	1614.4	13.4
Spot 83	879	660979	2.4	10.0412	0.9	4.0322	2.5	0.2938	2.3	0.94	1660.4	34.3	1640.7	20.3	1616.4	16.1	1616.4	16.1
Spot 9	147	528242	1.7	9.9944	0.8	3.9660	2.1	0.2876	1.9	0.93	1629.5	27.9	1627.3	16.9	1625.1	14.0	1625.1	14.0
Spot 72	854	6369131	342.8	9.9667	0.8	3.9451	2.2	0.2853	2.0	0.93	1618.0	28.8	1623.0	17.5	1630.3	14.5	1630.3	14.5
Spot 107	550	556486	5.8	9.8621	0.7	3.8822	2.2	0.2778	2.1	0.94	1580.3	29.2	1610.0	17.8	1649.9	13.4	1649.9	13.4
Spot 88	1039	646883	295.7	9.8089	0.7	4.2970	1.7	0.3058	1.6	0.92	1720.1	24.0	1692.8	14.3	1659.9	13.0	1659.9	13.0
Spot 102	689	229162	178.2	9.7769	0.9	4.3356	2.2	0.3076	2.0	0.92	1728.7	30.2	1700.2	17.9	1665.9	16.2	1665.9	16.2
Spot 101	597	255895	11.4	9.7129	0.9	4.2135	2.0	0.2970	1.8	0.89	1676.2	26.3	1676.7	16.5	1678.1	17.1	1678.1	17.1
Spot 41	636	2380581	126.9	9.7118	0.9	4.1983	2.6	0.2958	2.4	0.94	1670.6	35.4	1673.7	21.0	1678.3	16.1	1678.3	16.1
Spot 43	242	284212	1.4	9.6717	0.8	4.1285	2.3	0.2897	2.1	0.93	1640.2	31.0	1660.0	18.7	1685.9	15.3	1685.9	15.3
Spot 79	96	59669	2.8	9.6484	1.0	4.1359	2.4	0.2895	2.2	0.91	1639.3	31.4	1661.4	19.4	1690.4	17.9	1690.4	17.9
Spot 62	161	421141	2.6	9.6377	0.9	4.4522	2.5	0.3113	2.3	0.93	1747.3	35.7	1722.1	20.8	1692.4	17.1	1692.4	17.1
Spot 99	64	117855	1.5	9.6322	0.7	4.1723	2.7	0.2916	2.6	0.96	1649.5	37.6	1668.6	22.0	1693.5	13.8	1693.5	13.8
Spot 98	692	69866	17.5	9.6227	0.8	4.2903	2.2	0.2996	2.1	0.94	1689.1	30.5	1691.5	18.0	1695.3	14.0	1695.3	14.0
Spot 53	208	152007	1.1	9.6206	0.7	4.1177	2.6	0.2874	2.5	0.96	1628.7	35.7	1657.8	21.1	1695.7	13.5	1695.7	13.5
Spot 54	301	238253	2.5	9.5416	0.7	4.4299	2.6	0.3067	2.5	0.96	1724.4	37.1	1718.0	21.2	1710.9	13.5	1710.9	13.5
Spot 29	473	299252	10.3	9.5059	0.8	4.3846	2.1	0.3024	2.0	0.93	1703.3	29.4	1709.4	17.4	1717.8	13.9	1717.8	13.9

TABLE E2: U-TH-PB GEOCHRONOLOGIC ANALYSES

Analysis	U (ppm)	^{206}Pb / ^{204}Pb	U/Th	$^{206}Pb^*$ / $^{207}Pb^*$	± (%)	Isotope Ratios: $^{207}Pb^*$ / $^{235}U^*$	± (%)	$^{206}Pb^*$ / ^{238}U	± (%)	Error Corr.	Apparent Ages (Ma): $^{206}Pb^*$ / $^{238}U^*$	± (Ma)	$^{207}Pb^*$ / ^{235}U	± (Ma)	$^{206}Pb^*$ / $^{207}Pb^*$	± (Ma)	Best Age (Ma)	± (Ma)
Spot 36	1358	650645	3.6	9.4634	0.9	4.7231	2.2	0.3243	2.0	0.92	1810.8	32.2	1771.4	18.6	1726.0	15.9	1726.0	15.9
Spot 92	303	262961	3.1	9.4594	1.0	4.4210	2.1	0.3034	1.8	0.88	1708.3	27.5	1716.3	17.2	1726.8	17.8	1726.8	17.8
Spot 46	382	216801	8.2	9.4567	1.0	4.4023	2.7	0.3021	2.5	0.94	1701.5	37.9	1712.8	22.4	1727.3	17.5	1727.3	17.5
Spot 16	1194	785827	1.5	9.4564	0.9	4.7139	2.3	0.3234	2.1	0.91	1806.5	33.1	1769.7	19.3	1727.4	17.3	1727.4	17.3
Spot 19	311	702667	1.7	9.4562	0.8	4.5809	2.5	0.3143	2.3	0.95	1761.9	36.0	1745.8	20.6	1727.4	14.7	1727.4	14.7
Spot 66	611	206247	2.1	9.4131	1.0	4.5884	2.7	0.3134	2.5	0.94	1757.4	38.9	1747.2	22.5	1735.8	17.6	1735.8	17.6
Spot 5	760	6235002	5.6	9.4081	0.8	4.4440	2.8	0.3034	2.6	0.96	1708.0	39.5	1720.6	22.8	1736.7	14.6	1736.7	14.6
Spot 23	274	341400	3.4	9.4029	0.9	4.5448	2.5	0.3101	2.3	0.92	1741.1	34.7	1739.2	20.5	1737.8	17.3	1737.8	17.3
Spot 31	94	104729	1.8	9.3542	0.7	4.6962	2.4	0.3187	2.2	0.95	1783.6	35.1	1766.6	19.8	1747.3	13.6	1747.3	13.6
Spot 18	669	2255562	4.7	9.3485	1.0	4.6563	2.8	0.3158	2.7	0.94	1769.4	41.2	1759.4	23.7	1748.4	17.9	1748.4	17.9
Spot 90	447	1038994	3.0	9.3391	0.8	4.5544	2.7	0.3086	2.5	0.95	1733.9	38.3	1741.0	22.1	1750.2	15.3	1750.2	15.3
Spot 25	391	170575	1.8	9.2851	1.3	4.5992	2.5	0.3099	2.2	0.86	1740.0	33.0	1749.1	20.9	1760.8	23.0	1760.8	23.0
Spot 6	148	1933309	3.7	9.1853	0.9	4.5477	2.3	0.3031	2.1	0.91	1706.6	31.5	1739.7	19.2	1780.6	17.3	1780.6	17.3
Spot 70	200	241226	2.3	9.1509	0.8	4.8386	2.2	0.3213	2.1	0.94	1795.9	32.7	1791.6	18.7	1787.4	14.2	1787.4	14.2
Spot 97	98	49905	1.7	9.0534	0.6	5.0171	2.4	0.3296	2.3	0.97	1836.3	37.0	1822.2	20.3	1806.9	11.4	1806.9	11.4
Spot 37	878	75493	2.2	9.0238	0.9	4.2729	2.4	0.2798	2.2	0.93	1590.2	31.3	1688.2	19.6	1812.9	15.6	1812.9	15.6
Spot 68	129	2968727	3.5	8.7917	0.8	5.1946	2.8	0.3314	2.7	0.96	1845.0	43.2	1851.7	24.0	1860.0	15.0	1860.0	15.0
Spot 64	438	117703	4.1	6.4271	1.2	9.1935	2.6	0.4287	2.2	0.88	2300.0	43.2	2357.5	23.4	2408.3	20.9	2408.3	20.9
RS																		
Spot 90	1468	47889	5.0	23.3136	1.6	0.0665	30.4	0.0112	30.4	1.00	72.1	21.8	65.4	19.3	NA	NA	72.1	21.8

TABLE E2: U-TH-PB GEOCHRONOLOGIC ANALYSES

Analysis	U (ppm)	^{206}Pb / ^{204}Pb	U/Th	$^{206}Pb^*$ / $^{207}Pb^*$	± (%)	Isotope Ratios: $^{207}Pb^*$ / $^{235}U^*$	± (%)	$^{206}Pb^*$ / ^{238}U	± (%)	Error Corr.	Apparent Ages (Ma): $^{206}Pb^*$ / $^{238}U^*$	± (Ma)	$^{207}Pb^*$ / ^{235}U	± (Ma)	$^{206}Pb^*$ / $^{207}Pb^*$	± (Ma)	Best Age (Ma)	± (Ma)
Spot 3	1077	113303	4.9	16.7632	1.0	0.7670	3.0	0.0933	2.8	0.95	575.0	15.4	578.0	13.0	591.1	20.9	575.0	15.4
Spot 58	161	99158	1.6	11.2581	1.0	3.0898	2.5	0.2524	2.3	0.91	1450.8	29.7	1430.2	19.2	1400.4	19.4	1400.4	19.4
Spot 53	104	35358	1.7	11.2155	1.1	3.0524	2.3	0.2484	2.0	0.87	1430.2	25.3	1420.8	17.4	1407.6	21.5	1407.6	21.5
Spot 97	244	474834	3.6	11.2098	1.0	3.0539	2.6	0.2484	2.3	0.91	1430.2	30.1	1421.2	19.6	1408.6	19.9	1408.6	19.9
Spot 38	330	186361	1.2	11.2039	0.9	3.0582	2.6	0.2486	2.5	0.94	1431.3	31.8	1422.3	20.2	1409.6	17.1	1409.6	17.1
Spot 99	104	107328	1.6	11.1956	1.2	3.0628	2.7	0.2488	2.5	0.90	1432.3	31.7	1423.4	20.9	1411.0	22.4	1411.0	22.4
Spot 101	166	109217	1.0	11.1893	0.8	2.9290	2.8	0.2378	2.7	0.96	1375.2	33.6	1389.4	21.5	1412.1	15.4	1412.1	15.4
Spot 8	195	160194	2.4	11.1602	0.8	3.0520	2.9	0.2471	2.7	0.96	1423.7	35.0	1420.7	21.9	1417.1	15.7	1417.1	15.7
Spot 52	89	74270	2.0	11.1574	0.9	3.1255	3.5	0.2530	3.4	0.96	1454.1	44.0	1439.0	27.0	1417.6	17.8	1417.6	17.8
Spot 41	76	694808	1.5	11.1532	1.0	3.1376	2.7	0.2539	2.5	0.93	1458.6	32.5	1442.0	20.6	1418.3	18.8	1418.3	18.8
Spot 44	255	90660	2.7	11.1424	1.0	3.0816	2.5	0.2491	2.2	0.91	1434.0	28.6	1428.1	18.8	1420.1	19.6	1420.1	19.6
Spot 80	182	131568	1.7	11.1363	0.9	3.0118	2.6	0.2434	2.4	0.93	1404.2	30.6	1410.6	19.8	1421.2	17.9	1421.2	17.9
Spot 70	198	85676	1.9	11.1263	0.9	3.1322	2.2	0.2529	2.0	0.92	1453.2	25.9	1440.6	16.7	1422.9	16.6	1422.9	16.6
Spot 5	230	191824	5.0	11.1242	1.0	3.0883	2.8	0.2493	2.6	0.93	1434.7	33.7	1429.8	21.7	1423.3	20.0	1423.3	20.0
Spot 82	158	375319	1.2	11.1232	1.2	3.0529	3.3	0.2464	3.1	0.93	1419.8	38.9	1421.0	25.1	1423.4	23.0	1423.4	23.0
Spot 55	206	124066	1.4	11.1223	1.0	3.0282	3.1	0.2444	2.9	0.95	1409.4	37.0	1414.7	23.5	1423.6	18.4	1423.6	18.4
Spot 43	162	53360	1.4	11.1204	0.9	3.0574	2.8	0.2467	2.7	0.95	1421.4	33.9	1422.1	21.5	1423.9	17.5	1423.9	17.5
Spot 84	92	27665	1.7	11.1167	1.4	3.0252	2.6	0.2440	2.2	0.84	1407.6	28.0	1414.0	20.1	1424.5	27.2	1424.5	27.2
Spot 37	360	105004	2.5	11.0951	0.8	3.0762	2.6	0.2476	2.5	0.95	1426.3	32.0	1426.8	20.2	1428.3	15.7	1428.3	15.7

TABLE E2: U-TH-PB GEOCHRONOLOGIC ANALYSES

Analysis	U (ppm)	^{206}Pb ^{204}Pb	U/Th	$^{206}Pb^*$ $^{207}Pb^*$	± (%)	Isotope Ratios $^{207}Pb^*$ $^{235}U^*$	± (%)	$^{206}Pb^*$ ^{238}U	± (%)	Error Corr.	Apparent Ages (Ma) $^{206}Pb^*$ $^{238}U^*$	± (Ma)	$^{207}Pb^*$ ^{235}U	± (Ma)	$^{206}Pb^*$ $^{207}Pb^*$	± (Ma)	Best Age (Ma)	± (Ma)
Spot 98	115	276784	2.2	11.0919	1.2	3.1377	2.3	0.2525	2.0	0.86	1451.5	25.9	1442.0	17.8	1428.8	22.5	1428.8	22.5
Spot 46	68	41495	1.7	11.0842	1.1	3.0769	2.8	0.2475	2.5	0.92	1425.4	32.5	1427.0	21.2	1430.1	21.1	1430.1	21.1
Spot 75	125	104481	2.0	11.0701	1.1	3.1731	2.6	0.2549	2.3	0.90	1463.6	30.6	1450.6	20.0	1432.6	21.1	1432.6	21.1
Spot 42	201	618234	0.6	11.0631	0.9	3.1288	3.2	0.2512	3.0	0.96	1444.4	39.4	1439.8	24.5	1433.8	17.8	1433.8	17.8
Spot 15	100	40487	1.2	11.0601	1.1	3.1316	3.0	0.2513	2.8	0.93	1445.2	36.0	1440.5	23.1	1434.3	21.4	1434.3	21.4
Spot 20	75	54077	2.0	11.0495	1.2	3.1238	3.1	0.2504	2.8	0.92	1440.8	36.1	1438.6	23.5	1436.1	23.1	1436.1	23.1
Spot 104	96	48035	1.7	11.0490	1.1	3.0444	2.6	0.2441	2.3	0.91	1407.8	29.4	1418.8	19.5	1436.2	20.2	1436.2	20.2
Spot 48	360	276528	4.0	11.0417	1.0	3.1053	3.0	0.2488	2.8	0.94	1432.2	36.2	1434.0	23.0	1437.5	18.7	1437.5	18.7
Spot 45	90	57314	1.8	11.0322	1.0	3.1478	2.3	0.2520	2.1	0.90	1448.7	27.3	1444.5	18.0	1439.1	19.3	1439.1	19.3
Spot 72	119	30858	1.3	11.0271	1.1	3.0156	2.9	0.2413	2.7	0.92	1393.4	33.6	1411.6	22.1	1440.0	21.4	1440.0	21.4
Spot 92	170	2815037	2.3	11.0139	1.0	3.0529	2.6	0.2440	2.4	0.92	1407.3	30.0	1421.0	19.8	1442.3	19.3	1442.3	19.3
Spot 25	152	55821	1.8	11.0073	1.5	2.9987	3.0	0.2395	2.7	0.87	1384.1	33.2	1407.3	23.2	1443.4	28.1	1443.4	28.1
Spot 69	188	110769	1.6	11.0068	1.0	3.1859	1.9	0.2544	1.6	0.84	1461.3	20.6	1453.7	14.5	1443.5	19.3	1443.5	19.3
Spot 107	102	136447	1.5	11.0034	0.9	3.1335	2.6	0.2502	2.4	0.94	1439.4	31.6	1441.0	20.0	1444.1	16.7	1444.1	16.7
Spot 31	211	520165	1.1	10.9795	1.0	3.1859	3.1	0.2538	2.9	0.95	1458.1	38.2	1453.7	23.9	1448.2	18.4	1448.2	18.4
Spot 2	495	446659	8.6	10.9695	1.0	2.9272	2.3	0.2330	2.1	0.91	1350.1	25.9	1389.0	17.7	1450.0	18.5	1450.0	18.5
Spot 88	457	442868	0.9	10.9485	1.0	3.1519	3.0	0.2504	2.8	0.94	1440.5	36.3	1445.5	23.1	1453.6	19.5	1453.6	19.5
Spot 93	145	65337	2.3	10.9359	1.0	3.1174	2.9	0.2474	2.7	0.94	1424.9	35.0	1437.0	22.4	1455.8	18.8	1455.8	18.8
Spot 76	528	764188	11.2	10.9188	0.9	3.0784	2.7	0.2439	2.5	0.94	1406.9	32.2	1427.3	20.7	1458.8	17.2	1458.8	17.2

TABLE E2: U-TH-PB GEOCHRONOLOGIC ANALYSES

Analysis	U (ppm)	^{206}Pb / ^{204}Pb	U/Th	$^{206}Pb^*$ / $^{207}Pb^*$	± (%)	Isotope Ratios: $^{207}Pb^*$ / $^{235}U^*$	± (%)	$^{206}Pb^*$ / ^{238}U	± (%)	Error Corr.	Apparent Ages (Ma): $^{206}Pb^*$ / $^{238}U^*$	± (Ma)	$^{207}Pb^*$ / ^{235}U	± (Ma)	$^{206}Pb^*$ / $^{207}Pb^*$	± (Ma)	Best Age (Ma)	± (Ma)
Spot 74	77	18656	1.6	10.8983	0.9	3.0983	3.0	0.2450	2.8	0.96	1412.7	35.8	1432.3	22.7	1462.4	16.6	1462.4	16.6
Spot 34	261	496843	2.5	10.8958	0.9	3.2564	3.3	0.2574	3.1	0.96	1476.8	41.5	1470.7	25.4	1462.8	16.6	1462.8	16.6
Spot 11	151	135428	1.2	10.8877	1.0	3.2561	2.9	0.2572	2.8	0.94	1475.7	36.3	1470.6	22.8	1464.2	19.2	1464.2	19.2
Spot 7	128	39266	1.9	10.8245	1.2	3.1354	3.2	0.2463	2.9	0.92	1419.2	37.2	1441.4	24.4	1475.3	23.3	1475.3	23.3
Spot 1	406	276311	3.2	10.8208	0.8	3.0072	3.3	0.2361	3.2	0.97	1366.4	39.2	1409.4	25.1	1475.9	15.8	1475.9	15.8
Spot 77	69	108925	1.9	10.8204	1.0	3.3735	2.8	0.2649	2.6	0.93	1514.6	34.6	1498.3	21.6	1476.0	19.2	1476.0	19.2
Spot 24	356	417920	4.6	10.7794	0.9	3.0605	2.6	0.2394	2.5	0.94	1383.4	30.9	1422.9	20.3	1483.2	17.7	1483.2	17.7
Spot 54	353	149463	0.6	10.7188	0.9	3.0510	2.8	0.2373	2.7	0.95	1372.6	33.1	1420.5	21.6	1493.8	17.1	1493.8	17.1
Spot 105	133	271067	2.5	10.5316	1.0	3.3884	3.0	0.2589	2.9	0.95	1484.4	38.1	1501.7	23.8	1527.1	18.3	1527.1	18.3
Spot 47	209	27231	1.6	10.3772	1.4	3.2890	3.1	0.2476	2.7	0.88	1426.3	34.6	1478.4	23.8	1554.9	26.9	1554.9	26.9
Spot 13	277	315364	1.5	9.9180	1.1	3.9935	2.2	0.2874	1.9	0.88	1628.5	27.9	1632.9	18.0	1639.4	19.8	1639.4	19.8
Spot 100	717	503928	6.9	9.9112	0.8	3.8049	2.8	0.2736	2.7	0.96	1559.2	37.3	1593.8	22.6	1640.6	15.0	1640.6	15.0
Spot 59	300	325901	1.7	9.7852	1.0	4.2295	2.4	0.3003	2.2	0.91	1692.8	32.7	1679.8	19.8	1664.3	18.3	1664.3	18.3
Spot 14	114	254547	12.5	9.7748	1.3	4.1756	3.2	0.2962	2.9	0.92	1672.2	43.0	1669.3	26.1	1666.3	23.4	1666.3	23.4
Spot 85	404	405281	3.8	9.7469	0.7	4.1034	2.4	0.2902	2.3	0.95	1642.5	33.6	1655.0	19.9	1671.6	13.7	1671.6	13.7
Spot 60	998	935652	2.3	9.7443	1.0	4.2417	2.5	0.2999	2.2	0.91	1690.8	33.3	1682.1	20.3	1672.1	19.0	1672.1	19.0
Spot 87	188	290066	2.1	9.7437	1.3	4.1977	2.6	0.2968	2.3	0.86	1675.3	33.4	1673.6	21.5	1672.2	24.3	1672.2	24.3
Spot 65	422	475405	3.5	9.6905	1.2	4.1201	3.4	0.2897	3.2	0.93	1640.0	45.8	1658.3	27.7	1682.3	22.5	1682.3	22.5
Spot 103	363	3241500	4.5	9.5357	1.0	4.3858	2.8	0.3034	2.7	0.94	1708.4	40.1	1709.7	23.5	1712.0	17.8	1712.0	17.8

TABLE E2: U-TH-PB GEOCHRONOLOGIC ANALYSES

Analysis	U (ppm)	^{206}Pb / ^{204}Pb	U/Th	$^{206}Pb^*$ / $^{207}Pb^*$	± (%)	Isotope Ratios: $^{207}Pb^*$ / $^{235}U^*$	± (%)	$^{206}Pb^*$ / ^{238}U	± (%)	Error Corr.	Apparent Ages (Ma): $^{206}Pb^*$ / $^{238}U^*$	± (Ma)	$^{207}Pb^*$ / ^{235}U	± (Ma)	$^{206}Pb^*$ / $^{207}Pb^*$	± (Ma)	Best Age (Ma)	± (Ma)
Spot 78	491	254984	9.3	9.5344	1.0	4.0975	2.7	0.2835	2.5	0.93	1608.8	35.3	1653.8	21.9	1712.3	18.7	1712.3	18.7
Spot 96	481	250741	1.9	9.5327	1.2	4.1177	2.7	0.2848	2.5	0.91	1615.6	35.3	1657.8	22.2	1712.6	21.2	1712.6	21.2
Spot 27	529	2653230	1.9	9.5322	1.2	4.2797	2.7	0.2960	2.4	0.89	1671.5	35.0	1689.5	21.9	1712.7	22.2	1712.7	22.2
Spot 79	270	149269	1.8	9.5280	0.9	4.2639	2.5	0.2948	2.3	0.94	1665.3	34.2	1686.4	20.5	1713.5	16.1	1713.5	16.1
Spot 6	140	72226	17.1	9.5005	1.1	4.3985	2.7	0.3032	2.5	0.92	1707.2	37.2	1712.1	22.4	1718.8	19.7	1718.8	19.7
Spot 86	388	426491	1.3	9.4910	1.1	4.2568	2.8	0.2931	2.5	0.92	1657.2	37.2	1685.1	22.7	1720.6	19.6	1720.6	19.6
Spot 63	535	250786	3.0	9.4609	1.0	4.2595	2.7	0.2924	2.5	0.93	1653.5	36.7	1685.6	22.3	1726.5	18.5	1726.5	18.5
Spot 28	645	205840	14.3	9.4587	0.9	4.1333	2.1	0.2837	1.9	0.91	1609.8	27.3	1660.9	17.3	1726.9	16.1	1726.9	16.1
Spot 18	270	84575	2.3	9.4542	0.9	4.3149	2.6	0.2960	2.5	0.94	1671.4	36.2	1696.2	21.5	1727.8	15.8	1727.8	15.8
Spot 49	214	113899	2.3	9.4137	0.8	4.3340	2.0	0.2960	1.8	0.91	1671.6	26.4	1699.9	16.3	1735.7	15.4	1735.7	15.4
Spot 66	344	558291	2.5	9.4133	1.0	4.2839	2.8	0.2926	2.6	0.93	1654.5	37.7	1690.3	22.8	1735.7	18.0	1735.7	18.0
Spot 10	698	854140	2.7	9.3967	0.9	4.2499	2.3	0.2898	2.1	0.91	1640.3	30.0	1683.7	18.7	1739.0	17.0	1739.0	17.0
Spot 4	699	55407	4.4	9.3824	1.1	4.0074	2.8	0.2728	2.6	0.92	1555.0	35.5	1635.7	22.6	1741.8	19.4	1741.8	19.4
Spot 61	586	456898	1.8	9.3426	1.0	4.3666	2.6	0.2960	2.4	0.93	1671.5	35.0	1706.0	21.2	1749.5	17.6	1749.5	17.6
AM																		
Spot 65	1412	19163	1.5	21.3849	1.2	0.0427	2.8	0.0066	2.5	0.91	42.6	1.1	42.5	1.1	37.1	28.1	42.6	1.1
Spot 54	1601	234419	3.6	20.8810	0.9	0.0612	2.3	0.0093	2.1	0.91	59.5	1.2	60.3	1.3	93.9	22.1	59.5	1.2
Spot 93	48	17840	2.4	11.2867	0.9	3.0658	2.1	0.2511	1.9	0.90	1444.0	24.1	1424.2	15.8	1395.5	16.9	1395.5	16.9
Spot 46	52	37897	2.3	11.2668	0.9	3.1144	2.9	0.2546	2.7	0.95	1462.1	35.9	1436.2	22.1	1398.9	16.4	1398.9	16.4
Spot 47	91	52775	2.2	11.2233	0.9	3.1024	2.7	0.2526	2.6	0.94	1452.1	33.5	1433.3	20.9	1406.3	17.3	1406.3	17.3

TABLE E2: U-TH-PB GEOCHRONOLOGIC ANALYSES

Analysis	U (ppm)	^{206}Pb ^{204}Pb	U/Th	$^{206}Pb^*$ $^{207}Pb^*$	± (%)	Isotope Ratios $^{207}Pb^*$ $^{235}U^*$	± (%)	$^{206}Pb^*$ ^{238}U	± (%)	Error Corr.	Apparent Ages (Ma) $^{206}Pb^*$ $^{238}U^*$	± (Ma)	$^{207}Pb^*$ ^{235}U	± (Ma)	$^{206}Pb^*$ $^{207}Pb^*$	± (Ma)	Best Age (Ma)	± (Ma)
Spot 105	102	43473	1.4	11.2114	1.0	3.0300	3.2	0.2465	3.0	0.95	1420.3	38.5	1415.2	24.3	1408.3	18.9	1408.3	18.9
Spot 73	97	37492	1.8	11.2109	0.9	3.1461	2.4	0.2559	2.3	0.93	1468.9	29.8	1444.0	18.8	1408.4	17.4	1408.4	17.4
Spot 109	59	48648	2.1	11.2017	0.8	3.1443	2.1	0.2556	1.9	0.92	1467.1	25.0	1443.6	15.9	1410.0	15.4	1410.0	15.4
Spot 11	153	90678	1.5	11.1881	1.0	3.0596	2.5	0.2484	2.3	0.92	1430.1	29.9	1422.6	19.3	1412.3	18.7	1412.3	18.7
Spot 64	182	167494	2.1	11.1863	0.9	3.0336	2.4	0.2462	2.3	0.93	1419.0	28.8	1416.1	18.5	1412.6	16.8	1412.6	16.8
Spot 67	744	593742	12.6	11.1839	0.7	2.9228	2.2	0.2372	2.0	0.94	1372.0	25.1	1387.8	16.3	1413.0	13.7	1413.0	13.7
Spot 2	56	115954	1.9	11.1808	0.9	3.1006	2.9	0.2515	2.8	0.95	1446.4	35.9	1432.9	22.4	1413.6	17.9	1413.6	17.9
Spot 53	94	106913	1.3	11.1750	0.8	3.0458	2.4	0.2470	2.2	0.94	1422.8	28.3	1419.2	18.1	1414.6	15.6	1414.6	15.6
Spot 18	154	39985	2.8	11.1749	0.7	3.0607	2.2	0.2482	2.1	0.95	1429.0	26.9	1422.9	17.0	1414.6	13.7	1414.6	13.7
Spot 79	132	32172	0.8	11.1739	1.1	3.0706	2.7	0.2489	2.5	0.92	1433.1	32.0	1425.4	20.8	1414.7	20.7	1414.7	20.7
Spot 86	61	120340	2.2	11.1721	0.9	3.0751	2.4	0.2493	2.2	0.92	1434.8	28.6	1426.5	18.5	1415.1	17.8	1415.1	17.8
Spot 110	71	101937	1.9	11.1649	1.0	3.1183	2.3	0.2526	2.0	0.90	1452.0	26.6	1437.2	17.4	1416.3	18.7	1416.3	18.7
Spot 15	56	26392	2.3	11.1606	0.9	3.0751	2.5	0.2490	2.3	0.94	1433.4	29.5	1426.5	18.8	1417.0	16.5	1417.0	16.5
Spot 17	90	688111	2.1	11.1579	0.8	3.1321	2.5	0.2536	2.3	0.94	1456.9	30.1	1440.6	18.9	1417.5	16.2	1417.5	16.2
Spot 19	200	154305	2.1	11.1551	0.7	3.1434	2.0	0.2544	1.9	0.94	1461.3	24.8	1443.4	15.5	1418.0	12.7	1418.0	12.7
Spot 49	149	92368	2.1	11.1527	0.9	3.1128	2.8	0.2519	2.6	0.94	1448.3	33.7	1435.9	21.2	1418.4	17.9	1418.4	17.9
Spot 4	55	108456	2.1	11.1475	0.8	3.0602	2.3	0.2475	2.2	0.93	1425.7	27.8	1422.8	17.9	1419.3	16.2	1419.3	16.2
Spot 9	61	40091	2.0	11.1425	1.2	3.0951	2.6	0.2502	2.3	0.90	1439.7	29.9	1431.5	19.8	1420.1	22.0	1420.1	22.0
Spot 108	66	120823	2.0	11.1394	0.8	3.1304	2.7	0.2530	2.6	0.95	1454.0	33.4	1440.2	20.7	1420.6	15.4	1420.6	15.4

TABLE E2: U-TH-PB GEOCHRONOLOGIC ANALYSES

Analysis	U (ppm)	^{206}Pb / ^{204}Pb	U/Th	$^{206}Pb^*$ / $^{207}Pb^*$	± (%)	Isotope Ratios: $^{207}Pb^*$ / $^{235}U^*$	± (%)	$^{206}Pb^*$ / ^{238}U	± (%)	Error Corr.	Apparent Ages (Ma): $^{206}Pb^*$ / $^{238}U^*$	± (Ma)	$^{207}Pb^*$ / ^{235}U	± (Ma)	$^{206}Pb^*$ / $^{207}Pb^*$	± (Ma)	Best Age (Ma)	± (Ma)
Spot 8	158	62442	0.6	11.1258	0.6	3.0355	2.3	0.2450	2.2	0.96	1412.9	27.6	1416.6	17.3	1423.0	12.4	1423.0	12.4
Spot 24	178	92913	2.5	11.1252	0.9	3.0560	3.0	0.2467	2.9	0.95	1421.4	37.1	1421.7	23.3	1423.1	17.4	1423.1	17.4
Spot 30	44	7607325	2.0	11.1233	0.9	3.0905	3.2	0.2494	3.1	0.96	1435.5	39.3	1430.3	24.5	1423.4	17.4	1423.4	17.4
Spot 92	122	110856	1.5	11.1098	0.9	3.0319	2.5	0.2444	2.4	0.94	1409.6	30.1	1415.7	19.4	1425.7	16.9	1425.7	16.9
Spot 63	105	81233	2.8	11.1055	0.9	3.1617	2.6	0.2548	2.5	0.93	1463.0	32.2	1447.9	20.3	1426.5	18.1	1426.5	18.1
Spot 98	45	20142	2.2	11.0947	1.0	3.0937	2.7	0.2490	2.5	0.93	1433.6	31.8	1431.1	20.4	1428.3	18.6	1428.3	18.6
Spot 13	61	40427	1.7	11.0897	0.8	3.0432	2.4	0.2449	2.3	0.95	1412.0	29.3	1418.5	18.7	1429.2	15.2	1429.2	15.2
Spot 52	144	196655	0.9	11.0845	0.8	3.0445	2.2	0.2449	2.1	0.93	1411.9	26.1	1418.9	16.9	1430.1	15.9	1430.1	15.9
Spot 75	54	36538	2.3	11.0838	0.9	3.1175	2.8	0.2507	2.7	0.94	1442.2	34.5	1437.0	21.7	1430.2	17.7	1430.2	17.7
Spot 38	128	139304	2.4	11.0790	0.9	3.1478	2.3	0.2530	2.1	0.93	1454.2	27.5	1444.5	17.6	1431.0	16.2	1431.0	16.2
Spot 27	499	97757	13.5	11.0757	0.9	2.6286	2.4	0.2112	2.2	0.93	1235.4	25.1	1308.7	17.7	1431.6	16.9	1431.6	16.9
Spot 103	58	27501	2.3	11.0715	1.0	3.2092	2.3	0.2578	2.1	0.90	1478.6	27.4	1459.4	17.8	1432.3	18.9	1432.3	18.9
Spot 72	238	120637	1.7	11.0648	0.8	3.0644	2.8	0.2460	2.7	0.96	1418.0	34.5	1423.8	21.7	1433.5	15.7	1433.5	15.7
Spot 12	55	16564	2.1	11.0639	0.9	3.0763	2.3	0.2470	2.1	0.92	1422.8	26.8	1426.8	17.4	1433.6	16.6	1433.6	16.6
Spot 10	214	677348	2.2	11.0625	1.0	3.0651	2.8	0.2460	2.6	0.93	1417.9	32.7	1424.0	21.1	1433.9	18.8	1433.9	18.8
Spot 57	99	224934	0.7	11.0609	1.0	3.1358	2.0	0.2517	1.8	0.87	1447.1	22.7	1441.5	15.4	1434.2	18.5	1434.2	18.5
Spot 71	43	44701	1.4	11.0578	1.1	3.1093	2.4	0.2495	2.2	0.89	1435.7	27.8	1435.0	18.6	1434.7	21.2	1434.7	21.2
Spot 102	660	63070	0.4	11.0564	1.0	3.0241	2.5	0.2426	2.3	0.91	1400.2	29.0	1413.7	19.3	1434.9	19.7	1434.9	19.7
Spot 16	83	190815	2.7	11.0485	1.3	3.1951	3.2	0.2561	2.9	0.91	1470.1	38.3	1456.0	24.7	1436.3	24.9	1436.3	24.9

TABLE E2: U-TH-PB GEOCHRONOLOGIC ANALYSES

Analysis	U (ppm)	^{206}Pb / ^{204}Pb	U/Th	$^{206}Pb^*$ / $^{207}Pb^*$	± (%)	Isotope Ratios: $^{207}Pb^*$ / $^{235}U^*$	± (%)	$^{206}Pb^*$ / ^{238}U	± (%)	Error Corr.	Apparent Ages (Ma): $^{206}Pb^*$ / $^{238}U^*$	± (Ma)	$^{207}Pb^*$ / ^{235}U	± (Ma)	$^{206}Pb^*$ / $^{207}Pb^*$	± (Ma)	Best Age (Ma)	± (Ma)
Spot 51	362	931243	4.6	11.0468	0.8	3.1213	2.3	0.2502	2.1	0.93	1439.4	27.3	1438.0	17.5	1436.6	15.8	1436.6	15.8
Spot 26	111	422641	1.7	11.0420	0.8	3.1100	2.4	0.2492	2.2	0.95	1434.2	28.9	1435.2	18.2	1437.4	14.5	1437.4	14.5
Spot 68	108	93721	2.3	11.0411	0.8	3.1442	2.3	0.2519	2.2	0.94	1448.2	28.1	1443.6	17.8	1437.6	14.8	1437.6	14.8
Spot 81	110	129473	2.3	11.0388	0.9	3.0346	3.0	0.2431	2.8	0.95	1402.6	35.6	1416.4	22.8	1438.0	17.8	1438.0	17.8
Spot 32	82	233667	1.0	11.0362	0.8	3.1010	2.2	0.2483	2.0	0.93	1429.8	26.2	1432.9	16.9	1438.4	15.8	1438.4	15.8
Spot 77	53	33015	1.9	11.0331	0.9	3.0513	2.6	0.2443	2.4	0.93	1408.9	30.3	1420.6	19.6	1439.0	17.4	1439.0	17.4
Spot 39	52	21996	2.2	11.0055	0.8	3.0979	2.1	0.2474	1.9	0.92	1425.0	24.1	1432.2	15.8	1443.7	15.6	1443.7	15.6
Spot 42	546	201808	2.7	11.0046	0.6	3.0382	2.1	0.2426	2.0	0.96	1400.2	25.2	1417.3	16.0	1443.9	11.8	1443.9	11.8
Spot 48	158	6587799	0.7	11.0028	1.0	3.0637	2.8	0.2446	2.6	0.94	1410.5	33.2	1423.7	21.4	1444.2	18.3	1444.2	18.3
Spot 62	760	742613	19.7	10.9992	0.9	2.8342	2.4	0.2262	2.2	0.93	1314.5	26.1	1364.6	17.8	1444.8	16.8	1444.8	16.8
Spot 23	473	253103	7.7	10.9978	0.8	2.7957	2.3	0.2231	2.2	0.94	1298.2	25.3	1354.4	17.2	1445.1	15.1	1445.1	15.1
Spot 83	68	99371	2.2	10.9809	0.8	2.9795	2.4	0.2374	2.3	0.95	1373.1	28.1	1402.4	18.2	1448.0	14.6	1448.0	14.6
Spot 33	206	40776	0.9	10.9768	0.8	3.1049	2.6	0.2473	2.5	0.95	1424.5	31.5	1433.9	19.9	1448.7	15.4	1448.7	15.4
Spot 59	112	62196	2.4	10.9740	0.9	3.0504	2.3	0.2429	2.1	0.92	1401.7	26.8	1420.3	17.7	1449.2	17.3	1449.2	17.3
Spot 28	460	78230	2.1	10.9643	0.8	3.0561	2.2	0.2431	2.0	0.93	1402.9	25.3	1421.8	16.5	1450.9	14.9	1450.9	14.9
Spot 90	73	141407	1.9	10.9604	0.8	3.0668	2.4	0.2439	2.3	0.94	1406.9	29.1	1424.4	18.8	1451.6	16.0	1451.6	16.0
Spot 89	73	26663	2.2	10.9552	0.9	3.1388	2.7	0.2495	2.5	0.94	1435.9	32.0	1442.3	20.5	1452.5	17.9	1452.5	17.9
Spot 91	295	393188	0.7	10.9501	0.7	3.0482	2.6	0.2422	2.5	0.97	1398.1	31.2	1419.8	19.6	1453.3	12.6	1453.3	12.6
Spot 87	61	25671	2.1	10.9422	0.8	3.0374	2.5	0.2412	2.3	0.94	1392.7	29.0	1417.1	18.8	1454.7	15.6	1454.7	15.6

TABLE E2: U-TH-PB GEOCHRONOLOGIC ANALYSES

Analysis	U (ppm)	^{206}Pb / ^{204}Pb	U/Th	$^{206}Pb^*$ / $^{207}Pb^*$	± (%)	Isotope Ratios: $^{207}Pb^*$ / $^{235}U^*$	± (%)	$^{206}Pb^*$ / ^{238}U	± (%)	Error Corr.	Apparent Ages (Ma): $^{206}Pb^*$ / $^{238}U^*$	± (Ma)	$^{207}Pb^*$ / ^{235}U	± (Ma)	$^{206}Pb^*$ / $^{207}Pb^*$	± (Ma)	Best Age (Ma)	± (Ma)
Spot 69	73	75237	2.1	10.9396	0.8	3.1429	2.4	0.2495	2.3	0.94	1435.7	29.2	1443.3	18.5	1455.2	15.1	1455.2	15.1
Spot 56	75	61918	2.1	10.9324	0.9	3.0679	2.4	0.2434	2.2	0.93	1404.1	28.3	1424.7	18.4	1456.4	16.8	1456.4	16.8
Spot 100	78	65600	2.6	10.9318	0.7	3.1177	2.5	0.2473	2.4	0.96	1424.5	31.2	1437.1	19.6	1456.5	13.4	1456.5	13.4
Spot 96	110	47714	2.4	10.9222	0.9	3.0242	2.5	0.2397	2.3	0.94	1385.0	28.9	1413.8	18.9	1458.2	16.5	1458.2	16.5
Spot 58	63	55517	2.2	10.9120	0.9	3.1370	2.5	0.2484	2.4	0.94	1430.1	30.5	1441.8	19.5	1460.0	16.9	1460.0	16.9
Spot 101	65	58118	2.3	10.9018	0.7	3.1599	2.1	0.2500	2.0	0.95	1438.2	26.3	1447.4	16.6	1461.7	12.7	1461.7	12.7
Spot 14	283	156026	3.1	10.8773	0.9	3.1100	2.5	0.2455	2.4	0.94	1415.0	30.0	1435.2	19.3	1466.0	16.5	1466.0	16.5
Spot 80	113	77696	1.1	10.8750	1.0	3.1609	2.9	0.2494	2.7	0.94	1435.5	34.6	1447.7	22.2	1466.4	19.3	1466.4	19.3
Spot 22	85	120859	2.6	10.8593	0.9	3.1643	3.1	0.2493	3.0	0.96	1435.0	38.2	1448.5	24.0	1469.2	17.0	1469.2	17.0
Spot 34	645	1546278	13.3	10.8539	0.8	3.2084	2.6	0.2527	2.4	0.94	1452.2	31.5	1459.2	19.8	1470.1	16.0	1470.1	16.0
Spot 60	58	146403	2.1	10.8293	1.0	3.1046	2.6	0.2439	2.4	0.92	1407.2	30.9	1433.8	20.3	1474.4	19.2	1474.4	19.2
Spot 99	119	52554	1.7	10.7900	0.9	3.2085	2.6	0.2512	2.5	0.94	1444.7	32.0	1459.2	20.4	1481.3	17.7	1481.3	17.7
Spot 61	299	150544	0.5	10.6871	0.9	3.0266	2.6	0.2347	2.5	0.94	1359.1	30.1	1414.4	20.0	1499.5	17.1	1499.5	17.1
Spot 78	177	1518891	2.8	10.5221	1.2	3.3188	3.6	0.2534	3.4	0.95	1455.9	44.7	1485.5	28.3	1528.8	21.9	1528.8	21.9
Spot 1	1123	411495	1.8	10.4437	0.7	3.6101	2.1	0.2736	2.0	0.95	1558.9	27.3	1551.8	16.6	1542.9	12.8	1542.9	12.8
Spot 6	192	65322	5.4	10.0878	1.1	3.4247	3.2	0.2507	3.0	0.94	1441.9	39.1	1510.1	25.3	1607.8	20.8	1607.8	20.8
Spot 29	104	6391	0.9	9.8400	2.4	3.5328	3.5	0.2522	2.6	0.73	1450.0	33.5	1534.6	27.9	1654.0	44.6	1654.0	44.6
Spot 5	112	7657	2.0	9.8297	1.7	3.5343	2.9	0.2521	2.3	0.80	1449.2	30.2	1534.9	22.9	1656.0	31.8	1656.0	31.8
Spot 66	240	112102	3.4	9.8051	0.8	4.0609	3.1	0.2889	3.0	0.97	1636.1	43.9	1646.5	25.7	1660.6	15.1	1660.6	15.1
Spot 82	1418	77718	8.7	9.7930	0.7	4.1474	1.9	0.2947	1.8	0.94	1665.0	26.4	1663.7	15.7	1662.9	12.5	1662.9	12.5

TABLE E2: U-TH-PB GEOCHRONOLOGIC ANALYSES

Analysis	U (ppm)	^{206}Pb ^{204}Pb	U/Th	$^{206}Pb^*$ $^{207}Pb^*$	± (%)	Isotope Ratios $^{207}Pb^*$ $^{235}U^*$	± (%)	$^{206}Pb^*$ ^{238}U	± (%)	Error Corr.	Apparent Ages (Ma) $^{206}Pb^*$ $^{238}U^*$	± (Ma)	$^{207}Pb^*$ ^{235}U	± (Ma)	$^{206}Pb^*$ $^{207}Pb^*$	± (Ma)	Best Age (Ma)	± (Ma)
Spot 3	189	75982	3.1	9.7830	0.9	4.1736	2.2	0.2963	2.0	0.92	1672.7	30.1	1668.9	18.2	1664.8	16.0	1664.8	16.0
Spot 21	180	296409	3.0	9.7329	0.9	4.3897	2.6	0.3100	2.4	0.93	1740.7	36.5	1710.4	21.2	1674.3	17.1	1674.3	17.1
Spot 36	184	193486	2.7	9.7285	0.8	4.3882	2.0	0.3098	1.8	0.92	1739.5	27.7	1710.1	16.4	1675.1	14.3	1675.1	14.3
Spot 106	502	324521	48.6	9.7195	0.8	3.5413	2.3	0.2497	2.2	0.94	1437.2	28.3	1536.5	18.4	1676.8	14.2	1676.8	14.2
Spot 31	251	481625	4.9	9.7092	0.8	3.8366	2.2	0.2703	2.1	0.93	1542.2	28.4	1600.5	17.9	1678.8	15.3	1678.8	15.3
Spot 76	193	62010	2.0	9.6841	0.8	4.3893	2.5	0.3084	2.3	0.94	1732.9	35.3	1710.3	20.4	1683.6	15.1	1683.6	15.1
Spot 44	216	257429	7.2	9.6224	0.7	4.2740	1.8	0.2984	1.7	0.92	1683.4	25.2	1688.4	15.2	1695.3	13.0	1695.3	13.0
Spot 85	247	371528	5.3	9.6160	0.9	4.0227	2.5	0.2807	2.3	0.93	1594.8	32.2	1638.8	20.0	1696.6	17.2	1696.6	17.2
Spot 7	383	308021	7.9	9.6156	0.8	4.2971	2.2	0.2998	2.0	0.93	1690.4	30.0	1692.8	17.8	1696.6	14.4	1696.6	14.4
Spot 45	97	28635	2.0	9.6099	0.9	4.3092	2.6	0.3005	2.5	0.95	1693.6	37.1	1695.1	21.7	1697.7	15.8	1697.7	15.8
Spot 74	402	585187	3.4	9.5991	0.7	4.1427	2.2	0.2885	2.1	0.95	1634.2	29.7	1662.8	17.7	1699.8	12.7	1699.8	12.7
Spot 50	598	238408	3.4	9.5983	0.7	4.0395	2.5	0.2813	2.3	0.95	1598.0	33.2	1642.2	20.1	1700.0	13.8	1700.0	13.8
Spot 35	596	758325	4.4	9.5980	0.9	4.2539	2.8	0.2963	2.7	0.95	1672.7	39.4	1684.5	23.2	1700.0	16.4	1700.0	16.4
Spot 41	339	261975	3.3	9.5970	0.7	4.4058	2.9	0.3068	2.8	0.97	1724.9	42.1	1713.4	23.8	1700.2	13.2	1700.2	13.2
Spot 25	347	1686043	3.6	9.5838	0.6	4.2936	2.0	0.2986	1.9	0.96	1684.2	28.5	1692.1	16.5	1702.7	10.5	1702.7	10.5
Spot 40	356	135239	1.3	9.5829	0.9	4.3041	2.2	0.2993	2.1	0.92	1687.7	30.6	1694.1	18.5	1702.9	16.4	1702.9	16.4
Spot 84	84	135667	2.1	9.5574	0.8	4.2546	2.6	0.2950	2.4	0.95	1666.7	35.9	1684.6	21.2	1707.8	14.9	1707.8	14.9
Spot 94	406	308025	7.2	9.5088	0.9	4.3875	2.5	0.3027	2.3	0.93	1704.7	34.4	1710.0	20.3	1717.2	16.1	1717.2	16.1
Spot 95	67	10937	2.0	9.4827	3.7	3.6599	4.5	0.2518	2.6	0.57	1447.9	33.7	1562.7	36.2	1722.3	68.5	1722.3	68.5
Spot 70	131	133746	2.0	9.4814	1.0	4.3926	3.0	0.3022	2.9	0.95	1702.2	42.8	1710.9	25.0	1722.5	17.5	1722.5	17.5

TABLE E2: U-TH-PB GEOCHRONOLOGIC ANALYSES

						Isotope Ratios					Apparent Ages (Ma)							
Analysis	U (ppm)	^{206}Pb ^{204}Pb	U/Th	$^{206}Pb^*$ $^{207}Pb^*$	± (%)	$^{207}Pb^*$ $^{235}U^*$	± (%)	$^{206}Pb^*$ ^{238}U	± (%)	Error Corr.	$^{206}Pb^*$ $^{238}U^*$	± (Ma)	$^{207}Pb^*$ ^{235}U	± (Ma)	$^{206}Pb^*$ $^{207}Pb^*$	± (Ma)	**Best Age** (Ma)	± (Ma)
Spot 97	358	135705	1.9	9.4806	1.0	4.2359	2.9	0.2914	2.7	0.94	1648.4	39.5	1681.0	23.7	1722.7	18.1	1722.7	18.1
Spot 20	229	142446	2.2	9.4714	1.0	4.4719	2.9	0.3073	2.7	0.94	1727.5	41.0	1725.8	23.8	1724.4	17.7	1724.4	17.7
Spot 104	402	437011	1.7	9.4664	0.8	4.4053	2.3	0.3026	2.2	0.94	1704.1	32.6	1713.3	19.0	1725.4	13.9	1725.4	13.9
Spot 88	158	127697	2.1	9.4610	0.9	4.3205	2.6	0.2966	2.4	0.94	1674.4	35.6	1697.3	21.2	1726.5	16.3	1726.5	16.3
Spot 107	328	552934	3.9	9.4442	0.9	4.3731	3.3	0.2997	3.2	0.96	1689.7	46.9	1707.3	27.1	1729.7	15.9	1729.7	15.9
Spot 55	173	81451	8.4	9.1267	0.9	4.7723	2.6	0.3160	2.4	0.93	1770.3	37.0	1780.0	21.6	1792.2	17.1	1792.2	17.1
Spot 43	97	2871527	2.1	8.7614	0.7	5.1924	2.3	0.3301	2.2	0.95	1838.8	35.6	1851.4	19.9	1866.3	13.1	1866.3	13.1
Spot 47	349	861	1.6	30.2084	17.4	0.0252	17.6	0.0055	2.7	0.16	35.5	1.0	25.3	4.4	NA	NA	35.5	1.0
Spot 39	680	36247	2.4	21.2459	1.9	0.0431	3.7	0.0067	3.1	0.86	42.7	1.3	42.9	1.5	52.7	44.6	42.7	1.3
Spot 34	469	2771	2.7	18.8767	3.9	0.0494	4.7	0.0068	2.6	0.56	43.5	1.1	49.0	2.2	327.7	88.4	43.5	1.1
Spot 9	290	2760	2.6	22.4962	2.3	0.0435	3.4	0.0071	2.5	0.73	45.6	1.1	43.2	1.4	NA	NA	45.6	1.1
Spot 19	662	6082	8.1	21.0631	2.0	0.0601	3.5	0.0092	3.0	0.83	59.0	1.7	59.3	2.0	73.2	46.5	59.0	1.7
Spot 24	1929	118040	9.8	11.8158	1.1	2.6026	2.5	0.2231	2.2	0.90	1298.4	26.0	1301.4	18.0	1307.1	20.4	1307.1	20.4
Spot 58	117	15291	2.4	11.2756	1.0	3.0425	2.5	0.2489	2.4	0.93	1432.9	30.3	1418.3	19.4	1397.4	18.3	1397.4	18.3
Spot 5	417	452361	3.6	11.2433	0.9	3.0857	2.9	0.2517	2.7	0.95	1447.4	35.4	1429.2	22.0	1402.9	16.9	1402.9	16.9
Spot 37	58	12853	1.9	11.2388	1.0	3.0962	2.4	0.2525	2.2	0.92	1451.3	28.6	1431.8	18.4	1403.7	18.3	1403.7	18.3
Spot 28	69	11047	2.1	11.1995	1.1	3.0487	3.5	0.2477	3.3	0.95	1426.8	42.6	1419.9	26.7	1410.4	20.4	1410.4	20.4
Spot 112	87	33812	1.9	11.1990	1.2	3.1021	2.9	0.2521	2.6	0.90	1449.1	33.7	1433.2	22.0	1410.4	23.4	1410.4	23.4
Spot 16	129	130901	2.3	11.1725	1.1	3.0733	2.6	0.2491	2.4	0.91	1434.0	30.9	1426.1	20.2	1415.0	20.9	1415.0	20.9
Spot 44	739	56129	17.2	11.162	1.0	2.9904	3.0	0.2422	2.8	0.94	1398.1	35.7	1405.2	23.0	1416.8	19.6	1416.8	19.6

TABLE E2: U-TH-PB GEOCHRONOLOGIC ANALYSES

						Isotope Ratios					Apparent Ages (Ma)						Best Age	
Analysis	U (ppm)	$^{206}Pb/^{204}Pb$	U/Th	$^{206}Pb^*/^{207}Pb^*$	± (%)	$^{207}Pb^*/^{235}U^*$	± (%)	$^{206}Pb^*/^{238}U$	± (%)	Error Corr.	$^{206}Pb^*/^{238}U^*$	± (Ma)	$^{207}Pb^*/^{235}U$	± (Ma)	$^{206}Pb^*/^{207}Pb^*$	± (Ma)	(Ma)	± (Ma)
Spot 21	57	12919	2.1	11.1350	1.1	3.1030	2.5	0.2507	2.2	0.89	1442.1	28.3	1433.4	19.0	1421.4	21.9	1421.4	21.9
Spot 56	164	33587	3.5	11.1136	1.0	3.0636	2.8	0.2470	2.6	0.93	1423.2	33.1	1423.6	21.3	1425.1	19.2	1425.1	19.2
Spot 23	100	19268	2.5	11.1113	0.9	3.0587	3.0	0.2466	2.8	0.95	1420.9	36.1	1422.4	22.8	1425.5	17.9	1425.5	17.9
Spot 69	96	53177	2.0	11.0940	0.9	3.0331	2.7	0.2442	2.6	0.95	1408.3	32.5	1416.0	20.7	1428.5	16.7	1428.5	16.7
Spot 18	117	28160	2.5	11.0897	1.1	3.1139	2.8	0.2506	2.6	0.92	1441.4	33.1	1436.1	21.5	1429.2	21.5	1429.2	21.5
Spot 32	84	21004	2.3	11.0861	1.0	3.0857	2.5	0.2482	2.3	0.92	1429.2	29.7	1429.1	19.4	1429.8	19.2	1429.8	19.2
Spot 1	96	37780	1.3	11.0846	1.2	3.1333	3.0	0.2520	2.7	0.92	1448.8	35.7	1440.9	23.0	1430.1	22.3	1430.1	22.3
Spot 65	65	10080	1.6	11.0657	1.0	3.0355	2.6	0.2437	2.4	0.92	1406.0	30.7	1416.6	20.1	1433.3	19.4	1433.3	19.4
Spot 61	108	32215	1.4	11.0640	1.1	3.1857	2.6	0.2557	2.4	0.90	1468.0	31.0	1453.7	20.2	1433.6	21.4	1433.6	21.4
Spot 117	74	38299	2.3	11.0548	1.3	3.1301	2.5	0.2511	2.2	0.86	1444.0	28.1	1440.1	19.4	1435.2	24.2	1435.2	24.2
Spot 6	681	108148	31.4	11.0340	1.3	3.1221	3.1	0.2500	2.8	0.91	1438.2	35.7	1438.1	23.5	1438.8	24.5	1438.8	24.5
Spot 116	337	109724	1.8	11.0111	0.8	3.1185	2.7	0.2492	2.6	0.96	1434.1	32.9	1437.3	20.6	1442.8	15.0	1442.8	15.0
Spot 114	89	15155	1.8	11.0096	1.3	3.2213	3.3	0.2573	3.0	0.92	1476.2	39.6	1462.3	25.3	1443.0	24.4	1443.0	24.4
Spot 35	73	16549	1.6	11.0012	1.1	3.0885	2.8	0.2465	2.6	0.92	1420.6	32.5	1429.8	21.3	1444.5	21.0	1444.5	21.0
Spot 25	78	33991	2.5	10.9870	0.9	3.0816	3.0	0.2457	2.8	0.95	1416.1	35.8	1428.1	22.8	1446.9	18.0	1446.9	18.0
Spot 10	81	19347	1.7	10.9793	1.0	3.1037	2.7	0.2473	2.5	0.93	1424.3	31.5	1433.6	20.4	1448.3	19.2	1448.3	19.2
Spot 38	86	36000	2.2	10.9781	1.0	3.1618	2.7	0.2519	2.5	0.93	1448.0	32.9	1447.9	21.1	1448.5	19.3	1448.5	19.3
Spot 54	86	30086	2.1	10.9508	1.2	3.0825	2.8	0.2449	2.5	0.91	1412.2	32.2	1428.3	21.4	1453.2	22.4	1453.2	22.4
Spot 22	75	24366	2.1	10.937	0.9	3.1170	2.1	0.2474	1.9	0.89	1424.9	24.2	1436.9	16.3	1455.5	18.1	1455.5	18.1

TABLE E2: U-TH-PB GEOCHRONOLOGIC ANALYSES

Analysis	U (ppm)	^{206}Pb ^{204}Pb	U/Th	$^{206}Pb^*$ $^{207}Pb^*$	± (%)	Isotope Ratios $^{207}Pb^*$ $^{235}U^*$	± (%)	$^{206}Pb^*$ ^{238}U	± (%)	Error Corr.	Apparent Ages (Ma) $^{206}Pb^*$ $^{238}U^*$	± (Ma)	$^{207}Pb^*$ ^{235}U	± (Ma)	$^{206}Pb^*$ $^{207}Pb^*$	± (Ma)	Best Age (Ma)	± (Ma)
Spot 68	142	32930	0.5	10.9274	1.0	3.1096	2.5	0.2466	2.3	0.92	1420.7	29.3	1435.1	19.2	1457.3	19.0	1457.3	19.0
Spot 2	92	17241	1.6	10.8864	1.1	3.1183	2.4	0.2463	2.1	0.88	1419.4	26.5	1437.2	18.3	1464.4	21.7	1464.4	21.7
Spot 46	333	31813	1.8	10.8673	1.0	3.0568	2.6	0.2410	2.4	0.93	1392.0	29.8	1421.9	19.7	1467.8	18.5	1467.8	18.5
Spot 8	60	67639	2.5	10.8195	1.3	3.2133	3.5	0.2523	3.3	0.93	1450.1	42.3	1460.4	27.1	1476.1	24.5	1476.1	24.5
Spot 52	55	64989	1.7	10.7875	1.1	3.1453	3.0	0.2462	2.8	0.94	1418.8	36.2	1443.8	23.4	1481.8	20.2	1481.8	20.2
Spot 119	103	32341	0.7	10.7770	1.2	2.8794	2.6	0.2252	2.4	0.89	1309.1	28.0	1376.5	19.9	1483.6	22.3	1483.6	22.3
Spot 62	156	10576	1.4	10.5619	1.0	3.2259	2.3	0.2472	2.1	0.91	1424.1	26.8	1463.4	17.9	1521.7	18.4	1521.7	18.4
Spot 57	79	27902	1.4	10.2180	1.5	3.6047	3.1	0.2673	2.7	0.87	1526.9	36.9	1550.6	24.8	1583.9	28.8	1583.9	28.8
Spot 31	238	51044	14.9	10.1868	1.2	3.5331	3.1	0.2611	2.8	0.92	1495.7	37.9	1534.7	24.4	1589.6	22.7	1589.6	22.7
Spot 26	873	245741	19.0	10.1006	1.2	3.7042	3.1	0.2715	2.9	0.93	1548.3	39.8	1572.3	24.9	1605.4	21.6	1605.4	21.6
Spot 11	370	194860	2.8	9.8647	1.0	3.9690	3.1	0.2841	2.9	0.94	1611.9	41.8	1627.9	25.2	1649.4	19.4	1649.4	19.4
Spot 29	230	36875	7.0	9.8400	1.0	4.0933	2.9	0.2923	2.7	0.94	1652.8	39.6	1653.0	23.6	1654.0	18.7	1654.0	18.7
Spot 42	366	125221	5.7	9.7771	1.1	4.0761	3.4	0.2892	3.3	0.95	1637.3	47.4	1649.5	28.1	1665.9	19.6	1665.9	19.6
Spot 43	221	37665	2.2	9.7684	1.1	4.1417	2.8	0.2936	2.5	0.92	1659.3	37.0	1662.6	22.6	1667.5	20.3	1667.5	20.3
Spot 27	111	37028	1.5	9.7632	1.1	4.3095	3.0	0.3053	2.8	0.93	1717.5	42.3	1695.2	24.9	1668.5	20.6	1668.5	20.6
Spot 50	198	38342	2.1	9.7384	0.8	4.2998	1.9	0.3038	1.8	0.90	1710.3	26.3	1693.3	15.9	1673.2	15.3	1673.2	15.3
Spot 113	254	70837	5.0	9.7256	1.1	4.2062	2.8	0.2968	2.6	0.92	1675.5	37.8	1675.2	22.8	1675.7	19.6	1675.7	19.6
Spot 48	95	19556	2.4	9.7103	1.3	4.2831	2.5	0.3018	2.1	0.85	1700.1	31.6	1690.1	20.5	1678.6	24.1	1678.6	24.1
Spot 64	202	60605	2.4	9.6767	0.9	4.4186	2.4	0.3102	2.2	0.93	1741.9	33.5	1715.8	19.5	1685.0	16.1	1685.0	16.1
Spot 118	71	15397	2.1	9.6604	1.2	4.4886	3.3	0.3146	3.1	0.93	1763.4	47.1	1728.9	27.2	1688.1	22.2	1688.1	22.2

TABLE E2: U-TH-PB GEOCHRONOLOGIC ANALYSES

Analysis	U (ppm)	^{206}Pb / ^{204}Pb	U/Th	$^{206}Pb^*$ / $^{207}Pb^*$	± (%)	Isotope Ratios: $^{207}Pb^*$ / $^{235}U^*$	± (%)	$^{206}Pb^*$ / ^{238}U	± (%)	Error Corr.	Apparent Ages (Ma): $^{206}Pb^*$ / $^{238}U^*$	± (Ma)	$^{207}Pb^*$ / ^{235}U	± (Ma)	$^{206}Pb^*$ / $^{207}Pb^*$	± (Ma)	Best Age (Ma)	± (Ma)
Spot 36	580	4231137	2.4	9.6576	1.0	4.3103	3.1	0.3020	2.9	0.95	1701.4	43.2	1695.3	25.1	1688.6	17.9	1688.6	17.9
Spot 45	212	24352	2.1	9.6351	1.0	4.4393	3.0	0.3104	2.8	0.94	1742.5	42.5	1719.7	24.5	1692.9	18.3	1692.9	18.3
Spot 70	297	69164	6.0	9.6064	1.4	3.9873	2.7	0.2779	2.3	0.86	1580.9	32.8	1631.6	22.1	1698.4	25.8	1698.4	25.8
Spot 7	335	49868	2.4	9.6041	0.8	4.3771	2.6	0.3050	2.5	0.95	1716.2	37.4	1708.0	21.5	1698.8	14.2	1698.8	14.2
Spot 14	636	59743	3.1	9.5993	1.2	3.5084	2.9	0.2444	2.6	0.91	1409.3	33.3	1529.1	22.9	1699.8	22.3	1699.8	22.3
Spot 53	410	119365	1.9	9.5685	0.9	4.2930	2.8	0.2981	2.7	0.94	1681.6	39.9	1692.0	23.5	1705.7	17.2	1705.7	17.2
Spot 63	204	71970	2.4	9.5611	0.8	4.3864	2.4	0.3043	2.2	0.94	1712.6	33.8	1709.8	19.8	1707.1	15.0	1707.1	15.0
Spot 115	134	30108	2.1	9.5607	1.2	4.6107	2.8	0.3198	2.5	0.91	1789.0	39.1	1751.2	23.1	1707.2	21.4	1707.2	21.4
Spot 66	168	98458	1.6	9.5602	0.9	4.3273	2.9	0.3002	2.7	0.95	1692.2	40.5	1698.6	23.6	1707.3	16.0	1707.3	16.0
Spot 4	89	29187	1.8	9.5228	1.0	4.1792	3.1	0.2888	2.9	0.95	1635.4	42.0	1670.0	25.1	1714.5	18.0	1714.5	18.0
Spot 33	472	70502	2.0	9.5065	0.9	4.5040	2.8	0.3107	2.6	0.95	1744.0	40.3	1731.7	23.0	1717.6	15.7	1717.6	15.7
Spot 13	351	246190	2.9	9.4969	1.0	4.4928	2.4	0.3096	2.1	0.90	1738.7	32.4	1729.7	19.6	1719.5	18.9	1719.5	18.9
Spot 17	107	39953	3.6	9.4671	0.9	4.3451	2.5	0.2985	2.3	0.92	1683.7	33.7	1702.0	20.3	1725.3	17.3	1725.3	17.3
Spot 30	426	42620	2.4	9.4528	1.0	4.3688	2.5	0.2996	2.3	0.92	1689.6	34.7	1706.5	20.9	1728.1	18.0	1728.1	18.0
Spot 3	199	166091	2.0	9.4459	0.8	4.3604	2.5	0.2989	2.4	0.95	1685.6	34.9	1704.9	20.5	1729.4	14.6	1729.4	14.6
Spot 12	272	47486	3.7	9.4451	0.9	4.4325	3.3	0.3038	3.1	0.96	1710.0	47.2	1718.4	27.1	1729.6	16.7	1729.6	16.7
Spot 20	199	32766	3.1	9.3373	1.0	4.8203	2.5	0.3266	2.3	0.91	1821.7	36.5	1788.4	21.2	1750.6	18.7	1750.6	18.7
Spot 60	124	22660	5.0	9.2288	1.0	4.6081	2.8	0.3086	2.6	0.93	1733.7	39.3	1750.7	23.2	1772.0	18.9	1772.0	18.9
Spot 59	376	127444	1.9	8.6386	1.1	5.3607	2.8	0.3360	2.6	0.92	1867.4	41.6	1878.6	23.9	1891.7	19.7	1891.7	19.7
Spot 15	1135	342105	3.1	6.5682	1.1	8.5114	2.8	0.4056	2.6	0.92	2194.9	47.8	2287.1	25.3	2371.3	18.6	2371.3	18.6
MAX																		
Spot 34	169	380	1.1	103.6585	37.4	0.0069	37.5	0.0052	3.5	0.09	33.6	1.2	7.0	2.6	NA	NA	33.6	1.2

TABLE E2: U-TH-PB GEOCHRONOLOGIC ANALYSES

						Isotope Ratios					Apparent Ages (Ma)							
Analysis	U (ppm)	^{206}Pb ^{204}Pb	U/Th	$^{206}Pb^*$ $^{207}Pb^*$	± (%)	$^{207}Pb^*$ $^{235}U^*$	± (%)	$^{206}Pb^*$ ^{238}U	± (%)	Error Corr.	$^{206}Pb^*$ $^{238}U^*$	± (Ma)	$^{207}Pb^*$ ^{235}U	± (Ma)	$^{206}Pb^*$ $^{207}Pb^*$	± (Ma)	**Best Age** (Ma)	± (Ma)
Spot 6	392	902	2.8	29.7729	2.0	0.0243	4.2	0.0053	3.6	0.88	33.8	1.2	24.4	1.0	NA	NA	33.8	1.2
Spot 82	585	3021	0.6	22.8030	2.2	0.0320	3.7	0.0053	2.9	0.79	34.0	1.0	31.9	1.2	NA	NA	34.0	1.0
Spot 93	582	2304	1.4	23.9240	2.5	0.0306	4.1	0.0053	3.2	0.79	34.1	1.1	30.6	1.2	NA	NA	34.1	1.1
Spot 90	2314	82289	0.8	21.0400	1.6	0.0350	3.0	0.0053	2.6	0.85	34.3	0.9	34.9	1.0	75.8	37.0	34.3	0.9
Spot 77	1118	4849	1.1	21.8099	2.3	0.0338	3.1	0.0053	2.0	0.66	34.3	0.7	33.7	1.0	NA	NA	34.3	0.7
Spot 70	709	3665	1.2	22.4042	3.1	0.0329	3.8	0.0053	2.1	0.55	34.4	0.7	32.8	1.2	NA	NA	34.4	0.7
Spot 25	554	1100	1.1	25.1926	4.4	0.0293	5.7	0.0053	3.6	0.63	34.4	1.2	29.3	1.6	NA	NA	34.4	1.2
Spot 50	631	35913	1.9	20.9213	1.8	0.0353	3.2	0.0054	2.7	0.83	34.4	0.9	35.2	1.1	89.3	41.6	34.4	0.9
Spot 3	278	1251	1.9	25.0178	3.4	0.0295	4.6	0.0054	3.2	0.68	34.5	1.1	29.5	1.3	NA	NA	34.5	1.1
Spot 19	345	10597	1.4	17.8925	4.6	0.0413	5.9	0.0054	3.7	0.62	34.5	1.3	41.1	2.4	447.9	103.0	34.5	1.3
Spot 1	290	773	1.3	31.3768	7.4	0.0236	8.2	0.0054	3.5	0.42	34.5	1.2	23.6	1.9	NA	NA	34.5	1.2
Spot 89	765	3177	1.3	19.6050	4.2	0.0377	5.0	0.0054	2.7	0.54	34.5	0.9	37.6	1.9	241.2	97.9	34.5	0.9
Spot 85	379	2777	3.2	22.1584	3.1	0.0335	4.1	0.0054	2.7	0.66	34.6	0.9	33.4	1.4	NA	NA	34.6	0.9
Spot 6	925	6630	1.5	21.6304	3.0	0.0343	4.1	0.0054	2.8	0.68	34.6	1.0	34.2	1.4	9.7	73.2	34.6	1.0
Spot 109	673	2632	1.1	23.1370	3.5	0.0321	4.2	0.0054	2.3	0.54	34.7	0.8	32.1	1.3	NA	NA	34.7	0.8
Spot 78	1335	9926	1.5	21.0492	1.8	0.0353	3.3	0.0054	2.7	0.84	34.7	0.9	35.2	1.1	74.8	42.1	34.7	0.9
Spot 102	578	2035	0.9	23.9140	4.6	0.0311	5.2	0.0054	2.4	0.46	34.7	0.8	31.1	1.6	NA	NA	34.7	0.8
Spot 20	509	1626	1.6	24.6544	8.3	0.0302	8.6	0.0054	2.2	0.26	34.7	0.8	30.2	2.6	NA	NA	34.7	0.8
Spot 99	316	976	1.5	23.4267	10.9	0.0318	11.3	0.0054	2.9	0.26	34.7	1.0	31.8	3.5	NA	NA	34.7	1.0

TABLE E2: U-TH-PB GEOCHRONOLOGIC ANALYSES

						Isotope Ratios					Apparent Ages (Ma)							
Analysis	U (ppm)	$^{206}Pb/^{204}Pb$	U/Th	$^{206}Pb^*/^{207}Pb^*$	± (%)	$^{207}Pb^*/^{235}U^*$	± (%)	$^{206}Pb^*/^{238}U$	± (%)	Error Corr.	$^{206}Pb^*/^{238}U^*$	± (Ma)	$^{207}Pb^*/^{235}U$	± (Ma)	$^{206}Pb^*/^{207}Pb^*$	± (Ma)	**Best Age** (Ma)	± (Ma)
Spot 26	971	1317	0.7	28.5441	7.7	0.0261	8.2	0.0054	2.7	0.33	34.7	0.9	26.2	2.1	NA	NA	34.7	0.9
Spot 43	520	1730	1.5	24.7490	2.4	0.0302	3.8	0.0054	3.0	0.77	34.8	1.0	30.2	1.1	NA	NA	34.8	1.0
Spot 10	591	1961	0.5	24.4879	2.9	0.0305	4.1	0.0054	2.9	0.70	34.8	1.0	30.5	1.2	NA	NA	34.8	1.0
Spot 52	662	1783	1.0	23.9399	2.1	0.0312	3.2	0.0054	2.5	0.77	34.9	0.9	31.2	1.0	NA	NA	34.9	0.9
Spot 88	656	2009	1.4	24.2375	2.4	0.0309	3.3	0.0054	2.3	0.69	34.9	0.8	30.9	1.0	NA	NA	34.9	0.8
Spot 48	796	18178	0.5	20.2511	1.9	0.0369	3.5	0.0054	2.9	0.85	34.9	1.0	36.8	1.3	165.9	43.3	34.9	1.0
Spot 27	365	7724	1.4	21.9008	2.2	0.0342	3.5	0.0054	2.8	0.78	34.9	1.0	34.1	1.2	NA	NA	34.9	1.0
Spot 38	699	12378	1.3	20.4372	1.4	0.0366	2.4	0.0054	1.9	0.81	34.9	0.7	36.5	0.9	144.5	33.6	34.9	0.7
Spot 87	774	1858	1.5	25.1648	5.5	0.0298	6.0	0.0054	2.3	0.39	35.0	0.8	29.8	1.8	NA	NA	35.0	0.8
Spot 18	543	1487	1.2	25.5193	4.9	0.0294	5.6	0.0054	2.8	0.50	35.0	1.0	29.4	1.6	NA	NA	35.0	1.0
Spot 8	771	5148	0.7	21.0662	3.7	0.0356	4.5	0.0054	2.7	0.59	35.0	0.9	35.6	1.6	72.9	86.9	35.0	0.9
Spot 37	636	6636	1.0	21.4846	2.1	0.0349	3.9	0.0054	3.3	0.84	35.0	1.2	34.9	1.3	25.9	50.5	35.0	1.2
Spot 101	366	1476	1.3	24.8316	3.2	0.0302	4.4	0.0054	3.0	0.69	35.0	1.1	30.3	1.3	NA	NA	35.0	1.1
Spot 5	782	2360	2.2	23.0941	2.0	0.0325	4.1	0.0055	3.6	0.88	35.1	1.3	32.5	1.3	NA	NA	35.1	1.3
Spot 84	376	2872	1.3	23.2871	3.3	0.0323	4.1	0.0055	2.4	0.59	35.1	0.8	32.3	1.3	NA	NA	35.1	0.8
Spot 59	390	4815	2.0	21.3371	1.9	0.0353	3.4	0.0055	2.9	0.84	35.1	1.0	35.2	1.2	42.4	44.5	35.1	1.0
Spot 31	625	2504	1.4	21.8750	2.1	0.0344	3.6	0.0055	2.9	0.80	35.1	1.0	34.3	1.2	NA	NA	35.1	1.0
Spot 14	2728	177318	1.8	20.9422	1.1	0.0360	2.9	0.0055	2.7	0.93	35.1	1.0	35.9	1.0	86.9	25.9	35.1	1.0
Spot 2	515	4483	1.2	22.2016	2.7	0.0339	4.0	0.0055	2.9	0.73	35.2	1.0	33.9	1.3	NA	NA	35.2	1.0

TABLE E2: U-TH-PB GEOCHRONOLOGIC ANALYSES

Analysis	U (ppm)	^{206}Pb ^{204}Pb	U/Th	$^{206}Pb^*$ $^{207}Pb^*$	± (%)	Isotope Ratios $^{207}Pb^*$ $^{235}U^*$	± (%)	$^{206}Pb^*$ ^{238}U	± (%)	Error Corr.	Apparent Ages (Ma) $^{206}Pb^*$ $^{238}U^*$	± (Ma)	$^{207}Pb^*$ ^{235}U	± (Ma)	$^{206}Pb^*$ $^{207}Pb^*$	± (Ma)	Best Age (Ma)	± (Ma)
Spot 69	736	6917	1.8	21.8709	2.7	0.0345	3.9	0.0055	2.9	0.73	35.2	1.0	34.4	1.3	NA	NA	35.2	1.0
Spot 51	1081	6648	1.8	21.2718	2.0	0.0355	3.3	0.0055	2.6	0.79	35.2	0.9	35.4	1.1	49.8	48.0	35.2	0.9
Spot 51	643	2167	1.7	24.2509	4.2	0.0311	5.3	0.0055	3.3	0.61	35.2	1.1	31.1	1.6	NA	NA	35.2	1.1
Spot 24	380	2285	1.2	21.9717	7.4	0.0343	8.0	0.0055	3.0	0.38	35.2	1.1	34.3	2.7	NA	NA	35.2	1.1
Spot 92	1097	4886	0.8	22.1249	1.9	0.0341	3.1	0.0055	2.5	0.79	35.2	0.9	34.1	1.0	NA	NA	35.2	0.9
Spot 45	1049	22162	1.2	21.4514	1.4	0.0352	2.6	0.0055	2.2	0.85	35.2	0.8	35.1	0.9	29.7	32.8	35.2	0.8
Spot 42	519	2340	0.9	22.0292	3.1	0.0343	4.0	0.0055	2.6	0.63	35.2	0.9	34.2	1.4	NA	NA	35.2	0.9
Spot 31	1261	4817	1.2	22.4480	2.4	0.0336	3.2	0.0055	2.2	0.69	35.2	0.8	33.6	1.1	NA	NA	35.2	0.8
Spot 71	544	133044	1.3	20.7986	2.4	0.0363	3.3	0.0055	2.3	0.69	35.2	0.8	36.2	1.2	103.2	57.0	35.2	0.8
Spot 11	621	1936	0.6	24.4510	2.9	0.0309	4.1	0.0055	2.9	0.70	35.2	1.0	30.9	1.3	NA	NA	35.2	1.0
Spot 95	401	1993	1.1	23.9020	4.9	0.0316	5.9	0.0055	3.3	0.55	35.2	1.1	31.6	1.8	NA	NA	35.2	1.1
Spot 63	670	35931	2.3	20.6367	1.5	0.0366	3.1	0.0055	2.8	0.88	35.3	1.0	36.5	1.1	121.7	35.0	35.3	1.0
Spot 4	355	1139	1.8	26.9081	12.1	0.0281	12.5	0.0055	3.0	0.24	35.3	1.1	28.1	3.5	NA	NA	35.3	1.1
Spot 97	562	3052	1.4	22.7076	2.7	0.0333	4.1	0.0055	3.0	0.75	35.3	1.1	33.3	1.3	NA	NA	35.3	1.1
Spot 47	543	2510	1.2	23.6603	3.0	0.0320	3.5	0.0055	1.9	0.53	35.3	0.7	32.0	1.1	NA	NA	35.3	0.7
Spot 74	591	1510	2.1	25.3551	6.2	0.0299	6.6	0.0055	2.4	0.36	35.3	0.8	29.9	1.9	NA	NA	35.3	0.8
Spot 91	2399	38258	1.6	21.2780	1.5	0.0356	3.2	0.0055	2.8	0.88	35.3	1.0	35.5	1.1	49.0	35.8	35.3	1.0
Spot 37	838	9343	1.3	21.2564	2.1	0.0356	3.5	0.0055	2.9	0.81	35.3	1.0	35.6	1.2	51.5	49.6	35.3	1.0
Spot 83	551	8926	1.0	20.4993	2.5	0.0370	3.8	0.0055	2.9	0.76	35.4	1.0	36.9	1.4	137.4	57.9	35.4	1.0

TABLE E2: U-TH-PB GEOCHRONOLOGIC ANALYSES

Analysis	U (ppm)	^{206}Pb ^{204}Pb	U/Th	$^{206}Pb^*$ $^{207}Pb^*$	± (%)	Isotope Ratios $^{207}Pb^*$ $^{235}U^*$	± (%)	$^{206}Pb^*$ ^{238}U	± (%)	Error Corr.	Apparent Ages (Ma) $^{206}Pb^*$ $^{238}U^*$	± (Ma)	$^{207}Pb^*$ ^{235}U	± (Ma)	$^{206}Pb^*$ $^{207}Pb^*$	± (Ma)	Best Age (Ma)	± (Ma)
Spot 107	829	7491	1.1	21.0142	2.4	0.0361	3.9	0.0055	3.1	0.78	35.4	1.1	36.0	1.4	78.8	58.1	35.4	1.1
Spot 15	638	2645	1.4	22.8028	2.9	0.0333	4.0	0.0055	2.7	0.69	35.4	1.0	33.2	1.3	NA	NA	35.4	1.0
Spot 10	523	5972	1.2	21.3263	1.9	0.0356	2.7	0.0055	1.9	0.70	35.4	0.7	35.5	0.9	43.7	46.3	35.4	0.7
Spot 41	543	2425	1.2	24.4956	2.9	0.0310	3.8	0.0055	2.5	0.65	35.4	0.9	31.0	1.2	NA	NA	35.4	0.9
Spot 32	530	3049	1.3	20.8748	2.5	0.0364	4.0	0.0055	3.2	0.79	35.4	1.1	36.3	1.4	94.6	58.2	35.4	1.1
Spot 69	373	7468	1.5	22.2777	3.5	0.0341	4.2	0.0055	2.4	0.56	35.5	0.8	34.1	1.4	NA	NA	35.5	0.8
Spot 67	905	24157	3.1	21.0041	1.5	0.0362	2.9	0.0055	2.5	0.86	35.5	0.9	36.1	1.0	79.9	35.1	35.5	0.9
Spot 60	614	1914	1.6	23.2412	3.4	0.0327	4.4	0.0055	2.8	0.63	35.5	1.0	32.7	1.4	NA	NA	35.5	1.0
Spot 66	682	4161	1.6	21.1192	2.6	0.0360	3.8	0.0055	2.8	0.74	35.5	1.0	35.9	1.3	66.9	60.9	35.5	1.0
Spot 43	792	2063	1.1	21.7194	6.3	0.0350	6.9	0.0055	2.8	0.41	35.5	1.0	34.9	2.4	NA	NA	35.5	1.0
Spot 64	225	911	1.0	33.9699	6.6	0.0224	7.1	0.0055	2.4	0.35	35.5	0.9	22.5	1.6	NA	NA	35.5	0.9
Spot 65	354	994	1.2	29.7671	4.8	0.0256	5.2	0.0055	2.0	0.39	35.5	0.7	25.6	1.3	NA	NA	35.5	0.7
Spot 9	587	3591	1.2	21.2103	3.3	0.0359	4.3	0.0055	2.8	0.64	35.5	1.0	35.8	1.5	56.7	79.2	35.5	1.0
Spot 54	363	6461	1.4	22.6268	3.6	0.0337	4.4	0.0055	2.6	0.59	35.5	0.9	33.6	1.5	NA	NA	35.5	0.9
Spot 41	544	5595	1.2	22.4175	3.2	0.0340	3.8	0.0055	2.0	0.53	35.6	0.7	33.9	1.3	NA	NA	35.6	0.7
Spot 39	391	8587	1.6	5.1650	14.1	0.1476	14.3	0.0055	2.5	0.18	35.6	0.9	139.8	18.7	2773.1	231.9	35.6	0.9
Spot 100	1014	5486	1.4	20.9236	2.0	0.0364	3.2	0.0055	2.4	0.76	35.6	0.9	36.3	1.1	89.1	48.4	35.6	0.9
Spot 25	658	2693	1.2	24.4789	2.2	0.0312	3.3	0.0055	2.5	0.74	35.6	0.9	31.2	1.0	NA	NA	35.6	0.9
Spot 23	760	33992	1.4	20.1880	2.7	0.0378	3.7	0.0055	2.5	0.69	35.6	0.9	37.7	1.4	173.2	62.4	35.6	0.9
Spot 62	554	2046	1.3	23.580	3.6	0.0324	4.5	0.0055	2.7	0.60	35.6	1.0	32.3	1.4	NA	NA	35.6	1.0

TABLE E2: U-TH-PB GEOCHRONOLOGIC ANALYSES

Analysis	U (ppm)	$^{206}Pb/^{204}Pb$	U/Th	$^{206}Pb^*/^{207}Pb^*$	± (%)	Isotope Ratios $^{207}Pb^*/^{235}U^*$	± (%)	$^{206}Pb^*/^{238}U$	± (%)	Error Corr.	Apparent Ages (Ma) $^{206}Pb^*/^{238}U^*$	± (Ma)	$^{207}Pb^*/^{235}U$	± (Ma)	$^{206}Pb^*/^{207}Pb^*$	± (Ma)	Best Age (Ma)	± (Ma)
Spot 19	644	21047	1.7	20.7943	2.6	0.0367	4.0	0.0055	3.0	0.76	35.6	1.1	36.6	1.4	103.7	60.7	35.6	1.1
Spot 67	633	1196	0.8	20.8007	5.4	0.0367	6.1	0.0055	2.7	0.45	35.6	1.0	36.6	2.2	103.0	128.9	35.6	1.0
Spot 104	550	8608	1.8	20.7538	2.2	0.0368	3.4	0.0055	2.6	0.77	35.6	0.9	36.7	1.2	108.3	51.4	35.6	0.9
Spot 57	818	5585	1.3	21.9659	2.1	0.0348	3.6	0.0055	2.9	0.80	35.6	1.0	34.7	1.2	NA	NA	35.6	1.0
Spot 5	957	6750	1.5	21.5564	1.9	0.0354	3.1	0.0055	2.4	0.79	35.6	0.9	35.4	1.1	17.9	45.0	35.6	0.9
Spot 40	308	1710	1.7	22.9932	9.5	0.0332	10.0	0.0055	3.3	0.33	35.6	1.2	33.2	3.3	NA	NA	35.6	1.2
Spot 33	1018	4694	0.7	20.9518	2.5	0.0365	3.5	0.0055	2.4	0.70	35.6	0.9	36.4	1.3	85.9	59.8	35.6	0.9
Spot 65	388	2153	2.0	23.6753	2.5	0.0323	4.2	0.0055	3.4	0.80	35.7	1.2	32.3	1.3	NA	NA	35.7	1.2
Spot 7	625	976	1.0	29.6144	12.4	0.0258	12.6	0.0056	2.1	0.16	35.7	0.7	25.9	3.2	NA	NA	35.7	0.7
Spot 72	664	174137	1.5	19.5746	2.0	0.0391	3.4	0.0056	2.7	0.81	35.7	1.0	38.9	1.3	244.7	45.0	35.7	1.0
Spot 81	926	2608	1.2	23.9142	4.5	0.0320	5.1	0.0056	2.3	0.46	35.7	0.8	32.0	1.6	NA	NA	35.7	0.8
Spot 38	443	1526	2.4	24.9810	3.5	0.0306	4.4	0.0056	2.7	0.61	35.7	1.0	30.7	1.3	NA	NA	35.7	1.0
Spot 108	616	5210	1.1	21.3197	2.2	0.0359	3.6	0.0056	2.9	0.80	35.7	1.0	35.8	1.3	44.4	51.9	35.7	1.0
Spot 110	162	573	0.7	46.7191	9.8	0.0164	10.7	0.0056	4.3	0.41	35.7	1.5	16.5	1.8	NA	NA	35.7	1.5
Spot 106	313	697	2.4	36.6880	4.7	0.0209	5.5	0.0056	2.8	0.51	35.7	1.0	21.0	1.1	NA	NA	35.7	1.0
Spot 32	457	813	1.0	32.5435	3.5	0.0236	4.8	0.0056	3.2	0.67	35.8	1.1	23.6	1.1	NA	NA	35.8	1.1
Spot 50	408	891	0.8	31.5914	3.4	0.0243	4.5	0.0056	3.0	0.66	35.8	1.1	24.4	1.1	NA	NA	35.8	1.1
Spot 17	255	1790	2.3	23.9536	3.4	0.0320	4.8	0.0056	3.3	0.70	35.8	1.2	32.0	1.5	NA	NA	35.8	1.2
Spot 70	1663	36334	0.4	20.473	1.5	0.0375	3.2	0.0056	2.9	0.89	35.8	1.0	37.4	1.2	140.3	34.2	35.8	1.0

TABLE E2: U-TH-PB GEOCHRONOLOGIC ANALYSES

Analysis	U (ppm)	$^{206}Pb/^{204}Pb$	U/Th	$^{206}Pb^*/^{207}Pb^*$	± (%)	Isotope Ratios $^{207}Pb^*/^{235}U^*$	± (%)	$^{206}Pb^*/^{238}U$	± (%)	Error Corr.	Apparent Ages (Ma) $^{206}Pb^*/^{238}U^*$	± (Ma)	$^{207}Pb^*/^{235}U$	± (Ma)	$^{206}Pb^*/^{207}Pb^*$	± (Ma)	Best Age (Ma)	± (Ma)
Spot 57	471	4130	1.9	22.1311	1.8	0.0347	3.7	0.0056	3.3	0.88	35.8	1.2	34.6	1.3	NA	NA	35.8	1.2
Spot 75	496	5560	2.1	22.5068	2.5	0.0341	3.6	0.0056	2.6	0.71	35.8	0.9	34.1	1.2	NA	NA	35.8	0.9
Spot 98	653	4656	1.6	21.0776	2.6	0.0364	3.8	0.0056	2.8	0.73	35.8	1.0	36.3	1.4	71.6	61.5	35.8	1.0
Spot 16	1044	1845	3.7	24.5054	2.6	0.0314	3.7	0.0056	2.6	0.71	35.8	0.9	31.3	1.1	NA	NA	35.8	0.9
Spot 9	412	2142	1.6	23.2706	4.9	0.0330	5.8	0.0056	3.1	0.54	35.8	1.1	33.0	1.9	NA	NA	35.8	1.1
Spot 105	341	927	1.4	14.0780	10.5	0.0546	10.8	0.0056	2.7	0.25	35.9	1.0	54.0	5.7	958.3	215.1	35.9	1.0
Spot 8	316	32388	1.5	20.7268	3.4	0.0371	4.9	0.0056	3.6	0.73	35.9	1.3	37.0	1.8	111.4	80.1	35.9	1.3
Spot 24	626	1325	1.2	27.4519	9.6	0.0280	9.9	0.0056	2.6	0.27	35.9	0.9	28.1	2.7	NA	NA	35.9	0.9
Spot 59	542	1907	1.1	23.4343	9.4	0.0328	9.8	0.0056	2.7	0.28	35.9	1.0	32.8	3.2	NA	NA	35.9	1.0
Spot 76	418	10861	1.4	21.8763	2.9	0.0352	4.6	0.0056	3.5	0.77	35.9	1.3	35.1	1.6	NA	NA	35.9	1.3
Spot 55	360	2210	1.1	23.6979	7.8	0.0325	8.6	0.0056	3.6	0.42	35.9	1.3	32.5	2.7	NA	NA	35.9	1.3
Spot 62	1096	1635833	2.2	21.0835	1.6	0.0365	3.2	0.0056	2.7	0.87	35.9	1.0	36.4	1.1	71.0	37.5	35.9	1.0
Spot 39	676	11304	1.2	20.9146	2.1	0.0368	3.5	0.0056	2.8	0.80	35.9	1.0	36.7	1.2	90.1	49.3	35.9	1.0
Spot 64	509	6351	1.2	20.4750	2.5	0.0376	3.9	0.0056	3.0	0.77	35.9	1.1	37.5	1.4	140.2	58.1	35.9	1.1
Spot 36	535	1342	1.3	25.8540	4.3	0.0298	5.6	0.0056	3.6	0.64	35.9	1.3	29.8	1.6	NA	NA	35.9	1.3
Spot 44	434	2039	0.7	24.5780	4.2	0.0313	4.9	0.0056	2.5	0.52	35.9	0.9	31.3	1.5	NA	NA	35.9	0.9
Spot 80	533	3864	1.0	21.9198	5.0	0.0352	5.9	0.0056	3.1	0.53	35.9	1.1	35.1	2.0	NA	NA	35.9	1.1
Spot 68	773	9511	0.6	20.8987	1.9	0.0369	3.5	0.0056	3.0	0.85	36.0	1.1	36.8	1.3	91.9	44.9	36.0	1.1
Spot 103	1850	36386	0.8	20.277	1.6	0.0381	2.7	0.0056	2.2	0.81	36.0	0.8	38.0	1.0	162.9	36.9	36.0	0.8

TABLE E2: U-TH-PB GEOCHRONOLOGIC ANALYSES

Analysis	U (ppm)	^{206}Pb ^{204}Pb	U/Th	$^{206}Pb^*$ $^{207}Pb^*$	± (%)	Isotope Ratios $^{207}Pb^*$ $^{235}U^*$	± (%)	$^{206}Pb^*$ ^{238}U	± (%)	Error Corr.	Apparent Ages (Ma) $^{206}Pb^*$ $^{238}U^*$	± (Ma)	$^{207}Pb^*$ ^{235}U	± (Ma)	$^{206}Pb^*$ $^{207}Pb^*$	± (Ma)	**Best Age** (Ma)	± (Ma)
Spot 35	629	2539	0.9	22.968 7	2.7	0.0337	4.0	0.0056	3.0	0.75	36.1	1.1	33.6	1.3	NA	NA	36.1	1.1
Spot 66	604	31217	1.3	20.427 2	2.1	0.0379	4.1	0.0056	3.5	0.86	36.1	1.3	37.7	1.5	145.7	48.8	36.1	1.3
Spot 21	711	3808	1.2	23.423 3	2.6	0.0330	3.9	0.0056	3.0	0.75	36.1	1.1	33.0	1.3	NA	NA	36.1	1.1
Spot 11	483	3947	1.3	21.521 3	2.1	0.0360	3.5	0.0056	2.8	0.80	36.1	1.0	35.9	1.2	21.8	49.9	36.1	1.0
Spot 58	535	14727	1.3	20.646 2	1.9	0.0375	3.6	0.0056	3.0	0.85	36.1	1.1	37.4	1.3	120.6	43.8	36.1	1.1
Spot 56	694	3496	1.7	23.253 0	2.1	0.0333	3.7	0.0056	3.0	0.82	36.1	1.1	33.3	1.2	NA	NA	36.1	1.1
Spot 2	295	713	2.0	34.289 9	6.1	0.0226	6.7	0.0056	2.9	0.43	36.2	1.0	22.7	1.5	NA	NA	36.2	1.0
Spot 46	668	6037	1.2	21.692 5	2.2	0.0357	3.7	0.0056	3.0	0.80	36.2	1.1	35.7	1.3	2.8	53.5	36.2	1.1
Spot 16	704	50198	1.6	19.800 4	2.1	0.0393	3.5	0.0056	2.8	0.79	36.3	1.0	39.1	1.3	218.2	48.7	36.3	1.0
Spot 29	526	2878	2.0	23.764 2	6.4	0.0327	7.2	0.0056	3.4	0.47	36.3	1.2	32.7	2.3	NA	NA	36.3	1.2
Spot 36	593	3590	1.1	22.820 5	4.0	0.0341	4.5	0.0056	2.1	0.46	36.3	0.7	34.0	1.5	NA	NA	36.3	0.7
Spot 23	578	3324	1.0	21.480 2	5.2	0.0362	6.0	0.0056	3.0	0.50	36.3	1.1	36.1	2.1	26.4	125.1	36.3	1.1
Spot 53	701	1048	1.2	15.653 0	7.6	0.0498	8.0	0.0057	2.4	0.30	36.4	0.9	49.4	3.9	737.8	162.0	36.4	0.9
Spot 12	655	8743	1.2	21.549 7	2.9	0.0362	4.9	0.0057	3.9	0.80	36.4	1.4	36.1	1.7	18.7	70.6	36.4	1.4
Spot 29	392	7620	0.9	22.198 7	3.3	0.0352	4.6	0.0057	3.2	0.69	36.5	1.1	35.2	1.6	NA	NA	36.5	1.1
Spot 48	522	16099	0.9	21.424 1	3.1	0.0365	4.0	0.0057	2.5	0.62	36.5	0.9	36.4	1.4	32.7	75.4	36.5	0.9
Spot 63	637	3038	1.1	22.589 3	3.3	0.0347	4.2	0.0057	2.5	0.61	36.6	0.9	34.7	1.4	NA	NA	36.6	0.9
Spot 58	540	5585	1.1	21.549 7	2.4	0.0365	3.3	0.0057	2.3	0.68	36.6	0.8	36.4	1.2	18.7	58.0	36.6	0.8
Spot 1	624	2319	2.2	23.354	3.6	0.0336	4.5	0.0057	2.7	0.60	36.6	1.0	33.6	1.5	NA	NA	36.6	1.0

TABLE E2: U-TH-PB GEOCHRONOLOGIC ANALYSES

Analysis	U (ppm)	^{206}Pb ^{204}Pb	U/Th	$^{206}Pb^*$ $^{207}Pb^*$	± (%)	Isotope Ratios $^{207}Pb^*$ $^{235}U^*$	± (%)	$^{206}Pb^*$ ^{238}U	± (%)	Error Corr.	Apparent Ages (Ma) $^{206}Pb^*$ $^{238}U^*$	± (Ma)	$^{207}Pb^*$ ^{235}U	± (Ma)	$^{206}Pb^*$ $^{207}Pb^*$	± (Ma)	Best Age (Ma)	± (Ma)
Spot 73	446	2058	1.2	21.5210	8.2	0.0365	8.6	0.0057	2.6	0.30	36.7	0.9	36.4	3.1	21.9	197.9	36.7	0.9
Spot 21	323	1383	1.3	27.3061	4.1	0.0290	5.2	0.0057	3.2	0.62	36.9	1.2	29.0	1.5	NA	NA	36.9	1.2
Spot 52	499	7879	0.6	23.0452	2.3	0.0344	3.4	0.0057	2.5	0.74	36.9	0.9	34.3	1.1	NA	NA	36.9	0.9
Spot 30	574	4695	1.7	17.3562	3.6	0.0456	5.0	0.0057	3.4	0.69	37.0	1.3	45.3	2.2	515.2	79.0	37.0	1.3
Spot 28	513	8052	0.8	21.1921	2.9	0.0375	4.1	0.0058	2.9	0.71	37.1	1.1	37.4	1.5	58.7	69.5	37.1	1.1
Spot 96	456	661	1.1	12.4061	7.7	0.0645	8.1	0.0058	2.5	0.30	37.3	0.9	63.5	5.0	1211.9	151.6	37.3	0.9
Spot 30	531	4361	1.0	15.1973	5.9	0.0532	6.4	0.0059	2.5	0.39	37.7	0.9	52.6	3.3	800.0	123.9	37.7	0.9
Spot 54	442	1643	1.3	11.0415	10.6	0.0735	10.9	0.0059	2.5	0.22	37.8	0.9	72.0	7.6	1437.5	203.0	37.8	0.9
Spot 94	697	784	1.2	10.6357	14.6	0.0773	15.0	0.0060	3.3	0.22	38.4	1.3	75.6	10.9	1508.6	277.9	38.4	1.3
Spot 22	706	1768	1.5	22.8488	2.4	0.0360	3.9	0.0060	3.0	0.78	38.4	1.2	35.9	1.4	NA	NA	38.4	1.2
Spot 20	595	1189	2.2	21.2978	7.8	0.0388	8.3	0.0060	2.6	0.31	38.5	1.0	38.6	3.1	46.8	187.7	38.5	1.0
Spot 49	450	2407	1.1	12.9833	8.3	0.0640	8.7	0.0060	2.6	0.30	38.8	1.0	63.0	5.3	1121.7	166.4	38.8	1.0
Spot 13	683	2439	1.3	25.2152	2.5	0.0338	3.4	0.0062	2.4	0.69	39.7	0.9	33.7	1.1	NA	NA	39.7	0.9
Spot 15	675	595	1.2	7.1109	14.9	0.1209	15.3	0.0062	3.6	0.23	40.1	1.4	115.9	16.8	2234.9	259.7	40.1	1.4
Spot 49	588	273	1.2	4.3519	6.6	0.2240	8.4	0.0071	5.2	0.62	45.4	2.4	205.2	15.6	3050.5	105.4	45.4	2.4
Spot 53	370	126	1.8	2.2951	50.1	0.7142	52.4	0.0119	15.6	0.30	76.2	11.8	547.3	225.4	NA	NA	76.2	11.8
Spot 61	381	36016	98.7	11.3454	1.1	2.9138	2.8	0.2399	2.6	0.92	1386.0	32.4	1385.5	21.3	1385.5	21.0	1385.5	21.0
Spot 60	81	11037	1.2	11.1005	1.1	2.9972	2.3	0.2414	2.0	0.88	1394.0	25.1	1406.9	17.2	1427.3	20.2	1427.3	20.2
Spot 13	106	8437	1.4	11.0973	1.0	3.0255	2.6	0.2436	2.4	0.93	1405.5	30.4	1414.1	19.9	1427.9	18.8	1427.9	18.8

TABLE E2: U-TH-PB GEOCHRONOLOGIC ANALYSES

Analysis	U (ppm)	^{206}Pb / ^{204}Pb	U/Th	$^{206}Pb^*$ / $^{207}Pb^*$	± (%)	Isotope Ratios: $^{207}Pb^*$ / $^{235}U^*$	± (%)	$^{206}Pb^*$ / ^{238}U	± (%)	Error Corr.	Apparent Ages (Ma): $^{206}Pb^*$ / $^{238}U^*$	± (Ma)	$^{207}Pb^*$ / ^{235}U	± (Ma)	$^{206}Pb^*$ / $^{207}Pb^*$	± (Ma)	Best Age (Ma)	± (Ma)
Spot 34	377	75939	1.7	11.0767	0.9	3.0184	2.6	0.2426	2.5	0.93	1400.1	30.9	1412.3	20.0	1431.4	17.8	1431.4	17.8
Spot 44	141	127725	1.7	11.0459	1.1	3.0390	2.8	0.2436	2.6	0.92	1405.2	32.5	1417.5	21.4	1436.7	21.4	1436.7	21.4
Spot 17	730	134130	3.2	11.0033	1.0	2.8794	2.6	0.2299	2.4	0.93	1333.9	28.5	1376.5	19.3	1444.1	18.2	1444.1	18.2
Spot 18	92	79255	2.1	10.9932	1.0	3.0020	3.0	0.2395	2.8	0.94	1383.8	35.4	1408.1	23.1	1445.9	19.9	1445.9	19.9
Spot 42	62	35650	0.7	10.8405	1.3	3.0409	2.8	0.2392	2.4	0.88	1382.5	30.5	1418.0	21.3	1472.5	25.1	1472.5	25.1
Spot 27	240	16478	1.8	9.9570	0.9	4.0855	2.7	0.2952	2.5	0.94	1667.3	37.2	1651.4	22.0	1632.1	17.1	1632.1	17.1
Spot 33	933	129903	34.7	9.8603	1.2	3.6746	2.9	0.2629	2.7	0.92	1504.7	36.1	1565.9	23.4	1650.2	21.8	1650.2	21.8
Spot 79	444	65666	2.9	9.8551	1.1	4.0920	2.6	0.2926	2.3	0.91	1654.5	34.2	1652.7	21.0	1651.2	19.5	1651.2	19.5
Spot 12	893	34166	23.3	9.8367	1.1	3.9041	3.1	0.2786	2.8	0.93	1584.5	39.9	1614.5	24.7	1654.6	21.1	1654.6	21.1
Spot 86	463	36073	2.2	9.7709	1.0	4.1337	2.1	0.2931	1.9	0.88	1656.8	27.7	1661.0	17.6	1667.1	18.7	1667.1	18.7
Spot 35	830	143176	8.6	9.6854	1.0	4.0695	2.7	0.2860	2.5	0.93	1621.5	35.9	1648.2	21.8	1683.3	17.6	1683.3	17.6
Spot 40	434	94359	2.5	9.6624	0.9	4.3279	3.3	0.3034	3.2	0.96	1708.3	48.3	1698.7	27.6	1687.7	16.8	1687.7	16.8
Spot 26	266	38211	1.8	9.6533	1.1	4.1774	3.1	0.2926	2.9	0.93	1654.5	42.5	1669.6	25.6	1689.4	20.9	1689.4	20.9
Spot 68	746	789115	5.8	9.6521	1.0	4.2486	2.8	0.2975	2.7	0.94	1679.1	39.3	1683.5	23.3	1689.7	18.1	1689.7	18.1
Spot 3	462	401322	5.5	9.6162	0.9	4.2423	2.2	0.2960	2.0	0.91	1671.5	29.7	1682.3	18.2	1696.5	17.0	1696.5	17.0
Spot 61	355	47291	3.0	9.6135	1.0	3.8637	3.4	0.2695	3.2	0.95	1538.3	43.9	1606.1	27.1	1697.1	18.9	1697.1	18.9
Spot 46	193	29532	2.6	9.5697	0.9	4.2621	2.7	0.2959	2.5	0.94	1671.2	36.9	1686.1	22.0	1705.5	17.4	1705.5	17.4
Spot 22	147	26039	2.2	9.5677	1.0	4.4237	2.5	0.3071	2.3	0.92	1726.4	35.1	1716.8	20.8	1705.8	17.7	1705.8	17.7
Spot 55	273	50390	9.9	9.5572	0.9	4.2255	2.0	0.2930	1.8	0.89	1656.6	26.5	1679.0	16.8	1707.8	17.3	1707.8	17.3
Spot 7	195	35368	1.7	9.5331	1.1	4.2850	3.3	0.2964	3.2	0.95	1673.4	46.6	1690.5	27.5	1712.5	19.7	1712.5	19.7
Spot 47	126	134268	2.8	9.5271	1.1	4.3398	3.0	0.3000	2.8	0.93	1691.3	41.4	1701.0	24.8	1713.7	21.0	1713.7	21.0

TABLE E2: U-TH-PB GEOCHRONOLOGIC ANALYSES

Analysis	U (ppm)	^{206}Pb ^{204}Pb	U/Th	$^{206}Pb^*$ $^{207}Pb^*$	± (%)	Isotope Ratios $^{207}Pb^*$ $^{235}U^*$	± (%)	$^{206}Pb^*$ ^{238}U	± (%)	Error Corr.	Apparent Ages (Ma) $^{206}Pb^*$ $^{238}U^*$	± (Ma)	$^{207}Pb^*$ ^{235}U	± (Ma)	$^{206}Pb^*$ $^{207}Pb^*$	± (Ma)	Best Age (Ma)	± (Ma)
Spot 14	147	10618	5.8	9.5081	1.0	4.3624	2.6	0.3010	2.4	0.92	1696.1	35.5	1705.3	21.4	1717.3	18.9	1717.3	18.9
Spot 45	512	52112	4.0	9.4955	1.1	4.4872	2.9	0.3092	2.7	0.93	1736.6	40.9	1728.6	24.0	1719.8	19.9	1719.8	19.9
Spot 4	638	10277	2.1	9.4719	1.2	4.3590	3.8	0.2996	3.6	0.95	1689.2	53.6	1704.6	31.5	1724.3	22.5	1724.3	22.5
SAK-0502																		
Spot 75	2331	15731	1.2	21.7108	1.0	0.0321	2.4	0.0051	2.2	0.91	32.5	0.7	32.0	0.8	NA	NA	32.5	0.7
Spot 46	621	489235	2.7	21.0621	1.9	0.0342	4.2	0.0052	3.7	0.89	33.6	1.2	34.2	1.4	73.4	44.7	33.6	1.2
Spot 12	2105	169847	0.9	21.1174	1.2	0.0347	2.8	0.0053	2.6	0.91	34.2	0.9	34.7	1.0	67.1	28.0	34.2	0.9
Spot 52	572	3379	1.1	22.3792	2.1	0.0331	3.0	0.0054	2.1	0.71	34.5	0.7	33.0	1.0	NA	NA	34.5	0.7
Spot 11	533	89331	1.0	20.9408	2.2	0.0354	3.2	0.0054	2.4	0.73	34.6	0.8	35.3	1.1	87.1	51.7	34.6	0.8
Spot 17	939	19381	1.0	20.7871	1.5	0.0357	2.6	0.0054	2.1	0.81	34.6	0.7	35.6	0.9	104.5	35.4	34.6	0.7
Spot 13	551	6546	1.1	21.9839	1.7	0.0339	3.0	0.0054	2.4	0.82	34.8	0.8	33.9	1.0	NA	NA	34.8	0.8
Spot 104	974	7109	1.3	21.0373	2.8	0.0355	3.9	0.0054	2.7	0.70	34.8	0.9	35.4	1.4	76.1	66.5	34.8	0.9
Spot 72	1065	11764	1.5	21.2783	1.5	0.0351	3.1	0.0054	2.7	0.87	34.9	0.9	35.1	1.1	49.0	36.9	34.9	0.9
Spot 50	483	18815	1.2	18.2321	2.8	0.0411	3.7	0.0054	2.4	0.66	34.9	0.8	40.9	1.5	406.0	61.7	34.9	0.8
Spot 18	605	8764	0.4	21.0802	1.9	0.0356	3.6	0.0054	3.0	0.84	35.0	1.1	35.5	1.3	71.3	46.3	35.0	1.1
Spot 37	731	5541	0.9	21.8100	1.8	0.0344	3.6	0.0054	3.1	0.86	35.0	1.1	34.3	1.2	NA	NA	35.0	1.1
Spot 98	553	31091	1.0	20.0196	1.9	0.0375	3.6	0.0055	3.1	0.85	35.0	1.1	37.4	1.3	192.7	43.4	35.0	1.1
Spot 41	548	18754	1.1	20.5389	1.3	0.0367	2.7	0.0055	2.3	0.87	35.1	0.8	36.6	1.0	132.9	31.1	35.1	0.8
0Spot 21	977	26712	1.0	21.2545	1.3	0.0355	3.3	0.0055	3.1	0.92	35.2	1.1	35.4	1.2	51.7	30.6	35.2	1.1
Spot 10	754	5338	0.9	22.6221	1.6	0.0333	2.8	0.0055	2.3	0.81	35.2	0.8	33.3	0.9	NA	NA	35.2	0.8

TABLE E2: U-TH-PB GEOCHRONOLOGIC ANALYSES

Analysis	U (ppm)	^{206}Pb ^{204}Pb	U/Th	$^{206}Pb^*$ $^{207}Pb^*$	± (%)	Isotope Ratios $^{207}Pb^*$ $^{235}U^*$	± (%)	$^{206}Pb^*$ ^{238}U	± (%)	Error Corr.	Apparent Ages (Ma) $^{206}Pb^*$ $^{238}U^*$	± (Ma)	$^{207}Pb^*$ ^{235}U	± (Ma)	$^{206}Pb^*$ $^{207}Pb^*$	± (Ma)	Best Age (Ma)	± (Ma)
Spot 83	718	7529	1.2	21.3131	2.5	0.0354	3.5	0.0055	2.5	0.71	35.2	0.9	35.3	1.2	45.1	59.9	35.2	0.9
Spot 4	514	5470	1.2	21.9216	3.3	0.0344	3.8	0.0055	2.0	0.53	35.2	0.7	34.3	1.3	NA	NA	35.2	0.7
Spot 82	183	1489	0.7	27.9443	9.5	0.0270	10.0	0.0055	3.0	0.30	35.2	1.1	27.1	2.7	NA	NA	35.2	1.1
Spot 40	257	1668	1.1	24.6884	2.8	0.0306	3.7	0.0055	2.3	0.63	35.3	0.8	30.6	1.1	NA	NA	35.3	0.8
Spot 54	439	10864	1.1	19.3951	2.5	0.0390	4.0	0.0055	3.1	0.78	35.3	1.1	38.8	1.5	265.9	57.6	35.3	1.1
Spot 38	1334	28228	0.7	19.6787	1.1	0.0384	2.9	0.0055	2.6	0.92	35.3	0.9	38.3	1.1	232.5	26.1	35.3	0.9
Spot 19	728	31398	2.0	19.9777	2.3	0.0379	3.8	0.0055	3.1	0.80	35.3	1.1	37.7	1.4	197.6	53.0	35.3	1.1
Spot 96	1060	12709	1.4	20.9926	1.5	0.0361	3.1	0.0055	2.8	0.88	35.3	1.0	36.0	1.1	81.2	35.6	35.3	1.0
Spot 68	1208	11760	1.0	21.0223	1.5	0.0360	2.7	0.0055	2.3	0.85	35.3	0.8	35.9	1.0	77.8	34.7	35.3	0.8
Spot 20	914	80874	1.3	20.9046	1.3	0.0362	3.2	0.0055	2.9	0.91	35.3	1.0	36.1	1.1	91.2	31.5	35.3	1.0
Spot 26	494	17595	0.4	15.0986	2.0	0.0502	3.7	0.0055	3.1	0.84	35.3	1.1	49.7	1.8	813.7	42.6	35.3	1.1
Spot 103	584	6286	1.0	21.7418	1.8	0.0348	3.3	0.0055	2.8	0.84	35.3	1.0	34.8	1.1	NA	NA	35.3	1.0
Spot 9	524	9195	2.3	21.2342	2.0	0.0357	3.6	0.0055	3.1	0.84	35.4	1.1	35.6	1.3	54.0	47.2	35.4	1.1
Spot 1	566	9227	1.0	21.5968	2.6	0.0351	3.8	0.0055	2.8	0.74	35.4	1.0	35.1	1.3	13.4	61.4	35.4	1.0
Spot 65	878	53528	0.6	20.2209	1.7	0.0375	2.9	0.0055	2.4	0.82	35.4	0.9	37.4	1.1	169.4	39.5	35.4	0.9
Spot 100	547	11557	1.1	21.8201	2.0	0.0348	3.1	0.0055	2.4	0.77	35.4	0.9	34.7	1.1	NA	NA	35.4	0.9
Spot 42	666	26173	1.2	19.3384	3.1	0.0393	4.3	0.0055	3.0	0.69	35.4	1.0	39.1	1.6	272.6	70.5	35.4	1.0
Spot 102	1336	30302	1.2	20.9418	1.2	0.0363	2.9	0.0055	2.6	0.90	35.5	0.9	36.2	1.0	87.0	29.2	35.5	0.9
Spot 8	586	6249	1.1	20.5437	3.0	0.0370	4.2	0.0055	2.9	0.69	35.5	1.0	36.9	1.5	132.3	71.2	35.5	1.0

TABLE E2: U-TH-PB GEOCHRONOLOGIC ANALYSES

Analysis	U (ppm)	^{206}Pb / ^{204}Pb	U/Th	$^{206}Pb^*$ / $^{207}Pb^*$	± (%)	Isotope Ratios: $^{207}Pb^*$ / $^{235}U^*$	± (%)	$^{206}Pb^*$ / ^{238}U	± (%)	Error Corr.	Apparent Ages (Ma): $^{206}Pb^*$ / $^{238}U^*$	± (Ma)	$^{207}Pb^*$ / ^{235}U	± (Ma)	$^{206}Pb^*$ / $^{207}Pb^*$	± (Ma)	Best Age (Ma)	± (Ma)
Spot 2	747	46170	0.9	21.2701	1.9	0.0358	3.4	0.0055	2.9	0.84	35.5	1.0	35.7	1.2	50.0	44.2	35.5	1.0
Spot 107	752	22662	1.4	21.0369	1.7	0.0362	3.5	0.0055	3.1	0.87	35.5	1.1	36.1	1.2	76.2	40.8	35.5	1.1
Spot 49	542	2782	1.2	24.4662	2.5	0.0311	3.9	0.0055	2.9	0.75	35.5	1.0	31.1	1.2	NA	NA	35.5	1.0
Spot 28	658	12627	1.0	21.5737	1.9	0.0353	3.1	0.0055	2.5	0.79	35.5	0.9	35.2	1.1	16.0	46.1	35.5	0.9
Spot 93	417	25372	1.1	21.6427	2.4	0.0352	3.6	0.0055	2.7	0.74	35.5	1.0	35.1	1.2	8.3	58.3	35.5	1.0
Spot 92	482	5345	0.8	21.1934	2.5	0.0360	3.6	0.0055	2.6	0.71	35.6	0.9	35.9	1.3	58.6	60.7	35.6	0.9
Spot 53	694	16790	0.9	20.5650	1.9	0.0371	2.8	0.0055	2.1	0.73	35.6	0.7	37.0	1.0	129.9	45.7	35.6	0.7
Spot 74	731	115679	1.2	21.0709	1.6	0.0362	3.1	0.0055	2.6	0.85	35.6	0.9	36.1	1.1	72.4	39.2	35.6	0.9
Spot 56	922	6391	4.0	21.1874	2.2	0.0360	3.9	0.0055	3.1	0.81	35.6	1.1	35.9	1.4	59.3	53.6	35.6	1.1
Spot 110	1283	55091	0.7	20.8858	1.2	0.0365	2.9	0.0055	2.6	0.90	35.6	0.9	36.4	1.0	93.3	29.4	35.6	0.9
Spot 88	635	21403	1.2	20.4022	1.8	0.0374	3.8	0.0055	3.3	0.87	35.6	1.2	37.3	1.4	148.5	43.0	35.6	1.2
Spot 48	603	4374	1.1	23.1058	2.4	0.0330	3.4	0.0055	2.3	0.70	35.6	0.8	33.0	1.1	NA	NA	35.6	0.8
Spot 33	545	9977	1.4	22.0850	2.1	0.0346	3.6	0.0055	2.9	0.81	35.6	1.0	34.5	1.2	NA	NA	35.6	1.0
Spot 3	815	17121	1.0	21.4636	1.5	0.0356	2.9	0.0055	2.5	0.86	35.6	0.9	35.5	1.0	28.3	35.4	35.6	0.9
Spot 29	548	51540	1.3	20.4515	1.8	0.0373	3.0	0.0055	2.4	0.81	35.6	0.9	37.2	1.1	142.9	41.6	35.6	0.9
Spot 80	799	38648	0.9	16.7072	3.4	0.0457	4.5	0.0055	2.9	0.64	35.6	1.0	45.4	2.0	598.3	74.7	35.6	1.0
Spot 55	558	7135	1.0	21.9373	2.8	0.0348	4.0	0.0055	2.9	0.71	35.6	1.0	34.8	1.4	NA	NA	35.6	1.0
Spot 99	1550	40153	1.4	21.4843	1.5	0.0356	3.2	0.0055	2.8	0.88	35.7	1.0	35.5	1.1	26.0	36.4	35.7	1.0
Spot 59	265	3439	1.5	22.1863	3.5	0.0345	4.5	0.0055	2.9	0.63	35.7	1.0	34.4	1.5	NA	NA	35.7	1.0

TABLE E2: U-TH-PB GEOCHRONOLOGIC ANALYSES

						Isotope Ratios					Apparent Ages (Ma)							
Analysis	U (ppm)	^{206}Pb ^{204}Pb	U/Th	$^{206}Pb^*$ $^{207}Pb^*$	± (%)	$^{207}Pb^*$ $^{235}U^*$	± (%)	$^{206}Pb^*$ ^{238}U	± (%)	Error Corr.	$^{206}Pb^*$ $^{238}U^*$	± (Ma)	$^{207}Pb^*$ ^{235}U	± (Ma)	$^{206}Pb^*$ $^{207}Pb^*$	± (Ma)	**Best Age** (Ma)	± (Ma)
Spot 94	1089	10415	1.6	21.8276	1.6	0.0350	3.3	0.0055	2.9	0.88	35.7	1.0	35.0	1.1	NA	NA	35.7	1.0
Spot 7	1397	93173	1.1	20.7121	1.3	0.0369	2.7	0.0056	2.4	0.88	35.7	0.9	36.8	1.0	113.1	31.1	35.7	0.9
Spot 60	1075	11628	2.1	21.2247	1.7	0.0361	3.1	0.0056	2.5	0.83	35.7	0.9	36.0	1.1	55.0	40.9	35.7	0.9
Spot 15	934	33867	0.8	20.2081	1.7	0.0379	2.8	0.0056	2.2	0.80	35.7	0.8	37.8	1.0	170.9	39.2	35.7	0.8
Spot 91	515	20180	1.1	19.2018	3.4	0.0399	4.6	0.0056	3.2	0.69	35.7	1.1	39.7	1.8	288.9	76.7	35.7	1.1
Spot 51	531	11940	2.0	21.6336	2.1	0.0355	3.7	0.0056	3.0	0.82	35.8	1.1	35.4	1.3	9.3	50.8	35.8	1.1
Spot 78	542	20958	1.1	15.6639	3.6	0.0490	4.2	0.0056	2.0	0.48	35.8	0.7	48.6	2.0	736.4	77.3	35.8	0.7
Spot 108	883	97871	1.9	20.5382	1.1	0.0374	3.2	0.0056	3.1	0.94	35.8	1.1	37.3	1.2	132.9	25.2	35.8	1.1
Spot 84	893	12271	1.0	20.2933	2.2	0.0379	3.3	0.0056	2.5	0.76	35.8	0.9	37.7	1.2	161.1	50.4	35.8	0.9
Spot 85	500	9526	1.1	18.3254	2.3	0.0420	3.5	0.0056	2.6	0.75	35.9	0.9	41.7	1.4	394.6	51.0	35.9	0.9
Spot 63	571	9303	1.2	21.6219	1.8	0.0356	3.0	0.0056	2.4	0.80	35.9	0.9	35.5	1.1	10.7	43.8	35.9	0.9
Spot 31	2107	587848	0.8	21.3321	1.3	0.0361	3.1	0.0056	2.9	0.91	35.9	1.0	36.0	1.1	43.0	30.7	35.9	1.0
Spot 16	260	5476	0.9	22.8191	3.9	0.0338	4.7	0.0056	2.7	0.58	36.0	1.0	33.8	1.6	NA	NA	36.0	1.0
Spot 101	817	3633	0.2	12.3893	3.3	0.0623	4.0	0.0056	2.4	0.59	36.0	0.9	61.3	2.4	1214.5	64.4	36.0	0.9
Spot 36	529	7585	1.1	21.4215	1.8	0.0361	3.5	0.0056	3.0	0.86	36.1	1.1	36.0	1.2	33.0	43.0	36.1	1.1
Spot 57	469	15131	1.0	21.0784	2.1	0.0367	3.9	0.0056	3.2	0.83	36.1	1.2	36.6	1.4	71.5	51.0	36.1	1.2
Spot 14	303	8772	2.0	21.6083	2.7	0.0358	3.9	0.0056	2.8	0.73	36.1	1.0	35.7	1.4	12.1	64.0	36.1	1.0
Spot 87	441	15993	1.2	20.1387	3.7	0.0385	4.5	0.0056	2.6	0.58	36.1	0.9	38.3	1.7	178.9	86.5	36.1	0.9
Spot 79	655	480748	1.0	20.8435	2.1	0.0372	4.0	0.0056	3.5	0.86	36.1	1.2	37.1	1.5	98.1	49.0	36.1	1.2

TABLE E2: U-TH-PB GEOCHRONOLOGIC ANALYSES

Analysis	U (ppm)	^{206}Pb ^{204}Pb	U/Th	$^{206}Pb^*$ $^{207}Pb^*$	± (%)	Isotope Ratios $^{207}Pb^*$ $^{235}U^*$	± (%)	$^{206}Pb^*$ ^{238}U	± (%)	Error Corr.	Apparent Ages (Ma) $^{206}Pb^*$ $^{238}U^*$	± (Ma)	$^{207}Pb^*$ ^{235}U	± (Ma)	$^{206}Pb^*$ $^{207}Pb^*$	± (Ma)	Best Age (Ma)	± (Ma)
Spot 109	1709	96233	1.0	20.7564	1.7	0.0373	3.2	0.0056	2.7	0.85	36.2	1.0	37.2	1.2	108.0	40.5	36.2	1.0
Spot 32	581	33645	4.7	20.9629	2.2	0.0371	4.3	0.0056	3.7	0.86	36.2	1.4	36.9	1.6	84.6	52.1	36.2	1.4
Spot 62	443	30453	1.1	18.7499	2.8	0.0415	3.9	0.0056	2.7	0.69	36.3	1.0	41.2	1.6	343.0	62.9	36.3	1.0
Spot 58	443	2630	1.5	19.8663	3.7	0.0391	4.4	0.0056	2.5	0.56	36.3	0.9	39.0	1.7	210.6	85.7	36.3	0.9
Spot 64	503	13381	1.2	19.1254	2.6	0.0407	3.3	0.0056	2.1	0.62	36.3	0.7	40.5	1.3	297.9	59.8	36.3	0.7
Spot 106	472	23464	1.1	16.4715	2.8	0.0473	4.3	0.0056	3.2	0.76	36.3	1.2	46.9	2.0	629.0	60.1	36.3	1.2
Spot 6	991	63816	1.0	22.0472	1.4	0.0353	3.4	0.0057	3.1	0.92	36.3	1.1	35.3	1.2	NA	NA	36.3	1.1
Spot 22	671	4117	0.6	19.3408	3.0	0.0403	3.7	0.0057	2.2	0.60	36.3	0.8	40.1	1.5	272.3	67.9	36.3	0.8
Spot 81	1073	72341	0.5	21.3121	1.2	0.0367	2.7	0.0057	2.5	0.90	36.4	0.9	36.6	1.0	45.2	28.7	36.4	0.9
Spot 86	410	6597	1.3	22.4354	3.2	0.0349	3.9	0.0057	2.2	0.57	36.5	0.8	34.8	1.3	NA	NA	36.5	0.8
Spot 73	1466	10466	0.4	18.6138	2.3	0.0420	3.6	0.0057	2.7	0.75	36.5	1.0	41.8	1.5	359.5	53.0	36.5	1.0
Spot 43	549	7797	1.2	21.2155	1.6	0.0369	3.0	0.0057	2.6	0.85	36.5	0.9	36.8	1.1	56.1	37.9	36.5	0.9
Spot 25	454	7669	0.6	14.1420	4.3	0.0555	5.0	0.0057	2.5	0.49	36.6	0.9	54.9	2.7	949.1	88.4	36.6	0.9
Spot 45	863	9623	1.4	21.8314	2.3	0.0362	3.4	0.0057	2.5	0.74	36.8	0.9	36.1	1.2	NA	NA	36.8	0.9
Spot 61	1382	11082	1.0	19.5014	3.0	0.0405	3.9	0.0057	2.6	0.65	36.9	0.9	40.3	1.6	253.4	68.5	36.9	0.9
Spot 95	915	14031	0.9	21.8586	1.5	0.0363	2.9	0.0058	2.5	0.85	37.0	0.9	36.2	1.0	NA	NA	37.0	0.9
Spot 35	326	12714	1.7	22.3681	2.7	0.0356	4.0	0.0058	2.9	0.72	37.2	1.1	35.5	1.4	NA	NA	37.2	1.1
Spot 5	187	232729	0.8	22.3010	2.8	0.0358	4.1	0.0058	3.0	0.73	37.2	1.1	35.7	1.4	NA	NA	37.2	1.1
Spot 34	594	10641	1.1	21.4341	1.9	0.0373	3.3	0.0058	2.7	0.81	37.3	1.0	37.2	1.2	31.6	46.2	37.3	1.0

TABLE E2: U-TH-PB GEOCHRONOLOGIC ANALYSES

Analysis	U (ppm)	$^{206}Pb/^{204}Pb$	U/Th	$^{206}Pb^*/^{207}Pb^*$	± (%)	Isotope Ratios $^{207}Pb^*/^{235}U^*$	± (%)	$^{206}Pb^*/^{238}U$	± (%)	Error Corr.	Apparent Ages (Ma) $^{206}Pb^*/^{238}U^*$	± (Ma)	$^{207}Pb^*/^{235}U$	± (Ma)	$^{206}Pb^*/^{207}Pb^*$	± (Ma)	Best Age (Ma)	± (Ma)
Spot 90	991	285622	1.6	21.3692	1.6	0.0375	3.1	0.0058	2.6	0.85	37.3	1.0	37.3	1.1	38.8	38.8	37.3	1.0
Spot 77	237	2657	0.8	10.6364	12.5	0.0753	12.9	0.0058	3.5	0.27	37.3	1.3	73.7	9.2	1508.4	236.1	37.3	1.3
Spot 23	2530	68221	1.0	21.0918	1.1	0.0380	2.4	0.0058	2.2	0.90	37.4	0.8	37.9	0.9	70.0	25.3	37.4	0.8
Spot 44	1751	65511	1.2	20.1661	1.4	0.0398	2.9	0.0058	2.6	0.88	37.4	1.0	39.6	1.1	175.7	31.7	37.4	1.0
Spot 67	396	7879	1.3	19.0312	2.0	0.0421	3.6	0.0058	3.1	0.84	37.4	1.1	41.9	1.5	309.2	44.6	37.4	1.1
Spot 66	1386	17718	0.5	21.0254	1.0	0.0382	2.8	0.0058	2.6	0.93	37.4	1.0	38.0	1.1	77.5	24.6	37.4	1.0
Spot 27	787	9884	0.8	15.5477	4.9	0.0518	5.8	0.0058	3.2	0.54	37.6	1.2	51.3	2.9	752.1	103.8	37.6	1.2
Spot 47	949	115126	1.3	19.8886	1.7	0.0407	3.4	0.0059	3.0	0.87	37.7	1.1	40.5	1.4	208.0	39.0	37.7	1.1
Spot 89	548	8160	0.9	12.3468	9.7	0.0657	10.3	0.0059	3.3	0.32	37.9	1.3	64.7	6.5	1221.3	192.0	37.9	1.3
Spot 69	1089	35557	1.0	21.0351	1.5	0.0389	3.6	0.0059	3.2	0.90	38.2	1.2	38.8	1.4	76.4	36.5	38.2	1.2
Spot 105	482	15293	2.0	22.2787	2.1	0.0369	3.6	0.0060	2.9	0.81	38.4	1.1	36.8	1.3	NA	NA	38.4	1.1
Spot 39	710	51437	0.9	20.3859	1.9	0.0407	3.8	0.0060	3.3	0.87	38.7	1.3	40.5	1.5	150.4	44.8	38.7	1.3
Spot 24	562	1793	2.2	9.8910	12.2	0.0843	13.4	0.0060	5.5	0.41	38.9	2.1	82.2	10.5	1644.4	226.7	38.9	2.1
Spot 71	1009	13033	1.1	21.7937	1.6	0.0383	3.9	0.0061	3.6	0.92	38.9	1.4	38.1	1.5	NA	NA	38.9	1.4
Spot 30	606	4288	1.7	17.5972	3.2	0.0495	4.5	0.0063	3.1	0.69	40.6	1.3	49.1	2.1	484.9	71.3	40.6	1.3
Spot 76	1061	1628	1.6	6.4436	4.7	0.1368	5.6	0.0064	3.1	0.55	41.1	1.3	130.2	6.9	2403.9	80.3	41.1	1.3
Spot 97	154	1083	0.9	5.2264	9.2	0.1817	11.8	0.0069	7.3	0.62	44.3	3.2	169.5	18.4	2753.7	152.2	44.3	3.2
Spot 70	397	1102	0.7	5.4701	28.8	0.1737	30.0	0.0069	8.5	0.28	44.3	3.8	162.6	45.1	2678.5	487.7	44.3	3.8
Spot 31	143	359	1.5	1948.3116	699.7	0.0004	699.7	0.0051	3.2	0.00	32.9	1.0	0.4	2.6	NA	NA	32.9	1.0
Spot 24	1005	28254	0.7	21.0591	1.4	0.0343	2.9	0.0052	2.5	0.87	33.7	0.8	34.3	1.0	73.7	33.6	33.7	0.8

TABLE E2: U-TH-PB GEOCHRONOLOGIC ANALYSES

Analysis	U (ppm)	^{206}Pb ^{204}Pb	U/Th	$^{206}Pb^*$ $^{207}Pb^*$	± (%)	Isotope Ratios $^{207}Pb^*$ $^{235}U^*$	± (%)	$^{206}Pb^*$ ^{238}U	± (%)	Error Corr.	Apparent Ages (Ma) $^{206}Pb^*$ $^{238}U^*$	± (Ma)	$^{207}Pb^*$ ^{235}U	± (Ma)	$^{206}Pb^*$ $^{207}Pb^*$	± (Ma)	Best Age (Ma)	± (Ma)
Spot 74	1057	9866	0.7	21.0559	1.9	0.0346	3.1	0.0053	2.5	0.79	34.0	0.8	34.5	1.1	74.1	45.7	34.0	0.8
Spot 3	335	1452	1.6	26.2566	2.9	0.0280	4.0	0.0053	2.7	0.68	34.4	0.9	28.1	1.1	NA	NA	34.4	0.9
Spot 39	1682	3627	0.6	12.8423	7.0	0.0576	7.3	0.0054	2.0	0.28	34.5	0.7	56.8	4.0	1143.5	139.9	34.5	0.7
Spot 4	187	3127	1.6	22.8699	3.3	0.0324	4.4	0.0054	2.9	0.66	34.5	1.0	32.4	1.4	NA	NA	34.5	1.0
Spot 62	500	1200	1.5	29.3452	6.5	0.0253	6.9	0.0054	2.1	0.31	34.6	0.7	25.4	1.7	NA	NA	34.6	0.7
Spot 35	383	1846	1.5	26.2097	3.2	0.0285	4.0	0.0054	2.5	0.62	34.9	0.9	28.5	1.1	NA	NA	34.9	0.9
Spot 30	318	1744	1.6	26.7137	3.0	0.0280	4.7	0.0054	3.5	0.76	34.9	1.2	28.0	1.3	NA	NA	34.9	1.2
Spot 73	252	2090	3.3	22.3313	3.7	0.0335	4.6	0.0054	2.7	0.58	34.9	0.9	33.5	1.5	NA	NA	34.9	0.9
Spot 78	326	1472	1.7	25.5516	3.2	0.0293	3.9	0.0054	2.2	0.57	34.9	0.8	29.3	1.1	NA	NA	34.9	0.8
Spot 37	496	3036	1.2	22.3949	2.5	0.0335	3.6	0.0054	2.7	0.73	35.0	0.9	33.4	1.2	NA	NA	35.0	0.9
Spot 36	334	1687	2.0	23.2759	4.3	0.0323	5.2	0.0054	2.8	0.54	35.0	1.0	32.2	1.6	NA	NA	35.0	1.0
Spot 16	688	2278	1.4	17.2953	5.2	0.0435	6.2	0.0055	3.4	0.55	35.1	1.2	43.3	2.6	522.9	113.1	35.1	1.2
Spot 47	352	5310	2.2	21.1232	3.6	0.0357	4.2	0.0055	2.1	0.51	35.1	0.7	35.6	1.5	66.5	85.7	35.1	0.7
Spot 46	728	45835	1.1	21.8676	1.7	0.0344	2.9	0.0055	2.4	0.83	35.1	0.9	34.4	1.0	NA	NA	35.1	0.9
Spot 56	832	3042	1.6	23.0057	2.4	0.0328	4.0	0.0055	3.2	0.81	35.2	1.1	32.7	1.3	NA	NA	35.2	1.1
Spot 7	499	1647	1.4	25.4147	2.0	0.0297	3.3	0.0055	2.6	0.79	35.2	0.9	29.7	1.0	NA	NA	35.2	0.9
Spot 75	449	979	1.3	31.4848	2.6	0.0240	3.5	0.0055	2.4	0.69	35.3	0.9	24.1	0.8	NA	NA	35.3	0.9
Spot 19	337	4084	1.6	22.6709	4.8	0.0334	5.4	0.0055	2.6	0.47	35.3	0.9	33.3	1.8	NA	NA	35.3	0.9
Spot 68	325	10362	1.0	21.5053	2.6	0.0352	4.0	0.0055	3.0	0.76	35.3	1.1	35.1	1.4	23.6	62.6	35.3	1.1

TABLE E2: U-TH-PB GEOCHRONOLOGIC ANALYSES

Analysis	U (ppm)	^{206}Pb ^{204}Pb	U/Th	$^{206}Pb^*$ $^{207}Pb^*$	± (%)	Isotope Ratios $^{207}Pb^*$ $^{235}U^*$	± (%)	$^{206}Pb^*$ ^{238}U	± (%)	Error Corr.	Apparent Ages (Ma) $^{206}Pb^*$ $^{238}U^*$	± (Ma)	$^{207}Pb^*$ ^{235}U	± (Ma)	$^{206}Pb^*$ $^{207}Pb^*$	± (Ma)	Best Age (Ma)	± (Ma)
Spot 70	290	1094	1.7	30.2567	20.4	0.0250	20.7	0.0055	3.6	0.17	35.3	1.3	25.1	5.1	NA	NA	35.3	1.3
Spot 52	728	28408	1.2	21.2745	1.7	0.0356	3.0	0.0055	2.5	0.83	35.3	0.9	35.5	1.0	49.5	39.6	35.3	0.9
Spot 2	983	6763	0.7	21.3336	1.7	0.0355	2.5	0.0055	1.9	0.73	35.3	0.7	35.4	0.9	42.8	41.0	35.3	0.7
Spot 33	191	1083	2.9	16.8908	8.1	0.0448	8.4	0.0055	2.5	0.29	35.3	0.9	44.5	3.7	574.6	175.4	35.3	0.9
Spot 72	391	32590	1.4	19.3583	3.1	0.0392	4.1	0.0055	2.6	0.64	35.4	0.9	39.1	1.6	270.3	71.6	35.4	0.9
Spot 69	374	7255	1.4	21.7286	2.4	0.0350	3.5	0.0055	2.6	0.73	35.5	0.9	34.9	1.2	NA	NA	35.5	0.9
Spot 67	375	8237	1.5	21.1363	3.3	0.0360	4.3	0.0055	2.7	0.63	35.5	0.9	35.9	1.5	65.0	79.2	35.5	0.9
Spot 76	382	1383	1.4	26.4748	14.7	0.0287	14.9	0.0055	2.3	0.15	35.5	0.8	28.8	4.2	NA	NA	35.5	0.8
Spot 77	547	3509	1.8	22.9144	4.1	0.0332	4.7	0.0055	2.2	0.46	35.5	0.8	33.1	1.5	NA	NA	35.5	0.8
Spot 49	284	2423	1.9	23.9140	2.3	0.0319	3.3	0.0055	2.4	0.72	35.5	0.9	31.8	1.0	NA	NA	35.5	0.9
Spot 8	741	5550	1.5	20.6257	3.4	0.0370	4.7	0.0055	3.3	0.70	35.6	1.2	36.9	1.7	122.9	79.2	35.6	1.2
Spot 1	236	974	2.8	28.2133	10.4	0.0270	10.8	0.0055	2.6	0.25	35.6	0.9	27.1	2.9	NA	NA	35.6	0.9
Spot 79	353	1027	2.1	30.5933	9.7	0.0249	10.1	0.0055	2.7	0.27	35.6	1.0	25.0	2.5	NA	NA	35.6	1.0
Spot 48	222	664	0.9	40.2323	3.8	0.0190	4.6	0.0055	2.6	0.56	35.7	0.9	19.1	0.9	NA	NA	35.7	0.9
Spot 23	535	657	1.2	39.6130	44.4	0.0193	44.5	0.0056	3.1	0.07	35.7	1.1	19.4	8.6	NA	NA	35.7	1.1
Spot 58	201	5780	1.1	23.7227	2.7	0.0323	4.5	0.0056	3.6	0.80	35.7	1.3	32.2	1.4	NA	NA	35.7	1.3
Spot 43	1016	12357	2.1	22.5889	1.5	0.0339	2.4	0.0056	1.9	0.78	35.7	0.7	33.9	0.8	NA	NA	35.7	0.7
Spot 61	578	4909	1.4	21.6785	2.2	0.0354	3.1	0.0056	2.2	0.71	35.7	0.8	35.3	1.1	4.3	52.0	35.7	0.8
Spot 54	513	3934	0.7	23.2071	2.3	0.0330	3.4	0.0056	2.5	0.74	35.8	0.9	33.0	1.1	NA	NA	35.8	0.9

TABLE E2: U-TH-PB GEOCHRONOLOGIC ANALYSES

Analysis	U (ppm)	^{206}Pb ^{204}Pb	U/Th	$^{206}Pb^*$ $^{207}Pb^*$	± (%)	Isotope Ratios $^{207}Pb^*$ $^{235}U^*$	± (%)	$^{206}Pb^*$ ^{238}U	± (%)	Error Corr.	Apparent Ages (Ma) $^{206}Pb^*$ $^{238}U^*$	± (Ma)	$^{207}Pb^*$ ^{235}U	± (Ma)	$^{206}Pb^*$ $^{207}Pb^*$	± (Ma)	Best Age (Ma)	± (Ma)
Spot 10	392	1377	1.7	25.837 4	11.3	0.0297	11.8	0.0056	3.2	0.27	35.8	1.1	29.7	3.4	NA	NA	35.8	1.1
Spot 59	398	4118	1.6	18.251 0	4.5	0.0421	5.5	0.0056	3.1	0.57	35.8	1.1	41.8	2.2	403.7	100.7	35.8	1.1
Spot 64	602	5206	1.0	22.674 3	1.7	0.0339	3.2	0.0056	2.6	0.83	35.8	0.9	33.8	1.0	NA	NA	35.8	0.9
Spot 45	563	6301	1.1	15.584 2	5.1	0.0493	5.7	0.0056	2.6	0.46	35.9	0.9	48.9	2.7	747.1	107.2	35.9	0.9
Spot 13	344	1618	1.6	28.065 1	3.9	0.0274	4.7	0.0056	2.6	0.56	35.9	0.9	27.5	1.3	NA	NA	35.9	0.9
Spot 12	571	2182	1.4	23.184 2	3.5	0.0332	4.3	0.0056	2.6	0.60	35.9	0.9	33.2	1.4	NA	NA	35.9	0.9
Spot 71	381	2068	1.6	24.359 4	3.8	0.0316	4.9	0.0056	3.0	0.61	35.9	1.1	31.6	1.5	NA	NA	35.9	1.1
Spot 42	273	4407	1.6	22.195 7	3.2	0.0347	4.8	0.0056	3.6	0.74	35.9	1.3	34.7	1.6	NA	NA	35.9	1.3
Spot 41	362	7865	1.9	22.441 8	2.5	0.0344	3.5	0.0056	2.5	0.70	36.0	0.9	34.4	1.2	NA	NA	36.0	0.9
Spot 66	409	4752	2.4	22.648 3	2.4	0.0341	3.4	0.0056	2.4	0.71	36.1	0.9	34.1	1.1	NA	NA	36.1	0.9
Spot 11	356	5030	1.2	20.603 4	2.5	0.0375	3.4	0.0056	2.2	0.66	36.1	0.8	37.4	1.2	125.4	59.2	36.1	0.8
Spot 40	1465	25450	2.8	21.348 1	1.5	0.0362	3.0	0.0056	2.6	0.86	36.1	0.9	36.1	1.1	41.2	36.4	36.1	0.9
Spot 22	222	1460	1.3	29.844 4	3.4	0.0259	4.2	0.0056	2.5	0.58	36.1	0.9	26.0	1.1	NA	NA	36.1	0.9
Spot 25	495	16399	1.4	22.229 1	2.4	0.0348	3.8	0.0056	3.0	0.78	36.1	1.1	34.7	1.3	NA	NA	36.1	1.1
Spot 51	885	2156	1.6	18.903 5	5.3	0.0409	6.0	0.0056	3.0	0.49	36.1	1.1	40.7	2.4	324.5	119.3	36.1	1.1
Spot 57	306	942	1.0	33.220 5	12.3	0.0233	12.6	0.0056	2.6	0.21	36.1	0.9	23.4	2.9	NA	NA	36.1	0.9
Spot 6	592	5723	0.8	17.417 4	2.9	0.0446	3.8	0.0056	2.4	0.64	36.2	0.9	44.3	1.7	507.4	64.7	36.2	0.9
Spot 9	341	3929	1.9	21.669 1	4.7	0.0358	5.2	0.0056	2.2	0.42	36.2	0.8	35.7	1.8	5.4	113.4	36.2	0.8
Spot 44	341	1423	1.8	18.484 0	5.2	0.0421	6.0	0.0056	3.1	0.52	36.3	1.1	41.8	2.5	375.2	116.0	36.3	1.1

TABLE E2: U-TH-PB GEOCHRONOLOGIC ANALYSES

Analysis	U (ppm)	^{206}Pb ^{204}Pb	U/Th	$^{206}Pb^*$ $^{207}Pb^*$	± (%)	Isotope Ratios $^{207}Pb^*$ $^{235}U^*$	± (%)	$^{206}Pb^*$ ^{238}U	± (%)	Error Corr.	Apparent Ages (Ma) $^{206}Pb^*$ $^{238}U^*$	± (Ma)	$^{207}Pb^*$ ^{235}U	± (Ma)	$^{206}Pb^*$ $^{207}Pb^*$	± (Ma)	Best Age (Ma)	± (Ma)
Spot 34	518	5126	1.4	17.4215	5.0	0.0447	5.7	0.0057	2.9	0.50	36.3	1.0	44.4	2.5	506.9	109.2	36.3	1.0
Spot 28	911	4546	0.7	22.8205	1.9	0.0342	2.9	0.0057	2.2	0.76	36.5	0.8	34.2	1.0	NA	NA	36.5	0.8
Spot 5	379	1433	1.7	28.2411	11.9	0.0277	12.2	0.0057	2.9	0.23	36.6	1.0	27.8	3.4	NA	NA	36.6	1.0
Spot 55	403	3165	1.5	23.5237	2.6	0.0333	3.8	0.0057	2.8	0.74	36.6	1.0	33.3	1.2	NA	NA	36.6	1.0
Spot 60	364	2255	1.8	22.9480	6.6	0.0343	6.9	0.0057	2.1	0.31	36.7	0.8	34.2	2.3	NA	NA	36.7	0.8
Spot 29	769	3159	0.8	14.8746	3.5	0.0530	4.8	0.0057	3.3	0.68	36.8	1.2	52.4	2.5	844.9	73.0	36.8	1.2
Spot 26	701	2232	0.7	16.7536	5.2	0.0470	5.8	0.0057	2.4	0.41	36.8	0.9	46.7	2.6	592.3	113.6	36.8	0.9
Spot 20	292	4860	1.7	15.9235	6.5	0.0497	7.0	0.0057	2.6	0.37	36.9	1.0	49.2	3.4	701.5	138.6	36.9	1.0
Spot 50	259	1341	1.1	25.4746	5.1	0.0311	5.8	0.0057	2.8	0.48	37.0	1.0	31.1	1.8	NA	NA	37.0	1.0
Spot 15	556	4752	1.3	22.6694	4.0	0.0350	5.0	0.0058	3.1	0.61	37.1	1.1	35.0	1.7	NA	NA	37.1	1.1
Spot 53	438	496	1.3	10.9786	7.6	0.0726	8.3	0.0058	3.2	0.39	37.2	1.2	71.1	5.7	1448.4	145.3	37.2	1.2
Spot 80	762	46297	0.8	21.1173	1.8	0.0378	3.2	0.0058	2.7	0.83	37.2	1.0	37.6	1.2	67.1	42.6	37.2	1.0
Spot 27	496	4427	1.1	23.5312	4.3	0.0339	5.0	0.0058	2.4	0.48	37.2	0.9	33.9	1.7	NA	NA	37.2	0.9
Spot 14	267	7520	1.0	23.6829	2.1	0.0338	3.2	0.0058	2.4	0.76	37.4	0.9	33.8	1.1	NA	NA	37.4	0.9
Spot 18	2175	62010	1.8	21.6243	1.5	0.0371	3.4	0.0058	3.0	0.90	37.4	1.1	37.0	1.2	10.4	36.2	37.4	1.1
Spot 65	395	3451	2.0	11.5204	9.5	0.0699	10.1	0.0058	3.3	0.32	37.6	1.2	68.6	6.7	1356.1	183.8	37.6	1.2
Spot 32	440	1288	1.3	14.3904	5.7	0.0562	6.4	0.0059	2.9	0.45	37.7	1.1	55.5	3.4	913.3	117.1	37.7	1.1
Spot 17	334	7352	0.6	21.9317	2.3	0.0373	3.4	0.0059	2.5	0.75	38.1	1.0	37.2	1.2	NA	NA	38.1	1.0
Spot 21	468	4377	4.0	12.3453	8.9	0.0665	9.7	0.0060	4.0	0.41	38.3	1.5	65.4	6.2	1221.5	174.5	38.3	1.5

TABLE E2: U-TH-PB GEOCHRONOLOGIC ANALYSES

Analysis	U (ppm)	$^{206}Pb/^{204}Pb$	U/Th	$^{206}Pb^*/^{207}Pb^*$	± (%)	Isotope Ratios $^{207}Pb^*/^{235}U^*$	± (%)	$^{206}Pb^*/^{238}U$	± (%)	Error Corr.	Apparent Ages (Ma) $^{206}Pb^*/^{238}U^*$	± (Ma)	$^{207}Pb^*/^{235}U$	± (Ma)	$^{206}Pb^*/^{207}Pb^*$	± (Ma)	**Best Age** (Ma)	± (Ma)
Spot 38	427	876	1.4	10.0142	7.7	0.0835	8.8	0.0061	4.3	0.49	39.0	1.7	81.4	6.9	1621.4	143.6	39.0	1.7
Spot 63	102	24385	1.3	11.1656	0.8	2.9574	2.5	0.2396	2.3	0.94	1384.6	29.2	1396.7	18.9	1416.2	16.0	1416.2	16.0
SAK-0501																		
0501-38	258	2187	1.1	18.0675	38.8	0.0332	38.9	0.0043	3.5	0.09	28.0	1.0	33.1	12.7	426.3	896.1	28.0	1.0
0501-111	107	1682	0.9	25.0261	58.5	0.0292	59.1	0.0053	8.1	0.14	34.1	2.7	29.2	17.0	-353.6	1641.8	34.1	2.7
0501-81	222	7753	0.9	23.1111	40.4	0.0319	40.6	0.0053	4.8	0.12	34.4	1.6	31.9	12.8	-152.1	1038.9	34.4	1.6
0501-118	319	8399	0.4	16.4852	15.8	0.0450	16.1	0.0054	3.3	0.20	34.6	1.1	44.7	7.1	627.2	341.9	34.6	1.1
0501-73	122	6406	0.8	4.0010	456.4	~~0.1859~~	~~456.5~~	~~0.0054~~	~~9.2~~	~~0.02~~	34.7	3.2	173.1	912.4	3184.4	30.0	34.7	3.2
0501-43	214	2018	0.9	32.3578	59.8	0.0232	60.0	0.0055	5.7	0.09	35.1	2.0	23.3	13.8	-1068.6	1950.4	35.1	2.0
0501-21	455	6105	1.1	21.3248	14.9	0.0353	15.1	0.0055	2.4	0.16	35.1	0.8	35.2	5.2	43.8	357.2	35.1	0.8
0501-76	567	22140	1.0	22.4579	16.7	0.0336	17.3	0.0055	4.7	0.27	35.1	1.6	33.5	5.7	-81.4	410.4	35.1	1.6
0501-123	627	9672	2.0	20.8569	6.6	0.0364	7.4	0.0055	3.5	0.47	35.4	1.2	36.3	2.6	96.6	155.5	35.4	1.2
0501-07	344	3133	0.8	34.8245	29.8	0.0218	29.9	0.0055	2.8	0.09	35.4	1.0	21.9	6.5	-1295.4	961.4	35.4	1.0
0501-35	180	2231	0.9	26.8065	29.3	0.0284	30.4	0.0055	7.8	0.26	35.4	2.8	28.4	8.5	-534.5	801.0	35.4	2.8
0501-54	134	2693	0.8	12.2191	99.2	0.0622	99.4	0.0055	6.7	0.07	35.5	2.4	61.3	59.2	1241.7	#VALUE!	35.5	2.4
0501-39	190	2243	0.9	28.5412	30.4	0.0267	30.9	0.0055	5.5	0.18	35.5	1.9	26.7	8.2	-705.7	862.5	35.5	1.9
0501-85	370	7194	1.2	15.7792	32.3	0.0482	33.0	0.0055	6.7	0.20	35.5	2.4	47.8	15.4	720.8	703.6	35.5	2.4
0501-02	210	2750	1.0	16.0705	32.5	0.0473	32.9	0.0055	5.1	0.16	35.5	1.8	47.0	15.1	681.9	712.7	35.5	1.8
0501-68	436	12268	1.1	20.9894	16.3	0.0363	16.4	0.0055	2.0	0.12	35.5	0.7	36.2	5.8	81.6	388.7	35.5	0.7

TABLE E2: U-TH-PB GEOCHRONOLOGIC ANALYSES

Analysis	U (ppm)	$^{206}Pb/^{204}Pb$	U/Th	$^{206}Pb^*/^{207}Pb^*$	± (%)	Isotope Ratios $^{207}Pb^*/^{235}U^*$	± (%)	$^{206}Pb^*/^{238}U$	± (%)	Error Corr.	Apparent Ages (Ma) $^{206}Pb^*/^{238}U^*$	± (Ma)	$^{207}Pb^*/^{235}U$	± (Ma)	$^{206}Pb^*/^{207}Pb^*$	± (Ma)	Best Age (Ma)	± (Ma)
0501-10	430	6747	1.1	16.0168	13.7	0.0476	14.2	0.0055	3.6	0.25	35.5	1.3	47.2	6.5	689.0	294.1	35.5	1.3
0501-72	379	10691	1.2	26.8894	22.4	0.0284	23.5	0.0055	7.0	0.30	35.6	2.5	28.4	6.6	-542.8	608.8	35.6	2.5
0501-79	180	4699	0.9	28.0455	45.6	0.0273	46.1	0.0055	6.7	0.15	35.6	2.4	27.3	12.4	-657.2	1312.7	35.6	2.4
0501-114	412	28839	1.3	22.5332	19.0	0.0340	19.3	0.0056	3.6	0.19	35.7	1.3	33.9	6.4	-89.6	469.2	35.7	1.3
0501-127	473	11639	1.7	19.4745	22.1	0.0393	22.2	0.0056	2.4	0.11	35.7	0.9	39.2	8.5	256.5	513.0	35.7	0.9
0501-113	310	13359	1.0	23.8550	35.1	0.0321	35.2	0.0056	2.8	0.08	35.7	1.0	32.1	11.1	-231.3	908.4	35.7	1.0
0501-66	468	10327	1.1	24.1989	13.1	0.0317	13.2	0.0056	1.9	0.15	35.7	0.7	31.6	4.1	-267.5	333.9	35.7	0.7
0501-12	172	4830	0.9	19.9157	52.0	0.0385	52.3	0.0056	5.4	0.10	35.7	1.9	38.4	19.7	204.8	1290.3	35.7	1.9
0501-90	119	2804	1.0	14.1154	45.2	0.0545	45.7	0.0056	6.1	0.13	35.9	2.2	53.9	24.0	952.9	976.1	35.9	2.2
0501-27	337	7526	1.2	18.0718	20.3	0.0426	20.6	0.0056	3.6	0.18	35.9	1.3	42.3	8.5	425.8	456.7	35.9	1.3
0501-126	278	11195	0.9	24.6993	32.2	0.0312	32.4	0.0056	3.6	0.11	36.0	1.3	31.2	10.0	-319.8	843.8	36.0	1.3
0501-51	207	6625	0.6	22.6250	42.0	0.0341	42.5	0.0056	6.7	0.16	36.0	2.4	34.1	14.2	-99.6	1072.6	36.0	2.4
0501-125	457	13422	1.1	24.5242	23.5	0.0316	23.7	0.0056	3.4	0.14	36.1	1.2	31.6	7.4	-301.6	607.6	36.1	1.2
0501-117	396	15482	1.1	24.0785	30.2	0.0322	30.4	0.0056	2.9	0.10	36.2	1.1	32.2	9.6	-254.9	780.9	36.2	1.1
0501-69	216	12828	0.9	18.8919	29.8	0.0411	30.4	0.0056	6.3	0.21	36.2	2.3	40.9	12.2	325.9	689.7	36.2	2.3
0501-61	156	5209	1.0	25.8238	68.2	0.0301	68.3	0.0056	4.3	0.06	36.2	1.6	30.1	20.3	-435.4	2021.2	36.2	1.6
0501-56	418	7737	1.0	21.4442	20.9	0.0363	21.4	0.0056	4.7	0.22	36.3	1.7	36.2	7.6	30.5	505.6	36.3	1.7
0501-100	468	10530	0.9	22.2297	16.1	0.0350	16.2	0.0056	2.5	0.15	36.3	0.9	35.0	5.6	-56.4	393.2	36.3	0.9
0501-37	177	1757	0.6	26.4197	32.2	0.0295	33.2	0.0057	7.9	0.24	36.4	2.8	29.6	9.7	-495.7	876.1	36.4	2.8

TABLE E2: U-TH-PB GEOCHRONOLOGIC ANALYSES

						Isotope Ratios					Apparent Ages (Ma)							
Analysis	U (ppm)	^{206}Pb ^{204}Pb	U/Th	$^{206}Pb^*$ $^{207}Pb^*$	± (%)	$^{207}Pb^*$ $^{235}U^*$	± (%)	$^{206}Pb^*$ ^{238}U	± (%)	Error Corr.	$^{206}Pb^*$ $^{238}U^*$	± (Ma)	$^{207}Pb^*$ ^{235}U	± (Ma)	$^{206}Pb^*$ $^{207}Pb^*$	± (Ma)	**Best Age** (Ma)	± (Ma)
0501-28	394	8505	1.1	23.0399	16.1	0.0339	16.3	0.0057	2.7	0.17	36.4	1.0	33.9	5.4	-144.4	401.1	36.4	1.0
0501-36	274	7879	0.9	27.6061	61.8	0.0283	62.1	0.0057	5.5	0.09	36.5	2.0	28.4	17.4	-614.0	1847.9	36.5	2.0
0501-46	1860	21619	1.0	21.1307	2.8	0.0370	3.1	0.0057	1.2	0.39	36.5	0.4	36.9	1.1	65.6	67.2	36.5	0.4
0501-96	760	12206	0.5	20.7230	12.1	0.0378	12.5	0.0057	3.3	0.26	36.5	1.2	37.6	4.6	111.8	286.3	36.5	1.2
0501-49	195	11252	0.9	20.4193	22.4	0.0384	23.2	0.0057	6.0	0.26	36.5	2.2	38.2	8.7	146.6	531.6	36.5	2.2
0501-40	180	3418	0.9	33.2993	62.7	0.0236	63.2	0.0057	7.9	0.13	36.6	2.9	23.7	14.8	-1155.7	2108.0	36.6	2.9
0501-57	299	6569	1.1	18.7786	22.1	0.0419	22.6	0.0057	4.8	0.21	36.7	1.8	41.7	9.2	339.6	505.6	36.7	1.8
0501-45	786	10655	2.0	21.9394	11.5	0.0363	12.0	0.0058	3.3	0.27	37.1	1.2	36.2	4.3	-24.5	280.2	37.1	1.2
0501-42	540	8207	1.0	22.4660	16.5	0.0357	17.1	0.0058	4.5	0.26	37.4	1.7	35.7	6.0	-82.3	406.0	37.4	1.7
0501-83	357	13594	0.9	15.9701	27.5	0.0505	28.0	0.0058	5.0	0.18	37.6	1.9	50.0	13.6	695.2	597.1	37.6	1.9
0501-116	281	18387	0.9	22.5461	25.0	0.0358	25.4	0.0059	4.4	0.18	37.6	1.7	35.7	8.9	-91.0	621.0	37.6	1.7
0501-01	1126	14704	9.8	21.2107	3.8	0.0584	4.0	0.0090	1.3	0.33	57.7	0.8	57.7	2.2	56.6	89.8	57.7	0.8
0501-29	360	14970	16.5	21.8369	13.4	0.0665	13.6	0.0105	2.4	0.17	67.5	1.6	65.4	8.6	-13.2	325.3	67.5	1.6
0501-06	108	116265	1.2	11.1369	0.7	3.1209	1.2	0.2521	1.0	0.83	1449.2	12.4	1437.9	8.9	1421.1	12.5	1421.1	12.5
0501-112	100	161045	1.5	11.1107	1.1	3.1468	1.5	0.2536	1.1	0.70	1456.9	14.1	1444.2	11.9	1425.6	21.2	1425.6	21.2
0501-115	50	119917	0.9	11.0991	1.0	3.0935	2.5	0.2490	2.3	0.91	1433.4	29.7	1431.1	19.4	1427.6	19.5	1427.6	19.5
0501-03	314	164723	1.0	11.0754	0.5	3.0138	0.7	0.2421	0.5	0.65	1397.6	5.7	1411.1	5.3	1431.6	10.2	1431.6	10.2
0501-71	82	122961	1.0	11.0660	1.0	3.1275	1.8	0.2510	1.5	0.82	1443.7	19.3	1439.5	14.0	1433.3	19.9	1433.3	19.9
0501-15	88	52113	0.9	11.0623	1.2	3.1064	1.6	0.2492	1.1	0.66	1434.5	13.7	1434.3	12.4	1433.9	23.2	1433.9	23.2

TABLE E2: U-TH-PB GEOCHRONOLOGIC ANALYSES

Analysis	U (ppm)	^{206}Pb ^{204}Pb	U/Th	$^{206}Pb^*$ $^{207}Pb^*$	± (%)	Isotope Ratios $^{207}Pb^*$ $^{235}U^*$	± (%)	$^{206}Pb^*$ ^{238}U	± (%)	Error Corr.	Apparent Ages (Ma) $^{206}Pb^*$ $^{238}U^*$	± (Ma)	$^{207}Pb^*$ ^{235}U	± (Ma)	$^{206}Pb^*$ $^{207}Pb^*$	± (Ma)	Best Age (Ma)	± (Ma)
0501-41	66	31913	1.0	11.0548	1.5	3.2265	2.3	0.2587	1.8	0.78	1483.1	23.7	1463.5	17.8	1435.2	27.7	1435.2	27.7
0501-23	182	103311	0.8	11.0526	0.4	2.8260	1.4	0.2265	1.3	0.95	1316.3	15.5	1362.5	10.2	1435.6	7.9	1435.6	7.9
0501-91	105	195577	1.7	11.0420	1.1	3.1318	1.7	0.2508	1.3	0.75	1442.7	16.7	1440.5	13.2	1437.4	21.7	1437.4	21.7
0501-74	1277	634157	8.8	11.0409	0.1	3.1160	0.9	0.2495	0.9	0.99	1436.0	11.4	1436.6	6.8	1437.6	2.1	1437.6	2.1
0501-55	134	124694	1.0	11.0355	0.7	3.1077	2.0	0.2487	1.9	0.93	1431.9	24.1	1434.6	15.5	1438.5	14.0	1438.5	14.0
0501-82	115	197675	1.7	11.0234	1.1	3.1214	2.0	0.2496	1.7	0.84	1436.2	21.6	1438.0	15.4	1440.6	20.9	1440.6	20.9
0501-48	134	600384	1.2	11.0221	0.8	3.1864	1.4	0.2547	1.2	0.84	1462.8	15.9	1453.9	11.2	1440.9	15.0	1440.9	15.0
0501-94	246	333719	1.0	11.0191	0.3	3.1679	1.5	0.2532	1.5	0.98	1454.8	19.0	1449.4	11.5	1441.4	5.4	1441.4	5.4
0501-47	135	174893	1.7	11.0120	0.6	3.1412	1.3	0.2509	1.2	0.90	1443.0	15.7	1442.8	10.4	1442.6	11.0	1442.6	11.0
0501-60	413	483146	1.5	11.0107	0.3	3.1998	0.7	0.2555	0.6	0.90	1466.9	7.9	1457.1	5.1	1442.8	5.4	1442.8	5.4
0501-44	1135	612970	11.5	11.0054	0.1	3.2173	1.8	0.2568	1.8	1.00	1473.5	23.4	1461.3	13.8	1443.8	2.7	1443.8	2.7
0501-52	325	322616	8.3	10.9963	0.3	3.1227	0.7	0.2490	0.6	0.87	1433.5	7.6	1438.3	5.2	1445.3	6.3	1445.3	6.3
0501-105	607	563256	2.3	10.9945	0.2	3.0422	0.5	0.2426	0.4	0.88	1400.1	5.1	1418.3	3.5	1445.6	4.3	1445.6	4.3
0501-77	545	587363	2.8	10.9762	0.3	3.1644	1.1	0.2519	1.0	0.95	1448.3	13.3	1448.5	8.3	1448.8	6.5	1448.8	6.5
0501-80	86	111533	1.5	10.9661	1.4	3.1849	2.4	0.2533	1.9	0.82	1455.5	25.3	1453.5	18.4	1450.6	26.1	1450.6	26.1
0501-31	288	276810	1.6	10.9567	0.3	3.1607	1.2	0.2512	1.2	0.97	1444.5	14.9	1447.6	9.2	1452.2	5.8	1452.2	5.8
0501-22	175	308587	1.1	10.9521	0.6	3.1357	0.8	0.2491	0.5	0.65	1433.7	6.8	1441.5	6.2	1453.0	11.7	1453.0	11.7
0501-24	519	329162	1.4	10.9505	0.2	3.1505	1.1	0.2502	1.1	0.99	1439.6	14.6	1445.1	8.8	1453.3	3.4	1453.3	3.4
0501-19	193	108005	0.7	10.8869	0.8	3.1802	1.2	0.2511	1.0	0.77	1444.2	12.3	1452.4	9.5	1464.3	14.9	1464.3	14.9

TABLE E2: U-TH-PB GEOCHRONOLOGIC ANALYSES

Analysis	U (ppm)	^{206}Pb ^{204}Pb	U/Th	$^{206}Pb^*$ $^{207}Pb^*$	± (%)	Isotope Ratios $^{207}Pb^*$ $^{235}U^*$	± (%)	$^{206}Pb^*$ ^{238}U	± (%)	Error Corr.	Apparent Ages (Ma) $^{206}Pb^*$ $^{238}U^*$	± (Ma)	$^{207}Pb^*$ ^{235}U	± (Ma)	$^{206}Pb^*$ $^{207}Pb^*$	± (Ma)	Best Age (Ma)	± (Ma)
0501-30	191	109765	1.3	10.8848	0.6	3.2050	1.0	0.2530	0.8	0.81	1454.0	10.9	1458.4	7.9	1464.7	11.3	1464.7	11.3
0501-63	247	220184	1.3	10.8760	0.6	2.6102	3.2	0.2059	3.2	0.98	1206.9	35.1	1303.5	23.8	1466.3	10.8	1466.3	10.8
0501-86	61	78491	0.8	10.8316	1.2	3.0717	2.0	0.2413	1.6	0.80	1393.5	19.5	1425.7	15.0	1474.0	22.5	1474.0	22.5
0501-05	2766	195919	10.3	10.5081	0.8	1.0438	3.7	0.0796	3.6	0.98	493.5	17.3	725.8	19.3	1531.3	14.4	1531.3	14.4
0501-108	958	1536167	39.5	10.5068	0.3	3.1707	2.3	0.2416	2.2	0.99	1395.1	28.2	1450.0	17.5	1531.5	6.5	1531.5	6.5
0501-95	1374	1338141	6.9	10.2656	0.3	3.4610	5.5	0.2577	5.5	1.00	1478.0	72.9	1518.4	43.6	1575.2	6.1	1575.2	6.1
0501-09	401	305134	3.8	10.0482	0.7	4.1185	1.1	0.3001	0.9	0.82	1692.0	14.0	1658.0	9.4	1615.1	12.3	1615.1	12.3
0501-64	307	264451	4.7	9.6645	0.3	4.2475	1.0	0.2977	1.0	0.95	1680.0	14.1	1683.3	8.2	1687.3	5.5	1687.3	5.5
0501-124	315	516299	3.7	9.6472	0.7	4.2678	1.5	0.2986	1.4	0.90	1684.4	20.4	1687.2	12.6	1690.6	12.6	1690.6	12.6
0501-98	264	193026	0.9	9.6220	0.4	4.4519	1.6	0.3107	1.6	0.97	1744.0	24.2	1722.0	13.5	1695.4	7.2	1695.4	7.2
0501-62	255	252342	4.0	9.6185	0.9	3.9862	1.5	0.2781	1.2	0.81	1581.7	17.0	1631.4	12.2	1696.1	16.4	1696.1	16.4
0501-25	656	419574	3.3	9.6128	0.1	4.2660	0.9	0.2974	0.9	0.99	1678.5	13.3	1686.8	7.5	1697.2	2.0	1697.2	2.0
0501-34	481	268080	14.6	9.6121	0.2	4.3643	1.4	0.3043	1.4	0.99	1712.4	21.2	1705.6	11.8	1697.3	3.7	1697.3	3.7
0501-97	155	266915	0.7	9.6075	0.6	4.4053	1.1	0.3070	1.0	0.84	1725.7	14.5	1713.3	9.5	1698.2	11.6	1698.2	11.6
0501-13	103	131502	2.2	9.6016	1.1	4.3822	2.2	0.3052	2.0	0.88	1716.9	29.6	1709.0	18.5	1699.3	19.8	1699.3	19.8
0501-106	783	1023914	10.2	9.5995	0.1	4.2606	1.0	0.2966	1.0	0.99	1674.6	14.5	1685.8	8.1	1699.7	2.3	1699.7	2.3
0501-84	132	390854	2.9	9.5867	0.4	4.4237	1.9	0.3076	1.8	0.97	1728.8	27.5	1716.8	15.5	1702.2	8.0	1702.2	8.0
0501-107	206	305501	2.0	9.5820	0.4	4.4957	0.9	0.3124	0.8	0.91	1752.6	12.9	1730.2	7.7	1703.1	7.0	1703.1	7.0
0501-16	403	485259	2.2	9.5804	0.2	4.3060	0.8	0.2992	0.8	0.97	1687.3	11.2	1694.5	6.4	1703.4	3.7	1703.4	3.7
0501-17	462	546147	0.9	9.5796	0.2	4.3713	1.2	0.3037	1.2	0.98	1709.7	17.3	1706.9	9.7	1703.6	3.8	1703.6	3.8
0501-110	333	1386045	2.8	9.5737	0.2	4.4047	1.0	0.3058	0.9	0.98	1720.2	14.1	1713.2	7.9	1704.7	3.8	1704.7	3.8
0501-67	246	1080548	2.4	9.5700	0.4	4.4053	1.2	0.3058	1.1	0.93	1719.8	16.6	1713.3	9.8	1705.4	8.2	1705.4	8.2

TABLE E2: U-TH-PB GEOCHRONOLOGIC ANALYSES

						Isotope Ratios					Apparent Ages (Ma)							
Analysis	U (ppm)	^{206}Pb ^{204}Pb	U/Th	$^{206}Pb^*$ $^{207}Pb^*$	± (%)	$^{207}Pb^*$ $^{235}U^*$	± (%)	$^{206}Pb^*$ ^{238}U	± (%)	Error Corr.	$^{206}Pb^*$ $^{238}U^*$	± (Ma)	$^{207}Pb^*$ ^{235}U	± (Ma)	$^{206}Pb^*$ $^{207}Pb^*$	± (Ma)	**Best Age** (Ma)	± (Ma)
0501-87	369	287593	2.2	9.5685	0.2	4.4098	0.9	0.3060	0.9	0.97	1721.1	13.4	1714.2	7.6	1705.7	4.4	1705.7	4.4
0501-33	359	268034	2.4	9.5679	0.1	4.4086	0.6	0.3059	0.6	0.97	1720.6	9.5	1714.0	5.4	1705.8	2.7	1705.8	2.7
0501-92	292	516766	2.1	9.5575	0.2	4.4426	1.3	0.3080	1.3	0.99	1730.6	19.6	1720.3	10.9	1707.8	4.1	1707.8	4.1
0501-65	148	466938	2.0	9.5540	0.5	4.3075	1.2	0.2985	1.1	0.91	1683.7	16.0	1694.8	9.7	1708.5	8.9	1708.5	8.9
0501-120	383	736506	1.5	9.5479	0.2	4.4393	1.0	0.3074	1.0	0.99	1728.0	15.5	1719.7	8.6	1709.6	3.0	1709.6	3.0
0501-58	205	203234	2.1	9.5436	0.3	4.4136	0.8	0.3055	0.7	0.93	1718.5	10.7	1714.9	6.3	1710.5	5.2	1710.5	5.2
0501-121	264	993119	2.3	9.5417	0.3	4.4860	1.4	0.3104	1.4	0.98	1742.9	21.5	1728.4	11.9	1710.8	5.3	1710.8	5.3
0501-32	464	681303	2.8	9.5367	0.3	4.3993	1.1	0.3043	1.0	0.97	1712.5	15.7	1712.2	8.9	1711.8	4.6	1711.8	4.6
0501-122	187	337907	1.5	9.5264	0.5	4.4143	1.6	0.3050	1.5	0.95	1716.0	22.7	1715.0	13.2	1713.8	9.4	1713.8	9.4
0501-50	320	230301	1.7	9.5185	0.3	4.4719	1.3	0.3087	1.3	0.97	1734.4	19.6	1725.8	11.0	1715.3	5.7	1715.3	5.7
0501-109	390	362664	2.4	9.5171	0.4	3.9581	5.1	0.2732	5.1	1.00	1557.1	70.5	1625.7	41.5	1715.6	7.7	1715.6	7.7
0501-18	176	125610	2.0	9.5140	0.4	4.3965	1.6	0.3034	1.6	0.97	1708.0	24.0	1711.7	13.6	1716.2	7.2	1716.2	7.2
0501-59	767	1682279	2.0	9.5129	0.1	4.5449	1.4	0.3136	1.4	1.00	1758.3	21.7	1739.2	11.8	1716.4	2.5	1716.4	2.5
0501-89	103	198662	1.1	9.5116	0.8	4.4624	1.9	0.3078	1.7	0.90	1730.1	25.4	1724.0	15.4	1716.6	14.7	1716.6	14.7
0501-75	227	553403	1.6	9.4990	0.3	4.4081	0.8	0.3037	0.7	0.90	1709.6	10.5	1713.9	6.4	1719.1	6.1	1719.1	6.1
0501-26	331	206242	1.9	9.4504	0.3	4.1202	0.8	0.2824	0.7	0.93	1603.4	10.0	1658.3	6.2	1728.5	5.3	1728.5	5.3
0501-78	78	104250	1.3	9.3987	2.9	3.7443	3.7	0.2552	2.3	0.62	1465.4	30.1	1580.9	29.6	1738.6	53.1	1738.6	53.1
0501-53	164	212445	1.7	9.3884	1.7	4.5344	3.3	0.3088	2.9	0.87	1734.6	44.0	1737.3	27.8	1740.6	30.6	1740.6	30.6
0501-14	380	243312	1.2	9.3432	0.4	4.4692	3.2	0.3029	3.2	0.99	1705.4	48.3	1725.3	26.9	1749.4	6.7	1749.4	6.7
0501-119	138	204704	1.7	9.3107	0.4	4.7107	1.2	0.3181	1.2	0.95	1780.5	18.1	1769.1	10.3	1755.8	7.1	1755.8	7.1
0501-70	318	604448	2.1	9.0020	0.3	4.9354	1.5	0.3222	1.5	0.99	1800.6	23.0	1808.3	12.5	1817.3	4.6	1817.3	4.6
0501-101	412	1145697	1.1	8.9187	0.2	5.1445	0.6	0.3328	0.6	0.93	1851.8	9.4	1843.5	5.4	1834.1	4.3	1834.1	4.3
Spot 7	1999	128321	0.8	20.964 3	0.9	0.0347	3.1	0.0053	3.0	0.96	33.9	1.0	34.6	1.1	84.4	21.0	33.9	1.0

TABLE E2: U-TH-PB GEOCHRONOLOGIC ANALYSES

Analysis	U (ppm)	$^{206}Pb/^{204}Pb$	U/Th	$^{206}Pb^*/^{207}Pb^*$	± (%)	Isotope Ratios $^{207}Pb^*/^{235}U^*$	± (%)	$^{206}Pb^*/^{238}U$	± (%)	Error Corr.	Apparent Ages (Ma) $^{206}Pb^*/^{238}U^*$	± (Ma)	$^{207}Pb^*/^{235}U$	± (Ma)	$^{206}Pb^*/^{207}Pb^*$	± (Ma)	Best Age (Ma)	± (Ma)
Spot 108	805	23569	2.3	21.5680	1.2	0.0340	2.8	0.0053	2.5	0.90	34.2	0.9	34.0	0.9	16.6	29.3	34.2	0.9
Spot 42	57	1850	2.4	25.3960	4.7	0.0292	5.3	0.0054	2.4	0.45	34.6	0.8	29.2	1.5	NA	NA	34.6	0.8
Spot 10	128	4102	1.2	23.6855	3.1	0.0313	3.7	0.0054	2.1	0.57	34.6	0.7	31.3	1.2	NA	NA	34.6	0.7
Spot 106	384	4278	0.7	22.1370	2.0	0.0336	3.1	0.0054	2.4	0.77	34.7	0.8	33.6	1.0	NA	NA	34.7	0.8
Spot 77	206	6385	1.3	22.3254	1.9	0.0340	2.6	0.0055	1.7	0.67	35.4	0.6	33.9	0.9	NA	NA	35.4	0.6
Spot 50	72	7470	0.5	22.9235	4.3	0.0332	5.3	0.0055	3.1	0.59	35.5	1.1	33.1	1.7	NA	NA	35.5	1.1
Spot 65	129	14667	0.8	19.8332	3.1	0.0384	3.8	0.0055	2.3	0.60	35.5	0.8	38.3	1.4	214.5	71.0	35.5	0.8
Spot 82	220	19140	0.9	20.8363	2.2	0.0367	3.2	0.0055	2.3	0.72	35.7	0.8	36.6	1.1	98.9	52.5	35.7	0.8
Spot 53	279	5813	1.3	22.2367	3.2	0.0344	4.1	0.0056	2.5	0.61	35.7	0.9	34.3	1.4	NA	NA	35.7	0.9
Spot 46	140	3682	1.0	21.2713	3.0	0.0360	4.1	0.0056	2.7	0.67	35.7	1.0	35.9	1.4	49.8	71.6	35.7	1.0
Spot 17	153	10359	0.7	21.6221	2.8	0.0354	3.5	0.0056	2.1	0.60	35.7	0.7	35.3	1.2	10.6	66.7	35.7	0.7
Spot 12	168	34763	1.4	20.8411	2.6	0.0368	3.3	0.0056	2.0	0.62	35.8	0.7	36.7	1.2	98.4	60.4	35.8	0.7
Spot 85	74	1264	1.2	26.9237	6.3	0.0285	6.6	0.0056	2.0	0.30	35.8	0.7	28.5	1.9	NA	NA	35.8	0.7
Spot 26	187	23995	1.3	23.0204	2.2	0.0334	2.9	0.0056	1.9	0.67	35.8	0.7	33.3	1.0	NA	NA	35.8	0.7
Spot 75	226	3251	0.9	23.6970	2.1	0.0324	2.8	0.0056	1.8	0.64	35.8	0.6	32.4	0.9	NA	NA	35.8	0.6
Spot 88	300	19667	1.1	20.6921	1.7	0.0373	2.3	0.0056	1.5	0.64	36.0	0.5	37.2	0.8	115.4	41.2	36.0	0.5
Spot 35	259	6616	1.0	21.7372	1.9	0.0355	3.2	0.0056	2.5	0.79	36.0	0.9	35.5	1.1	NA	NA	36.0	0.9
Spot 109	225	23856	0.9	21.9829	2.2	0.0351	3.3	0.0056	2.4	0.75	36.0	0.9	35.1	1.1	NA	NA	36.0	0.9
Spot 80	245	32417	1.4	21.2367	2.2	0.0365	2.9	0.0056	1.8	0.63	36.1	0.7	36.4	1.0	53.7	53.6	36.1	0.7

TABLE E2: U-TH-PB GEOCHRONOLOGIC ANALYSES

Analysis	U (ppm)	^{206}Pb ^{204}Pb	U/Th	$^{206}Pb^*$ $^{207}Pb^*$	± (%)	Isotope Ratios $^{207}Pb^*$ $^{235}U^*$	± (%)	$^{206}Pb^*$ ^{238}U	± (%)	Error Corr.	Apparent Ages (Ma) $^{206}Pb^*$ $^{238}U^*$	± (Ma)	$^{207}Pb^*$ ^{235}U	± (Ma)	$^{206}Pb^*$ $^{207}Pb^*$	± (Ma)	Best Age (Ma)	± (Ma)
Spot 69	270	39608	1.4	19.9859	2.2	0.0388	3.1	0.0056	2.1	0.70	36.2	0.8	38.7	1.2	196.7	51.0	36.2	0.8
Spot 41	194	6624	1.1	21.7758	2.7	0.0357	3.8	0.0056	2.8	0.72	36.2	1.0	35.6	1.3	NA	NA	36.2	1.0
Spot 81	288	7710	1.4	20.9386	1.3	0.0371	2.7	0.0056	2.4	0.89	36.3	0.9	37.0	1.0	87.4	29.7	36.3	0.9
Spot 34	186	10903	0.8	23.0154	2.6	0.0338	3.7	0.0056	2.7	0.71	36.3	1.0	33.8	1.2	NA	NA	36.3	1.0
Spot 14	174	6665	1.1	21.9009	2.3	0.0356	3.3	0.0057	2.3	0.71	36.3	0.8	35.5	1.1	NA	NA	36.3	0.8
Spot 47	299	7476	1.0	22.9007	3.0	0.0340	3.7	0.0057	2.3	0.61	36.4	0.8	34.0	1.2	NA	NA	36.4	0.8
Spot 3	240	25282	1.4	21.2691	1.6	0.0366	2.6	0.0057	2.0	0.78	36.4	0.7	36.5	0.9	50.1	38.1	36.4	0.7
Spot 38	195	8057	1.1	21.1516	2.5	0.0369	3.6	0.0057	2.6	0.72	36.4	0.9	36.8	1.3	63.3	59.4	36.4	0.9
Spot 64	103	2140	1.0	24.9221	5.6	0.0314	5.9	0.0057	1.9	0.32	36.5	0.7	31.4	1.8	NA	NA	36.5	0.7
Spot 97	79	8222	1.2	22.2884	3.9	0.0353	4.5	0.0057	2.3	0.51	36.7	0.9	35.2	1.6	NA	NA	36.7	0.9
Spot 70	65	14486	1.2	21.9178	4.2	0.0360	5.0	0.0057	2.8	0.56	36.8	1.0	35.9	1.8	NA	NA	36.8	1.0
Spot 56	70	51801	1.1	21.1904	4.3	0.0372	5.4	0.0057	3.3	0.61	36.8	1.2	37.1	2.0	58.9	101.5	36.8	1.2
Spot 27	136	7416	1.8	21.6400	2.5	0.0367	6.1	0.0058	5.6	0.92	37.1	2.1	36.6	2.2	8.6	59.2	37.1	2.1
Spot 13	63	45305	1.1	20.8742	3.4	0.0382	4.0	0.0058	2.2	0.55	37.2	0.8	38.1	1.5	94.6	79.9	37.2	0.8
Spot 31	83	2225	1.1	19.6106	6.0	0.0411	6.6	0.0059	2.7	0.42	37.6	1.0	40.9	2.6	240.5	137.7	37.6	1.0
Spot 89	89	54089	0.7	21.1495	3.6	0.0381	4.8	0.0059	3.1	0.65	37.6	1.2	38.0	1.8	63.5	86.4	37.6	1.2
Spot 37	90	83302	0.7	21.9089	3.0	0.0369	15.2	0.0059	14.9	0.98	37.7	5.6	36.8	5.5	NA	NA	37.7	5.6
Spot 8	184	6319	1.1	23.4684	3.0	0.0355	3.7	0.0060	2.1	0.57	38.8	0.8	35.4	1.3	NA	NA	38.8	0.8
Spot 55	216	14429	4.4	21.4992	1.8	0.0441	2.5	0.0069	1.7	0.69	44.2	0.8	43.8	1.1	24.3	43.0	44.2	0.8

TABLE E2: U-TH-PB GEOCHRONOLOGIC ANALYSES

Analysis	U (ppm)	^{206}Pb ^{204}Pb	U/Th	$^{206}Pb^*$ $^{207}Pb^*$	± (%)	Isotope Ratios $^{207}Pb^*$ $^{235}U^*$	± (%)	$^{206}Pb^*$ ^{238}U	± (%)	Error Corr.	Apparent Ages (Ma) $^{206}Pb^*$ $^{238}U^*$	± (Ma)	$^{207}Pb^*$ ^{235}U	± (Ma)	$^{206}Pb^*$ $^{207}Pb^*$	± (Ma)	Best Age (Ma)	± (Ma)
Spot 48	811	79759	5.6	20.9947	1.1	0.0601	2.4	0.0092	2.1	0.89	58.7	1.2	59.2	1.4	81.0	26.1	58.7	1.2
Spot 63	321	17521	21.5	20.4573	2.2	0.0701	3.1	0.0104	2.1	0.70	66.7	1.4	68.8	2.0	142.2	51.4	66.7	1.4
Spot 67	542	503985	39.7	11.5385	0.9	2.9419	2.1	0.2463	1.9	0.91	1419.4	24.1	1392.8	15.7	1353.1	16.7	1353.1	16.7
Spot 44	86	97148	1.4	11.3270	0.7	3.0660	2.5	0.2520	2.4	0.96	1448.7	31.1	1424.2	19.2	1388.7	14.0	1388.7	14.0
Spot 21	87	105259	1.5	11.3050	0.8	3.0601	2.3	0.2510	2.2	0.95	1443.7	28.4	1422.8	17.8	1392.4	14.5	1392.4	14.5
Spot 24	527	390902	16.1	11.2735	0.8	3.0218	1.9	0.2472	1.8	0.92	1423.9	22.8	1413.1	14.8	1397.7	14.4	1397.7	14.4
Spot 107	68	249810	2.1	11.2732	0.8	3.0105	2.3	0.2462	2.2	0.94	1419.1	27.9	1410.3	17.7	1397.8	14.8	1397.8	14.8
Spot 68	529	269431	5.3	11.2710	0.8	2.6911	2.1	0.2201	1.9	0.91	1282.3	22.1	1326.0	15.4	1398.2	16.1	1398.2	16.1
Spot 73	53	103658	1.8	11.2592	0.8	3.0921	2.6	0.2526	2.5	0.96	1451.9	32.1	1430.7	19.8	1400.2	14.7	1400.2	14.7
Spot 103	78	114450	1.8	11.2585	0.7	3.0581	2.0	0.2498	1.8	0.93	1437.5	23.8	1422.3	15.1	1400.3	13.4	1400.3	13.4
Spot 5	41	43648	1.2	11.2417	0.9	3.0944	2.0	0.2524	1.7	0.88	1450.9	22.6	1431.3	15.2	1403.2	17.9	1403.2	17.9
Spot 83	152	1417488	0.9	11.2235	0.8	3.0907	2.2	0.2517	2.1	0.94	1447.2	27.3	1430.4	17.2	1406.3	14.7	1406.3	14.7
Spot 110	49	35125	1.5	11.2040	0.9	3.0888	2.2	0.2511	2.0	0.91	1444.2	26.4	1429.9	17.2	1409.6	17.6	1409.6	17.6
Spot 84	240	119782	4.0	11.1873	0.8	3.1238	2.3	0.2536	2.1	0.94	1456.9	28.0	1438.6	17.6	1412.5	15.1	1412.5	15.1
Spot 96	48	69870	2.1	11.1803	0.7	3.1816	2.1	0.2581	2.0	0.94	1480.1	25.9	1452.7	16.1	1413.6	13.5	1413.6	13.5
Spot 79	150	307440	2.0	11.1779	0.7	3.0402	2.1	0.2466	2.0	0.95	1420.8	25.5	1417.8	16.1	1414.1	12.5	1414.1	12.5
Spot 22	68	117115	1.8	11.1645	0.7	3.1050	2.1	0.2515	2.0	0.94	1446.3	25.5	1433.9	16.0	1416.4	13.3	1416.4	13.3
Spot 76	175	136738	2.2	11.1575	0.8	3.1680	2.1	0.2565	1.9	0.93	1471.8	25.2	1449.4	16.0	1417.6	15.0	1417.6	15.0
Spot 25	145	207561	1.6	11.1518	0.8	3.1125	2.2	0.2519	2.1	0.94	1448.0	26.9	1435.8	17.0	1418.5	14.9	1418.5	14.9

TABLE E2: U-TH-PB GEOCHRONOLOGIC ANALYSES

Analysis	U (ppm)	^{206}Pb ^{204}Pb	U/Th	$^{206}Pb^*$ $^{207}Pb^*$	± (%)	Isotope Ratios $^{207}Pb^*$ $^{235}U^*$	± (%)	$^{206}Pb^*$ ^{238}U	± (%)	Error Corr.	Apparent Ages (Ma) $^{206}Pb^*$ $^{238}U^*$	± (Ma)	$^{207}Pb^*$ ^{235}U	± (Ma)	$^{206}Pb^*$ $^{207}Pb^*$	± (Ma)	Best Age (Ma)	± (Ma)
Spot 19	92	46195	1.4	11.1422	0.7	3.0826	2.7	0.2492	2.6	0.96	1434.4	32.9	1428.4	20.4	1420.2	14.2	1420.2	14.2
Spot 11	71	100059	1.4	11.1402	0.8	3.1069	2.3	0.2511	2.1	0.93	1444.3	27.5	1434.4	17.6	1420.5	16.1	1420.5	16.1
Spot 49	368	218134	0.8	11.1334	0.7	3.0137	2.1	0.2435	2.0	0.95	1404.6	25.5	1411.1	16.3	1421.7	13.0	1421.7	13.0
Spot 90	268	261964	1.8	11.1206	0.5	3.0825	2.1	0.2487	2.0	0.97	1431.9	26.1	1428.3	16.1	1423.9	9.8	1423.9	9.8
Spot 94	117	709879	1.1	11.0885	0.8	3.0743	2.3	0.2473	2.1	0.94	1424.8	27.2	1426.3	17.4	1429.4	15.1	1429.4	15.1
Spot 23	242	92555	0.9	11.0787	0.7	3.0505	2.5	0.2452	2.4	0.96	1413.7	30.0	1420.4	18.9	1431.1	13.3	1431.1	13.3
Spot 78	352	69986	5.9	11.0728	0.9	2.9955	2.1	0.2407	1.9	0.91	1390.2	23.5	1406.5	15.7	1432.1	16.4	1432.1	16.4
Spot 28	40	517292	1.1	11.0689	0.8	3.1511	1.9	0.2531	1.7	0.91	1454.3	22.6	1445.3	14.8	1432.8	15.2	1432.8	15.2
Spot 20	65	97859	1.6	11.0621	0.7	3.1477	1.9	0.2527	1.8	0.92	1452.1	22.8	1444.4	14.7	1433.9	14.2	1433.9	14.2
Spot 32	81	828296	1.1	11.0491	0.8	3.1935	2.0	0.2560	1.9	0.93	1469.5	24.5	1455.6	15.6	1436.2	14.4	1436.2	14.4
Spot 33	34	34416	1.2	10.9702	1.1	3.1355	2.2	0.2496	1.9	0.88	1436.3	25.1	1441.5	17.1	1449.8	20.3	1449.8	20.3
Spot 74	43	47648	1.3	10.9530	0.9	3.0475	3.3	0.2422	3.1	0.96	1398.1	39.3	1419.6	24.9	1452.8	17.6	1452.8	17.6
Spot 98	349	465782	3.8	10.5049	1.1	3.3695	2.0	0.2568	1.6	0.82	1473.6	21.3	1497.3	15.4	1531.9	21.2	1531.9	21.2
Spot 39	683	3777424	19.5	10.4895	0.8	3.7178	2.3	0.2830	2.2	0.94	1606.3	31.0	1575.2	18.5	1534.6	14.7	1534.6	14.7
Spot 105	727	2012307	7.0	10.4084	0.7	3.7715	1.8	0.2848	1.7	0.92	1615.7	23.7	1586.7	14.5	1549.3	13.4	1549.3	13.4
Spot 2	637	1594112	3.7	10.2234	0.8	3.8080	1.9	0.2825	1.8	0.92	1603.8	25.3	1594.4	15.6	1582.9	14.5	1582.9	14.5
Spot 59	355	630667	3.4	9.9076	0.7	4.1928	1.9	0.3014	1.8	0.92	1698.3	26.5	1672.6	15.8	1641.3	13.8	1641.3	13.8
Spot 6	115	259700	2.6	9.8557	0.6	4.1066	2.0	0.2937	1.9	0.96	1659.8	28.3	1655.6	16.5	1651.1	10.7	1651.1	10.7
Spot 54	182	130895	3.3	9.8217	0.5	4.1559	1.7	0.2962	1.6	0.95	1672.3	23.8	1665.4	13.9	1657.5	10.0	1657.5	10.0
Spot 91	123	171733	2.5	9.7790	0.6	4.3048	2.4	0.3054	2.4	0.97	1718.3	35.6	1694.3	20.0	1665.5	10.3	1665.5	10.3

TABLE E2: U-TH-PB GEOCHRONOLOGIC ANALYSES

						Isotope Ratios					Apparent Ages (Ma)							
Analysis	U (ppm)	^{206}Pb ^{204}Pb	U/Th	$^{206}Pb^*$ $^{207}Pb^*$	± (%)	$^{207}Pb^*$ $^{235}U^*$	± (%)	$^{206}Pb^*$ ^{238}U	± (%)	Error Corr.	$^{206}Pb^*$ $^{238}U^*$	± (Ma)	$^{207}Pb^*$ ^{235}U	± (Ma)	$^{206}Pb^*$ $^{207}Pb^*$	± (Ma)	**Best Age** (Ma)	± (Ma)
Spot 95	244	168922	3.0	9.7413	0.7	4.0838	2.0	0.2886	1.9	0.94	1634.8	26.8	1651.1	16.1	1672.7	12.7	1672.7	12.7
Spot 99	145	168574	3.8	9.7358	0.9	4.2299	2.2	0.2988	2.0	0.92	1685.4	29.8	1679.8	17.9	1673.7	15.9	1673.7	15.9
Spot 51	92	103979	1.9	9.7325	0.8	4.2769	2.1	0.3020	1.9	0.93	1701.3	29.1	1688.9	17.2	1674.3	13.9	1674.3	13.9
Spot 92	115	156762	1.5	9.7172	0.8	4.3037	2.1	0.3034	2.0	0.94	1708.4	30.1	1694.1	17.7	1677.2	13.9	1677.2	13.9
Spot 62	191	2240598	3.7	9.6975	0.7	4.2086	2.4	0.2961	2.3	0.96	1672.1	33.3	1675.7	19.4	1681.0	12.7	1681.0	12.7
Spot 45	133	292139	1.6	9.6974	0.9	4.3848	2.6	0.3085	2.4	0.94	1733.5	36.8	1709.5	21.3	1681.0	16.0	1681.0	16.0
Spot 100	199	551869	4.1	9.6879	0.7	4.1509	2.2	0.2918	2.1	0.95	1650.4	31.0	1664.4	18.4	1682.8	13.4	1682.8	13.4
Spot 4	163	323071	2.7	9.6799	0.6	4.2812	2.1	0.3007	2.0	0.96	1694.7	30.4	1689.8	17.5	1684.4	11.3	1684.4	11.3
Spot 66	103	129634	3.5	9.6780	0.8	4.3423	2.2	0.3049	2.1	0.93	1715.7	31.2	1701.4	18.3	1684.7	14.8	1684.7	14.8
Spot 104	276	1164789	2.1	9.6732	0.8	4.3503	2.3	0.3053	2.1	0.94	1717.7	32.1	1703.0	18.7	1685.6	14.2	1685.6	14.2
Spot 15	217	299840	4.0	9.6686	0.6	3.9833	2.1	0.2794	2.0	0.95	1588.6	28.3	1630.8	17.1	1686.5	11.9	1686.5	11.9
Spot 101	157	132353	2.2	9.6587	0.9	4.3129	2.4	0.3023	2.2	0.93	1702.5	32.9	1695.8	19.5	1688.4	16.4	1688.4	16.4
Spot 61	196	173371	1.7	9.6578	0.7	4.3478	2.5	0.3047	2.4	0.96	1714.4	35.8	1702.5	20.5	1688.6	13.5	1688.6	13.5
Spot 72	313	373245	2.3	9.6407	0.6	4.3844	2.0	0.3067	1.9	0.95	1724.4	28.7	1709.4	16.5	1691.8	11.5	1691.8	11.5
Spot 93	275	290907	3.5	9.6324	0.7	4.1490	2.4	0.2900	2.3	0.96	1641.4	33.7	1664.0	19.8	1693.4	12.6	1693.4	12.6
Spot 29	194	628131	3.2	9.6225	0.8	4.4215	2.3	0.3087	2.2	0.94	1734.4	33.4	1716.4	19.3	1695.3	14.4	1695.3	14.4
Spot 30	305	4221641	15.6	9.6154	0.6	4.2499	2.4	0.2965	2.3	0.97	1674.0	34.5	1683.7	19.8	1696.7	11.1	1696.7	11.1
Spot 16	126	210936	2.0	9.5808	0.7	4.3377	2.5	0.3015	2.4	0.96	1699.0	35.5	1700.6	20.5	1703.3	13.4	1703.3	13.4
Spot 58	113	115705	1.1	9.5758	1.0	4.2664	2.5	0.2964	2.3	0.92	1673.6	33.6	1686.9	20.4	1704.3	17.7	1704.3	17.7
Spot 57	317	431230	3.2	9.5585	0.8	4.3370	2.8	0.3008	2.7	0.95	1695.2	39.6	1700.4	23.0	1707.6	15.4	1707.6	15.4
Spot 60	279	344180	1.6	9.5574	0.9	4.4907	3.0	0.3114	2.8	0.95	1747.7	43.0	1729.2	24.6	1707.8	17.1	1707.8	17.1
Spot 40	200	4301082	1.9	9.5447	0.7	4.0985	2.3	0.2838	2.1	0.94	1610.7	30.5	1654.0	18.5	1710.3	13.7	1710.3	13.7
Spot 1	434	553845	8.9	9.5220	0.8	4.4805	2.5	0.3096	2.3	0.95	1738.5	35.5	1727.4	20.4	1714.6	14.1	1714.6	14.1
Spot 18	107	103362	2.5	9.4345	0.6	4.6443	2.1	0.3179	2.0	0.96	1779.6	31.6	1757.3	17.7	1731.6	10.7	1731.6	10.7

TABLE E2: U-TH-PB GEOCHRONOLOGIC ANALYSES

Analysis	U (ppm)	^{206}Pb ^{204}Pb	U/Th	$^{206}Pb^*$ $^{207}Pb^*$	± (%)	Isotope Ratios $^{207}Pb^*$ $^{235}U^*$	± (%)	$^{206}Pb^*$ ^{238}U	± (%)	Error Corr.	Apparent Ages (Ma) $^{206}Pb^*$ $^{238}U^*$	± (Ma)	$^{207}Pb^*$ ^{235}U	± (Ma)	$^{206}Pb^*$ $^{207}Pb^*$	± (Ma)	Best Age (Ma)	± (Ma)
Spot 9	105	10907	1.5	9.0731	3.6	3.9617	4.5	0.2608	2.7	0.60	1494.0	36.5	1626.4	36.8	1803.0	65.9	1803.0	65.9
CDC																		
Spot 90	93	1461	0.7	25.3420	13.8	0.0264	14.1	0.0049	2.9	0.20	31.3	0.9	26.5	3.7	NA	NA	31.3	0.9
Spot 20	43	591	0.9	51.9465	67.8	0.0138	67.9	0.0052	3.5	0.05	33.4	1.2	13.9	9.4	NA	NA	33.4	1.2
Spot 42	249	22122	0.5	20.6874	2.9	0.0348	4.1	0.0052	2.9	0.71	33.6	1.0	34.8	1.4	115.9	67.8	33.6	1.0
Spot 22	759	41447	1.2	20.7612	1.5	0.0353	3.4	0.0053	3.0	0.89	34.2	1.0	35.2	1.2	107.5	36.4	34.2	1.0
Spot 52	281	4156	0.6	22.5935	3.4	0.0325	4.5	0.0053	3.0	0.66	34.3	1.0	32.5	1.4	NA	NA	34.3	1.0
Spot 78	602	814902	3.0	21.0663	1.7	0.0349	3.0	0.0053	2.5	0.83	34.3	0.8	34.8	1.0	72.9	39.5	34.3	0.8
Spot 72	273	2807	0.6	21.5720	3.7	0.0342	4.7	0.0054	2.8	0.61	34.4	1.0	34.2	1.6	16.2	89.8	34.4	1.0
Spot 97	507	6114	1.9	20.2930	2.2	0.0365	3.3	0.0054	2.4	0.72	34.5	0.8	36.4	1.2	161.1	52.6	34.5	0.8
Spot 15	34	807	1.5	68.2742	65.4	0.0109	65.4	0.0054	3.2	0.05	34.6	1.1	11.0	7.1	NA	NA	34.6	1.1
Spot 28	680	41110	0.5	21.6837	1.4	0.0342	3.3	0.0054	3.0	0.91	34.6	1.0	34.2	1.1	3.7	33.3	34.6	1.0
Spot 17	1650	33197	1.0	21.4512	1.4	0.0346	2.8	0.0054	2.5	0.88	34.6	0.9	34.5	1.0	29.7	32.9	34.6	0.9
Spot 82	1330	109191	0.6	20.8915	1.5	0.0356	3.2	0.0054	2.8	0.88	34.7	1.0	35.5	1.1	92.7	35.1	34.7	1.0
Spot 73	1449	21051	2.3	21.6342	1.2	0.0345	2.6	0.0054	2.3	0.90	34.8	0.8	34.4	0.9	9.3	27.7	34.8	0.8
Spot 74	247	1996	0.6	22.4031	2.4	0.0333	4.1	0.0054	3.3	0.80	34.8	1.1	33.2	1.3	NA	NA	34.8	1.1
Spot 87	374	28663	1.3	20.0518	2.6	0.0372	3.9	0.0054	2.9	0.75	34.8	1.0	37.1	1.4	189.0	60.6	34.8	1.0
Spot 56	853	9394	2.0	22.1947	2.2	0.0337	3.2	0.0054	2.3	0.72	34.9	0.8	33.6	1.1	NA	NA	34.9	0.8
Spot 58	1177	9021	1.6	21.6675	1.4	0.0345	3.1	0.0054	2.8	0.89	34.9	1.0	34.5	1.1	5.6	34.1	34.9	1.0
Spot 9	937	39284	2.9	21.5384	1.4	0.0348	2.5	0.0054	2.2	0.85	35.0	0.8	34.8	0.9	20.0	32.7	35.0	0.8

TABLE E2: U-TH-PB GEOCHRONOLOGIC ANALYSES

Analysis	U (ppm)	^{206}Pb ^{204}Pb	U/Th	$^{206}Pb^*$ $^{207}Pb^*$	± (%)	Isotope Ratios $^{207}Pb^*$ $^{235}U^*$	± (%)	$^{206}Pb^*$ ^{238}U	± (%)	Error Corr.	Apparent Ages (Ma) $^{206}Pb^*$ $^{238}U^*$	± (Ma)	$^{207}Pb^*$ ^{235}U	± (Ma)	$^{206}Pb^*$ $^{207}Pb^*$	± (Ma)	Best Age (Ma)	± (Ma)
Spot 2	775	11986	1.8	21.8022	1.5	0.0344	3.0	0.0054	2.5	0.86	35.0	0.9	34.3	1.0	NA	NA	35.0	0.9
Spot 110	990	12719	2.8	21.7970	1.3	0.0344	2.7	0.0054	2.4	0.87	35.0	0.8	34.4	0.9	NA	NA	35.0	0.8
Spot 67	520	23315	1.2	21.1225	2.3	0.0356	3.4	0.0055	2.6	0.75	35.0	0.9	35.5	1.2	66.6	53.7	35.0	0.9
Spot 4	471	5322	2.5	22.2099	1.8	0.0338	3.2	0.0055	2.7	0.84	35.1	1.0	33.8	1.1	NA	NA	35.1	1.0
Spot 6	474	12908	1.4	20.6756	2.2	0.0364	3.3	0.0055	2.4	0.75	35.1	0.8	36.3	1.2	117.2	51.0	35.1	0.8
Spot 105	1551	25666	1.3	21.0986	1.5	0.0357	3.1	0.0055	2.7	0.88	35.1	0.9	35.6	1.1	69.3	34.7	35.1	0.9
Spot 66	286	12193	1.5	22.6125	2.0	0.0333	3.9	0.0055	3.3	0.85	35.1	1.2	33.3	1.3	NA	NA	35.1	1.2
Spot 61	545	17889	1.6	21.7726	1.9	0.0346	2.8	0.0055	2.1	0.74	35.2	0.7	34.5	1.0	NA	NA	35.2	0.7
Spot 94	191	6106	1.2	21.1051	2.9	0.0358	4.5	0.0055	3.5	0.78	35.2	1.2	35.7	1.6	68.5	67.9	35.2	1.2
Spot 75	159	2047	1.1	23.8831	8.9	0.0317	9.7	0.0055	3.9	0.40	35.3	1.4	31.6	3.0	NA	NA	35.3	1.4
Spot 26	136	5003	1.2	19.2008	4.4	0.0394	5.2	0.0055	2.8	0.53	35.3	1.0	39.2	2.0	289.0	101.2	35.3	1.0
Spot 49	313	18204	0.8	21.2952	2.5	0.0356	3.5	0.0055	2.4	0.68	35.3	0.8	35.5	1.2	47.2	60.6	35.3	0.8
Spot 43	812	8075	2.8	21.8292	1.4	0.0347	2.8	0.0055	2.5	0.87	35.3	0.9	34.6	1.0	NA	NA	35.3	0.9
Spot 23	1199	33915	1.6	21.4451	1.4	0.0353	2.6	0.0055	2.2	0.84	35.3	0.8	35.2	0.9	30.3	34.1	35.3	0.8
Spot 46	1562	55179	1.4	21.1465	1.4	0.0358	3.6	0.0055	3.4	0.93	35.3	1.2	35.7	1.3	63.8	32.8	35.3	1.2
Spot 54	804	13536	1.4	21.6577	1.1	0.0350	3.1	0.0055	2.9	0.93	35.3	1.0	34.9	1.1	6.7	27.4	35.3	1.0
Spot 18	633	17053	0.6	20.9425	1.9	0.0362	2.9	0.0055	2.1	0.74	35.3	0.7	36.1	1.0	86.9	45.6	35.3	0.7
Spot 44	1260	42398	2.6	21.6583	1.2	0.0350	2.8	0.0055	2.5	0.91	35.4	0.9	35.0	1.0	6.6	28.4	35.4	0.9
Spot 83	729	7728	1.1	19.2199	2.3	0.0395	3.5	0.0055	2.6	0.75	35.4	0.9	39.4	1.3	286.7	52.4	35.4	0.9

TABLE E2: U-TH-PB GEOCHRONOLOGIC ANALYSES

						Isotope Ratios					Apparent Ages (Ma)							
Analysis	U (ppm)	^{206}Pb ^{204}Pb	U/Th	$^{206}Pb^*$ $^{207}Pb^*$	± (%)	$^{207}Pb^*$ $^{235}U^*$	± (%)	$^{206}Pb^*$ ^{238}U	± (%)	Error Corr.	$^{206}Pb^*$ $^{238}U^*$	± (Ma)	$^{207}Pb^*$ ^{235}U	± (Ma)	$^{206}Pb^*$ $^{207}Pb^*$	± (Ma)	**Best Age** (Ma)	± (Ma)
Spot 64	886	17895	1.7	21.8178	1.3	0.0348	2.6	0.0055	2.2	0.86	35.4	0.8	34.8	0.9	NA	NA	35.4	0.8
Spot 65	269	24343	1.6	20.5464	2.8	0.0370	3.9	0.0055	2.7	0.69	35.4	1.0	36.9	1.4	132.0	66.4	35.4	1.0
Spot 24	214	2276	1.1	24.5410	2.4	0.0310	3.5	0.0055	2.5	0.72	35.5	0.9	31.0	1.1	NA	NA	35.5	0.9
Spot 95	430	5297	1.4	22.9996	2.2	0.0331	3.5	0.0055	2.8	0.79	35.5	1.0	33.1	1.2	NA	NA	35.5	1.0
Spot 62	836	54079	1.8	15.3756	4.3	0.0496	5.1	0.0055	2.8	0.55	35.6	1.0	49.2	2.5	775.6	89.5	35.6	1.0
Spot 92	839	40338	1.0	19.3990	2.3	0.0393	4.2	0.0055	3.6	0.85	35.6	1.3	39.2	1.6	265.5	51.7	35.6	1.3
Spot 84	332	30874	1.3	20.1392	2.7	0.0379	4.0	0.0055	2.9	0.73	35.6	1.0	37.8	1.5	178.8	63.7	35.6	1.0
Spot 21	1125	91891	1.8	19.4569	1.5	0.0392	2.9	0.0055	2.4	0.85	35.6	0.9	39.1	1.1	258.6	35.0	35.6	0.9
Spot 33	217	3038	1.0	21.7915	3.1	0.0350	3.7	0.0055	2.1	0.57	35.6	0.8	35.0	1.3	NA	NA	35.6	0.8
Spot 45	257	11919	1.1	22.2515	2.5	0.0343	3.8	0.0055	2.8	0.75	35.6	1.0	34.3	1.3	NA	NA	35.6	1.0
Spot 47	895	168779	0.7	21.4220	1.5	0.0358	2.7	0.0056	2.2	0.83	35.7	0.8	35.7	0.9	32.9	36.3	35.7	0.8
Spot 27	353	1690	1.2	23.9745	2.2	0.0320	3.2	0.0056	2.3	0.73	35.8	0.8	32.0	1.0	NA	NA	35.8	0.8
Spot 50	287	139572	1.2	21.2859	2.6	0.0360	3.8	0.0056	2.8	0.73	35.8	1.0	35.9	1.3	48.2	61.6	35.8	1.0
Spot 30	156	12741	1.5	21.0683	4.2	0.0365	5.2	0.0056	3.0	0.59	35.9	1.1	36.4	1.9	72.7	99.7	35.9	1.1
Spot 86	516	1352247	1.3	17.2219	4.0	0.0446	4.6	0.0056	2.3	0.50	35.9	0.8	44.3	2.0	532.3	88.1	35.9	0.8
Spot 77	420	25623	1.0	21.2914	2.1	0.0362	3.4	0.0056	2.6	0.78	36.0	0.9	36.1	1.2	47.6	50.6	36.0	0.9
Spot 89	1275	34344	0.9	21.2688	1.4	0.0363	2.8	0.0056	2.4	0.87	36.0	0.9	36.2	1.0	50.1	32.7	36.0	0.9
Spot 80	114	1433	0.8	23.9016	5.2	0.0324	6.2	0.0056	3.4	0.55	36.1	1.2	32.4	2.0	NA	NA	36.1	1.2
Spot 55	318	130969	1.3	13.0447	8.1	0.0594	8.7	0.0056	3.4	0.39	36.1	1.2	58.6	5.0	1112.3	161.2	36.1	1.2

TABLE E2: U-TH-PB GEOCHRONOLOGIC ANALYSES

Analysis	U (ppm)	^{206}Pb ^{204}Pb	U/Th	$^{206}Pb^*$ $^{207}Pb^*$	± (%)	Isotope Ratios $^{207}Pb^*$ $^{235}U^*$	± (%)	$^{206}Pb^*$ ^{238}U	± (%)	Error Corr.	Apparent Ages (Ma) $^{206}Pb^*$ $^{238}U^*$	± (Ma)	$^{207}Pb^*$ ^{235}U	± (Ma)	$^{206}Pb^*$ $^{207}Pb^*$	± (Ma)	Best Age (Ma)	± (Ma)
Spot 5	293	10997	1.2	21.6845	2.3	0.0358	3.6	0.0056	2.7	0.77	36.2	1.0	35.7	1.2	3.7	54.7	36.2	1.0
Spot 68	1383	6159	0.7	16.1958	3.6	0.0479	4.4	0.0056	2.6	0.59	36.2	0.9	47.5	2.1	665.3	76.9	36.2	0.9
Spot 108	1102	20601	1.7	20.9116	1.4	0.0372	3.0	0.0056	2.7	0.89	36.3	1.0	37.1	1.1	90.4	32.4	36.3	1.0
Spot 70	331	32788	0.8	21.0401	2.0	0.0370	3.6	0.0056	3.0	0.84	36.3	1.1	36.9	1.3	75.8	46.9	36.3	1.1
Spot 8	307	4721	1.3	22.9829	3.0	0.0339	3.8	0.0057	2.4	0.62	36.3	0.9	33.8	1.3	NA	NA	36.3	0.9
Spot 100	208	2495	1.4	22.3869	4.8	0.0348	5.4	0.0057	2.4	0.44	36.4	0.9	34.8	1.8	NA	NA	36.4	0.9
Spot 38	311	8905	1.4	21.2863	2.5	0.0366	4.3	0.0057	3.4	0.80	36.4	1.2	36.5	1.5	48.1	60.8	36.4	1.2
Spot 29	410	34330	1.1	21.1376	2.0	0.0370	4.2	0.0057	3.7	0.88	36.4	1.3	36.9	1.5	64.9	48.2	36.4	1.3
Spot 37	301	16674	1.3	20.2828	2.1	0.0386	4.1	0.0057	3.6	0.86	36.5	1.3	38.4	1.6	162.3	48.5	36.5	1.3
Spot 107	464	32762	1.7	21.1562	1.8	0.0370	3.2	0.0057	2.6	0.83	36.6	1.0	36.9	1.1	62.7	42.5	36.6	1.0
Spot 48	900	31130	1.3	21.3231	1.4	0.0368	3.0	0.0057	2.7	0.88	36.6	1.0	36.7	1.1	44.0	34.3	36.6	1.0
Spot 98	418	55698	1.1	12.6176	5.2	0.0621	5.9	0.0057	2.7	0.46	36.6	1.0	61.2	3.5	1178.5	103.2	36.6	1.0
Spot 51	312	6878	1.1	21.1099	3.3	0.0372	4.0	0.0057	2.2	0.56	36.6	0.8	37.0	1.5	68.0	78.7	36.6	0.8
Spot 60	554	7929	1.3	22.5333	1.7	0.0349	2.5	0.0057	1.9	0.75	36.7	0.7	34.8	0.9	NA	NA	36.7	0.7
Spot 96	132	3689	0.7	20.9398	4.8	0.0375	5.7	0.0057	3.1	0.53	36.7	1.1	37.4	2.1	87.2	114.9	36.7	1.1
Spot 14	501	11197	0.7	21.3109	2.1	0.0369	3.1	0.0057	2.3	0.74	36.7	0.8	36.8	1.1	45.4	49.2	36.7	0.8
Spot 88	712	6659	1.2	14.6499	4.8	0.0538	5.7	0.0057	3.1	0.54	36.7	1.1	53.2	3.0	876.4	100.1	36.7	1.1
Spot 109	1697	19523	0.6	21.6560	1.3	0.0364	2.5	0.0057	2.2	0.86	36.7	0.8	36.3	0.9	6.9	30.3	36.7	0.8
Spot 71	427	421226	1.2	20.4546	2.4	0.0386	3.5	0.0057	2.6	0.72	36.9	0.9	38.5	1.3	142.5	57.3	36.9	0.9

TABLE E2: U-TH-PB GEOCHRONOLOGIC ANALYSES

Analysis	U (ppm)	^{206}Pb ^{204}Pb	U/Th	$^{206}Pb^*$ $^{207}Pb^*$	± (%)	Isotope Ratios $^{207}Pb^*$ $^{235}U^*$	± (%)	$^{206}Pb^*$ ^{238}U	± (%)	Error Corr.	Apparent Ages (Ma) $^{206}Pb^*$ $^{238}U^*$	± (Ma)	$^{207}Pb^*$ ^{235}U	± (Ma)	$^{206}Pb^*$ $^{207}Pb^*$	± (Ma)	Best Age (Ma)	± (Ma)
Spot 102	207	43745	1.2	20.9857	3.0	0.0378	4.1	0.0058	2.8	0.68	37.0	1.0	37.7	1.5	82.0	71.6	37.0	1.0
Spot 31	303	2871	0.9	10.7109	10.4	0.0777	11.0	0.0060	3.4	0.31	38.8	1.3	76.0	8.0	1495.2	197.6	38.8	1.3
Spot 40	212	6554	1.1	7.5810	14.3	0.1117	14.9	0.0061	4.3	0.29	39.5	1.7	107.5	15.2	2123.5	251.1	39.5	1.7
Spot 106	447	1010480	1.4	12.8884	0.8	1.9764	2.2	0.1848	2.0	0.93	1093.3	20.5	1107.5	14.8	1136.4	16.3	1136.4	16.3
Spot 81	643	108415	2.3	11.7450	0.6	2.3321	2.4	0.1987	2.3	0.97	1168.6	24.8	1222.1	17.0	1318.8	11.4	1318.8	11.4
Spot 53	80	75268	1.1	11.2154	1.1	3.0515	2.5	0.2483	2.3	0.91	1429.8	29.5	1420.6	19.4	1407.7	20.5	1407.7	20.5
Spot 25	197	344607	0.7	11.0309	1.0	2.8988	3.2	0.2320	3.0	0.95	1345.0	36.8	1381.6	24.0	1439.3	18.7	1439.3	18.7
Spot 69	841	117971	7.0	9.9549	0.8	3.2349	3.2	0.2337	3.1	0.97	1353.7	37.4	1465.6	24.6	1632.5	15.3	1632.5	15.3
Spot 34	559	763735	3.3	9.9278	0.9	4.1196	2.7	0.2968	2.5	0.94	1675.2	37.2	1658.2	21.9	1637.5	16.6	1637.5	16.6
Spot 32	222	110916	2.6	9.8672	1.0	4.1442	2.9	0.2967	2.7	0.94	1674.9	39.9	1663.1	23.5	1648.9	17.8	1648.9	17.8
Spot 36	180	9343772	2.4	9.7239	1.1	4.3012	3.0	0.3035	2.8	0.93	1708.5	41.9	1693.6	24.6	1676.0	19.6	1676.0	19.6
Spot 59	343	399837	3.1	9.7056	1.1	4.2054	2.8	0.2962	2.6	0.93	1672.2	38.3	1675.1	23.0	1679.5	19.4	1679.5	19.4
Spot 63	561	210171	3.4	9.6847	0.8	3.9050	2.8	0.2744	2.6	0.96	1563.1	36.7	1614.7	22.3	1683.4	14.8	1683.4	14.8
Spot 85	327	956310	3.4	9.6697	1.1	4.2525	2.9	0.2984	2.7	0.92	1683.2	39.8	1684.2	23.9	1686.3	20.7	1686.3	20.7
Spot 1	171	105398	2.2	9.6650	0.7	4.4361	2.5	0.3111	2.4	0.96	1746.1	36.4	1719.1	20.5	1687.2	12.0	1687.2	12.0
Spot 7	258	212564	1.8	9.6593	0.8	4.2466	2.6	0.2976	2.4	0.94	1679.5	35.9	1683.1	21.1	1688.3	15.5	1688.3	15.5
Spot 16	355	375246	2.0	9.6565	0.8	4.2949	2.6	0.3009	2.4	0.94	1695.9	36.0	1692.4	21.1	1688.8	15.5	1688.8	15.5
Spot 91	225	109898	1.7	9.6250	0.9	4.3016	2.6	0.3004	2.4	0.93	1693.4	35.6	1693.7	21.1	1694.8	16.9	1694.8	16.9
Spot 11	252	756666	1.6	9.6181	0.9	4.3037	2.8	0.3003	2.7	0.95	1693.0	40.3	1694.1	23.4	1696.2	15.7	1696.2	15.7
Spot 39	288	6600821	2.9	9.5886	1.1	4.3244	2.7	0.3009	2.5	0.92	1695.6	36.9	1698.0	22.2	1701.8	19.7	1701.8	19.7
Spot 93	381	201064	2.9	9.5881	0.9	4.1737	3.0	0.2904	2.8	0.95	1643.4	41.1	1668.9	24.5	1701.9	17.5	1701.9	17.5
Spot 19	234	123635	1.5	9.5860	1.0	4.2874	3.2	0.2982	3.0	0.95	1682.4	44.5	1690.9	26.1	1702.3	18.4	1702.3	18.4

TABLE E2: U-TH-PB GEOCHRONOLOGIC ANALYSES

Analysis	U (ppm)	^{206}Pb ^{204}Pb	U/Th	$^{206}Pb^*$ $^{207}Pb^*$	± (%)	Isotope Ratios $^{207}Pb^*$ $^{235}U^*$	± (%)	$^{206}Pb^*$ ^{238}U	± (%)	Error Corr.	Apparent Ages (Ma) $^{206}Pb^*$ $^{238}U^*$	± (Ma)	$^{207}Pb^*$ ^{235}U	± (Ma)	$^{206}Pb^*$ $^{207}Pb^*$	± (Ma)	Best Age (Ma)	± (Ma)
Spot 12	426	245247	2.0	9.5701	0.9	4.2495	3.0	0.2951	2.8	0.95	1666.9	41.2	1683.6	24.3	1705.4	17.1	1705.4	17.1
Spot 35	229	386880	3.2	9.5700	0.8	4.3176	2.3	0.2998	2.1	0.94	1690.4	31.7	1696.7	18.7	1705.4	14.1	1705.4	14.1
Spot 10	295	822498	1.9	9.5460	1.0	4.3254	3.1	0.2996	2.9	0.95	1689.3	43.0	1698.2	25.2	1710.0	18.0	1710.0	18.0
Spot 101	430	256887	4.4	9.5231	0.8	4.3853	2.3	0.3030	2.1	0.94	1706.2	32.1	1709.6	18.8	1714.4	14.4	1714.4	14.4
Spot 99	211	245037	4.3	9.5045	0.7	4.3462	2.9	0.2997	2.9	0.97	1690.0	42.5	1702.2	24.3	1718.0	13.0	1718.0	13.0
Spot 103	127	357772	1.6	9.5013	0.8	4.4384	2.7	0.3060	2.5	0.96	1720.9	38.4	1719.5	22.0	1718.6	14.4	1718.6	14.4
Spot 76	143	281235	2.1	9.4399	1.0	4.3271	2.9	0.2964	2.7	0.94	1673.3	39.9	1698.5	23.9	1730.6	18.7	1730.6	18.7
Spot 57	485	237409	3.0	9.4078	0.9	3.9148	2.7	0.2672	2.5	0.95	1526.7	34.2	1616.7	21.5	1736.8	15.8	1736.8	15.8
Spot 104	348	1681927	2.0	9.3321	0.9	4.3014	3.1	0.2913	3.0	0.96	1647.8	43.8	1693.6	25.9	1751.6	15.9	1751.6	15.9
SQG																		
SQG-66	701	6374	1.0	18.5224	22.1	0.0255	22.4	0.0034	3.4	0.15	22.0	0.8	25.5	5.6	370.6	503.1	22.0	0.8
SQG-200	649	15143	1.6	19.4746	10.9	0.0335	12.0	0.0047	5.1	0.43	30.4	1.6	33.4	4.0	256.5	250.6	30.4	1.6
SQG-166	315	6552	0.5	28.6927	14.0	0.0239	15.9	0.0050	7.7	0.48	32.0	2.5	24.0	3.8	-720.4	391.4	32.0	2.5
SQG-95	504	5283	0.9	18.9262	26.3	0.0365	27.5	0.0050	7.9	0.29	32.2	2.5	36.4	9.8	321.8	607.6	32.2	2.5
SQG-42	991	9388	1.1	20.1988	8.1	0.0345	8.2	0.0050	1.3	0.16	32.5	0.4	34.4	2.8	171.9	190.2	32.5	0.4
SQG-64	162	3127	0.5	25.5078	59.2	0.0273	60.1	0.0051	9.9	0.17	32.5	3.2	27.4	16.2	-403.1	1681.9	32.5	3.2
SQG-06	122	1132	1.8	19.2200	68.8	0.0363	69.3	0.0051	7.9	0.11	32.6	2.6	36.2	24.7	286.7	1801.3	32.6	2.6
SQG-01	412	3178	0.9	28.2074	43.5	0.0248	43.8	0.0051	4.8	0.11	32.7	1.6	24.9	10.8	-673.1	1251.4	32.7	1.6
SQG-44	1209	20893	1.4	20.5464	7.7	0.0343	8.0	0.0051	2.0	0.25	32.9	0.7	34.3	2.7	132.0	182.4	32.9	0.7
SQG-57	509	4654	0.7	23.1625	10.6	0.0304	10.7	0.0051	1.7	0.15	32.9	0.5	30.5	3.2	-157.6	263.9	32.9	0.5
SQG-76	146	2384	1.3	9.0898	187.8	0.0777	188.0	0.0051	8.0	0.04	32.9	2.6	76.0	138.5	1799.6	234.9	32.9	2.6

TABLE E2: U-TH-PB GEOCHRONOLOGIC ANALYSES

						Isotope Ratios					Apparent Ages (Ma)							
Analysis	U (ppm)	^{206}Pb ^{204}Pb	U/Th	$^{206}Pb^*$ $^{207}Pb^*$	± (%)	$^{207}Pb^*$ $^{235}U^*$	± (%)	$^{206}Pb^*$ ^{238}U	± (%)	Error Corr.	$^{206}Pb^*$ $^{238}U^*$	± (Ma)	$^{207}Pb^*$ ^{235}U	± (Ma)	$^{206}Pb^*$ $^{207}Pb^*$	± (Ma)	**Best Age** (Ma)	± (Ma)
SQG-62	1558	19960	1.6	21.8048	4.1	0.0327	4.5	0.0052	2.0	0.44	33.2	0.7	32.6	1.5	-9.6	98.0	33.2	0.7
SQG-67	1719	27474	1.7	20.7103	5.4	0.0345	5.5	0.0052	1.0	0.18	33.3	0.3	34.4	1.8	113.3	127.1	33.3	0.3
SQG-78	886	24684	0.9	20.0954	9.1	0.0355	9.3	0.0052	1.6	0.18	33.3	0.5	35.5	3.2	183.9	212.4	33.3	0.5
SQG-56	1519	25713	1.6	21.4798	7.9	0.0332	8.5	0.0052	2.9	0.34	33.3	1.0	33.2	2.8	26.5	190.8	33.3	1.0
SQG-83	1431	61495	0.8	18.6048	7.4	0.0385	7.6	0.0052	1.4	0.18	33.4	0.5	38.4	2.9	360.5	168.2	33.4	0.5
SQG-16	1451	15660	0.8	20.4182	7.3	0.0351	7.4	0.0052	1.5	0.20	33.5	0.5	35.1	2.6	146.7	171.4	33.5	0.5
SQG-128	437	7308	1.0	14.9097	44.1	0.0482	44.5	0.0052	6.1	0.14	33.5	2.1	47.8	20.8	839.9	965.6	33.5	2.1
SQG-13	403	7067	1.2	25.1357	29.7	0.0286	30.0	0.0052	4.3	0.14	33.5	1.4	28.6	8.5	-364.9	784.0	33.5	1.4
SQG-108	1395	70991	1.9	20.5967	11.9	0.0349	12.1	0.0052	2.0	0.17	33.5	0.7	34.8	4.1	126.2	282.0	33.5	0.7
SQG-175	1510	23708	2.3	21.3694	5.9	0.0337	6.0	0.0052	1.2	0.19	33.6	0.4	33.7	2.0	38.8	141.4	33.6	0.4
SQG-133	1727	51303	2.7	21.5951	5.0	0.0334	5.2	0.0052	1.4	0.26	33.6	0.5	33.4	1.7	13.6	120.2	33.6	0.5
SQG-126	1608	21177	1.2	21.1414	4.6	0.0342	4.7	0.0052	0.8	0.16	33.7	0.3	34.1	1.6	64.4	109.3	33.7	0.3
SQG-111	1046	12710	1.5	21.0104	6.2	0.0345	6.5	0.0053	1.6	0.25	33.8	0.5	34.5	2.2	79.2	148.5	33.8	0.5
SQG-49	244	5953	1.1	23.1842	35.0	0.0313	35.3	0.0053	4.9	0.14	33.8	1.7	31.3	10.9	-159.9	893.6	33.8	1.7
SQG-82	1043	12751	1.1	22.2596	12.7	0.0326	12.9	0.0053	2.3	0.18	33.8	0.8	32.6	4.1	-59.7	310.6	33.8	0.8
SQG-77	388	6641	0.9	22.2357	16.4	0.0327	17.0	0.0053	4.4	0.26	33.9	1.5	32.6	5.5	-57.1	402.9	33.9	1.5
SQG-118	1583	25846	1.6	21.1834	6.9	0.0343	7.1	0.0053	1.7	0.23	33.9	0.6	34.3	2.4	59.7	164.5	33.9	0.6
SQG-28	3069	29460	0.9	21.0038	2.6	0.0347	2.7	0.0053	0.6	0.21	34.0	0.2	34.7	0.9	79.9	62.1	34.0	0.2
SQG-127	873	9857	1.2	21.9979	15.4	0.0332	15.5	0.0053	2.1	0.14	34.0	0.7	33.1	5.1	-31.0	375.0	34.0	0.7

TABLE E2: U-TH-PB GEOCHRONOLOGIC ANALYSES

Analysis	U (ppm)	$^{206}Pb/^{204}Pb$	U/Th	$^{206}Pb^*/^{207}Pb^*$	± (%)	Isotope Ratios $^{207}Pb^*/^{235}U^*$	± (%)	$^{206}Pb^*/^{238}U$	± (%)	Error Corr.	Apparent Ages (Ma) $^{206}Pb^*/^{238}U^*$	± (Ma)	$^{207}Pb^*/^{235}U$	± (Ma)	$^{206}Pb^*/^{207}Pb^*$	± (Ma)	Best Age (Ma)	± (Ma)
SQG-182	1447	19096	1.3	21.4076	11.4	0.0341	11.5	0.0053	0.7	0.06	34.0	0.3	34.0	3.8	34.5	274.7	34.0	0.3
SQG-177	1570	26551	2.1	21.3616	9.4	0.0342	9.4	0.0053	1.3	0.14	34.0	0.4	34.1	3.2	39.7	224.2	34.0	0.4
SQG-185	123	2454	0.9	15.1598	108.8	0.0482	109.2	0.0053	9.2	0.08	34.1	3.1	47.8	51.0	805.2	501.2	34.1	3.1
SQG-18	1198	21038	1.5	21.6047	12.1	0.0338	12.1	0.0053	1.2	0.10	34.1	0.4	33.8	4.0	12.5	291.1	34.1	0.4
SQG-162	971	13272	1.3	19.9508	6.7	0.0367	7.9	0.0053	4.1	0.53	34.1	1.4	36.6	2.8	200.7	155.5	34.1	1.4
SQG-40	880	11710	0.6	18.6369	6.1	0.0393	6.4	0.0053	1.8	0.29	34.1	0.6	39.1	2.5	356.7	138.4	34.1	0.6
SQG-115	890	14105	1.9	22.9720	10.7	0.0319	11.0	0.0053	2.3	0.21	34.2	0.8	31.9	3.4	-137.1	266.1	34.2	0.8
SQG-117	496	9780	1.1	20.2343	13.1	0.0363	13.5	0.0053	3.3	0.24	34.2	1.1	36.2	4.8	167.8	307.5	34.2	1.1
SQG-100	482	23444	0.9	20.2970	20.8	0.0362	20.9	0.0053	2.3	0.11	34.2	0.8	36.1	7.4	160.6	490.1	34.2	0.8
SQG-69	1940	53657	2.4	20.9024	6.8	0.0351	6.8	0.0053	1.0	0.14	34.2	0.3	35.1	2.4	91.4	160.5	34.2	0.3
SQG-39	632	6831	1.2	21.0691	12.2	0.0349	12.4	0.0053	2.3	0.18	34.3	0.8	34.8	4.3	72.6	292.0	34.3	0.8
SQG-25	1713	16767	2.4	22.5853	8.6	0.0326	8.7	0.0053	0.6	0.07	34.3	0.2	32.5	2.8	-95.3	212.2	34.3	0.2
SQG-19	989	12542	0.6	24.0217	14.9	0.0307	15.0	0.0053	1.7	0.11	34.4	0.6	30.7	4.5	-248.9	378.9	34.4	0.6
SQG-43	1451	15664	1.0	19.6570	5.1	0.0375	5.4	0.0054	1.9	0.36	34.4	0.7	37.4	2.0	235.1	116.7	34.4	0.7
SQG-17	2091	26466	1.4	21.1700	3.9	0.0350	4.1	0.0054	1.1	0.27	34.5	0.4	34.9	1.4	61.2	94.0	34.5	0.4
SQG-33	1282	16468	1.8	22.1034	6.9	0.0335	7.0	0.0054	1.3	0.19	34.5	0.5	33.4	2.3	-42.6	168.0	34.5	0.5
SQG-85	2124	25219	1.9	20.5069	1.9	0.0361	2.2	0.0054	1.1	0.52	34.5	0.4	36.0	0.8	136.5	44.0	34.5	0.4
SQG-156	469	12517	1.1	24.7844	18.8	0.0299	19.0	0.0054	2.6	0.13	34.6	0.9	29.9	5.6	-328.6	486.7	34.6	0.9
SQG-141	666	5501	1.9	22.3196	8.0	0.0332	8.2	0.0054	1.8	0.22	34.6	0.6	33.2	2.7	-66.3	195.9	34.6	0.6

TABLE E2: U-TH-PB GEOCHRONOLOGIC ANALYSES

Analysis	U (ppm)	^{206}Pb ^{204}Pb	U/Th	$^{206}Pb^*$ $^{207}Pb^*$	± (%)	Isotope Ratios $^{207}Pb^*$ $^{235}U^*$	± (%)	$^{206}Pb^*$ ^{238}U	± (%)	Error Corr.	Apparent Ages (Ma) $^{206}Pb^*$ $^{238}U^*$	± (Ma)	$^{207}Pb^*$ ^{235}U	± (Ma)	$^{206}Pb^*$ $^{207}Pb^*$	± (Ma)	Best Age (Ma)	± (Ma)
SQG-97	105	1340	0.4	25.5913	37.7	0.0290	38.6	0.0054	8.6	0.22	34.6	3.0	29.1	11.1	-411.7	1014.5	34.6	3.0
SQG-15	1479	17588	2.4	20.7063	10.8	0.0359	10.9	0.0054	1.5	0.13	34.6	0.5	35.8	3.8	113.7	256.4	34.6	0.5
SQG-139	837	8407	1.5	22.0876	9.5	0.0336	10.3	0.0054	3.9	0.38	34.7	1.4	33.6	3.4	-40.9	231.9	34.7	1.4
SQG-189	1012	29796	1.0	21.6867	3.5	0.0343	3.9	0.0054	1.7	0.44	34.7	0.6	34.3	1.3	3.5	84.2	34.7	0.6
SQG-07	981	9190	1.3	21.3908	12.0	0.0348	12.2	0.0054	2.4	0.20	34.7	0.8	34.8	4.2	36.4	287.9	34.7	0.8
SQG-73	607	11990	0.8	23.7503	11.6	0.0314	11.9	0.0054	2.8	0.23	34.7	1.0	31.4	3.7	-220.2	292.5	34.7	1.0
SQG-184	1008	16880	1.6	22.1662	5.5	0.0336	6.5	0.0054	3.5	0.53	34.7	1.2	33.6	2.1	-49.5	133.7	34.7	1.2
SQG-26	503	5127	1.1	23.0338	28.7	0.0323	28.7	0.0054	2.3	0.08	34.7	0.8	32.3	9.1	-143.8	722.6	34.7	0.8
SQG-61	338	6448	1.0	23.7657	33.0	0.0314	33.2	0.0054	3.5	0.10	34.8	1.2	31.4	10.3	-221.9	851.1	34.8	1.2
SQG-10	1481	8515	1.5	22.7467	9.2	0.0328	9.8	0.0054	3.1	0.32	34.8	1.1	32.8	3.1	-112.8	227.9	34.8	1.1
SQG-31	1350	14955	1.6	22.1662	9.5	0.0337	9.8	0.0054	2.4	0.24	34.8	0.8	33.6	3.3	-49.5	232.7	34.8	0.8
SQG-53	1386	40127	1.4	21.9483	3.4	0.0340	4.0	0.0054	2.1	0.54	34.8	0.7	34.0	1.3	-25.5	81.2	34.8	0.7
SQG-194	1095	10483	1.4	21.3024	7.3	0.0351	7.5	0.0054	1.8	0.24	34.9	0.6	35.0	2.6	46.3	175.0	34.9	0.6
SQG-79	508	2898	1.1	23.7468	13.0	0.0315	14.7	0.0054	7.0	0.47	34.9	2.4	31.5	4.6	-219.9	327.0	34.9	2.4
SQG-112	1293	10850	2.0	21.7034	6.1	0.0345	6.8	0.0054	3.0	0.43	34.9	1.0	34.4	2.3	1.6	148.0	34.9	1.0
SQG-72	227	6806	1.0	24.9908	18.2	0.0299	19.5	0.0054	6.8	0.35	34.9	2.4	30.0	5.7	-350.0	474.2	34.9	2.4
SQG-96	654	5689	1.1	23.2074	6.0	0.0323	6.3	0.0054	2.1	0.33	34.9	0.7	32.2	2.0	-162.4	149.3	34.9	0.7
SQG-116	454	3042	1.1	29.9026	47.9	0.0250	48.1	0.0054	3.4	0.07	34.9	1.2	25.1	11.9	-837.1	1440.3	34.9	1.2
SQG-157	352	6820	1.7	20.2997	10.1	0.0369	11.4	0.0054	5.2	0.46	35.0	1.8	36.8	4.1	160.3	237.9	35.0	1.8

TABLE E2: U-TH-PB GEOCHRONOLOGIC ANALYSES

						Isotope Ratios					Apparent Ages (Ma)							
Analysis	U (ppm)	^{206}Pb ^{204}Pb	U/Th	$^{206}Pb^*$ $^{207}Pb^*$	± (%)	$^{207}Pb^*$ $^{235}U^*$	± (%)	$^{206}Pb^*$ ^{238}U	± (%)	Error Corr.	$^{206}Pb^*$ $^{238}U^*$	± (Ma)	$^{207}Pb^*$ ^{235}U	± (Ma)	$^{206}Pb^*$ $^{207}Pb^*$	± (Ma)	**Best Age** (Ma)	± (Ma)
SQG-122	385	6056	1.0	28.0631	21.1	0.0267	21.2	0.0054	2.4	0.12	35.0	0.9	26.8	5.6	-658.9	584.6	35.0	0.9
SQG-134	1067	17144	1.5	21.7051	5.9	0.0346	6.2	0.0054	1.9	0.30	35.0	0.6	34.5	2.1	1.4	142.2	35.0	0.6
SQG-02	716	3992	1.2	25.7099	19.3	0.0292	19.3	0.0055	1.1	0.05	35.1	0.4	29.3	5.6	-423.8	509.1	35.1	0.4
SQG-196	972	11315	1.1	21.6553	14.1	0.0347	14.2	0.0055	1.6	0.11	35.1	0.6	34.7	4.8	6.9	340.4	35.1	0.6
SQG-138	548	16386	1.6	20.4287	16.5	0.0369	16.9	0.0055	3.9	0.23	35.1	1.4	36.8	6.1	145.5	388.2	35.1	1.4
SQG-170	384	16665	0.8	26.2725	45.7	0.0287	45.8	0.0055	2.6	0.06	35.2	0.9	28.7	13.0	-480.8	1268.1	35.2	0.9
SQG-110	238	3168	1.3	23.4328	22.3	0.0322	22.5	0.0055	2.9	0.13	35.2	1.0	32.2	7.1	-186.5	562.2	35.2	1.0
SQG-153	271	4357	0.8	28.4217	45.4	0.0266	46.0	0.0055	7.4	0.16	35.2	2.6	26.6	12.1	-694.0	1314.5	35.2	2.6
SQG-102	196	6239	0.9	19.0886	39.0	0.0396	39.2	0.0055	3.2	0.08	35.2	1.1	39.4	15.1	302.4	922.1	35.2	1.1
SQG-101	1753	12618	1.6	15.9658	6.8	0.0474	6.9	0.0055	1.3	0.19	35.3	0.5	47.0	3.2	695.8	144.9	35.3	0.5
SQG-161	471	5975	2.1	21.3561	16.0	0.0354	16.4	0.0055	3.6	0.22	35.3	1.3	35.4	5.7	40.3	385.6	35.3	1.3
SQG-74	505	5107	1.0	25.1322	12.7	0.0301	13.1	0.0055	3.0	0.23	35.3	1.1	30.1	3.9	-364.6	331.2	35.3	1.1
SQG-143	868	31222	1.6	21.0457	9.2	0.0360	9.4	0.0055	1.8	0.19	35.3	0.6	35.9	3.3	75.2	219.3	35.3	0.6
SQG-160	1920	29399	1.5	21.0970	5.0	0.0359	5.2	0.0055	1.5	0.29	35.3	0.5	35.8	1.8	69.4	118.5	35.3	0.5
SQG-197	129	1289	0.9	17.7824	55.4	0.0426	56.0	0.0055	8.2	0.15	35.4	2.9	42.4	23.3	461.6	1330.1	35.4	2.9
SQG-123	1011	6514	1.7	21.4314	6.2	0.0354	6.3	0.0055	0.9	0.15	35.4	0.3	35.3	2.2	31.9	148.4	35.4	0.3
SQG-50	2029	45671	1.3	21.7913	3.1	0.0348	3.3	0.0055	1.1	0.34	35.4	0.4	34.8	1.1	-8.1	74.8	35.4	0.4
SQG-37	850	13568	0.9	20.0966	9.4	0.0378	9.5	0.0055	1.8	0.18	35.4	0.6	37.7	3.5	183.8	218.8	35.4	0.6
SQG-203	1883	21733	2.4	21.1461	4.0	0.0359	4.2	0.0055	1.3	0.30	35.4	0.5	35.8	1.5	63.9	96.3	35.4	0.5

TABLE E2: U-TH-PB GEOCHRONOLOGIC ANALYSES

Analysis	U (ppm)	^{206}Pb ^{204}Pb	U/Th	$^{206}Pb^*$ $^{207}Pb^*$	± (%)	Isotope Ratios $^{207}Pb^*$ $^{235}U^*$	± (%)	$^{206}Pb^*$ ^{238}U	± (%)	Error Corr.	Apparent Ages (Ma) $^{206}Pb^*$ $^{238}U^*$	± (Ma)	$^{207}Pb^*$ ^{235}U	± (Ma)	$^{206}Pb^*$ $^{207}Pb^*$	± (Ma)	**Best Age** (Ma)	± (Ma)
SQG-155	373	5269	1.6	17.4443	24.3	0.0437	24.5	0.0055	2.7	0.11	35.6	0.9	43.4	10.4	504.0	542.1	35.6	0.9
SQG-88	1474	21251	0.8	21.5533	8.6	0.0354	8.7	0.0055	1.5	0.18	35.6	0.6	35.4	3.0	18.3	206.7	35.6	0.6
SQG-171	1117	13190	1.8	22.1532	11.2	0.0345	11.3	0.0055	1.5	0.13	35.6	0.5	34.4	3.8	-48.1	272.3	35.6	0.5
SQG-63	538	5749	1.1	23.5869	19.3	0.0324	19.7	0.0055	3.7	0.19	35.6	1.3	32.4	6.3	-202.9	488.8	35.6	1.3
SQG-90	513	9565	1.2	20.1757	20.4	0.0379	20.6	0.0055	2.4	0.12	35.6	0.9	37.8	7.6	174.6	481.3	35.6	0.9
SQG-154	1117	17948	1.9	21.5916	4.2	0.0354	4.4	0.0055	1.3	0.29	35.6	0.5	35.3	1.5	14.0	100.4	35.6	0.5
SQG-199	693	6798	0.7	20.5348	9.3	0.0372	9.8	0.0055	3.0	0.30	35.6	1.1	37.1	3.6	133.3	219.6	35.6	1.1
SQG-195	404	5852	0.9	26.2151	31.7	0.0292	32.0	0.0055	4.8	0.15	35.7	1.7	29.2	9.2	-475.0	856.8	35.7	1.7
SQG-120	339	3532	1.1	24.2858	42.1	0.0315	42.3	0.0055	3.2	0.08	35.7	1.2	31.5	13.1	-276.7	1115.2	35.7	1.2
SQG-14	3278	39192	1.9	20.2473	3.9	0.0378	5.0	0.0056	3.1	0.62	35.7	1.1	37.7	1.8	166.3	91.5	35.7	1.1
SQG-05	498	8577	1.0	22.3624	33.6	0.0342	33.7	0.0056	3.1	0.09	35.7	1.1	34.2	11.3	-71.0	840.3	35.7	1.1
SQG-92	706	10409	1.6	21.0878	9.5	0.0363	9.9	0.0056	2.7	0.27	35.7	1.0	36.2	3.5	70.5	226.1	35.7	1.0
SQG-55	603	10081	1.0	20.3054	13.8	0.0377	14.0	0.0056	2.5	0.18	35.7	0.9	37.6	5.2	159.7	323.2	35.7	0.9
SQG-151	508	9762	1.2	24.3746	19.3	0.0315	19.5	0.0056	2.9	0.15	35.8	1.0	31.5	6.1	-285.9	496.5	35.8	1.0
SQG-174	569	7757	1.2	18.9940	12.2	0.0404	12.6	0.0056	3.0	0.24	35.8	1.1	40.2	5.0	313.7	278.2	35.8	1.1
SQG-129	422	8111	0.8	22.9250	18.6	0.0335	19.0	0.0056	3.9	0.21	35.8	1.4	33.4	6.3	-132.0	463.7	35.8	1.4
SQG-27	587	18306	1.1	20.6447	11.7	0.0372	11.9	0.0056	2.3	0.20	35.8	0.8	37.1	4.3	120.7	275.4	35.8	0.8
SQG-173	497	6103	1.2	19.7320	19.5	0.0390	19.7	0.0056	3.0	0.15	35.8	1.1	38.8	7.5	226.3	453.9	35.8	1.1
SQG-59	330	9268	0.8	20.7373	21.3	0.0371	21.7	0.0056	4.0	0.18	35.9	1.4	37.0	7.9	110.2	507.7	35.9	1.4

TABLE E2: U-TH-PB GEOCHRONOLOGIC ANALYSES

Analysis	U (ppm)	^{206}Pb ^{204}Pb	U/Th	$^{206}Pb^*$ $^{207}Pb^*$	± (%)	Isotope Ratios $^{207}Pb^*$ $^{235}U^*$	± (%)	$^{206}Pb^*$ ^{238}U	± (%)	Error Corr.	Apparent Ages (Ma) $^{206}Pb^*$ $^{238}U^*$	± (Ma)	$^{207}Pb^*$ ^{235}U	± (Ma)	$^{206}Pb^*$ $^{207}Pb^*$	± (Ma)	Best Age (Ma)	± (Ma)
SQG-172	475	6590	1.1	25.7686	24.2	0.0299	24.3	0.0056	2.6	0.11	35.9	0.9	29.9	7.2	-429.8	642.5	35.9	0.9
SQG-144	692	7985	1.8	21.7119	6.4	0.0355	6.7	0.0056	1.9	0.29	36.0	0.7	35.4	2.3	0.7	154.3	36.0	0.7
SQG-206	780	10450	2.0	23.7968	10.0	0.0324	10.3	0.0056	2.4	0.23	36.0	0.9	32.4	3.3	-225.2	251.9	36.0	0.9
SQG-191	1162	12576	1.9	19.5728	15.2	0.0395	15.4	0.0056	2.4	0.15	36.0	0.8	39.3	5.9	244.9	351.7	36.0	0.8
SQG-84	223	2524	0.9	23.7938	44.4	0.0325	44.8	0.0056	6.1	0.14	36.1	2.2	32.5	14.3	-224.9	1167.7	36.1	2.2
SQG-08	1078	9034	0.9	21.6614	7.7	0.0357	7.8	0.0056	1.3	0.17	36.1	0.5	35.6	2.7	6.2	185.3	36.1	0.5
SQG-152	2046	27953	1.9	21.5834	6.0	0.0358	6.2	0.0056	1.7	0.27	36.1	0.6	35.8	2.2	14.9	144.2	36.1	0.6
SQG-188	666	5831	1.1	22.1333	14.4	0.0350	14.5	0.0056	1.8	0.13	36.1	0.7	34.9	5.0	-45.9	350.6	36.1	0.7
SQG-201	1048	17790	1.4	20.7483	8.6	0.0374	8.7	0.0056	1.1	0.13	36.2	0.4	37.3	3.2	109.0	203.2	36.2	0.4
SQG-60	546	5301	1.0	17.2602	10.8	0.0450	11.3	0.0056	3.3	0.29	36.2	1.2	44.7	4.9	527.4	237.8	36.2	1.2
SQG-174	470	11173	1.1	23.5044	24.6	0.0331	24.7	0.0056	1.9	0.08	36.2	0.7	33.0	8.0	-194.1	624.1	36.2	0.7
SQG-41	512	4168	0.8	22.9596	18.5	0.0339	18.8	0.0056	3.7	0.19	36.3	1.3	33.8	6.3	-135.8	460.4	36.3	1.3
SQG-183	404	16255	0.5	17.1875	17.0	0.0453	17.3	0.0056	3.2	0.19	36.3	1.2	45.0	7.6	536.6	373.5	36.3	1.2
SQG-12	452	5717	0.9	22.5480	34.4	0.0346	34.4	0.0057	1.6	0.05	36.3	0.6	34.5	11.7	-91.2	865.4	36.3	0.6
SQG-164	474	6340	1.0	19.6698	14.3	0.0396	15.4	0.0057	5.6	0.36	36.4	2.0	39.5	6.0	233.6	332.7	36.4	2.0
SQG-165	166	2161	0.9	18.6467	68.2	0.0418	68.7	0.0057	8.2	0.12	36.4	3.0	41.6	28.0	355.5	1758.5	36.4	3.0
SQG-211	317	11363	3.0	21.6302	20.9	0.0361	21.5	0.0057	4.7	0.22	36.4	1.7	36.0	7.6	9.7	508.2	36.4	1.7
SQG-210	1124	26121	1.5	21.8695	5.2	0.0357	5.4	0.0057	1.4	0.27	36.4	0.5	35.6	1.9	-16.8	125.4	36.4	0.5
SQG-104	423	5479	1.0	21.8000	33.8	0.0358	34.3	0.0057	5.5	0.16	36.4	2.0	35.8	12.0	-9.1	837.9	36.4	2.0

TABLE E2: U-TH-PB GEOCHRONOLOGIC ANALYSES

Analysis	U (ppm)	^{206}Pb ^{204}Pb	U/Th	$^{206}Pb^*$ $^{207}Pb^*$	± (%)	Isotope Ratios $^{207}Pb^*$ $^{235}U^*$	± (%)	$^{206}Pb^*$ ^{238}U	± (%)	Error Corr.	Apparent Ages (Ma) $^{206}Pb^*$ $^{238}U^*$	± (Ma)	$^{207}Pb^*$ ^{235}U	± (Ma)	$^{206}Pb^*$ $^{207}Pb^*$	± (Ma)	Best Age (Ma)	± (Ma)
SQG-71	492	5265	1.0	15.3194	12.4	0.0512	12.9	0.0057	3.4	0.27	36.5	1.2	50.7	6.4	783.3	261.8	36.5	1.2
SQG-30	547	6959	1.0	17.6127	20.2	0.0445	20.3	0.0057	2.4	0.12	36.6	0.9	44.2	8.8	482.9	450.4	36.6	0.9
SQG-176	468	4744	1.1	24.5150	20.5	0.0320	20.7	0.0057	3.0	0.14	36.6	1.1	32.0	6.5	-300.6	529.4	36.6	1.1
SQG-198	431	4300	1.5	17.9783	17.1	0.0437	17.3	0.0057	2.7	0.15	36.6	1.0	43.4	7.4	437.3	383.7	36.6	1.0
SQG-158	143	1118	0.9	26.8236	51.9	0.0293	52.5	0.0057	8.0	0.15	36.6	2.9	29.3	15.2	-536.2	1478.5	36.6	2.9
SQG-65	616	9427	0.9	22.3900	14.4	0.0351	15.2	0.0057	5.0	0.33	36.7	1.8	35.1	5.2	-74.0	352.8	36.7	1.8
SQG-36	523	4834	0.6	20.0526	14.9	0.0394	15.5	0.0057	4.2	0.27	36.8	1.6	39.2	6.0	188.9	349.1	36.8	1.6
SQG-99	139	2110	1.2	35.7610	142.6	0.0221	142.7	0.0057	5.3	0.04	36.8	1.9	22.2	31.3	-1380.4	0.0	36.8	1.9
SQG-209	550	9190	1.1	19.5240	9.9	0.0408	10.1	0.0058	1.9	0.18	37.2	0.7	40.6	4.0	250.7	228.0	37.2	0.7
SQG-149	538	6029	1.0	21.5683	11.8	0.0370	12.1	0.0058	3.0	0.25	37.2	1.1	36.9	4.4	16.6	283.3	37.2	1.1
SQG-214	1063	21707	1.4	21.2593	9.0	0.0376	9.2	0.0058	1.8	0.20	37.2	0.7	37.4	3.4	51.2	215.4	37.2	0.7
SQG-181	456	7373	1.1	22.5059	21.6	0.0356	21.7	0.0058	2.1	0.10	37.4	0.8	35.6	7.6	-86.6	534.6	37.4	0.8
SQG-167	177	2316	0.9	19.9689	15.5	0.0404	16.7	0.0059	6.0	0.36	37.7	2.3	40.3	6.6	198.6	362.7	37.7	2.3
SQG-142	1992	28756	2.2	22.0020	2.8	0.0369	5.3	0.0059	4.5	0.85	37.9	1.7	36.8	1.9	-31.4	67.8	37.9	1.7
SQG-208	547	10939	1.6	20.0397	17.8	0.0405	18.5	0.0059	5.1	0.27	37.9	1.9	40.4	7.3	190.4	417.7	37.9	1.9
SQG-205	364	3882	1.9	22.3150	22.5	0.0367	22.7	0.0059	3.1	0.14	38.2	1.2	36.6	8.2	-65.8	554.4	38.2	1.2
SQG-213	229	6146	0.7	22.3160	30.3	0.0371	30.4	0.0060	2.7	0.09	38.5	1.0	36.9	11.0	-65.9	753.3	38.5	1.0
SQG-150	473	14350	1.1	16.2815	7.8	0.0508	8.8	0.0060	4.1	0.47	38.6	1.6	50.3	4.3	653.9	166.8	38.6	1.6
SQG-24	460	6249	1.2	8.9025	25.2	0.0934	25.9	0.0060	5.7	0.22	38.7	2.2	90.6	22.5	1837.4	465.1	38.7	2.2
SQG-147	1414	13350	1.3	16.255	10.9	0.0513	12.6	0.0060	6.3	0.50	38.8	2.4	50.8	6.2	657.4	234.7	38.8	2.4

TABLE E2: U-TH-PB GEOCHRONOLOGIC ANALYSES

Analysis	U (ppm)	^{206}Pb ^{204}Pb	U/Th	$^{206}Pb^*$ $^{207}Pb^*$	± (%)	Isotope Ratios $^{207}Pb^*$ $^{235}U^*$	± (%)	$^{206}Pb^*$ ^{238}U	± (%)	Error Corr.	Apparent Ages (Ma) $^{206}Pb^*$ $^{238}U^*$	± (Ma)	$^{207}Pb^*$ ^{235}U	± (Ma)	$^{206}Pb^*$ $^{207}Pb^*$	± (Ma)	**Best Age** (Ma)	± (Ma)
SQG-202	806	16838	3.2	21.8346	7.2	0.0593	7.4	0.0094	1.7	0.23	60.3	1.0	58.5	4.2	-12.9	174.5	60.3	1.0
SQG-105	3592	66854	1.2	20.8715	0.9	0.0630	5.0	0.0095	4.9	0.98	61.2	3.0	62.0	3.0	94.9	21.9	61.2	3.0
SQG-75	64	2133	1.0	24.3524	38.5	0.0584	39.1	0.0103	6.7	0.17	66.2	4.4	57.7	21.9	-283.6	1014.0	66.2	4.4
SQG-132	336	4509	3.1	21.2287	24.3	0.0685	24.4	0.0105	1.4	0.06	67.6	0.9	67.3	15.9	54.6	587.9	67.6	0.9
SQG-168	462	21065	1.8	21.5166	7.7	0.0851	7.9	0.0133	1.9	0.24	85.0	1.6	82.9	6.3	22.4	184.6	85.0	1.6
SQG-212	606	59331	1.8	11.4275	0.7	0.6861	1.1	0.0569	0.8	0.73	356.5	2.8	530.5	4.5	1371.7	14.4	356.5	2.8
SQG-86	162	25333	1.7	17.2073	3.1	0.6616	3.4	0.0826	1.4	0.41	511.4	6.8	515.6	13.6	534.1	67.3	511.4	6.8
SQG-145	140	52430	1.1	13.4656	0.7	1.8847	1.3	0.1841	1.0	0.82	1089.1	10.5	1075.7	8.5	1048.6	14.7	1048.6	14.7
SQG-29	283	84883	2.4	12.7222	0.9	2.0794	3.1	0.1919	3.0	0.95	1131.5	30.7	1142.0	21.3	1162.1	18.5	1162.1	18.5
SQG-135	92	43737	2.2	11.3263	0.9	2.8357	1.2	0.2329	0.8	0.64	1349.9	9.3	1365.0	9.0	1388.8	17.7	1388.8	17.7
SQG-193	50	38178	1.3	11.0603	1.3	3.2744	1.4	0.2627	0.6	0.42	1503.5	8.1	1475.0	11.2	1434.3	25.0	1434.3	25.0
SQG-130	102	47315	1.7	11.0532	0.7	3.0273	2.2	0.2427	2.1	0.95	1400.6	26.8	1414.5	17.1	1435.5	13.3	1435.5	13.3
SQG-45	138	68348	1.0	11.0482	0.6	3.1330	1.3	0.2510	1.2	0.91	1443.9	15.3	1440.8	10.1	1436.3	10.6	1436.3	10.6
SQG-190	351	121487	3.7	11.0409	0.5	3.0944	1.0	0.2478	0.9	0.88	1427.1	11.2	1431.3	7.7	1437.6	9.2	1437.6	9.2
SQG-169	138	78252	1.0	11.0178	0.9	3.1515	1.1	0.2518	0.7	0.65	1447.9	9.7	1445.4	8.8	1441.6	16.5	1441.6	16.5
SQG-87	229	153891	1.7	11.0125	0.6	3.1344	1.0	0.2503	0.8	0.78	1440.3	10.2	1441.2	7.8	1442.5	12.1	1442.5	12.1
SQG-04	270	89594	1.0	10.9926	0.8	3.0201	1.5	0.2408	1.2	0.84	1390.8	15.6	1412.7	11.4	1446.0	15.5	1446.0	15.5
SQG-91	233	457088	1.3	10.9797	0.6	3.1589	1.0	0.2516	0.8	0.82	1446.5	10.8	1447.2	7.8	1448.2	11.0	1448.2	11.0
SQG-179	168	108149	1.6	10.976	0.9	3.2493	2.1	0.2587	1.9	0.91	1483.0	25.2	1469.0	16.3	1448.8	17.0	1448.8	17.0

TABLE E2: U-TH-PB GEOCHRONOLOGIC ANALYSES

Analysis	U (ppm)	^{206}Pb ^{204}Pb	U/Th	$^{206}Pb^*$ $^{207}Pb^*$	± (%)	Isotope Ratios $^{207}Pb^*$ $^{235}U^*$	± (%)	$^{206}Pb^*$ ^{238}U	± (%)	Error Corr.	Apparent Ages (Ma) $^{206}Pb^*$ $^{238}U^*$	± (Ma)	$^{207}Pb^*$ ^{235}U	± (Ma)	$^{206}Pb^*$ $^{207}Pb^*$	± (Ma)	Best Age (Ma)	± (Ma)
SQG-186	178	203864	1.0	10.9720	0.5	3.1660	1.7	0.2519	1.6	0.95	1448.5	21.2	1448.9	13.2	1449.5	9.7	1449.5	9.7
SQG-22	248	134930	1.3	10.9479	0.4	2.7764	1.4	0.2204	1.3	0.95	1284.3	15.7	1349.2	10.5	1453.7	8.2	1453.7	8.2
SQG-20	148	56172	1.3	10.9473	1.2	3.1859	1.7	0.2530	1.2	0.73	1453.7	16.0	1453.7	13.1	1453.8	22.0	1453.8	22.0
SQG-47	169	71235	1.2	10.8902	0.5	3.0502	2.1	0.2409	2.0	0.97	1391.4	25.0	1420.3	15.7	1463.8	9.0	1463.8	9.0
SQG-103	263	223093	1.2	10.8889	0.5	3.1044	1.7	0.2452	1.6	0.95	1413.5	20.7	1433.8	13.2	1464.0	10.1	1464.0	10.1
SQG-23	276	183713	1.5	10.7744	0.8	3.1919	1.6	0.2494	1.4	0.86	1435.5	17.7	1455.2	12.3	1484.0	15.3	1484.0	15.3
SQG-107	92	34061	1.4	10.6153	3.1	3.2275	3.7	0.2485	2.0	0.54	1430.6	25.4	1463.8	28.6	1512.2	58.7	1512.2	58.7
SQG-58	130	43761	1.0	10.4470	2.3	3.2416	2.7	0.2456	1.3	0.49	1415.8	16.5	1467.2	20.7	1542.3	43.9	1542.3	43.9
SQG-32	283	210640	2.4	9.9076	0.9	3.7813	2.5	0.2717	2.3	0.93	1549.5	32.4	1588.8	20.3	1641.3	17.6	1641.3	17.6
SQG-52	396	238876	6.8	9.8403	0.5	3.9262	1.7	0.2802	1.6	0.96	1592.4	22.8	1619.1	13.6	1654.0	8.3	1654.0	8.3
SQG-137	694	1601990	2.7	9.6902	0.3	3.6819	6.9	0.2588	6.9	1.00	1483.5	91.7	1567.5	55.4	1682.4	5.8	1682.4	5.8
SQG-180	471	304841	1.9	9.5741	0.3	4.2497	1.5	0.2951	1.5	0.98	1666.9	21.6	1683.7	12.3	1704.6	5.1	1704.6	5.1
SQG-119	422	421211	2.8	9.5672	0.1	4.1073	1.1	0.2850	1.1	0.99	1616.5	16.0	1655.8	9.2	1705.9	2.1	1705.9	2.1
SQG-70	413	356054	2.1	9.5623	0.2	4.0082	1.6	0.2780	1.6	0.99	1581.2	21.9	1635.9	12.9	1706.9	4.5	1706.9	4.5
SQG-68	625	620516	2.4	9.5577	0.1	3.9972	1.0	0.2771	1.0	0.99	1576.7	13.8	1633.6	8.1	1707.8	2.3	1707.8	2.3
SQG-187	209	293123	1.6	9.5550	0.5	4.3170	0.7	0.2992	0.5	0.75	1687.2	7.7	1696.6	5.7	1708.3	8.4	1708.3	8.4
SQG-80	243	615823	1.6	9.5536	0.3	4.2173	1.8	0.2922	1.8	0.98	1652.6	26.0	1677.4	14.9	1708.5	6.3	1708.5	6.3
SQG-192	227	157936	3.4	9.5514	0.3	4.5063	1.4	0.3122	1.4	0.97	1751.4	21.5	1732.1	12.0	1709.0	6.3	1709.0	6.3
SQG-125	464	244026	1.9	9.5406	0.2	4.2600	0.4	0.2948	0.4	0.87	1665.3	5.5	1685.7	3.6	1711.1	3.9	1711.1	3.9
SQG-11	245	114270	2.3	9.5398	0.6	4.1546	1.1	0.2875	0.9	0.83	1628.8	13.3	1665.1	9.1	1711.2	11.4	1711.2	11.4
SQG-54	476	658481	2.5	9.5371	0.3	4.1687	0.8	0.2883	0.8	0.94	1633.3	10.9	1667.9	6.6	1711.7	4.8	1711.7	4.8

TABLE E2: U-TH-PB GEOCHRONOLOGIC ANALYSES

Analysis	U (ppm)	^{206}Pb ^{204}Pb	U/Th	$^{206}Pb^*$ $^{207}Pb^*$	± (%)	Isotope Ratios $^{207}Pb^*$ $^{235}U^*$	± (%)	$^{206}Pb^*$ ^{238}U	± (%)	Error Corr.	Apparent Ages (Ma) $^{206}Pb^*$ $^{238}U^*$	± (Ma)	$^{207}Pb^*$ ^{235}U	± (Ma)	$^{206}Pb^*$ $^{207}Pb^*$	± (Ma)	Best Age (Ma)	± (Ma)
SQG-124	318	295428	1.6	9.5366	0.4	4.0998	1.8	0.2836	1.8	0.98	1609.3	25.0	1654.3	14.7	1711.8	7.3	1711.8	7.3
SQG-48	434	201195	2.2	9.5319	0.3	4.3375	1.0	0.2999	0.9	0.94	1690.6	13.3	1700.5	7.8	1712.7	5.8	1712.7	5.8
SQG-09	189	66197	1.0	9.5318	1.1	4.1768	1.5	0.2887	1.0	0.68	1635.3	14.2	1669.5	11.9	1712.8	19.8	1712.8	19.8
SQG-46	386	310102	1.7	9.5115	0.2	4.3349	1.4	0.2990	1.4	0.99	1686.5	20.4	1700.0	11.5	1716.7	3.9	1716.7	3.9
SQG-207	134	54827	1.5	9.5092	0.7	4.5687	1.1	0.3151	0.8	0.78	1765.7	12.9	1743.6	8.9	1717.1	12.3	1717.1	12.3
SQG-35	290	242563	1.2	9.5087	0.4	4.4982	1.5	0.3102	1.4	0.97	1741.7	21.8	1730.6	12.2	1717.2	6.5	1717.2	6.5
SQG-21	628	258739	2.8	9.5053	0.3	4.0436	4.3	0.2788	4.3	1.00	1585.1	60.6	1643.0	35.2	1717.9	5.4	1717.9	5.4
SQG-114	285	175568	1.7	9.5001	0.3	4.4639	1.2	0.3076	1.1	0.96	1728.7	17.2	1724.3	9.8	1718.9	6.3	1718.9	6.3
SQG-51	296	105423	2.0	9.4878	0.7	4.2669	2.2	0.2936	2.1	0.94	1659.6	30.8	1687.0	18.4	1721.3	13.7	1721.3	13.7
SQG-98	325	889617	2.5	9.4694	0.3	4.5295	4.4	0.3111	4.4	1.00	1746.0	66.9	1736.4	36.5	1724.8	5.2	1724.8	5.2
SQG-215	651	372074	3.8	9.4561	0.5	4.1547	3.1	0.2849	3.1	0.99	1616.2	43.9	1665.1	25.4	1727.4	8.3	1727.4	8.3
SQG-94	545	371287	1.7	9.4550	0.1	4.0719	1.6	0.2792	1.6	1.00	1587.5	22.2	1648.7	12.9	1727.6	1.4	1727.6	1.4
SQG-109	576	231077	3.0	9.4501	0.3	3.8172	6.2	0.2616	6.2	1.00	1498.1	83.0	1596.4	50.0	1728.6	6.1	1728.6	6.1
SQG-106	575	399510	7.2	9.4407	0.1	3.9668	1.1	0.2716	1.1	0.99	1548.9	15.3	1627.4	9.1	1730.4	2.3	1730.4	2.3
SQG-178	419	361836	3.8	9.4374	0.3	4.4096	0.6	0.3018	0.5	0.86	1700.3	8.2	1714.1	5.3	1731.0	6.0	1731.0	6.0
SQG-140	513	270717	2.2	9.3164	0.3	4.6956	2.1	0.3173	2.1	0.99	1776.4	32.3	1766.4	17.6	1754.7	5.8	1754.7	5.8
SQG-03	103	89186	3.4	6.0509	0.6	10.5553	1.2	0.4632	1.0	0.84	2453.8	19.9	2484.8	10.8	2510.2	10.6	2510.2	10.6
SQG-93	63	78181	1.6	4.4254	0.3	16.1025	6.2	0.5168	6.2	1.00	2685.7	135.6	2882.9	59.2	3023.7	5.6	3023.7	5.6
PS																		
Spot 7	110	449	0.8	85.3269	41.6	0.0080	41.8	0.0050	3.7	0.09	31.8	1.2	8.1	3.4	NA	NA	31.8	1.2
Spot 10	141	662	1.1	33.8802	12.8	0.0202	13.6	0.0050	4.6	0.34	31.9	1.5	20.3	2.7	NA	NA	31.9	1.5
Spot 58	46	318	1.3	318.5789	79.4	0.0022	79.5	0.0050	3.9	0.05	32.1	1.2	2.2	1.7	NA	NA	32.1	1.2
Spot 92	88	526	1.1	31.744	7.1	0.0217	8.0	0.0050	3.7	0.46	32.2	1.2	21.8	1.7	NA	NA	32.2	1.2

TABLE E2: U-TH-PB GEOCHRONOLOGIC ANALYSES

						Isotope Ratios					Apparent Ages (Ma)							
Analysis	U (ppm)	^{206}Pb ^{204}Pb	U/Th	$^{206}Pb^*$ $^{207}Pb^*$	± (%)	$^{207}Pb^*$ $^{235}U^*$	± (%)	$^{206}Pb^*$ ^{238}U	± (%)	Error Corr.	$^{206}Pb^*$ $^{238}U^*$	± (Ma)	$^{207}Pb^*$ ^{235}U	± (Ma)	$^{206}Pb^*$ $^{207}Pb^*$	± (Ma)	**Best Age** (Ma)	± (Ma)
Spot 9	206	1102	0.9	29.4600	5.4	0.0235	6.6	0.0050	3.8	0.57	32.3	1.2	23.6	1.5	NA	NA	32.3	1.2
Spot 107	528	3594	0.9	23.3030	2.1	0.0299	4.0	0.0051	3.4	0.85	32.5	1.1	29.9	1.2	NA	NA	32.5	1.1
Spot 79	140	709	1.0	36.9525	40.2	0.0192	40.4	0.0051	3.0	0.07	33.0	1.0	19.3	7.7	NA	NA	33.0	1.0
Spot 77	84	772	1.1	37.0274	5.0	0.0194	6.3	0.0052	3.8	0.60	33.4	1.3	19.5	1.2	NA	NA	33.4	1.3
Spot 40	115	312	1.3	284.5638	161.0	0.0025	161.0	0.0052	3.9	0.02	33.5	1.3	2.6	4.1	NA	NA	33.5	1.3
Spot 69	105	481	0.9	68.7872	20.5	0.0105	20.9	0.0053	3.9	0.19	33.8	1.3	10.6	2.2	NA	NA	33.8	1.3
Spot 54	103	793	1.5	36.1678	20.5	0.0202	20.8	0.0053	3.6	0.17	34.1	1.2	20.3	4.2	NA	NA	34.1	1.2
Spot 65	1195	28106	1.1	20.8089	1.4	0.0352	3.4	0.0053	3.1	0.91	34.2	1.0	35.2	1.2	102.0	33.1	34.2	1.0
Spot 31	889	12656	0.8	21.4121	1.6	0.0343	3.0	0.0053	2.6	0.85	34.2	0.9	34.2	1.0	34.0	38.8	34.2	0.9
Spot 99	982	114837	2.6	20.2579	1.7	0.0363	3.0	0.0053	2.5	0.82	34.3	0.9	36.2	1.1	165.1	40.7	34.3	0.9
Spot 55	124	1242	1.3	18.3461	7.0	0.0401	7.8	0.0053	3.3	0.42	34.3	1.1	39.9	3.0	392.1	158.2	34.3	1.1
Spot 75	251	3597	0.9	21.3182	3.0	0.0346	4.6	0.0053	3.5	0.76	34.4	1.2	34.5	1.6	44.6	70.9	34.4	1.2
Spot 72	118	2828	1.0	20.1102	4.5	0.0367	5.8	0.0053	3.7	0.63	34.4	1.3	36.6	2.1	182.2	105.7	34.4	1.3
Spot 12	119	1208	0.6	24.7361	6.8	0.0299	7.5	0.0054	3.0	0.41	34.4	1.0	29.9	2.2	NA	NA	34.4	1.0
Spot 100	1236	118491	2.9	20.9050	1.5	0.0356	3.8	0.0054	3.5	0.92	34.7	1.2	35.5	1.3	91.1	36.1	34.7	1.2
Spot 37	1048	6505	1.1	21.7104	2.0	0.0346	3.3	0.0055	2.6	0.79	35.1	0.9	34.6	1.1	NA	NA	35.1	0.9
Spot 30	95	1684	1.1	25.8461	5.5	0.0291	6.6	0.0055	3.6	0.55	35.1	1.3	29.1	1.9	NA	NA	35.1	1.3
Spot 108	138	18582	1.1	21.6170	3.7	0.0349	4.8	0.0055	3.0	0.62	35.2	1.0	34.8	1.6	11.2	89.5	35.2	1.0
Spot 53	113	2108	0.9	23.613	5.0	0.0320	5.8	0.0055	3.0	0.51	35.2	1.1	32.0	1.8	NA	NA	35.2	1.1

TABLE E2: U-TH-PB GEOCHRONOLOGIC ANALYSES

Analysis	U (ppm)	^{206}Pb ^{204}Pb	U/Th	$^{206}Pb^*$ $^{207}Pb^*$	± (%)	Isotope Ratios $^{207}Pb^*$ $^{235}U^*$	± (%)	$^{206}Pb^*$ ^{238}U	± (%)	Error Corr.	Apparent Ages (Ma) $^{206}Pb^*$ $^{238}U^*$	± (Ma)	$^{207}Pb^*$ ^{235}U	± (Ma)	$^{206}Pb^*$ $^{207}Pb^*$	± (Ma)	**Best Age** (Ma)	± (Ma)
Spot 13	429	3021	2.1	23.2016	5.8	0.0326	6.9	0.0055	3.7	0.53	35.3	1.3	32.6	2.2	NA	NA	35.3	1.3
Spot 41	128	449	1.0	73.9214	70.1	0.0102	70.2	0.0055	3.3	0.05	35.3	1.2	10.3	7.2	NA	NA	35.3	1.2
Spot 20	126	2278	1.0	22.6917	4.0	0.0334	4.9	0.0055	2.9	0.59	35.3	1.0	33.3	1.6	NA	NA	35.3	1.0
Spot 24	170	13098	0.9	20.0085	3.6	0.0378	4.7	0.0055	3.0	0.64	35.3	1.1	37.7	1.7	194.0	83.3	35.3	1.1
Spot 8	121	4187	0.9	20.5261	4.3	0.0371	5.3	0.0055	3.1	0.59	35.5	1.1	36.9	1.9	134.3	100.2	35.5	1.1
Spot 56	139	2971	0.7	20.6387	4.2	0.0372	5.7	0.0056	3.9	0.68	35.8	1.4	37.0	2.1	121.4	98.0	35.8	1.4
Spot 67	84	335	1.1	8.7824	7.2	0.0877	8.0	0.0056	3.4	0.43	35.9	1.2	85.4	6.5	1862.0	130.5	35.9	1.2
Spot 78	127	6391	1.0	20.0851	4.2	0.0384	5.3	0.0056	3.2	0.61	36.0	1.1	38.3	2.0	185.1	97.2	36.0	1.1
Spot 57	515	5347	1.1	20.9806	2.5	0.0370	3.8	0.0056	2.9	0.75	36.2	1.0	36.9	1.4	82.6	59.9	36.2	1.0
Spot 93	87	240	1.1	6.8502	23.1	0.1160	23.4	0.0058	3.7	0.16	37.1	1.4	111.5	24.7	2299.4	403.0	37.1	1.4
Spot 51	269	1125	0.8	21.7400	3.9	0.0372	5.2	0.0059	3.4	0.66	37.7	1.3	37.0	1.9	NA	NA	37.7	1.3
Spot 89	145	4013	2.4	21.0475	4.1	0.2156	4.6	0.0329	2.1	0.45	208.9	4.2	198.3	8.3	75.0	98.5	208.9	4.2
Spot 29	175	17398	2.3	17.9097	1.9	0.4824	3.8	0.0627	3.3	0.86	392.0	12.4	399.7	12.6	445.8	43.1	392.0	12.4
Spot 23	420	12048	9.3	18.3328	1.3	0.4967	3.8	0.0661	3.6	0.94	412.4	14.2	409.5	12.8	393.7	29.9	412.4	14.2
Spot 3	151	11749	1.7	17.7291	1.5	0.5402	3.2	0.0695	2.8	0.87	433.1	11.6	438.6	11.2	468.3	33.9	433.1	11.6
Spot 18	173	34063	3.8	15.4723	1.2	1.0341	3.5	0.1161	3.3	0.95	708.1	22.5	721.0	18.3	762.4	24.3	708.1	22.5
Spot 50	63	19404	3.5	14.0529	1.3	1.4938	3.0	0.1523	2.7	0.90	913.9	23.2	927.9	18.5	962.0	27.5	962.0	27.5
Spot 64	167	34360	2.3	13.2142	1.0	1.8829	2.8	0.1805	2.6	0.94	1069.9	26.1	1075.1	18.7	1086.5	19.1	1086.5	19.1
Spot 34	118	85332	4.7	12.6673	1.2	1.9953	2.8	0.1834	2.5	0.91	1085.5	25.2	1113.9	18.8	1170.7	23.0	1170.7	23.0

TABLE E2: U-TH-PB GEOCHRONOLOGIC ANALYSES

Analysis	U (ppm)	^{206}Pb ^{204}Pb	U/Th	$^{206}Pb^*$ $^{207}Pb^*$	± (%)	Isotope Ratios $^{207}Pb^*$ $^{235}U^*$	± (%)	$^{206}Pb^*$ ^{238}U	± (%)	Error Corr.	Apparent Ages (Ma) $^{206}Pb^*$ $^{238}U^*$	± (Ma)	$^{207}Pb^*$ ^{235}U	± (Ma)	$^{206}Pb^*$ $^{207}Pb^*$	± (Ma)	Best Age (Ma)	± (Ma)
Spot 101	138	25923	2.2	11.6318	0.9	2.7257	2.5	0.2300	2.4	0.94	1334.7	28.7	1335.5	18.8	1337.5	16.5	1337.5	16.5
Spot 17	447	94026	1.7	11.5490	0.9	2.8713	2.9	0.2406	2.7	0.95	1389.9	34.0	1374.4	21.5	1351.3	17.0	1351.3	17.0
Spot 87	112	23572	2.4	11.4173	1.4	2.8603	3.3	0.2370	3.0	0.91	1370.8	37.3	1371.5	25.0	1373.4	26.4	1373.4	26.4
Spot 1	31	16822	1.5	11.2992	1.5	2.8881	3.0	0.2368	2.6	0.87	1369.9	32.6	1378.8	22.9	1393.4	28.6	1393.4	28.6
Spot 14	166	27605	1.2	11.1260	0.8	3.1321	3.0	0.2528	2.9	0.96	1453.1	37.3	1440.6	22.9	1423.0	15.5	1423.0	15.5
Spot 44	89	60468	2.5	11.0931	0.8	3.1470	2.5	0.2533	2.4	0.95	1455.5	30.7	1444.3	19.2	1428.6	15.2	1428.6	15.2
Spot 81	585	4123313	2.9	11.0615	1.1	3.0361	3.2	0.2437	3.0	0.94	1405.8	38.2	1416.8	24.7	1434.1	21.7	1434.1	21.7
Spot 6	84	116628	1.4	11.0283	1.2	3.1500	3.5	0.2521	3.3	0.94	1449.1	43.4	1445.0	27.3	1439.8	22.2	1439.8	22.2
Spot 38	328	571721	54.9	11.0190	0.9	2.8654	3.7	0.2291	3.6	0.97	1329.8	42.9	1372.9	27.7	1441.4	17.1	1441.4	17.1
Spot 66	73	45898	1.2	11.0053	1.1	3.0829	2.7	0.2462	2.5	0.91	1418.7	31.2	1428.4	20.6	1443.8	20.7	1443.8	20.7
Spot 68	47	14652	1.5	10.9920	1.2	3.2395	3.0	0.2584	2.7	0.92	1481.5	36.2	1466.7	23.0	1446.1	21.9	1446.1	21.9
Spot 33	136	38005	0.7	10.9770	1.3	3.1213	2.8	0.2486	2.5	0.88	1431.3	31.9	1438.0	21.7	1448.7	25.5	1448.7	25.5
Spot 97	132	30898	1.3	10.9517	1.0	3.1614	2.6	0.2512	2.4	0.92	1444.8	31.4	1447.8	20.3	1453.1	19.0	1453.1	19.0
Spot 96	107	43691	1.5	10.9447	1.0	3.1821	3.1	0.2527	3.0	0.95	1452.4	38.6	1452.8	24.2	1454.3	18.8	1454.3	18.8
Spot 88	111	61183	1.2	10.9152	1.1	3.1639	2.9	0.2506	2.7	0.92	1441.5	34.7	1448.4	22.5	1459.4	21.6	1459.4	21.6
Spot 90	208	36853	1.8	10.8979	1.1	3.1439	2.6	0.2486	2.3	0.91	1431.3	30.0	1443.5	19.8	1462.4	20.4	1462.4	20.4
Spot 70	71	60155	1.3	10.8546	1.2	3.0312	3.2	0.2387	3.0	0.93	1380.1	37.6	1415.5	24.8	1470.0	22.2	1470.0	22.2
Spot 98	1406	35385	3.6	10.7634	1.1	2.9254	2.8	0.2285	2.6	0.92	1326.5	30.9	1388.5	21.1	1486.0	20.1	1486.0	20.1
Spot 5	374	318756	16.8	10.5572	0.9	3.3194	3.0	0.2543	2.8	0.96	1460.5	37.2	1485.6	23.2	1522.5	16.6	1522.5	16.6

TABLE E2: U-TH-PB GEOCHRONOLOGIC ANALYSES

Analysis	U (ppm)	^{206}Pb ^{204}Pb	U/Th	$^{206}Pb^*$ $^{207}Pb^*$	± (%)	Isotope Ratios $^{207}Pb^*$ $^{235}U^*$	± (%)	$^{206}Pb^*$ ^{238}U	± (%)	Error Corr.	Apparent Ages (Ma) $^{206}Pb^*$ $^{238}U^*$	± (Ma)	$^{207}Pb^*$ ^{235}U	± (Ma)	$^{206}Pb^*$ $^{207}Pb^*$	± (Ma)	Best Age (Ma)	± (Ma)
Spot 19	498	1062981	7.2	10.3992	0.8	3.6787	3.8	0.2776	3.8	0.98	1579.1	52.6	1566.7	30.7	1550.9	15.9	1550.9	15.9
Spot 86	92	31830	1.8	9.9883	1.2	4.0455	2.9	0.2932	2.7	0.92	1657.5	39.5	1643.4	24.0	1626.2	21.7	1626.2	21.7
Spot 48	811	99462	2.0	9.7271	0.9	4.2758	2.5	0.3018	2.3	0.93	1700.1	34.9	1688.7	20.7	1675.4	17.5	1675.4	17.5
Spot 71	789	70684	2.0	9.7041	1.0	4.0968	2.3	0.2885	2.0	0.90	1633.8	29.5	1653.7	18.5	1679.7	18.0	1679.7	18.0
Spot 102	202	125645	4.3	9.6928	0.8	4.0116	2.5	0.2821	2.4	0.95	1602.1	33.7	1636.6	20.4	1681.9	14.9	1681.9	14.9
Spot 103	93	19443	1.3	9.6854	1.1	4.3100	3.5	0.3029	3.3	0.95	1705.6	49.6	1695.3	28.7	1683.3	20.0	1683.3	20.0
Spot 52	46	13304	3.9	9.6823	1.2	4.3336	2.9	0.3045	2.6	0.91	1713.4	39.3	1699.8	23.8	1683.9	22.4	1683.9	22.4
Spot 21	286	52559	2.4	9.6243	0.9	4.3540	3.1	0.3040	3.0	0.96	1711.3	45.2	1703.6	25.9	1695.0	16.4	1695.0	16.4
Spot 73	157	30479	3.5	9.6106	0.9	4.3902	3.2	0.3061	3.1	0.96	1721.7	47.0	1710.5	26.7	1697.6	16.1	1697.6	16.1
Spot 74	168	616464	1.7	9.5754	1.2	4.0764	3.1	0.2832	2.9	0.92	1607.6	40.9	1649.6	25.4	1704.4	22.0	1704.4	22.0
Spot 76	396	59233	3.2	9.5419	1.0	4.3738	3.7	0.3028	3.5	0.97	1705.3	53.0	1707.4	30.3	1710.8	17.6	1710.8	17.6
Spot 15	386	35520	2.4	9.5239	1.0	4.3414	2.5	0.3000	2.3	0.92	1691.3	34.2	1701.3	20.7	1714.3	18.2	1714.3	18.2
Spot 49	135	43058	3.6	9.5239	0.8	4.4282	2.4	0.3060	2.2	0.93	1721.0	33.2	1717.6	19.5	1714.3	15.5	1714.3	15.5
Spot 36	277	113189	3.2	9.4881	0.9	4.4225	3.3	0.3045	3.1	0.96	1713.4	47.2	1716.6	27.1	1721.2	16.8	1721.2	16.8
Spot 47	323	2416173	2.6	9.4869	1.1	4.5670	3.1	0.3144	2.9	0.94	1762.2	44.8	1743.3	25.9	1721.4	20.2	1721.4	20.2
Spot 39	195	46043	2.8	9.4828	0.9	4.5703	3.0	0.3145	2.8	0.95	1762.6	43.6	1743.9	24.8	1722.2	17.2	1722.2	17.2
Spot 11	223	73973	2.8	9.4684	0.9	4.4884	2.5	0.3084	2.3	0.94	1732.6	35.7	1728.8	20.8	1725.0	16.1	1725.0	16.1
Spot 32	203	60900	2.6	9.4638	0.9	4.4234	2.3	0.3037	2.1	0.92	1709.9	31.5	1716.7	18.8	1725.9	16.0	1725.9	16.0
Spot 43	115	445422	2.7	9.4572	0.8	4.3602	2.8	0.2992	2.7	0.96	1687.3	39.8	1704.8	23.1	1727.2	14.7	1727.2	14.7
Spot 94	183	1525293	3.5	9.4554	0.8	4.5457	3.1	0.3119	3.0	0.96	1749.9	46.1	1739.4	26.0	1727.6	15.2	1727.6	15.2
Spot 42	248	71694	3.6	9.4518	1.3	4.1767	3.3	0.2864	3.0	0.92	1623.7	43.1	1669.5	26.7	1728.2	23.4	1728.2	23.4
Spot 16	150	74401	3.7	9.4227	1.0	4.4743	2.7	0.3059	2.5	0.92	1720.5	37.2	1726.2	22.2	1733.9	18.8	1733.9	18.8
Spot 26	441	72233	2.8	9.4019	0.9	4.4959	2.9	0.3067	2.8	0.95	1724.5	41.7	1730.2	24.1	1738.0	16.6	1738.0	16.6

TABLE E2: U-TH-PB GEOCHRONOLOGIC ANALYSES

Analysis	U (ppm)	$^{206}Pb/^{204}Pb$	U/Th	$^{206}Pb^*/^{207}Pb^*$	± (%)	Isotope Ratios $^{207}Pb^*/^{235}U^*$	± (%)	$^{206}Pb^*/^{238}U$	± (%)	Error Corr.	Apparent Ages (Ma) $^{206}Pb^*/^{238}U^*$	± (Ma)	$^{207}Pb^*/^{235}U$	± (Ma)	$^{206}Pb^*/^{207}Pb^*$	± (Ma)	Best Age (Ma)	± (Ma)
Spot 4	191	53107	2.6	9.4014	1.2	4.3664	3.0	0.2979	2.8	0.92	1680.7	40.7	1706.0	24.7	1738.0	21.1	1738.0	21.1
Spot 2	86	66180	3.7	9.3867	1.1	4.4131	2.5	0.3006	2.2	0.89	1694.1	33.2	1714.8	20.7	1740.9	20.6	1740.9	20.6
Spot 91	161	94866	2.7	9.3523	0.8	4.4490	2.7	0.3019	2.6	0.96	1700.8	39.2	1721.5	22.7	1747.6	14.6	1747.6	14.6
Spot 28	128	109929	3.5	9.3250	1.0	4.5431	2.5	0.3074	2.3	0.91	1727.8	34.2	1738.9	20.7	1753.0	19.1	1753.0	19.1
Spot 95	164	61062	3.1	9.2978	0.8	4.4646	3.0	0.3012	2.9	0.96	1697.2	43.4	1724.4	25.1	1758.3	14.8	1758.3	14.8
Spot 35	374	352843	2.9	9.2632	0.7	4.3975	3.1	0.2956	3.0	0.97	1669.3	44.0	1711.9	25.5	1765.2	13.7	1765.2	13.7
Spot 27	71	132265	2.0	5.0189	1.0	14.6386	2.8	0.5331	2.6	0.94	2754.4	59.2	2792.0	26.8	2820.0	16.2	2820.0	16.2
Spot 22	62	28137	2.5	5.0130	0.8	15.5549	3.0	0.5658	2.9	0.96	2890.5	67.2	2849.9	28.7	2822.0	13.7	2822.0	13.7
UTCK																		
Spot 14	3207	38460	2.9	20.4990	1.0	0.0328	1.9	0.0049	1.6	0.84	31.4	0.5	32.8	0.6	137.4	23.8	31.4	0.5
Spot 135	137	451	0.9	54.9331	8.2	0.0136	8.9	0.0054	3.4	0.39	34.9	1.2	13.7	1.2	NA	NA	34.9	1.2
Spot 46	89	628	0.9	39.5049	37.0	0.0192	37.1	0.0055	2.9	0.08	35.4	1.0	19.3	7.1	NA	NA	35.4	1.0
Spot 34	129	422	1.2	68.1831	65.1	0.0112	65.1	0.0055	2.8	0.04	35.5	1.0	11.3	7.3	NA	NA	35.5	1.0
Spot 156	132	113163	0.9	20.3288	3.9	0.0383	4.8	0.0056	2.9	0.59	36.3	1.0	38.1	1.8	156.9	91.2	36.3	1.0
Spot 22	150	2629	1.1	22.6583	3.3	0.0347	4.3	0.0057	2.8	0.65	36.7	1.0	34.7	1.5	NA	NA	36.7	1.0
Spot 140	202	2148	1.2	24.7492	3.9	0.0318	4.8	0.0057	2.8	0.58	36.7	1.0	31.8	1.5	NA	NA	36.7	1.0
Spot 145	173	10003	0.8	22.3924	3.0	0.0355	4.3	0.0058	3.0	0.71	37.0	1.1	35.4	1.5	NA	NA	37.0	1.1
Spot 124	116	2120	1.0	23.3344	4.4	0.0342	5.0	0.0058	2.4	0.48	37.2	0.9	34.1	1.7	NA	NA	37.2	0.9
Spot 116	230	3998	0.6	22.9797	3.2	0.0349	4.3	0.0058	2.9	0.67	37.4	1.1	34.8	1.5	NA	NA	37.4	1.1
Spot 53	119	12016	1.2	23.4081	3.9	0.0343	5.2	0.0058	3.4	0.66	37.5	1.3	34.3	1.8	NA	NA	37.5	1.3
Spot 149	255	1511	0.9	26.8227	3.7	0.0309	4.8	0.0060	3.1	0.64	38.7	1.2	30.9	1.5	NA	NA	38.7	1.2

TABLE E2: U-TH-PB GEOCHRONOLOGIC ANALYSES

Analysis	U (ppm)	^{206}Pb ^{204}Pb	U/Th	$^{206}Pb^*$ $^{207}Pb^*$	± (%)	Isotope Ratios $^{207}Pb^*$ $^{235}U^*$	± (%)	$^{206}Pb^*$ ^{238}U	± (%)	Error Corr.	Apparent Ages (Ma) $^{206}Pb^*$ $^{238}U^*$	± (Ma)	$^{207}Pb^*$ ^{235}U	± (Ma)	$^{206}Pb^*$ $^{207}Pb^*$	± (Ma)	Best Age (Ma)	± (Ma)
Spot 144	36	309	1.6	444.1400	116.9	0.0030	117.0	0.0096	3.3	0.03	61.4	2.0	3.0	3.5	NA	NA	61.4	2.0
Spot 2	40	269	2.2	75.6784	106.0	0.0175	106.0	0.0096	2.7	0.03	61.6	1.7	17.6	18.5	NA	NA	61.6	1.7
Spot 127	32	213	1.6	65.0969	88.6	0.0203	88.7	0.0096	3.0	0.03	61.6	1.8	20.4	17.9	NA	NA	61.6	1.8
Spot 155	27	463	1.8	43.9185	14.4	0.0302	14.9	0.0096	3.8	0.25	61.7	2.3	30.2	4.4	NA	NA	61.7	2.3
Spot 18	26	198	2.5	115.3769	15.0	0.0116	15.5	0.0097	3.9	0.25	62.3	2.4	11.7	1.8	NA	NA	62.3	2.4
Spot 60	33	237	1.1	41.9002	17.0	0.0320	17.3	0.0097	3.4	0.20	62.4	2.1	32.0	5.4	NA	NA	62.4	2.1
Spot 123	55	330	1.2	415.3412	41.7	0.0033	41.8	0.0099	2.8	0.07	63.4	1.8	3.3	1.4	NA	NA	63.4	1.8
Spot 54	30	556	1.3	30.2922	11.4	0.0450	11.8	0.0099	2.8	0.24	63.4	1.8	44.7	5.2	NA	NA	63.4	1.8
Spot 25	57	523	1.2	23.2997	11.3	0.0590	11.8	0.0100	3.4	0.28	63.9	2.1	58.2	6.7	NA	NA	63.9	2.1
Spot 32	40	409	1.6	72.3681	7.6	0.0190	8.1	0.0100	2.9	0.36	64.0	1.8	19.1	1.5	NA	NA	64.0	1.8
Spot 17	45	1311	1.2	23.8348	5.1	0.0579	5.9	0.0100	3.0	0.51	64.3	1.9	57.2	3.3	NA	NA	64.3	1.9
Spot 136	35	341	1.1	243.5316	306.6	0.0057	306.6	0.0100	3.5	0.01	64.3	2.2	5.7	17.6	NA	NA	64.3	2.2
Spot 30	58	587	1.0	41.7064	21.0	0.0332	21.1	0.0100	2.6	0.12	64.4	1.7	33.1	6.9	NA	NA	64.4	1.7
Spot 69	49	310	1.3	172.0151	21.1	0.0081	21.3	0.0101	2.8	0.13	64.6	1.8	8.2	1.7	NA	NA	64.6	1.8
Spot 56	36	411	1.5	69.3237	67.2	0.0201	67.3	0.0101	3.3	0.05	65.0	2.1	20.3	13.5	NA	NA	65.0	2.1
Spot 153	36	334	2.0	250.6380	215.7	0.0056	215.7	0.0102	3.2	0.01	65.5	2.1	5.7	12.2	NA	NA	65.5	2.1
Spot 24	41	1399	1.4	26.9938	4.9	0.0521	6.1	0.0102	3.6	0.59	65.5	2.4	51.6	3.1	NA	NA	65.5	2.4
Spot 3	43	3005	2.2	22.4056	4.8	0.0632	6.0	0.0103	3.6	0.60	65.9	2.4	62.2	3.6	NA	NA	65.9	2.4
Spot 9	32	1182	2.0	25.0029	6.4	0.0568	7.3	0.0103	3.6	0.49	66.1	2.4	56.1	4.0	NA	NA	66.1	2.4

TABLE E2: U-TH-PB GEOCHRONOLOGIC ANALYSES

Analysis	U (ppm)	^{206}Pb ^{204}Pb	U/Th	$^{206}Pb^*$ $^{207}Pb^*$	± (%)	Isotope Ratios $^{207}Pb^*$ $^{235}U^*$	± (%)	$^{206}Pb^*$ ^{238}U	± (%)	Error Corr.	Apparent Ages (Ma) $^{206}Pb^*$ $^{238}U^*$	± (Ma)	$^{207}Pb^*$ ^{235}U	± (Ma)	$^{206}Pb^*$ $^{207}Pb^*$	± (Ma)	Best Age (Ma)	± (Ma)
Spot 10	48	3678	2.3	20.6720	5.0	0.0688	5.9	0.0103	3.1	0.53	66.2	2.1	67.6	3.9	117.6	118.0	66.2	2.1
Spot 58	26	814	2.0	28.5340	8.9	0.0501	9.4	0.0104	3.0	0.32	66.6	2.0	49.7	4.6	NA	NA	66.6	2.0
Spot 15	87	1135	1.1	27.7994	3.5	0.0516	4.3	0.0104	2.6	0.60	66.7	1.7	51.0	2.1	NA	NA	66.7	1.7
Spot 31	47	2404	1.2	19.9860	5.2	0.0718	5.9	0.0104	2.8	0.48	66.8	1.9	70.4	4.0	196.6	121.1	66.8	1.9
Spot 8	73	35813	1.4	20.6338	4.1	0.0696	4.9	0.0104	2.5	0.52	66.8	1.7	68.3	3.2	122.0	97.5	66.8	1.7
Spot 112	37	1089	1.4	25.5907	6.0	0.0562	7.0	0.0104	3.5	0.51	66.9	2.3	55.5	3.8	NA	NA	66.9	2.3
Spot 66	92	3111	1.0	24.1564	3.3	0.0596	4.0	0.0104	2.3	0.57	67.0	1.5	58.8	2.3	NA	NA	67.0	1.5
Spot 63	78	732	1.1	28.8675	9.7	0.0499	10.1	0.0104	3.0	0.29	67.0	2.0	49.4	4.9	NA	NA	67.0	2.0
Spot 42	127	3072	1.3	22.0563	2.6	0.0654	3.4	0.0105	2.3	0.67	67.2	1.5	64.4	2.1	NA	NA	67.2	1.5
Spot 21	129	6981	0.9	21.8151	2.4	0.0664	3.5	0.0105	2.5	0.71	67.4	1.6	65.3	2.2	NA	NA	67.4	1.6
Spot 26	83	3852	1.0	21.2879	3.7	0.0681	4.9	0.0105	3.2	0.65	67.5	2.1	66.9	3.2	48.0	88.9	67.5	2.1
Spot 126	81	1195	0.9	27.7482	4.9	0.0523	5.7	0.0105	2.8	0.50	67.6	1.9	51.8	2.9	NA	NA	67.6	1.9
Spot 159	73	3208	1.1	22.9499	3.3	0.0633	4.7	0.0105	3.4	0.71	67.6	2.3	62.3	2.9	NA	NA	67.6	2.3
Spot 50	33	884	2.0	29.0072	6.6	0.0502	7.1	0.0106	2.6	0.37	67.7	1.8	49.7	3.5	NA	NA	67.7	1.8
Spot 48	586	10540	4.0	21.3553	1.6	0.0683	3.2	0.0106	2.8	0.88	67.9	1.9	67.1	2.1	40.4	37.2	67.9	1.9
Spot 28	47	1683	1.3	20.6579	5.1	0.0707	5.8	0.0106	2.7	0.47	68.0	1.8	69.4	3.9	119.3	119.7	68.0	1.8
Spot 59	75	1878	1.2	23.6343	3.2	0.0618	4.2	0.0106	2.7	0.65	68.0	1.9	60.9	2.5	NA	NA	68.0	1.9
Spot 137	32	919	1.2	31.4892	16.7	0.0465	17.0	0.0106	3.2	0.19	68.1	2.2	46.1	7.7	NA	NA	68.1	2.2
Spot 128	69	1587	1.3	25.5591	4.0	0.0578	4.5	0.0107	2.1	0.47	68.8	1.4	57.1	2.5	NA	NA	68.8	1.4

TABLE E2: U-TH-PB GEOCHRONOLOGIC ANALYSES

Analysis	U (ppm)	^{206}Pb ^{204}Pb	U/Th	$^{206}Pb^*$ $^{207}Pb^*$	± (%)	Isotope Ratios $^{207}Pb^*$ $^{235}U^*$	± (%)	$^{206}Pb^*$ ^{238}U	± (%)	Error Corr.	Apparent Ages (Ma) $^{206}Pb^*$ $^{238}U^*$	± (Ma)	$^{207}Pb^*$ ^{235}U	± (Ma)	$^{206}Pb^*$ $^{207}Pb^*$	± (Ma)	Best Age (Ma)	± (Ma)
Spot 38	304	8426	2.5	21.4496	1.6	0.0705	2.8	0.0110	2.3	0.82	70.4	1.6	69.2	1.9	29.8	38.6	70.4	1.6
Spot 157	157	2317	1.0	21.1606	2.0	0.1764	2.9	0.0271	2.1	0.72	172.3	3.6	165.0	4.5	62.3	48.5	172.3	3.6
Spot 118	93	39139	1.8	17.1488	1.2	0.6662	2.4	0.0829	2.1	0.87	513.4	10.5	518.4	9.9	541.5	26.2	513.4	10.5
Spot 70	75	12298	1.2	11.2151	1.1	2.9405	3.0	0.2393	2.8	0.93	1383.0	35.1	1392.4	23.0	1407.7	21.4	1407.7	21.4
Spot 147	132	27908	2.8	10.1206	0.9	3.6340	2.3	0.2669	2.1	0.92	1524.8	29.1	1557.0	18.5	1601.7	16.6	1601.7	16.6
Spot 130	1088	118260	9.4	9.9966	1.0	3.1043	2.8	0.2252	2.6	0.93	1309.1	31.0	1433.8	21.5	1624.7	18.5	1624.7	18.5
Spot 141	831	108159	11.0	9.9610	0.7	3.5226	2.6	0.2546	2.5	0.96	1462.1	32.1	1532.3	20.2	1631.3	13.1	1631.3	13.1
Spot 133	247	47003	6.7	9.9282	0.8	4.0545	2.1	0.2921	2.0	0.93	1651.9	28.6	1645.2	17.2	1637.5	14.6	1637.5	14.6
Spot 33	518	96043	8.9	9.8966	0.9	3.9231	2.4	0.2817	2.2	0.93	1600.0	31.8	1618.5	19.6	1643.4	16.6	1643.4	16.6
Spot 44	205	95641	2.1	9.8557	1.0	4.2873	2.3	0.3066	2.0	0.91	1723.9	30.9	1690.9	18.6	1651.1	17.8	1651.1	17.8
Spot 11	490	143929	21.3	9.8423	0.7	4.0250	2.7	0.2874	2.6	0.97	1628.7	38.1	1639.3	22.2	1653.6	12.8	1653.6	12.8
Spot 65	87	8514	1.4	9.7972	1.0	4.2159	2.2	0.2997	2.0	0.89	1689.8	29.7	1677.1	18.3	1662.1	18.5	1662.1	18.5
Spot 152	741	1970764	12.4	9.7793	0.9	3.8099	2.6	0.2703	2.5	0.94	1542.5	33.6	1594.8	21.0	1665.5	16.6	1665.5	16.6
Spot 132	251	24378	2.7	9.7757	0.8	4.2832	2.0	0.3038	1.8	0.91	1710.2	26.7	1690.1	16.1	1666.1	15.0	1666.1	15.0
Spot 125	162	325991	1.9	9.7633	0.7	4.2696	2.0	0.3025	1.9	0.94	1703.5	28.4	1687.5	16.6	1668.5	12.5	1668.5	12.5
Spot 6	997	96775	8.2	9.7572	1.2	3.4591	2.5	0.2449	2.2	0.89	1412.1	27.8	1517.9	19.5	1669.7	21.3	1669.7	21.3
Spot 27	115	38868	2.7	9.7490	0.9	4.2351	3.2	0.2996	3.1	0.96	1689.2	46.5	1680.9	26.7	1671.2	15.7	1671.2	15.7
Spot 113	131	83190	2.0	9.7365	0.9	4.2493	2.3	0.3002	2.1	0.92	1692.3	30.8	1683.6	18.5	1673.6	16.5	1673.6	16.5
Spot 61	163	36261	1.8	9.7105	1.0	4.3631	2.2	0.3074	2.0	0.90	1728.0	30.6	1705.4	18.5	1678.5	17.9	1678.5	17.9
Spot 158	141	55363	2.4	9.6996	0.9	4.2401	2.1	0.2984	1.9	0.90	1683.4	27.9	1681.8	17.3	1680.6	17.2	1680.6	17.2
Spot 143	447	1675353	3.3	9.6798	0.8	4.1976	2.5	0.2948	2.4	0.95	1665.6	35.1	1673.5	20.7	1684.4	14.5	1684.4	14.5
Spot 7	224	200339	4.5	9.6795	0.8	4.3205	2.2	0.3034	2.1	0.93	1708.3	31.2	1697.3	18.3	1684.4	14.7	1684.4	14.7
Spot 122	72	33125	2.3	9.6779	1.0	4.3986	2.5	0.3089	2.3	0.91	1735.2	34.7	1712.1	20.7	1684.7	18.7	1684.7	18.7

TABLE E2: U-TH-PB GEOCHRONOLOGIC ANALYSES

Analysis	U (ppm)	^{206}Pb ^{204}Pb	U/Th	$^{206}Pb^*$ $^{207}Pb^*$	± (%)	Isotope Ratios $^{207}Pb^*$ $^{235}U^*$	± (%)	$^{206}Pb^*$ ^{238}U	± (%)	Error Corr.	Apparent Ages (Ma) $^{206}Pb^*$ $^{238}U^*$	± (Ma)	$^{207}Pb^*$ ^{235}U	± (Ma)	$^{206}Pb^*$ $^{207}Pb^*$	± (Ma)	Best Age (Ma)	± (Ma)
Spot 20	202	59892	2.0	9.6743	0.9	4.3315	2.4	0.3041	2.2	0.93	1711.4	33.0	1699.4	19.5	1685.4	15.9	1685.4	15.9
Spot 57	367	141682	2.6	9.6733	0.8	4.2809	2.3	0.3005	2.1	0.94	1693.6	31.7	1689.7	18.6	1685.6	13.9	1685.6	13.9
Spot 64	387	273203	8.2	9.6662	0.8	4.2847	2.2	0.3005	2.0	0.92	1693.9	30.0	1690.4	17.9	1687.0	15.4	1687.0	15.4
Spot 68	289	57778	8.2	9.6597	1.0	4.3712	2.4	0.3064	2.2	0.91	1722.9	33.3	1706.9	19.9	1688.2	18.0	1688.2	18.0
Spot 4	238	175487	4.1	9.6573	0.7	4.2064	2.1	0.2947	2.0	0.94	1665.2	29.0	1675.3	17.3	1688.7	13.2	1688.7	13.2
Spot 45	146	63385	2.4	9.6566	0.7	4.2030	2.1	0.2945	2.0	0.94	1663.9	29.6	1674.6	17.6	1688.8	13.4	1688.8	13.4
Spot 62	136	2066963	2.3	9.6506	0.9	4.0287	2.2	0.2821	2.0	0.90	1601.9	28.4	1640.0	18.0	1689.9	17.5	1689.9	17.5
Spot 120	364	137899	7.5	9.6476	0.9	4.1398	1.9	0.2898	1.7	0.89	1640.5	24.9	1662.2	15.9	1690.5	16.5	1690.5	16.5
Spot 131	616	66581	7.2	9.6428	0.9	3.8146	2.6	0.2669	2.4	0.94	1525.0	32.8	1595.8	20.8	1691.4	16.8	1691.4	16.8
Spot 154	267	790253	2.3	9.6422	0.8	4.4700	2.4	0.3127	2.2	0.94	1754.1	34.1	1725.4	19.7	1691.5	15.4	1691.5	15.4
Spot 12	159	34420	5.0	9.6303	0.8	4.3718	2.1	0.3055	2.0	0.93	1718.4	29.8	1707.0	17.5	1693.8	14.2	1693.8	14.2
Spot 23	171	104581	4.6	9.6284	1.0	4.2757	2.0	0.2987	1.8	0.88	1684.9	26.2	1688.7	16.6	1694.2	18.0	1694.2	18.0
Spot 29	385	39388	1.8	9.6257	1.2	3.8380	3.5	0.2681	3.3	0.94	1530.9	44.4	1600.7	27.9	1694.7	21.2	1694.7	21.2
Spot 40	195	31406	2.1	9.6193	0.9	4.3102	2.7	0.3008	2.6	0.95	1695.5	38.7	1695.3	22.6	1695.9	16.0	1695.9	16.0
Spot 151	178	107219	2.3	9.6042	1.0	4.3309	2.1	0.3018	1.9	0.89	1700.3	28.6	1699.3	17.7	1698.8	18.0	1698.8	18.0
Spot 121	70	1257970	2.9	9.6013	0.8	4.2630	2.3	0.2970	2.2	0.94	1676.4	32.6	1686.3	19.2	1699.4	14.3	1699.4	14.3
Spot 13	322	95105	1.3	9.5978	0.8	4.2864	2.1	0.2985	2.0	0.94	1683.9	29.6	1690.8	17.6	1700.1	13.9	1700.1	13.9
Spot 49	140	413948	2.9	9.5969	1.0	4.2623	2.4	0.2968	2.2	0.91	1675.4	32.9	1686.1	20.0	1700.2	18.2	1700.2	18.2
Spot 37	287	160810	1.7	9.5948	1.0	4.2607	2.6	0.2966	2.4	0.92	1674.5	34.7	1685.8	21.1	1700.6	18.9	1700.6	18.9
Spot 114	252	39375	3.9	9.5944	0.8	4.3254	2.4	0.3011	2.3	0.95	1696.8	33.6	1698.2	19.6	1700.7	13.8	1700.7	13.8
Spot 1	264	114316	7.8	9.5888	1.1	4.3677	3.0	0.3039	2.8	0.93	1710.5	41.4	1706.3	24.5	1701.8	20.5	1701.8	20.5
Spot 16	135	250834	2.9	9.5771	1.0	4.3194	2.5	0.3002	2.4	0.93	1692.1	35.1	1697.1	21.0	1704.0	17.5	1704.0	17.5
Spot 129	183	21073	2.0	9.5752	0.8	4.1970	2.3	0.2916	2.1	0.93	1649.5	30.5	1673.4	18.6	1704.4	15.6	1704.4	15.6
Spot 67	216	86193	1.3	9.5706	1.0	4.3106	2.5	0.2993	2.3	0.92	1688.0	34.5	1695.4	20.8	1705.3	18.3	1705.3	18.3

TABLE E2: U-TH-PB GEOCHRONOLOGIC ANALYSES

Analysis	U (ppm)	$^{206}Pb/^{204}Pb$	U/Th	$^{206}Pb^*/^{207}Pb^*$	± (%)	Isotope Ratios $^{207}Pb^*/^{235}U^*$	± (%)	$^{206}Pb^*/^{238}U$	± (%)	Error Corr.	Apparent Ages (Ma) $^{206}Pb^*/^{238}U^*$	± (Ma)	$^{207}Pb^*/^{235}U$	± (Ma)	$^{206}Pb^*/^{207}Pb^*$	± (Ma)	Best Age (Ma)	± (Ma)
Spot 41	128	40870	2.2	9.5687	0.7	4.3164	2.6	0.2997	2.5	0.97	1689.7	37.5	1696.5	21.5	1705.7	12.2	1705.7	12.2
Spot 142	195	65546	3.0	9.5597	0.7	4.3988	2.2	0.3051	2.1	0.94	1716.6	31.1	1712.1	18.1	1707.4	13.4	1707.4	13.4
Spot 134	256	242451	3.9	9.5356	0.9	4.1659	2.3	0.2882	2.1	0.92	1632.7	30.8	1667.3	19.0	1712.0	16.5	1712.0	16.5
Spot 39	175	141242	2.5	9.5309	0.8	4.3145	2.5	0.2984	2.4	0.95	1683.2	35.5	1696.1	20.8	1712.9	14.7	1712.9	14.7
Spot 146	379	195366	5.6	9.5189	1.1	4.1011	2.9	0.2833	2.7	0.93	1607.7	38.2	1654.5	23.6	1715.3	19.7	1715.3	19.7
Spot 119	155	25604	1.8	9.5067	0.9	4.2371	2.6	0.2923	2.5	0.94	1652.9	36.2	1681.2	21.8	1717.6	16.9	1717.6	16.9
Spot 43	217	49373	3.7	9.4914	0.7	4.3533	1.9	0.2998	1.8	0.93	1690.3	26.7	1703.5	16.0	1720.6	13.5	1720.6	13.5
Spot 150	64	50620	1.8	9.4888	0.9	4.1253	2.4	0.2840	2.3	0.93	1611.6	32.5	1659.3	19.9	1721.1	16.0	1721.1	16.0
Spot 36	140	24878	1.7	9.4788	0.9	4.3279	2.3	0.2977	2.1	0.92	1679.7	31.1	1698.7	18.9	1723.0	16.9	1723.0	16.9
Spot 5	202	97351	3.7	9.4464	0.7	4.3595	2.4	0.2988	2.3	0.95	1685.4	34.2	1704.7	20.0	1729.3	13.3	1729.3	13.3
Spot 19	155	4384	2.3	8.9879	1.2	4.3079	2.4	0.2809	2.1	0.87	1596.1	29.9	1694.9	20.1	1820.1	22.1	1820.1	22.1
SDA																		
Spot 14	63	504	0.8	74.4211	111.4	0.0090	111.5	0.0049	3.5	0.03	31.4	1.1	9.1	10.1	NA	NA	31.4	1.1
Spot 110	57	344	0.9	60.1897	135.5	0.0113	135.5	0.0049	3.7	0.03	31.7	1.2	11.4	15.3	NA	NA	31.7	1.2
Spot 88	98	449	0.7	48.6943	29.9	0.0140	30.1	0.0049	3.2	0.11	31.7	1.0	14.1	4.2	NA	NA	31.7	1.0
Spot 25	43	628	0.8	21.6291	8.9	0.0315	9.5	0.0049	3.3	0.35	31.8	1.1	31.5	3.0	9.8	215.6	31.8	1.1
Spot 81	80	325	1.0	190.6888	151.1	0.0036	151.1	0.0049	2.6	0.02	31.8	0.8	3.6	5.5	NA	NA	31.8	0.8
Spot 98	91	578	0.8	40.5810	22.2	0.0169	22.4	0.0050	2.8	0.12	32.0	0.9	17.0	3.8	NA	NA	32.0	0.9
Spot 11	86	2553	0.7	25.2850	5.3	0.0273	6.0	0.0050	2.9	0.48	32.2	0.9	27.4	1.6	NA	NA	32.2	0.9
Spot 79	97	610	0.9	35.0867	20.4	0.0198	20.6	0.0050	2.5	0.12	32.4	0.8	19.9	4.1	NA	NA	32.4	0.8
Spot 5	51	3575	0.8	24.0564	4.8	0.0289	5.7	0.0050	3.2	0.55	32.4	1.0	28.9	1.6	NA	NA	32.4	1.0
Spot 6	48	2824	1.1	18.591	7.2	0.0375	7.9	0.0051	3.3	0.41	32.5	1.1	37.3	2.9	362.1	163.2	32.5	1.1

TABLE E2: U-TH-PB GEOCHRONOLOGIC ANALYSES

Analysis	U (ppm)	$^{206}Pb/^{204}Pb$	U/Th	$^{206}Pb^*/^{207}Pb^*$	± (%)	Isotope Ratios $^{207}Pb^*/^{235}U^*$	± (%)	$^{206}Pb^*/^{238}U$	± (%)	Error Corr.	Apparent Ages (Ma) $^{206}Pb^*/^{238}U^*$	± (Ma)	$^{207}Pb^*/^{235}U$	± (Ma)	$^{206}Pb^*/^{207}Pb^*$	± (Ma)	Best Age (Ma)	± (Ma)
Spot 73	83	807	1.1	30.6587	23.1	0.0228	23.4	0.0051	3.4	0.15	32.6	1.1	22.9	5.3	NA	NA	32.6	1.1
Spot 46	116	1097	0.8	26.5745	16.8	0.0264	17.1	0.0051	2.9	0.17	32.7	0.9	26.5	4.5	NA	NA	32.7	0.9
Spot 54	369	2025	0.5	23.2386	2.9	0.0303	4.1	0.0051	2.9	0.70	32.9	0.9	30.3	1.2	NA	NA	32.9	0.9
Spot 93	146	477	0.7	54.8183	88.2	0.0129	88.2	0.0051	2.5	0.03	32.9	0.8	13.0	11.4	NA	NA	32.9	0.8
Spot 13	433	3296	0.6	21.6932	2.6	0.0326	3.3	0.0051	2.1	0.63	33.0	0.7	32.6	1.1	2.7	62.5	33.0	0.7
Spot 53	127	807	0.7	33.1395	27.2	0.0214	27.3	0.0051	3.1	0.11	33.1	1.0	21.5	5.8	NA	NA	33.1	1.0
Spot 94	34	351	0.9	614.4261	103.1	0.0012	103.2	0.0052	4.0	0.04	33.2	1.3	1.2	1.2	NA	NA	33.2	1.3
Spot 36	134	621	1.0	39.1682	5.5	0.0182	6.4	0.0052	3.3	0.51	33.2	1.1	18.3	1.2	NA	NA	33.2	1.1
Spot 31	690	4234	0.6	21.3478	2.2	0.0334	3.4	0.0052	2.6	0.76	33.3	0.9	33.4	1.1	41.3	52.4	33.3	0.9
Spot 33	157	1018	1.0	29.5318	7.8	0.0242	8.4	0.0052	3.2	0.38	33.3	1.1	24.3	2.0	NA	NA	33.3	1.1
Spot 45	218	728	1.1	30.4712	5.6	0.0235	6.2	0.0052	2.8	0.44	33.3	0.9	23.5	1.5	NA	NA	33.3	0.9
Spot 99	50	839	0.9	27.3692	9.1	0.0262	9.6	0.0052	3.1	0.33	33.5	1.0	26.3	2.5	NA	NA	33.5	1.0
Spot 34	327	1120	0.9	28.1523	3.9	0.0255	4.9	0.0052	2.8	0.59	33.5	1.0	25.6	1.2	NA	NA	33.5	1.0
Spot 50	86	572	1.0	37.9172	29.0	0.0190	29.7	0.0052	6.3	0.21	33.6	2.1	19.1	5.6	NA	NA	33.6	2.1
Spot 20	18	2034	0.8	29.1337	6.6	0.0248	8.3	0.0052	5.0	0.60	33.7	1.7	24.9	2.0	NA	NA	33.7	1.7
Spot 40	1133	123149	0.6	20.2115	1.2	0.0359	2.6	0.0053	2.3	0.89	33.8	0.8	35.8	0.9	170.5	27.2	33.8	0.8
Spot 39	108	3142	0.8	19.6779	3.5	0.0370	4.7	0.0053	3.1	0.67	33.9	1.1	36.9	1.7	232.6	80.2	33.9	1.1
Spot 102	666	3349	0.7	21.8507	2.8	0.0333	3.4	0.0053	2.0	0.58	34.0	0.7	33.3	1.1	NA	NA	34.0	0.7
Spot 72	152	7578	0.6	19.927	3.1	0.0366	4.3	0.0053	3.0	0.69	34.0	1.0	36.5	1.5	203.4	72.4	34.0	1.0

TABLE E2: U-TH-PB GEOCHRONOLOGIC ANALYSES

						Isotope Ratios					Apparent Ages (Ma)						Best Age	
Analysis	U (ppm)	$^{206}Pb/^{204}Pb$	U/Th	$^{206}Pb^*/^{207}Pb^*$	± (%)	$^{207}Pb^*/^{235}U^*$	± (%)	$^{206}Pb^*/^{238}U$	± (%)	Error Corr.	$^{206}Pb^*/^{238}U^*$	± (Ma)	$^{207}Pb^*/^{235}U$	± (Ma)	$^{206}Pb^*/^{207}Pb^*$	± (Ma)	(Ma)	± (Ma)
Spot 48	106	1152	0.7	15.0791	10.9	0.0484	11.3	0.0053	2.8	0.25	34.0	1.0	48.0	5.3	816.4	229.2	34.0	1.0
Spot 43	435	4483	0.7	20.5726	3.8	0.0355	4.4	0.0053	2.3	0.52	34.1	0.8	35.4	1.5	129.0	89.0	34.1	0.8
Spot 66	609	11366	0.5	20.6832	1.7	0.0353	3.0	0.0053	2.5	0.82	34.1	0.8	35.2	1.1	116.3	40.8	34.1	0.8
Spot 63	147	1691	0.8	21.3045	5.0	0.0344	5.8	0.0053	3.0	0.52	34.2	1.0	34.3	2.0	46.1	119.8	34.2	1.0
Spot 68	543	36367	0.8	20.1690	1.5	0.0365	2.9	0.0053	2.4	0.84	34.3	0.8	36.4	1.0	175.4	35.9	34.3	0.8
Spot 83	140	8969	0.9	19.7857	3.8	0.0376	4.4	0.0054	2.2	0.50	34.7	0.7	37.4	1.6	220.0	87.4	34.7	0.7
Spot 103	107	42622	0.7	18.4319	4.1	0.0403	4.9	0.0054	2.8	0.57	34.7	1.0	40.1	1.9	381.6	91.7	34.7	1.0
Spot 37	1288	5749	2.5	20.2076	1.6	0.0370	2.9	0.0054	2.4	0.84	34.9	0.8	36.9	1.0	170.9	36.7	34.9	0.8
Spot 97	126	52927	0.8	16.5779	4.6	0.0452	5.4	0.0054	2.9	0.54	34.9	1.0	44.9	2.4	615.1	98.5	34.9	1.0
Spot 41	128	943	0.7	24.9268	9.4	0.0301	9.9	0.0055	3.1	0.32	35.1	1.1	30.2	2.9	NA	NA	35.1	1.1
Spot 26	1028	10346	0.9	20.3628	1.5	0.0371	2.7	0.0055	2.2	0.82	35.2	0.8	37.0	1.0	153.0	35.9	35.2	0.8
Spot 29	329	33840	1.2	20.2958	1.8	0.0374	3.3	0.0055	2.8	0.84	35.4	1.0	37.3	1.2	160.7	41.7	35.4	1.0
Spot 55	540	14675	0.6	18.3980	1.6	0.0413	3.0	0.0055	2.6	0.86	35.4	0.9	41.1	1.2	385.7	35.4	35.4	0.9
Spot 24	129	1231	0.5	21.8609	9.1	0.0350	9.5	0.0056	2.9	0.31	35.7	1.0	34.9	3.3	NA	NA	35.7	1.0
Spot 44	382	3217	1.1	19.2788	3.3	0.0402	4.1	0.0056	2.5	0.61	36.1	0.9	40.0	1.6	279.7	75.1	36.1	0.9
Spot 12	170	73333	0.8	18.9926	2.3	0.0410	3.6	0.0057	2.7	0.76	36.4	1.0	40.8	1.4	313.9	53.1	36.4	1.0
Spot 92	423	35833	0.8	19.1282	1.2	0.0409	2.8	0.0057	2.5	0.91	36.5	0.9	40.7	1.1	297.6	27.1	36.5	0.9
Spot 109	619	9046	0.7	20.7081	1.8	0.0379	3.3	0.0057	2.7	0.83	36.6	1.0	37.7	1.2	113.5	43.6	36.6	1.0
Spot 4	255	23529	0.9	16.166	2.8	0.0489	3.5	0.0057	2.2	0.61	36.9	0.8	48.5	1.7	669.1	60.3	36.9	0.8

TABLE E2: U-TH-PB GEOCHRONOLOGIC ANALYSES

Analysis	U (ppm)	^{206}Pb ^{204}Pb	U/Th	$^{206}Pb^*$ $^{207}Pb^*$	± (%)	Isotope Ratios $^{207}Pb^*$ $^{235}U^*$	± (%)	$^{206}Pb^*$ ^{238}U	± (%)	Error Corr.	Apparent Ages (Ma) $^{206}Pb^*$ $^{238}U^*$	± (Ma)	$^{207}Pb^*$ ^{235}U	± (Ma)	$^{206}Pb^*$ $^{207}Pb^*$	± (Ma)	Best Age (Ma)	± (Ma)
Spot 32	95	10420	0.9	18.2015	4.2	0.0436	5.4	0.0058	3.5	0.64	37.1	1.3	43.4	2.3	409.8	93.3	37.1	1.3
Spot 75	212	27926	0.9	19.1440	3.0	0.0419	4.2	0.0058	3.0	0.70	37.4	1.1	41.7	1.7	295.8	68.1	37.4	1.1
Spot 38	256	5513	1.5	11.6008	2.0	0.3000	4.6	0.0252	4.1	0.90	160.7	6.5	266.4	10.8	1342.7	39.4	160.7	6.5
Spot 84	199	6290	1.7	12.0148	1.1	0.3781	2.9	0.0330	2.7	0.92	209.1	5.5	325.7	8.1	1274.6	21.8	209.1	5.5
Spot 80	950	158286	18.9	11.5155	0.9	2.9476	2.8	0.2463	2.7	0.95	1419.3	33.8	1394.2	21.2	1356.9	16.9	1356.9	16.9
Spot 47	243	107382	6.1	11.3266	1.1	2.8340	2.6	0.2329	2.4	0.91	1349.7	29.1	1364.6	19.6	1388.7	20.3	1388.7	20.3
Spot 16	71	27288	1.2	11.2665	0.7	2.9815	2.4	0.2437	2.3	0.96	1406.1	29.2	1402.9	18.4	1398.9	13.6	1398.9	13.6
Spot 87	367	274629	4.9	11.2240	0.8	2.9482	2.9	0.2401	2.8	0.96	1387.2	34.3	1394.4	21.8	1406.2	15.7	1406.2	15.7
Spot 3	148	32279	1.5	11.2214	1.0	3.0411	2.4	0.2476	2.2	0.91	1426.1	27.9	1418.0	18.3	1406.6	19.0	1406.6	19.0
Spot 108	228	26007	1.3	11.2020	0.8	3.0786	2.9	0.2502	2.8	0.96	1439.6	35.7	1427.4	22.0	1409.9	15.0	1409.9	15.0
Spot 78	214	153031	4.7	11.1760	0.9	3.0216	2.6	0.2450	2.5	0.94	1412.8	31.5	1413.1	20.2	1414.4	17.3	1414.4	17.3
Spot 1	240	69929	1.8	11.1561	1.3	3.0721	2.6	0.2487	2.3	0.88	1431.6	29.9	1425.8	20.3	1417.8	24.1	1417.8	24.1
Spot 91	308	31155	1.5	11.1362	0.9	3.1070	3.1	0.2511	3.0	0.96	1443.9	38.7	1434.4	24.0	1421.2	17.4	1421.2	17.4
Spot 42	101	38363	2.1	11.1192	0.9	3.0201	2.7	0.2437	2.6	0.95	1405.7	32.5	1412.7	20.7	1424.1	16.3	1424.1	16.3
Spot 7	61	31845	1.6	11.1128	1.1	3.0838	2.3	0.2487	2.1	0.89	1431.5	26.9	1428.7	18.0	1425.2	20.2	1425.2	20.2
Spot 35	434	122965	2.3	11.1108	0.9	3.0848	2.3	0.2487	2.1	0.92	1431.7	27.4	1428.9	17.8	1425.6	17.1	1425.6	17.1
Spot 8	522	89335	1.8	11.0752	0.9	3.0659	2.0	0.2464	1.8	0.89	1419.7	22.8	1424.2	15.4	1431.7	17.4	1431.7	17.4
Spot 101	59	35296	1.8	11.0171	0.9	2.9955	2.6	0.2395	2.5	0.93	1383.9	30.7	1406.5	20.1	1441.7	18.1	1441.7	18.1
Spot 89	104	91028	1.6	10.944	0.9	3.1540	2.3	0.2505	2.1	0.91	1440.8	26.7	1446.0	17.5	1454.4	17.6	1454.4	17.6

TABLE E2: U-TH-PB GEOCHRONOLOGIC ANALYSES

Analysis	U (ppm)	^{206}Pb ^{204}Pb	U/Th	$^{206}Pb^*$ $^{207}Pb^*$	± (%)	Isotope Ratios $^{207}Pb^*$ $^{235}U^*$	± (%)	$^{206}Pb^*$ ^{238}U	± (%)	Error Corr.	Apparent Ages (Ma) $^{206}Pb^*$ $^{238}U^*$	± (Ma)	$^{207}Pb^*$ ^{235}U	± (Ma)	$^{206}Pb^*$ $^{207}Pb^*$	± (Ma)	Best Age (Ma)	± (Ma)
Spot 58	331	39809	1.2	10.9426	1.0	3.1251	3.0	0.2481	2.8	0.95	1428.8	36.2	1438.9	23.0	1454.6	18.3	1454.6	18.3
Spot 21	96	39372	1.5	10.9033	0.8	3.0903	2.6	0.2445	2.5	0.95	1410.0	31.3	1430.3	20.1	1461.5	16.0	1461.5	16.0
Spot 15	579	74267	22.2	10.6919	0.8	3.2758	2.5	0.2541	2.4	0.95	1459.8	31.1	1475.3	19.4	1498.6	14.3	1498.6	14.3
Spot 86	439	15130	1.4	10.6870	1.2	3.1802	2.9	0.2466	2.7	0.91	1420.9	34.3	1452.4	22.8	1499.5	22.7	1499.5	22.7
Spot 100	48	46496	1.4	10.2448	1.1	3.3994	3.1	0.2527	2.9	0.94	1452.3	37.5	1504.3	24.1	1578.9	19.9	1578.9	19.9
Spot 90	720	573204	22.4	9.9623	0.8	3.7591	2.3	0.2717	2.1	0.93	1549.6	29.4	1584.1	18.4	1631.1	15.4	1631.1	15.4
Spot 18	354	223527	3.9	9.8455	0.9	3.9693	2.5	0.2836	2.4	0.94	1609.2	33.8	1627.9	20.5	1653.0	15.9	1653.0	15.9
Spot 67	126	37028	4.8	9.8430	0.9	4.2920	2.7	0.3065	2.5	0.94	1723.6	37.9	1691.8	21.9	1653.4	16.7	1653.4	16.7
Spot 71	128	31040	3.6	9.6050	1.1	4.4020	3.2	0.3068	3.1	0.95	1724.9	46.2	1712.7	26.7	1698.7	19.4	1698.7	19.4
Spot 107	193	164201	2.9	9.5995	1.0	4.4263	2.5	0.3083	2.4	0.93	1732.4	35.7	1717.3	21.1	1699.7	17.8	1699.7	17.8
Spot 17	118	158804	3.9	9.5902	0.8	4.4457	2.0	0.3094	1.8	0.91	1737.5	28.0	1720.9	16.7	1701.5	15.5	1701.5	15.5
Spot 96	135	228867	3.4	9.5423	0.8	4.4516	2.5	0.3082	2.4	0.95	1731.9	36.3	1722.0	21.0	1710.7	15.2	1710.7	15.2
Spot 19	94	131688	4.2	9.5421	0.9	4.5898	2.7	0.3178	2.5	0.94	1778.9	39.0	1747.4	22.2	1710.8	16.7	1710.8	16.7
Spot 95	159	48690	3.7	9.5374	1.0	4.4125	2.4	0.3054	2.2	0.92	1717.8	33.3	1714.7	19.9	1711.7	17.6	1711.7	17.6
Spot 10	102	24150	4.4	9.5349	1.1	4.4802	2.8	0.3100	2.6	0.92	1740.5	39.5	1727.3	23.4	1712.2	20.4	1712.2	20.4
Spot 85	334	197236	1.8	9.5213	0.9	4.3899	2.7	0.3033	2.5	0.95	1707.5	38.1	1710.4	22.2	1714.8	15.9	1714.8	15.9
Spot 106	279	95636	1.3	9.5203	0.9	4.3558	1.9	0.3009	1.7	0.89	1695.7	25.9	1704.0	16.1	1715.0	16.3	1715.0	16.3
Spot 64	111	29193	4.0	9.5131	0.8	4.3804	2.0	0.3024	1.9	0.93	1703.0	28.3	1708.6	16.8	1716.4	13.9	1716.4	13.9
Spot 52	207	33051	2.9	9.5017	0.8	4.4927	2.5	0.3097	2.3	0.94	1739.4	35.3	1729.6	20.4	1718.6	14.8	1718.6	14.8
Spot 30	131	23980	3.1	9.4839	1.1	4.4621	2.6	0.3070	2.4	0.91	1726.2	35.8	1723.9	21.5	1722.0	19.5	1722.0	19.5
Spot 65	218	1082582	2.7	9.4809	0.8	4.3653	2.3	0.3003	2.1	0.93	1692.8	31.4	1705.8	18.8	1722.6	15.6	1722.6	15.6
Spot 23	176	81420	3.2	9.4731	0.7	4.5922	2.2	0.3156	2.1	0.94	1768.4	32.8	1747.9	18.7	1724.1	13.5	1724.1	13.5

TABLE E2: U-TH-PB GEOCHRONOLOGIC ANALYSES

Analysis	U (ppm)	$^{206}Pb/^{204}Pb$	U/Th	$^{206}Pb^*/^{207}Pb^*$	± (%)	Isotope Ratios $^{207}Pb^*/^{235}U^*$	± (%)	$^{206}Pb^*/^{238}U$	± (%)	Error Corr.	Apparent Ages (Ma) $^{206}Pb^*/^{238}U^*$	± (Ma)	$^{207}Pb^*/^{235}U$	± (Ma)	$^{206}Pb^*/^{207}Pb^*$	± (Ma)	Best Age (Ma)	± (Ma)
Spot 70	124	66034	3.7	9.4615	0.8	4.4462	2.4	0.3052	2.3	0.94	1717.2	34.2	1721.0	20.1	1726.4	15.4	1726.4	15.4
Spot 60	347	41781	7.7	9.4566	1.1	4.2841	2.7	0.2940	2.5	0.92	1661.3	36.6	1690.3	22.4	1727.3	19.9	1727.3	19.9
Spot 56	122	30466	3.5	9.4493	1.0	4.4409	2.9	0.3045	2.7	0.94	1713.5	40.8	1720.0	23.9	1728.7	17.7	1728.7	17.7
Spot 74	208	14523875	2.7	9.4345	1.3	4.6047	2.6	0.3152	2.3	0.87	1766.3	35.5	1750.1	22.0	1731.6	23.4	1731.6	23.4
Spot 76	199	36145	2.9	9.4106	0.9	4.4489	2.1	0.3038	1.9	0.92	1710.0	29.3	1721.5	17.6	1736.3	15.7	1736.3	15.7
Spot 62	104	51429	3.6	9.3823	1.0	4.4933	2.6	0.3059	2.4	0.92	1720.4	36.8	1729.7	22.0	1741.8	18.7	1741.8	18.7
Spot 28	151	39483	3.5	9.3803	0.7	4.5159	2.3	0.3074	2.2	0.95	1727.7	33.3	1733.9	19.3	1742.2	13.6	1742.2	13.6
Spot 9	151	112505	3.1	9.3419	0.8	4.5310	2.4	0.3071	2.3	0.94	1726.6	34.3	1736.7	20.0	1749.7	14.9	1749.7	14.9
Spot 104	353	324847	1.6	9.3291	0.9	4.3800	2.2	0.2965	2.0	0.91	1673.8	29.0	1708.6	17.8	1752.2	16.0	1752.2	16.0
Spot 61	167	32633	3.5	9.3193	0.8	4.4605	2.2	0.3016	2.0	0.92	1699.3	29.9	1723.7	18.0	1754.1	15.3	1754.1	15.3
Spot 77	145	98693	3.3	9.3189	0.9	4.4102	2.4	0.2982	2.2	0.93	1682.4	32.9	1714.3	19.9	1754.2	16.6	1754.2	16.6
Spot 22	295	84213	2.7	9.3087	0.9	4.4796	2.1	0.3026	1.9	0.90	1704.0	27.9	1727.2	17.2	1756.2	16.5	1756.2	16.5
Spot 27	196	3508	3.9	8.8189	1.2	4.6248	3.3	0.2959	3.1	0.93	1671.1	45.5	1753.8	27.6	1854.5	21.5	1854.5	21.5
Spot 2	186	33703	4.2	8.6757	1.1	4.8298	3.2	0.3040	3.0	0.94	1711.3	45.8	1790.1	27.2	1884.0	19.4	1884.0	19.4
Spot 51	587	112583	1.7	6.2151	0.8	10.9235	2.4	0.4926	2.2	0.94	2582.0	47.2	2516.6	22.0	2465.1	13.9	2465.1	13.9
HOW-01																		
Spot 66	343	2162	1.3	24.3397	3.8	0.0234	4.8	0.0041	3.0	0.62	26.6	0.8	23.5	1.1	NA	NA	26.6	0.8
Spot 90	319	994	2.1	30.7338	15.2	0.0196	15.5	0.0044	2.7	0.18	28.1	0.8	19.7	3.0	NA	NA	28.1	0.8
Spot 87	69	206	1.0	43.7972	39.3	0.0149	39.5	0.0047	3.8	0.10	30.4	1.2	15.0	5.9	NA	NA	30.4	1.2
Spot 44	72	203	0.6	25.5919	51.1	0.0255	51.2	0.0047	3.2	0.06	30.4	1.0	25.6	12.9	NA	NA	30.4	1.0
Spot 29	59	200	0.7	34.8192	18.7	0.0188	18.9	0.0047	3.0	0.16	30.5	0.9	18.9	3.5	NA	NA	30.5	0.9
Spot 102	50	249	0.9	132.30	108.2	0.0050	108.	0.0048	3.7	0.03	31.0	1.1	5.1	5.5	NA	NA	31.0	1.1

TABLE E2: U-TH-PB GEOCHRONOLOGIC ANALYSES

Analysis	U (ppm)	$^{206}Pb/^{204}Pb$	U/Th	$^{206}Pb^*/^{207}Pb^*$	± (%)	Isotope Ratios $^{207}Pb^*/^{235}U^*$	± (%)	$^{206}Pb^*/^{238}U$	± (%)	Error Corr.	Apparent Ages (Ma) $^{206}Pb^*/^{238}U^*$	± (Ma)	$^{207}Pb^*/^{235}U$	± (Ma)	$^{206}Pb^*/^{207}Pb^*$	± (Ma)	Best Age (Ma)	± (Ma)
Spot 27	42	277	0.9	190.4381	70.9	0.0035	71.0	0.0048	3.6	0.05	31.0	1.1	3.5	2.5	NA	NA	31.0	1.1
Spot 67	43	381	0.8	73.0358	149.6	0.0091	149.7	0.0048	3.7	0.02	31.1	1.1	9.2	13.7	NA	NA	31.1	1.1
Spot 79	61	473	0.8	34.4087	27.9	0.0194	28.2	0.0048	4.5	0.16	31.1	1.4	19.5	5.5	NA	NA	31.1	1.4
Spot 89	57	679	0.9	26.7362	7.7	0.0253	8.7	0.0049	4.0	0.46	31.5	1.3	25.3	2.2	NA	NA	31.5	1.3
Spot 99	134	1762	1.0	31.4313	5.1	0.0215	6.0	0.0049	3.1	0.51	31.5	1.0	21.6	1.3	NA	NA	31.5	1.0
Spot 40	1443	5004	2.0	21.8352	1.4	0.0311	2.9	0.0049	2.5	0.87	31.6	0.8	31.0	0.9	NA	NA	31.6	0.8
Spot 42	43	629	0.6	34.8109	17.5	0.0195	17.9	0.0049	4.0	0.22	31.7	1.3	19.6	3.5	NA	NA	31.7	1.3
Spot 95	89	732	1.1	27.3687	6.6	0.0250	7.5	0.0050	3.6	0.48	31.9	1.1	25.1	1.9	NA	NA	31.9	1.1
Spot 65	100	710	0.7	32.5559	16.3	0.0210	16.7	0.0050	3.4	0.20	32.0	1.1	21.1	3.5	NA	NA	32.0	1.1
Spot 53	103	370	0.8	72.5240	30.8	0.0094	31.0	0.0050	2.9	0.09	32.0	0.9	9.5	2.9	NA	NA	32.0	0.9
Spot 68	399	1215	0.7	25.0954	10.8	0.0273	11.0	0.0050	2.3	0.21	32.0	0.7	27.4	3.0	NA	NA	32.0	0.7
Spot 75	205	533	1.0	51.4073	6.3	0.0134	6.6	0.0050	2.1	0.31	32.1	0.7	13.5	0.9	NA	NA	32.1	0.7
Spot 50	116	2114	0.8	27.7647	4.2	0.0249	5.0	0.0050	2.7	0.54	32.2	0.9	24.9	1.2	NA	NA	32.2	0.9
Spot 46	102	790	1.3	28.6508	6.5	0.0241	7.8	0.0050	4.3	0.55	32.2	1.4	24.2	1.9	NA	NA	32.2	1.4
Spot 104	48	560	0.8	73.7104	31.4	0.0094	31.7	0.0050	4.4	0.14	32.3	1.4	9.5	3.0	NA	NA	32.3	1.4
Spot 96	79	321	1.0	454.1426	575.6	0.0015	575.6	0.0050	3.2	0.01	32.4	1.0	1.6	8.9	NA	NA	32.4	1.0
Spot 34	86	2356	0.7	19.9634	5.4	0.0348	6.6	0.0050	3.7	0.57	32.4	1.2	34.8	2.3	199.3	126.6	32.4	1.2
Spot 55	157	1702	0.8	21.1993	4.5	0.0328	5.5	0.0050	3.1	0.56	32.5	1.0	32.8	1.8	57.9	107.7	32.5	1.0
Spot 83	425	4622	0.6	21.986	2.8	0.0317	4.2	0.0051	3.1	0.75	32.5	1.0	31.7	1.3	NA	NA	32.5	1.0

TABLE E2: U-TH-PB GEOCHRONOLOGIC ANALYSES

						Isotope Ratios					Apparent Ages (Ma)							
Analysis	U (ppm)	^{206}Pb ^{204}Pb	U/Th	$^{206}Pb^*$ $^{207}Pb^*$	± (%)	$^{207}Pb^*$ $^{235}U^*$	± (%)	$^{206}Pb^*$ ^{238}U	± (%)	Error Corr.	$^{206}Pb^*$ $^{238}U^*$	± (Ma)	$^{207}Pb^*$ ^{235}U	± (Ma)	$^{206}Pb^*$ $^{207}Pb^*$	± (Ma)	**Best Age** (Ma)	± (Ma)
Spot 86	267	718	0.6	36.2213	37.4	0.0192	37.6	0.0051	3.8	0.10	32.5	1.2	19.4	7.2	NA	NA	32.5	1.2
Spot 72	59	601	0.8	32.3815	9.9	0.0215	10.4	0.0051	3.1	0.30	32.5	1.0	21.6	2.2	NA	NA	32.5	1.0
Spot 47	38	2720	0.8	19.8245	7.3	0.0353	7.9	0.0051	3.0	0.37	32.6	1.0	35.2	2.7	215.4	170.0	32.6	1.0
Spot 36	227	820	0.6	30.6472	13.2	0.0229	13.5	0.0051	2.8	0.21	32.7	0.9	22.9	3.1	NA	NA	32.7	0.9
Spot 39	404	1985	0.7	23.5838	9.0	0.0297	9.5	0.0051	3.0	0.32	32.7	1.0	29.7	2.8	NA	NA	32.7	1.0
Spot 100	50	696	0.7	26.6019	7.0	0.0264	8.0	0.0051	4.0	0.50	32.8	1.3	26.5	2.1	NA	NA	32.8	1.3
Spot 70	36	314	1.0	110.6024	54.2	0.0064	54.4	0.0051	4.8	0.09	32.8	1.6	6.4	3.5	NA	NA	32.8	1.6
Spot 48	214	1834	0.5	22.8471	4.2	0.0308	4.9	0.0051	2.6	0.53	32.8	0.8	30.8	1.5	NA	NA	32.8	0.8
Spot 43	554	5861	0.7	21.4224	2.2	0.0329	3.6	0.0051	2.8	0.79	32.8	0.9	32.8	1.2	32.9	52.5	32.8	0.9
Spot 57	60	2383	0.7	19.8023	6.4	0.0356	7.4	0.0051	3.7	0.50	32.9	1.2	35.5	2.6	218.1	148.7	32.9	1.2
Spot 97	127	788	0.7	35.4369	19.2	0.0199	19.6	0.0051	3.6	0.18	32.9	1.2	20.0	3.9	NA	NA	32.9	1.2
Spot 52	142	1302	0.8	25.2951	4.3	0.0279	5.2	0.0051	3.1	0.58	32.9	1.0	27.9	1.4	NA	NA	32.9	1.0
Spot 64	91	576	0.5	51.8045	8.4	0.0136	9.1	0.0051	3.4	0.37	32.9	1.1	13.7	1.2	NA	NA	32.9	1.1
Spot 80	201	1050	0.6	30.3864	13.8	0.0232	14.0	0.0051	2.5	0.18	32.9	0.8	23.3	3.2	NA	NA	32.9	0.8
Spot 28	268	54062	0.7	21.3983	2.8	0.0331	3.4	0.0051	1.9	0.57	33.0	0.6	33.0	1.1	35.6	66.6	33.0	0.6
Spot 73	615	11785	1.0	21.6504	1.9	0.0327	3.0	0.0051	2.3	0.77	33.0	0.7	32.7	1.0	7.5	45.7	33.0	0.7
Spot 71	578	2192	0.7	24.2749	2.7	0.0292	3.7	0.0051	2.5	0.68	33.1	0.8	29.2	1.1	NA	NA	33.1	0.8
Spot 98	131	2496	0.7	21.8013	5.1	0.0326	6.0	0.0052	3.2	0.54	33.2	1.1	32.6	1.9	NA	NA	33.2	1.1
Spot 78	197	1294	0.9	25.788	5.7	0.0276	6.3	0.0052	2.7	0.43	33.2	0.9	27.6	1.7	NA	NA	33.2	0.9

TABLE E2: U-TH-PB GEOCHRONOLOGIC ANALYSES

						Isotope Ratios					Apparent Ages (Ma)						Best Age	
Analysis	U (ppm)	$^{206}Pb/^{204}Pb$	U/Th	$^{206}Pb^*/^{207}Pb^*$	± (%)	$^{207}Pb^*/^{235}U^*$	± (%)	$^{206}Pb^*/^{238}U$	± (%)	Error Corr.	$^{206}Pb^*/^{238}U^*$	± (Ma)	$^{207}Pb^*/^{235}U$	± (Ma)	$^{206}Pb^*/^{207}Pb^*$	± (Ma)	(Ma)	± (Ma)
Spot 92	100	2124	1.3	20.9465	5.7	0.0339	6.6	0.0052	3.3	0.50	33.2	1.1	33.9	2.2	86.5	136.4	33.2	1.1
Spot 37	108	1451	1.2	22.6361	5.7	0.0314	6.7	0.0052	3.4	0.51	33.2	1.1	31.4	2.1	NA	NA	33.2	1.1
Spot 74	94	2554	0.7	20.9831	5.3	0.0339	6.2	0.0052	3.2	0.52	33.2	1.1	33.9	2.1	82.3	125.0	33.2	1.1
Spot 63	666	16368	1.0	20.6931	1.6	0.0344	2.9	0.0052	2.4	0.83	33.2	0.8	34.4	1.0	115.3	38.5	33.2	0.8
Spot 94	599	3213	1.0	22.6382	2.3	0.0316	3.5	0.0052	2.7	0.76	33.3	0.9	31.5	1.1	NA	NA	33.3	0.9
Spot 33	200	1950	0.5	22.4667	7.2	0.0318	8.0	0.0052	3.5	0.44	33.3	1.2	31.8	2.5	NA	NA	33.3	1.2
Spot 103	240	6852	0.6	18.9673	2.6	0.0377	3.5	0.0052	2.3	0.67	33.3	0.8	37.6	1.3	316.8	58.3	33.3	0.8
Spot 105	186	6881	0.6	23.3711	3.0	0.0306	4.0	0.0052	2.5	0.64	33.4	0.8	30.6	1.2	NA	NA	33.4	0.8
Spot 41	881	33451	0.7	20.6725	1.7	0.0347	3.2	0.0052	2.8	0.85	33.5	0.9	34.7	1.1	117.6	39.8	33.5	0.9
Spot 101	39	4730	0.9	22.7059	6.7	0.0316	8.2	0.0052	4.7	0.57	33.5	1.6	31.6	2.6	NA	NA	33.5	1.6
Spot 107	405	8619	0.9	20.5490	1.9	0.0350	3.4	0.0052	2.8	0.83	33.5	0.9	34.9	1.2	131.7	43.8	33.5	0.9
Spot 25	50	908	0.9	26.4814	6.6	0.0272	7.6	0.0052	3.8	0.50	33.5	1.3	27.2	2.0	NA	NA	33.5	1.3
Spot 45	138	16195	1.0	19.5607	4.5	0.0368	5.6	0.0052	3.3	0.59	33.5	1.1	36.7	2.0	246.4	103.7	33.5	1.1
Spot 22	218	14654	0.6	21.2739	3.3	0.0338	4.4	0.0052	2.9	0.66	33.6	1.0	33.8	1.5	49.6	78.3	33.6	1.0
Spot 24	227	7761	0.7	19.9476	2.6	0.0361	3.7	0.0052	2.6	0.70	33.6	0.9	36.0	1.3	201.1	61.0	33.6	0.9
Spot 21	371	5600	0.6	22.1794	2.8	0.0325	4.0	0.0052	2.9	0.72	33.6	1.0	32.4	1.3	NA	NA	33.6	1.0
Spot 85	232	1356	0.6	27.7668	9.4	0.0259	9.9	0.0052	2.8	0.29	33.6	0.9	26.0	2.5	NA	NA	33.6	0.9
Spot 91	283	1984	0.6	25.7532	3.0	0.0280	3.6	0.0052	2.0	0.55	33.7	0.7	28.1	1.0	NA	NA	33.7	0.7
Spot 60	413	1721	0.5	24.697	2.8	0.0293	3.9	0.0053	2.8	0.71	33.8	0.9	29.4	1.1	NA	NA	33.8	0.9

TABLE E2: U-TH-PB GEOCHRONOLOGIC ANALYSES

Analysis	U (ppm)	^{206}Pb ^{204}Pb	U/Th	$^{206}Pb^*$ $^{207}Pb^*$	± (%)	Isotope Ratios $^{207}Pb^*$ $^{235}U^*$	± (%)	$^{206}Pb^*$ ^{238}U	± (%)	Error Corr.	Apparent Ages (Ma) $^{206}Pb^*$ $^{238}U^*$	± (Ma)	$^{207}Pb^*$ ^{235}U	± (Ma)	$^{206}Pb^*$ $^{207}Pb^*$	± (Ma)	Best Age (Ma)	± (Ma)
Spot 56	96	3989	1.2	20.5536	3.9	0.0353	4.9	0.0053	2.9	0.59	33.9	1.0	35.2	1.7	131.1	92.6	33.9	1.0
Spot 19	89	1198	1.0	25.1432	5.2	0.0289	5.9	0.0053	2.8	0.47	34.0	0.9	29.0	1.7	NA	NA	34.0	0.9
Spot 59	413	2019	1.3	24.1399	9.2	0.0302	9.6	0.0053	2.8	0.29	34.0	0.9	30.2	2.8	NA	NA	34.0	0.9
Spot 58	148	2866	0.7	22.6413	3.6	0.0322	4.8	0.0053	3.1	0.65	34.0	1.0	32.1	1.5	NA	NA	34.0	1.0
Spot 109	276	4059	0.7	20.5279	2.5	0.0355	3.3	0.0053	2.3	0.68	34.0	0.8	35.4	1.2	134.1	57.7	34.0	0.8
Spot 38	194	3102	0.8	22.1567	3.6	0.0330	4.2	0.0053	2.1	0.50	34.1	0.7	33.0	1.3	NA	NA	34.1	0.7
Spot 62	265	2180	0.8	23.8659	5.2	0.0307	6.0	0.0053	3.0	0.50	34.2	1.0	30.7	1.8	NA	NA	34.2	1.0
Spot 88	172	730	0.8	20.1108	7.0	0.0365	7.9	0.0053	3.6	0.46	34.2	1.2	36.4	2.8	182.1	164.4	34.2	1.2
Spot 35	96	1555	0.8	10.5700	10.2	0.0694	10.7	0.0053	3.0	0.28	34.2	1.0	68.1	7.0	1520.2	193.3	34.2	1.0
Spot 77	95	1378	0.6	23.2275	5.3	0.0317	6.2	0.0053	3.2	0.51	34.4	1.1	31.7	1.9	NA	NA	34.4	1.1
Spot 82	502	1029	1.1	10.9532	4.1	0.0679	4.6	0.0054	2.1	0.46	34.7	0.7	66.7	3.0	1452.8	78.3	34.7	0.7
Spot 69	254	11007	0.7	17.6376	2.7	0.0426	4.0	0.0055	3.0	0.75	35.1	1.1	42.4	1.7	479.8	59.1	35.1	1.1
Spot 54	35	911	1.3	30.9120	5.7	0.0447	6.6	0.0100	3.4	0.51	64.3	2.2	44.4	2.9	NA	NA	64.3	2.2
Spot 23	623	18764	2.2	20.6541	1.3	0.0842	2.4	0.0126	2.0	0.84	80.9	1.6	82.1	1.9	119.7	30.2	80.9	1.6
Spot 106	160	7859	0.8	21.0431	2.1	0.0830	3.3	0.0127	2.5	0.77	81.2	2.1	81.0	2.6	75.5	49.9	81.2	2.1
Spot 26	261	38677	1.6	19.9952	1.8	0.1831	3.0	0.0266	2.4	0.79	169.0	4.0	170.7	4.7	195.6	42.5	169.0	4.0
Spot 31	249	37050	2.0	11.1118	0.8	3.0064	2.6	0.2424	2.4	0.95	1399.1	30.6	1409.3	19.5	1425.4	15.5	1425.4	15.5
Spot 30	118	307318	1.8	11.0948	0.9	3.1290	2.3	0.2519	2.1	0.93	1448.2	27.7	1439.8	17.7	1428.3	16.4	1428.3	16.4
Spot 108	204	34534	3.8	9.6792	1.0	4.0434	3.1	0.2840	2.9	0.94	1611.3	41.3	1643.0	25.0	1684.5	18.6	1684.5	18.6

TABLE E2: U-TH-PB GEOCHRONOLOGIC ANALYSES

Analysis	U (ppm)	$^{206}Pb/^{204}Pb$	U/Th	$^{206}Pb^*/^{207}Pb^*$	± (%)	Isotope Ratios $^{207}Pb^*/^{235}U^*$	± (%)	$^{206}Pb^*/^{238}U$	± (%)	Error Corr.	Apparent Ages (Ma) $^{206}Pb^*/^{238}U^*$	± (Ma)	$^{207}Pb^*/^{235}U$	± (Ma)	$^{206}Pb^*/^{207}Pb^*$	± (Ma)	Best Age (Ma)	± (Ma)
Spot 51	395	8168	1.8	9.6737	0.7	3.8719	2.3	0.2718	2.1	0.95	1549.8	29.5	1607.8	18.3	1685.5	13.6	1685.5	13.6
Spot 32	47	36422	1.2	9.6108	0.9	4.2579	2.6	0.2969	2.5	0.94	1676.0	36.8	1685.3	21.8	1697.6	16.4	1697.6	16.4
Spot 20	127	43223	3.4	9.6073	1.0	4.3219	2.9	0.3013	2.7	0.94	1697.6	40.6	1697.5	23.9	1698.2	18.2	1698.2	18.2
Spot 61	218	40267	3.3	9.3930	0.9	4.5511	2.2	0.3102	2.0	0.92	1741.6	30.5	1740.4	18.1	1739.7	15.7	1739.7	15.7
Spot 76	118	175139	2.9	9.3917	1.1	4.4460	2.9	0.3030	2.7	0.93	1706.0	41.1	1720.9	24.4	1739.9	19.5	1739.9	19.5
Spot 49	213	25509	2.6	9.3909	1.0	4.3319	2.4	0.2952	2.2	0.91	1667.3	31.7	1699.5	19.6	1740.1	18.5	1740.1	18.5
Spot 86	787	3020	1.9	22.7766	2.1	0.0180	3.1	0.0030	2.3	0.75	19.1	0.4	18.1	0.6	NA	NA	19.1	0.4
Spot 21	809	34086	1.7	20.5435	1.6	0.0200	3.1	0.0030	2.7	0.86	19.2	0.5	20.1	0.6	132.3	37.3	19.2	0.5
Spot 17	133	6995	1.5	22.2247	3.2	0.0286	4.4	0.0046	3.0	0.68	29.6	0.9	28.6	1.3	NA	NA	29.6	0.9
Spot 89	1004	3584	1.7	22.4957	1.6	0.0292	2.6	0.0048	2.1	0.80	30.6	0.6	29.2	0.7	NA	NA	30.6	0.6
Spot 109	376	4591	1.0	19.8458	1.8	0.0335	3.3	0.0048	2.7	0.83	31.1	0.8	33.5	1.1	212.9	42.5	31.1	0.8
Spot 70	31	191	0.8	34.9889	45.9	0.0191	46.0	0.0048	3.6	0.08	31.2	1.1	19.2	8.7	NA	NA	31.2	1.1
Spot 20	1484	34715	3.0	20.7664	1.0	0.0323	2.8	0.0049	2.6	0.94	31.3	0.8	32.3	0.9	106.9	22.9	31.3	0.8
Spot 103	47	201	0.7	31.8939	14.1	0.0213	14.6	0.0049	3.6	0.25	31.7	1.1	21.4	3.1	NA	NA	31.7	1.1
Spot 66	534	5109	0.5	21.0470	2.2	0.0325	3.1	0.0050	2.2	0.70	31.9	0.7	32.5	1.0	75.1	52.2	31.9	0.7
Spot 60	735	7177	0.7	21.2545	2.6	0.0322	3.8	0.0050	2.7	0.73	32.0	0.9	32.2	1.2	51.7	61.9	32.0	0.9
Spot 95	88	204	0.8	43.8152	8.2	0.0157	8.9	0.0050	3.4	0.38	32.0	1.1	15.8	1.4	NA	NA	32.0	1.1
Spot 24	517	19845	1.3	20.3651	1.6	0.0338	2.8	0.0050	2.2	0.81	32.1	0.7	33.7	0.9	152.8	38.4	32.1	0.7
Spot 4	516	4278	1.2	21.3540	3.0	0.0323	3.7	0.0050	2.2	0.58	32.2	0.7	32.3	1.2	40.6	72.7	32.2	0.7
Spot 76	131	367	0.6	125.1280	22.9	0.0055	23.1	0.0050	2.8	0.12	32.3	0.9	5.6	1.3	NA	NA	32.3	0.9
Spot 92	65	475	0.8	58.107	43.8	0.0119	43.9	0.0050	3.5	0.08	32.3	1.1	12.0	5.3	NA	NA	32.3	1.1

TABLE E2: U-TH-PB GEOCHRONOLOGIC ANALYSES

Analysis	U (ppm)	$^{206}Pb/^{204}Pb$	U/Th	$^{206}Pb^*/^{207}Pb^*$	± (%)	Isotope Ratios $^{207}Pb^*/^{235}U^*$	± (%)	$^{206}Pb^*/^{238}U$	± (%)	Error Corr.	Apparent Ages (Ma) $^{206}Pb^*/^{238}U^*$	± (Ma)	$^{207}Pb^*/^{235}U$	± (Ma)	$^{206}Pb^*/^{207}Pb^*$	± (Ma)	Best Age (Ma)	± (Ma)
Spot 53	46	225	0.7	48.7120	16.7	0.0142	17.0	0.0050	3.2	0.19	32.3	1.0	14.3	2.4	NA	NA	32.3	1.0
Spot 61	78	318	0.8	169.7331	86.0	0.0041	86.1	0.0050	3.3	0.04	32.4	1.1	4.1	3.6	NA	NA	32.4	1.1
Spot 31	82	361	0.8	46.9856	7.1	0.0148	7.5	0.0050	2.4	0.32	32.4	0.8	14.9	1.1	NA	NA	32.4	0.8
Spot 3	126	689	1.0	38.8517	9.0	0.0179	9.5	0.0050	3.1	0.32	32.5	1.0	18.0	1.7	NA	NA	32.5	1.0
Spot 16	81	491	0.8	75.6853	13.3	0.0092	13.5	0.0051	2.4	0.18	32.5	0.8	9.3	1.2	NA	NA	32.5	0.8
Spot 5	335	3688	0.5	21.7088	1.9	0.0322	3.4	0.0051	2.8	0.83	32.6	0.9	32.1	1.1	1.0	45.7	32.6	0.9
Spot 74	55	367	0.7	103.0969	123.1	0.0068	123.1	0.0051	3.7	0.03	32.6	1.2	6.9	8.4	NA	NA	32.6	1.2
Spot 18	43	401	0.8	105.9884	60.4	0.0066	60.6	0.0051	4.3	0.07	32.7	1.4	6.7	4.0	NA	NA	32.7	1.4
Spot 2	864	3410	1.1	21.1163	1.8	0.0332	2.9	0.0051	2.3	0.80	32.7	0.8	33.1	1.0	67.2	42.0	32.7	0.8
Spot 40	45	815	0.9	27.3421	6.2	0.0256	6.8	0.0051	2.7	0.40	32.7	0.9	25.7	1.7	NA	NA	32.7	0.9
Spot 62	234	1986	1.0	24.1776	3.0	0.0291	4.0	0.0051	2.7	0.67	32.8	0.9	29.1	1.1	NA	NA	32.8	0.9
Spot 22	53	778	0.7	33.8498	12.1	0.0208	12.5	0.0051	3.4	0.27	32.9	1.1	20.9	2.6	NA	NA	32.9	1.1
Spot 79	75	475	0.9	36.9359	35.3	0.0191	35.5	0.0051	3.3	0.09	32.9	1.1	19.2	6.7	NA	NA	32.9	1.1
Spot 110	232	1134	0.6	26.9880	3.1	0.0261	4.5	0.0051	3.2	0.72	32.9	1.1	26.2	1.2	NA	NA	32.9	1.1
Spot 26	459	40848	1.2	20.3935	2.2	0.0346	3.3	0.0051	2.5	0.75	32.9	0.8	34.5	1.1	149.5	51.2	32.9	0.8
Spot 7	57	562	1.1	36.1829	10.5	0.0195	11.0	0.0051	3.2	0.29	32.9	1.1	19.6	2.1	NA	NA	32.9	1.1
Spot 51	107	651	0.6	43.9902	12.7	0.0160	13.0	0.0051	2.7	0.21	32.9	0.9	16.2	2.1	NA	NA	32.9	0.9
Spot 71	288	1148	0.6	26.8231	4.4	0.0264	5.4	0.0051	3.2	0.60	33.0	1.1	26.4	1.4	NA	NA	33.0	1.1
Spot 45	87	357	0.7	131.15	256.6	0.0054	256.	0.0051	2.8	0.01	33.0	0.9	5.5	14.0	NA	NA	33.0	0.9

TABLE E2: U-TH-PB GEOCHRONOLOGIC ANALYSES

Analysis	U (ppm)	$^{206}Pb/^{204}Pb$	U/Th	$^{206}Pb^*/^{207}Pb^*$	± (%)	Isotope Ratios $^{207}Pb^*/^{235}U^*$	± (%)	$^{206}Pb^*/^{238}U$	± (%)	Error Corr.	Apparent Ages (Ma) $^{206}Pb^*/^{238}U^*$	± (Ma)	$^{207}Pb^*/^{235}U$	± (Ma)	$^{206}Pb^*/^{207}Pb^*$	± (Ma)	Best Age (Ma)	± (Ma)
Spot 90	753	11974	1.0	21.1909	1.6	0.0335	2.5	0.0051	1.9	0.77	33.1	0.6	33.4	0.8	58.9	38.0	33.1	0.6
Spot 78	37	713	0.8	27.3550	6.4	0.0259	7.3	0.0052	3.4	0.47	33.1	1.1	26.0	1.9	NA	NA	33.1	1.1
Spot 30	261	2083	0.9	22.5339	2.5	0.0315	4.4	0.0052	3.6	0.82	33.1	1.2	31.5	1.4	NA	NA	33.1	1.2
Spot 54	223	737	0.5	23.5546	6.9	0.0302	7.4	0.0052	2.8	0.38	33.2	0.9	30.2	2.2	NA	NA	33.2	0.9
Spot 43	389	8582	0.6	21.6032	2.1	0.0331	3.1	0.0052	2.3	0.75	33.3	0.8	33.0	1.0	12.7	49.8	33.3	0.8
Spot 28	184	1459	0.8	26.4073	7.9	0.0271	8.4	0.0052	2.9	0.34	33.3	1.0	27.1	2.3	NA	NA	33.3	1.0
Spot 65	103	798	0.5	35.2713	33.6	0.0203	33.6	0.0052	2.0	0.06	33.4	0.7	20.4	6.8	NA	NA	33.4	0.7
Spot 10	407	6309	1.8	21.4989	2.1	0.0333	3.2	0.0052	2.4	0.75	33.4	0.8	33.3	1.1	24.3	51.4	33.4	0.8
Spot 85	70	1190	0.8	22.8796	8.4	0.0313	8.9	0.0052	2.9	0.32	33.4	1.0	31.3	2.7	NA	NA	33.4	1.0
Spot 12	61	518	0.6	40.4649	12.4	0.0177	12.7	0.0052	2.9	0.23	33.5	1.0	17.8	2.2	NA	NA	33.5	1.0
Spot 69	129	1227	0.6	27.2318	5.4	0.0263	6.5	0.0052	3.7	0.57	33.5	1.2	26.4	1.7	NA	NA	33.5	1.2
Spot 11	150	4773	1.0	21.7724	3.2	0.0330	4.2	0.0052	2.8	0.65	33.5	0.9	32.9	1.4	NA	NA	33.5	0.9
Spot 102	90	2957	0.7	23.2344	4.0	0.0309	5.0	0.0052	3.0	0.60	33.5	1.0	30.9	1.5	NA	NA	33.5	1.0
Spot 64	179	552	1.1	51.2792	71.5	0.0140	71.5	0.0052	2.2	0.03	33.5	0.8	14.1	10.0	NA	NA	33.5	0.8
Spot 88	203	1365	0.8	25.8271	5.2	0.0279	6.3	0.0052	3.4	0.55	33.6	1.1	27.9	1.7	NA	NA	33.6	1.1
Spot 23	35	1050	0.9	36.7859	18.5	0.0196	18.9	0.0052	4.0	0.21	33.6	1.4	19.7	3.7	NA	NA	33.6	1.4
Spot 83	172	1460	0.7	26.3776	6.2	0.0273	6.6	0.0052	2.3	0.34	33.6	0.8	27.4	1.8	NA	NA	33.6	0.8
Spot 35	176	7567	0.8	21.6805	3.2	0.0332	4.0	0.0052	2.4	0.60	33.6	0.8	33.2	1.3	4.1	77.8	33.6	0.8
Spot 87	348	5242	0.4	20.406	3.1	0.0353	4.0	0.0052	2.6	0.65	33.6	0.9	35.2	1.4	148.0	71.6	33.6	0.9

TABLE E2: U-TH-PB GEOCHRONOLOGIC ANALYSES

Analysis	U (ppm)	^{206}Pb ^{204}Pb	U/Th	$^{206}Pb^*$ $^{207}Pb^*$	± (%)	Isotope Ratios $^{207}Pb^*$ $^{235}U^*$	± (%)	$^{206}Pb^*$ ^{238}U	± (%)	Error Corr.	Apparent Ages (Ma) $^{206}Pb^*$ $^{238}U^*$	± (Ma)	$^{207}Pb^*$ ^{235}U	± (Ma)	$^{206}Pb^*$ $^{207}Pb^*$	± (Ma)	**Best Age** (Ma)	± (Ma)
Spot 105	170	868	1.0	28.5039	8.2	0.0253	8.6	0.0052	2.6	0.30	33.6	0.9	25.4	2.2	NA	NA	33.6	0.9
Spot 13	289	4298	0.6	21.9596	2.8	0.0329	3.8	0.0052	2.5	0.67	33.7	0.9	32.8	1.2	NA	NA	33.7	0.9
Spot 80	115	1577	0.9	19.1622	9.8	0.0377	10.2	0.0052	2.8	0.27	33.7	0.9	37.6	3.8	293.6	224.6	33.7	0.9
Spot 108	187	1410	0.7	24.7977	6.4	0.0291	6.9	0.0052	2.6	0.37	33.7	0.9	29.2	2.0	NA	NA	33.7	0.9
Spot 73	76	662	0.9	37.9619	22.5	0.0190	22.7	0.0052	3.3	0.15	33.7	1.1	19.2	4.3	NA	NA	33.7	1.1
Spot 15	174	802	0.5	31.6612	10.6	0.0228	11.1	0.0052	3.3	0.29	33.7	1.1	22.9	2.5	NA	NA	33.7	1.1
Spot 101	62	1016	0.6	25.1123	5.4	0.0288	6.1	0.0053	2.8	0.46	33.8	0.9	28.9	1.7	NA	NA	33.8	0.9
Spot 55	587	83458	1.1	19.9953	1.5	0.0362	3.0	0.0053	2.6	0.87	33.8	0.9	36.1	1.1	195.6	34.3	33.8	0.9
Spot 97	169	25377	0.5	19.8462	2.7	0.0365	4.0	0.0053	3.0	0.75	33.8	1.0	36.4	1.4	212.9	61.7	33.8	1.0
Spot 63	273	1285	0.6	25.4723	4.7	0.0285	5.4	0.0053	2.6	0.49	33.8	0.9	28.5	1.5	NA	NA	33.8	0.9
Spot 68	33	1091	0.9	38.4069	5.3	0.0189	6.6	0.0053	4.0	0.60	33.8	1.3	19.0	1.3	NA	NA	33.8	1.3
Spot 49	365	2438	0.9	23.7171	2.3	0.0307	4.0	0.0053	3.2	0.81	33.9	1.1	30.7	1.2	NA	NA	33.9	1.1
Spot 47	144	898	0.7	30.5193	6.4	0.0238	7.1	0.0053	3.1	0.44	34.0	1.1	23.9	1.7	NA	NA	34.0	1.1
Spot 104	102	464	0.7	58.5283	14.7	0.0125	15.0	0.0053	3.1	0.21	34.0	1.1	12.6	1.9	NA	NA	34.0	1.1
Spot 77	115	1810	1.1	25.4895	3.1	0.0287	4.1	0.0053	2.7	0.66	34.1	0.9	28.7	1.2	NA	NA	34.1	0.9
Spot 98	522	3762	1.0	21.7769	2.2	0.0336	3.2	0.0053	2.3	0.72	34.1	0.8	33.5	1.0	NA	NA	34.1	0.8
Spot 84	60	4884	0.7	21.9504	4.4	0.0334	5.7	0.0053	3.6	0.63	34.2	1.2	33.3	1.9	NA	NA	34.2	1.2
Spot 39	150	956	0.7	27.5294	7.0	0.0266	7.8	0.0053	3.5	0.44	34.2	1.2	26.7	2.1	NA	NA	34.2	1.2
Spot 56	46	450	0.7	52.452	22.5	0.0140	22.7	0.0053	3.0	0.13	34.2	1.0	14.1	3.2	NA	NA	34.2	1.0

TABLE E2: U-TH-PB GEOCHRONOLOGIC ANALYSES

Analysis	U (ppm)	^{206}Pb ^{204}Pb	U/Th	$^{206}Pb^*$ $^{207}Pb^*$	± (%)	Isotope Ratios $^{207}Pb^*$ $^{235}U^*$	± (%)	$^{206}Pb^*$ ^{238}U	± (%)	Error Corr.	Apparent Ages (Ma) $^{206}Pb^*$ $^{238}U^*$	± (Ma)	$^{207}Pb^*$ ^{235}U	± (Ma)	$^{206}Pb^*$ $^{207}Pb^*$	± (Ma)	Best Age (Ma)	± (Ma)
Spot 82	222	2561	1.2	22.2261	2.5	0.0331	3.7	0.0053	2.7	0.73	34.3	0.9	33.0	1.2	NA	NA	34.3	0.9
Spot 6	181	1671	0.8	23.9955	4.9	0.0307	5.7	0.0053	2.8	0.50	34.3	1.0	30.7	1.7	NA	NA	34.3	1.0
Spot 32	147	8254	0.9	19.7699	2.8	0.0372	3.6	0.0053	2.3	0.64	34.3	0.8	37.1	1.3	221.8	64.2	34.3	0.8
Spot 29	64	614	0.8	40.6066	8.7	0.0181	9.1	0.0053	2.8	0.31	34.3	1.0	18.2	1.7	NA	NA	34.3	1.0
Spot 96	123	435	0.5	64.0319	11.7	0.0115	12.3	0.0054	3.6	0.29	34.4	1.2	11.6	1.4	NA	NA	34.4	1.2
Spot 19	32	3075	0.8	19.7788	6.7	0.0373	7.6	0.0054	3.7	0.48	34.4	1.3	37.2	2.8	220.8	155.0	34.4	1.3
Spot 48	32	1871	0.7	23.3580	6.7	0.0316	7.6	0.0054	3.5	0.46	34.4	1.2	31.6	2.4	NA	NA	34.4	1.2
Spot 37	181	4326	0.8	23.2806	2.9	0.0320	4.4	0.0054	3.3	0.75	34.8	1.2	32.0	1.4	NA	NA	34.8	1.2
Spot 9	157	1956	0.9	24.0954	4.0	0.0310	5.1	0.0054	3.0	0.60	34.9	1.1	31.0	1.5	NA	NA	34.9	1.1
Spot 33	66	287	0.9	197.7294	78.1	0.0038	78.1	0.0054	2.9	0.04	34.9	1.0	3.8	3.0	NA	NA	34.9	1.0
Spot 107	154	3284	0.7	22.0638	3.8	0.0341	4.2	0.0055	1.9	0.46	35.1	0.7	34.0	1.4	NA	NA	35.1	0.7
Spot 81	199	1279	1.0	27.2545	13.3	0.0276	13.6	0.0055	2.8	0.21	35.1	1.0	27.7	3.7	NA	NA	35.1	1.0
Spot 34	610	98524	0.5	20.2154	1.9	0.0373	3.1	0.0055	2.5	0.80	35.1	0.9	37.1	1.1	170.0	43.5	35.1	0.9
Spot 99	53	1469	0.8	19.6866	4.8	0.0384	5.9	0.0055	3.4	0.58	35.3	1.2	38.3	2.2	231.6	110.3	35.3	1.2
Spot 46	194	37817	0.6	20.6651	3.0	0.0366	4.6	0.0055	3.5	0.76	35.3	1.2	36.5	1.6	118.4	71.1	35.3	1.2
Spot 91	147	4631	0.6	22.3828	3.5	0.0338	4.8	0.0055	3.3	0.69	35.3	1.2	33.7	1.6	NA	NA	35.3	1.2
Spot 36	172	1311	0.7	13.6540	5.7	0.0555	6.7	0.0055	3.6	0.53	35.3	1.3	54.8	3.6	1020.5	115.6	35.3	1.3
Spot 14	48	2737	0.6	23.6268	5.4	0.0348	6.1	0.0060	2.8	0.45	38.3	1.1	34.7	2.1	NA	NA	38.3	1.1
Spot 44	219	146871	1.2	14.164	0.9	1.5675	2.5	0.1611	2.4	0.94	962.9	21.4	957.4	15.7	945.8	17.7	945.8	17.7

TABLE E2: U-TH-PB GEOCHRONOLOGIC ANALYSES

Analysis	U (ppm)	^{206}Pb ^{204}Pb	U/Th	$^{206}Pb^*$ $^{207}Pb^*$	± (%)	Isotope Ratios $^{207}Pb^*$ $^{235}U^*$	± (%)	$^{206}Pb^*$ ^{238}U	± (%)	Error Corr.	Apparent Ages (Ma) $^{206}Pb^*$ $^{238}U^*$	± (Ma)	$^{207}Pb^*$ ^{235}U	± (Ma)	$^{206}Pb^*$ $^{207}Pb^*$	± (Ma)	Best Age (Ma)	± (Ma)
Spot 59	97	44977	2.0	11.2670	0.9	3.0337	2.2	0.2480	2.0	0.92	1428.2	25.9	1416.1	16.9	1398.9	16.9	1398.9	16.9
Spot 100	506	80840	5.1	9.7138	1.0	3.4424	3.0	0.2426	2.9	0.94	1400.4	36.0	1514.1	23.9	1677.9	18.8	1677.9	18.8
Spot 72	158	173588	1.1	9.6560	0.9	4.2681	2.4	0.2990	2.3	0.94	1686.5	33.7	1687.2	20.0	1688.9	15.8	1688.9	15.8
Spot 50	105	39866	2.0	9.5992	0.7	4.4341	2.6	0.3088	2.5	0.96	1735.0	37.9	1718.7	21.5	1699.8	13.1	1699.8	13.1
Spot 52	305	324000	2.0	9.5900	0.8	4.1996	2.4	0.2922	2.3	0.95	1652.6	33.3	1673.9	19.8	1701.6	14.4	1701.6	14.4
Spot 38	117	86844	3.9	9.4862	0.9	4.4433	2.8	0.3058	2.6	0.94	1720.2	39.5	1720.4	23.0	1721.6	16.7	1721.6	16.7
Spot 93	118	41676	3.7	9.4809	0.5	4.5263	2.7	0.3114	2.6	0.98	1747.5	39.9	1735.8	22.2	1722.6	10.1	1722.6	10.1
Spot 27	471	419692	2.9	9.4268	1.0	4.6521	2.7	0.3182	2.5	0.93	1780.9	39.5	1758.7	22.9	1733.1	18.8	1733.1	18.8
Spot 106	69	31701	4.1	9.3770	0.9	4.7068	2.8	0.3202	2.6	0.95	1790.9	41.1	1768.4	23.3	1742.8	16.6	1742.8	16.6
Spot 8	194	290646	3.5	9.3754	0.9	4.5632	2.5	0.3104	2.3	0.93	1742.7	35.0	1742.6	20.6	1743.1	17.2	1743.1	17.2
Spot 25	184	101565	3.1	9.2164	1.0	4.6421	2.9	0.3104	2.7	0.93	1742.8	41.1	1756.9	24.1	1774.4	18.8	1774.4	18.8
Spot 94	417	221763	2.7	9.0850	0.9	4.6914	2.4	0.3093	2.2	0.93	1737.0	34.1	1765.7	20.1	1800.6	15.9	1800.6	15.9
HOW-02																		
02-36	467	3128	0.4	22.3520	17.5	0.0179	19.3	0.0029	8.1	0.42	18.6	1.5	18.0	3.4	-69.8	431.4	18.6	1.5
02-34	254	2292	1.2	23.4001	42.7	0.0180	42.9	0.0030	4.1	0.09	19.6	0.8	18.1	7.7	-183.0	1110.4	19.6	0.8
02-46	96	1177	0.6	22.1693	51.8	0.0302	54.0	0.0048	15.1	0.28	31.2	4.7	30.2	16.1	-49.8	1345.2	31.2	4.7
02-02	1835	12251	1.3	22.0046	3.9	0.0309	4.0	0.0049	0.8	0.20	31.7	0.3	30.9	1.2	-31.7	94.5	31.7	0.3
02-35	93	1585	0.6	21.2981	39.5	0.0319	41.1	0.0049	11.5	0.28	31.7	3.6	31.9	12.9	46.8	977.5	31.7	3.6
02-21	45	629	0.8	9.1342	174.3	~~0.0763~~	~~174.6~~	~~0.0051~~	~~10.0~~	~~0.06~~	32.5	3.3	74.6	126.3	1790.7	178.5	32.5	3.3
02-40	146	2308	0.6	21.3827	66.6	0.0330	66.8	0.0051	6.1	0.09	32.9	2.0	33.0	21.7	37.3	1796.7	32.9	2.0

TABLE E2: U-TH-PB GEOCHRONOLOGIC ANALYSES

						Isotope Ratios					Apparent Ages (Ma)							
Analysis	U (ppm)	$^{206}Pb/^{204}Pb$	U/Th	$^{206}Pb^*/^{207}Pb^*$	± (%)	$^{207}Pb^*/^{235}U^*$	± (%)	$^{206}Pb^*/^{238}U$	± (%)	Error Corr.	$^{206}Pb^*/^{238}U^*$	± (Ma)	$^{207}Pb^*/^{235}U$	± (Ma)	$^{206}Pb^*/^{207}Pb^*$	± (Ma)	**Best Age** (Ma)	± (Ma)
02-17	64	4660	0.7	0.9413	1998.4	~~0.7534~~	~~1998.5~~	~~0.0051~~	~~18.9~~	~~0.01~~	33.1	6.2	570.2	#NUM!	NA	NA	33.1	6.2
02-26	575	13398	0.4	21.1472	8.2	0.0336	8.6	0.0052	2.6	0.30	33.2	0.9	33.6	2.9	63.8	196.2	33.2	0.9
02-32	192	3697	0.6	26.9079	51.8	0.0264	52.0	0.0052	4.7	0.09	33.2	1.6	26.5	13.6	-544.6	1477.3	33.2	1.6
02-01	74	507	0.6	9.6129	186.4	~~0.0747~~	~~187.0~~	~~0.0052~~	~~15.3~~	~~0.08~~	33.5	5.1	73.2	132.8	1697.2	303.3	33.5	5.1
02-08	162	1945	0.5	22.8091	72.8	0.0315	73.0	0.0052	5.0	0.07	33.6	1.7	31.5	22.7	-119.5	2087.9	33.6	1.7
02-43	622	16931	0.9	22.0319	7.0	0.0327	7.2	0.0052	1.8	0.25	33.6	0.6	32.6	2.3	-34.7	169.3	33.6	0.6
02-30	124	1726	0.7	28.7408	154.8	0.0251	155.0	0.0052	6.9	0.04	33.7	2.3	25.2	38.6	-725.1	0.0	33.7	2.3
02-16	102	1575	0.6	6.6913	373.6	~~0.1081~~	~~373.7~~	~~0.0052~~	~~9.7~~	~~0.03~~	33.7	3.3	104.2	388.1	2339.6	503.0	33.7	3.3
02-38	664	7741	0.5	19.6505	10.2	0.0368	10.3	0.0052	1.8	0.17	33.8	0.6	36.7	3.7	235.8	235.5	33.8	0.6
02-37	281	15067	0.4	22.3454	21.6	0.0324	22.0	0.0052	4.4	0.20	33.8	1.5	32.4	7.0	-69.1	531.6	33.8	1.5
02-20	193	2434	0.5	12.6329	135.0	~~0.0578~~	~~135.2~~	~~0.0053~~	~~7.0~~	~~0.05~~	34.1	2.4	57.1	75.2	1176.1	408.4	34.1	2.4
02-48	108	2586	0.5	9.1547	225.6	~~0.0798~~	~~225.8~~	~~0.0053~~	~~9.9~~	~~0.04~~	34.1	3.4	78.0	171.2	1786.7	414.1	34.1	3.4
02-13	165	2784	0.7	27.9284	61.6	0.0262	62.6	0.0053	11.4	0.18	34.1	3.9	26.2	16.2	-645.7	1850.6	34.1	3.9
02-06	133	1506	0.6	24.4648	60.3	0.0300	60.8	0.0053	8.4	0.14	34.2	2.9	30.0	18.0	-295.4	1682.2	34.2	2.9
02-14	629	12145	1.0	21.6624	7.9	0.0339	8.0	0.0053	1.4	0.18	34.2	0.5	33.8	2.7	6.2	190.6	34.2	0.5
02-23	274	2148	0.6	14.4676	8.9	0.0516	12.9	0.0054	9.4	0.73	34.8	3.3	51.1	6.4	902.3	183.4	34.8	3.3
02-42	314	16448	0.6	21.0894	22.3	0.0357	22.5	0.0055	2.8	0.12	35.1	1.0	35.6	7.9	70.3	536.2	35.1	1.0
02-19	69	1107	0.8	-3.8100	607.4	~~-0.2041~~	~~607.6~~	~~0.0056~~	~~13.3~~	~~0.02~~	36.3	4.8	-231.8	#NUM!	NA	NA	36.3	4.8
02-11	83	6528	0.8	20.5566	21.2	0.1618	21.3	0.0241	2.0	0.09	153.7	3.0	152.3	30.1	130.8	504.0	153.7	3.0

TABLE E2: U-TH-PB GEOCHRONOLOGIC ANALYSES

						Isotope Ratios					Apparent Ages (Ma)							
Analysis	U (ppm)	^{206}Pb ^{204}Pb	U/Th	$^{206}Pb^*$ $^{207}Pb^*$	± (%)	$^{207}Pb^*$ $^{235}U^*$	± (%)	$^{206}Pb^*$ ^{238}U	± (%)	Error Corr.	$^{206}Pb^*$ $^{238}U^*$	± (Ma)	$^{207}Pb^*$ ^{235}U	± (Ma)	$^{206}Pb^*$ $^{207}Pb^*$	± (Ma)	**Best Age** (Ma)	± (Ma)
02-31	542	18677	0.8	20.5835	2.3	0.1758	2.4	0.0262	0.5	0.23	167.0	0.9	164.4	3.6	127.8	54.5	167.0	0.9
02-03	386	14792	1.1	20.2051	3.5	0.1807	3.7	0.0265	1.3	0.36	168.4	2.2	168.6	5.8	171.2	80.9	168.4	2.2
02-27	17	14905	1.6	13.5587	9.6	1.7349	9.6	0.1706	1.0	0.10	1015.4	8.9	1021.6	62.2	1034.7	194.2	1034.7	194.2
02-18	1014	646550	18.1	9.7660	0.2	3.8050	0.9	0.2695	0.9	0.98	1538.3	12.2	1593.8	7.3	1668.0	2.9	1668.0	2.9
02-05	355	174149	3.0	9.7138	0.2	4.3631	1.8	0.3074	1.8	1.00	1727.8	26.8	1705.4	14.7	1677.9	3.3	1677.9	3.3
02-28	104	95391	2.4	9.5965	0.7	4.3781	0.9	0.3047	0.6	0.64	1714.7	9.0	1708.2	7.7	1700.3	13.1	1700.3	13.1
02-41	74	136649	2.6	9.5772	1.1	4.4027	1.3	0.3058	0.8	0.59	1720.1	11.5	1712.9	10.8	1704.0	19.4	1704.0	19.4
02-04	175	80363	4.5	9.5269	0.5	4.5136	0.6	0.3119	0.3	0.57	1749.9	5.1	1733.5	4.9	1713.7	8.9	1713.7	8.9
02-33	257	331246	2.7	9.5002	0.3	4.4728	0.4	0.3082	0.3	0.79	1731.8	5.0	1725.9	3.5	1718.9	4.8	1718.9	4.8
02-24	128	190725	2.3	9.3784	0.8	4.5936	1.1	0.3125	0.7	0.70	1752.8	11.4	1748.1	8.8	1742.5	13.9	1742.5	13.9
02-45	173	208914	2.9	9.3756	0.5	4.6070	1.0	0.3133	0.8	0.86	1756.8	12.8	1750.5	8.1	1743.1	8.9	1743.1	8.9
02-15	120	103387	3.2	9.3563	0.6	4.6178	0.7	0.3134	0.4	0.58	1757.2	6.2	1752.5	5.7	1746.9	10.2	1746.9	10.2
02-44	208	227474	2.6	9.2206	0.4	4.6497	5.4	0.3109	5.4	1.00	1745.3	82.1	1758.2	45.0	1773.6	7.9	1773.6	7.9
02-07	590	447615	0.9	9.1883	0.3	4.9659	3.9	0.3309	3.9	1.00	1842.9	63.0	1813.5	33.3	1780.0	5.5	1780.0	5.5
02-12	143	139182	1.6	9.0638	1.4	4.4718	2.5	0.2940	2.1	0.84	1661.3	31.1	1725.8	20.9	1804.8	24.8	1804.8	24.8
02-29	42	25350	1.7	8.6550	6.1	4.8296	6.4	0.3032	1.8	0.28	1707.0	26.7	1790.1	53.8	1888.3	110.5	1888.3	110.5
Spot 106	294	1156	1.3	29.5919	4.1	0.0143	4.9	0.0031	2.6	0.54	19.7	0.5	14.4	0.7	NA	NA	19.7	0.5
Spot 67	65	659	0.9	39.1445	12.3	0.0175	12.7	0.0050	3.3	0.26	31.9	1.0	17.6	2.2	NA	NA	31.9	1.0
Spot 91	68	675	0.9	39.4852	29.5	0.0174	29.7	0.0050	3.1	0.11	32.1	1.0	17.5	5.2	NA	NA	32.1	1.0
Spot 36	53	895	0.6	26.8129	11.7	0.0258	12.2	0.0050	3.4	0.28	32.3	1.1	25.9	3.1	NA	NA	32.3	1.1
Spot 35	45	461	0.7	41.2371	32.9	0.0168	33.1	0.0050	3.2	0.10	32.3	1.0	16.9	5.5	NA	NA	32.3	1.0
Spot 24	74	1256	0.8	22.6552	14.4	0.0306	14.9	0.0050	4.0	0.27	32.3	1.3	30.6	4.5	NA	NA	32.3	1.3

TABLE E2: U-TH-PB GEOCHRONOLOGIC ANALYSES

Analysis	U (ppm)	^{206}Pb ^{204}Pb	U/Th	$^{206}Pb^*$ $^{207}Pb^*$	± (%)	Isotope Ratios $^{207}Pb^*$ $^{235}U^*$	± (%)	$^{206}Pb^*$ ^{238}U	± (%)	Error Corr.	Apparent Ages (Ma) $^{206}Pb^*$ $^{238}U^*$	± (Ma)	$^{207}Pb^*$ ^{235}U	± (Ma)	$^{206}Pb^*$ $^{207}Pb^*$	± (Ma)	Best Age (Ma)	± (Ma)
Spot 71	353	2052	0.5	25.0663	3.1	0.0277	4.3	0.0050	3.1	0.71	32.3	1.0	27.7	1.2	NA	NA	32.3	1.0
Spot 54	240	46909	0.5	21.8247	3.4	0.0319	4.0	0.0051	2.2	0.54	32.5	0.7	31.9	1.3	NA	NA	32.5	0.7
Spot 97	194	3149	0.6	22.1232	4.3	0.0315	7.6	0.0051	6.3	0.83	32.6	2.0	31.5	2.4	NA	NA	32.6	2.0
Spot 94	97	3693	0.9	20.8859	5.4	0.0336	6.3	0.0051	3.4	0.53	32.8	1.1	33.6	2.1	93.3	127.2	32.8	1.1
Spot 64	167	3574	0.4	20.7929	3.6	0.0338	4.6	0.0051	2.9	0.63	32.8	0.9	33.8	1.5	103.9	84.7	32.8	0.9
Spot 38	176	2277	1.0	26.2272	9.2	0.0269	9.6	0.0051	2.5	0.26	32.9	0.8	26.9	2.5	NA	NA	32.9	0.8
Spot 90	348	4533	0.8	22.3822	2.3	0.0315	3.3	0.0051	2.5	0.74	32.9	0.8	31.5	1.0	NA	NA	32.9	0.8
Spot 47	199	5143	0.6	23.0898	3.6	0.0306	4.2	0.0051	2.2	0.52	33.0	0.7	30.6	1.3	NA	NA	33.0	0.7
Spot 19	99	3555	0.9	21.3854	4.7	0.0331	5.7	0.0051	3.1	0.55	33.0	1.0	33.0	1.8	37.0	113.3	33.0	1.0
Spot 20	480	5521	0.5	21.3991	2.8	0.0332	3.5	0.0052	2.1	0.60	33.1	0.7	33.1	1.2	35.5	67.9	33.1	0.7
Spot 28	189	1931	0.7	23.0772	6.4	0.0308	6.9	0.0052	2.7	0.39	33.1	0.9	30.8	2.1	NA	NA	33.1	0.9
Spot 40	339	25259	0.5	22.2198	2.0	0.0320	2.7	0.0052	1.8	0.67	33.2	0.6	32.0	0.9	NA	NA	33.2	0.6
Spot 32	282	8223	0.6	21.4450	2.8	0.0332	4.0	0.0052	2.9	0.72	33.2	1.0	33.1	1.3	30.3	67.5	33.2	1.0
Spot 101	161	27900	0.8	19.7928	4.0	0.0359	5.0	0.0052	3.0	0.60	33.2	1.0	35.8	1.8	219.1	93.1	33.2	1.0
Spot 70	92	2395	0.6	19.1201	5.2	0.0372	6.5	0.0052	3.9	0.60	33.2	1.3	37.1	2.4	298.6	118.9	33.2	1.3
Spot 23	71	1651	0.5	16.1513	6.9	0.0441	7.8	0.0052	3.5	0.45	33.2	1.2	43.8	3.3	671.1	148.0	33.2	1.2
Spot 80	966	48815	0.9	21.3382	1.8	0.0335	2.7	0.0052	2.0	0.73	33.4	0.6	33.5	0.9	42.3	44.2	33.4	0.6
Spot 62	110	1816	0.9	25.8286	11.2	0.0277	11.7	0.0052	3.2	0.27	33.4	1.1	27.7	3.2	NA	NA	33.4	1.1
Spot 4	1207	58194	1.0	21.5652	1.3	0.0333	2.6	0.0052	2.2	0.86	33.5	0.7	33.2	0.8	16.9	32.0	33.5	0.7

TABLE E2: U-TH-PB GEOCHRONOLOGIC ANALYSES

Analysis	U (ppm)	^{206}Pb ^{204}Pb	U/Th	$^{206}Pb^*$ $^{207}Pb^*$	± (%)	Isotope Ratios $^{207}Pb^*$ $^{235}U^*$	± (%)	$^{206}Pb^*$ ^{238}U	± (%)	Error Corr.	Apparent Ages (Ma) $^{206}Pb^*$ $^{238}U^*$	± (Ma)	$^{207}Pb^*$ ^{235}U	± (Ma)	$^{206}Pb^*$ $^{207}Pb^*$	± (Ma)	Best Age (Ma)	± (Ma)
Spot 86	173	1461	0.8	27.9186	2.5	0.0257	3.8	0.0052	2.8	0.75	33.5	0.9	25.8	1.0	NA	NA	33.5	0.9
Spot 42	213	4570	0.9	21.0135	3.8	0.0342	4.6	0.0052	2.5	0.55	33.5	0.8	34.1	1.5	78.8	91.2	33.5	0.8
Spot 37	327	11116	0.7	21.3647	2.5	0.0337	3.1	0.0052	1.8	0.58	33.5	0.6	33.6	1.0	39.4	59.7	33.5	0.6
Spot 73	928	23405	0.9	21.8830	1.5	0.0329	2.7	0.0052	2.3	0.83	33.6	0.8	32.9	0.9	NA	NA	33.6	0.8
Spot 95	1119	30392	1.4	21.7212	1.6	0.0332	2.9	0.0052	2.4	0.83	33.6	0.8	33.1	0.9	NA	NA	33.6	0.8
Spot 99	671	29533	0.7	20.7468	2.2	0.0347	3.4	0.0052	2.6	0.76	33.6	0.9	34.7	1.1	109.1	51.4	33.6	0.9
Spot 25	505	15385	0.9	21.0919	2.3	0.0342	3.5	0.0052	2.7	0.75	33.6	0.9	34.1	1.2	70.0	55.3	33.6	0.9
Spot 30	169	4073	0.5	21.5665	5.5	0.0336	6.3	0.0053	3.1	0.49	33.9	1.0	33.6	2.1	16.8	132.1	33.9	1.0
Spot 82	53	5138	0.9	21.1493	5.0	0.0343	6.0	0.0053	3.3	0.55	33.9	1.1	34.3	2.0	63.6	118.9	33.9	1.1
Spot 29	1203	20095	1.3	20.9585	1.6	0.0347	2.8	0.0053	2.3	0.82	33.9	0.8	34.6	1.0	85.1	38.4	33.9	0.8
Spot 108	81	4148	0.9	19.2848	6.4	0.0377	7.3	0.0053	3.4	0.47	34.0	1.2	37.6	2.7	279.0	146.8	34.0	1.2
Spot 14	252	4525	0.6	21.9658	2.8	0.0333	3.4	0.0053	2.0	0.59	34.2	0.7	33.3	1.1	NA	NA	34.2	0.7
Spot 74	190	3382	1.1	19.5623	5.0	0.0385	5.6	0.0055	2.5	0.45	35.1	0.9	38.4	2.1	246.2	114.6	35.1	0.9
Spot 18	220	1937	0.8	18.2672	4.8	0.0415	5.6	0.0055	2.9	0.52	35.4	1.0	41.3	2.3	401.7	106.9	35.4	1.0
Spot 103	587	6472	1.1	22.0394	1.7	0.0348	2.7	0.0056	2.1	0.78	35.8	0.8	34.7	0.9	NA	NA	35.8	0.8
Spot 53	1025	22375	0.8	21.8371	1.8	0.0353	3.1	0.0056	2.5	0.81	35.9	0.9	35.2	1.1	NA	NA	35.9	0.9
Spot 41	703	13246	1.2	20.7910	1.6	0.0831	2.4	0.0125	1.8	0.75	80.3	1.4	81.1	1.9	104.1	37.8	80.3	1.4
Spot 9	248	110164	2.3	19.7451	1.1	0.2882	2.6	0.0413	2.4	0.90	260.8	6.0	257.1	5.9	224.7	26.3	260.8	6.0
Spot 27	102	42811	2.5	18.5832	1.3	0.4398	2.3	0.0593	1.8	0.80	371.4	6.6	370.1	7.0	363.2	30.4	371.4	6.6

TABLE E2: U-TH-PB GEOCHRONOLOGIC ANALYSES

Analysis	U (ppm)	^{206}Pb ^{204}Pb	U/Th	$^{206}Pb^*$ $^{207}Pb^*$	± (%)	Isotope Ratios $^{207}Pb^*$ $^{235}U^*$	± (%)	$^{206}Pb^*$ ^{238}U	± (%)	Error Corr.	Apparent Ages (Ma) $^{206}Pb^*$ $^{238}U^*$	± (Ma)	$^{207}Pb^*$ ^{235}U	± (Ma)	$^{206}Pb^*$ $^{207}Pb^*$	± (Ma)	Best Age (Ma)	± (Ma)
Spot 68	335	34691	0.8	18.5139	1.0	0.4618	2.5	0.0620	2.3	0.92	388.0	8.6	385.5	8.0	371.6	22.0	388.0	8.6
Spot 31	88	19125	2.2	18.0615	1.3	0.5040	2.7	0.0660	2.4	0.88	412.3	9.6	414.4	9.3	427.0	29.4	412.3	9.6
Spot 11	195	35312	1.6	17.8294	1.0	0.5357	2.5	0.0693	2.4	0.93	431.9	9.8	435.6	9.0	455.8	21.4	431.9	9.8
Spot 1	427	68900	1.8	17.9467	0.9	0.5542	2.1	0.0722	1.8	0.89	449.2	8.0	447.7	7.4	441.2	20.6	449.2	8.0
Spot 21	184	79872	1.0	17.8298	1.0	0.5820	3.0	0.0753	2.8	0.94	467.9	12.7	465.7	11.1	455.8	21.7	467.9	12.7
Spot 43	955	346175	4.1	17.2604	0.8	0.6733	2.1	0.0843	1.9	0.93	521.9	9.7	522.7	8.5	527.4	17.0	521.9	9.7
Spot 69	204	78781	2.0	16.5742	1.1	0.8305	2.4	0.0999	2.2	0.89	613.7	12.6	613.9	11.1	615.6	23.5	613.7	12.6
Spot 81	87	22811	1.1	16.2697	1.1	0.8965	2.5	0.1058	2.3	0.90	648.5	13.9	649.9	12.1	655.5	24.0	648.5	13.9
Spot 96	175	90334	1.4	16.2961	1.0	0.9247	2.7	0.1093	2.5	0.93	668.9	16.0	664.8	13.2	652.0	20.7	668.9	16.0
Spot 8	15	5471	1.6	13.9428	1.8	1.6201	3.3	0.1639	2.8	0.84	978.4	25.0	978.0	20.6	978.0	36.4	978.0	36.4
Spot 89	71	21023	4.1	13.9261	1.3	1.6129	2.9	0.1630	2.6	0.89	973.3	23.3	975.2	18.2	980.5	27.2	980.5	27.2
Spot 15	171	262439	1.8	13.8003	1.0	1.6582	2.3	0.1660	2.1	0.90	990.2	18.9	992.7	14.5	998.9	20.4	998.9	20.4
Spot 105	533	13598181	5.1	13.6226	0.9	1.7547	2.4	0.1734	2.3	0.93	1031.1	21.5	1028.9	15.7	1025.2	18.4	1025.2	18.4
Spot 34	332	338612	2.9	13.5649	0.9	1.7681	2.2	0.1740	2.0	0.91	1034.2	19.5	1033.8	14.4	1033.8	18.2	1033.8	18.2
Spot 12	55	13737	0.5	13.3755	1.2	1.8802	2.4	0.1825	2.1	0.86	1080.5	20.6	1074.1	15.9	1062.2	24.4	1062.2	24.4
Spot 104	1383	1884791	4.8	13.2312	0.8	1.8883	2.2	0.1813	2.0	0.93	1074.0	19.8	1077.0	14.3	1083.9	15.7	1083.9	15.7
Spot 107	95	147521	1.2	13.2250	0.9	1.9745	2.5	0.1895	2.4	0.93	1118.5	24.2	1106.9	17.0	1084.9	18.0	1084.9	18.0
Spot 6	152	94065	2.3	12.9297	1.2	2.0265	2.4	0.1901	2.1	0.88	1122.0	22.0	1124.4	16.6	1130.0	23.5	1130.0	23.5
Spot 17	55	53341	1.9	12.7323	1.0	2.0624	2.4	0.1905	2.2	0.91	1124.2	22.7	1136.4	16.5	1160.6	19.4	1160.6	19.4

TABLE E2: U-TH-PB GEOCHRONOLOGIC ANALYSES

Analysis	U (ppm)	^{206}Pb ^{204}Pb	U/Th	$^{206}Pb^*$ $^{207}Pb^*$	± (%)	Isotope Ratios $^{207}Pb^*$ $^{235}U^*$	± (%)	$^{206}Pb^*$ ^{238}U	± (%)	Error Corr.	Apparent Ages (Ma) $^{206}Pb^*$ $^{238}U^*$	± (Ma)	$^{207}Pb^*$ ^{235}U	± (Ma)	$^{206}Pb^*$ $^{207}Pb^*$	± (Ma)	Best Age (Ma)	± (Ma)
Spot 33	103	30328	2.1	12.4458	1.1	2.1934	2.6	0.1981	2.3	0.90	1165.0	24.8	1179.0	18.0	1205.5	22.1	1205.5	22.1
Spot 83	210	205574	1.7	11.9964	0.8	2.5610	2.1	0.2229	1.9	0.92	1297.3	22.8	1289.6	15.4	1277.6	16.2	1277.6	16.2
Spot 51	251	121819	1.0	11.2849	0.8	3.0702	2.5	0.2514	2.4	0.96	1445.6	31.5	1425.3	19.5	1395.8	14.4	1395.8	14.4
Spot 65	67	296820	1.1	11.2580	1.0	2.8262	2.7	0.2309	2.5	0.93	1339.0	30.6	1362.5	20.4	1400.4	19.2	1400.4	19.2
Spot 78	360	825366	2.0	11.2566	0.8	3.0532	2.4	0.2494	2.2	0.93	1435.2	28.4	1421.0	18.1	1400.6	16.1	1400.6	16.1
Spot 52	455	123611	3.8	11.2561	0.8	2.9992	3.4	0.2450	3.3	0.97	1412.4	41.5	1407.4	25.6	1400.7	15.3	1400.7	15.3
Spot 2	282	4561117	1.4	11.2308	0.7	3.1089	2.0	0.2533	1.8	0.93	1455.7	23.8	1434.9	15.1	1405.0	14.2	1405.0	14.2
Spot 93	210	203471	3.2	11.2217	0.7	2.9331	2.2	0.2388	2.0	0.94	1380.6	25.4	1390.5	16.4	1406.6	13.8	1406.6	13.8
Spot 26	195	110366	2.3	11.0589	0.9	3.0837	2.1	0.2474	1.9	0.91	1425.3	24.9	1428.6	16.4	1434.5	17.0	1434.5	17.0
Spot 75	232	362815	1.2	10.9851	1.1	3.0797	3.0	0.2455	2.8	0.93	1415.1	35.0	1427.7	22.7	1447.3	20.9	1447.3	20.9
Spot 102	152	27990	1.6	10.8795	0.8	3.0769	2.7	0.2429	2.6	0.95	1401.7	33.0	1427.0	21.0	1465.6	15.5	1465.6	15.5
Spot 16	630	238792	3.1	10.7170	0.9	3.2824	2.2	0.2552	2.0	0.92	1465.5	26.2	1476.9	16.9	1494.2	16.2	1494.2	16.2
Spot 56	402	200520	2.7	10.6508	0.8	3.5483	2.3	0.2742	2.1	0.93	1562.1	29.4	1538.0	18.1	1505.9	15.9	1505.9	15.9
Spot 85	193	103514	2.3	10.1535	0.7	3.8135	2.1	0.2810	2.0	0.94	1596.1	27.8	1595.6	16.9	1595.7	13.7	1595.7	13.7
Spot 3	331	158936	1.8	9.8994	0.9	4.1950	2.7	0.3013	2.6	0.94	1697.9	38.1	1673.0	22.3	1642.8	17.2	1642.8	17.2
Spot 59	192	307642	2.5	9.8093	0.7	4.1766	2.3	0.2973	2.2	0.95	1677.8	31.8	1669.4	18.5	1659.8	12.5	1659.8	12.5
Spot 92	162	79583	0.9	9.7561	0.9	4.1411	2.0	0.2931	1.8	0.90	1657.2	26.1	1662.5	16.3	1669.9	16.3	1669.9	16.3
Spot 66	209	85633	2.0	9.7516	0.8	4.1664	2.3	0.2948	2.2	0.94	1665.5	31.9	1667.4	19.0	1670.7	14.9	1670.7	14.9
Spot 13	358	137071	2.2	9.7189	0.9	4.2212	2.2	0.2977	2.0	0.91	1679.8	29.8	1678.1	18.2	1676.9	16.9	1676.9	16.9
Spot 87	558	842465	5.6	9.7123	0.8	4.1834	2.2	0.2948	2.0	0.92	1665.5	29.2	1670.8	17.7	1678.2	15.3	1678.2	15.3
Spot 63	433	373194	1.9	9.6964	0.8	4.3131	2.3	0.3035	2.1	0.94	1708.4	32.3	1695.9	18.9	1681.2	14.5	1681.2	14.5

TABLE E2: U-TH-PB GEOCHRONOLOGIC ANALYSES

Analysis	U (ppm)	^{206}Pb ^{204}Pb	U/Th	$^{206}Pb^*$ $^{207}Pb^*$	± (%)	Isotope Ratios $^{207}Pb^*$ $^{235}U^*$	± (%)	$^{206}Pb^*$ ^{238}U	± (%)	Error Corr.	Apparent Ages (Ma) $^{206}Pb^*$ $^{238}U^*$	± (Ma)	$^{207}Pb^*$ ^{235}U	± (Ma)	$^{206}Pb^*$ $^{207}Pb^*$	± (Ma)	Best Age (Ma)	± (Ma)
Spot 44	301	92947	2.3	9.6837	0.9	4.3996	2.5	0.3091	2.3	0.94	1736.4	35.6	1712.3	20.7	1683.6	16.2	1683.6	16.2
Spot 79	78	95580	1.8	9.6571	0.7	4.2370	2.2	0.2969	2.0	0.94	1675.9	30.1	1681.2	17.8	1688.7	13.6	1688.7	13.6
Spot 100	284	90232	1.4	9.6095	0.8	4.1914	2.3	0.2922	2.2	0.93	1652.7	31.7	1672.3	19.1	1697.8	15.3	1697.8	15.3
Spot 50	343	1447223	4.2	9.6030	0.7	4.4744	1.8	0.3118	1.7	0.92	1749.4	25.3	1726.2	15.0	1699.1	13.2	1699.1	13.2
Spot 77	192	78747	1.3	9.5758	1.0	4.4765	2.3	0.3110	2.1	0.91	1745.8	32.2	1726.6	19.2	1704.3	17.6	1704.3	17.6
Spot 72	404	295296	2.5	9.5437	0.9	4.2001	2.2	0.2908	2.0	0.91	1645.8	28.7	1674.0	17.9	1710.5	16.7	1710.5	16.7
Spot 46	270	185974	3.2	9.5080	0.8	4.5711	2.2	0.3154	2.0	0.93	1767.0	30.9	1744.0	17.9	1717.4	14.7	1717.4	14.7
Spot 10	182	287303	2.3	9.4714	0.9	4.5461	2.4	0.3124	2.2	0.93	1752.6	33.6	1739.4	19.7	1724.4	16.4	1724.4	16.4
Spot 39	216	104801	2.6	9.4460	0.7	4.4186	2.5	0.3028	2.4	0.96	1705.4	36.0	1715.8	20.7	1729.4	12.8	1729.4	12.8
Spot 98	519	298705	2.0	9.4255	0.7	4.4246	2.1	0.3026	2.0	0.94	1704.2	29.3	1717.0	17.2	1733.4	13.0	1733.4	13.0
Spot 88	252	136916	2.4	9.3734	0.7	4.4687	3.1	0.3039	3.0	0.97	1710.7	45.7	1725.2	26.0	1743.5	13.3	1743.5	13.3
Spot 60	243	184494	2.8	9.3526	1.0	4.4781	2.2	0.3039	2.0	0.90	1710.6	30.0	1726.9	18.4	1747.6	17.4	1747.6	17.4
Spot 49	272	111682	1.6	9.3451	0.9	4.5564	2.9	0.3090	2.8	0.95	1735.5	42.2	1741.3	24.3	1749.1	16.6	1749.1	16.6
Spot 5	293	130109	1.6	9.3407	0.8	4.5640	2.0	0.3093	1.8	0.91	1737.4	27.8	1742.7	16.7	1749.9	15.5	1749.9	15.5
Spot 58	113	73623	3.5	9.2511	1.1	4.6390	2.6	0.3114	2.4	0.91	1747.6	36.1	1756.3	21.7	1767.5	19.6	1767.5	19.6
Spot 109	186	97542	1.9	9.0982	0.8	4.4463	2.3	0.2935	2.2	0.94	1659.1	31.5	1721.0	19.0	1797.9	14.2	1797.9	14.2
Spot 110	41	184061460	1.1	8.5482	0.8	5.4829	2.1	0.3401	1.9	0.93	1887.0	31.2	1897.9	17.7	1910.6	13.9	1910.6	13.9
Spot 57	262	30880	1.2	8.1451	0.7	5.8495	2.0	0.3457	1.8	0.93	1914.0	30.6	1953.8	17.2	1996.9	12.8	1996.9	12.8
Spot 76	16	537666	1.3	7.7450	1.0	6.7055	2.4	0.3768	2.2	0.90	2061.5	38.2	2073.4	21.2	2085.9	18.2	2085.9	18.2
Spot 48	225	939841	1.6	5.4064	0.7	12.9988	2.8	0.5099	2.7	0.96	2656.3	58.2	2679.6	26.1	2697.9	12.0	2697.9	12.0
Spot 55	253	356274	0.6	5.3646	0.7	13.3406	1.7	0.5193	1.6	0.92	2696.1	34.7	2704.1	16.3	2710.7	11.4	2710.7	11.4
DMH																		
Spot 78	117	392	0.9	82.3121	37.5	0.0076	37.6	0.0045	2.9	0.08	29.1	0.8	7.7	2.9	NA	NA	29.1	0.8

TABLE E2: U-TH-PB GEOCHRONOLOGIC ANALYSES

Analysis	U (ppm)	^{206}Pb ^{204}Pb	U/Th	$^{206}Pb^*$ $^{207}Pb^*$	± (%)	Isotope Ratios $^{207}Pb^*$ $^{235}U^*$	± (%)	$^{206}Pb^*$ ^{238}U	± (%)	Error Corr.	Apparent Ages (Ma) $^{206}Pb^*$ $^{238}U^*$	± (Ma)	$^{207}Pb^*$ ^{235}U	± (Ma)	$^{206}Pb^*$ $^{207}Pb^*$	± (Ma)	Best Age (Ma)	± (Ma)
Spot 12	949	12865	1.9	21.5928	2.0	0.0291	3.0	0.0046	2.1	0.72	29.3	0.6	29.1	0.8	13.9	49.3	29.3	0.6
Spot 17	136	266	0.7	34.7212	10.5	0.0186	11.1	0.0047	3.4	0.31	30.1	1.0	18.7	2.0	NA	NA	30.1	1.0
Spot 86	110	316	0.9	80.7372	201.9	0.0080	201.9	0.0047	3.8	0.02	30.2	1.1	8.1	16.3	NA	NA	30.2	1.1
Spot 15	71	352	1.3	36.9147	17.6	0.0177	17.9	0.0047	3.1	0.18	30.5	1.0	17.8	3.2	NA	NA	30.5	1.0
Spot 91	163	556	0.8	43.4525	56.6	0.0151	56.7	0.0048	3.3	0.06	30.6	1.0	15.2	8.6	NA	NA	30.6	1.0
Spot 89	281	699	0.8	30.1786	7.8	0.0219	8.2	0.0048	2.4	0.30	30.8	0.7	22.0	1.8	NA	NA	30.8	0.7
Spot 65	107	720	0.8	14.6045	10.4	0.0458	10.8	0.0049	2.9	0.27	31.2	0.9	45.5	4.8	882.9	216.1	31.2	0.9
Spot 24	129	1191	0.8	19.7752	5.3	0.0340	5.7	0.0049	2.1	0.38	31.3	0.7	33.9	1.9	221.2	121.8	31.3	0.7
Spot 10	177	687	0.8	27.0264	14.8	0.0250	15.1	0.0049	2.6	0.17	31.6	0.8	25.1	3.7	NA	NA	31.6	0.8
Spot 34	87	938	1.1	12.1557	10.9	0.0557	11.4	0.0049	3.5	0.31	31.6	1.1	55.1	6.1	1251.9	213.3	31.6	1.1
Spot 102	137	3708	1.5	21.2258	4.4	0.0328	5.3	0.0050	3.0	0.57	32.4	1.0	32.7	1.7	54.9	104.3	32.4	1.0
Spot 21	363	3706	0.8	16.8924	4.8	0.0439	5.7	0.0054	3.1	0.54	34.6	1.1	43.6	2.4	574.4	104.5	34.6	1.1
Spot 109	175	376	0.9	40.9029	8.8	0.0184	20.2	0.0055	18.2	0.90	35.2	6.4	18.6	3.7	NA	NA	35.2	6.4
Spot 29	68	3628	2.4	17.6058	2.1	0.6328	3.5	0.0808	2.8	0.79	501.1	13.5	497.8	13.8	483.8	47.2	501.1	13.5
Spot 5	67	8956	3.1	17.0193	1.4	0.6668	2.7	0.0823	2.3	0.85	510.1	11.1	518.8	10.8	558.1	30.8	510.1	11.1
Spot 62	103	29948	2.2	16.9824	1.4	0.6689	2.9	0.0824	2.5	0.87	510.6	12.5	520.0	11.9	562.8	31.1	510.6	12.5
Spot 9	114	18650	2.5	16.8640	1.4	0.6736	2.5	0.0824	2.1	0.83	510.6	10.4	522.9	10.4	578.0	30.6	510.6	10.4
Spot 3	119	6156	3.6	17.2707	1.3	0.6592	3.0	0.0826	2.7	0.90	511.7	13.1	514.1	12.0	526.1	28.5	511.7	13.1
Spot 94	166	23164	2.6	17.0159	0.9	0.6711	2.4	0.0829	2.2	0.93	513.1	10.8	521.4	9.7	558.5	19.5	513.1	10.8

TABLE E2: U-TH-PB GEOCHRONOLOGIC ANALYSES

Analysis	U (ppm)	^{206}Pb ^{204}Pb	U/Th	$^{206}Pb^*$ $^{207}Pb^*$	± (%)	Isotope Ratios $^{207}Pb^*$ $^{235}U^*$	± (%)	$^{206}Pb^*$ ^{238}U	± (%)	Error Corr.	Apparent Ages (Ma) $^{206}Pb^*$ $^{238}U^*$	± (Ma)	$^{207}Pb^*$ ^{235}U	± (Ma)	$^{206}Pb^*$ $^{207}Pb^*$	± (Ma)	Best Age (Ma)	± (Ma)
Spot 101	299	10942	3.0	16.8095	1.0	0.6808	2.8	0.0830	2.6	0.94	514.2	13.1	527.2	11.6	585.1	21.4	514.2	13.1
Spot 27	1000	217147	2.3	17.0680	0.8	0.6715	1.9	0.0832	1.7	0.91	515.0	8.4	521.6	7.6	551.8	16.9	515.0	8.4
Spot 95	104	27462	1.8	16.6441	1.2	0.6893	2.8	0.0832	2.5	0.90	515.4	12.3	532.4	11.5	606.5	26.4	515.4	12.3
Spot 85	111	9668	3.4	16.9906	1.6	0.6768	2.7	0.0834	2.2	0.81	516.6	10.8	524.8	11.0	561.8	34.3	516.6	10.8
Spot 96	366	73385	2.7	16.7268	1.3	0.6875	2.6	0.0834	2.2	0.86	516.6	11.0	531.3	10.6	595.8	28.1	516.6	11.0
Spot 83	1182	148352	4.0	17.2784	0.7	0.6662	1.9	0.0835	1.7	0.92	517.1	8.7	518.4	7.7	525.0	16.4	517.1	8.7
Spot 36	150	4380	3.0	17.3507	1.0	0.6637	2.2	0.0836	1.9	0.89	517.3	9.7	516.9	8.9	515.9	22.0	517.3	9.7
Spot 84	113	6679	2.9	17.1348	1.5	0.6736	2.5	0.0837	1.9	0.79	518.4	9.7	522.9	10.0	543.3	32.7	518.4	9.7
Spot 18	197	321350	2.8	16.7899	0.9	0.6883	2.2	0.0839	2.0	0.91	519.1	9.9	531.8	9.1	587.6	20.2	519.1	9.9
Spot 38	74	13954	1.8	16.5623	1.6	0.6979	3.4	0.0839	3.0	0.88	519.2	15.0	537.5	14.3	617.1	35.2	519.2	15.0
Spot 99	251	25509	5.6	16.9959	1.0	0.6810	2.9	0.0840	2.7	0.93	519.8	13.7	527.4	12.1	561.1	22.9	519.8	13.7
Spot 108	306	26743	2.8	17.2066	0.9	0.6732	2.2	0.0840	2.0	0.91	520.2	10.0	522.6	9.0	534.2	20.6	520.2	10.0
Spot 13	108	7300	3.1	17.2131	1.5	0.6746	2.2	0.0843	1.7	0.76	521.5	8.6	523.5	9.2	533.4	31.9	521.5	8.6
Spot 11	205	31725	3.8	16.9872	0.9	0.6839	2.2	0.0843	1.9	0.90	521.7	9.7	529.2	8.9	562.2	20.5	521.7	9.7
Spot 104	477	225716	2.0	17.0132	1.0	0.6836	2.5	0.0844	2.3	0.91	522.2	11.5	528.9	10.3	558.9	22.3	522.2	11.5
Spot 60	231	15655	2.4	17.2012	1.1	0.6776	2.7	0.0846	2.5	0.92	523.3	12.3	525.3	11.0	534.9	23.4	523.3	12.3
Spot 49	230	7038	4.1	17.3898	1.5	0.6713	2.8	0.0847	2.4	0.85	524.1	12.1	521.5	11.5	511.0	32.1	524.1	12.1
Spot 37	152	12929	1.9	16.7437	1.5	0.6987	2.3	0.0849	1.8	0.76	525.2	9.0	538.0	9.8	593.6	33.2	525.2	9.0
Spot 7	243	34665	2.4	16.6471	0.9	0.7032	2.7	0.0849	2.5	0.94	525.5	12.8	540.7	11.3	606.1	19.8	525.5	12.8

TABLE E2: U-TH-PB GEOCHRONOLOGIC ANALYSES

Analysis	U (ppm)	^{206}Pb ^{204}Pb	U/Th	$^{206}Pb^*$ $^{207}Pb^*$	± (%)	Isotope Ratios $^{207}Pb^*$ $^{235}U^*$	± (%)	$^{206}Pb^*$ ^{238}U	± (%)	Error Corr.	Apparent Ages (Ma) $^{206}Pb^*$ $^{238}U^*$	± (Ma)	$^{207}Pb^*$ ^{235}U	± (Ma)	$^{206}Pb^*$ $^{207}Pb^*$	± (Ma)	Best Age (Ma)	± (Ma)
Spot 47	219	174128	4.1	17.0839	1.2	0.6855	2.4	0.0850	2.1	0.86	525.7	10.4	530.1	9.9	549.8	26.7	525.7	10.4
Spot 105	516	131491	2.9	16.8954	1.0	0.6938	3.1	0.0850	2.9	0.94	526.2	14.7	535.1	12.8	574.0	22.6	526.2	14.7
Spot 82	144	37475	7.3	16.6494	1.1	0.7048	3.0	0.0851	2.8	0.93	526.8	14.1	541.7	12.5	605.8	23.2	526.8	14.1
Spot 46	209	22731	3.1	16.9586	0.9	0.6927	2.4	0.0852	2.2	0.92	527.3	11.2	534.4	10.0	565.9	20.6	527.3	11.2
Spot 77	485	229888	3.1	17.3478	1.0	0.6774	2.2	0.0853	1.9	0.88	527.5	9.7	525.2	8.9	516.2	22.9	527.5	9.7
Spot 48	315	39100	3.2	16.9114	1.0	0.6952	2.4	0.0853	2.1	0.90	527.7	10.7	535.9	9.8	572.0	22.6	527.7	10.7
Spot 63	438	23220	5.9	17.0908	0.9	0.6881	2.5	0.0853	2.3	0.94	527.9	11.7	531.7	10.2	549.0	18.7	527.9	11.7
Spot 106	626	50820	2.5	17.1976	0.9	0.6856	2.4	0.0855	2.3	0.93	529.1	11.6	530.1	10.1	535.3	19.4	529.1	11.6
Spot 32	269	59506	4.2	16.9191	0.9	0.6972	2.5	0.0856	2.4	0.93	529.4	12.1	537.1	10.6	570.9	20.1	529.4	12.1
Spot 23	213	30757	2.2	16.9134	1.1	0.7005	2.1	0.0860	1.8	0.86	531.6	9.4	539.1	8.9	571.7	23.6	531.6	9.4
Spot 68	319	33995	4.6	17.2203	1.2	0.6888	2.8	0.0861	2.5	0.90	532.2	12.7	532.1	11.4	532.5	25.8	532.2	12.7
Spot 98	399	7041	2.7	16.5479	1.4	0.7217	2.3	0.0866	1.8	0.79	535.7	9.3	551.6	9.7	619.0	29.8	535.7	9.3
Spot 28	247	28256	3.6	17.2539	1.0	0.6955	2.2	0.0871	1.9	0.89	538.2	10.0	536.1	9.1	528.2	22.0	538.2	10.0
Spot 71	207	30186	3.6	11.2163	1.0	3.0937	2.1	0.2518	1.9	0.89	1447.6	24.7	1431.1	16.4	1407.5	18.8	1407.5	18.8
Spot 69	78	18933	1.8	11.1099	0.9	3.1862	2.1	0.2568	2.0	0.91	1473.7	25.8	1453.8	16.6	1425.7	16.9	1425.7	16.9
Spot 103	917	77335	3.5	10.8886	1.0	3.0511	2.5	0.2411	2.3	0.92	1392.2	29.2	1420.5	19.5	1464.0	19.3	1464.0	19.3
Spot 92	401	56966	12.1	10.6874	0.9	3.4008	2.4	0.2637	2.2	0.93	1508.8	30.1	1504.6	18.8	1499.4	16.3	1499.4	16.3
Spot 20	147	46396	3.1	10.2881	1.0	3.7545	2.6	0.2803	2.4	0.93	1592.7	33.5	1583.1	20.5	1571.0	17.9	1571.0	17.9
Spot 8	161	59182	4.6	9.8112	0.7	4.0321	2.2	0.2870	2.0	0.94	1626.7	29.2	1640.7	17.5	1659.4	13.3	1659.4	13.3
Spot 50	77	51079	3.6	9.7967	0.8	4.0695	2.7	0.2893	2.5	0.96	1637.9	36.7	1648.2	21.7	1662.2	14.5	1662.2	14.5

TABLE E2: U-TH-PB GEOCHRONOLOGIC ANALYSES

						Isotope Ratios					Apparent Ages (Ma)							
Analysis	U (ppm)	^{206}Pb ^{204}Pb	U/Th	$^{206}Pb^*$ $^{207}Pb^*$	± (%)	$^{207}Pb^*$ $^{235}U^*$	± (%)	$^{206}Pb^*$ ^{238}U	± (%)	Error Corr.	$^{206}Pb^*$ $^{238}U^*$	± (Ma)	$^{207}Pb^*$ ^{235}U	± (Ma)	$^{206}Pb^*$ $^{207}Pb^*$	± (Ma)	**Best Age** (Ma)	± (Ma)
Spot 72	288	481034	2.4	9.7741	0.8	4.0735	2.0	0.2889	1.8	0.91	1636.0	26.4	1649.0	16.3	1666.4	15.1	1666.4	15.1
Spot 26	79	31573	1.8	9.7593	1.1	4.1896	2.5	0.2967	2.2	0.90	1674.8	32.9	1672.0	20.3	1669.3	19.8	1669.3	19.8
Spot 31	70	14029	123.7	9.7454	1.0	4.1766	2.4	0.2953	2.2	0.91	1668.1	32.3	1669.4	19.8	1671.9	18.6	1671.9	18.6
Spot 88	206	159229	2.9	9.7449	1.1	4.0738	3.0	0.2880	2.7	0.93	1631.8	39.4	1649.1	24.1	1672.0	20.7	1672.0	20.7
Spot 2	227	57710	4.2	9.6924	1.0	4.3009	2.4	0.3025	2.2	0.91	1703.5	32.3	1693.5	19.5	1682.0	18.1	1682.0	18.1
Spot 40	112	34613	3.3	9.6917	0.7	4.2563	2.6	0.2993	2.5	0.96	1687.9	36.7	1685.0	21.2	1682.1	13.2	1682.1	13.2
Spot 75	216	125557	2.1	9.6839	0.9	4.4222	2.4	0.3107	2.2	0.92	1744.3	33.4	1716.5	19.6	1683.6	16.7	1683.6	16.7
Spot 59	61	24048	2.7	9.6598	1.2	4.2121	3.3	0.2952	3.0	0.93	1667.6	44.2	1676.4	26.7	1688.2	22.7	1688.2	22.7
Spot 64	23	7455	4.0	9.6597	1.3	4.3153	2.5	0.3025	2.2	0.86	1703.5	32.4	1696.3	20.7	1688.2	23.3	1688.2	23.3
Spot 87	153	85144	3.5	9.6212	0.9	4.2002	3.1	0.2932	2.9	0.95	1657.6	43.1	1674.1	25.4	1695.6	17.3	1695.6	17.3
Spot 52	86	37616	5.9	9.6126	0.9	4.2869	2.6	0.2990	2.4	0.93	1686.3	35.6	1690.8	21.2	1697.2	17.1	1697.2	17.1
Spot 110	242	95130	2.6	9.6096	0.8	4.3086	2.4	0.3004	2.3	0.94	1693.4	33.6	1695.0	19.7	1697.8	14.8	1697.8	14.8
Spot 1	372	109886	3.4	9.5754	0.9	4.4337	2.9	0.3080	2.7	0.95	1731.1	41.6	1718.7	23.8	1704.4	16.2	1704.4	16.2
Spot 79	25	8095	2.5	9.5291	1.4	4.2169	3.2	0.2916	2.8	0.89	1649.3	41.0	1677.3	25.9	1713.3	25.9	1713.3	25.9
Spot 6	349	61634	4.7	9.5207	0.8	4.3675	2.3	0.3017	2.2	0.93	1699.8	32.6	1706.2	19.3	1714.9	15.5	1714.9	15.5
Spot 19	899	25919	12.0	9.5081	0.9	4.2222	2.3	0.2913	2.1	0.92	1647.9	30.3	1678.3	18.6	1717.3	16.1	1717.3	16.1
Spot 14	142	122158	2.5	9.4920	1.0	4.3194	2.4	0.2975	2.2	0.92	1678.8	32.9	1697.1	20.0	1720.5	17.9	1720.5	17.9
Spot 53	279	177279	4.1	9.4886	0.8	4.4085	2.5	0.3035	2.3	0.95	1708.7	35.2	1713.9	20.6	1721.1	14.9	1721.1	14.9
Spot 30	760	180627	3.6	9.4310	0.8	4.3810	2.6	0.2998	2.5	0.95	1690.3	36.4	1708.8	21.3	1732.3	14.5	1732.3	14.5
Spot 93	307	38791	3.0	9.4287	0.7	4.4909	2.5	0.3072	2.4	0.96	1727.1	37.0	1729.3	21.1	1732.7	13.0	1732.7	13.0
Spot 80	151	51540	4.4	9.4251	0.9	4.2857	2.9	0.2931	2.8	0.95	1656.9	40.2	1690.6	23.8	1733.4	15.9	1733.4	15.9
Spot 100	659	819802	3.1	9.4132	0.9	4.4187	2.3	0.3018	2.1	0.92	1700.2	32.0	1715.9	19.3	1735.8	17.0	1735.8	17.0
Spot 33	305	63258	3.3	9.4037	0.9	4.4000	2.6	0.3002	2.5	0.94	1692.4	37.0	1712.3	21.9	1737.6	16.7	1737.6	16.7
Spot 4	177	30319	4.8	9.3911	0.9	3.7321	2.4	0.2543	2.2	0.93	1460.7	28.6	1578.3	18.8	1740.1	15.8	1740.1	15.8

TABLE E2: U-TH-PB GEOCHRONOLOGIC ANALYSES

Analysis	U (ppm)	$^{206}Pb/^{204}Pb$	U/Th	$^{206}Pb^*/^{207}Pb^*$	± (%)	Isotope Ratios $^{207}Pb^*/^{235}U^*$	± (%)	$^{206}Pb^*/^{238}U$	± (%)	Error Corr.	Apparent Ages (Ma) $^{206}Pb^*/^{238}U^*$	± (Ma)	$^{207}Pb^*/^{235}U$	± (Ma)	$^{206}Pb^*/^{207}Pb^*$	± (Ma)	Best Age (Ma)	± (Ma)
Spot 39	324	56143	3.6	9.3739	0.9	4.5733	2.6	0.3111	2.4	0.94	1745.9	36.9	1744.4	21.4	1743.4	16.1	1743.4	16.1
Spot 81	23	19308	2.5	9.3371	1.1	4.2550	2.8	0.2883	2.6	0.92	1632.9	37.8	1684.7	23.4	1750.6	20.1	1750.6	20.1
Spot 35	119	7373	2.9	8.8846	1.5	4.6332	2.7	0.2987	2.3	0.83	1684.8	33.7	1755.3	22.8	1841.0	27.3	1841.0	27.3
MCH																		
MCH-47	630	7367	1.7	21.7229	11.1	0.0286	11.3	0.0045	2.3	0.20	29.0	0.7	28.6	3.2	-0.6	267.6	29.0	0.7
MCH-36	246	2289	1.6	25.4811	21.9	0.0289	22.1	0.0053	3.2	0.15	34.3	1.1	28.9	6.3	-400.4	575.6	34.3	1.1
MCH-65	757	7606	1.3	20.4646	16.2	0.0363	16.2	0.0054	1.2	0.08	34.6	0.4	36.2	5.8	141.3	381.6	34.6	0.4
MCH-60	184	2889	0.7	32.9245	91.5	0.0226	91.7	0.0054	6.1	0.07	34.6	2.1	22.6	20.5	-1121.1	1873.3	34.6	2.1
MCH-37	2032	18536	1.1	21.9006	5.2	0.0341	5.2	0.0054	0.8	0.15	34.8	0.3	34.0	1.7	-20.2	124.8	34.8	0.3
MCH-04	172	1198	0.5	22.7585	38.4	0.0328	39.2	0.0054	8.2	0.21	34.8	2.8	32.8	12.7	-114.1	977.1	34.8	2.8
MCH-76	212	3651	0.5	12.6531	115.2	0.0595	115.3	0.0055	4.9	0.04	35.1	1.7	58.7	65.9	1173.0	288.5	35.1	1.7
MCH-54	496	5788	1.3	24.1390	16.6	0.0312	16.9	0.0055	2.8	0.17	35.1	1.0	31.2	5.2	-261.2	424.0	35.1	1.0
MCH-63	299	3456	0.7	22.0622	19.2	0.0342	19.5	0.0055	3.6	0.19	35.2	1.3	34.1	6.5	-38.1	469.0	35.2	1.3
MCH-33	174	5113	0.8	-4.0066	863.7	~~-0.1890~~	~~863.7~~	~~0.0055~~	~~6.8~~	~~0.01~~	35.3	2.4	-212.7	#NUM!	NA	NA	35.3	2.4
MCH-34	815	11305	0.9	19.4389	8.6	0.0390	8.9	0.0055	2.2	0.25	35.3	0.8	38.8	3.4	260.8	198.4	35.3	0.8
MCH-25	561	4236	1.6	22.9606	13.5	0.0331	13.7	0.0055	2.0	0.14	35.4	0.7	33.0	4.4	-135.9	336.5	35.4	0.7
MCH-14	801	8062	2.3	19.4339	16.3	0.0391	16.4	0.0055	1.6	0.10	35.4	0.6	38.9	6.3	261.3	377.0	35.4	0.6
MCH-01	400	2317	1.2	22.4036	18.8	0.0339	19.0	0.0055	2.5	0.13	35.4	0.9	33.9	6.3	-75.5	463.9	35.4	0.9
MCH-26	283	1309	0.9	29.8101	22.9	0.0255	23.6	0.0055	5.5	0.23	35.4	1.9	25.6	5.9	-828.2	661.0	35.4	1.9
MCH-20	394	5133	2.1	23.7957	15.6	0.0320	15.8	0.0055	2.2	0.14	35.5	0.8	31.9	5.0	-225.1	395.9	35.5	0.8

TABLE E2: U-TH-PB GEOCHRONOLOGIC ANALYSES

						Isotope Ratios					Apparent Ages (Ma)						Best Age	±
Analysis	U (ppm)	^{206}Pb / ^{204}Pb	U/Th	$^{206}Pb^*$ / $^{207}Pb^*$	± (%)	$^{207}Pb^*$ / $^{235}U^*$	± (%)	$^{206}Pb^*$ / ^{238}U	± (%)	Error Corr.	$^{206}Pb^*$ / $^{238}U^*$	± (Ma)	$^{207}Pb^*$ / ^{235}U	± (Ma)	$^{206}Pb^*$ / $^{207}Pb^*$	± (Ma)	(Ma)	(Ma)
MCH-40	425	2389	1.6	19.5341	24.3	0.0389	24.4	0.0055	2.1	0.09	35.5	0.8	38.8	9.3	249.5	566.4	35.5	0.8
MCH-52	1053	9156	1.1	21.2793	4.7	0.0358	4.8	0.0055	1.0	0.21	35.5	0.4	35.7	1.7	48.9	111.6	35.5	0.4
MCH-68	105	1314	0.8	19.2102	200.1	0.0397	200.3	0.0055	7.6	0.04	35.5	2.7	39.5	77.8	287.9	0.0	35.5	2.7
MCH-22	227	2753	1.2	24.4327	29.2	0.0312	29.3	0.0055	2.5	0.08	35.6	0.9	31.2	9.0	-292.0	758.5	35.6	0.9
MCH-31	462	6280	0.9	20.8775	14.8	0.0366	15.1	0.0055	3.2	0.21	35.6	1.1	36.5	5.4	94.3	351.9	35.6	1.1
MCH-07	780	6095	1.5	22.5997	10.6	0.0338	10.9	0.0055	2.5	0.23	35.6	0.9	33.8	3.6	-96.8	261.5	35.6	0.9
MCH-77	404	9621	1.0	24.7662	30.0	0.0309	30.1	0.0056	1.5	0.05	35.7	0.5	30.9	9.2	-326.7	786.0	35.7	0.5
MCH-78	902	7837	1.6	22.0677	8.8	0.0348	9.0	0.0056	1.7	0.19	35.8	0.6	34.7	3.1	-38.7	215.1	35.8	0.6
MCH-70	542	7640	2.2	23.2280	21.5	0.0330	21.6	0.0056	2.2	0.10	35.8	0.8	33.0	7.0	-164.6	539.9	35.8	0.8
MCH-03	172	2191	1.1	24.5114	70.7	0.0314	70.7	0.0056	3.3	0.05	35.8	1.2	31.4	21.8	-300.2	2067.8	35.8	1.2
MCH-09	516	5041	3.2	22.4515	10.8	0.0343	11.3	0.0056	3.2	0.29	35.9	1.2	34.3	3.8	-80.7	266.2	35.9	1.2
MCH-45	263	2797	1.3	20.6113	15.5	0.0374	15.9	0.0056	3.8	0.24	36.0	1.4	37.3	5.8	124.5	366.1	36.0	1.4
MCH-56	170	2252	0.8	27.9595	52.9	0.0277	53.2	0.0056	5.2	0.10	36.1	1.9	27.7	14.5	-648.8	1547.3	36.1	1.9
MCH-16	379	5628	1.6	20.5278	13.1	0.0378	13.3	0.0056	2.2	0.16	36.2	0.8	37.7	4.9	134.1	310.0	36.2	0.8
MCH-50	1020	5510	2.0	20.2671	13.5	0.0384	13.6	0.0056	1.3	0.09	36.3	0.5	38.3	5.1	164.0	317.3	36.3	0.5
MCH-61	686	13499	1.4	18.4719	5.2	0.0423	6.0	0.0057	2.9	0.49	36.4	1.1	42.0	2.5	376.7	117.7	36.4	1.1
MCH-43	301	5224	1.4	24.2950	19.7	0.0323	20.3	0.0057	4.9	0.24	36.5	1.8	32.2	6.5	-277.6	506.3	36.5	1.8
MCH-42	642	7386	1.3	21.0824	8.2	0.0372	8.3	0.0057	0.7	0.08	36.6	0.2	37.1	3.0	71.1	195.9	36.6	0.2
MCH-11	154	2192	0.8	24.4595	55.6	0.0325	55.7	0.0058	3.8	0.07	37.1	1.4	32.5	17.8	-294.8	1527.2	37.1	1.4

TABLE E2: U-TH-PB GEOCHRONOLOGIC ANALYSES

						Isotope Ratios					Apparent Ages (Ma)						Best Age	
Analysis	U (ppm)	^{206}Pb / ^{204}Pb	U/Th	$^{206}Pb^*$ / $^{207}Pb^*$	± (%)	$^{207}Pb^*$ / $^{235}U^*$	± (%)	$^{206}Pb^*$ / ^{238}U	± (%)	Error Corr.	$^{206}Pb^*$ / $^{238}U^*$	± (Ma)	$^{207}Pb^*$ / ^{235}U	± (Ma)	$^{206}Pb^*$ / $^{207}Pb^*$	± (Ma)	(Ma)	± (Ma)
MCH-19	196	3088	0.9	27.3170	64.0	0.0291	64.4	0.0058	7.0	0.11	37.1	2.6	29.2	18.5	-585.3	1916.8	37.1	2.6
MCH-57	182	2480	0.9	21.8199	36.1	0.0366	36.7	0.0058	6.6	0.18	37.2	2.4	36.5	13.1	-11.3	897.6	37.2	2.4
MCH-44	89	1318	1.0	9.9948	124.4	0.0799	124.6	0.0058	6.0	0.05	37.2	2.2	78.0	93.8	1625.0	39.1	37.2	2.2
MCH-58	163	2463	0.8	18.6379	28.8	0.0430	29.2	0.0058	4.7	0.16	37.3	1.8	42.7	12.2	356.5	662.4	37.3	1.8
MCH-73	115	1839	0.9	12.5793	39.5	0.0638	39.9	0.0058	6.0	0.15	37.4	2.2	62.8	24.3	1184.5	812.2	37.4	2.2
MCH-02	506	1567	1.0	16.4865	8.8	0.0492	9.1	0.0059	2.1	0.23	37.8	0.8	48.7	4.3	627.0	191.1	37.8	0.8
MCH-15	240	4448	0.7	23.8133	22.1	0.0343	22.3	0.0059	2.8	0.13	38.1	1.1	34.3	7.5	-226.9	563.2	38.1	1.1
MCH-69	166	1834	1.0	19.3648	67.6	0.0422	67.9	0.0059	5.8	0.08	38.1	2.2	42.0	27.9	269.5	1764.4	38.1	2.2
MCH-46	1435	18206	2.3	21.4597	4.2	0.0383	4.5	0.0060	1.5	0.34	38.3	0.6	38.1	1.7	28.7	100.4	38.3	0.6
MCH-32	189	2840	1.5	8.7301	12.8	0.0982	14.1	0.0062	6.0	0.43	40.0	2.4	95.1	12.8	1872.7	231.2	40.0	2.4
MCH-23	413	1996	0.7	11.5448	33.9	0.0764	34.3	0.0064	5.6	0.16	41.1	2.3	74.8	24.8	1352.0	673.7	41.1	2.3
MCH-13	196	5010	0.6	23.9993	18.6	0.0575	18.8	0.0100	3.1	0.16	64.2	2.0	56.8	10.4	-246.6	473.0	64.2	2.0
MCH-06	105	1427	0.8	27.8203	24.9	0.0518	25.3	0.0104	4.7	0.18	67.0	3.1	51.3	12.7	-635.1	690.4	67.0	3.1
MCH-08	75	1116	0.9	34.2602	76.4	0.0430	76.5	0.0107	5.0	0.07	68.6	3.4	42.8	32.1	-1244.0	1003.6	68.6	3.4
MCH-38	65	23572	0.9	18.0040	8.2	0.6385	8.6	0.0834	2.5	0.30	516.3	12.6	501.4	34.1	434.1	183.4	516.3	12.6
MCH-79	244	74692	2.3	17.3806	1.5	0.6636	1.9	0.0837	1.3	0.65	517.9	6.3	516.8	7.9	512.1	32.5	517.9	6.3
MCH-05	206	83046	1.9	11.0314	0.5	3.1282	0.9	0.2503	0.7	0.82	1439.9	9.5	1439.7	6.9	1439.2	9.8	1439.2	9.8
MCH-62	141	87746	3.8	11.0128	0.6	3.2850	1.9	0.2624	1.8	0.95	1502.0	24.2	1477.5	14.7	1442.5	11.0	1442.5	11.0
MCH-72	66	54365	1.5	9.6696	1.1	4.3847	1.7	0.3075	1.4	0.79	1728.4	20.5	1709.5	14.2	1686.3	19.4	1686.3	19.4
MCH-27	59	66812	1.6	9.6263	1.2	4.3416	2.0	0.3031	1.6	0.80	1706.7	23.8	1701.3	16.4	1694.6	21.8	1694.6	21.8

TABLE E2: U-TH-PB GEOCHRONOLOGIC ANALYSES

Analysis	U (ppm)	^{206}Pb ^{204}Pb	U/Th	$^{206}Pb^*$ $^{207}Pb^*$	± (%)	Isotope Ratios $^{207}Pb^*$ $^{235}U^*$	± (%)	$^{206}Pb^*$ ^{238}U	± (%)	Error Corr.	Apparent Ages (Ma) $^{206}Pb^*$ $^{238}U^*$	± (Ma)	$^{207}Pb^*$ ^{235}U	± (Ma)	$^{206}Pb^*$ $^{207}Pb^*$	± (Ma)	Best Age (Ma)	± (Ma)
MCH-18	219	124670	2.6	9.5642	0.4	4.4447	1.0	0.3083	0.9	0.93	1732.4	14.1	1720.7	8.2	1706.5	6.6	1706.5	6.6
MCH-74	397	344660	2.1	9.5587	0.1	4.3516	2.4	0.3017	2.4	1.00	1699.6	36.0	1703.2	19.9	1707.6	2.7	1707.6	2.7
MCH-24	152	73750	2.5	9.5459	0.5	4.4049	1.0	0.3050	0.8	0.88	1715.9	12.7	1713.3	8.0	1710.0	8.5	1710.0	8.5
MCH-12	139	84524	2.3	9.5454	0.4	4.5078	1.6	0.3121	1.5	0.96	1750.9	23.4	1732.4	13.2	1710.1	8.1	1710.1	8.1
MCH-10	105	47284	2.1	9.5452	0.5	4.3899	0.7	0.3039	0.5	0.67	1710.6	7.5	1710.4	6.1	1710.2	10.1	1710.2	10.1
MCH-64	672	390860	1.6	9.4925	0.3	4.3029	1.1	0.2962	1.0	0.97	1672.6	15.1	1693.9	8.7	1720.3	4.6	1720.3	4.6
MCH-75	201	186424	2.9	9.4774	0.5	4.4212	1.9	0.3039	1.9	0.96	1710.6	28.2	1716.3	16.1	1723.3	9.4	1723.3	9.4
MCH-49	204	115652	1.7	9.4720	0.4	4.5746	1.9	0.3143	1.9	0.98	1761.7	29.1	1744.7	16.0	1724.3	7.0	1724.3	7.0
MCH-21	153	104815	2.2	9.4667	0.6	4.4066	1.3	0.3025	1.2	0.89	1703.9	17.4	1713.6	10.7	1725.4	10.7	1725.4	10.7
MCH-53	112	86982	1.7	9.4540	0.6	4.5351	1.0	0.3110	0.7	0.77	1745.4	11.3	1737.4	8.0	1727.8	11.3	1727.8	11.3
MCH-39	374	184226	4.1	9.4377	0.5	4.5022	3.6	0.3082	3.5	0.99	1731.7	53.4	1731.4	29.6	1731.0	10.0	1731.0	10.0
MCH-17	303	279409	1.7	9.4309	0.8	4.3905	1.7	0.3003	1.5	0.87	1692.9	22.5	1710.6	14.3	1732.3	15.4	1732.3	15.4
MCH-59	186	98534	1.7	9.3811	0.4	4.0930	5.7	0.2785	5.7	1.00	1583.7	79.8	1652.9	46.5	1742.0	7.6	1742.0	7.6
MCH-35	340	231370	5.2	9.3794	0.4	4.4566	0.8	0.3032	0.7	0.86	1707.0	10.7	1722.9	6.9	1742.3	7.8	1742.3	7.8
MCH-55	233	248554	2.8	9.3767	0.2	4.5559	1.3	0.3098	1.3	0.99	1739.9	20.1	1741.2	11.1	1742.9	4.2	1742.9	4.2
MCH-71	110	102812	3.7	9.3534	0.4	4.5813	1.2	0.3108	1.1	0.93	1744.6	16.8	1745.9	9.8	1747.4	7.9	1747.4	7.9
MCH-48	280	100524	2.4	9.3348	0.7	4.6904	2.3	0.3175	2.2	0.96	1777.8	34.8	1765.5	19.6	1751.1	12.4	1751.1	12.4
MCH-66	120	56856	1.6	9.2896	0.9	4.7226	2.1	0.3182	1.9	0.91	1780.9	30.0	1771.3	17.8	1759.9	16.3	1759.9	16.3
MCH-67	186	112400	1.1	9.1409	1.5	4.4571	4.5	0.2955	4.3	0.94	1668.9	62.7	1723.0	37.6	1789.4	27.8	1789.4	27.8
MCH-41	145	90837	1.4	8.8716	1.1	5.1160	4.2	0.3292	4.0	0.97	1834.4	64.3	1838.8	35.4	1843.7	19.8	1843.7	19.8
MAR																		
Spot 30	246	6098	1.5	21.9639	3.4	0.0325	3.8	0.0052	1.7	0.45	33.3	0.6	32.4	1.2	NA	NA	33.3	0.6
Spot 78	1240	6647	2.7	22.0869	1.3	0.0327	1.6	0.0052	1.0	0.62	33.7	0.3	32.7	0.5	NA	NA	33.7	0.3

TABLE E2: U-TH-PB GEOCHRONOLOGIC ANALYSES

Analysis	U (ppm)	^{206}Pb ^{204}Pb	U/Th	$^{206}Pb^*$ $^{207}Pb^*$	± (%)	Isotope Ratios $^{207}Pb^*$ $^{235}U^*$	± (%)	$^{206}Pb^*$ ^{238}U	± (%)	Error Corr.	Apparent Ages (Ma) $^{206}Pb^*$ $^{238}U^*$	± (Ma)	$^{207}Pb^*$ ^{235}U	± (Ma)	$^{206}Pb^*$ $^{207}Pb^*$	± (Ma)	Best Age (Ma)	± (Ma)
Spot 32	240	4915	1.5	21.8132	2.3	0.0339	2.6	0.0054	1.1	0.45	34.5	0.4	33.8	0.9	NA	NA	34.5	0.4
Spot 18	243	4990	1.2	21.6917	3.7	0.0347	3.9	0.0055	1.4	0.35	35.2	0.5	34.7	1.3	2.9	88.1	35.2	0.5
Spot 54	523	5408	1.8	22.0379	1.7	0.0344	2.3	0.0055	1.5	0.66	35.4	0.5	34.4	0.8	NA	NA	35.4	0.5
Spot 26	169	2915	1.1	21.8682	2.5	0.0351	3.5	0.0056	2.6	0.72	35.8	0.9	35.0	1.2	NA	NA	35.8	0.9
Spot 89	193	1297	1.6	22.0101	3.7	0.0352	4.1	0.0056	1.6	0.40	36.2	0.6	35.2	1.4	NA	NA	36.2	0.6
Spot 27	369	3721	1.2	11.3095	6.1	0.0714	6.2	0.0059	1.3	0.21	37.6	0.5	70.0	4.2	1391.6	117.1	37.6	0.5
Spot 109	111	8870	1.7	21.3200	2.9	0.0382	3.4	0.0059	1.8	0.52	38.0	0.7	38.1	1.3	44.4	69.8	38.0	0.7
Spot 88	127	9043	1.0	21.6488	2.5	0.0381	3.0	0.0060	1.6	0.52	38.5	0.6	38.0	1.1	7.7	61.3	38.5	0.6
Spot 8	255	3149	1.8	10.7596	8.4	0.0769	8.6	0.0060	2.1	0.24	38.6	0.8	75.2	6.3	1486.6	158.9	38.6	0.8
Spot 38	272	697	0.9	2.9947	50.0	0.3987	50.3	0.0087	5.6	0.11	55.6	3.1	340.7	146.7	3635.2	NA	55.6	3.1
Spot 83	187	49753	3.2	13.2501	0.7	1.9028	1.1	0.1829	0.8	0.72	1083.0	7.6	1082.1	7.1	1081.1	15.0	1081.1	15.0
Spot 105	478	363722	5.7	11.2001	0.7	3.0331	1.4	0.2465	1.1	0.85	1420.3	14.6	1416.0	10.4	1410.3	13.8	1410.3	13.8
Spot 103	577	2473551	25.9	11.1748	0.5	3.0246	0.9	0.2452	0.7	0.82	1413.9	9.2	1413.8	6.8	1414.6	9.9	1414.6	9.9
Spot 102	211	96737	4.2	11.1696	0.8	3.0751	1.4	0.2492	1.2	0.84	1434.4	15.4	1426.5	11.0	1415.5	15.1	1415.5	15.1
Spot 81	73	651742	2.5	11.0749	0.9	3.0858	2.4	0.2480	2.2	0.93	1428.0	27.9	1429.2	18.0	1431.7	16.9	1431.7	16.9
Spot 4	293	74125	2.9	11.0643	0.7	2.9027	1.2	0.2330	1.0	0.83	1350.4	12.4	1382.6	9.2	1433.6	12.9	1433.6	12.9
Spot 87	69	37886	1.6	11.0602	0.8	3.1789	1.3	0.2551	1.0	0.78	1464.8	13.4	1452.0	10.1	1434.3	15.6	1434.3	15.6
Spot 86	228	62449	8.1	11.0560	0.7	3.1520	2.5	0.2529	2.4	0.96	1453.2	31.0	1445.5	19.2	1435.0	14.0	1435.0	14.0
Spot 45	77	64072	1.8	11.0105	0.8	3.1218	1.3	0.2494	1.0	0.79	1435.4	12.8	1438.1	9.7	1442.9	14.8	1442.9	14.8
Spot 82	61	99882	2.0	11.006	0.7	3.1420	1.2	0.2509	1.0	0.80	1443.3	12.8	1443.0	9.5	1443.5	14.1	1443.5	14.1

TABLE E2: U-TH-PB GEOCHRONOLOGIC ANALYSES

Analysis	U (ppm)	^{206}Pb ^{204}Pb	U/Th	$^{206}Pb^*$ $^{207}Pb^*$	± (%)	Isotope Ratios $^{207}Pb^*$ $^{235}U^*$	± (%)	$^{206}Pb^*$ ^{238}U	± (%)	Error Corr.	Apparent Ages (Ma) $^{206}Pb^*$ $^{238}U^*$	± (Ma)	$^{207}Pb^*$ ^{235}U	± (Ma)	$^{206}Pb^*$ $^{207}Pb^*$	± (Ma)	Best Age (Ma)	± (Ma)
Spot 48	151	119821	2.2	10.9623	0.8	3.1322	1.5	0.2491	1.2	0.85	1434.0	15.9	1440.6	11.2	1451.2	14.8	1451.2	14.8
Spot 13	139	44941	1.5	10.7895	0.5	3.3036	1.1	0.2586	0.9	0.86	1482.8	12.2	1481.9	8.3	1481.4	10.4	1481.4	10.4
Spot 39	194	47091	0.7	10.6084	0.7	3.1486	1.2	0.2424	1.0	0.80	1398.9	12.2	1444.7	9.3	1513.4	13.5	1513.4	13.5
Spot 91	249	91412	5.4	10.0513	0.7	3.8441	1.3	0.2804	1.1	0.86	1593.2	15.8	1602.0	10.4	1614.5	12.3	1614.5	12.3
Spot 80	345	89493	3.3	9.9171	0.6	3.8537	1.1	0.2773	1.0	0.87	1577.7	13.5	1604.0	9.0	1639.5	10.2	1639.5	10.2
Spot 71	371	119705	2.5	9.8244	0.6	4.1085	1.2	0.2929	1.0	0.86	1655.9	14.8	1656.0	9.7	1656.9	11.4	1656.9	11.4
Spot 36	122	600797	1.4	9.8089	1.2	4.1915	1.9	0.2983	1.5	0.80	1683.0	23.0	1672.4	15.8	1659.9	21.3	1659.9	21.3
Spot 7	247	116527	2.6	9.7636	0.8	4.1847	1.5	0.2965	1.3	0.87	1673.7	19.7	1671.0	12.7	1668.4	14.3	1668.4	14.3
Spot 41	269	371544	6.0	9.7585	0.7	3.9151	1.4	0.2772	1.3	0.88	1577.3	17.7	1616.8	11.7	1669.4	12.7	1669.4	12.7
Spot 67	172	78449	4.8	9.7382	0.8	4.0101	1.4	0.2833	1.1	0.80	1608.2	16.2	1636.2	11.6	1673.3	15.7	1673.3	15.7
Spot 97	115	77694	3.6	9.7304	0.7	4.4257	1.1	0.3125	0.9	0.79	1752.8	13.4	1717.2	9.2	1674.7	12.5	1674.7	12.5
Spot 75	467	211034	3.4	9.7268	0.9	4.2980	1.5	0.3033	1.3	0.83	1707.8	19.0	1693.0	12.6	1675.4	15.9	1675.4	15.9
Spot 74	171	68570	2.3	9.7153	0.7	4.0203	1.9	0.2834	1.8	0.93	1608.5	25.7	1638.3	15.8	1677.6	13.3	1677.6	13.3
Spot 107	280	731654	5.3	9.7080	0.7	4.2753	1.2	0.3012	1.0	0.80	1697.0	14.5	1688.6	10.0	1679.0	13.5	1679.0	13.5
Spot 70	344	110978	3.6	9.6922	0.7	4.2725	1.2	0.3005	1.0	0.79	1693.6	14.2	1688.1	9.9	1682.0	13.4	1682.0	13.4
Spot 77	68	34362	2.7	9.6897	0.6	4.4285	1.2	0.3114	1.1	0.87	1747.4	16.5	1717.7	10.3	1682.5	11.5	1682.5	11.5
Spot 93	465	53918	6.3	9.6494	0.8	3.8852	1.4	0.2720	1.2	0.84	1551.1	16.7	1610.6	11.7	1690.2	14.5	1690.2	14.5
Spot 3	121	90615	3.3	9.6491	0.7	4.3019	1.3	0.3012	1.2	0.86	1697.2	17.2	1693.7	11.1	1690.2	12.8	1690.2	12.8
Spot 68	259	107584	4.9	9.6308	0.9	4.0410	1.7	0.2824	1.4	0.84	1603.4	20.2	1642.5	13.8	1693.7	16.9	1693.7	16.9
Spot 49	392	270775	8.1	9.6263	0.7	3.9446	1.6	0.2755	1.4	0.91	1568.8	19.8	1622.9	12.7	1694.6	12.3	1694.6	12.3
Spot 94	142	91456	3.7	9.6237	0.8	4.3602	1.4	0.3045	1.1	0.80	1713.4	16.7	1704.8	11.5	1695.1	15.6	1695.1	15.6
Spot 40	740	81100	1.8	9.6197	0.7	4.2813	1.1	0.2988	0.9	0.81	1685.5	13.2	1689.8	9.1	1695.9	12.0	1695.9	12.0

TABLE E2: U-TH-PB GEOCHRONOLOGIC ANALYSES

Analysis	U (ppm)	^{206}Pb ^{204}Pb	U/Th	$^{206}Pb^*$ $^{207}Pb^*$	± (%)	Isotope Ratios $^{207}Pb^*$ $^{235}U^*$	± (%)	$^{206}Pb^*$ ^{238}U	± (%)	Error Corr.	Apparent Ages (Ma) $^{206}Pb^*$ $^{238}U^*$	± (Ma)	$^{207}Pb^*$ ^{235}U	± (Ma)	$^{206}Pb^*$ $^{207}Pb^*$	± (Ma)	Best Age (Ma)	± (Ma)
Spot 69	113	108688	3.3	9.6196	0.6	4.4000	1.3	0.3071	1.1	0.89	1726.5	17.4	1712.3	10.6	1695.9	10.6	1695.9	10.6
Spot 110	192	146343	2.0	9.6190	0.8	4.3372	1.1	0.3027	0.8	0.73	1704.7	12.2	1700.5	9.1	1696.0	13.9	1696.0	13.9
Spot 6	159	400363	2.4	9.6099	0.7	3.9453	1.4	0.2751	1.1	0.84	1566.6	15.9	1623.0	11.0	1697.7	13.6	1697.7	13.6
Spot 98	338	338460	3.1	9.6096	0.7	4.3368	1.3	0.3024	1.1	0.84	1703.1	16.3	1700.4	10.6	1697.8	12.8	1697.8	12.8
Spot 59	593	67102	10.8	9.6012	0.8	3.5222	1.6	0.2454	1.4	0.86	1414.6	18.0	1532.2	13.0	1699.4	15.4	1699.4	15.4
Spot 65	234	168761	2.5	9.5855	0.7	4.1914	1.8	0.2915	1.7	0.93	1649.1	24.2	1672.3	14.7	1702.4	12.5	1702.4	12.5
Spot 96	252	76223	6.1	9.5813	0.8	4.1922	1.7	0.2914	1.5	0.89	1648.7	22.2	1672.5	14.0	1703.2	14.1	1703.2	14.1
Spot 33	91	27455	2.2	9.5783	0.8	4.3302	1.4	0.3009	1.2	0.83	1696.0	17.4	1699.1	11.6	1703.8	14.6	1703.8	14.6
Spot 23	168	185531	2.0	9.5758	0.8	4.2895	1.3	0.2980	1.0	0.75	1681.6	14.3	1691.3	10.5	1704.3	15.5	1704.3	15.5
Spot 104	115	142143	2.7	9.5742	0.7	4.4093	1.2	0.3063	1.0	0.82	1722.5	14.8	1714.1	9.8	1704.6	12.3	1704.6	12.3
Spot 17	198	96535	1.9	9.5718	0.8	4.3745	1.2	0.3038	1.0	0.78	1710.2	14.5	1707.5	10.2	1705.0	14.2	1705.0	14.2
Spot 22	270	127594	5.1	9.5716	0.7	4.1731	1.2	0.2898	1.0	0.84	1640.6	14.9	1668.8	10.1	1705.1	12.4	1705.1	12.4
Spot 90	534	232637	2.8	9.5703	0.6	4.4658	1.0	0.3101	0.9	0.83	1741.3	13.0	1724.6	8.6	1705.3	10.8	1705.3	10.8
Spot 76	259	910417	5.4	9.5564	0.7	4.0075	1.5	0.2779	1.3	0.87	1580.7	18.1	1635.7	12.0	1708.0	13.3	1708.0	13.3
Spot 100	406	177228	4.2	9.5554	0.7	4.1462	1.2	0.2875	1.0	0.84	1628.9	14.8	1663.5	10.0	1708.2	12.3	1708.2	12.3
Spot 84	359	1029580	2.2	9.5331	0.7	4.4110	1.4	0.3051	1.2	0.86	1716.6	18.2	1714.4	11.6	1712.5	13.0	1712.5	13.0
Spot 52	152	39697	3.8	9.5294	0.6	4.2960	1.0	0.2970	0.8	0.81	1676.6	12.2	1692.6	8.4	1713.2	11.1	1713.2	11.1
Spot 12	196	68446	5.7	9.5229	0.8	4.3041	1.2	0.2974	1.0	0.79	1678.4	14.3	1694.2	10.1	1714.5	13.9	1714.5	13.9
Spot 101	487	1902135	5.0	9.5186	0.6	4.1504	1.3	0.2866	1.1	0.87	1624.8	16.3	1664.3	10.7	1715.3	11.8	1715.3	11.8
Spot 55	236	32381	6.1	9.5049	0.6	4.1214	1.2	0.2842	1.0	0.85	1612.7	14.7	1658.6	10.0	1717.9	11.9	1717.9	11.9
Spot 24	350	96598	4.3	9.5011	0.6	4.2905	1.0	0.2958	0.8	0.83	1670.4	12.3	1691.5	8.3	1718.7	10.2	1718.7	10.2
Spot 50	278	270541	3.8	9.4937	0.7	4.3148	1.2	0.2972	1.0	0.80	1677.5	14.3	1696.2	10.0	1720.1	13.2	1720.1	13.2
Spot 14	650	57211	10.5	9.4825	0.8	4.0392	1.6	0.2779	1.4	0.87	1580.8	19.0	1642.1	12.7	1722.3	14.2	1722.3	14.2
Spot 19	132	66906	5.4	9.4683	0.7	4.5773	1.2	0.3145	1.0	0.84	1762.6	15.4	1745.1	9.9	1725.0	12.0	1725.0	12.0

TABLE E2: U-TH-PB GEOCHRONOLOGIC ANALYSES

Analysis	U (ppm)	^{206}Pb ^{204}Pb	U/Th	$^{206}Pb^*$ $^{207}Pb^*$	± (%)	Isotope Ratios $^{207}Pb^*$ $^{235}U^*$	± (%)	$^{206}Pb^*$ ^{238}U	± (%)	Error Corr.	Apparent Ages (Ma) $^{206}Pb^*$ $^{238}U^*$	± (Ma)	$^{207}Pb^*$ ^{235}U	± (Ma)	$^{206}Pb^*$ $^{207}Pb^*$	± (Ma)	**Best Age** (Ma)	± (Ma)
Spot 72	225	156123	4.7	9.4657	1.0	4.2245	1.4	0.2901	1.0	0.72	1642.3	14.4	1678.8	11.4	1725.5	17.7	1725.5	17.7
Spot 53	144	95261	3.4	9.4590	0.8	4.4614	1.1	0.3062	0.8	0.70	1722.0	11.6	1723.8	9.1	1726.8	14.2	1726.8	14.2
Spot 47	116	25721	2.4	9.4587	0.7	4.4198	1.2	0.3033	1.0	0.80	1707.8	14.4	1716.1	9.9	1726.9	13.0	1726.9	13.0
Spot 46	554	46388	3.2	9.4335	0.7	4.1170	1.4	0.2818	1.2	0.85	1600.4	16.4	1657.7	11.2	1731.8	13.4	1731.8	13.4
Spot 9	740	31159	5.5	9.4171	0.8	3.8292	1.7	0.2616	1.5	0.89	1498.2	20.3	1598.9	13.8	1735.0	14.6	1735.0	14.6
Spot 57	90	57631	3.1	9.4156	0.8	4.4282	1.6	0.3025	1.4	0.86	1703.8	20.2	1717.6	13.0	1735.3	14.5	1735.3	14.5
Spot 31	86	134339	2.0	9.4146	0.9	4.3951	1.4	0.3002	1.1	0.79	1692.5	16.6	1711.4	11.7	1735.5	16.1	1735.5	16.1
Spot 42	76	25241	2.1	9.3932	0.9	4.6527	1.6	0.3171	1.3	0.84	1775.6	20.7	1758.8	13.3	1739.6	15.8	1739.6	15.8
Spot 10	391	199771	1.4	9.3744	0.7	4.2382	1.2	0.2883	1.0	0.83	1632.9	14.8	1681.5	10.1	1743.3	12.6	1743.3	12.6
Spot 95	220	404483	4.5	9.3715	0.8	4.6147	1.5	0.3138	1.3	0.85	1759.3	19.7	1751.9	12.6	1743.9	14.7	1743.9	14.7
Spot 28	286	108193	3.3	9.3272	0.6	3.6505	3.0	0.2471	2.9	0.98	1423.3	37.6	1560.6	24.0	1752.6	11.8	1752.6	11.8
Spot 20	646	39411	4.2	9.3094	0.7	3.6579	1.4	0.2471	1.2	0.86	1423.4	15.3	1562.2	11.2	1756.1	13.2	1756.1	13.2
Spot 21	188	37184	8.4	9.3055	0.8	3.7652	1.4	0.2542	1.2	0.85	1460.2	15.9	1585.4	11.5	1756.8	13.8	1756.8	13.8
Spot 5	303	258110	2.6	9.2992	0.6	4.3943	1.3	0.2965	1.1	0.86	1673.9	16.2	1711.3	10.6	1758.1	11.8	1758.1	11.8
Spot 37	149	92261	2.9	9.2893	0.7	4.3809	1.5	0.2953	1.2	0.86	1667.8	18.3	1708.7	12.0	1760.0	13.7	1760.0	13.7
Spot 61	48	5083	1.6	7.5808	1.0	6.0357	1.4	0.3320	1.0	0.71	1848.0	15.7	1981.0	12.0	2123.6	17.1	2123.6	17.1

REFERENCES

Brady, R., Wernicke, B.P., and Fryxell, J., 2000, Kinematic evolution of a large-offset continental normal fault system, South Virgin Mountains, Nevada: Geological Society of America Bulletin, v. 112, p. 1375–1397, doi:10.1130/0016-7606 (2000)112<1375:KEOALO>2.0.CO;2.

Bryant, B., and Naeser, C. W., 1980, The significance of fission-track ages of apatite in relation to the tectonic history of the Front and Sawatch Ranges, Colorado: Geological Society of America Bulletin, v. 91, p. 156–164.

Cunningham, C. G., Naeser, C. W., and Marvin, R. F., 1977, New ages for intrusive rocks in the Colorado mineral belt: U.S. Geological Survey Open-File Report 77-573, 7 p.

House, M.A., Kelley, S.A., Roy, M., 2003, Refining the footwall cooling history of a rift flank uplift, Rio Grande rift, New Mexico, Tectonics, v. 22, no. 5, 1060, doi:10.1029/2002TC001418.

Karlstrom, K.E., Crow, R., Crossey, L.J., Coblentz, D., and Van Wijk, J.W., 2008, Model for tectonically driven incision of the younger than 6 Ma Grand Canyon: Geology, v. 36, p. 835–838, doi:10.1130/G25032A.1.

Kelley, S. A., Chapin, C. E., and Corrigan, A. J., 1992, Late Mesozoic to Cenozoic Cooling Histories of the Flank of the Northern and Central Rio Grande Rift, Colorado and New Mexico: New Mexico Bureau of Mines Mineral Resources, v. 145, p. 1–40.

Kelley, S. A., and Chapin, C. E., 1997, Cooling histories of mountain ranges in the southern Rio Grande rift based on apatite fission-track analysis—a reconnaissance survey: New Mexico Bureau of Mines Mineral Resources, v. 19, n. 1, p. 1–14.

Kelley, S.A., Duncan, I.J., 1986, Late Cretaceous to Middle Tertiary tectonic history of the northern Rio Grande rift, New Mexico: Journal of Geophysical Research, v. 91, p. 6246–6262, doi:10.1029/JB091iB06p06246.

Klein, T.L., Evans, K.V., and DeWitt, E.H., 2010, Geochronology database for central Colorado: U.S. Geological Survey Data Series 489, 17 p.

Landman, R., and Flowers, R. M., 2013, (U-Th)/He thermochronologic constraints on the evolution of the northern Rio Grande Rift, Gore Range, Colorado, and implications for rift propagation models: Geosphere, v. 9, n. 1, p. 170–187.

Leonard, E. M., 2002, Geomorphic and tectonic forcing of late Cenozoic warping of the Colorado piedmont, Geology, v. 30, n. 7, p. 595–598.

McMillan, M.E., Heller, P.L., and Wing, S.L., 2006, History and causes of post-Laramide relief in the Rocky Mountain orogenic plateau: Geological Society of America Bulletin, v. 118, p. 393–405, doi:10.1130/B25712.1.

Naeser, C. W., Bryant, B., Kunk, M. J., Kellogg, K., Donelick, R. A., and Perry, W. J. Jr., 2002, Tertiary cooling and tectonic history of the White River uplift, Gore Range, and western Front Range, central Colorado: Evidence from fission-track and $^{39}Ar/^{40}Ar$ ages: Geological Society of America Special Papers, v. 366, p. 31–53.

Ricketts, J. W., Kelley, S. A., Karlstrom, K. E., Schmandt, B., Donahue, M. S., and van Wijk, J., 2016, Synchronous opening of the Rio Grande rift along its entire length at 25–10 Ma supported by apatite (U-Th)/He and fission-track thermochronology, and evaluation of possible driving mechanisms: Geological Society of America Bulletin, v. 128, n. 3-4, p. 397–424. doi.org/10.1130/B31223.1.

Thomson, S.N., Soreghan, G.S., Reiners, P.W., Peyton, S.L., and Murray, K.E., 2016, A definitive 6 Ma start date for carving of the northeastern Colorado Plateau Canyonlands: Geological Society of America Abstracts with Programs, v. 48, no. 7, doi:10.1130/abs/2016AM-287583.